Springer Geochemistry/Mineralogy

Faqin Dong *Editor*

Proceedings of the 11th International Congress for Applied Mineralogy (ICAM)

ICAM
International Council for Applied Mineralogy

Springer

Springer Geochemistry/Mineralogy

More information about this series at
http://www.springer.com/series/10171

Faqin Dong
Editor

Proceedings of the 11th International Congress for Applied Mineralogy (ICAM)

Springer

Editor
Faqin Dong
Key Laboratory of Solid Waste Treatment and
the Resource Recycle, Ministry of Education
Southwest University of Science & Technology
Mianyang City
Sichuan
China

ISSN 2194-3176 ISSN 2194-3184 (electronic)
Springer Geochemistry/Mineralogy
ISBN 978-3-319-13947-0 ISBN 978-3-319-13948-7 (eBook)
DOI 10.1007/978-3-319-13948-7

Library of Congress Control Number: 2015934693

Springer Cham Heidelberg New York Dordrecht London

Printed on acid-free paper

Springer International Publishing AG Switzerland is part of Springer Science+Business Media (www.springer.com)

Preface

These proceedings comprise the consolidated Full Paper contributions submitted to the 11th International Congress for Applied Mineralogy (ICAM), held at the Southwest University of Science and Technology (SWUST) in Mianyang, China, on 5–10 July 2013.

68 Proceedings were submitted to the 11th ICAM for a journal-style peer review. Of these 68 contributions, 60 have been finally accepted, 4 were rejected as outside of ICAM scope or being of insufficient quality, 2 were withdrawn by the authors, and 1 had been submitted too late. In all, 134 review assignments have been completed, of which 12 review invitations were initially declined and reassigned to another reviewer, and another 2 were terminated by the Editor-in-Chief. On average, 2.19 reviews were required per submission until final acceptance, varying from 1 to 3 per individual contribution. I am greatly indebted to the Publication Committee without whom the whole review process would have been infeasible.

The post-conference publication of the 11th ICAM consists of two parts, including these electronic proceedings in charge of Springer and the special issue published in *Mineralogy and Petrology*. Of 60 accepted contributions, 15 better-qualified papers were recommended to *Mineralogy and Petrology*, and 9 papers (*Appendix*) have been finally accepted after going through standard journal review processes.

These are fascinating times for research in applied mineralogy with multiple and diverse opportunities being offered by emerging analytical techniques and novel instrumentation to authenticate all-new insights or to critically reassess established verities. However, as scientists, we must remain aware of the interim character of the knowledge we have garnered: whereas some findings have stood "forever," others have turned obsolete before long. The letter should not make us sad: new ground has been broken, and new uncharted areas lay galore to be explored.

As proceedings are rich in content, involving a wide-ranging as well as huge editorial workload, coupled with time constraints, the collection, review, editing, and publishing must have been inadequate. We thank the author and reader for understanding and putting forward valuable opinions.

Enjoy the 11th ICAM Proceedings!

Mianyang, China Faqin Dong
July 2013

Contents

Microparagenetic Associations of Gold in Ore-Forming Minerals from Deposits of Different Geological and Industrial Types of Kazakhstan 1
Adilkhan Baibatsha, Kulyash Dyussembayeva, and Aimkhan Kassenova

Calcium Phosphate Mineralization of Bacteria 9
Anatoly T. Titov, Piter M. Larionov, and Vladimir I. Zaikovskii

Economical Potential of an Ultramafic Rock at the Kvaløya Island, North Norway 19
Anna Pryadunenko and Kåre Kullerud

Synthesis and Characterization of Mesoporous Carbon Using Attapulgite Template 29
Xi Cao and Xiuyun Chuan

Gold Characterization by MLA and Technological Tests: Discussion of Sample Preparation and Results 39
Carina Ulsen, Henrique Kahn, Guilherme Nery, Daniel Uliana, and Juliana L. Antoniassi

Analyzing the Characteristics and Available Attributes of Skarn Gold Deposit Tailings 51
Yunhong Cheng, Fei Huang, Guanglu Li, Qingyu Yang, Han Peng, and Rui Liu

Reciprocity Effect Between Silicate Bacterium and Wollastonite 59
Qunwei Dai, Faqin Dong, Yulian Zhao, Jianjun Deng, and Junda Lu

Process Mineralogy of Lateritic Nickel Ore 71
Daniel Uliana, M. Manuela M. Lé Tassinari, Henrique Kahn, and Marco Antonio Angora

The Optimal Conditions of Preparation of Phosphogypsum-Based Calcium Sulfate Hemihydrate Whiskers by Hydrothermal Method Using Phosphogypsum 81
Faqin Dong, Hua He, Ping He, Wei Yang, and Longhua Xu

Ore Mineral Textures of Late Cretaceous Volcanogenic Massive Sulfide Deposits of Turkey: Proposed Paragenetic Sequence 91
Emin Çiftçi, Abdurrahman Lermi, and Bülent Yalçınalp

Micronized Calcite Potential, Production, and Principal Characteristics of Nigde (Turkey) 99
Emin Çiftçi and İsmail Erdağ

Lime-Assisted Cyanide Leaching of Refractory Gold Ores from Ajialongwa Mine 107
Kaibin Fu, Shu Chen, Zhen Wang, Junhui Xiao, and Deqiang Luo

Growth Mechanism and Stability Study on the Fe_3S_4 Nanocrystals Synthesized Under Thermal and Humid Conditions 115
Shang Gao, Fei Huang, Dan Song, Guanglu Li, Qiang Liu, Taiwei Feng, Ran Zhao, Jia Liu, and Wenyuan Gao

Antarcticite: A Phase Change Material for Thermal Energy Storage—Experiments and Simulation 125
Xiaobin Gu, Jingjing Niu, and Shan Qin

Illite–Smectite Mixed-Layer Minerals in the Alteration Volcanic Ashes Under Submarine Environment 137
Hanlie Hong, Wenpeng Gao, Ke Yin, Zhaohui Li, and Chaowen Wang

The Occurrence of Sc, Co, and Ni in Lithiophorite-type Manganese Ore 151
Qiuyang Hong, Lili Zhang, and Bo Li

Cytotoxicity of Quartz and Montmorillonite in Human Lung Epithelial Cells (A549) 159
Tingting Huo, Faqin Dong, Mingcui Wang, Shiyong Sun, Jianjun Deng, Qingbi Zhang, and Siwang Yu

Assessment and Characterization of REE Minerals from an Alkali-Carbonatitic Complex 173
Juliana Lívi Antoniassi, Daniel Uliana, Henrique Kahn, M. Manuela M. Lé Tassinari, and Carina Ulsen

Study on Influencing Factors and Planning Model of Mining Quantity About Mineral Resources in Open Pit 187
Lihua Ke and Jie Chen

Effect of Temperature upon Fe–Mg Composition of Garnet in Pelitic System 197
Ying Li, Jianguo Du, Chao Xie, and Zhihua Zhou

An Overview of Process Mineralogy of Tungsten and Its Associated Elements 205
Dongyun Liang, Qiuyang Hong, Bo Li, and Lili Zhang

Light Absorption Characteristics of Multi-morphology FeS_2 Granular Synthesized Under Hydrothermal Conditions 213
Jia Liu, Fei Huang, Guanglu Li, Lin Meng, Haoran Yu, Yinghua Chen, Weifeng Wang, Shang Gao, and Wenyuan Gao

Bolshetagninskoe Deposit Microcline–Pyrochlore Ore Process Mineralogy 223
Liudmila Azarnova

The Roughness on Polished Gemstone Surfaces 233
Angela V. Nadur, Rainer A.S. Gütller, Sheila S. Carmo, and H. Kahn

Minerals of Bauxites and Residues: Problems of Processing and Enrichment (Russia) 241
Olga Kotova, Galina Gasaleeva, and Aleksandr Vakhrushev

Effects of Sintering Temperature on Crystallization Behavior and Performance of Glass Ceramics from Coal Fly Ash 253
Tongjiang Peng, Chao Cao, and Hongjuan Sun

The Oxidation–Reduction Mineralogical Features of Graphite Deposit in Pingdu, Shandong 263
Lang Qin and Xiuyun Chuan

Study on the Effect and Mechanism of Calcination of Asbestos Tailings Mixed with Ammonium Sulfate 275
Bei Song, Chao Liu, Shuilin Zheng, Tongtong Wang, and Jian Zhao

Heavy-Ion Radiation Stability of $Gd_2Zr_2O_7$-Pyrochlore Glass-Ceramic Wasteforms Doped by Simulated Actinides 283
Sijin Su, Faqin Dong, Xirui Lu, Jingyou Tang, and Xiaoli Wang

Veins, Dikes, and Pods of the UAE Mantle Peridotites: Possible Industrial Raw Materials 291
Sulaiman Alaabed

Dissolution Characteristic Study on Dustfall in Citric Acid 305
Jun Tang, Faqin Dong, Qunwei Dai, Yuequan Deng, Shiping Zhou, and Wu Chen

Graphite and Graphite-Like Materials from Black-Shale and Magmatic Ores: Raman Spectroscopy Data 313
Tatyana Moroz, Victor Ponomarchuk, Sergey Goryainov, Konstantin Kovalev, and Nadezhda Palchik

Analysis of Impurity Density in the Structure of Arsenopyrite of the Panimba Deposit 325
Victor V. Onufrienok and Maarten A.T.M. Broekmans

Research on Preparation and Influencing Factors of High Calcium High Sulfate Ash to Autoclaved Aerated Concrete 335
Jun Wan and Shaohui Jia

Preliminary Discussion on Comprehensive Utilization of Tailings 343
Fudong Wang, Xiaoqing Zhu, Zhonggang Wang, Tao Han, Zengsheng Li, Xiaohui Sun, and Kunyue Ling

Study on the Thermal Conductivity of Compacted Buffer/Backfill Materials 351
Maoli Wang, Facheng Yi, Zhe Wang, Zhongyan Wan, Chong Wang, and Jianwei Wang

Study on Performances of the Concrete Pavement from Zincilate 365
Yong Wang and Ya'nan Yan

Preparation of Carbon-Coated Tourmaline and the Degradation of Methylene Blue 373
Yuesong Wang, Xiuyun Chuan, Lin Li, and Dubin Huang

Raman Spectroscopic Core Scanning for Iron Ore and BIF Characterization 387
M.A. Wells and E.R. Ramanaidou

Comprehensive Utilization and Purified Research on Kaolin Ores in Huichang 397
Caibin Wu and Guiming Shi

Using Goethite as a Heterogeneous Fenton Catalyst for the Removal of Tetracycline Hydrochloride: Effects of Its Adsorptive and Reductive Activities 405
Honghai Wu, Fenfen Jiang, Shaoyou Lu, Yufeng Guan, Dayi Deng, and Xiaoling Chen

Palygorskite in the Late Miocene Red Clay Sediment from the Chinese Loess Plateau and Its Paleoclimatic Implications 425
Qiaoqin Xie, Gao Qiu, Tianhu Chen, Xiaochun Xu, Xiaoyong Wang, Huayu Lu, Huifang Xu, and Junfeng Ji

Preparation of Cristobalite and Its Thermal Characteristics 441
Ying Yan and Yongheng Zhou

Removal of Cu (II) from Aqueous Solutions Using Colloidal Pyrite Calcined Under Inert Atmosphere 447
Yan Yang, Tianhu Chen, Ping Li, Haibo Liu, Yadan Shi, and Xinmin Zhan

N Reagents in the Reverse Flotation of Carbonate-Containing Iron Ores 459
Wanzhong Yin, Jizhen Wang, and Longhua Xu

The Study on Genotoxicity of $PM_{2.5}$ Mineral Dusts to A_{549} Cells 471
Yali Zeng, Tingting Huo, Faqin Dong, Limin Wang, and Jianjun Deng

The Effect of Gum Arabic on the Dispersion of Cement Pastes 483
Cuiting Zhao, Qinglin Zhao, Yulin Zhang, and Mingkai Zhou

Reservoir Features of Carboniferous Sand-Mudstone Member and Effects of Diagenesis in Lunnan Region 495
Xueqin Zhao, Jin Fang, Jianghua Deng, and Tiejun Yin

The Mineral Geochemistry Identification and Its Influence on the Pore Evolution of the Upper Ordovician Carbonate Cements in Tazhong Oil Field 509
Xueqin Zhao, Yunfeng Zhang, Zhenyu Wang, Qin Ma, and Tiejun Yin

Chemical and Mineralogical Characterizations of High Ti-Bearing Blast Furnace Slag in Panzhihua, China 521
Guobiao Zhou, Tongjiang Peng, Hongjuan Sun, and Haiyang Xian

Secondary Minerals of Weathered Orpiment–Realgar-Bearing Tailings in Shimen Carbonate-Type Realgar Mine, Changde, Central China 531
Xiangyu Zhu, Rucheng Wang, Xiancai Lu, Huan Liu, Juan Li, Bingjie Ouyang, and Jianjun Lu

Appendix 555

Index 557

Introduction

The biennial International Congress for Applied Mineralogy (ICAM) is the most important gathering of applied mineralogists, organized every odd year by the ICAM Council. The 11th ICAM in the series will be held at the Southwest University of Science and Technology—SWUST in Mianyang, China, on 05–10 July 2013.

The field of Applied Mineralogy responds to the ever-increasing demands from society, increasingly, as existing demands get redefined and entirely new demands emerge. Thirty-two years after the inception of the first ICAM in Johannesburg, South Africa, in 1981, Applied Mineralogy is more than ever before a hot topic.

In a bidding competition during the 10th ICAM in Trondheim, Norway, in 2011, China won the votes to host the 11th ICAM in 2013. The possibility of visiting a country in blazing development, with numerous mineral resources and a scientific proliferation to match, combined with the continuation of the effective paperless publishing of ICAM proceedings (with printing-on-demand), the highly interactive Guided Poster Sessions, and exciting excursion destinations convinced delegates to vote in favor of China. Anyone still in doubt was easily converted by prospects of tasty and spicy food and the proverbial Chinese "hospitality with a smile."

All the above and more have been implemented in the program for the 11th ICAM. As per June 20, over 200 delegates from 18 countries have registered to the congress and 146 abstracts have been submitted. They comprise a diverse collection of applied mineralogy, including Process Mineralogy, Advanced Materials, Mining and Metallurgy, Geometallurgy, Industrial Minerals, Solid Waste Treatment and Recycling (also known as Urban Mining), and Environmental and Medical Mineralogy. The highly exciting disciplines of Bio-mimetic Mineral Materials and Interaction of Ultrafine Minerals with Micro-Organisms lend ICAM 2013 a special Asian flavor and high degree of sophistication. I am confident that the 11th ICAM delegates will be satisfied with content as well as performance!

The field of Applied Mineralogy has been able to match society's pace by continuously reinventing itself, quickly adopting new technologies and instrumentation as they became available, and put them to work at the service of mankind

living in a world substantially relying on minerals. Over the past decennia, Applied Mineralogy has evolved into a trendsetting discipline, staking out course for science and engineering and research and development, for the benefit of society. Contrary to popular layman belief, mineral resources are limited, and we are obliged to our heirs to use them responsibly.

The 11th ICAM presents something new and exciting to learn for everyone. I guarantee each one of you will exclaim at least one time "hey, I didn't know that!" That will not signify lack of knowledge, but far more importantly, it will demonstrate something learned. Ultimately, "learning" is the main reason why ICAM delegates want to meet. I look forward to a very reworded 11th ICAM Congress in Mianyang, China!

Maarten A.T.M. Broekmans

Historical overview of past ICAM congresses

Edition	Year	Venue	Congress chair
11th	2013	Mianyang, China	Faqin Dong
10th	2011	Trondheim, Norway	Maarten Broekmans
9th	2008	Brisbane, Australia	Ying Gu
8th	2004	Aguas de Lindoia, Brazil	Henrique Kahn
7th	2000	Göttingen/Hannover, Germany	Robert B. Heimann
6th	1996	Warsaw, Poland	Andrzej Szymanski
5th	1993	Perth, Australia	Jim Graham
4th	1991	Pretoria, South Africa	Sybrand de Waal
3rd	1989	Montréal, Canada	Bill Petruk
2nd	1984	Los Angeles, USA	Donald Hausen
1st	1981	Johannesburg, South Africa	Sybren Hiemstra

International Council for Applied Mineralogy

Prof.	Faqin Dong	*President*	Southwest University of Science and Technology (SWUST), Mianyang, China
Prof.	Emin Çiftçi	*Vice President*	Department of Geological Engineering, ITU, Istanbul, Turkey
Dr.	Maarten A.T.M. Broekmans	*Past President*	Geological Survey of Norway (NGU), Trondheim, Norway
Dr.	Deshenthree Chetty	*Secretary*	Mintek, Johannesburg, South Africa

11th ICAM Organizing Committee		
Prof.	Xiao Zhengxue	Southwest University of Science and Technology
Prof.	Liu Congqiang	Chinese Society for Mineralogy, Petrology and Geochemistry
Prof.	Chai Yucheng	National Natural Science Foundation of China
Prof.	He Hongping	Guangzhou Institute of Geochemistry, Chinese Academy of Sciences
Prof.	Wang Yanxin	China University of Geosciences (Wuhan)
Prof.	Liu Jiongtian	China University of Mining and Technology
Prof.	Wang Rucheng	Nanjing University
Prof.	Zhu Lixin	Chinese Academy of Geological Science, Geological Society of Chinese
Prof.	Lu Anhuai	Peking University
Prof.	Ni Wen	University of Science and Technology Beijing
Prof.	Cao Xiping	The Geological Museum of China

11th ICAM Publication Committee			
Prof.	Faqin Dong	Southwest University of Science and Technology	Editor-in-Chief
Prof.	Liu Congqiang	Chinese Society for Mineralogy and Geochemistry	Associate Editor
Prof.	Chai Yucheng	National Natural Science Foundation of China	Associate Editor
Prof.	He Hongping	Guangzhou Institute of Geochemistry, Chinese Academy of Sciences	Associate Editor
Prof.	Wang Yanxin	China University of Geosciences (Wuhan)	Associate Editor
Prof.	Liu Jiongtian	China University of Mining and Technology	Associate Editor
Prof.	Wang Rucheng	Nanjing University	Associate Editor
Prof.	Lu Anhuai	Peking University	Associate Editor
Prof.	Jin Zhisheng	Acta Mineralogica Sinica	Associate Editor
Dr.	Zhao Xueqin	Southwest University of Science and Technology	Associate Editor

11th ICAM Scientific Committee					
Prof.	Faqin Dong (Chairman)	China	Prof.	Cai Jianhui	China
Dr.	Maarten A.T.M. Broekmans	Norway	Prof.	Hong Hanlie	China
Dr.	Ying Gu	Australia	Prof.	Jin Zhisheng	China
Prof.	Jonathan W.C. Wong	Hong Kong	Prof.	Lu Anhuai	China
Prof.	Dogan Paktunc	Canada	Prof.	Li Shengrong	China
Prof.	Dong Hailiang	USA	Prof.	Lian Bin	China
Dr.	Özge Andiç-Çakır	Turkey	Prof.	Liao Libing	China
Dr.	Geólogo Reiner Neumann	Brazil	Prof.	Lu Xiancai	China
Prof.	Xie Xiande	China	Prof.	Ni Wen	China
Prof.	Ye Danian	China	Prof.	Ning Ping	China
Prof.	Chen Qianwang	China	Prof.	Peng Tongjiang	China
Prof.	Feng Qiming	China	Prof.	Wang Gehui	China
Prof.	He Hongping	China	Prof.	Wang Ling	China
Prof.	Zhao Qinling	China	Prof.	Zheng Shuilin	China

Microparagenetic Associations of Gold in Ore-Forming Minerals from Deposits of Different Geological and Industrial Types of Kazakhstan

Adilkhan Baibatsha, Kulyash Dyussembayeva, and Aimkhan Kassenova

Abstract All endogenous gold deposits have the same productive mineral associations, which do not depend on the age of the deposits, geological and tectonic position, and compositions of the deep substrate and host rocks. These include the following associations: gold–pyrite–arsenopyrite, gold–polysulfide, gold–telluride, gold–antimonite, and gold–vermilion. These associations are sustained. Geological conditions will affect the shape of its release—the macro-, micro-, nanomineral, or isomorphic. These associations are also found in different gold deposits of Kazakhstan.

Keywords Deposit • Ore • Mineral • Association • Gold • Micromineral • Sulfides • Quartz

1 Introduction

Comparative analyses of paragenetic associations in complex ores of gold–pyrite–polymetallic deposits (Ridder-Sokolnoe—eastern Kazakhstan, Abyz, Maikain—central Kazakhstan) show consecutive associations from early to late associations, with some deviations. But Maikain deposits have unusual baryte–copper ores that contain rare minerals of tin, germanium, and indium, which are formed at the end of mineralization. The ore-forming sulfides have a common trend to allocate sequentially in all complex ores of gold–pyrite–polymetallic deposits. This is pyrite–chalcopyrite–sphalerite-faded ore galena.

In the gold–sulfide–quartz deposits, gold–pyrite–arsenopirite association is early, which includes arsenopyrite, as the earliest sulfide. Later associations (gold–bismuth–pyrite–quartz–arsenopirite in Altyntau—northern Kazakhstan deposit and gold–sulfosolt in Akbakai—southern Kazakhstan) are overlaid at the early gold–pyrite–quartz–arsenopirite association. They contain bismuth

A. Baibatsha • K. Dyussembayeva • A. Kassenova (✉)
Kazakh National Technical University named after K. Satpayev, Satpaev st., 22, Almaty, Kazakhstan
e-mail: baibatsha48@mail.ru

F. Dong (ed.), *Proceedings of the 11th International Congress for Applied Mineralogy (ICAM)*, Springer Geochemistry/Mineralogy,
DOI 10.1007/978-3-319-13948-7_1

minerals—sulfotellurides of bismuth, lead, copper, and bismuth telluride. In ores of Kulazhon deposit, bismuth minerals are not found. The next gold–polymetallic association, which is in the deposits of this type, is manifested in different ways. The latest associations with antimonite (quartz–carbonate–antimonite–tetraedrite in Altyntau) and (gold–antimonite–vermilion in Akbakai) complete the process of mineralization, weakly auriferous. However, they can serve as an indicator of hidden gold mineralization (Kulazhon deposit—eastern Kazakhstan).

2 Research

2.1 Microparagenetic Associations of Gold in the Main Minerals of Deposits of Gold–Pyrite–Polymetallic Type

This type of gold bearing is complex. Gold in them is concentrated in quartz and in the main ore-forming sulfides. The main sulfides (pyrite, chalcopyrite, sphalerite, galena) composing lodes of deep horizons of Ridder-Sokolnoe deposit, according to their ratio, belong to the gold–polymetallic, ores of Abyz to the gold–pyrite–copper–zinc, and ores of Maykain to the gold–pyrite–barite–polymetallic. Each of these deposits has its own features. At the Abyz and Maykain deposits, the massive ores are mainly developed, and the disseminated ores have subordinate importance. In the Ridder-Sokolnoe deposit, the massive ores at depth are replaced with the rich sulfide veined mineralization. Each deposit includes several types of ores, which are composed of the relevant paragenetic associations. Among them the paragenetic associations with which gold and silver relate are highlighted. The latest associations are usually productive.

The ores of the Ridder-Sokolnoe deposit include the following paragenetic mineral associations with which the gold is bound: gold–pyrite–quartz, gold–chalcopyrite–quartz–sericite, gold–sphalerite–tetrahedrite–sulfosalt–chalcopytite–quartz, galena–gold–telluride, gold–telluride, and gold–quartz (no sulfides) poorly-sulfide–quartz–carbonate. Rare microminerals are in intergrowths with gold and form microparagenetic associations with the main and secondary sulfides (Fig. 1). They are in the following productive paragenetic associations: gold–sphalerite–tetrahedrite–sulfosalt–chalcopytite–quartz, galena–gold–telluride, and gold–telluride (Table 1). Their compositions are studied by electron microprobe analysis.

The Abyz deposit includes the following paragenetic mineral associations with which the gold relates: pyrite, pyrite–chalcopyrite, pyrite–sphalerite, galena–sphalerite, significantly gold–telluride, and gold–silver. Among them two are the most latest productive associations: galena–sphalerite and gold–telluride.

In the Maykain deposit, rare microminerals are part of the following paragenetic associations: chalcopyrite–sphalerite–galena–barite, barite–enargite–luzonite, and barite–bornite–chalcocite–tennantite. In associations are presented not only those

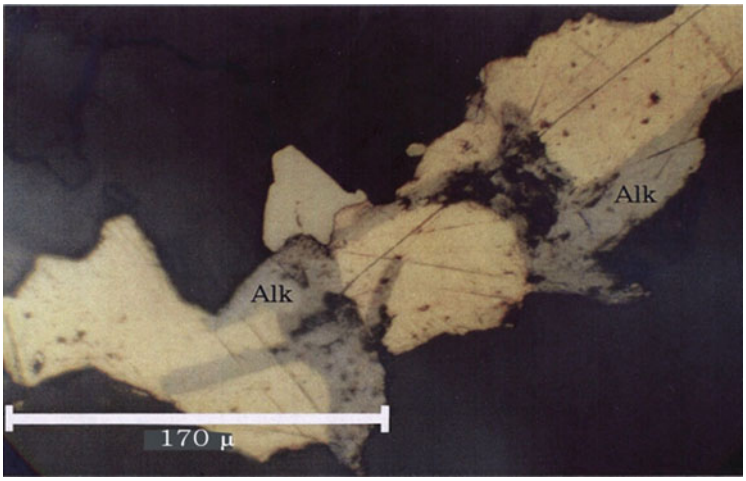

Fig. 1 Gold (*yellow*) in intergrowths with aleksite (Alk) and grain of pyrite in quartz

typical ones for ores of gold–pyrite–polymetallic type of minerals, such as tellurides, but such atypical rare minerals of germanium, indium, and tin associated with late barite–bornite–chalcosine–tennantite association (Table 1).

2.2 Microparagenetic Associations of Gold in the Main Minerals of Deposits of Gold–Sulfide–Quartz Type

Gold–quartz–sulfide stockwork Altyntau and gold–sulfide–quartz vein Akbakai are significant and relate to the deposits of the gold–sulfide–quartz type. Kulazhon deposit represents a combination of quartz vein and stockwork mineralization. According to M. Raphailovich [1], Altyntau deposit is the gold–arsenic–bismuth–copper type, and Akbakai is the gold–arsenic–antimony type.

Ores of gold–sulfide–quartz are vein disseminated and disseminated. The content of sulfides reaches 10 %. The main ore minerals at the Altyntau and Akbakai deposits are arsenopyrite and nonmetallic vein quartz. The main part of gold is in a free form in vein quartz. "Resistant gold" is mainly related to arsenopyrite. In the Kulazhon deposit, gold is in vein quartz and late sulfide antimonite. Compositions of rare minerals are studied by microprobe analysis.

At the Altyntau deposit, the following paragenetic mineral associations with which the gold is bound are identified: gold–pyrite–arsenopyrite–quartz, gold–bismuth–pyrite–arsenopyrite–quartz, gold–polymetallic, and quartz–carbonate–antimonite–tetrahedrite. The bulk of the gold is associated with pyrite–arsenopyrite–quartz and bismuth–arsenopyrite–pyrite–quartz associations and it is in quartz and arsenopyrite. Table 2 gives rare microminerals within these

Table 1 Microminerals in the ores of the deposits of gold–pyrite–polymetallic type

Ridder-Sokolnoe (deep horizons)	Abyz	Maykain
Paragenetic associations and microminerals relating to them		
Alloy standard of gold 665–*900*	Alloy standard of gold *610–980*	Alloy standard of gold *650–950*
Gold–sphalerite–tetrahedirite–Sulfosalt–chalcopyrite–quartz:	*Gold–sphalerite–tetrahedirite–Sulfosalt–chalcopyrite–quartz:*	*Gold–chalcopyrite–sphalerite–galena–barite:*
Native gold	Native gold	Native gold
Electrum	Electrum	Electrum
Tetrahedrite	Tennantite–tetrahedrite	Kustelite
Bismuth	Tetrahedrite	Tennantite
Galena–gold–telluride and Gold-telluride:	Bismuth	Argirodite
Electrum	Aikinite	Hessite
Hessite	*Galena–gold–telluride and Gold–telluride:*	Altaite
Telluro Bismutite	Electrum	Tetradymite
Hedleyite	Hessite	Telluro Bismutite
Pilzenite	Altaite	Pearceite
Tetradymite	Tellur	Molybdenite
Telluro Joseite	Coloradoite	Arsenopyrite
Aleksite	Telluro Bismutite	Pyrrhotine
Bursaite	Petzite	*Gold barite–enargite–luzonite:*
Bournonite	*Gold and silver:*	Electrum
Lead sulfide?	Electrum	Chalkosine
	Kustelite	Covelline
	Arsenopolibazite	Enargite
	Proustite	Luzonite
	Proustite–pyrargyrite	Tennantite
	Stephanite	Germanite
	Tennantite	*Gold–barite–barnite–chalcosine–tennantite:*
		Electrum
		Bomite
		Chalkosine
		Enargite
		Tennantite
		Idaite
		Stromeyerite
		Jalpaite
		Betehtenite
		Stannin
		Stannoidite
		Mawsonite
		Renierite
		Roquesite
		Germanite

associations, in which bismuth minerals—bismuthinite and native bismuth—have industrial importance.

At the Akbakai deposit, the following paragenetic mineral associations with which the gold is bound are identified: gold–pyrite–arsenopyrite, gold–sulfosalt,

Table 2 Microminerals in the ores of the deposits of gold–sulfide–quartz type

Ridder-Sokolnoe (deep horizons)	Abyz	Maykain
Paragenetic associations and microminerals relating to them		
Alloy standard of gold 665–*900*	Alloy standard of gold *610–980*	Alloy standard of gold *650–950*
Gold–pyrite–arsenopyrite–quartz: Native gold Pyrrhotine Loellingite *Gold–bismuth–pyrite–arsenopyrite–quartz:* Native gold Electrum Molybdenite Scheelite Bismuthin Bismuth Telluro Bismutite Cubanite Tetradymite Aikinite Cosalite Tennantite–tetrahedrite *Gold–pdynaallic:* Native gold Electrum Tennantite Tellurides *Quartz–carbonate–antimonite–tetraedrite:* Tetrahedrite Antimonite	*Gold–pyrite–arsenopyrite–quartz:* Native gold *Gold–sulfosalt:* Native gold Electrum Tennantite Tennantite–tetrahedrite Tetrahedrite Gersdorffite Bismuth Bismuthin Boumonite Boulangerite Jemesonite Molybdenite Scheelite *Gold–pdynaallic:* Native gold Electrum Aikinite Cosalite Linneite Enargite Hessite Altaite Krennerite Petzite *Gold antimonite–vermilion:* Native gold Electrum Antimonite Native antimony Vermilion Native silver	*Gold–pyrite–arsenopyrite and gold–polymetallic::* Native gold *Gold–polymetallic combined with gold–antimony–pressure mercury association:* Native gold Antimonite Native antimony Antimony oxides

gold–polymetallic, and gold–antimonite–vermilion. The first three of the associations have industrial importance. Gold–antimonite–vermilion is latter term and weakly manifested. Rare microminerals are given in Table 2.

At the Kulazhon deposit, the following paragenetic mineral associations with which the gold is bound are identified: gold–pyrite–arsenopyrite and gold–polymetallic and gold–polymetallic combined with gold–antimonite–pressure mercury association (Fig. 2). Gold is found in quartz and antimonite.

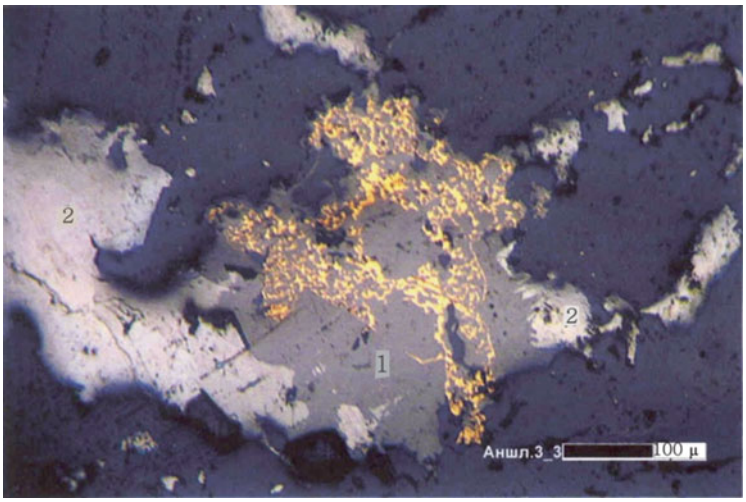

Fig. 2 Dendritic native gold (*yellow*) in antimony oxides (1) developed among antimonite

3 Results

The results of the study ore deposits of gold–pyrite–polymetallic type show the following: (1) productive for gold are the two or three of the latest paragenetic associations, which are connected rarely with microminerals; (2) the purity of gold ranges from relatively low grade to high grade. There is a decrease in alloy standard of gold from early to late associations; (3) the gold of early associations is fine grained and associated mainly with quartz and pyrite. All are relatively large particles of gold formed in the later stages of the process of mineralization; and (4) according to the classification [2], there is microscopic and macroscopic gold in the ores.

Results of the study ore deposits of gold–sulfide–quartz type show the following: (1) Everywhere early gold–pyrite–arsenopyrite paragenetic association is manifested (Table 2); (2) Gold–polymetallic association is typical for all too. However, in ores of Altyntau and Akbakai deposits, there are paragenetic associations—gold–bismuth–pyrite–arsenopyrite–quartz (Altyntau) and gold–sulfosalt (Akbakai)—that emerge before the gold–polymetallic association; (3) Process of mineral formation is usually completed by weak auriferous associations in which antimonite is typomorphous (Altyntau and Akbakai); (4) A distinctive feature of the ores in Kulazhon is the late productive gold–antimony–pressure mercury association.

4 Discussion

According to D. Rundquist, all of gold deposits, regardless of genetic types, have steady consecutive parageneses of gold: /Au-W/Au-Mo/Au-As/Au-Cu-Pb-Zn/Au-Te/Au-Ag/Au-Sb/Au-Sb-As-Hg/ [3]. The studies of A. Kremenetsky and E. Mincer [4] have led to the fact that all of the endogenous gold deposits, regardless of the age, geological and tectonic setting, compositions, and depth of substrate and host rocks have in general the following standard set of mineral types of associations: the gold–pyrite–arsenopyrite gold–polysulfide, gold–telluride, gold–antimonite, and gold–vermilion. Sustainable regular consecutive parageneses of gold are revealed. R. Koneev conducts an analysis of the mineral compositions of ores from different deposits of gold in Uzbekistan which allowed, regardless of their location, host rocks, metasomatism, and shapes of the ore bodies, etc., on all of gold deposits to reveal under different names of six mineral associations, corresponding to the six gold geochemical parageneses: /Au-W/Au-As/Au-Te/Au-Ag/Au-Sb/Au-Hg/ [5].

In the gold ore deposits in Kazakhstan, consistent pattern in the allocation of paragenetic associations of gold was revealed too. They are as follows: (1) In the complex ores of gold–pyrite–polymetallic deposits, the gold–pyrite–quartz association is early, usually less gold bearing in comparison with the latest paragenetic associations. The gold is fine grained and associated with early pyrite. This type of deposit is completely absent or is a rare arsenopyrite. (2) The earliest gold–pyrite–arsenopyrite–quartz association with fine-grained gold in arsenopyrite is typical for deposits of gold–sulfide–quartz and gold–skarn copper–gold–sulfide types in terrigenous strata (Bakyrchik). (3) All types of deposits are characterized by the latest gold–polymetallic association in which the gold consolidates, and falls into alloy standard of gold, and electrum is the predominant mineral. Here, earlier gold is redistributed with its consolidated and introduces its additional portions. In many deposits, what is allocated before the gold–polymetallic is the association with bismuth minerals, sulfosalts, and sulfotellurides of bismuth, lead, and copper and faded ore is usually presented tetrahedrite. (4) The gold–telluride association is final and it is after the gold–polymetallic or galena–sphalerite with a decrease in the activity of sulfur. However, each deposit has its own specific characteristics. In Ridder-Sokolnoe and Abyz, this association is manifested quite clearly, but in the ores of Maykain received poor development. The gold–telluride association also is manifested in the deposits of gold–copper skarn (Sayak IV) and gold–sulfide–quartz type (Altyntau, Akbakai) and absolutely not expressed in ores of Kulazhon. (5) The latest association with antimonite is the final in mineralization process and is manifested in the ores of gold–sulfide–quartz type (Altyntau, Akbakai, Kulazhon). As a rule it is weakly auriferous. However, in Kulazhon, most of the gold is associated with oxides of antimony in antimonite. The latter has no place in the ores of gold–pyrite–polymetallic type.

5 Conclusion

A sequence /Au-W/Au-As/Au-Te/Au-Ag/Au-Sb/Au-Hg/ which specified in [5] has at the gold fields of Kazakhstan, too. The completeness of this sequence depends on the level of erosion and on the size of the deposit. It should be noted that industrial interest is usually determined by two or three parageneses.

References

1. Rafailovich MS (2009) Gold mineral resources of Kazakhstan: geology, metallogeny, forecast-search model. Almaty, p 304
2. Moiseyenko VG (2008) Nanogeochemistry of gold: Proceedings of the Symposium, Vladivostok, pp 6–25
3. Rundquist DV (1997) The factor of time in the formation of hydrothermal deposits: periods, epochs, stages and stages of mineralization: Geology of Ore Deposits, No. 1, pp 11–24
4. Kremenetsky AA, Mintzer EF (1995) Universality of gold systems—a key criterion for the regional forecast of industrial mineralization: National Geology, No. 1, pp 19–27
5. Koneev RI (2006) Nanomineralogy of gold. DELTA, St. Petersburg, p 216

Calcium Phosphate Mineralization of Bacteria

Anatoly T. Titov, Piter M. Larionov, and Vladimir I. Zaikovskii

Abstract The morphology, structure, and chemistry of calcifications upon native and bioprosthetic heart valves infected with *Staphylococcus aureus* have been investigated using high-resolution transmission and scanning electron microscopy, electron diffraction, and energy-dispersive X-ray spectroscopy. Additionally, calcium phosphate mineralization of bacteria has been studied experimentally under the conditions simulating the major ion composition of blood plasma (Ca, P, Mg, NaCl). The experiments address the capacity of hydroxyapatite isolated from calcified valves to adsorb bacteria and the mineralization ability of bacteria (*S. aureus*). The bacteria were found out to activate formation of calcium phosphate in the blood plasma of patients.

Keywords Mineralization of bacteria • Hydroxyapatite • Blood plasma • Scanning and transmission electron microscopy

1 Introduction

The exceptional role of bacteria in the formation of calcium phosphate has been understood since the last century. However, abundant publications on this issue report mainly geological data and experiments with natural phosphates (e.g., [1, 2]). The morphology of particles is commonly referred to as principal evidence for microbial mediation in phosphate genesis. Such publications have become more numerous with the advent of electron microscopy and often contain inferences of the bacterial origin of phosphates [3]. Bacteriomorphic phosphate particles found in many regions worldwide are often interpreted as mineralized bacteria (Fig. 1). However, high-resolution transmission electron microscopy (HRTEM) allowed us

A.T. Titov (✉)
Institute of Geology and Mineralogy SB RAS, Acad. Koptyug, av., 3, Novosibirsk, Russia
e-mail: titov@igm.nsc.ru

P.M. Larionov
Institute of Traumatology and Orthopedy, Novosibirsk, Russia

V.I. Zaikovskii
Institute of Catalysis of SB RAS, Novosibirsk, Russia

F. Dong (ed.), *Proceedings of the 11th International Congress for Applied Mineralogy (ICAM)*, Springer Geochemistry/Mineralogy,
DOI 10.1007/978-3-319-13948-7_2

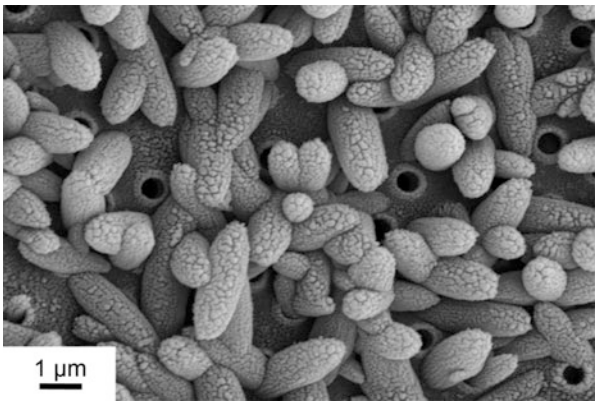

Fig. 1 Bacteriomorphic calcium phosphate particles upon diatoms from recent marine phosphates

to suggest a different formation mechanism for such particles from recent marine phosphorites [4]. Calcium phosphate crystals often appear on heart valves and become a subject of medical research. Unlike the medical literature concerning mostly the meditative role of bacteria in calcification, we address mineralization of bacteria themselves. Specifically, this chapter is devoted to mineralization of cocci, especially *Staphylococcus aureus* widespread in humans. We report electron microscopy data on calcifications upon infected native and bioprosthetic heart valves and the results of experiments on bacteria adsorption by hydroxyapatite and on mineralization ability of bacteria.

2 Materials and Methods

2.1 Materials

In this study, we used samples of calcified native mitral and aortal heart valves taken intraoperatively from patients with acquired infective valvular diseases, as well as porcine bioprosthetic heart valves removed during revalving. All valve samples were subjected to preliminary macroscopy and histology analyses.

Altogether about 50 samples of native and bioprosthetic heart valves were examined. SEM images revealed 1–5 μm spherical particles in calcium phosphate inclusions from the valves. After detailed SEM examination, five samples were selected in which the sizes of many spherical particles approached the common sizes of *S. aureus* bacteria in humans (Fig. 2a). The mineral fraction of the deposits was divided into two parts: one was examined on a transmission electron microscope and the other was embedded in epoxy resin and polished to highlight the particle cross sections. The mineralization of bacterial cultures was investigated with a strain of *S. aureus* from the collection of the Gamaleya Institute of

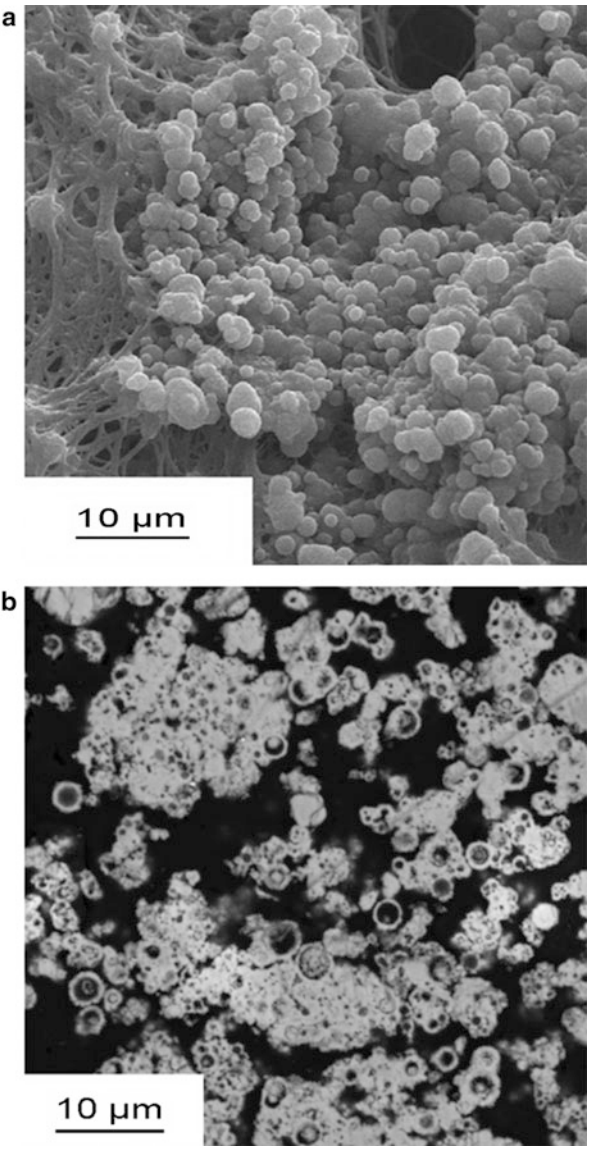

Fig. 2 Photomicrographs of calcified *S. aureus* upon a bioprosthetic heart valve: an SEM image of bacteria surface in secondary electrons (**a**) and a BSE image of calcification section as in a (**b**)

Epidemiology and Microbiology of the Russian Academy of Medical Sciences (Moscow).

2.2 Methods

The inventory of methods applied in the reported study included high-resolution transmission electron microscopy (HRTEM), scanning electron microscopy

(SEM), electron diffraction, and energy-dispersive X-ray spectroscopy (EDX). The instruments were a JEOL JEM2010 transmission electron microscope (acceleration voltage 200 kV, resolution 1.4 Å) equipped with an EDAX EDS detector (spectral resolution 130 eV) and an LEO1430 VP scanning electron microscope with an OXFORD EDS detector (resolution 128 eV) and INKA ENERGY software for the elemental analysis; Gatan DigitalMicrograph software was used for processing the electron microscopic images.

2.3 *Experimental Conditions: Bacteria Sorption on Hydroxyapatite*

The experiment was carried out to study sorption of bacteria on hydroxyapatite (HA) isolated from heavily mineralized heart valves. Hydroxyapatite was separated from the organic part of the valves in the following way. The calcified material was first separated mechanically from the valves and placed into vials with distilled water, and then dispersed at 22 kHz for 10 min using a USD-2 ultrasonic dispersant. After the coarse particles were let to precipitate for a short while, the remainder solution was poured into vials. Then the precipitate of fine HA particles was annealed for 1 h in a muffle furnace in air at 600 °C.

The adsorption was studied using nylon wool columns in 10 ml syringes, with hydroxyapatite as a tested sorbent and activated carbon–mineral sorbent as a control (activated charcoal + aluminum oxide used currently in clinical practice). The HA-to-sorbent volume ratios were 1:1 in the first series of the experiments and 1:2 in the second series. The bacterial cultures passing through the columns contained 1×10^5 bacterial cells, which corresponds to the maximum cell count detectable in the hemoculture of venous blood in the case of transient bacteriemia. The bacteriological control was carried out with standard growth media.

2.4 *Experimental Conditions: Mineralization of* S. Aureus

The microbial culture of *S. aureus* was grown on solid agar. Then the microbial culture was placed in a Petri dish with the solution containing calcium, phosphorus, and salt ions in the initial amounts of 1.33 mM Ca^{2+}, 1.5 mM P^{5+}, 0.8 mM Mg^{2+}, and 0.15 M $Na^{+}Cl^{-}$ at a temperature 37 °C. The aqueous solution with these concentrations of Ca, P, Mg ions and NaCl and with pH = 7.4 simulated the ionic composition of blood in healthy adults [5]. Under these conditions, no calcium phosphate normally forms even in several years, which is proven by the absence of precipitates in the solution. A similar microbial culture grown in a standard medium was used for reference. After exposure to the experimental conditions, the

precipitate samples were prepared for SEM examination by dehydrating, drying, mounting, and coating with carbon.

3 Results

The obtained SEM images of calcified heart valves with abscesses have revealed complex bacterial colonization patterns with zonal growth and several layers. Bacteria formed clusters consisting either of cocci and rod-shaped bacteria (bacilli) or cocci only. The cocci were noted to preferentially colonize the mineral aggregates during the zonal and colonial growth, while the bacilli more frequently grew on the organic abscess components. The endothelial layer in the abscess regions showed some variations. In some cases, it was clearly polymorphic, with its part being prone to swelling, or in other cases, the mineral component was populated with erythrocytes and blood plasma proteins, this being evidence of an intravital contact of the mineral component with blood.

In terms of morphology, HA deposits in the periphery of heart valve calcifications are commonly spherical particles of the sizes similar to or larger than the cocci (1–5 μm). In the calcified heart valve samples we studied, they were about the sizes of natural bacteria (Fig. 2a).

In BSE images, some spherical calcium phosphate particles retain organic material in the center: see the contours of *S. aureus* bacteria mineralized from the surface in Fig. 2b. They are of different sizes, the difference being the result of polishing the calcified spherical particles at different levels. However, many bacteria are mineralized also in the interior part, which cannot be due to contamination while polishing. The absence of this contamination is proven by the absence of polisher at the respective sites analyzed by EDS.

The TEM micrographs image the bioprosthetic calcification samples mostly as composed of acicular nanometer HA crystals about 150 nm long and 5 nm wide (Fig. 3). Some layers of such HA crystals, of uniform sizes, lie upon collagen fibers and are aligned with them (Fig. 3a). Other mineral layers consist of larger randomly oriented HA crystals similar in structure and morphology to the fine ones (Fig. 3b). They remain as large as 300–500 nm even after ultrasonic dispersing applied during the preparation of samples for HRTEM examination. The acicular habit of the nanometer HA crystals is typical of calcifications, but their ordered patterns on collagen fibers differ from the random orientations in the remainder part of the selected samples.

Calcium phosphate mineralization activated by *S. aureus* occurs mainly on the surface of bacteria and inside them. Unlike the collagen fibers, the HA crystals do not show any preferred orientation with respect to bacteria surfaces.

Then we studied the sorption capacity of hydroxyapatite isolated from the heart valves in two series of tests with different HA-to-sorbent volume ratios (1:1 in the first series and 1:2 in the second series of the experiments; see above). After the *S. aureus* culture passed twice through the control activated carbon sorbent, there

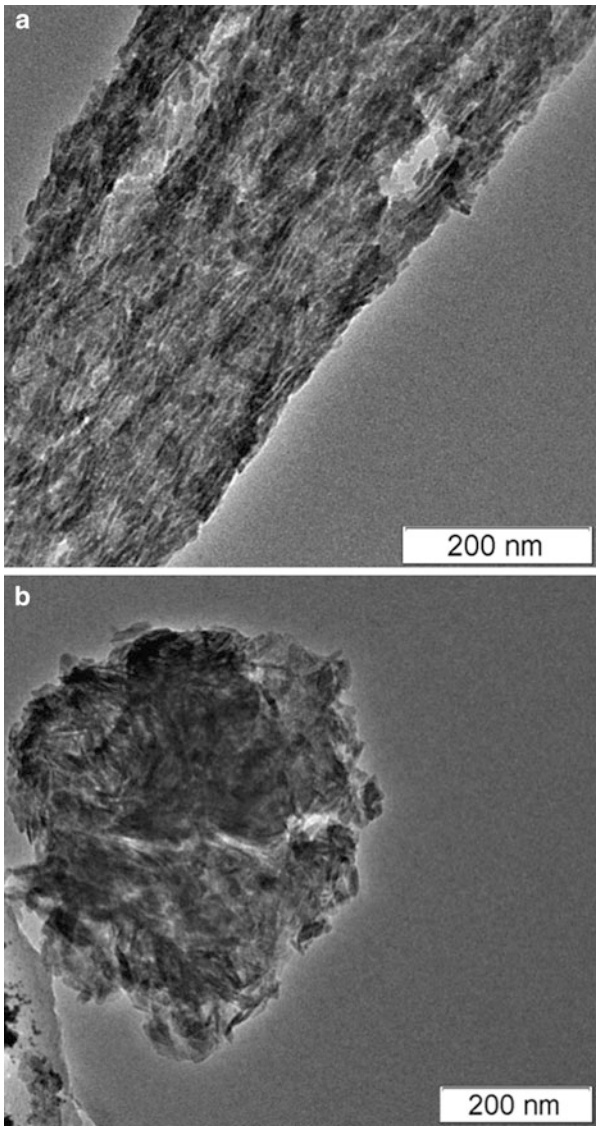

Fig. 3 A HRTEM image of calcification on a bioprosthetic heart valve: nanometer hydroxyapatite crystals upon collagen fibers (**a**) and presumably in the bacterial cell interior (**b**)

remained 3.75×10^4 and 1.23×10^4 cells, respectively, in the first and second runs. However, hydroxyapatite from the calcified heart valves adsorbed almost all bacterial cells in the first run. The second series of tests, under similar conditions, gave similar results: almost all bacterial cells were adsorbed on HA, though its amount was twice smaller than that of the control carbon sorbent.

The result of the bacteria mineralization test was likewise positive. Calcium phosphate precipitates appeared on the surface of some bacteria in the *S. aureus*

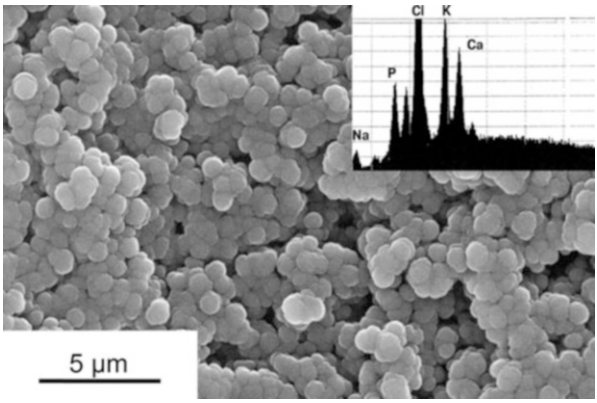

Fig. 4 A colony of *S. aureus* grown in 4 days on solid agar in a solution with the initial amounts of 1.33 mM Ca^{2+}, 1.5 mM P^{5+}, 0.8 mM Mg^{2+}, and 0.15 M $Na^{+}Cl^{-}$. *Inset* shows an EDX spectrum of a single mineralized bacterium

culture already in 4 days (Fig. 4). The mineral component showed a calcium-to-phosphorus ratio corresponding to that in hydroxyapatite, according to EDX data.

4 Discussion

The blood of humans and vertebrate animals is to some approximation an analog of seawater as to the concentrations of calcium, phosphorus, sodium, and magnesium. For this reason, new results in mineralogy obtained for natural marine phosphorite are often used in medicine. On the other hand, experimental results which simulate the formation of bone apatite and pathological calcium phosphates in humans likewise can be useful for modeling marine mineral formation [6]. Dissolved inorganic phosphorus in seawater and in artesian fluids comes mostly from biodegradation of organic matter. It serves as a preferable nutrient for microorganisms and plants or can precipitate as authigenic apatite [3]. However, our HRTEM data on the structure of bacteriomorphic HA particles from recent marine phosphorite [4] contradict their bacterial origin. Note in this respect that the morphological similarity is a necessary but not sufficient criterion to prove mineralization of bacteria. Therefore, our study of the role the bacteria can play in heart valve calcification has been integrated with clinical and histological results.

Calcifications of native or bioprosthetic heart valves have a propensity for bacterial colonization, and patients with a calcified aortic valve run a ten times greater risk for infective endocarditis than others [7]. Infective endocarditis is among the most complicated and acute problems in the surgery of acquired valvular diseases. Clinicopathologic correlation between bacterial endocarditis, caused mainly by *S. aureus*, and calcification was also reported in Mambo et al. [8].

Abscesses in calcified heart valves arise commonly at the late mineralization stage, which follows from numerous observations and is supported by our experimental results. Calcium phosphates typically precipitate inside the tissue of native heart valves. In these conditions, hydroxyapatite cannot interact with bacteria

which are too large to penetrate into the intratissular space. However, the conditions at the late stages of intratissular calcification may be favorable for *S. aureus* vegetation due to endothelium injury, tissue degradation, or direct penetration of bacteria onto the hydroxyapatite. The contact with blood is proved by the presence of erythrocytes in the samples.

According to the tests, nanocrystalline hydroxyapatite formed in the process of heart valve calcification has a very high sorption capacity, and the bacteria it adsorbs from the blood stream can proliferate upon the valves. The bioprosthetic heart valves, with weaker protective functions than their native counterparts (being void of endothelium, etc.), are more vulnerable to the infection associated with calcification.

On the other hand, our experimental results show that *S. aureus* itself is prone to mineralization in blood plasma at the concentrations of calcium, phosphorus, and magnesium ions as in blood of healthy adults. Furthermore, increase in calcium and/or phosphorus ions in human blood at some pathologies may lead to a higher solubility product, which is sometimes expressed as the Ca and P product, and may eventually induce enhanced pathological HA precipitation.

The medical practitioners know how *S. aureus* is harmful for humans, but its ability of activating its own calcium phosphate mineralization in blood plasma remained so far unknown.

5 Conclusions

Calcified native and bioprosthetic heart valves are commonly prone to abscesses at late stages of mineralization. The infecting *S. aureus* bacteria turn out to be able to activate calcium phosphate formation in humans, which increases the risks of cardiovascular diseases, especially those complicated by calcification.

References

1. Lucas J, Prevot L (1985) The synthesis of apatite by bacterial activity: mechanism. Sci Geol Metallogenia 77:83–92
2. Lamboy M (1990) Microbial mediation in phosphogenesis: new data from the Cretaceous phosphatic chalks in Northern France. Geology Soc Spec Publ 52:157–167
3. Blake RE, O'Neil JR, Garsia GA (1998) Effects of microbial activity on the δ (18)O of dissolved inorganic phosphate and textural features of synthetic apatites. Am Mineral 83:1516–1531
4. Titov AT, Baturin GN (2008) Microstructure and formation mechanism of calcium phosphate in resent phosphorites. Dokl Earth Sci 419(2):312–315
5. Titov AT, Larionov PM, Ivanova AI et al (2004) Hydroxyapatite formation in human blood. In: Pecchio et al (eds) Applied mineralogy. ICAM-BR, Sao-Paulo, pp 207–210. ISBN 85-98656-01-1

6. Sanchez-Navasi A, Martin-Algarra A (2001) Genesis of apatite in phosphate stromatolites. Eur J Mineral 13(2):361–376
7. Bischof T, Schneider J (1992) Degenerative calcification of mitral and aortic valves. Schweiz Rundsch Med Prax 81(19):626–631
8. Mambo NC, Silver MD, Brunsdon DF (1978) Bacterial endocarditis of the mitral valve associated with annual calcification. Can Med Assoc J 119(4):323–326

Economical Potential of an Ultramafic Rock at the Kvaløya Island, North Norway

Anna Pryadunenko and Kåre Kullerud

Abstract A low-grade metamorphic ultramafic rock at the Kvaløya Island, North Norway, shows Ni content up to 5,600 ppm and an average content of 2,500 ppm Ni. Olivine is absent from the rock, and Ni is principally bonded in pentlandite, violarite, and millerite. The rock might be considered as a low-grade ore, with 0.2–0.56 wt% Ni. Other metals that might be of economic interest to extract from the rock include Co (from pentlandite and violarite) and Cr and Fe (from magnetite).

However, traditional mining of such a low-grade ore would result in large volumes of waste material, which could represent a serious environmental problem. The future challenge for developing low-grade ore deposits like this is to find alternative uses of the minerals that are left after extraction of the economically interesting ore minerals, in order to reduce the volumes of waste materials from mining. One possible use of many of the traditional waste minerals from mining is for CO_2 sequestration, i.e., by reacting the waste minerals with CO_2 in order to permanently store CO_2 in carbonates. Traditional mining of the Ni-bearing ultramafic rock described here would result in large volumes of tailings dominated by serpentine. If value could be added by reacting serpentine from these tailings with CO_2 in order to sequestrate CO_2 in magnesite, extraction of Ni from such a marginal grade deposit could be of economical interest.

Keywords Ultramafic rock • Ni-sulfides • Serpentine • CO_2 sequestration

1 Introduction

During recent years, there has been an increasing global demand for metals, resulting in a significant increase in metal prices. A consequence of this is that low-grade ores which earlier were of no economic interest might today be considered as economically interesting. Extraction of metals from low-grade ores, however, results in large amounts of waste material, which might represent serious environmental problems. For modern mining industry, it is therefore important to

A. Pryadunenko (✉) • K. Kullerud
Department of Geology, University of Tromsø, 9037 Tromsø, Norway
e-mail: a.pryadunenko@gmail.com

F. Dong (ed.), *Proceedings of the 11th International Congress for Applied Mineralogy (ICAM)*, Springer Geochemistry/Mineralogy,
DOI 10.1007/978-3-319-13948-7_3

investigate the potential for other uses of the waste material. One possible use of waste materials from mining is for carbon sequestration (e.g., [1]). In this chapter, we give a description of a Ni-bearing metamorphic ultramafic rock, which with 0.2–0.56 wt% Ni might be considered as a potential low-grade ore. The waste material after extracting ore minerals from this rock would be dominated by serpentine, which can be reacted with CO_2 to form magnesite and quartz. Thus, even though a low-grade ore is of marginal economic interest if only extraction of metals is considered, it might turn out to be economical if value is added by minimizing the waste materials from mining through CO_2 sequestration.

2 Geological Setting

The rock described here occurs in the NE part of the Kvaløya Island, which belongs to the West Troms Basement Complex (WTBC). The WTBC represents a tectonic window within the Norwegian Caledonides and makes up the NW margin of the Fennoscandian Shield (Fig. 1). The main geological units of the island are represented by TTG gneisses, mainly Archaean in age, Neoarchaean and Paleoproterozoic metasupracrustal rocks (2.85–1.97 Ga), early Paleoproterozoic mafic dyke swarms (2.4–2.22 Ga), and plutonic suites (1.8–1.76 Ga) intruded during the Svecofennian Orogeny [2–5]. All rock units of WTBC show only gentle metamorphic overprint as a result of the Caledonian Orogeny [5].

The studied ultramafic rock occurs within the TTG gneisses as lens-shaped bodies, up to 300 m long and 10–30 m wide. The mineral content of the rock is dominated by serpentine, talc, chlorite, and opaque minerals. No olivine or pyroxene has been observed. These observations suggest that the rock has undergone metamorphism under greenschist to lower amphibolite facies conditions.

3 Whole Rock Chemistry

3.1 Analytical Procedure

Whole rock chemical analyses were carried out by wavelength-dispersive X-ray fluorescence spectrometry on a Bruker Tiger SX8 instrument at the Department of Geology, University of Tromsø. Major and minor elements were analyzed on fused $Li_2B_4O_7$ glass beads, while trace elements were analyzed on pressed pellets.

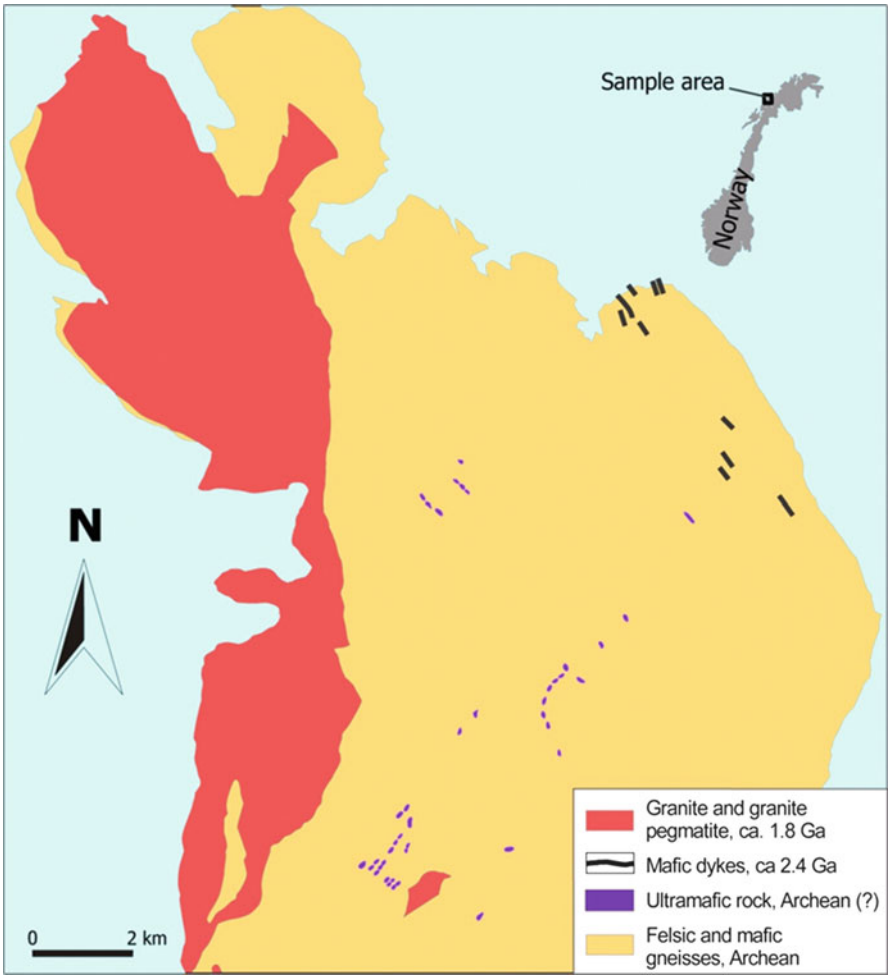

Fig. 1 Schematic map of the NE part of the Kvaløya Island. See *inset map* for location. Modified from [6, 7]

3.2 Results

Whole rock chemical analyses were performed for 40 samples. The major element composition of the rock is characterized by low SiO_2 (38–43.7 wt%), high MgO (23–35 wt%), Fe_2O_3 in the range 10–14 wt%, Al_2O_3 up to 5.5 wt%, highly variable CaO (0.21–6.1 wt%), TiO_2 <1.1 wt%, Cr_2O_3 <0.9 wt%, and total alkalis <0.6 wt%.

One of the samples shows 700 ppm Ni; however, the rest show Ni in the range 1,500–5,600 ppm, with an average of 2,500 ppm Ni. The Co content of the rock varies in the range 80–140 ppm. The Cr content reaches up to 4,000 ppm for some

samples. Other elements such as Pb, Zn, and Cu show significantly lower concentrations than the average of ultramafic rocks. The rock shows insignificant Au content (5 ppb for the richest sample) and Pt and Pd up to 11 and 15 ppb, respectively. However, according to unpublished data of G. Motuza (personal communication 2011), concentrations up to 300 ppb Pd have been determined from the ultramafic rock.

4 Ore Mineralogy

Ultramafic rocks often contain elevated concentrations of Ni. Commonly, however, Ni in ultramafic rocks is not of economic interest, because the element is strongly bonded in the crystal lattice of olivine. For the rock studied here, however, olivine has broken completely down, and Ni occurs in a range of sulfide minerals. Table 1 presents a list of opaque minerals that have been revealed in the studied rock during reflected light microscopy. The presence of the minerals has been confirmed by electron microprobe analyses.

The opaque mineral content of the rock is dominated by magnetite and ilmenite, with magnetite as most abundant. The sulfides present in the rock are dominated by pyrrhotite and pentlandite, which show approximately equal modal abundances. Pyrite and chalcopyrite were also found in all thin sections, but their modal abundances are much lower than for pyrrhotite and pentlandite. Galena and sphalerite were occasionally observed. Sphalerite sometimes occurs separated from other sulfides, while galena only has been observed in aggregates together with other sulfides. Galena also occurs as inclusions in pyrite. Millerite was observed in five thin sections as coarse individual crystals or together with pentlandite.

Magnetite shows different types of intergrowths and aggregates. The grain size varies from <0.01 mm up to several mm. Magnetite shows anhedral grain shapes,

Table 1 Ore minerals observed from the Kvaløya ultramafic rock

Mineral	Chemical composition
Oxides	
Magnetite	Fe_2O_3
Ilmenite	$FeTiO_3$
Sulfides	
Pentlandite	$(Fe,Ni)_9S_8$
Pyrrhotite	$Fe_{1-x}S$
Pyrite	FeS_2
Chalcopyrite	$CuFeS_2$
Sphalerite	ZnS
Galena	PbS
Millerite	NiS
Violarite	$(Ni,Fe,Co)_3S_4$
Gersdorffite	NiAsS

but subhedral grains are also observed. Magnetite is often intergrown with other ore minerals, most commonly with ilmenite (Fig. 2a). Intergrowth of magnetite with pyrrhotite and pentlandite is also common.

Pyrrhotite has been observed as anhedral grains in all studied samples (Fig. 2b, f). The mineral is commonly observed intergrown with pentlandite. The size of pyrrhotite grains and pyrrhotite–pentlandite aggregates varies from <0.01 mm up to about 1 mm. Pyrrhotite also occurs together with chalcopyrite, sphalerite, and occasionally galena and pyrite (Fig. 2f). Pyrrhotite commonly contains inclusions of other minerals, such as chalcopyrite and pentlandite.

Pentlandite occurs as separate crystals as well as intergrowths with pyrrhotite, millerite, ilmenite, and magnetite (Fig. 2b–f). The mineral can frequently be observed in mineral assemblages together with chalcopyrite, sometimes also with sphalerite and galena (Fig. 2f). Occasionally, subhedral grains are observed. Chalcopyrite is sometimes observed as small inclusions in pentlandite. Pentlandite also occurs as flame-shaped or semicircular segregations in pyrrhotite, which are inferred as exsolution lamellae formed during the breakdown of pyrrhotite–pentlandite solid solution.

Chalcopyrite occurs as separate individual grains or as a part of mineral assemblages, as well as in intergrowths with pentlandite and as inclusions in pentlandite (Fig. 2f). Chalcopyrite also occurs as small inclusions in sphalerite. Sometimes, small grains of chalcopyrite are associated with magnetite. The shape of isolated grains is irregular, with jagged edges.

Sphalerite is always associated with pentlandite, pyrrhotite, pyrite, chalcopyrite, and sometimes with magnetite (Fig. 2f). It occurs as inclusions, sometimes together with galena in pyrite grains. Some grains of sphalerite have isometric, close to circular shape. Such grains often contain small inclusions of elliptic or stilliform grains of chalcopyrite. Some grains of sphalerite are partially replaced by chalcopyrite.

Only a few grains of galena have been observed in the studied samples. The mineral is most often present as small inclusions in pyrite, together with inclusions of sphalerite. In one single case, galena was observed as a part of the matrix mineral assemblage.

The modal content of pyrite is approximately half of that of pyrrhotite. The grain shape is often euhedral, but the crystals are mostly fractured. Apparently there are two generations of pyrite present in studied samples (Fig. 2g, h). The earliest generation shows fractured crystals, partially replaced by Fe-hydroxides along the rim of an internal crack. The grain size of this generation does not exceed 1 mm. Pyrite crystals of a second, later, generation is larger; their sizes sometimes come up to 3 mm. They do not show any evidence of deformation, but they have a lot of early minerals as inclusions, such as small rounded grains of sphalerite and galena entrapped during mineral growth.

Millerite has been observed in five samples. It occurs in granular aggregates, up to 0.4–0.5 mm in diameter and as 0.01–0.02 mm long acicular crystals (Fig. 2e). Millerite occurs together with pentlandite, probably being a product of pentlandite decomposition. Violarite has been observed in close association with pentlandite.

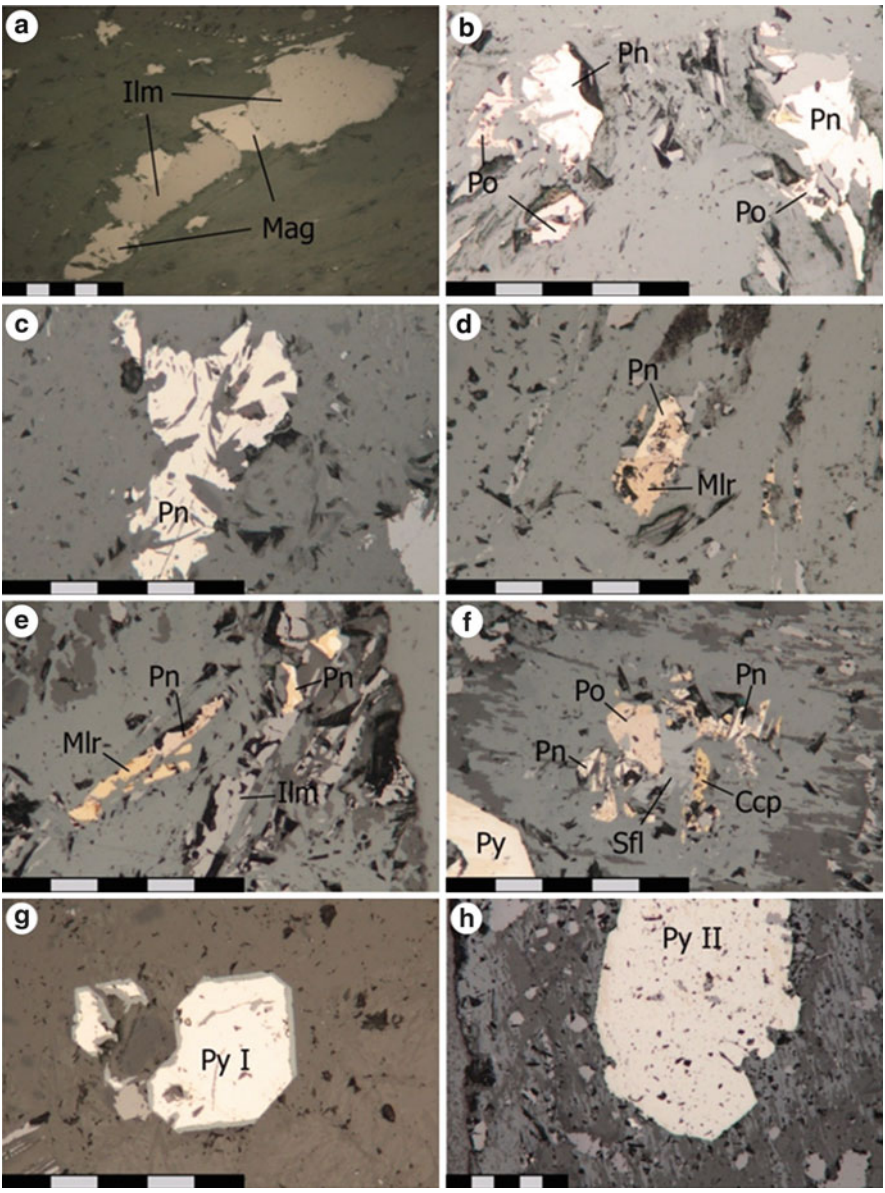

Fig. 2 Reflected light photomicrographs of ore minerals from the Kvaløya ultramafic rock. (**a**) Intergrowth of magnetite with ilmenite. (**b**) Pyrrhotite with pentlandite. (**c**) Typical occurrence of pentlandite. (**d**) Pentlandite with millerite. (**e**) Pentlandite and millerite. (**f**) Cluster of pentlandite, pyrrhotite, sphalerite, and chalcopyrite. (**g**) Pyrite (I generation). Along the rim, pyrite is overgrown by iron-hydroxides. (**h**) Grain of pyrite (II generation) with inclusions of magnetite and sphalerite. Abbreviations of mineral names: *Ilm* ilmenite, *Mag* magnetite, *Mlr* millerite, *Pn* pentlandite, *Po* pyrrhotite, *Py* pyrite, *Sfl* sphalerite, *Ccp* chalcopyrite. Length of *scale bar* is 0.5 mm

5 Ore Mineral Compositions

5.1 Analytical Procedures

Mineral analyses were performed at the Department of Geosciences at the University of Oslo, Norway, with a Cameca SX100 electron microprobe. The analyses were carried out at 15 kV accelerating voltage, 15 nA beam current, focused beam, and 10 s counting time on peak for major and 20 s or 30 s for minor elements. Synthetic oxides, metals, and natural minerals were used as standards. PAP matrix corrections were applied.

5.2 Results

The compositional variations of the Ni-bearing sulfides from the Kvaløya ultramafic rock are shown in Fig. 3. Pentlandite varies in composition between $Fe_{4.37}Ni_{4.25}Co_{0.29}S_8$ and $Fe_{3.52}Ni_{5.47}S_8$. Violarite shows compositions varying between $Fe_{0.96}Ni_{1.48}Co_{0.5}S_4$ and $Fe_{0.64}Ni_{1.8}Co_{0.48}S_4$, indicating solid solution toward siegenite $[(Ni,Co)_3S_4]$. Millerite contains some iron and gives a structural formula corresponding to $Ni_{0.97}Fe_{0.02}S$.

Pyrite contains up to 2.5 wt% Ni, up to 2.3 wt% Co, and up to 0.3 wt% Cu. The one pyrrhotite analysis that was performed shows a Ni content of 0.12 wt%, while chalcopyrite contains <0.3 wt% Ni.

Magnetite contains above 4 wt% Cr, but only trace amounts of Ti, Mn, and Ni, while ilmenite shows above 3.6 wt% Mn and about 0.3 wt% Mg.

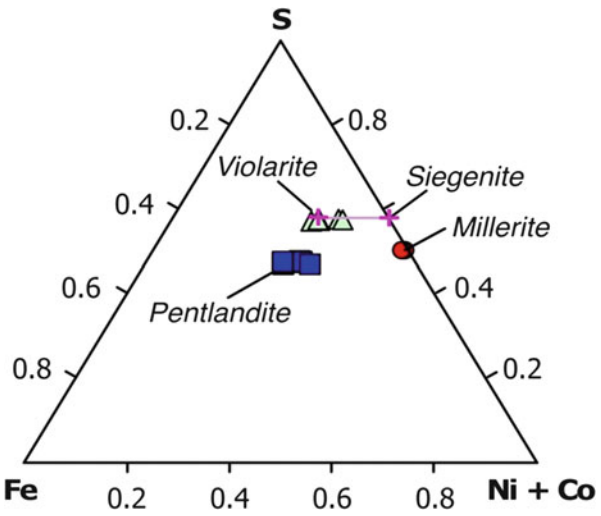

Fig. 3 Compositions of pentlandite, violarite, and millerite from the Kvaløya ultramafic rock in the ternary diagram Fe–Ni + Co–S. Ideal composition of violarite and siegenite are indicated with *pink crosses*

6 Discussion

6.1 Formation of the Ore Minerals

The relatively high contents of Ca of the rock suggest that clinopyroxene initially was present in the ultramafic rock. However, all olivine, clinopyroxene, and orthopyroxene have been completely altered during metamorphism under greenschist to lower amphibolite facies conditions. Magnetite probably formed during alteration of olivine to serpentine, since serpentine is not able to incorporate the same amount of iron as olivine. Further, alteration of olivine most likely liberated Ni that was bonded in the crystal lattice of olivine.

The Ni that was liberated during olivine breakdown and serpentinization was incorporated in pentlandite and violarite, which crystallized together with pyrrhotite and pyrite, as well as chalcopyrite, sphalerite, and galena in small quantities. The presence of two generations of pyrite indicates several stages of sulfide mineral formation in the rock. Millerite is rather late mineral and was probably formed due to decomposition of pentlandite. The modal ratio between the two most abundant sulfide minerals, pentlandite and pyrrhotite, is 1.5/1, which suggests that the rock is very rich in Ni relative to S compared to many other Ni-ores. The presence of millerite, which has high nickel content relative to S, is also important. The high nickel content of some of the whole rock samples (>5,000 ppm) suggests that the rock may be of economic importance.

6.2 Economical Evaluation of the Rock

The investigated rock shows an average of 2,500 ppm Ni, but some samples contain up to 5,600 ppm Ni. Based on today's prices, Ni sulfide ore with Ni content of 2–5 wt% is considered as high-grade ore, while ore with Ni content of 0.3–1 wt% is considered as low-grade ore. Thus, based on the Ni content of the rock, it might be considered as a potential low-grade ore, with 0.2–0.56 % Ni. Other metals that might be of economic interest include Co (from pentlandite and violarite) and Cr and Fe (from magnetite).

Traditional mining of a low-grade ore as reported here for only the metals mentioned above would represent a serious environmental problem, because it would create large amounts of waste rock. One of the most important challenges for modern mining is to find new ways to use the materials that traditionally have been deposited in tailings. Since the excess material after extracting Ni, Co, Cr, and Fe from the ultramafic rock would be dominated by serpentine, there is a possible use of this material that might be of economic interest, namely for CO_2 sequestration. The reaction between serpentine and CO_2 can be formulated accordingly:

$$Mg_3Si_2O_5(OH)_4 + 3CO_2 = 3MgCO_3 + 2SiO_2 + 2H_2O$$

which shows that CO_2 through reaction with serpentine can be permanently sequestrated in magnesite. Carbonation of large volumes of serpentine in excess from mining may in this way be used for permanent storage of large quantities of CO_2. Furthermore, magnesite being produced during this process might also be of economic interest. Through comprehensive Aspen modeling, Brent et al. [1] proposed that co-location of mineral carbonation plants and CO_2 producing industries could lead to synergies and added value for both parts. Therefore, for a complete evaluation of the economical potential of a Ni deposit as studied here, the economic benefits of carbon sequestration using the materials in excess from metal extraction should be evaluated in a larger context, in order to decide whether the deposit is economic or not.

Acknowledgments Norwegian Centre for International Cooperation in Education (SIU) is thanked for financing this project. Muriel Erambert is thanked for great assistance during the microprobe work.

References

1. Brent GF, Allen DJ, Eichler BR, Petrie JG, Mann JP, Haynes BS (2011) Mineral carbonation as the core of an industrial symbiosis for energy-intensive minerals conversion. J Ind Ecol 16 (1):94–104
2. Corfu F, Armitage PEB, Kullerud K, Bergh SG (2003) Preliminary U-Pb geochronology in the west troms basement complex, North Norway: Archaean and paleoproterozoic events and younger overprints. Norgesgeologiskeundersøkelse Bull 441:61–72
3. Kullerud K, Corfu F, Bergh SG, Davidsen B, Ravna EK (2006) U-Pb constraints on the archaean and early proterozoic evolution of the west troms basement complex, North Norway. Abstr Bull Geol Soc Finl Spec Issue I, 79
4. Kullerud K, Skjerlie KP, Corfu F, De La Rosa J (2006) The 2.40 Ga Ringvassøy mafic dykes, west troms basement complex, Norway: the concluding act of early palaeoproterozoic continental breakup. Precambrian Res 150:183–200
5. Bergh SG, Kullerud K, Armitage PEB, Zwaan KB, Corfu F, Ravna EJK, Myhre PI (2010) Neoarchaean to Svecofennian tectono-magmatic evolution of the west troms basement complex, North Norway. Norweg J Geol 90:21–48
6. Zwaan KB (2001) Berggrunnskart TROMSØ 1534 III, M 1:50.000. Norges Geologiske Undersøkelse, 1
7. Zwaan KB, Fareth E, Grogan PW (1998) Geologisk kart over Norge, berggrunnskart Tromsø, M 1:250.000. Norges Geologiske Undersøkelse

Synthesis and Characterization of Mesoporous Carbon Using Attapulgite Template

Xi Cao and Xiuyun Chuan

Abstract The template carbonization method was utilized for the production of mesoporous carbon using attapulgite as a template and sucrose as a carbon precursor. Sucrose was polymerized and carbonized in the tubes of natural attapulgite using a sulfuric acid catalyst. The structure of the template and carbon was investigated by powder X-ray diffraction, transmission electron microscopy, and nitrogen adsorption analysis techniques. At the micrometer level, the resultant carbon material templated by natural attapulgite had a similar morphology. Nitrogen adsorption analysis showed that the obtained porous carbon possessed a wide pore-size distribution and a large pore volume, especially in the range of mesopores.

Keywords Attapulgite • Templated carbons • Mesoporous carbons

1 Introduction

Porous carbon materials are widely used in both traditional areas such as gas separation, water purification, catalyst support, chromatography columns, and storage of natural gas and advanced areas such as electric double-layer capacitors due to the hydrophobic nature of their surfaces, high surface area, large pore volumes, chemical inertness, good mechanical stability, and good thermal stability. In recent years, much attention has been paid to mesopore-rich carbon materials because they can adsorb giant molecules such as dyes, vitamins, polymers, and biomolecules, which cannot be adsorbed by microporous carbons [1–3]. There are mainly three methods to prepare mesoporous carbons: carbonization and activation of carbon precursors, the sol–gel process, and the template method [4]. Compared with other methods, the template approach has been proved to be an efficient way to prepare mesoporous carbons with well-controlled pore sizes and mesopore volume fraction. A lot of studies proved that the highly ordered mesoporous carbon

X. Cao • X. Chuan (✉)
Key Laboratory of Orogenic and Crustal Evolution, School of Earth and Space Sciences, Peking University, 5 Yiheyuan Road, Beijing, People's Republic of China
e-mail: xychuan@pku.edu.cn

F. Dong (ed.), *Proceedings of the 11th International Congress for Applied Mineralogy (ICAM)*, Springer Geochemistry/Mineralogy,
DOI 10.1007/978-3-319-13948-7_4

molecular sieves can be synthesized by using ordered mesoporous silica molecular sieves, like MCM and SBA series [5]. However, the high cost of artificial templates leads to the high cost of the resultant mesoporous carbons using this method; thus natural clay minerals are quite good template candidates due to their porous properties and especially low prices. Kyotani et al. [6–8] first synthesized wrinkled, thin carbon films using montmorillonite, taeniolite, and saponite as templates and acrylonitrile, furfuryl alcohol, and vinyl acetate as carbon precursors from the late 1980s. From then on, a lot of minerals have been studied as templates to prepare carbon materials, such as the lithium form of taeniolite [9, 10], Na^+-montmorillonite [11], porous clay (montmorillonite) heterostructures containing iron, zinc, or copper [12], and Turkish natural zeolite [13]. However, all of these carbons contain mesopore volume fraction lower than 75 %. Therefore, it is important to prepare mesoporous carbon with a high mesopore volume fraction by choosing an appropriate natural clay template.

Recently, we have synthesized mesopore- and macropore-rich carbons with a mesopore volume fraction of 85 % using halloysite as a template and sucrose/furfuryl alcohol as carbon precursors [4, 14]. Attapulgite, widely distributed in China, is a kind of natural hydrous magnesium–aluminum silicate fibrillar mineral containing ribbons. It has open microchannels of 0.38×0.63 nm oriented longitudinally with the fibers, as well as a high proportion of mesopores formed between the nanofibers [15]. Lingmin Shi [16] synthesized mesoporous carbons with a mesopore volume fraction greater than 86 % by using attapulgite as template and furfuryl alcohol as the carbon source through a vapor deposition polymerization (VDP) method. In this chapter, we tried to prepare mesoporous carbon reflecting the morphology and pore structure of the attapulgite template using sucrose as the carbon source by a liquid impregnation method.

2 Materials and Methods

2.1 Materials and Carbon Preparation

The template used in this study was attapulgite, a natural magnesium–aluminum silicate mineral, with ideal molecular formula of $[Si_8Mg_5O_{20}(OH)_2(H_2O)_4{\cdot}4H_2O]$, supplied by Jiu Chuan Nami Material Technology Co., Ltd from Xuyi, Jiangsu Province, China, denoted as APT. It was ground and sieved by a 200-mesh sieve and then dried at 110 °C for 24 h before use. Sucrose (AR) and sulfuric acid (98 %) were purchased from Beijing Yili Fine Chemicals Co., Ltd. Sulfuric acid was used as the acid catalyst to polymerize and solidify the sucrose used in the process in order to prepare porous carbons [17].

In the first case, 25.0 g of sucrose was dissolved in 50.0 g of deionized water to prepare the sucrose solution. The sucrose solution was introduced into 5.0 g of attapulgite matrix by liquid impregnation at room temperature, under vacuum.

Afterward, 2.8 g of sulfuric acid was added to the mixture of attapulgite and sucrose solution. This mixture was stirred for 24 h at room temperature. The mixture was then polymerized at 100 °C for 6 h and subsequently heated at 160 °C for another 6 h. For the carbonization, the polymerized composite was heat treated under a nitrogen atmosphere from room temperature to 700 °C at a heating rate of 5 °C/min and then kept for 3 h in order to complete the carbonization.

After carbonization, the attapulgite–carbon composite (denoted as APT-C) was leached in HF (40 wt%) solution at room temperature and stirred for 3 h, then kept overnight to dissolve the mineral framework, followed by washing with deionized water, and treating with 36 wt% HCl solution under stirring overnight. This demineralization procedure was repeated twice to completely remove the inorganic matrix. The resultant mesoporous carbon was obtained by filtering, washing with deionized water, and drying in an oven at 110 °C overnight. The carbon was denoted as C-700.

2.2 Samples Characterization

2.2.1 X-ray Powder Diffraction

Powder X-ray diffraction pattern of the sample was recorded using X-ray diffractometer (Rigaku, *D*/Max with CuKa radiation, $k = 1.5406$ Å) operated at 40 kV and 100 mA. The step width was 0.02° in the range of 5°–70° 2θ. The analyzed samples were spread as thin layers on a glass slide. Low-angle X-ray diffraction pattern of the resultant sample was also recorded with a *D*/Max diffractometer with a step width of 0.02° in the range of 0.06°–3.0° 2θ.

2.2.2 Scanning Electron Microscopy

The scanning electron microscopy (SEM) images were taken with a Cambridge S-360 microscope equipped with a cold field-emission gun operating at 20 kV and all SEM images were captured by CCD (charge-coupled device) cameras. The specimen was mounted on SEM mount with a carbon tape.

2.2.3 Transmission Electron Microscopy

Transmission electron microscopy (TEM) images of samples were obtained on a Hitachi H9000NAR microscope equipped with a cold field-emission gun. The acceleration voltage was 100 kV, and all TEM images were captured by CCD (charge-coupled device) cameras. The specimens were prepared by the following procedure: the sample was ultrasonically dispersed in ethanol for 15 min, and then a drop of the suspension was placed onto a carbon-coated copper grid, which was left to stand for 10 min before transferred to the microscope.

2.2.4 Surface Area Measurements

N_2 adsorption isotherms (at 77 K) were obtained using an Accelerated Surface Area Porosimeter (ASAP 2020) from Micromeritics. The samples were outgassed for 2 h before measurements at 200 °C in a vacuum at about 10^{-3} Torr. All adsorbed amounts are expressed per gram of outgassed sample. The specific surface area of the samples was calculated by the Brunauer–Emmett–Teller (BET) method using the adsorption data in the relative pressure range of 0.05–0.20 as all materials contained micropores, which prevented a proper determination of their specific surface areas by the BET method. The total pore volume was estimated to be the liquid volume at a relative pressure, P/P_0, of 0.99($V_{0.99}$). The micropore volume (V_{mic}) was calculated using the t-plot method. The mesopore volume (V_{meso}) was determined by subtracting the micropore volume from the total volume. The pore-size distribution (PSD) curves were obtained using the Brunauer–Joyner–Halenda (BJH) method from the desorption branch. Mesopore volume fraction was calculated by V_{meso}/V_{total}.

3 Results

3.1 X-ray Powder Diffraction

The X-ray powder diffraction (XRD) patterns of the template and resultant carbon are shown in Fig. 1. The template used consists mostly of attapulgite, with the typical diffraction peak observed at $2\theta = 8.6°$, which corresponds to a basal spacing of 10.4 Å, attributed to the primary diffraction of the (001) plane [18]. Other peaks observed at $2\theta = 13.6$, 16.1, and 19.7° were attributed to the (020), (310), (400)

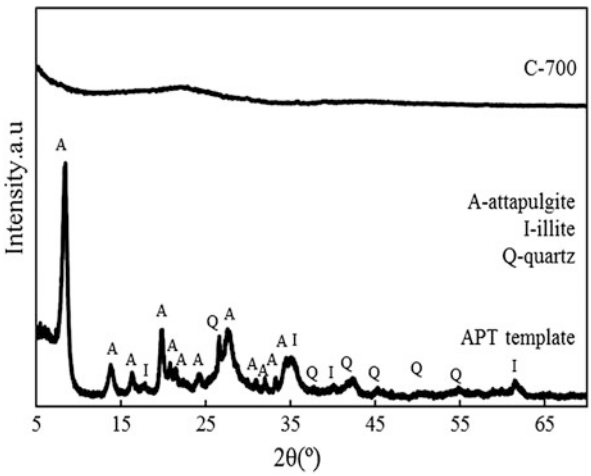

Fig. 1 XRD patterns of the template APT and the resultant carbon C-700

planes, respectively [19]. Quartz and illite impurities were also detected as shown by their most intense peaks situated at $2\theta = 26.5^\circ$ ($d = 0.334$ nm) and $2\theta = 34.9^\circ$ ($d = 0.257$ nm), respectively. The XRD pattern of the resultant carbon shows two broad diffraction peaks observed at $2\theta = 22.3^\circ$ and 44.0°, which are characteristic of a disordered carbonaceous structure; the broad peak at $2\theta = 22.3^\circ$ represents the (002) reflection of carbon due to the stacking structure of aromatic layers. The XRD result indicates the resultant carbon has an amorphous structure.

3.2 TEM and SEM Observation

Figures 2, 3, and 4 showed TEM and SEM images of the original attapulgite APT and the resultant carbon C-700. It is shown that the attapulgite exhibited a one-dimensional structure with diameters at the manometer scale under TEM. Most of the nanorods were separated after being treated by ultrasonic wave during TEM sample preparation. The attapulgite nanorods showed the typical dimensions of 100–1,000 nm in length and 20–40 nm in diameter (Fig. 2). Therefore, if the surface of attapulgite was coated with carbon, we can expect the formation of the porous carbon reflecting the morphology when the carbon is extracted from the attapulgite framework.

Just as expected, the resultant carbon C-700 shows a tubular-like morphology (Fig. 3), with ca. 20–40 nm in diameter tubes as shown in Fig. 4, which is similar to the attapulgite, and demonstrates that sucrose was mainly deposited on the external surface of the template, and the carbon preserved after carbonization and demineralization, thus, the attapulgite shows the templating effect.

3.3 Surface Area Measurements

The nitrogen adsorption–desorption isotherm and pore size distribution (PSD) of attapulgite are shown in Fig. 5. From Fig. 5, we can see that the isotherm shows a type IV isotherm and type H3 hysteresis loops according to IUPAC classification [19], with a high adsorption in the high-pressure section and a pronounced capillary condensation step at relative pressures of 0.7. This indicates that the attapulgite possesses a high proportion of slit-shape mesopores and almost no micropores, and the pores were formed by the packing of flake particles, which is very common in the layered clay porous minerals. The result is in accordance with previous work, which pointed out that the nitrogen adsorption of attapulgite belongs to outer surface adsorption, rather than its channel surface [20]. There are also some macropores as suggested from the final raising tail at relative pressure near 1.0 [11]. The BET-specific surface area value of attapulgite is 126.34 $m^2\ g^{-1}$ (see Table 1). The original attapulgite has a large mesoporosity of 99.5 % and a large specific surface area and pore volume. From the BJH pore-size distributions

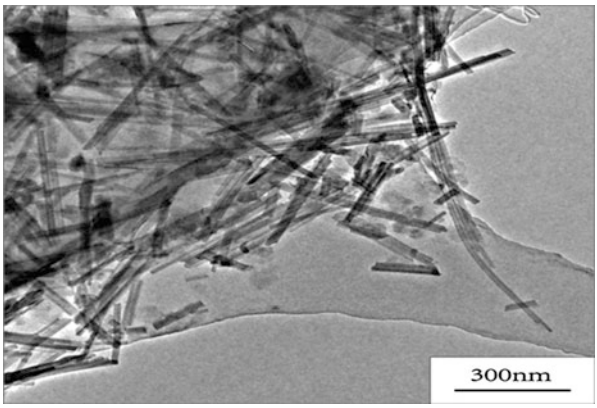

Fig. 2 TEM image of the attapulgite APT

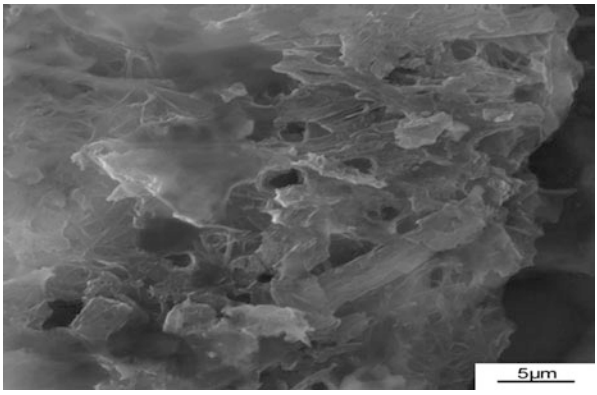

Fig. 3 SEM image of the resultant carbon C-700

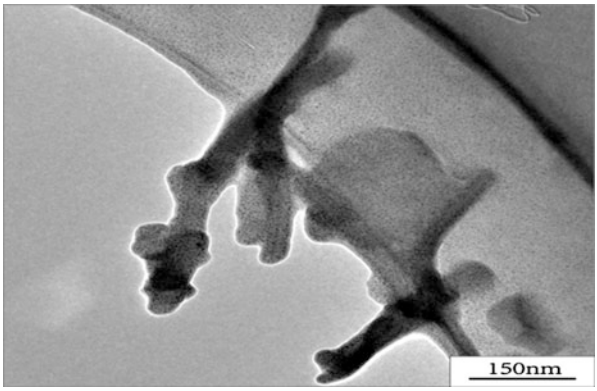

Fig. 4 TEM image of the resultant carbon C-700

obtained, shown in Fig. 5 (inset), it can be seen that the attapulgite exhibits a relatively broad PSD between 3 and 40 nm with maxima at 3.7 and 31.6 nm.

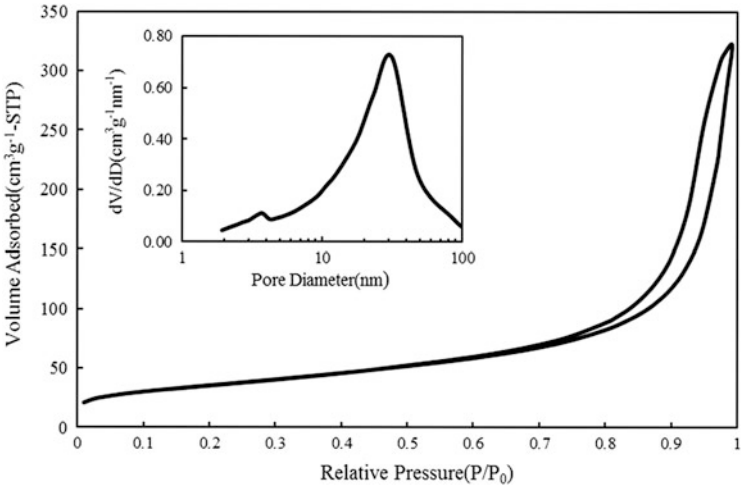

Fig. 5 N_2 adsorption isotherms and pore-size distribution (*inset*) of the attapulgite

The nitrogen adsorption–desorption isotherm and pore-size distribution (PSD) of the resultant carbon C-700 are shown in Fig. 6. The isotherm of the resultant carbon also shows a type IV isotherm and type H3 hysteresis loops. This suggests the existence of a high proportion of mesopores with pores being slit shaped. In addition, the appearance of hysteresis loops at a relative pressure higher than $P/P_0 = 0.44$ indicates that the resultant carbon has a broad PSD [21]. In Fig. 6 (inset), it can be seen that the carbon material exhibits a pore structure with maxima at 3.85 and 9.36 nm and a relatively broad PSD between 30 and 70 nm, which is also in accordance with TEM results, indicating that the resultant carbon partially inherits or replicates the morphology of the template. The increase of the adsorbed volume at low relative pressure reveals the presence of a small amount of micropores in the carbon [11]. The BET-specific surface area value of the resultant carbon is 368.80 $m^2\ g^{-1}$ (Table 1), with a large mesoporosity of 87.3 %, indicating that it is a mesopore-rich carbon material.

4 Discussion

The resultant carbon prepared by using attapulgite as a template and sucrose as a carbon source through liquid impregnation without a high-temperature graphitization can be identified as amorphous carbon from the XRD patterns. The small-angle X-ray diffraction result also shows that carbon does not possess a regular structure, in accordance with other studies [4, 5, 17].

During carbon preparation, the sucrose mainly deposited on the external surface of the template, and the resultant carbon partially inherits or replicates the morphology of the template and exhibits a tubular morphology, as shown in the TEM

Table 1 Specific surface areas and pore characteristics of attapulgite and resultant carbon

Sample	SBET ($m^2\ g^{-1}$)	S_{Mic} ($m^2\ g^{-1}$)	S_{Ext} ($m^2\ g^{-1}$)	V_{total} ($cm^3\ g^{-1}$)	V_{micro} ($cm^3\ g^{-1}$)	V_{meso} ($cm^3\ g^{-1}$)	Mesoporosity (%)
APT	126.34	6.50	119.83	0.497	0.002	0.495	99.5
C-700	368.80	112.75	256.05	0.465	0.059	0.406	87.3

SBET BET-specific surface area, S_{mic} micropore-specific surface area, S_{ext} external specific surface area, V_{total} total pore volume, V_{meso} mesopore volume, V_{micro} micropore volume, mesoporosity $= V_{meso}/V_{total}$

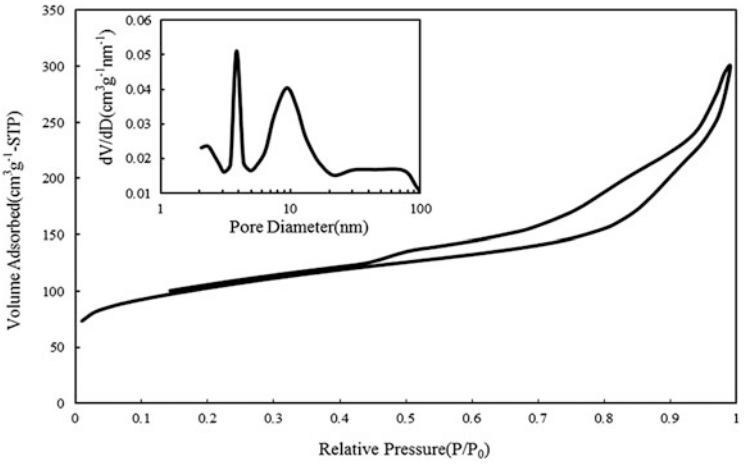

Fig. 6 N_2 adsorption isotherms and pore-size distribution (*inset*) of the resultant carbon C-700

images, which demonstrates a "template effect." The same result can be acquired from the N_2 adsorption results, which show that the resultant carbon exhibits a pore structure with a relatively broad PSD between 30 and 70 nm and reflects the morphology of the attapulgite.

5 Conclusions

Mesoporous carbon with high mesoporosity (87 %) and a large total pore volume can be prepared by using two cheap, eco-friendly materials: one-dimensional nanorod-like attapulgite as a template and sucrose as a carbon precursor. The method proved to be an efficient, simple way to prepare carbon with a high mesoporosity and tubular structures, and it may be an appropriate method for the mass production of porous carbons.

References

1. Sakintuna B, Yurum Y (2005) Templated porous carbons: a review article. Ind Eng Chem Res 44:2893–2902
2. Xu DP, Yoon SH, Mochida I (2008) Synthesis of mesoporous carbon and its adsorption property to biomolecules. Micropor Mesopor Mater 115:461–468
3. Lee JW, Yoon SH, Hyeon TH (1999) Synthesis of a new mesoporous carbon and its application to electrochemical double-layer capacitors. Chem Commun 21:2177–2178

4. Wang AP, Kang FY, Huang ZH (2008) Synthesis of mesoporous carbon nanosheets using tubular halloysite and furfuryl alcohol by a template-like method. Micropor Mesopor Mater 108:318–324
5. Lu AH, Schüth F (2006) Nanocasting: a versatile strategy for creating nanostructured porous materials. Adv Mater 18:1793–1805
6. Kyotani T, Sonobe N, Tomita A (1988) Formation of highly oriented graphite from polyacrylonitrile by using a two-dimensional space between montmorllonite lamellae. Nature 28:331–333
7. Sonobe N, Kyotani T, Tomita A (1990) Carbonization of polyfurfuryl alcohol and polyvinyl acetate between the lamellae of montmorllonite. Carbon 28:483–488
8. Kyotani T, Yamada H, Sonobe N (1994) Heat-treatment of polyfurfuryl alcohol prepared between taeniolite lamellae. Carbon 32:627
9. Bandosz TJ, Jagiello J, Putyera K (1995) Sieving properties of carbons obtained by template carbonization of polyfurfuryl alcohol within mineral matrices. Langmuir 11:3964–3969
10. Bandosz TJ, Jagiello J, Putyera K (1996) Pore structure of carbon-mineral nanocomposites and derived carbons obtained by template carbonization. Chem Mater 8:2023–2029
11. Bakandritsos A, Steriotis T, Petridis D (2004) High surface area montmorillonite-carbon composites and derived carbons. Chem Mater 16:1551–1559
12. Nguyen-Thanh D, Bandosz TJ (2006) Metal-loaded carbonaceous adsorbents templated from porous clay heterostructures. Micropor Mesopor Mater 92:47–55
13. Sakintuna B, Yürüm Y (2006) Preparation and characterization of mesoporous carbons using a Turkish natural zeolitic template/furfuryl alcohol system. Micropor Mesopor Mater 93:304–312
14. Liu GY, Kang FY, Li BH (2006) Characterization of the porous carbon prepared by using halloysite as template and its application to EDLC. J Phys Chem Solid 67:1186–1189
15. Bradley WF (1940) The structural scheme of attapulgite. Am Mineral 25:405–410
16. Shi LM, Yao JF, Jiang JL (2009) Preparation of mesopore-rich carbons using attapulgite as templates and furfuryl alcohol as carbon source through a vapor deposition polymerization method. Micropor Mesopor Mater 122:294–300
17. Joo SH, Jun S, Ryoo R (2001) Synthesis of ordered mesoporous carbon molecular sieves CMK-1. Micropor Mesopor Mater 44–45:153–158
18. Smith DK, Mrose ME, Berry LG (1974) Selected powder diffraction data for minerals. Joint Committee on Powder Diffraction Standards
19. Sing KSW, Everett DH, Haul RAW (1985) Reporting physisorption data for gas solid systems with special reference to the determination of surface-area and porosity (Recommendations 1984). Pure Appl Chem 57:603–619
20. Galan E (1996) Properties and applications of Palygorskite-sepiolite clays. Clay Miner 31:443–453
21. Böhme K, Einicke WD, Klepel O (2005) Templated synthesis of mesoporous carbon from sucrose—the way from the silica pore filling to the carbon material. Carbon 43:1918

Gold Characterization by MLA and Technological Tests: Discussion of Sample Preparation and Results

Carina Ulsen, Henrique Kahn, Guilherme Nery, Daniel Uliana, and Juliana L. Antoniassi

Abstract Gold has been present throughout the history of mankind and used to make jewelry and coins, and recently, it is put into use in industry. The price of gold in international market had a significant increase, surpassing 100 % in the last 5 years. Thereby, deposits with low levels of gold content as well as gold with complex associations or in a very fine particle size became exploitable again, allowing new projects and expansion of existing ones. However, as maximum process efficiency is indispensable and deep knowledge of the characteristics of these minerals and their behavior in face of beneficiation processes. Consequently, an accurate routine for mineralogical and technological characterization is essential. This chapter presents a methodology for characterizing low-grade ores with fine-grained gold. The procedure was conducted in three different samples from different regions, mineralogical assemblages, and grades.

Gold grains and their associations were characterized by SEM-based automated image analysis using the MLA SPL_Lt method, which consists in the initial search of gold, as well as other quite heavy minerals (e.g., platinum, silver, etc.), by atomic number contrast (backscattered electrons) and further identification of these phases and their mineral associations by EDS spectra. The automated routine is set up for allowing the identification of gold grains measuring down to 0.5 μm. Gold extraction assays were accomplished by amalgamation and cyanidation leaching of products from heavy liquid separation. The grades and partition of gold among mineral separation products are discussed in order to evaluate the significance of the gold density preconcentration prior to the characterization by an automated image analysis system. The results attained at mineralogical studies are correlated to the extraction of gold.

Keywords Gold characterization • Image analysis • Sample preparation

C. Ulsen (✉) • H. Kahn • G. Nery • D. Uliana • J.L. Antoniassi
Mining and Petroleum Engineering Department, Polytechnic School, University of Sao Paulo, Av. Prof. Mello Moraes, 2373 Sao Paulo, SP, Brazil
e-mail: carina@lct.poli.usp.br

F. Dong (ed.), *Proceedings of the 11th International Congress for Applied Mineralogy (ICAM)*, Springer Geochemistry/Mineralogy,
DOI 10.1007/978-3-319-13948-7_5

1 Introduction

Gold always has been present throughout the history of mankind. Its brilliance and rarity have made it much sought after for jewelry and coin manufacturing. More recently, gold has been acquired several industrial noblest uses. Moreover, gold is a highly required commodity in times of crisis, and due to the current situation of uncertainty in the global economy, its price had a significant increase in its value, surpassing 100 % in the last 5 years (www.goldprice.com).

Thereby, deposits with low levels of gold content and gold with complex associations or in a very fine particle size became exploitable, allowing new projects and expansion of existing ones. However, maximum process efficiency is indispensable and deep knowledge of the characteristics of these minerals and their behavior in face of beneficiation processes. Therefore, an accurate process mineralogy routine is essential.

Characterization of gold ores differs from the conventional approach since there is a great difficulty to find gold grains for qualitative and quantitative analyses due to the low content of gold (mostly <2 ppm in Brazil) and sparse distribution in mineral deposits. Regarding the high density of gold (19.3 g/cm^3), it is usual to perform a density concentration in order to enrich the heavy products with gold and other heavy minerals to enable a faster analysis on a large number of gold grains or gold-bearing particles without spending much hours searching in multiple polished sections [1].

Density concentration can be carried out by different methods: Wilfrey Table [2], centrifuges, heavy liquid separation, Mozley table, elutriation, and hydro separator [3]. The aim of all these methods is to promote a high-efficient concentration of gold associated with low content of light phases.

The automated methods of image analysis, which are gaining importance in the mining sector due to reliability of the results obtained and the statistical significance afforded by the analysis of large numbers of particles [4], are aiming to obtain the mineralogical composition of the sample, the mineral assemblages, the chemical composition of each phase identified, the partition of elements, the liberation curves of phases of interest, as well as other information.

Automated image analysis by SEM is an efficient and effective mean of identifying visible gold occurrences and distribution, but it is limited on the identification of "invisible" gold [4], which is considered a solid solution or colloidal gold in the range from 0.1 to 0.001 μm [2]. The most sensitive analytical techniques available for the detection of "invisible" gold and other trace elements in minerals are microbeam techniques. These methods can give sensitivities down to the low ppm and even low ppb range, which can detect nanometer-sized micro inclusions and effectively identify "invisible" gold [2].

Although the automated routine through an automated SEM-based mineral liberation analysis system is suitable for the identification of visible gold, due to the difference of spatial resolution magnitude between BSE (0.1–0.02 μm) and

X-ray (2–5 μm) [5], the traditional methodologies are well suited to the determination of particles greater than 5 μm.

This study involves the characterization of the forms of occurrence of gold and its association by quantitative mineralogy by electron beam at an MLA system, and technological tests are to evaluate the recovery of gold by amalgamation and cyanidation in three gold ore samples. The sizes of gold grains are also highlighted since they occur mostly below 5 μm. The grades and partition of gold among mineral separation products (light, intermediate, and heavy products) are discussed in order to evaluate the significance of the gold density preconcentration prior to the characterization by an automated image analysis system. The results attained by cyanide leaching and MLA are compared.

2 Materials and Methods

2.1 Sample Preparation and Gold Technological Tests

The study was carried out in three samples: one from oxidized ore and two from sulfide ore, from two different Brazilian deposits and composed by drill core fragments (approximately 400 kg of each sample). The samples were identified, according to the main composition and origin, as high-grade samples from the same deposit—OXI-HG and SULF-HG and low-grade samples from another deposit—SULF-LG.

The sample preparation comprised sequential steps of comminution, homogenization, and sampling to obtain representative aliquots for this study, comminuted below 0.30 mm. The importance of the sampling is particularly relevant for low-grade ores because of the great care taken on splitting—it was always conducted with rotary sample dividers, both for sample preparation and for the chemical analysis.

The samples were screened in narrow sieve fractions down to 0.037 mm (0.21, 0.15, 0.074, and 0.037 mm) and each sieve fraction was separated by heavy liquid (bromoform) at 2.8 g/cm^3. The sink product of each fraction was then elutriated under controlled conditions to simulate a concentration at higher density and generated the intermediate and the heavy products. So, at the end of mineral separations, there were three products: light (float at 2.8 g/cm^3), intermediate (sink at 2.8 g/cm^3 and light from elutriation), and heavy (sink at 2.8 g/cm^3 and heavy from elutriation). One representative aliquot of the heavy product was taken for SEM-MLA analyses.

Gold extraction assays comprised cyanidation leaching of the light and intermediate products and amalgamation plus cyanidation for the heavy products (coarse gold is recovered at the amalgam and the remaining gold can be accessible to the cyanide solution or not). All cyanide solutions containing gold, as well as the

amalgam and the solid residues, were assessed for the determination of the gold content.

The amalgamation was conducted in the weight proportion of 1:20 (Hg/sample) in a 50 % w/w solids suspension for 15 h; after that, the amalgam (Hg + Au + Ag) was separated from the ore by elutriation (density separation). The cyanidation was performed with a sodium cyanide (NaCN) solution and a concentration of 2,000 ppm of NaCN in a 50 % w/w solid suspension, whose pH was balanced between 10 and 11 with sodium hydroxide (NaOH) under agitation for 48 h. The final solution and the residue were recovered by filtration.

The content of gold in each product, amalgam, cyanide solution, and solid residue was evaluated by fire assay at an international certified laboratory (gold assessed by fire assay with lower limit of 0.01 ppm or 0.01 mg/l).

2.2 SEM-MLA Settings

Due to the low grades of gold, a density concentration previous to SEM analysis was performed by heavy liquid separation and elutriation in order to enrich the sink products and increase the concentration of gold grains in the products to be characterized. To provide statistical robust data on the quantification of gold associations, 26 polished sections were analyzed by MLA.

The gold characterization was carried out by systematic analysis on scanning electron microscopy (SEM) with a field emission source (FEG) coupled with an energy-dispersive spectrometer (EDS) in order to identify gold bearing particles and determine the gold grain composition. The search for gold grains was done automatically by MLA software (Mineral Liberation Analyser—FEI), considering the atomic number (gray levels contrast—backscattered electrons) and chemical composition (EDS microanalysis). It was determined by the gold mineral association, gold liberation-exposed perimeter, and gold grains' size distribution.

The gold grains and their associations were characterized by MLA-SPL_Lt method, which consists in the initial identification of gold by atomic number contrast (backscattered electrons) and EDS spectrum and further identification of the associated phases (perimeter of contact). The operating conditions permitted the identification of gold grains with sizes down to 0.5 μm.

3 Results

3.1 Technological Characterization and Gold Extraction Tests

The weight distribution by sieve fraction, the grades, and the distribution of gold by fraction are shown in Table 1. The grade of gold is around 3 ppm for samples from the high-grade deposit (tendency to enrichment towards the coarse faction) and 0.51 ppm for the low-grade sample (increasing at the finest fraction).

The particle size distribution demonstrates that oxidized sample presents a significant higher amount of fine fraction (below 0.037 mm) than sulfide samples; despite the origin of sulfide samples, the total content of gold associated with the fines represents around 26 % of the total gold from the sample, while this value is 37 % for the oxidized sample. This result demonstrates once more the importance of characterizing gold in fine grains and also the development of technologies to improve their recovery.

The summary of the results of technological characterization studies (total composed from fractions below 0.30 and above 0.037 mm) considering the grades of gold, weight, and gold distribution in each product is shown in Table 2.

The preconcentration done in three steps demonstrates that the heavy products (submitted to MLA analysis) represent different mass recovery and depend on the composition; for sulfide samples, this product represents around 10 and 11 % in mass; however, for oxidized samples the heavy products account for less than 3 % in mass.

The content of gold in heavy products exceeds 30 ppm (mass recovery of 2.8 % in assay) for the oxidized samples and 30 % of gold in assay. For sulfide samples, despite the content of gold in the sample (low- or high-grade ore), the content of gold is around 50 ppm in heavy products (mass recovery around 10 % in assay).

The content of gold in intermediate products is relatively low for sulfide sample, but relatively high for oxidized sample; so, mineralogical analysis carried out in

Table 1 Particle size distribution and gold content and distribution (samples comminuted below 0.30 mm)

Sieve fraction (mm)	OXI-HG			SULF-HG			SUL-LG		
	wt (%)	Au (ppm)	Dist (%)	wt (%)	Au (ppm)	Dist (%)	wt (%)	Au (ppm)	Dist (%)
−0.30 + 0.21	15.2	3.66	19.8	18.2	4.57	23.2	19.0	0.51	19.0
−0.21 + 0.15	11.8	3.19	13.3	14.8	3.35	13.9	17.5	0.48	16.7
−0.15 + 0.074	16.5	3.03	17.8	22.8	3.16	20.2	24.6	0.44	21.3
−0.074 + 0.037	13.5	2.56	12.3	17.3	3.38	16.4	19.7	0.45	17.6
−0.037	43.0	2.40	36.8	26.9	3.50	26.3	19.1	0.68	25.5
Total −0.30	100.0	2.81	100.0	100.0	3.57	100.0	100.0	0.51	100.0

Table 2 Results of density separation for the fraction size above 0.037 mm (samples comminuted below 0.30 mm)

Sample −0.30 +0.037 mm	Products	Weight (%)		Grades	Distribution Au (%)	
		Assay	Sample	Au (ppm)	Assay	Sample
OXI-HG	Light	84.6	48.20	0.88	23.80	15.00
	Intermediate	12.6	7.20	11.50	46.50	29.40
	Heavy	2.8	1.60	32.90	29.70	18.80
	Total calc.	100.0	57.00	3.12	100.00	63.30
SULF-HG	Light	48.3	35.30	0.73	9.83	7.24
	Intermediate	40.4	29.50	3.21	36.10	26.60
	Heavy	11.3	8.30	17.20	54.10	39.80
	Total calc.	100.0	73.10	3.60	100.00	73.70
SULF-LG	Light	77.7	62.9	0.16	26.60	19.80
	Intermediate	12.1	9.83	0.90	23.40	17.40
	Heavy	10.2	8.21	2.31	50.00	37.30
	Total calc.	100.0	80.90	0.47	100.00	74.50

oxidized sample can also consider a preconcentration step, but it has to be lower than the density established for sulfide samples, taking into account the density of the separation (gold associated with other phases besides sulfides).

The content of gold in light product is at least three times lower than that in the fraction and represents the largest amount of sample; the analysis of this product by MLA will bring additional difficulties in terms of gold identification and number of polished sections to be analyzed.

The extraction of gold by cyanidation for light and intermediate products and by amalgamation and cyanidation for the heavy products is presented in Table 3.

The extraction of gold by cyanide leaching (liquor) in the light and intermediate products is similar to each sample, suggesting that the association of gold in both products is similar, though the gold recovery varies significantly among the samples. The high losses of gold in the solid residue are related to inaccessible gold or refractory gold.

The content of gold associated with the amalgam varies markedly among the samples and is related to the gold grains in particle's surface (exposed gold); the much higher grades of gold recovered by amalgamation of OXI-HG sample are probably associated with the presence of a gold nugget than to higher proportion of fine gold grains in exposed surface.

3.2 Gold Association by SEM-MLA for the Heavy Products

The total amount of gold-bearing particles and the number of gold grains identified by MLA routine are exposed in Table 4. For OXI-HG sample, it is notable the high

Table 3 Results of amalgamation and leaching tests for the density separation products (samples comminuted below 0.30 mm)

Samples, total −0.30 +0.037 mm		OXI-HG			SULF-HG			SULF-LG		
			Dist. Au (%)			Dist. Au (%)			Dist. Au (%)	
Products from amalgamation/cyanidation		Au (ppm)	Assay	Sample	Au (ppm)	Assay	Sample	Au (ppm)	Assay	Sample
Float	Liquor	0.61	69.6	10.50	0.42	57.1	4.14	0.12	76.30	15.10
	Residue	0.27	30.4	4.57	0.32	42.9	3.11	0.04	23.70	4.70
	Total calc.	0.88	100.0	15.00	0.73	100.0	7.24	0.16	100.00	19.80
Intermediate	Liquor	7.29	63.2	18.60	1.59	49.5	13.20	0.61	72.70	12.70
	Residue	4.25	36.8	10.80	1.62	50.5	13.40	0.25	27.30	4.74
	Total calc.	11.50	100.0	29.40	3.21	100.0	26.60	0.90	100.00	17.40
Sink	Amalgam	25.40	77.2	14.50	10.60	61.6	24.60	0.02	0.69	0.26
	Liquor	1.55	4.7	0.88	2.18	12.7	5.07	1.64	70.90	26.40
	Residue	5.96	18.1	3.40	4.40	25.7	10.20	0.66	28.40	10.60
	Total calc.	32.90	100.0	18.80	17.20	100.0	39.80	2.31	100.00	37.30

Table 4 Gold-bearing particles and grains (samples comminuted below 0.30 mm)

Fraction (mm)	OXI-HG		SULF-HG		SULF-LG	
	Part.	Grains	Part.	Grains	Part.	Grains
−0.3 +0.21	95	139	50	54	23	43
−0.21 +0.15	73	109	37	38	34	41
−0.15 +0.074	46	85	20	21	56	68
−0.074 +0.037	62	159	10	13	14	16
Total +0.037	276	492	117	126	127	168

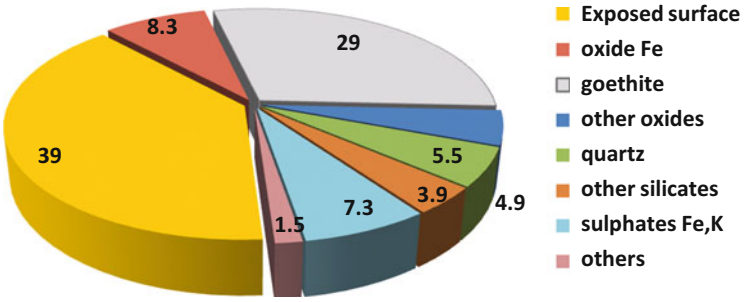

Fig. 1 Gold associations (% of perimeter of contact), sample OXI-HG

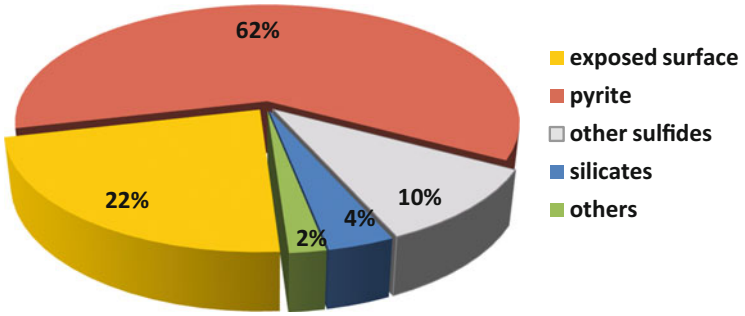

Fig. 2 Gold associations (% of perimeter of contact), sample SULF-HG

quantity of gold grains identified at the microscope (492 grains and 276 bearing particles—most particles contain more than one gold grain) is due to the very high grade of gold in heavy product in this sample (>30 ppm). On sulfide samples, the quantity of gold grains identified is also considerable, for both samples, with 17 and 2.3 ppm of gold in heavy products, respectively.

The main gold associations determined by the perimeter of contact with other minerals (gold carrier) are shown in Figs. 1, 2, and 3. An accurate ore characterization is essential in determining how an ore behaves in a traditional recovery circuit and this way to know the amenability of an ore to different process options

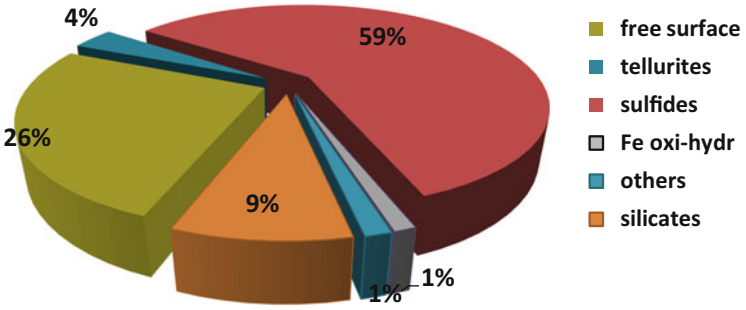

Fig. 3 Gold associations (% of perimeter of contact), sample SULF-LG

[2]. For example, flotation could be indicated if gold is exposed in particle's surface or locked in sulfide particles; cyanidation, if gold grains are very fine or associated with silicates; density concentration, if gold occurs in coarse grains; and so on.

For sample OXI-HG, the average gold association for the heavy products (−0.30 +0.037 mm) indicates that 39 % of the perimeter of gold grains is exposed in particle's surface. Gold grains in locked particles are essentially associated with iron hydroxides (29 %) and oxides (8.3 %) and secondarily to silicates and other oxides.

For sample SULF-HG, the average gold association for the heavy products (−0.30+0.037 mm) indicates that 22 % of the perimeter of gold grains is exposed in particle's surface. Gold in locked particles is essentially associated with pyrite (62 %) and secondarily to other sulfides (chalcopyrite—4 %, CuS—3 % and others—4 %), followed by silicates (4 %) and other minerals (2 %).

For sample SULF-LG, the average gold association for the heavy products (−0.30+0.037 mm) demonstrates the exposed gold grains correspond to 26 % of the total gold perimeter; the main association of the gold is with sulfides (59 %, mainly pyrite and more rarely pyrrhotite and chalcopyrite), followed by silicates (9 %), telluride (4 %), and other minerals (2 %). In this sample, a gold nugget is identified on fraction −0.074+0.037 mm, influencing the gold grain size distribution and exposed surface proportion.

3.3 Gold Grain Size

The size distribution of gold grains (absolute number of grains and frequency) is shown in Fig. 4, in terms of ECD (equivalent circle diameter).

For sample OXI-HG, it was found 466 grains of gold with ECD below 5 μm (91 % of the total grains identified), for sample SULF-HG, this amount corresponds to 78 % (102 gold grains); for sample SULF-LG (159 gold grains), 95 %. Due to the relative amount of fine grains of gold, it is fundamental that the characterization procedure enables the identification of them.

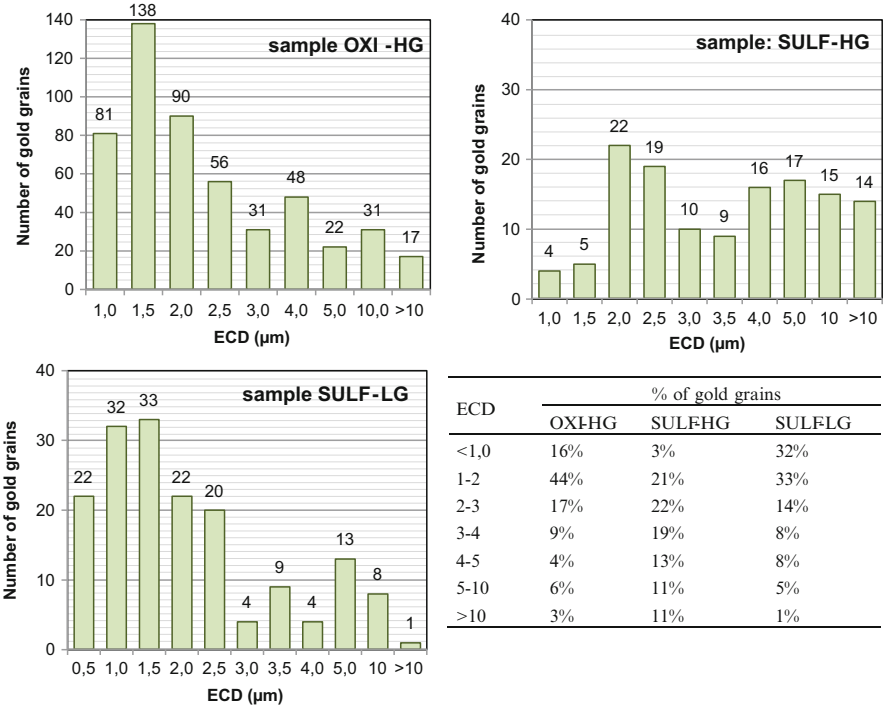

ECD	% of gold grains		
	OXI-HG	SULF-HG	SULF-LG
<1,0	16%	3%	32%
1-2	44%	21%	33%
2-3	17%	22%	14%
3-4	9%	19%	8%
4-5	4%	13%	8%
5-10	6%	11%	5%
>10	3%	11%	1%

Fig. 4 Gold grain size distribution

4 Discussion and Conclusions

This chapter compares the results of mineralogical and technological characterization of three samples with different grades of gold and origin. The density preconcentration step prior to MLA analysis demonstrates that the heavy products (submitted to MLA analysis) obtained for each fraction represent different mass recovery and depend on the composition of the sample.

Considering the enrichment of gold in sink product, a density preconcentration step can be carried out even in oxidized sample for mineralogical analysis, but it has to be lower than the density established for sulfide samples, taking into account the density of the separation, since the occurrence of gold is associated with other phases besides sulfides.

Methods for gold characterization and extraction have to consider the finer particles, since a huge amount of gold can be associated with fractions below 37 µm.

The extraction of gold by cyanide leaching in the light and intermediate product is similar to each sample; though the gold recovery varies significantly among the samples, indicating that the gold associations play a major role in gold recovery, regardless of the content of gold in the sample.

The higher recovery of gold by amalgamation in OXI-HG sample is in agreement with the higher proportion of free surface gold in this sample.

The identification of a large number of gold grains demonstrates the robustness of the established procedure on the search of gold by the MLA and also the effectiveness of the density separation on sample preparation.

Gold grains with ECD below 5 μm correspond to almost all gold in sample (78 %, 91 % and 95 %), so it is fundamental to establish a characterization procedure that enables the identification of them.

Acknowledgments The authors acknowledge the financial support as well as the Coordination for the Improvement of Higher Education Personnel (CAPES).

References

1. Nuemann R, Schneider CL, Alcover Neto A (2002) Caracterização tecnológica de minérios. In: Technical communication prepared for the 3rd edition of Tratamento de Minérios, pp 81
2. Goodall WR, Scales PJ, Butcher AR (2005) The use of QEMSCAM and diagnostic leaching in the characterization of visible gold in complex ores. Miner Eng 18:877–886
3. Cabri LJ, Beattie M, Rudashevsky NS, Rudashevsky VN (2005) Process mineralogy of Au, Pd and Pt ores from Skaegaard intrusion, Greenland, using new technology. Miner Eng 18:888–897
4. Goodall WR, Scales PJ (2007) An overview of the advantages and disadvantages of the determination of gold mineralogy by automated mineralogy. Miner Eng 20:506–517
5. Gu Y (2003) Automated scanning electron microscope based mineral liberation analysis. An introduction to JKMRC/FEI Mineral Liberation Analyser. J Miner Mater Charact Eng 2(1):33–41
6. Chryssoulius SL, Cabri LJ (1990) Significance of gold mineralogical balances in mineral processing. Trans Inst Min Metall, Sect C 99(January–April):C1–C10

Analyzing the Characteristics and Available Attributes of Skarn Gold Deposit Tailings

Yunhong Cheng, Fei Huang, Guanglu Li, Qingyu Yang, Han Peng, and Rui Liu

Abstract Skarn gold deposit tailings are a kind of tailings which are difficult to be utilized effectively. Taking skarn gold deposit tailings from Hubei province, in China, as an example, this chapter has tested and analyzed the tailings, studied the characteristics and available attributes of the tailings, and provided scientific and efficient utilization approaches of tailings in the area of building materials further. The results show that major mineral phase in the tailings is quartz, particle sizes of the tailings mainly existed in 10–100 μm, and the tailings have no pozzolanic activity. As a result, this kind of tailings can be used for building sand and can be used as auxiliary cementing material for concrete based on mechano-chemistry.

Keywords Skarn gold deposit • Tailings • Available attributes

1 Introduction

Skarn gold deposit is a main type of gold deposit [1]. Skarn gold deposit is widely distributed all over the world, which contains a much higher economical value [2–7]. Including gold mine associated with deposits of copper, iron, lead, and zinc, the reserves of skarn gold deposit in China account for 20 % of the whole country's gold reserves [8].

Due to the particularity of gold ore (industrial grade measures in g/ton), as beneficiation process leads to a large accumulation of tailings, it causes very serious environmental stress. The mineral composition in skarn gold tailings is very complex. It contains garnet, diopside, wollastonite, epidote, tourmaline, actinolite, chlorite, quartz, etc. Nonmetal ores like garnet, wollastonite, etc., which contain much industrial value, are recycled by beneficiation [9–12]. However, the total availability of tailings is still very low. Some mines use skarn tailings as mine filling

Y. Cheng • F. Huang (✉) • G. Li • H. Peng • R. Liu
College of Resources and Civil Engineering, Northeastern University, Shenyang, Liaoning, People's Republic of China
e-mail: huangfei@mail.neu.edu.cn

Q. Yang
Jilongshan Gold Mining Co., Ltd, Huangshi, Hubei, People's Republic of China

F. Dong (ed.), *Proceedings of the 11th International Congress for Applied Mineralogy (ICAM)*, Springer Geochemistry/Mineralogy,
DOI 10.1007/978-3-319-13948-7_6

material, but the tailing granules are too small for padding. In the research of developing and utilizing tailings like these, we found skarn gold tailings contain little SiO_2, normally less than 60 % [13]. Its complex composition and stable structure made it hard to be utilized. Therefore, a systematic study, objectively evaluating and scientifically utilizing its available characteristics, could help to improve the efficiency and provide basis for developing highly value-added products.

Based on a systematic study on the characteristics of tailings, this chapter selects one skarn gold tailing from Hubei Province to scientifically evaluate its useable attributes and, hence, to propose a scientific way to utilize the tailings in construction material field.

2 Basic Characteristics of Skarn Gold Tailings

2.1 Chemical Constituents

Chemical compositions of the tailings are shown in Table 1.

Table 1 shows SiO_2, CaO, Fe_2O_3, and Al_2O_3 are the main chemical compositions of these Hubei skarn gold tailings.

2.2 Phase Analysis

The tailing's XRD diffraction pattern is shown in Fig. 1.

Figure 1 shows the minerals contained in these Hubei skarn gold tailings are quartz, calcite, and hematite.

2.3 Particle Size Analysis

Measured by the laser particle size analyzer in the experiment center, which is owned by the College of resources and civil engineering, Northeastern University, the results are shown in Fig. 2.

Figure 2 shows this Hubei skarn gold tailing's particle size distribution is within the range of 10–100 μm.

Table 1 Chemical compositions of the tailings

	wt%						
	SiO_2	CaO	Fe_2O_3	Al_2O_3	MgO	K_2O	SO_3
1	39.1296	31.6354	14.8089	6.3496	4.4438	1.4850	0.6630
2	40.2984	30.2432	13.3886	7.2404	4.3982	1.8724	0.6268
3	41.2927	29.7331	12.2873	7.6230	4.5781	1.8714	0.6798
Average	40.2402	30.5372	13.4949	7.0710	4.4734	1.7429	0.6565
	Na_2O	MnO	TiO_2	P_2O_5	PbO	CuO	Cr_2O_3
1	0.6568	0.3075	0.2510	0.1027	–	0.0488	0.0325
2	0.7693	0.4845	0.3205	0.1169	0.0680	0.0406	–
3	0.8515	0.4458	0.2944	0.1232	0.0704	0.0373	–
Average	0.7592	0.4126	0.2886	0.1143	–	0.0422	–
	Cl	SrO	ZnO	ZrO_2	Rb_2O	Y_2O_3	Nb_2O_5
1	0.0320	0.0313	0.0100	0.0071	0.0053	–	–
2	0.0376	0.0442	0.0330	0.0107	0.0049	0.0018	0.0003
3	–	0.0437	0.0330	0.0270	0.0042	–	0.0041
Average	–	0.0397	0.0253	0.0149	0.0005	–	–

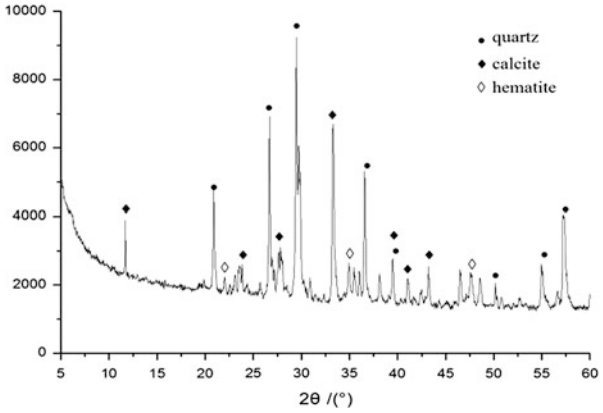

Fig. 1 XRD pattern of the tailings

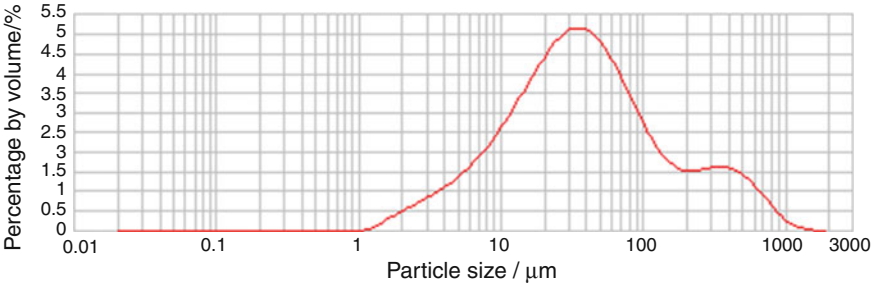

Fig. 2 Laser particle size analysis of the tailings

3 The Skarn Tailings Activity Analysis

According to GB/T12957-2005 "Test method for activity of industrial waste slag used as addition to cement" and appendix A of GB/T2847-2005 "Pozzolanic material used for cement production," the College of sciences, Northeastern University, arranged pozzolanic ash test for the tailings.

1. Under 40 °C for 8 days

   Total Alkalinity determination and calculation:

$$X_{OH^-} = 40 \times c(\mathrm{HCl}) \times V_4 = 40 \times 0.09672 \times 13.25 = 51.26\,\mathrm{mmol/L} \quad (1)$$

   Calcium oxide content determination and calculation:

$$X_{CaO} = 40 \times T_{CaO} \times V_5/56.08 = (40 \times 0.8331 \times 19.3)/56.08 = 11.468\,\mathrm{mmol/L} \quad (2)$$

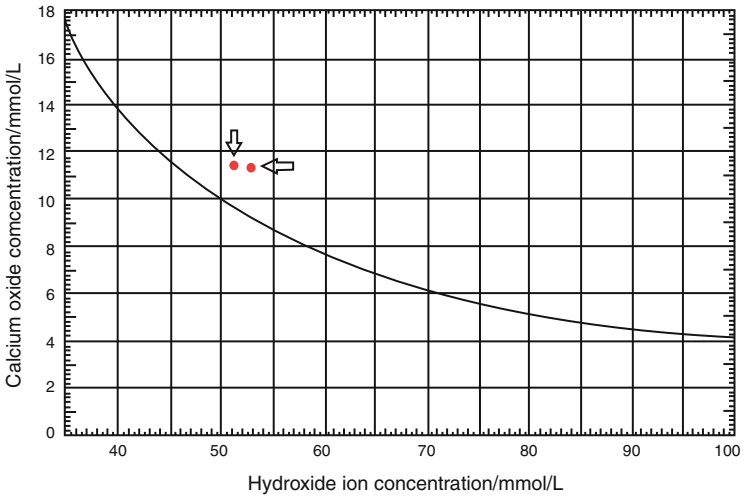

Fig. 3 Curve for assessment of pozzolanic activity

2. Under 40 °C for 15 days

Total Alkalinity determination and calculation:

$$X_{OH^-} = 40 \times c(\text{HCl}) \times V_4 = 40 \times 0.09672 \times 13.8 = 53.39 \text{ mmol/L} \quad (3)$$

Calcium oxide content determination and calculation:

$$X_{CaO} = 40 \times T_{CaO} \times V_5/56.08 = (40 \times 0.8331 \times 18.5)/56.08 = 10.99 \text{ mmol/L} \quad (4)$$

Considering total alkalinity (hydroxide ion concentration) as the abscissa and calcium oxide content as the ordinate, the test results are marked in the pozzolanic activity diagram and shown in Fig. 3. We could figure out both the test results located above the curve (40 °C calcium hydroxide solubility curve). So, pozzolanic ash test result for the tailings is not qualified.

4 Available Property Analysis for Skarn Tailings

The skarn gold tailings used in this study mainly contain minerals like quartz, calcite, and hematite; chemical composition analysis shows that the main component is SiO_2, but it mainly exists in quartz form of non-active silicon and the content is very low. There are also some other compositions like CaO, Fe_2O_3, Al_2O_3, and MgO, and very few of some other metals, all of which exist in the form of

steady-state oxide. Activity analysis showed that the tailings were not qualified for pozzolanic ash test. The particle size of the tailings distributed between 10 and 100 μm and its shape is rubbly.

Based on the above test and analysis, such tailings can be considered as the usage of following aspects.

4.1 Building Sand

Based on the chemical composition, mineral composition, and particle morphology analysis, we could consider to manually grade the tailings to several levels to meet the requirement for the sand used in construction in GB/T14684-2001 " Sand for building" and JGJ52-2006 "Standard for technical requirements and test method of sand and crushed stone (or gravel) for ordinary concrete." Usage as below:

1. Directly use the sand made from tailings as aggregate to blend concrete. It can be used singly or mixed with other ordinary sand in proportion. Sand is the main component of mortar and concrete, which were much needed in the construction field. So, the sand made from tailings could get a lot of applications in such a way.
2. The sand made from tailings could be used as material to prepare building products, such as bricks made from tailings sand. As the gradual expansion of construction scale, building products, including building clinker, road brick, and decorative brick, etc., have a very broad application prospect.

4.2 Auxiliary Cementing Agent for Concrete

According to the basic theory of cementing material, auxiliary cementing agent in concrete can be summarized as physical and chemical effects. Physical effects mainly refer to the role of micro-aggregate filling and the role of providing sediment core for hydrates. Chemical effect means the auxiliary cementing materials can chemically react with the hydrates, which coexisted within the concrete, to show hydration reactivity. The physical effects require the auxiliary cementing agent to be powder with fine particles, while chemical reaction requires chemical activity like pozzolanicity.

Mechano-chemistry is a science to research the fundamental principles, rules, and applications of solid, while physical energy is applied. It studies the change of solid on shape, crystal structure, and physical and chemical characters. The solid particles change under mechanical force, which is not only the volume of the solid particle getting smaller and the specific surface area becoming larger, but also the internal structure, chemical reactivity, and physical and chemical characters change a lot relevantly.

This study shows that these skarn gold tailings don't have pozzolanic activity, and the particle size is too large. The main ingredient of these tailings is SiO_2, but the content is very low. So, we can increase the SiO_2 content by adding proper amount of quartz. Based on this, we could consider to mechano-chemically activate tailings to make it suitable for auxiliary cementing.

By mechano-chemical activation, on one hand, we could reduce the particle size of tailings, thereby to improve the physical filling effect of the tailings as concrete auxiliary cementing materials; on the other hand, under the Mechano-chemistry force of grinding, the crystalline degree of quartz in the tailings was decreased and gradually turned into amorphous form. SiO_2 in amorphous form shows vitreous structure and has potential chemical reactivity. It can chemically react with calcium hydroxide, the hydration products of cement in the concrete, to form calcium silicate hydrate (the products of cement hydration in concrete). Thus, after the mechano-chemical activation, such tailings formed amorphous SiO_2 structure and extremely fine particle size, which is the basis for such tailings to be used as auxiliary cementing agent for concrete.

5 Conclusions

1. Quartz is the main component of the skarn gold tailings we chose in this study. But its content is not very high and with a very low chemical activity.
2. Such skarn gold tailings can be manually graded to several levels to be used as building sand; meanwhile, we can add proper amount of ordinary sand to increase the content of SiO_2 and make it suitable as auxiliary cementing material for concrete by mechano-chemical activation.
3. As the scale of construction increasing, both of the above applications have very good prospects.

References

1. Chen YJ, Qin S, Li X (1997) Mineralization time, space, geodynamic background and metallogenic model of the skarn gold deposits, China. Acta Sci Nat Univ Pekin 33(4):456–466 (in Chinese)
2. Meinert LD, Lentzd R, Newberry RJ (2000) Special issue devoted to skarn deposits. Econ Geol 95(6):1183–1184
3. Chen YJ (1996) Skarn gold deposits in China. Resour Geol 46:369–376
4. Zhao YM, Zhang YN, Bi CS (1999) Geology of goldbearing skarn deposits in the middle and lower Yangtze River Valley and adjacent regions. Ore Geol Rev 14:227–249
5. Sill Itoe RH (2002) Some metallogenic features of gold and copper deposits related to alkaline rocks and consequences for exploration. Mineral Deposita 37:4–13
6. Muller D (2002) Gold–copper mineralization in alkaline rocks. Mineral Deposita 37:1–3

7. Pan YM, Dong P (1999) The Lower Changjiang (Yangzi/Yangtze River) metallogenic belt, east central China: Intrusion and wall rockhosted Cu–Fe–Au, Mo, Zn, Pb, Ag deposits. Ore Geol Rev 15:177–242
8. Chen YJ, Chen HY, Zaw K, Pirajno F, Zhang ZJ (2004) The geodynamic setting of large-scale metallogenesis mainland China, exemplified by skarn type gold deposits. Earth Sci Front 11 (1):57–83 (in Chinese)
9. Lei CY, Wang XW, Gou ZB, Zhang Q (2012) The integrated utilization of garnet in skarn type ore of Jiama copper polymetallic deposit in Tibet. China Min Mag 21(2):68–70 (in Chinese)
10. Shen SH, Li AL (2005) Exploitation of garnet resources in metallic ores in Shizhuyuan, Hunan province. Miner Resour Geol 19(4):432–435 (in Chinese)
11. Lei CY, Wang XW, Gou ZB, Zhang Q (2012) The comprehensive utilization of wollastonite in skarn type ore of Jiama copper polymetallic deposit in Tibet. Multipurpose Util Mineral Resour 1:51–52 (in Chinese)
12. Tian ZH, Wang B, Li JT (2001) Analysis on silica resources and its comprehensive utilization in Luanchuan molybdenum mine. China Molybdenum Ind 25(1):23–26 (in Chinese)
13. Liu L, Hao QQ, Hao ZG, Zhang JQ, Fei HC (2012) The state of the comprehensive utilization of Skarn-type deposits tailings. China Min Mag 12(11):52–54 (in Chinese)

Reciprocity Effect Between Silicate Bacterium and Wollastonite

Qunwei Dai, Faqin Dong, Yulian Zhao, Jianjun Deng, and Junda Lu

Abstract This chapter studies the reciprocity effect between wollastonite and a strain of silicate bacterium isolated from purple soil. The changes of pH value, glucose (GLU) residual concentration, electrolyte, and Mn, Si, Fe, etc., in the culture liquid with wollastonite after 48 h were analyzed. The results show that the GLU consumption of silicate bacterium with wollastonite was 2.5 times of the bacterial control. It indicates that wollastonite can obviously promote silicate bacterium growth, but the silicate bacteria cells were badly broken and even distorted observed by SEM. The solubilization of Si element by silicate bacterium from wollastonite reached above ten times that of the wollastonite control. At the same time, three typical peak intensities in FTIR of wollastonite (898 cm^{-1}, 925 cm^{-1}, 962 cm^{-1}) lowered obviously after the interaction with silicate bacterium, which shows that a great deal of Si has dissolved. Therefore, it is clear that wollastonite has a remarkable effect on the growth of silicate bacterium and there has been an obvious solubilization of Si.

Keywords Reciprocity • Wollastonite • Silicate bacterium • Solubilization • Autolysis

1 Introduction

The interaction between microorganisms and minerals is a kind of geological action that takes place extensively on the earth. In recent years, it has been a popular cross-research realm of mineralogy, microbiology, chemistry, and environmental sciences; the reportorial literatures were extraordinary. So a large number of theories

Q. Dai • F. Dong (✉) • Y. Zhao
Key Laboratory of Solid Waste Treatment and the Resource Recycle, Ministry of Education, Southwest University of Science and Technology, Mianyang, Sichuan 621010, China
e-mail: fqdong@swust.edu.cn

J. Deng
The Medical Laboratory, 404 Hospital, Mianyang, Sichuan 621000, China

J. Lu
Beijing University of Technology, Beijing 100124, China

F. Dong (ed.), *Proceedings of the 11th International Congress for Applied Mineralogy (ICAM)*, Springer Geochemistry/Mineralogy,
DOI 10.1007/978-3-319-13948-7_7

and application researches of its environmental meaning have come out [1, 2]. The recent researches show that minerals can supply microorganisms with energy, little nourishment, and the electronic embracer that metabolic activities need, which is one of indispensability conditions of the microorganism's survival and propagation. On the contrary, microbial metabolism activity also has important influence on mineral deliquescence and deposition [3, 4].

Silicate bacterium is a kind of normal microorganism living in soil. Now they are used to divide impurity from ore and float and raise the valuable metals and there are some researches on ceramics and porcelain craft, industrial wastewater management of mineral smelt, and mineral microorganism fertilizer and microorganism flocculation reagent exploitation realms and have been fruitful [5–8].

Wollastonite is a calcium inosilicate mineral ($CaSiO_3$) that may contain small amounts of iron, magnesium, and manganese substituting for calcium. It is usually white. In 2005, the British Geological Survey reported that China was the top producer of wollastonite with at least 50 % world share followed by India and the USA. Wollastonite has industrial importance worldwide [9]. It is used in many industries, mostly by tile factories which have incorporated it into the manufacturing of ceramic to improve many aspects, and this is due to its fluxing properties, freedom from volatile constituents, whiteness, and acicular particle shape [10–12]. It also can be used in plastic, paint, paper, and friction products [13, 14]. The reports about reciprocity between wollastonite and microorganism are infrequent. The geologic effect of microorganism between wollastonite is also not clear.

This chapter studies the reciprocity effect between wollastonite and a strain of silicate bacterium. It is based on microbe-mineral and maybe provides some references to further research on the intersect domain of mineralogy, microbiology, chemistry, and environmentology.

2 Material and Methods

2.1 Sample Preparation

Minerals: wollastonite was collected from Panshi of Jilin province. All the experimental wollastonite samples were grinded by ceramics and porcelain muller and then sifted by a 200-mesh sifter.

Bactria: The silicate bacteria S35 was provided by Sichuan Agricultural University, isolated from moderate purple soil with pH = 7.26.

2.2 Experimental Method

300 mL nutrient broth and 100 mL glucose solution with the concentration of 3×10^2 mg/mL were confected and then sterilized at 121.3 °C and 1 atm for 20 min.

6 mL glucose solution was added into nutrient broth and shaked up. 160 mg wollastonite samples were weighed and mixed in 10 mL nutrient broth. Then 0.4 mL wollastonite suspension was taken and mixed with 3.4 mL broth and 0.2 mL silicate bacterium suspension solution. 0.2 mL silicate bacterium suspension solution and 3.8 mL nutrient broth were cultured as control. 0.4 mL dust suspension solution and 3.6 mL nutrient broth were mixed and used to wollastonite control without silicate bacterium.

All above testing tubes were cultured for 48 h at 35 °C in the culture box. Firstly, the SEM samples were prepared. Secondly, the residual mixture of each tube was centrifuged 30 min at a speed of 4,000 r/min, and then the upside clear liquid was tested for pH values, GLU, Ca, Mg, etc., and trace elements of Si, Fe, and Mn. The sediment was prepared as FTIR samples.

2.3 Instruments

Biochemical index analysis: STATMT-type biochemistry emergency analysis instrument (America); 7060-type automated biochemistry analysis instrument (Japan). Dust chemical composition analysis: PW1404-type automatic X-ray fluorescence spectroscopic analysis instrument (Holland). SEM analysis: S440-type scanning electron microscopy (Britain). Trace element analysis: autoscan advantage ICP-AES (America). FTIR analysis: Nicolet5700-type FTIR spectrometer (America).

2.4 Scanning Electron Microscopy

Samples were fixed with glutaraldehyde solution (2.5 %) for about 20 h. After fixation, a dehydration series (30–100 %, 20 min) was performed using ethanol and then mounted on metal disks, dried at 30 °C for about 2 h, and coated with gold. The samples were then analyzed using an SEM (LE-S440, England) at an accelerating voltage of 20 kV.

3 Results and Analysis

3.1 Dust Characteristic

The primary characteristic of wollastonite was shown in Table 1. The XRF analysis result showed that experimental wollastonite was mostly made up of a higher content of SiO_2 (50.83 %) and CaO (44.27 %) and a lower content of MgO (0.46 %), Al_2O_3 (0.40 %), and Fe_2O_3 (0.23 %). Otherwise, the characteristic of

Table 1 The chemical component analysis of wollastonite (unit: %)

Index	SiO_2	TiO_2	Al_2O_3	Fe_2O_3	MnO	CaO	MgO	Na_2O	K_2O	P_2O_5	LOI	SNM
Content	50.83	0.05	0.40	0.23	0.03	44.27	0.46	0.05	0.08	0.07	3.49	99.96

Note: *LOI* losing percent of quantity after burning

experimental wollastonite was pH = 8.75 and conductance (κ) = 1.34×10^2 μS/cm in 40 °C water.

3.2 Biochemical Indexes Testing

As shown in Table 2, the GLU residual concentration of testing groups consisted of more than two kinds of control groups. As the initial concentrations of all tubes were same, a small amount of residual concentration implies that the GLU metabolizable quantity of silicate bacteria was much more. It shows that GLU metabolizable quantity was best under the reaction of wollastonite. To a certain extent, it can represent growth status of silicate bacteria under the reaction of wollastonite. The pH value was 6.70 of experimental group, which was between two control groups. The concentrations of Ca^{2+}, Fe^{3+}, and Si^{4+} were higher than two control groups in solution. The concentration of Si element was 30 ppm, and this was equivalent to 7.5 % of the total silicon in wollastonite. It reached 13 times to that of control of mineral, which indicated that silicate bacteria have some stimulative effects to Si element's dissolution.

3.3 SEM Analysis Results

Figure 1 shows the SEM results of the reciprocity between silicate bacterium and wollastonite after 48 h. The surfaces of silicate bacteria cells whose lengths are about 3 μm are smooth and have sunken ditches in them after being cultured for 48 h in broth culture medium in normal conditions (Fig. 1a). Some cells broke due to the autolysis of silicate bacteria (Fig. 1b). The autolysis began from the cell's end, while cells became withered and cell wall broke to appear like lace. Figure 1c and d shows that the cracked phenomenon of silicate bacterial cells was serious. The cell autolysis did not begin from one end, but "fissure" appeared along the bacterial length direction. At the same time, the cells had different degrees of distortions as well as the cell wall became bumpy and fossilized, and cell sizes were different. The interfacial contact degree was very high between cells and wollastonite particles. All the above phenomena show that the growth of environmental change affected the cell shape and autolyzing manner and that they have solubilization effect on mineral elements. Accordingly it affected the growth course of silicate bacteria.

Table 2 The testing results of action between wollastonite and silicate bacterium

Groups	GLU (mmol/L)	pH	Ca^{2+} (mmol/L)	Mg^{2+} (mmol/L)	Na^{+} (mmol/L)	K^{+} (mmol/L)	P^{5+} (mmol/L)	Mn^{2+} 10^{-6}	Si^{4+} 10^{-6}	Fe^{3+} 10^{-6}
I	14.68	6.46	0.18	0.37	134.4	2.65	0.86	0.022	3.203	0.716
II	4.32	6.70	4.07	0.48	135.1	2.80	0.64	0.053	30.450	2.412
III	21.46	7.35	1.29	0.37	135.3	2.65	0.76	0.026	2.412	0.707

Note: I—dust action tubes; II—dust control tubes without bacteria; III—bacterial control tubes without dusts; all the above results are the average values of three teams' experiment

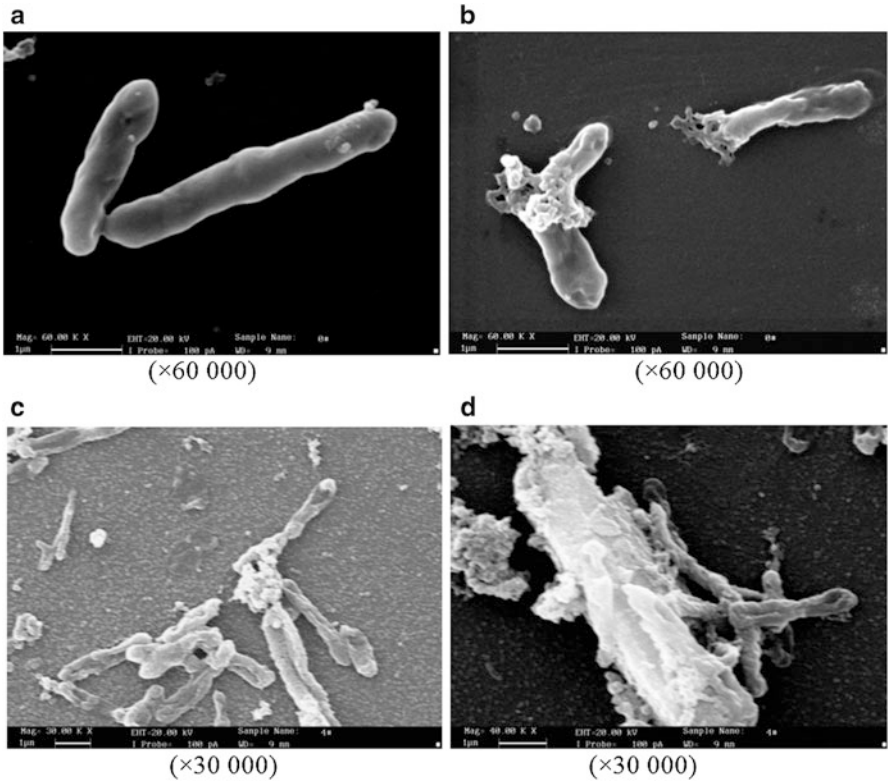

Fig. 1 SEM photos of silicate bacterium after the action of wollastonite. (**a**) Silicate bacterium cells in normal conditions; (**b**) the autolysis of silicate bacterium cells in normal conditions; (**c**) and (**d**) silicate bacterium cells under the action of wollastonite

3.4 FTIR Analysis Results

The FTIR spectra of wollastonite before and after the action with silicate bacterium in the range of 400–4,000 cm^{-1} were taken and the results were showed in Fig. 2. The FTIR spectra of wollastonite can be divided into two parts (in Fig. 2a). The first part is 900–1,100 cm^{-1}, which belongs to the absorption band of Si–O–Si asymmetry stretching vibration and O–Si–O stretching vibration. The second part is 600–700 cm^{-1}, which belongs to the absorption band of Si–O–Si symmetry stretching vibration in silico-oxy tetrahedron of wollastonite crystalloid. As shown in Fig. 2b, three adsorption bands descended obviously at 898 cm^{-1}, 925 cm^{-1}, and 962 cm^{-1}. The intensity ratios of adsorption band between 1,060 cm^{-1} and 898 cm^{-1}, 925 cm^{-1}, and 962 cm^{-1} were shown in Table 3. These can influence the change of groups' vibration in the range of 900–1,100 cm^{-1} and imply the dissolution results of Si element.

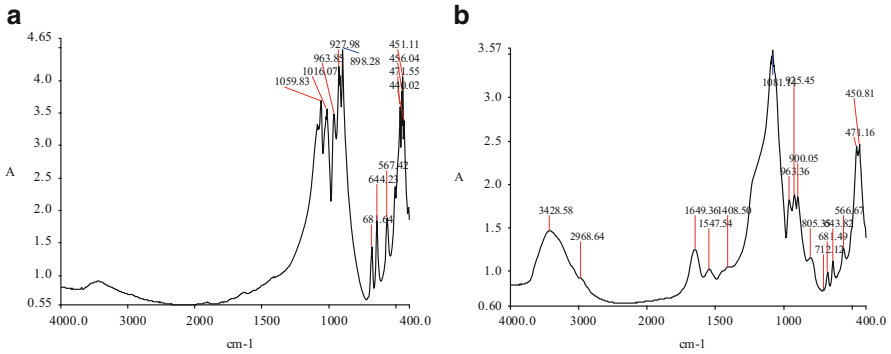

Fig. 2 Infrared absorbency spectra of silicate bacterium with the action of wollastonite. (**a**) Wollastonite control; (**b**) wollastonite under the action of silicate bacterium

Table 3 Infrared absorbency spectra apexes' intensity ratios of silicate bacterium with the action of wollastonite

Intensity ratio	Wollastonite (A)	Wollastonite and silicate bacterium (B)	Comparison
D1060/D962	1.072	1.768	B>A>1.0
D1060/D925	0.914	1.714	B>1.0>A
D1060/D898	0.822	1.741	B>1.0>A

4 Discussions

Bacterial proteins, similar to other proteins, are composed of a series of amino acids. Amino acids are known as zwitterions and have both amine and carboxylic acid functional groups, therefore both an acid and a base at the same time. At a certain pH known as the isoelectric point, an amino acid has no overall charge, and the number of protonated ammonium groups (positive charges) and deprotonated carboxylate groups (negative charges) is equal. The isoelectric of bacterial cell is always in pH 2–5. As the experimental liquid pH values are always above 6.0, the silicate bacterium cell presents negative charges in the course of the action with wollastonite particles. The zeta potential of wollastonite particles is about −20 mV. Ca^{2+} is dissolved by the action of acid and mineral particle surfaces of residues (hydrate of SiO_2) take more negative charges. When silicate bacterium cell autolysis began, positive charges inside cell encounter the negative charges outside environment, the cell autolysis effect accelerated.

The concentration of Si element was 30 ppm in solution, and it was 10 times to that of the control group without silicate bacterium. In recent years, many researches about the mechanisms of desilication from the interaction between silicate mineral and silicate bacterium were reported, but explanations were not quite similar. Some reports expounded desilication as a mechanism by which the mineral structure was broken by silicate bacterium. The mineral components dissolved by organic acid (such as oxalic acid and citric acid, etc.) from silicate

bacterium and particulates emerged outside from bauxite ore. Other researchers considered that abundant amylase outside cells was produced, while little was produced in the course of silicate bacterium growth. Each mineral particulate has good dispersion in this amylose, especially quartz. As other mineral components deposited quickly, the silicon could be bioleached from bauxite ore. The main mechanism of desilication of bauxite ore is bio-floatation by the action of outside cells' amylose. Our experimental result was more in accord with the former mechanism.

The mechanism of pH value change in the liquid with wollastonite is as follows: $CaSiO_3 = Ca^{2+} + [SiO_3]^{2-}$; the groups of $[SiO_3]^{2-}$ are unstable and hydrolyzed as $[SiO_3]^{2-} + 2H_2O = H_2SiO_3 + 2OH^-$; $[SiO_3]^{2-}$ hydrolysis can promote the ionization of wollastonite. Wollastonite has huge dissolved potential in organic acid liquid, and its dissolution has strong relation to functional groups of organic acids. In organic acid liquid with many kinds of function groups, not only Ca element can be dissolved, but also Si element can be dissolved. It includes two reaction courses: the phase of sour alkali neutralizes reaction and the phase of silicon organism forms compounds with the redissolved SiO_2. As silicate bacterium could metabolize glucose and produce organism acid, the dissolution speed of Si element was accelerated in our experiment.

As wollastonite has an abundance of Ca elements, when experimental silicate bacterium acted with wollastonite particles, the Ca element largely dissolved, while only some of Mg element dissolved. There are obvious effects of silicate bacteria on wollastonite in experimental conditions, while there was obvious solubilization of Si element under the action of silicate bacterium. Its mechanism is as follows: Ca and Mg are the absolutely necessary elements in the growth of bacteria. They all drop out of cellularity and are in the state of ion. Mg^{2+} can activate many enzymatic reactions, and it is important in controlling the polymerization of nucleus albumen. Ca controls bacterial physiological state and has contradictory function in some toxicity cations. The pH value of the culture liquid decreases and counteracts almost of OH^- and accelerates the dissolution of dusts by adding main metabolizability products (such as glucose and pyruvic acid) in the course of culturing silicate bacterium. The dissolution of wollastonite can provide necessary nourishment, such as mineral elements (Ca, Mg, Fe, Mn, etc.), to the growth of silicate bacterium. It promotes matter metabolizability, especially glucose metabolizability, and allows the addition of silicate bacterium. At the same time, it adds content of organism acids and energy of some enzymes.

5 Conclusions

1. GLU consumption and pH values had been obviously increased after the interaction between silicate bacterium and wollastonite relative to normal control. This can promote the growth of silicate bacterium. But SEM analysis showed

that the silicate bacterium cell's autolyzing degree increased, the cell distorted, and their surfaces become dry, rot, and lose water badly. This is mainly because Ca and Si have been dissolved from dusts ($CaSiO_3$) in the culture liquid.
2. The concentration of Si element was 30 ppm, and this was equivalent to 7.5 % of the total silicon in wollastonite. It reached 13 times to that of control of mineral, which indicated that silicate bacterium have some stimulative to Si element's dissolution.
3. Three peaks in the FTIR spectra of wollastonite (898 cm^{-1}, 925 cm^{-1}, 962 cm^{-1}) descended obviously after the action of silicate bacterium, which shows that Si has dissolved.

The growth effect research of silicate bacterium to wollastonite and the other minerals on surface electricity, shape, elementary characteristic, etc., still need further experiment.

Acknowledgements The authors gratefully acknowledge the following institutions for their support: the National Nature Science Foundation of China and China Academy of Engineering Physics for financial Grant of NSAF (11176028), the National Natural Science Foundation of China (41102212, 41130746), Sichuan Province Department of Education fund (11ZB105), and the Natural Science Foundation of Southwest University of Science and Technology (12ZX7121).

References

1. Xie XD, Zhang GS (2001) Environmental significance of the interaction between minerals and microbes. Acta Petrol Mineral 20(4):382–386
2. Dopson M, Lövgren L, Boström D (2009) Silicate mineral dissolution in the presence of acidophilic microorganisms: implications for heap bioleaching. Hydrometallurgy 96 (4):288–293
3. Dai QW, Dong FQ, Deng JJ (2009) Effect of several kinds of mineral dusts to the growth of silicate bacterium S35. Acta Geol Sin 22(2):179–183
4. Chaerun SK, Tazaki K, Asada R, Kogure K (2005) Interaction between clay minerals and hydrocarbon-utilizing. Clay Miner 40:105–114
5. Feng YL, Wang HJ, Li HR et al (2008) A bioflocculant-producing silicate bacterium screening and its flocculating activity. J Cent South Univ Sci Technol 39(5):934–939
6. Lian B, Fu PQ, Mo DM (2002) A comprehensive review of the mechanism of potassium releasing by silicate bacterium. Acta Mineral Sin 22(2):179–183
7. Niu YJ, Qiu GZ, Zhou JK (2004) Screening of silicate bacterium and bioleaching silicon from bauxite. Chin J Nonferrous Met 14(2):280–285
8. Yilmaz EI (2003) Metal tolerance and biosorption capacity of bacillus circulans strain EB1. Res Microbiol 154(6):409–415
9. Virta RL, Revette D (2006) Wollastonite. Min Eng 58(6):61–62
10. Cannillo V, Pierli F, Sampath S et al (2009) Thermal and physical characterisation of apatite/wollastonite bioactive glass-ceramics. J Eur Ceram Soc 29(4):611–619
11. Vakifahmetoglu C, Park J, Korkusuz F et al (2009) Production and properties of apatite-wollastonite ceramics for biomedical applications. InterCeram Int Ceram Rev 58(2–3):86–90

12. Ransinchung RNGD, Kumar B (2010) Investigations on pastes and mortars of ordinary portland cement admixed with wollastonite and microsilica. J Mater Civil Eng 22(4):305–313
13. Xin RL, Zhang QY, Gao JH (2010) Identification of the wollastonite phase in sintered 45S5 bioglass and its effect on in vitro bioactivity. J Non Cryst Solids 356(23–24):1180–1184
14. Sarang S, Misra RDK (2004) Strain rate sensitive behavior of wollastonite-reinforced ethylene-propylene copolymer composites. Mater Sci Eng A 381(1–2):259–272

Process Mineralogy of Lateritic Nickel Ore

Daniel Uliana, M. Manuela M. Lé Tassinari, Henrique Kahn, and Marco Antonio Angora

Abstract This chapter presents a methodology for studying low-grade lateritic nickel ore, which usually presents complex mineralogy, with widespread nickel in several mineral phases. The study is focused on determining the mineralogy and the distribution of nickel in the bearing minerals. Laboratory assays comprise homogenization, sampling, and particle size analysis. Chemical analyses by X-ray fluorescence are performed in all fraction sizes, while mineralogical assessments by X-ray diffraction are carried out for the head samples. The mineralogical composition of the samples and the partition of main elements in the bearing minerals are assayed by size fraction through automated image analysis software (MLA) coupled with a scanning electron microscope (SEM). The chemical compositions of the several minerals identified in MLA are determined during systematic observations on SEM with energy-dispersive spectrometer (EDS).

Two samples of lateritic nickel ore have been characterized, one silicate and other oxidized, with nickel grades of 0.60 and 0.28 wt%, respectively. The nickel grades in the oxidized ore vary from 0.16 to 0.26 wt% above 0.037 mm, increasing to 0.41–0.42 wt% below this fraction, where 79 wt% of total nickel is contained. In the silicate ore, the nickel grades vary from 0.42 to 0.47 wt% above 0.15 mm, where 36 wt% of the total nickel are present, while the nickel grades below this fraction increase, varying from 0.60 to 0.68 wt%; the fraction −0.020 mm is responsible for 38 % of total nickel present in the sample.

The silicate ore mineralogy consists mainly of clay minerals with nickel (67 wt%; vermiculite/smectite group) and pyroxene (22 wt%), besides minor phases like goethite, kaolinite, quartz, Cr-spinel, and other minerals. The oxidized ore is composed essentially of goethite (49 wt%) and Cr-spinel (41 wt%), besides quartz, kaolinite, Ni clay minerals, hematite, and other minor phases. Considering the interval −0.30 +0.020 mm, in the silicate ore, the clay minerals are responsible for 93 wt% of total nickel contained, while goethite responds for 93 wt% of total nickel present in the oxidized ore.

D. Uliana (✉) • M.M.M. Lé Tassinari • H. Kahn
Mining and Petroleum Engineering Department, Polytechnic School, University of Sao Paulo, Av. Prof. Mello Mores, 2373 Sao Paulo, SP, Brazil
e-mail: daniel@lct.poli.usp.br

M.A. Angora
Votorantim Metais, Nickel Business Unit, Av. Dr. José Artur Nova, 1309 Sao Paulo, SP, Brazil

F. Dong (ed.), *Proceedings of the 11th International Congress for Applied Mineralogy (ICAM)*, Springer Geochemistry/Mineralogy,
DOI 10.1007/978-3-319-13948-7_8

Keywords Nickel ore • Process mineralogy • Automated mineralogy • Image analysis

1 Introduction

Although about 70 % of world nickel reserves are contained in laterites, they account for only 40 % of the world's nickel production, as the major source is still dominated by sulfide ores since its discovery in the early twentieth century. However, most of the expansion in nickel production capacity over the next years will come from processing of lateritic ores [1]. Chemical and mineralogical compositions of laterites from different origins and depths can vary quite significantly, thus requiring different alternatives in the metallurgical process [2].

The nickel lateritic deposits are formed by intense weathering of ultramafic rocks, mostly from Cenozoic age. They occur mainly in the area of tropical climate like in New Caledonia, Philippines, and Brazil [3]. Some Brazilian lateritic nickel ores are not only derived from the weathering of dunite and peridotite but from the weathering of pyroxenite, with Ni-rich smectite as a major Ni-bearing mineral present, different from most of the world's nickeliferous laterite deposits [4].

The objective of this work is to characterize two Brazilian lateritic nickel ore types from different weathering horizons, focusing on the determination of mineralogical composition and distribution of nickel in the bearing minerals.

2 Materials and Methods

2.1 Studied Samples

The studies were performed on two samples of low-grade lateritic nickel ores from different horizons of the weathering mantle: the first corresponds to a silicate ore (saprolitic/smectite-rich horizon) and the second is related to an oxidized ore (limonitic/goethite-rich horizon). The initial weight of each sample was about 5 kg.

2.2 Sample Preparation

The layout of the experimental procedure adopted is displayed in Fig. 1 and included the activities described as follows.

The homogenization and sampling of representative aliquots were performed by elongated piles and Jones splitter, while the sieve-size analysis was carried out by wet screening with screen size apertures of 0.30, 0.15, 0.10, 0.074, 0.044, 0.037, and 0.020 mm.

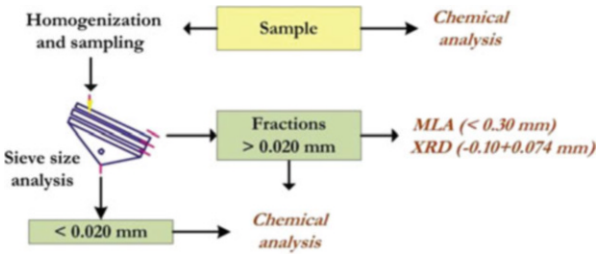

Fig. 1 Experimental procedure layout

Mineralogical assessments were conducted by SEM-based automated search for the sizes fractions between 0.30 and 0.020 mm, as well as X-ray diffraction analysis was performed in −0.10+0.074 mm size fraction of each sample.

Chemical analyses were held in all generated fractions and also in the head samples.

2.3 Methods for Assessment and Analysis

2.3.1 Chemical Analysis

Chemical analyses were carried out by X-ray fluorescence (XRF) in pressed pellets, by means of Axios Advanced spectrometer (PANalytical) with determination of Ni, Cr, Fe, SiO_2, Al_2O_3, CaO, MgO, TiO_2, and MnO. Loss on ignition (LOI) was also performed by sample calcinations in a muffle furnace at 1,050 °C for 1 h.

2.3.2 X-ray Diffraction

The mineralogical analysis by X-ray diffraction (XRD) was performed by powder method in X-ray diffractometer X'Pert PRO with X'Celerator detector (PANalytical). The identification of crystalline phases was obtained by comparing the diffraction patterns with the database ICDD—International Centre for Diffraction Data (2003).

2.3.3 SEM-Based Automated Mineralogy

The study by scanning electron microscopy (SEM) was carried out in polished sections, previously coated with a carbon film.

The qualitative and semiquantitative evaluation of chemical elements present in the several minerals was accomplished by Stereoscan 440 microscope (LEO) with energy-dispersive spectrometer (EDS, Oxford) with Si detector and microanalysis system INCA (Oxford).

The mineralogical composition of the samples and the partition of the main elements in the bearing minerals were performed through automated image analysis software (Mineral Liberation Analyzer—MLA) coupled with a scanning electron microscope Quanta 600 FEG (FEI) with EDS (Bruker) and microanalysis system Esprit (Bruker). The automated mineralogic search was held by XBSE mode, considering such the atomic number contrast as the chemical composition of each mineral phase (backscattered electron images and characteristic X-ray spectra by EDS).

3 Results

3.1 Chemical Composition

The chemical compositions of the samples are presented in Table 1. The Ni grade in silicate ore is 0.60 wt%, while in oxidized ore is 0.28 wt%. On one hand, silicate ore presents the highest grades of SiO_2 (50.1 wt%), MgO (10.9 wt%), and CaO (4.88 wt%), against 10.1, 2.42, and 0.50 wt% in the oxidized ore, respectively. On the other hand, oxidized ore shows the highest grades of Fe (35.9 wt%), Al_2O_3 (11.2 wt%), and Cr (10.8 wt%), against 11.6, 7.56, and 0.85 wt%, respectively. The grades of TiO_2 are comprehended between 0.25 and 0.42 wt%, while MnO grades range from 0.39 to 0.56 wt%. Loss on ignition (LOI) corresponds to 6.91 wt% in the silicate ore and 7.03 wt% in the oxidized ore.

3.2 Particle Size Analysis

Cumulative distribution curves for weight, Ni, Fe, SiO_2, Al_2O_3, and MgO are presented in Fig. 2.

In the silicate ore, the distribution curves of Ni as well as Al_2O_3 and Fe show a concentration trend in the fine size fractions: about 40–45 wt% of total nickel, aluminum, and iron present in the sample are contained below 0.020 mm. Otherwise, MgO has the opposite behavior, with only 15 wt% below 0.020 mm and 60 wt% between 0.30 and 0.020 mm.

For the oxidized ore, 61 wt% of total nickel and iron present in the sample are contained below 0.020 mm. In the meantime, MgO total content between 0.30 and 0.020 mm corresponds to about 80 wt%.

Table 1 Chemical compositions of head samples

	Grades (wt%)									
Sample	Ni	Cr	Fe	SiO_2	Al_2O_3	CaO	MgO	TiO_2	MnO	LOI
Silicate	0.60	0.85	11.60	50.10	7.56	4.88	10.90	0.42	0.39	6.91
Oxidized	0.28	10.80	35.90	10.10	11.20	0.50	2.42	0.25	0.56	7.03

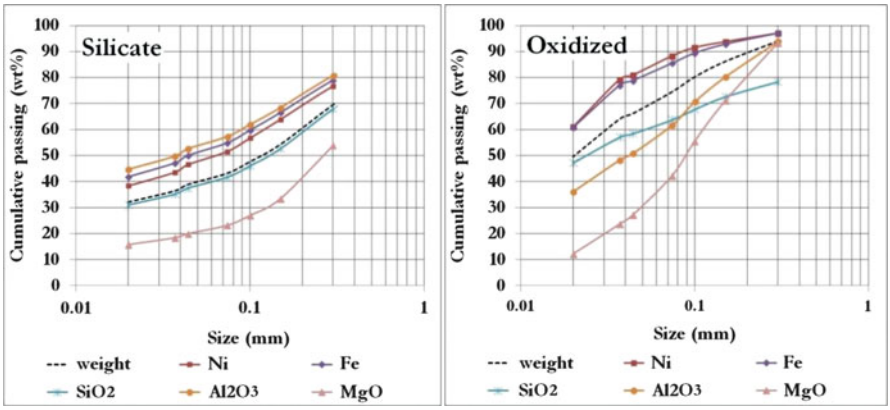

Fig. 2 Weight and major elements distribution by grain size

Table 2 Mineralogical composition of the studied samples—MLA (total −0.30+0.020 mm)

Size fraction (mm)	Total −0.30 +0.020	−0.30 +0.15	−0.15 +0.10	−0.10 +0.074	−0.074 +0.44	−0.044 +0.037	−0.037 +0.020
Silicate							
Ni clay minerals	67.0	56.0	74.0	72.0	75.0	76.0	80.0
Enstatite	8.1	13.0	6.0	5.9	3.2	3.2	2.0
Diopside	14.0	22.0	10.0	11.0	9.0	6.7	5.5
Quartz	2.2	2.2	2.3	2.1	2.1	2.0	2.2
Kaolinite	2.9	2.4	2.6	3.3	3.5	4.0	3.8
Goethite	3.2	2.5	3.1	3.0	4.1	5.2	3.9
Cr-spinel	1.4	1.1	0.9	1.8	2.1	2.1	1.6
Others	0.6	0.5	0.6	0.6	0.7	0.6	0.7
Oxidized							
Ni clay minerals	0.4	0.4	0.5	0.5	0.5	0.3	0.2
Quartz	3.8	6.0	5.8	5.4	4.7	3.6	0.6
Kaolinite	3.5	4.2	3.6	3.8	4.4	1.8	2.7
Goethite	49.0	13.0	15.0	31.0	45.0	43.0	93.0
Hematite	2.6	2.8	2.7	3.1	3.7	4.9	1.3
Cr-spinel	41.0	73.0	72.0	56.0	42.0	47.0	2.4
Others	0.2	0.3	0.5	0.2	0.2	0.3	0.1

3.3 Mineralogical Composition

The mineralogical composition of the samples (total $-0.30+0.020$ mm), highlighted in Table 2, was determined by MLA and supported by XRD and SEM/EDS analyses.

Analysis by XRD of silicate ore indicates the presence of clay minerals from vermiculite and/or smectite group, besides pyroxene (diopside and enstatite) and quartz. In the oxidized ore, the XRD results show the presence of spinel, goethite, hematite, quartz, and incipient kaolinite.

The silicate ore is constituted by 67 wt% of clay minerals with Ni (verified in the SEM/EDS analysis), 22 wt% of pyroxene (14 wt% diopside and 8.1 wt% enstatite), besides goethite and kaolinite (around 3 wt% each), quartz (2.2 wt%), and Cr-spinel (1.4 wt%).

The mineralogical composition of oxidized ore comprises mostly goethite (49 wt%) and Cr-spinel (41 wt%), in addition to quartz (3.8 wt%), kaolinite (3.5 wt%), and hematite (2.6 wt%).

Other trace minerals such as ilmenite, manganese oxides, feldspar, apatite, carbonates, and sulfides are present in both samples.

3.4 Characteristics of Nickel Bearing Minerals

Some features of the main nickel bearing minerals observed in SEM/EDS analysis are illustrated from Photomicrographs 1, 2, 3 to 4.

In the silicate ore, the clay minerals hold the most part of nickel present in the sample, with nickel grades ranging from 0.3 up to 11 wt%. Otherwise, nickel contained in the oxidized ore is mainly associated with goethite, which has nickel grades varying from 0.3 to 1.5 wt%.

The average composition of these clay minerals, estimated by several SEM-EDS measurements, comprises 58 wt% of SiO_2, 10 wt% of Fe, 7.1 wt% of MgO, 6.6 wt% of Al_2O_3, and 1.0 wt% of Ni. Traces of calcium, titanium, chromium, and copper are also observed. Likewise, the average composition estimated for goethite consists of 55 wt% of Fe, 5.0 wt% of Al_2O_3, 2.9 wt% of Cr, 2.3 wt% of SiO_2, and 0.5 wt%

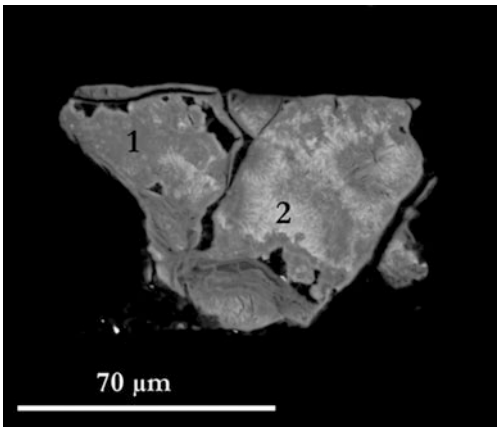

Photomicrograph 1 Detail of clay minerals with compositional zoning: nickel content ranges from 1.3 (1) to 11 wt% (2); chromium grades are between 0.3 and 0.5 %

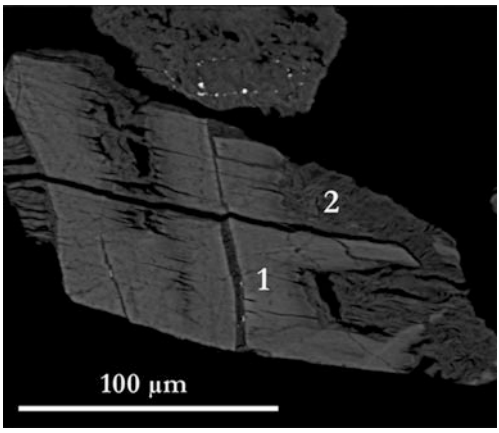

Photomicrograph 2 Clay minerals with nickel grades between 0.5 wt% (2) and 5.6 wt% (1)

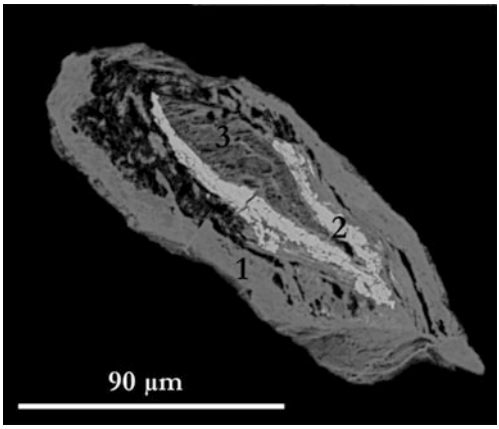

Photomicrograph 3 Relict hematite (2) free of nickel, amidst goethite (1 and 3) with nickel grades between 0.5 and 0.7 wt%

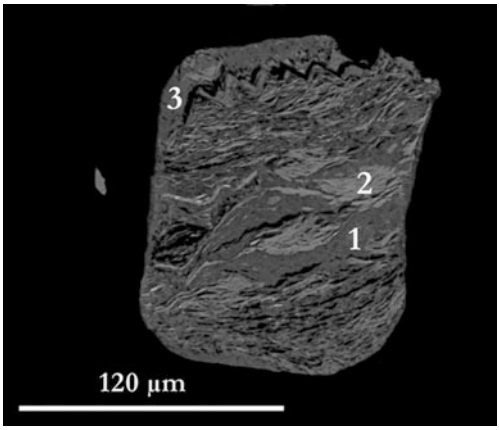

Photomicrograph 4 Detail of microcrystalline goethite/limonite with different hydration degrees, containing 0.5–0.6 wt% of nickel

of Ni and MnO, besides traces of TiO_2. These average compositions are then inputted in MLA mineral database for elemental distribution calculations.

3.5 Validation of MLA Results

The comparison of XRF-assayed grades with MLA-calculated grades shows good correlation for Ni, Cr, Fe, Al_2O_3, and MgO contents ($R2 > 0.95$), thus ensuring the reliability of the sample splitting and polished sections preparation as well as the average chemical compositions inputted for major mineral phases identified in MLA. Fig. 3 illustrates the correlation between XRF-assayed and MLA-calculated nickel grades for both samples.

3.6 Elemental Distribution

The distributions of nickel in the bearing minerals are shown in Fig. 4. For the silicate ore, the clay minerals respond for 93 wt% of total nickel present in the sample, whereas 3 wt% are associated with goethite, 2 wt% to enstatite, and 2 wt% to Cr-spinel. In a different way, goethite is responsible for 93 wt% of total nickel content in the oxidized ore; clay minerals account for 6 wt% and Cr-spinel for only 1 wt%.

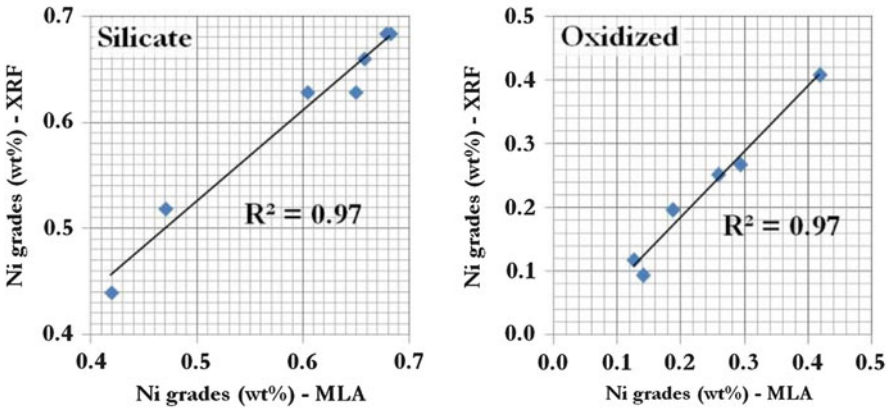

Fig. 3 Comparison between XRF-assayed Ni grades and MLA-calculated Ni grades

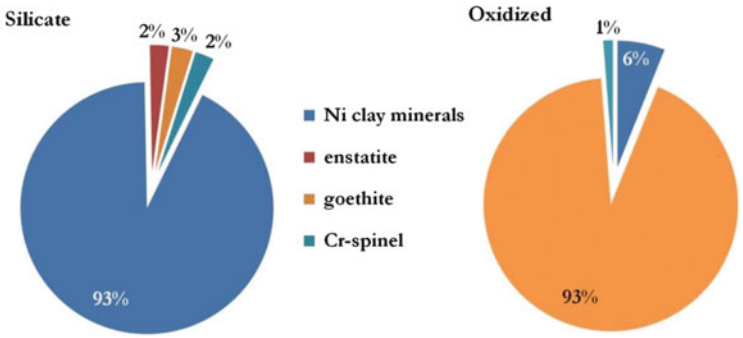

Fig. 4 Distribution of nickel in the bearing minerals—MLA

4 Final Considerations

Based on the results obtained in the mineralogical characterization of the two samples studied, it was possible to highlight the main differences between the two ore types, with a primary focus on the mineralogy and distribution of nickel in bearing minerals in order to guide the type of process to be used for nickel recovery for each type of ore.

The silicate ore sample, which has nickel content of 0.60 %, presents also a high content of SiO_2 (50.1 wt%) and significant amounts of MgO and CaO (10.9 and 4.88 wt%, respectively). About 40 wt% of nickel present in the sample are contained below 0.020 mm. Considering the range −0.30+0.020 mm, the sample is composed of 67 wt% of clay minerals from smectite group, which have an average grade of 1 % nickel and are responsible for 93 % of nickel contained in the particle size range studied.

Regarding the oxidized ore, which presents nickel content of 0.28 %, it has a high iron content (35.9 wt%) with significant amounts of Al_2O_3, SiO_2, and Cr (11.2, 10.8, and 10,1 wt%, respectively). Approximately 60 wt% of nickel contained in the sample is present below 0.020 mm. Concerning the particle size range studied (total −0.30+0.020 mm), the sample is predominantly composed of goethite (49 wt%) and Cr-spinel (41 wt%). The main nickel bearing mineral in oxidized ore is goethite, which presents the average nickel content of 0.5 wt% and accounts for 93 % present.

Acknowledgments The authors are grateful to Votorantim Metais, Nickel Business Unit, for permitting the publication of these study results and also to the financial support of FAPESP—Sao Paulo Research Foundation, process 2009-54007-0 to carry out this research.

References

1. Dalvi AD, Bacon WG, Osborne RC (2004) The past and the future of nickel laterites. Inco Limited, Ontario
2. Wang B, Guo Q, Wei G, Zhang P, Qu J, Qi T (2012) Characterization and atmospheric hydrochloric acid leaching of a limonitic laterite from Indonesia. Hydrometallurgy 129–130:7–13
3. Oliveira SMBD (1990) Estágio atual do conhecimento a cerca do minério laterítico de níquel no Brasil e no mundo. Rev Inst Geol 11(2):49–57
4. Colin F, Nahon D, Trescases JJ, Melfi AJ (1990) Lateritic weathering of pyroxenites at Niquelandia, Goias, Brazil; the supergene behavior of nickel. Econ Geol 85(5):1010–1023

The Optimal Conditions of Preparation of Phosphogypsum-Based Calcium Sulfate Hemihydrate Whiskers by Hydrothermal Method Using Phosphogypsum

Faqin Dong, Hua He, Ping He, Wei Yang, and Longhua Xu

Abstract Calcium sulfate hemihydrate whisker was prepared successfully by hydrothermal method with phosphogypsum; the morphology and synthesis rate of calcium sulfate hemihydrate whisker were very sensitive to reaction temperature, reaction time, and additives. Therefore, L25(5^6) orthogonal experiments were carried out to obtain the optimal conditions. Composition, morphology, and structure of calcium sulfate hemihydrate whisker were characterized by SEM, XRD, and FT-IR. The results showed that the optimal conditions were ball-milling time 1.5 h, reaction temperature 160 °C, reaction time 2 h, solid–liquid mass ratio 1:20, V (glycerol)/V (solution) = 10 %, and drying temperature 140 °C. Calcium sulfate hemihydrate whisker synthesis rate was 95 %; its aspect ratio was up to 45.

Keywords PG • Hydrothermal method • Calcium sulfate hemihydrate whisker • Optimal conditions

F. Dong (✉)
School of Environmental Resource and Engineering, SWUST, 59 Qinglong Road, Mianyang, Sichuan, People's Republic of China

Key Laboratory of Solid Waste Treatment and Resource Recycle, Ministry of Education, School of Materials Science and Engineering, SWUST, 59 Qinglong Road, Mianyang, Sichuan, People's Republic of China
e-mail: fqdong@swust.edu.cn

H. He • P. He • W. Yang
School of Environmental Resource and Engineering, SWUST, 59 Qinglong Road, Mianyang, Sichuan, People's Republic of China

L. Xu
Key Laboratory of Solid Waste Treatment and Resource Recycle, Ministry of Education, School of Materials Science and Engineering, SWUST, 59 Qinglong Road, Mianyang, Sichuan, People's Republic of China

F. Dong (ed.), *Proceedings of the 11th International Congress for Applied Mineralogy (ICAM)*, Springer Geochemistry/Mineralogy,
DOI 10.1007/978-3-319-13948-7_9

1 Introduction

Phosphogypsum (PG) as a by-product was obtained from the production of phosphoric acid [6]. PG contains $CaSO_4 \cdot 2H_2O$ mainly and some impurities such as phosphates, fluorides, silicon [2], etc. Over 150 million and 10 million tons of PG were produced per year in the world and China, but only 4.3–4.6 % and 2–3 % were reasonably utilized [12]. A great quantity of PG was dumped as residue which caused heavy financial burden and environmental pollution such as occupying lots of lands and polluting water resources [9]. Therefore, the reasonable processing and effective utilization of PG brook no delay.

Calcium sulfate hemihydrate (HH) whisker is a kind of fiber-shaped single crystal with the mean diameter of 1–3 μm and the mean aspect ratio of 30–80 [13]. HH whisker was the most promising reinforcement and seemed to be calcium sulfate based due to its high intensity, high corrosion resistance, good thermal stability, nonpoisonous nature, and low price [11]. Thus, HH whisker combines reinforcement with low price, both improving mechanical performance and extending application area [10].

Hydrothermal homogeneous precipitation is a useful method of preparing large and non-aggregated crystals and whiskers with high crystallinity, controllable aspect ratio, high purity, and low dislocation density [1]. To control the crystallization of calcium sulfate, many researchers have studied the factors that govern the precipitation and dissolution of the sparingly soluble calcium salts, including temperature, supersaturation, seeding, organic or inorganic additives [3], etc. Despite considerable research on the formation of calcium sulfate in aqueous media, many uncertainties remain concerning the formation of these salts under variable conditions of the solutions, especially hydrothermal conditions [5].

To obtain the optimal conditions of preparation of HH whisker by hydrothermal method of using PG, in this present work, L25(56) orthogonal experiments were carried out to explore the effect of ball-milling time, reaction temperature, reaction time, solid–liquid mass ratio, V (glycerol)/V (solution), and drying temperature on the morphology, pattern, and productivity of the as-prepared HH whisker.

2 Materials and Methods

2.1 Materials

Glycerol of analytical grade was bought from Chengdu Kelong Chemical Regent Factory, China. Phosphogypsum was provided by the Guangxi Luzhai Chemical Fertilizer Company. Distilled water was self-made.

2.2 Methods

Phosphogypsum, pretreated with 0–2 h ball-milling and distilled water [8], was firstly added into the Teflon stainless steel autoclave with an inner volume of 50 cm^3, and then 20 ml distilled water and designated volume of glycerol were added into the reactor, respectively, stirring it with a glass rod and aged at 100–180 °C for 1–5 h. Then the autoclave was cooled down to room temperature naturally and product was washed with distilled water and dried at 100–180 °C for 5 h.

2.3 Analysis

The morphology of the samples was examined with scanning electron microscope (SEM, TM-1000, Hitachi Ltd., Japan). The pattern of the samples was identified by an X-ray powder diffractometer (XRD, X'pert PRO, Panake, Holland) using Cu Kα radiation ($\lambda = 1.54178$ Å). Crystal morphology and the length and diameter of the samples were measured by the optical microscope (Nikon Corporation, Japan, ECLIPSE E200). The aspect ratio of samples was calculated by the statistical method.

3 Results

The results of L25(56) orthogonal experiments were shown in Table 1. The results show that the optimal conditions of preparation of HH whisker by hydrothermal method using PG were the following: ball-milling time was 1.5 h, reaction temperature was 160 °C, reaction time was 2 h, solid–liquid mass ratio was 1:20, V (glycerol)/V (solution) = 10 %, and dry temperature was 140 °C. The morphology and pattern of HH whisker prepared on the condition of the optimal condition were shown in Figs. 1 and 2.

4 Discussion

As we know, the morphology, pattern, and productivity of HH whisker are very sensitive to the preparing conditions [4], and we have the same conclusion in our work. It was found that the reaction temperature, reaction time, ball-milling time, dry temperature, and solid–liquid mass ratio were all the factors [7].

Table 1 L25(56) orthogonal experimental results, the optimal conditions were ball-milling time 1.5 h, reaction temperature 160 °C, reaction time 2 h, solid–liquid mass ratio 1:20, V (glycerol)/V (solution) 10 %, and dry temperature 140 °C

Factors numbers	Ball-milling time (h)	Reaction temperature (°C)	Reaction time (h)	Solid–liquid mass ratio	V (glycerol)/V (solution)	Dry temperature (°C)	Mean aspect ratio	Synthetic ratio (%)	Total points
1	0	100	1	1:5	10 %	100	0	0	0
2	0	120	2	1:10	30 %	120	26	24	50
3	0	140	3	1:15	50 %	140	42	63	105
4	0	160	4	1:20	70 %	160	45	87	132
5	0	180	5	1:25	90 %	180	38	29	67
6	0.5	100	2	1:15	70 %	180	0	0	0
7	0.5	120	3	1:20	90 %	100	27	25	52
8	0.5	140	4	1:25	10 %	120	44	80	124
9	0.5	160	5	1:5	30 %	140	43	78	121
10	0.5	180	1	1:10	50 %	160	35	88	123
11	1	100	3	1:25	30 %	160	0	0	0
12	1	120	4	1:5	50 %	180	28	27	55
13	1	140	5	1:10	70 %	100	43	83	126
14	1	160	1	1:15	90 %	120	42	85	127
15	1	180	2	1:20	10 %	140	35	93	128
16	1.5	100	4	1:10	90 %	140	0	0	0
17	1.5	120	5	1:15	10 %	160	33	38	71
18	1.5	140	1	1:20	30 %	180	43	94	137
19	1.5	160	2	1:25	50 %	100	45	95	140
20	1.5	180	3	1:5	70 %	140	36	65	101
21	2	100	5	1:20	50 %	120	0	0	0
22	2	120	1	1:25	70 %	140	30	32	62
23	2	140	2	1:5	90 %	160	43	90	133

24	2	160	3	1:10	10 %	180	40	88	128
25	2	180	4	1:15	30 %	100	34	70	104
K1	70.800	0.000	89.800	82.000	92.600	84.400			
K2	84.000	58.000	90.200	87.800	82.400	60.200			
K3	87.200	125.000	79.600	81.400	84.600	103.400			
K4	89.8000	132.000	83.000	89.800	84.200	91.800			
K5	87.8000	104.600	77.000	78.600	75.800	79.800			
Range	19.000	132.000	13.200	11.200	16.800	43.200			

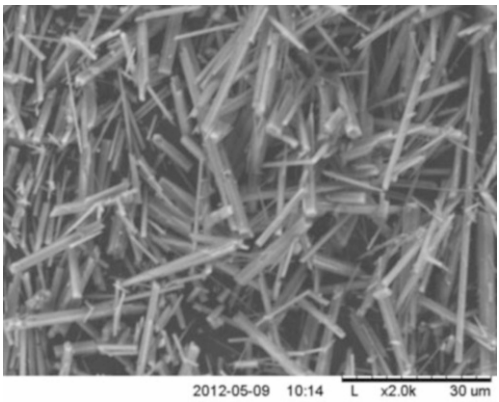

Fig. 1 SEM characterization of HH whisker

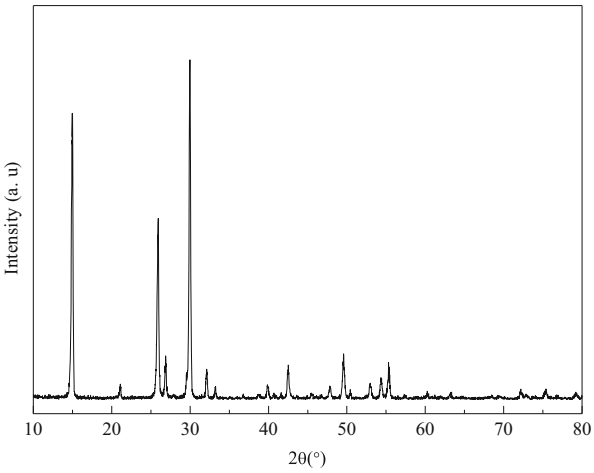

Fig. 2 XRD pattern of HH whisker

4.1 Effect of Ball-Milling Time

The granularity of PG was directly determined by the ball-milling time. Too large granularity goes ill with the dissolution of PG; it took a longer time for the solution to reach saturation, so the quantity of formation of crystal nucleus was little, and the morphology, crystallinity, and productivity of as-prepared HH whisker were poor. However, too small granularity of PG causes the solution to easily dissolve and reach saturation very fast and results in the formation of a large number of crystal nuclei, so the length of HH whisker was very short and the aspect ratio was small. Thus, appropriate quantity of crystal nucleus should be formed at proper granularity of PG, we chose 0, 0.5, 1, 1.5, and 2 h as ball-milling time in our experiments; it was indicated that the morphology, pattern, and productivity of HH whisker were better when the ball-milling time was 1.5 h.

4.2 Effect of Reaction Temperature

Reaction temperature plays an important role in the preparation of HH whisker by hydrothermal method using PG, which affected the dissolution rate of PG and the solution compositions. The product formed at 100 °C was mainly composed of irregular $CaSO_4 \cdot 2H_2O$ plates and amount of minor poor crystalline $CaSO_4 \cdot 0.5H_2O$. Increase of temperature from 100 to 160 °C led to an increase of crystallinity of $CaSO_4 \cdot 0.5H_2O$ and aspect ratio. The product formed at 160 °C was composed of crystalline $CaSO_4 \cdot 0.5H_2O$ completely. The above results indicated that the conversion of $CaSO_4 \cdot 2H_2O$ to $CaSO_4 \cdot 0.5H_2O$ might have taken place via the dissolution–precipitation route. $CaSO_4 \cdot 0.5H_2O$ whiskers with varying morphologies formed at 120–180 °C. Irregular whiskers appeared at 120 °C and crystalline whisker, aspect ratio 0–45, was produced at 120–180 °C. Further increase of temperature to 180 °C led to the formation of the $CaSO_4 \cdot 0.5H_2O$ whisker with thinner diameters and shorter lengths. The gradual decrease of crystallinity of $CaSO_4 \cdot 0.5H_2O$ with increasing temperature from 160 to 180 °C indicated that the maximum stability of $CaSO_4 \cdot 0.5H_2O$ is at 160 °C. The conversion of the calcium sulfates took place via the dissolution–precipitation route and depended closely on temperature.

4.3 Effect of Reaction Time

As we know, the formation of HH whisker includes the formation of crystal nucleus, crystal growth along the c axis, second growth, and growth stop stage. The process of preparation of HH whisker took a long time, so a proper reaction time was needed. Otherwise, the length of HH whisker was too short and resulted in small aspect ratio, and the morphology, crystallinity, and productivity of as-prepared HH whisker were poor. It was found that the growth of whisker was not complete, and the length and diameter of the whisker were uneven when the reaction time was 1 h. With the increase of reaction time from 2 to 5 h, the length and diameter of whiskers increased and the structure became regular. But the aggregation became serious with the increase of reaction time. Furthermore, the secondary nucleation occurred on the surface of whiskers and the original crystals gradually dissolved or broke. Considering both the performance of as-prepared production and consumption of energy, 2 h was the optimal reaction time.

4.4 Effect of Solid–Liquid Mass Ratio and V (Glycerol)/V (Solution)

$CaSO_4 \cdot 2H_2O$ was a kind of insoluble salt, so glycerol was added in our experiments to promote the solubility of $CaSO_4 \cdot 2H_2O$ as well as to help the formation of HH whisker. If the initial solid–liquid mass ratio was too large, the reaction solution reached saturation immediately, the HH whisker was short, and the productivity was low. However, when the initial solid–liquid mass ratio was too small, the mass transfer rate slowed down, it took a long time for the reaction solution to reach saturation, the consumption of energy was huge, and the cost of HH whiskers increased. 1:20 was the optimal initial solid–liquid mass ratio.

Although the addition of glycerol could promote the solubility of $CaSO_4 \cdot 2H_2O$ and the formation of HH whisker, when V (glycerol)/V (solution) was large and the viscosity of the reaction solution was large, it resulted in slowed down mass transfer rate and the aggregation of HH whiskers became serious. That could affect the performance of HH whisker used in organic modification. It was found that there was not even HH whisker formed in pure glycerol solution by hydrothermal method using PG. It was indicated that V (glycerol)/V (solution) = 10 % was the optimal. The reason was that the nucleation of whisker increased significantly with the increase of supersaturation, which changed the radial and axial growth rate of the whiskers and resulted in the increase of whisker diameter and decrease of length to diameter ratio.

4.5 Effect of Dry Temperature

Higher drying temperature could shorten the drying time and decrease the cost of HH whiskers. But when the dry temperature exceeds 180 °C, $CaSO_4 \cdot 0.5H_2O$ will lose 0.5 water, which resulted in HH whisker effectiveness. So we chose 100–180 °C as drying temperature in our experiments; comprehensively considering the effectiveness of drying and the cost of HH whisker, it was found that 140 °C was the optimal drying temperature.

5 Conclusions

HH whisker, with good morphology and good crystallization, was successfully prepared by hydrothermal method using PG. The morphology, crystallization, and productivity of HH whisker were very sensitive to the preparation conditions. The results of L25(56) orthogonal experiments show that the optimal conditions of preparation of HH whisker by hydrothermal method using PG were the following: ball-milling time was 1.5 h, reaction temperature was 160 °C, reaction time was 2 h,

solid–liquid mass ratio was 1:20, V (glycerol)/V (solution) = 10 %, and drying temperature was 140 °C.

References

1. Amani A-O, Demopoulos GP (2009) Gypsum crystallization and hydrochloric acid regeneration by reaction of calcium chloride solution with sulfuric acid. Hydrometallurgy 96:95–102
2. Canut MMC, Jacomino VMF, Bratveit K, Gomes AM, Yoshida MI (2008) Microstructural analyses of phosphogypsum generated by Brazilian fertilizer industries. Mater Charact 59:365–373
3. Chindaprasirt P, Boonserm K, Chairuangsri T, Vichit-Vadakan W, Eaimsin T, Sato T, Pimraksa K (2011) Plaster materials from waste calcium sulfate containing chemicals, organic fibers and inorganic additives. Constr Build Mater 25:3193–3203
4. Guan BH, Yang LC, Wu ZB, Shen ZX, Ma XF, Ye QQ (2009) Preparation of alpha-calcium sulfate hemihydrate from FGD gypsum in K, Mg-containing concentrated Cacl(2) solution under mild conditions. Fuel 88:1286–1293
5. Han YX, Wang YB, Yuan ZT, Yin WZ (2008) Hydration of hemihydrated calcium sulfate whiskers. J Northeast Univ Nat Sci 29:1490–1493
6. Huang ZY, Dong FQ (2010) Preparation of calcium sulfate whisker using waste residue of phosphogypsum by hydrothermal method. 2010 4th International conference on bioinformatics and biomedical engineering (iCBBE 2010)
7. Li CF, Liu SG, Li GC, Bai JH, Wang WW, Du QY (2011) Hydrothermal synthesis of large-sized hydroxyapatite whiskers regulated by glutamic acid in solutions with low supersaturation of precipitation. Adv Powder Technol 22:537–543
8. Shen W, Gan GJ, Dong R, Chen H, Tan Y, Zhou MK (2012) Utilization of solidified phosphogypsum as portland cement retarder. J Mater Cycles Waste Manage 14:228–233
9. Shweikani R, Kousa M, Mizban F (2013) The use of phosphogypsum in Syrian cement industry: radiation dose to public. Ann Nucl Energy 54:197–201
10. Viswanath B, Ravishankar N (2008) Controlled synthesis of plate-shaped hydroxyapatite and implications for the morphology of the apatite phase in bone. Biomaterials 29:4855–4863
11. Wang HG, Mu B, Ren JF, Jian LQ, Zhang JY, Yang SR (2009) Mechanical and tribological behaviors of PA66/PVDF blends filled with calcium sulphate whiskers. Polym Compos 30:1326–1332
12. Zhang DY, Luo HM, Zheng LW, Wang KJ, Li HX, Wang Y, Feng HX (2012) Utilization of waste phosphogypsum to prepare hydroxyapatite nanoparticles and its application towards removal of fluoride from aqueous solution. J Hazard Mater 241:418–426
13. Zhu ZC, Xu L, Chen GA, Li YL (2010) Optimization on tribological properties of aramid fibre and $CaSO_4$ whisker reinforced non-metallic friction material with analytic hierarchy process and preference ranking organization method for enrichment evaluations. Mater Des 31:551–555

Ore Mineral Textures of Late Cretaceous Volcanogenic Massive Sulfide Deposits of Turkey: Proposed Paragenetic Sequence

Emin Çiftçi, Abdurrahman Lermi, and Bülent Yalçınalp

Abstract Most of the massive sulfide deposits (VMS) occurring from Precambrian to Cenozoic throughout the world have been subsequently metamorphosed at various grades. Thus, all the original textures have been either completely destroyed or strongly modified. However, there are a very few examples, rather younger deposits such as late Cretaceous Turkish VMS deposits and Miocene Kuroko deposits of Japan in which representative and original ore textures are preserved. The Turkish massive sulfide deposits are mainly Cu–Zn–Pb type and entirely hosted by Late Cretaceous felsic volcanic rocks within a paleoarc geotectonic setting.

Major ore minerals are base metal sulfides (pyrite, chalcopyrite, bornite, chalcocite, covellite, sphalerite, and galena) and sulfosalts along with quartz, barite, and calcite gangue. In general, dissemination and veinlet textures are extremely abundant in the stockwork and siliceous ore zones that mainly form the base of the massive ore bodies and around the vent through which the ore-forming fluids traversed. In the massive ore, particularly in the central zone of the lenses, fine-grained massive sulfide minerals show a wide variety of replacement and colloform textures. In the lateral zones, clastic or fragmental ore textures may be present if the deposit has undergone a slumping. In the case of cone-shaped deposits, the brecciated ore textures tend to be dominant in the central part of the lens. Most of the minerals are very fine grained, and the larger grains of the major minerals are in the order of 100–300 μm in size, but most of the minor and trace minerals are much smaller, typically in the order of 1–20 μm in across. Most of the minerals are anhedral with the exception of pyrite, quartz, and barite that commonly occur as euhedral to subhedral crystals.

Four major mineralization stages have been determined at the regional scale. First-stage minerals are two generations of pyrite and chalcopyrite followed by the

E. Çiftçi (✉)
Department of Geological Engineering, ITU, 34469 Maslak, Istanbul, Turkey
e-mail: eciftci@itu.edu.tr

A. Lermi
Department of Geological Engineering, Niğde University, 51100 Niğde, Turkey

B. Yalçınalp
Department of Geological Engineering, KTU, 61100 Trabzon, Turkey

F. Dong (ed.), *Proceedings of the 11th International Congress for Applied Mineralogy (ICAM)*, Springer Geochemistry/Mineralogy,
DOI 10.1007/978-3-319-13948-7_10

second-stage minerals including sphalerite, galena, and sulfosalts (mainly tennantite and subordinate tetrahedrite). In the third stage, second generation of chalcopyrite occurs replacing all the earlier phases. This stage is absent in black ore dominating deposits. Bornite prevails in the last stage (aka supergene enrichment) along with chalcocite and covellite, which replaces all the other phases including gangue minerals.

Keywords Ore textures • Eastern Pontides • Late Cretaceous • Volcanogenic massive sulfides (VMS) • Turkey

1 Introduction

The study area is situated within the Eastern Pontides, one of the major tectonic units of Turkey [1, 2] (Fig. 1). This belt is about 500 km long and has a very complex volcanic island arc structure evolved during Alpine-Himalayan orogeny. The region is a host to numerous volcanogenic massive sulfide (VMS) deposits dominantly of Late Cretaceous age. Moreover, the number of VMS deposits, across about 250 km of the Black Sea coast, makes the region one of the most significant ore districts in the world [3, 4]. The VMS deposits of the region are considered to be Kuroko type in a broad sense. The eastern Pontide metallogenic belt has been a major source for base metal production in Turkey for the past 30 years. Almost all of this production comes from the volcanogenic massive sulfide deposits of the region.

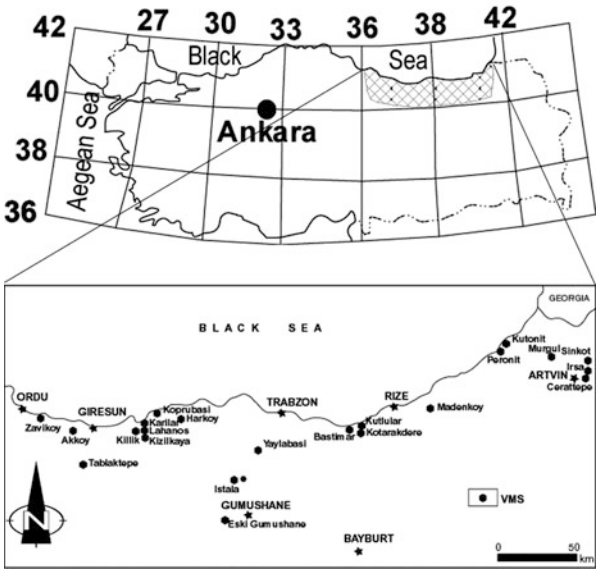

Fig. 1 Location map of the Turkish VMS deposits

2 Regional Geology

The oldest rocks in region are Devonian-Early Carboniferous metamorphic rocks and the Gümüşhane Granite of Permian age that intrudes them. Although volcanic rocks are prevalent in the region, sedimentary rocks are also present, varying from Late Carboniferous–Early Permian to Oligocene–Miocene in age [5]. However, the igneous rocks intruded the volcanic and sedimentary units in at least three major pulses in the region [6].

The Jurassic–Lower Cretaceous volcanic complex, which is known as the "Lower Basic Volcanic Complex" (LBC) in Turkish literature, discordantly overlies the basement metamorphic rocks. This complex consists mainly of basalt, basaltic agglomerates, locally spilitized basalts, andesite, andesitic agglomerates, and tuffs. Locally, intercalated marble or recrystallized limestone lenses occur within the complex, and they may contain skarn-type mineralization at their contacts with the younger acidic intrusions. The Lower Basic Volcanic Complex is overlain by Late Dogger–Malm–Early Cretaceous carbonates.

One of the major granitoid emplacements occurred between Early Cretaceous and Late Cretaceous epochs. The Artvin granite in the easternmost corner of the region and the Harşit granite in the central to western part of the eastern Pontides are major intrusions that occurred during this interval. These two granitoids are related to the formation of the felsic volcanic complex of Late Cretaceous age and, thus, the formation of the VMS deposits of the region [4].

The felsic rocks, known as the "pyritized dacites," are of particular interest due to their close association with the region's VMS deposits. This volcanic complex consists of lava flow, tuff, and pyroclastics often containing disseminated pyrite and it is overlain by marl-limestone (locally mudstone)-barren dacite sequence, regionally known as the purple dacite, of Maastrichtian–Paleocene age. Middle–Late Eocene in the region is represented by basaltic-andesitic rocks and intercalated sedimentary rocks: these rocks are known as the Upper Basic Volcanic Complex (UBC) [7] (Fig. 2).

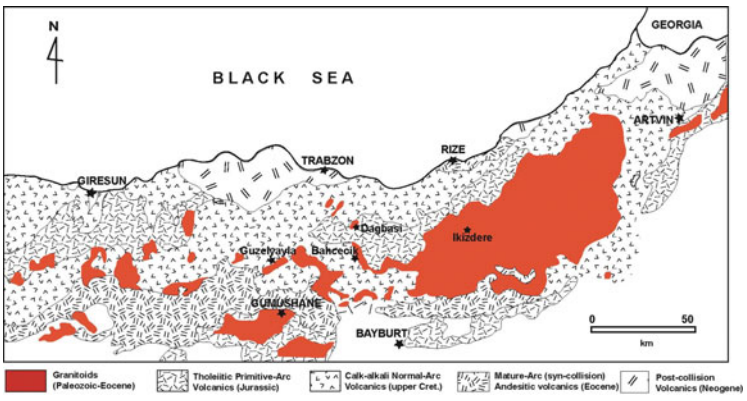

Fig. 2 Generalized geological map of the eastern Pontide metallogenic belt [8]

3 Materials and Methods

Samples were collected from the major VMS deposits including Cerattepe, İrsahan, Kuvarshan, Murgul, Akarşen, Kutonit, Tunca, Çayeli, Kutlular, Kanköy, Yaylabaşı, Köprübaşı, Lahanos, Kızılkaya, and Killik. These are considered to be representative of the major ore types. Polished sections were prepared for reflected-light microscopy (RLM) examination employing a Nikon L150 reflected light microscope. Secondary Electron Microscope-Energy Dispersive Spectra (SEM-EDS) and optical cathodoluminescence microscopy (CLM) were routinely used for assurance when needed.

4 Ore Mineralogy and Ore Textures

The most ubiquitous ore mineral in the VMS deposits is pyrite. Chalcopyrite, sphalerite, and galena form the second mineral group in terms of abundance. Sulfosalts (tetrahedrite and tennantite) and bornite are the third most abundant. Pyrrhotite and marcasite also occur at much lower abundances. Gangue minerals typically include quartz, barite, gypsum, anhydrite, and carbonates (mainly calcite and dolomite).

Ore mineral paragenesis is determined essentially by the deposit type, whether it is yellow ore or black ore or semi-black ore dominating. Thus, each type has dominating mineral assemblages and ore mineral textures. Pyrite occurs as very large euhedral crystals, suggesting that they formed at higher temperatures and slower deposition process. The yellow ore zone is composed mainly of pyrite–chalcopyrite with minor to trace sphalerite and trace galena. Anhedral chalcopyrite appears to have filled the matrix of euhedral to subhedral pyrite grains. Colloform texture is rare but present. The black ore zone is an essentially polymetallic sulfide zone and comprises sphalerite, galena, pyrite, and sulfosalts with minor chalcopyrite. Bornite is also common in minor to major quantities.

Considering most of the VMS deposits of the world have been subsequently metamorphosed and, thus, all the original textures have been either completely destroyed or strongly modified, younger deposits including Japanese Miocene VMS deposits and Turkish Upper Cretaceous VMS deposits are very unique in that representative and original ore textures are preserved.

In general, dissemination and veinlet textures are extremely abundant in the stockwork and siliceous ore zones that mainly formed the base of the massive ore body and the vent through which the ore-forming fluids traversed. In the massive ore, particularly in the central zone, fine-grained massive sulfide minerals show a wide variety of replacement and colloform textures. In the lateral zones, clastic or fragmental ore textures may be present if the deposit has undergone a slumping event (Fig. 3a–f).

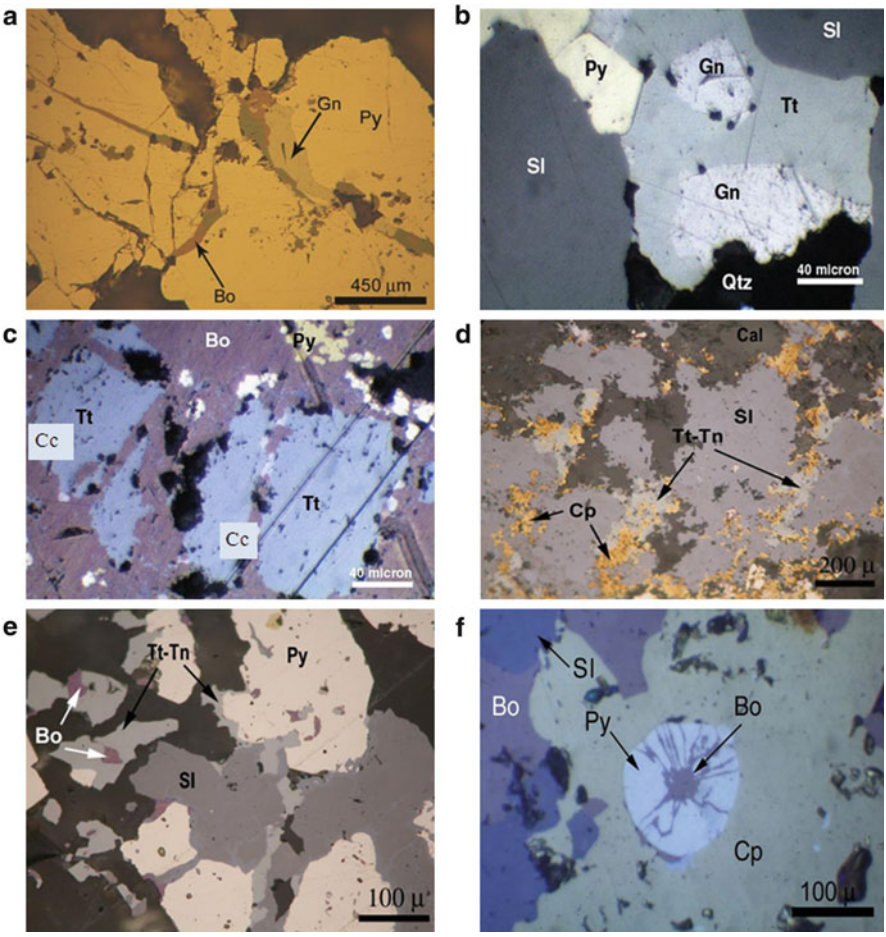

Fig. 3 (**a**) Early pyrite (Py) replaced first by galena (Gn) and later by late bornite in Kanköy deposit; (**b**) tetrahedrite (Tt-Tn) replacement over galena in Köprübaşı deposit; (**c**) bornite (Bo) replacement over chalcocite (Cc) in Lahanos deposit; (**d**) tennantite replacement of sphalerite (Sl) and replacement of both by second generation of chalcopyrite (Cp) in Çayeli deposit; (**e**) tennantite replacement of sphalerite and pyrite in İrsahan deposit; and (**f**) late bornite selective replacement of early pyrite and chalcopyrite in Murgul deposit

Most of the minerals are very fine grained, and the larger grains of the major minerals are in the order of 100–300 µm in diameter, but most of the minor and trace minerals are much smaller, typically in the order of 1–20 µm in diameter. Most of the minerals are anhedral with the exception of pyrite, quartz, and barite that commonly occur as euhedral to subhedral crystals. In general, the grain sizes decrease upward most probably due to decreasing temperature. Based on the RLM study of a significant number of polished sections, a generalized ore mineral paragenetic sequence was proposed for the Turkish VMS deposits (Fig. 4).

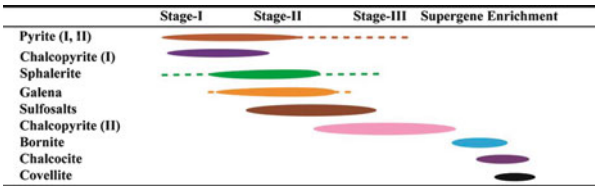

Fig. 4 Generalized paragenetic sequence for the ore minerals determined in the Turkish VMS

5 Conclusions

Turkish VMS deposits are hosted by the Upper Cretaceous felsic volcanics.

Major ore minerals are base metal sulfides (pyrite, chalcopyrite, bornite, chalcocite, sphalerite, and galena) and sulfosalts (mainly tetrahedrite and tennantite) along with quartz, barite, and calcite gangue.

Most of the minerals are very fine grained, and the larger grains of the major minerals are in the order of 100–300 μm in size, but most of the minor and trace minerals are much smaller, typically in the order of 1–20 μm in size. Most of the minerals are anhedral with the exception of pyrite, quartz, and barite that commonly occur as euhedral to subhedral crystals.

Primary ore textures are preserved and could be used to decipher the mineralization conditions and paragenetic sequence.

Turkish massive sulfide deposits are mainly Cu–Zn–Pb type due mainly to the Cu-rich underlying rock section.

Common ore textures are dissemination and veinlet textures in the stockwork and siliceous ore zones, whereas replacement and colloform textures become prevalent in the massive ore, particularly in the central zone of the lenses. In the lateral zones, clastic or fragmental ore textures may be present if the deposit has undergone a slumping event.

In the case of cone-shaped deposits, the brecciated ore textures tend to be dominant in the central part of the lens.

References

1. Ketin I (1966) Anadolunun Tektonik Birlikleri. M.T.A. Bull. 66:20–34. Ankara, Turkey
2. Ketin I, Canıtez N (1972) Yapısal Jeoloji. İ.T.Ü. Kütüphanesi, no. 520. Istanbul, Turkey
3. Pejatovic S (1979) Metallogeny of the pontide-type massive sulfide deposits. M.T.A., no: 177. Ankara, Turkey
4. Ciftci E (2000) Mineralogy, paragenetic sequence, geochemistry, and genesis of the gold and silver bearing upper cretaceous mineral deposits, Northeastern Turkey. Ph.D. Dissertation, University of Missouri-Rolla, pp 251, Missouri, USA
5. Okay AI, Şahintürk Ö (1997) Geology of the Eastern Pontides. In: Robinson AG (ed) Regional and petroleum geology of the black sea and surrounding region. AAPG Memoir 68, pp 291–311

6. Moore WJ, McKee EH, Akinci O (1986) Chemistry and chronology of plutonic rocks in the Pontid mountains, northern Turkey. European Copper Deposits, Belgrade, pp 209–216
7. Korkmaz S, Tuysuz N, Er M, Musaoglu A, Keskin I (1992) Geology of the Black Sea Region. In: Proceedings of the International Symposium on the Geology of the Black Sea Region, Ankara, Turkey
8. Aslaner M (1977) Türkiye Cu-Pb-Zn Yataklarının Jeolojik ve Bölgesel Sınıflamasıyla Plaka Tektoniği Yönünden İncelemesi. K.T.Ü. Yer. Bil. Fak. Yayınları, no: 12, Trabzon, Turkey

Micronized Calcite Potential, Production, and Principal Characteristics of Nigde (Turkey)

Emin Çiftçi and İsmail Erdağ

Abstract Marble, which is exploited for micronized calcite production in Nigde area (South Central Turkey), occurs in the Upper Cretaceous Gümüşler, Aşıgediği, and Kaleboynu Formations of the Nigde Massif. Although there are a few marble producing quarries in the area, it is long been known that the marbles of this area are generally highly fractured and don't yield large blocks or suitable slabs meeting the industrial demands. Thus, most of the production is currently carried out mainly as building stone, crushed stone, and micronized calcite. Due mainly to its high demand, micronized calcite has become a significant export product for the state's economy. Because the Nigde marbles are coarse grained with high $CaCO_3$ content, high purity, and whiteness, they are considered to be the highest quality micronized calcite quarries in the country. Consequently, the area drew many national and international investors resulting in significant increase in the number and extent of micronized calcite plants in the area. In the early 1980s, the city of Nigde had only one or two plants, it is now well over five including foreign investors and joint ventures. Annual production is also considerably increased from 20,000 to 30,000 t to almost half a million tons and it is still in increasing trend.

Keywords Micronized calcium carbonate • Calcite • Marble • Gümüşler Formation • Nigde Massif • Turkey

1 Introduction

Turkey is one of the countries with significant marble reserves in the world. Economically most important marble reserves are in the cities of the western and central Anatolia. Travertine and onyx deposits are also significant in state's economy and found in various parts of western and central Anatolia. Among these

E. Çiftçi (✉)
Department of Geological Engineering, ITU, 34469 Maslak, Istanbul, Turkey
e-mail: eciftci@itu.edu.tr

İ. Erdağ
Nahita Mining Co, 51100 Nigde, Turkey

F. Dong (ed.), *Proceedings of the 11th International Congress for Applied Mineralogy (ICAM)*, Springer Geochemistry/Mineralogy,
DOI 10.1007/978-3-319-13948-7_11

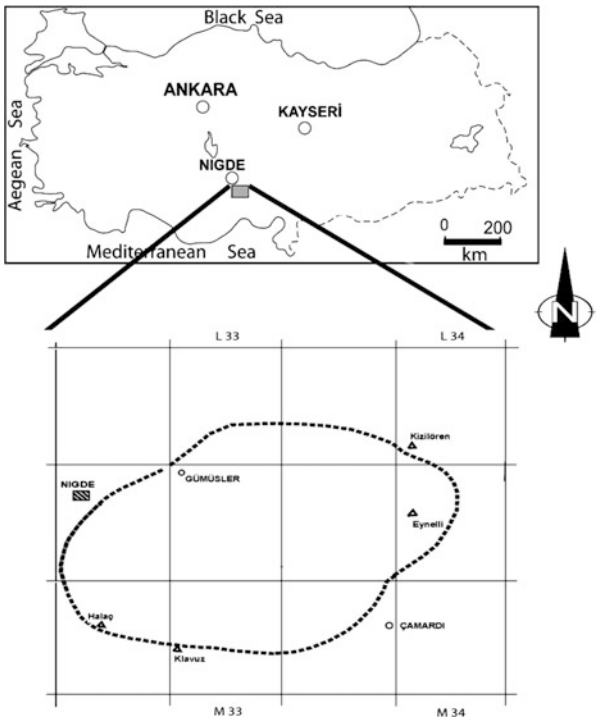

Fig. 1 Occurrences of the Nigde-white marbles in the region

places, the Nigde region (Fig. 1) prevails in terms of the reserves for high purity (low iron oxide and silica) calcium carbonate deposits.

Micronized calcium carbonate (down to 0.1 μm) production has been increasing due to the high demand from a wide variety of industrial applications, as well being an environment-friendly mineral. It has been consumed as mineral additive to soils and as acid neutralizing agent to treat wastewater and polluted lakes in many countries. Micronized calcium carbonate is also used as a filler and/or pigment by paint, paper, plastics, and ink industries. It is often used as a cheap alternative filler and pigment to replace more expensive products like titanium-dioxide, zinc oxide, and barium sulfate. According to the official records (data acquired thru personal request from the State Planning Organization), micronized calcium carbonate production increased almost fivefold during the 2004–2008 period (from about 3 million tones to over 13 million tons). Although there was a small downturn in production in 2005, the production is still showing an increasing trend [1]. More than half of this production is supplied from the city of Nigde.

Production of micronized calcium carbonate is a good approach to use calcareous rocks that are otherwise not suitable for classical applications such as slab and block marble. The major steps in production of micron-sized calcite are crushing, grinding, sizing, coating (if required), quality control, and packaging. Major industries that use micronized calcium carbonate are ink, paint, paper, plastics, construction, adhesive, leather, detergent, ceramics, food, carpet, and glass industries

Fig. 2 Field view of the Nigde-white marbles showing intense fracturing

(http://www.reade.com/es/Products/Carbonate-Compounds%2C-Powder/Calcium-Carbonate-$CaCO_3$-Powder.html; http://www.vimalmicrons.com). Coated micronized calcium carbonate is preferred for certain applications where properties such as hydrophobicity, chemical durability, high strength, and easy dispersion are needed.

The Nigde region is one of the major producers of micronized calcium carbonate. The Nigde-white marbles (as being industrial name for the marble produced in this area) crop out around the city within Gümüşler, Aşıgediği, and Kaleboynu Formations of the Nigde Massif. Most of the marbles are intensively deformed (Fig. 2); thus they are useable only as micronized calcium carbonate, dimension stone, crushed stone, and construction stone; essentially colored ones due to iron oxides staining are preferred in construction. Only a few small-scale quarries are currently operating for block production particularly from marbles of the Gümüşler Formation.

2 Regional Geological Setting

The Nigde Massif (in broad sense), representing southernmost segment of the Kırşehir Massif (or Central Anatolia Massif), which is itself a large metamorphic mass, is located in the SE of the city of Nigde, after which it is named. Southern morphology of the Massif resembles a dome with a long axis. In its north and west, it is covered and/or surrounded by Neogene tuffs (products of the Mount Hasan and Erciyes), by sediments of Mesozoic-Lower Tertiary age of Ulukışla basin in the south, and by the Ecemiş corridor (or fault zone) sediments in the east. It is first named by [2]. Blumenthal [3, 4] determined the stratigraphy and used the term "Nigde Complex," suggesting that the rocks of this massif are partially crystalline schists originated from fossil-free Paleozoic rocks. Oktay [5] prepared 1/100,000-scale geological map and made detailed petrographic determinations of the rocks. It is composed of, progressing upward, Gümüşler Formation (gneiss-amphibolite-intercalated thin marble-quartzite layers), Kaleboynu Formation (similar lithology

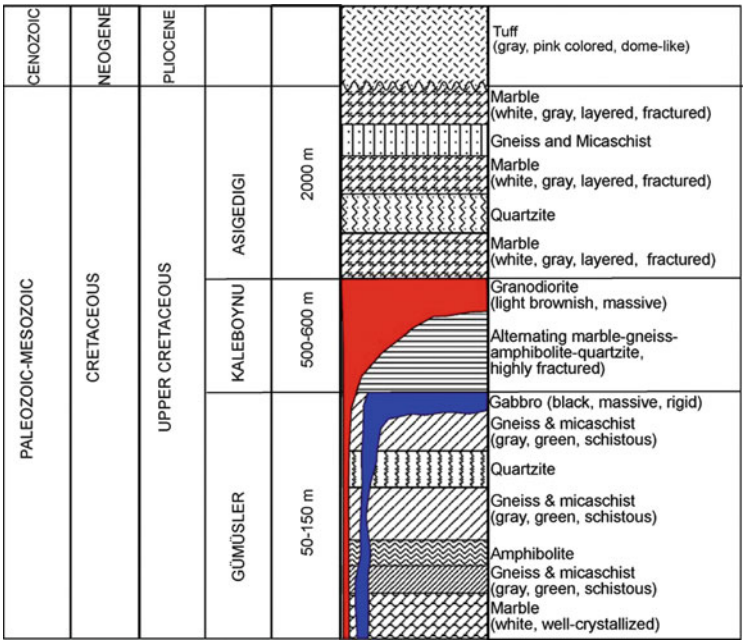

Fig. 3 Generalized geological columnar section of the study area (modified from [7, 8])

but layering is more evident), Aşıgediği Formation (white marbles—thin intercalations of amphibolite-quartzite-gneiss-calcsilicates), and Sineksizyayla Metagabbro and cut by post-metamorphism/tectonism Üçkapılı Granodiorite [6] (Fig. 3).

3 Experimental Methods

The Nigde-white marbles and micronized calcites were characterized by applying optical, physical, and chemical techniques. These include petrographic characterization of the starting materials, size distribution analyses (laser diffraction for smaller particles and sieve analyses for coarser grains), whiteness tests (using Color Eye XTH), abrasiveness (demanded by paper industry), moisture content (demanded by plastic industry), extent of coating (filler for plastic industry), scanning electron microscope analyses, chemical analyses, X-ray diffraction (XRD), percent undissolved solids in HCl, pH measurements, and oil-doped (flax oil with density of 0.98 g/cm^3) absorption values.

Table 1 Major physical parameters measured for the Nigde-white marbles [7]

Parameter	Value
Specific gravity	2.62 g/cm^3
Unit bulk weight	2.60 g/cm^3
Hardness (Moh's)	3–3.5
Water absorption by wt. and by volume under atmosphere	0.10 %, 0.25 %
Water absorption by wt. and by volume in boiling water	0.17 %, 0.27 %
Apparent porosity and porosity	0.28 %, 0.92 %
Ultrasound permeability	5,454 kg/cm^2
Compression strength	566 kg/cm^2
Percussion strength	15.6 kg/cm^2
Abrasion strength	15.9 g/cm^2
Porosity	0.92 %

Table 2 Major characteristic parameters measured for the micronized calcite produced from the Nigde-white marbles [8]

Parameter	Value	Industry requirement
Whiteness	98.68–99.64	96
Abrasiveness	8.8–11 mg/100 g	Qualified
Moisture ratio	0.15–0.28 %	Max 0.3 %
Undissolved matter ratio in HCl	0.40 %	Qualified
Mineral phases by XRD	Calcite only	Qualified
pH	9.11–9.35	Qualified
DOP absorption rate (down to 1 μm)	15–31	15–35
Oil absorption rate (down to 1 μm)	15–20	20–25
Coatability rate of coated powders (down to <2 μm)	1.22–1.48	1.50

3.1 Characteristics of Nigde Marble

Petrographic investigations of the selected samples representing the Nigde-white marble indicated that calcite occurs as chiefly equidimensional large euhedral to subhedral crystals and showed emphasized relief pleocroizm. No intergranular spaces were observed. Crystals clamped together perfectly presenting well-developed mosaic texture. Indications of tectonic deformation are clearly observed in the form of polysynthetic twinnings, calcite bucklings, and cracks. The physical parameters of the Nigde marble are listed in Table 1 [7]. Average test results for the micronized calcite samples are summarized in Tables 2 and 3 [8].

Most striking features of micronized calcium carbonates produced from the Nigde marble are their high $CaCO_3$ content up to (wt. 99 %), lower iron and silica content, and whiteness. Higher whiteness is particularly required by the dye and plastics industries in order to consume lesser TiO_2 and in paper industry to use less

Table 3 Chemical composition of selected samples for the major oxides (in wt. %) [8]

Test sample	CaO%	MgO%	Fe_2O_3%	SiO_2%	Al_2O_3%	CO_2%
UF[a] (%90 <2 μm)	53.9	0.5	<0.05	<0.05	0.15	43.8
95 (%80 <2 μm)	53.95	0.6	<0.05	<0.05	0.15	43.2
1 (%50 <2 μm)	54.4	0.55	<0.05	<0.05	0.1	43.4
2 (%40 <2 μm)	54.85	0.6	<0.05	<0.05	0.05	43.2

[a]*UF* Ultrafine

Table 4 Major micronized calcite producers in the Nigde area (Turkey)

Manufacturer	Capacity (tpy)	Product name family	PVC profile grade	Coated products	Mine ownership and operation	Distance to loading port
Esen Mikronize	70,000	Esen A	E400	Yes	Yes	20 km
Erciyes Mikronize	50,000	Ermikal	Sf1c	Yes	No	450 km
			Sf2c			
Komsar (Former Hisar)	100,000	Normcal Hydrocal	St99	Yes	No	400 km
Turmet	30,000	Turmet	None	No	Yes	350 km
Mikron'S	110,000	Turkcarb	Sm1c	Yes	Yes	350 km
Mikro Kalsit	50,000	Mikrocarb	None	No	Yes	10 km
Nigtas Mikronize	55,000	Nigkal	None	No	Yes	350 km

optical whitening. Table 4 lists major companies in the micronized calcium carbonate business in Turkey.

4 Conclusions

Subject area is located within the boundaries of Nigde, a south-central Anatolian city. High-quality micronized calcium carbonate is produced from coarse-grained, white marbles, known as the Nigde-white marbles that dominantly crop out in the Nigde Massif. The Nigde-white marbles occur in the Gümüşler, Aşıgediği, and Kaleboynu Formations. At present a few small-scale slab and block-yielding quarries are in operation in the Gümüşler Formation. The geomechanical experiments [7, 8] show that the Nigde-white marble is not suitable for slab/block marble production as a result of tectonic deformations taking place subsequent to their deposition. This study shows that the Nigde-white marbles are more suitable for the filler and pigment markets due mainly to their natural high purity and whiteness.

References

1. DPT Report 2007–2013 (2006) Dokuzuncu Kalkınma Planı 2007–2013, Madencilik Özel İhtisas Raporu, Ankara (in Turkish)
2. Tchihatcheff PDe (1869) Asie mineure (description physique) Quatrieme partie goologie III, Paris, pp 552
3. Blumenthal M (1941) A general review of the geology of the Taurides between Nigde and Adana. General Directorate of Mineral Research and Exploration (MTA) Publications vol B. No. 6, pp 48, Ankara (in Turkish)
4. Blumenthal M (1952) Geographical, stratigraphical and tectonical features of the high aladag mountains. Publications of the Mineral Research and Exploration Institute (MTA) of Turkey D6, pp 179, Ankara (in Turkish)
5. Oktay AC (1955) Niğde, Çamardı ve Ulukışla Arasındaki Bölgenin Jeolojisi. M.T.A. Report No: 2383 (in Turkish)
6. Göncüoğlu MC (1977) Geologie des westlichen Niğde Massivs. Bonn Univ. Ph.D. Thesis, pp 181 (in German)
7. Üçok S (2001) Marble deposits of the Gümüsler (Nigde) Region. Nigde Univ. M.S. Thesis, pp 106 (in Turkish)
8. Erdağ İ (2005) Investigation of suitability of Nigde-Hidirlik Marbles for industrial Use. Nigde Univ. M.S. Thesis, pp 79 (in Turkish)

Lime-Assisted Cyanide Leaching of Refractory Gold Ores from Ajialongwa Mine

Kaibin Fu, Shu Chen, Zhen Wang, Junhui Xiao, and Deqiang Luo

Abstract Heap leaching is a promising, less expensive, alternative technology for processing low-grade gold ores compared with traditional, energy-intensive processes (e.g., autoclave/tank leaching). The effects of lime on the heap leaching of gold ores from Ajialongwa gold mine in China were investigated. Leach tests included column leach tests, the pilot plant tests, and the commercial plant. The leach experiments were performed using cyanide leaching solutions at pH = 10–11. The results show that the presence of lime greatly increased gold leaching rates. Column leaching experiments show that there was 35.2 % of gold leached without the addition of lime. When 4 % lime was added to gold ores, Au extraction reached 50.56 %. Lime-assisted cyanide of refractory gold was also proved by the pilot plant tests and the commercial plant.

Keywords Lime • Gold ores • Column leaching • Heap leaching

1 Introduction

Ajialongwa gold mine, owned by the Xinshun Mining Co. Ltd., Sichuan, is located in southwest Ganzi Tibetan Autonomous Prefecture, Sichuan Province, approximately 30 km from Litang county, at 100°04′45″–100°05′15″ E, 30°25′15″–30°25′45″ W, covering an area of 1.7 km^2. The mining area is located in east Tibet Plateau, 4,000–5,000 m above sea level. The average atmospheric temperature at mine is less than 1.5 °C, the lowest temperature in winter is −15 °C, and the highest in summer is 25.6 °C. The annual rainfall is 600–650 mm. The cold weather is a big challenge to heap leaching. Since the discovery of Ajialongwa gold desposit in 1989, many researchers have investigated the geology, zonation of alteration, geochemistry, and characteristics of the mineralizing fluids in the mineral field. These studies have recognized that the Au-bearing oxide ore is in the upper zone of

K. Fu (✉) • S. Chen • Z. Wang • J. Xiao • D. Luo
School of environmental resource and engineering, SWUST, 59 Qinglong Road, Mianyang, Sichuan, People's Republic of China
e-mail: fukaibin@126.com

F. Dong (ed.), *Proceedings of the 11th International Congress for Applied Mineralogy (ICAM)*, Springer Geochemistry/Mineralogy,
DOI 10.1007/978-3-319-13948-7_12

the ore system characterized by Au-bearing primary ore at deeper levels. Ajialongwa gold deposit is a medium-size ore deposit with total gold ore reserves of 2,170,000 t at an average grade of 1.5–3.6 g/t total gold [1–4].

Heap leaching is a widely used extraction method for low-grade minerals, including those of copper, gold, silver, and uranium [5]. The most common leaching process for gold dissolution involves cyanidation, which is a process that has been practiced for over a century [6]. During the past three decades, the development of heap leaching technology for low-grade ore has extended the world resource base considerably. This method has new applications including nonmetallic minerals such as saltpeter [7] and soil remediation [8]. Heap leaching can avoid ambient contamination caused by conventional pyrometallurgical process and economical advantages for low-grade minerals [9]. Since 2002, Ajialongwa gold mine has employed the low-cost technology—heap leaching to recover gold. With the depletion of the oxidized ore, Au extraction decreased.

In general, the use of alkalis, such as calcium oxide and caustic soda, prevents the decomposition of cyanide in solution to form hydrogen cyanide gas. However, because of the remoteness of Ajialongwa gold mine, caustic soda was used to adjust the pH of leach solution before the technology was updated. This chapter mainly reviews the pilot plant tests together with the introduction of the laboratory tests and the commercial plant. The effects of lime, cement, and lime–cement ratio on the heap leach of Ajialongwa gold ores were compared. The viability of substituting lime for caustic soda was investigated.

2 Materials and Methods

2.1 Materials

The gold-bearing ores in this study were obtained from the Ajialongwa deposit. Elemental analysis of the sample is presented in Table 1. The metal sulfide ores consist mainly of arsenopyrite and pyrite. Chalcopyrite, galena, and sphalerite were also detected. The metal oxide consists of limonite, hematite, and scorodite. Quartz was the main nonmetallic minerals in the ore; however, dolomite, calcite, feldspar, and a small quantity of sericite were also present. The chemical composition of the ore sample and the leach solution was determined by atomic absorption spectrometry (AAS).

Table 1 Chemical composition of ore sample

Elements	Au (ppm)	Ag (ppm)	Cu	Pb	Zn	Fe	S	C
Content (%)	3.06	4.72	0.01	0.004	0.01	5.87	0.78	1.89
Elements	As	Sb	Bi	CaO	MgO	Al_2O_3	SiO_2	
Content (%)	0.94	0.014	0.04	3.270	3.25	12.09	60.08	

2.2 Leach Tests

Leach experiments consist of column leach tests, pilot plant tests, and commercial plant. The column leaching of the gold ore was carried out in PVC percolation column with an effective length of 3,000 mm and a 300 mm diameter. Each column was charged with 300 kg of ore. The leaching procedure consists of four stages: water washing, alkali washing, cyanide leaching, and spraying bleach solution. The pH of the column effluents was adjusted to values in the range of 10–11 by adding caustic soda. The solutions were then recycled to the top of the columns and were circulated continuously in this way to allow gold-cyanide complexion to accumulate. The leach pad below the heap is a significant element of a heap leach design. For pilot plant tests and commercial plant, the design of leach pad was identical. The pad consists of 150–300 mm of compacted clay-rich soil (engineered to a permeability of 10^{-6} cm/s), plastic liner (usually 1.50–2.00 mm thick HDPE or LLDPE), and geotextile cover (which may be placed above the plastic to prevent damage of the plastic by rocks in the drainage layer).

3 Results

3.1 Column Leach Tests

The column tests were carried out at ambient temperatures ranging from 20 to 35 °C with NaCN. The samples were crushed to −40 mm. The effects of the ratio of lime and cement on Au extractions of Ajialongwa gold ore were investigated. A column with a diameter of 300 and a height of 3,000 mm was used. The irrigation rate at 35–45 L/m^2/h was applied to the column leach. The effects of the ratio of lime and cement on gold extraction are shown in Fig. 1.

The results indicate that a gold dissolution of 35.2 % is attained at a residence time of 31 days for the blank test, but higher gold extraction is obtained by the addition of lime and cement. After 31 days of leaching, Au extracted from gold ores at blank, 4 % lime, 2 % lime + 2 % cement, and 4 % cement were 35.2 %, 50.56 %, 40.28 %, and 43.58 %, respectively. The leaching rate at 4 % lime was 15.36 % greater than that at blank tests; the result indicates that lime assists in leaching of gold. The maximal gold recovery was attained at 4 % lime.

3.2 Pilot Plant Tests

The ores came from the strip mine and were crushed before being fed to the heap leach. The pilot plant with a treatment capacity of 4,000 t/a gold ores consists of two

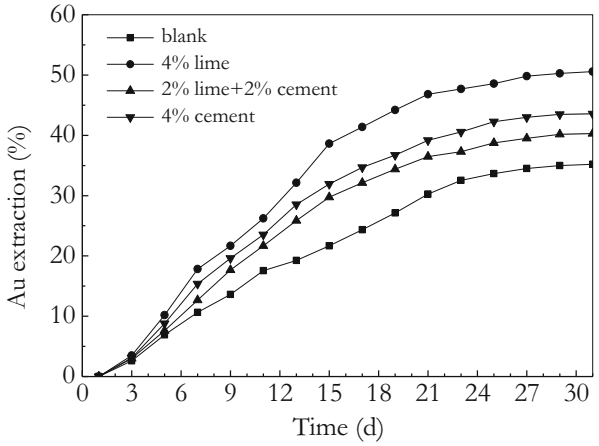

Fig. 1 Column leaching with NaCN

leach heaps and two solution collection systems. Pilot plant tests started up from January 2003.

Gold ores from an open pit mine were crushed to −50 mm and then transported by trucks to the leach heaps and stacked. 4,000 t of ore, with size of −50 mm at an average grade of 2.58 g/t total gold, has been stacked to leach Heap 1 and Heap 2, respectively. The lift height for each heap is 2.3 m. Lime (4%) was added to Heap 2 during stacking; however, nothing was added to Heap 1. For Heap 1, the use of sodium hydroxide prevents the decomposition of cyanide in solution to form hydrogen cyanide gas. For Heap 2, a small amount of sodium hydroxide was used as protective alkali in the initial stage. Wobblers supplied a solution at an irrigation rate of 25–25 L/m^2.H, with a rest–rinse cycle, and a 1-h rest period every 3 h. After leaching for 35 days, gold dissolution reached 33.3 % for Heap 1; however, 46.9 % of gold for Heap 2 with 4 % lime was dissolved (Fig. 2).

3.3 Commercial Plant

The commercial plant with a capacity of 100,000/a gold ores was commissioned by the end of 2004. Open-cast mining system supplies 2,000 t ore per day at an average grade of 2.97 g/t gold. Temporary heaps would be adopted for cyanide leaching. A two-stage crushing plant is designed to crush ore to a size of 100 % passing 50 mm. Granular activated carbon adsorption column was designed to recover gold. After 35 days of heap leaching, Au recovery reached 32.58 % before the technology was updated, while Au recovery increased to 45.68 % after the technology was updated (Fig. 3).

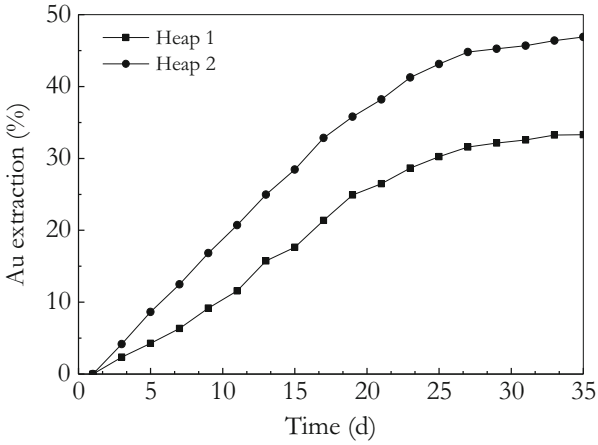

Fig. 2 Au extractions of the 2,000 t/a pilot plant

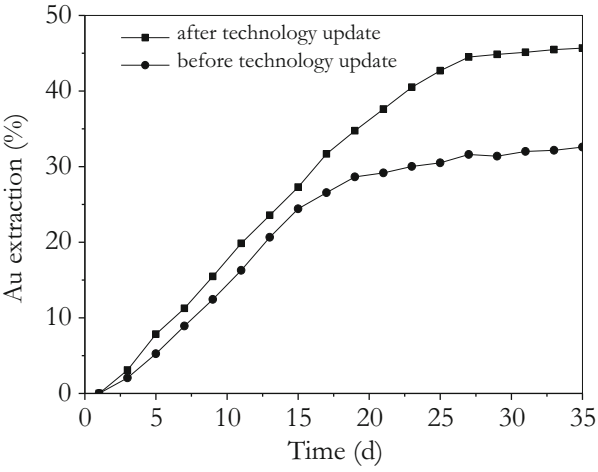

Fig. 3 Au extractions of the 100,000 t/a commercial plant

4 Discussion

Gold cyanidation has been reported to involve the chemical reactions shown in Eq. (1) [10] and Eq. (3) [11], where Eq. (3) can be treated as the sum of the two partial reactions shown in Eqs. (1) and (2). Hydrogen peroxide produced at the interface by reduction of oxygen can react with gold (Eq. 2), or with cyanide ion (Eq. 4), or disproportionate to $H_2O + 0.5\ O_2$, while cyanate produced in solution further degrades to other products.

$$2Au + 4CN^- + O_2 + 2H_2O = 2Au(CN)\,2^- + 2OH^- + H_2O_2 \quad (1)$$

$$2Au + 4CN^- + H_2O_2 = 2Au(CN)_{2^-} + 2OH^- \quad (2)$$

$$4Au + 8CN^- + O_2 + 2H_2O = 4Au(CN)_{2^-} + 4OH^- \quad (3)$$

$$CN^- + H_2O_2 = CNO^- + H_2O \quad (4)$$

Because of the remoteness of Ajialongwa gold mine, sodium hydroxide was used as protective alkali before technology reformation. This is attributed to the transportation cost. Low Au extraction resulted in an attempt to substitute lime with caustic soda. The result shows that lime assisted in leaching of gold. The reasons are as follows: firstly, lime can result in the coagulation of fine-grain minerals and enhance the permeability of ore pile. Secondly, coagulation causes fine particles to adhere directly to each other, decreases the coverage of slime on the surface of coarse particle, and improves the contact of CN^- and mineral. At last, lime is able to fix the arsenic in the ores. Arsenic metal is very rarely in its pure form in nature. The most common arsenic mineral is arsenopyrite (FeAsS), a compound of iron, arsenic, and sulfur. Several other, less-common minerals contain arsenic, including orpiment (As_2S_3), realgar (As_2S_2), and enargite, which are arsenic sulfides. The immobilization mechanism of arsenic by lime is as follows:

$$2As_2S_3 + 6Ca(OH)_2 = Ca_3(ASO_3)_2 + Ca_3(AsS_3)_2 + 6H_2O \quad (5)$$

$$Ca_3(AsS_3)_2 + 6Ca(OH)_2 = Ca_3(ASO_3)_2 + 6CaS + 6H_2O \quad (6)$$

$$2CaS + 2O_2 + H_2O = CaS_2O_3 + Ca(OH)_2 \quad (7)$$

$$2CaS + 2NaCN + 2H_2O + O_2 = 2NaCNS + 2Ca(OH)_2 \quad (8)$$

$$Ca_3(AsS_3)_2 + 2NaCN + 3O_2 = 6NaCNS + Ca_3(ASO_3)_2 \quad (9)$$

$$As_2S_3 + 3CaS = Ca_3(AsS_3)_2 \quad (10)$$

$$6As_2S_2 + 3O_2 = 2As_2O_3 + 4As_2S_3 \quad (11)$$

$$6As_2S_2 + 3O_2 + 18Ca(OH)_2 = 4Ca_3(ASO_3)_2 + 2Ca_3(AsS_3)^{2+}18H_2O \quad (12)$$

Significant quantities of arsenic can be converted to relatively stable calcium arsenate, and fixed in the ores.

5 Conclusions

The column leach tests, the pilot plant tests, and the commercial plant have demonstrated that it was viable to substitute lime for caustic soda and that lime assisted in cyanide leaching of gold ores from Ajialongwa mine. Column leaching experiments show that there was 35.2 % gold leached without the addition of lime. When 4 % lime was added to gold ores, Au extraction reached 50.56 %. Lime-assisted cyanide of refractory gold was also proved by the pilot plant tests and the

commercial plant. The reasons are as follows: firstly, lime can result in the coagulation of fine-grain minerals and enhance the permeability of ore pile. Secondly, coagulation causes fine particles to adhere directly to each other, decreases the coverage of slime on the surface of coarse particle, and improves the contact of CN^- and mineral. At last, lime is able to fix the arsenic in the ores.

Acknowledgment The authors would like to thank the support for this research of research fund for the development and construction plans of Key Laboratory of Solid Waste Treatment and Resource Recycle of Ministry of Education (Grant No. 13zxgk07)

References

1. Yang YP, Yang LY (2007) Geological features and prospecting potential of the Ajialongwa-Yahuo Au-(Cu) Ore Zone, Litang, Sichuan. Acta Geol Sichuan 27(3):0–176
2. Zhu HP (2007) Geological characteristics and genesis of Ajialongwa gold deposit, Sichuan province. Gold 28(6):18–20
3. Xia TG, Sun CM, Li L, Wang YZ, Liu C, Yang YP (2006) Geological features and prospecting criteria of the Ajialongwa gold deposit, Sichuan. Geol Prospect 42(3):53–55
4. Huan WJ, Yuan WM, Li N (2011) Study on the mineral electron microprobe evidence of the formation conditions and fission track of gold deposits in Ganzi-Litang gold belt, Western Sichuan Province. Geoscience 25(2):261–270
5. Padilla GA, Cisternas LA, Cueto JY (2008) On the optimization of heap leaching. Miner Eng 21(9):673–678
6. Dai XW, Simons A, Breuer P (2012) A review of copper cyanide recovery technologies for the cyanidation of copper containing gold ores. Miner Eng 25(1):1–13
7. Valencia JA, Mendez DA, Cueto JY, Cisternas LA (2008) Saltpeter extraction and modelling of caliche mineral heap leaching. Hydrometallurgy 90(2–4):103–114
8. Hanson AT, Dwyer B, Samani ZA, York D (1993) Remediation of chromium-containing soils by heap leaching: column study. J Environ Eng 199(5):825–841
9. Karimi P, Abdollahi H, Amini A, Noaparast M, Shafaei SZ, Habashi F (2010) Cyanidation of gold ores containing copper, silver, lead, arsenic and antimony. Int J Miner Process 95 (1–4):68–77
10. Bodlander G (1896) Die chemie des cyanidverfahrens. Angew Chem 9(19):583–587
11. Elsner L (1846) Uber das verhalten verschiedener metalle in einer wassrigen losung von zyankalium. J Prakt Chem 37(2):441–446

Growth Mechanism and Stability Study on the Fe_3S_4 Nanocrystals Synthesized Under Thermal and Humid Conditions

Shang Gao, Fei Huang, Dan Song, Guanglu Li, Qiang Liu, Taiwei Feng, Ran Zhao, Jia Liu, and Wenyuan Gao

Abstract Greigite (Fe_3S_4) is important magnetic mineral that can not only instruct reducing environment but also provide paleomagnetic signal for the paleoenvironment research. Generally Fe_3S_4 exists as an unstable intermediate, whose preparation condition is rigorous. Previous studies have accumulated rich results, but the research on its stable conditions, formation mechanism, and evolution process remains to be verified. This study simulates the mineral growth and carries out experimental research systematically under thermal and humid conditions. Pure Fe_3S_4 is synthesized under the conditions of 200 °C, $t = 30$ h, pH = 4–5. The morphology of Fe_3S_4 is nanoscale particles. Fe_3S_4 stably exists at 200 °C, $t = 30$ h, and transforms to FeS_2 with increasing time. The experimental results broaden the stability range of Fe_3S_4 in the Fe–S binary phase diagram. This study has typomorphic significance on geological conditions and provides a scientific basis for the preparation of Fe_3S_4 nano-magnetic materials.

Keywords Stability • Fe_3S_4 • Synthesize • Thermal and humid conditions

1 Introduction

Greigite was first discovered in magnetotactic bacteria of California Tertiary lake sediments in 1964 [1]. Previously it was thought to be a rare mineral and did not attract people's attention. In recent years, due to the in-depth study on rock magnetism and geochemistry, Fe_3S_4 is widely found in various types of sediments [2–4].

Fund: Supported by National Natural Science Foundation (Grant No.:40872045; 41172047); The Opening Project of Key Laboratory of Solid Waste Treatment and Resource Recycle (SWUST), Ministry of Education (12zxgk01).

S. Gao • F. Huang (✉) • D. Song • G. Li • Q. Liu • T. Feng • R. Zhao • J. Liu • W. Gao
College of Resources and Civil Engineering, Northeastern University, Wenhua Road, Shenyang, Liaoning, People's Republic of China
e-mail: huangfei@mail.neu.edu.cn

F. Dong (ed.), *Proceedings of the 11th International Congress for Applied Mineralogy (ICAM)*, Springer Geochemistry/Mineralogy,
DOI 10.1007/978-3-319-13948-7_13

Scholars have made some research on the formation of Fe_3S_4 in the sedimentary environment [5–9]. As an authigenic ferrimagnetic mineral, the magnetic characteristic of Fe_3S_4 is widely investigated [10, 11]. It helps to identify and interpret the paleomagnetic signal of sedimentary rocks containing Fe_3S_4 and provides clues for the research on the environmental magnetic mechanism. The symbiotic evolution phenomenon of Fe–S series is widespread in various geological environments [12–15]. Gu Lianxing et al. [14] observed the symbiotic evolution phenomenon of iron sulfide such as Fe_3S_4, FeS_2, and $Fe_{1-x}S$ in various jet-sedimentary deposits. Zeng Pusheng et al. [15] studied the genesis of the Fe_3S_4 generally exists as an unstable intermediate [16–19]. It is easily oxidized at high temperature or exposures to the air. So it is stringent in preparation conditions [7, 20]. Previous research has accumulated rich results, but the formation mechanism and stable physical and chemical conditions of Fe_3S_4 still lack an in-depth understanding.

2 Materials and Methods

2.1 Experimental Methods and Procedures

The Fe_3S_4 widely exists and the symbiotic evolution phenomenon of Fe–S series is common in typical jet-sedimentary deposits. Thus, the experimental conditions are designed by simulating natural geological conditions [12, 13]. The comparison of experimental conditions and the geological conditions is shown in Table 1.

2.2 Experimental Methods and Procedures

To further clarify the stable conditions and evolution process of the Fe_3S_4 intermediates, this research made Na_2S and $Na_2S_2O_3$ as sulfur source and $FeSO_4{\bullet}7H_2O$ as iron source and conducted the laboratory experiments using the vacuum heating equipment at different temperatures and times. When the vacuum heating equipment cooled spontaneously, we obtained black solid powder. Experimental conditions are shown in Table 1.

2.3 Methods for Assessment and Analysis

2.3.1 X-Ray Powder Diffraction

Use the agate mortar to grind the experimental samples for X-Ray Powder Diffraction (XRD) phase analysis. XRD of Northeastern University is PW3040/60X. Test conditions: CuKα target ($\lambda = 0.154056$ nm); Continuous scan range: 5°–90°; Step size: 0.033°; The consecutive scan time: approximately 7 min.

Table 1 The experimental conditions

pH	Concentration of Fe source (mol/L)	Fe:S	Heating temperature (°C)	Heating time (h)
4–5	0.30	3:4	160	30–50
4–5	0.30	3:4	200	30
4–5	0.30	3:4	260	30
4–5	0.30	3:4	290	30
4–5	0.30	3:4	320	30
4–5	0.30	3:4	350	30
4–5	0.30	3:4	380	30

2.3.2 Scanning Electron Microscope

Use the conductive adhesive to fix the samples and spray gold on it for Scanning Electron Microscope (SEM) morphology observation and element analysis (Energy spectrum diffraction (EDS)). SEM of Northeastern University is SSX—550. Resolution: 3.5 nm; Magnification: 20–300,000; Acceleration voltage: 0.5–30 kV; EDS energy resolution: 144 eV; Element: C–U; The minimum range $<1\mu m$.

2.3.3 Transmission Electron Microscopy

Grind samples in the anhydrous ethanol solution and oscillate it for 10 min by ultrasonic to disperse the sample particles. Use double micro grating to gain the dispersed fine powder and dry it for Transmission Electron Microscopy (TEM) observation and structure determination. TEM of Northeastern University is TecnaiG220. Point resolution: 0.23 nm; Line resolution: 0.14 nm; Acceleration voltage: 200 kV; Magnification: 20–1,000,000×.

3 Results

Pure Fe_3S_4 was prepared under the conditions of 200 °C, $t = 30$ h, pH = 4–5. X-ray diffraction analysis results are shown in Fig. 1.

The SEM and TEM observations results are shown in Fig. 2. The morphology of Fe_3S_4 is mainly spherical granular. Its particle size is uniform, about 30 nm (Fig. 2a, b). According to the electron diffraction spectrum test data, calibrate the crystal structure by the Comprehensive Analysis of Electron Diffraction Pattern Application Version 2.0.0 [21]. The calculative result is [202] crystal zone of Fe_3S_4 (Fig. 2c). The element analysis shows Fe, S peak, and Fe:S = 3:4 (Fig. 2d). It confirms that these small grains are Fe_3S_4 authentically, which belongs to the cubic system. The unit cell parameter is $a = 9.88$ Å; $\alpha = 90°$.

At 160 °C, the effects of different heating times on the experimental products have been investigated. Use XRD to analyze the main compositions and variation

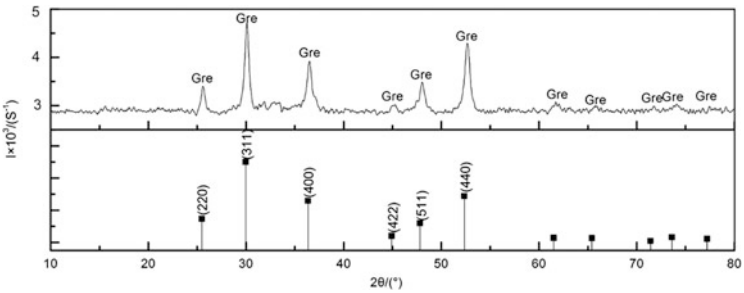

Fig. 1 The XRD analysis results of Fe_3S_4. Gre—Fe_3S_4

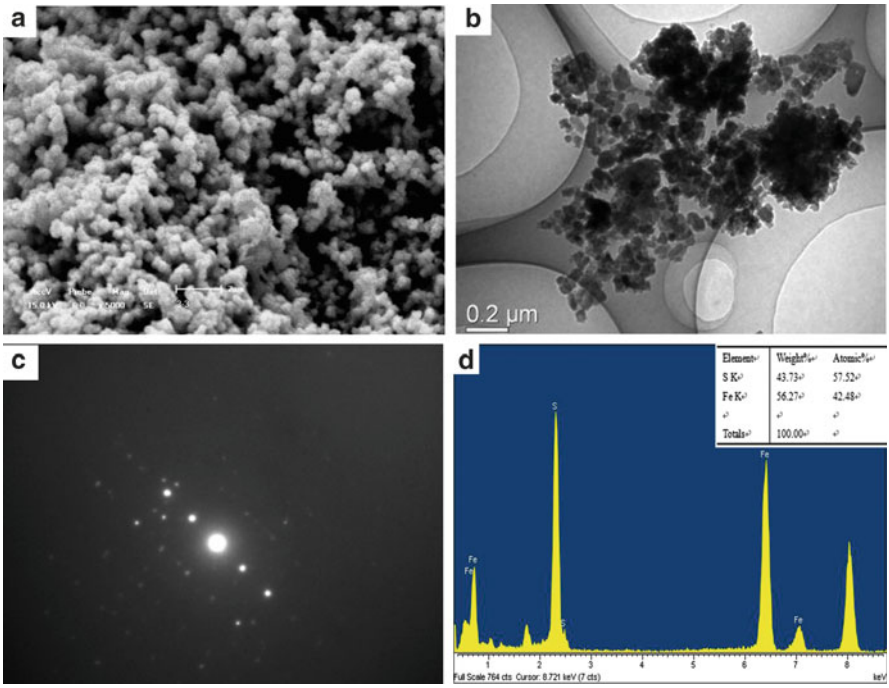

Fig. 2 The morphology and structure observation of Fe_3S_4. (**a**) Granular Fe_3S_4 under SEM, (**b**) Fe_3S_4 nanocrystals under TEM, (**c**) Selected area electron diffraction spectrum of Fe_3S_4, (**d**) The energy spectrum component analysis of Fe_3S_4

characteristics of the experimental products. From the XRD patterns (Fig. 3), the main phases of products are FeS, greigite, pyrite, and elemental sulfur when heating for 30 h. While the heating time increased to 50 h, FeS peaks disappeared and greigite and elemental sulfur peaks' intensity reduced. Meanwhile, the pyrite diffraction peaks increased instead. Due to the low temperature, the crystallization degree of experiment products is poor.

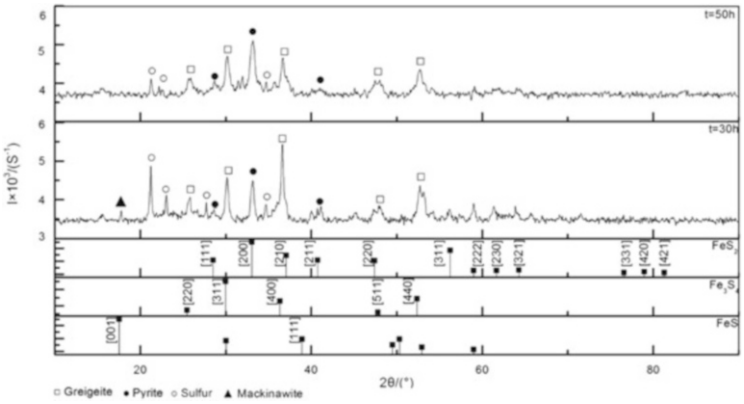

Fig. 3 XRD analysis results of the products of different heating times at 160 °C

4 Discussion

4.1 Growth Mechanism of Fe_3S_4 Nanocrystals

The growth of Fe_3S_4 nanocrystals experienced two processes of nucleation and growth [22]. The nucleation process is critical to obtain monodispersed nanoparticles. At any instant when the parent phase and the new phase achieve equilibrium, due to the thermal fluctuation, some local areas always have the density fluctuation that deviates from the equilibrium in the system. At this time, the atoms or molecules in original state may come together and become the new phase nuclei.

According to crystal growth theory [23], for the spherical nuclei:

$$\Delta G = (4\pi/3)\mathrm{r}^3\Delta G_{\mathrm{v}}^{\mathrm{o}} + 4\pi\mathrm{r}^2\Delta G_{\mathrm{s}}^{\mathrm{o}} \tag{1}$$

In the formula: $\Delta G_{\mathrm{v}}^{\mathrm{o}}$ and $\Delta G_{\mathrm{s}}^{\mathrm{o}}$ mean the decrease of free energy when per unit volume new phase forms and the increase on the interface of per unit area old and new phase, respectively; r represents the radius of the nucleus.

According to Fig. 4, ΔG in the system increases with the increasing r. When $r = r_{\mathrm{c}}$ (the critical radius), ΔG begins to decline; $r > r_{\mathrm{c}}$; and crystal nucleus can be stable; otherwise nucleation can't exist. The critical radius r_{c} of the nucleus is inversely proportional to the degree of supersaturation. When the system has a high degree of supersaturation, crystal nucleus can be saved stably as long as it reaches the smaller radius. In contrast, in low supersaturation condition, only the crystal nucleus with large radius can grow into crystals. Therefore, to prepare nanoparticles with uniform size, nucleation should occur at the mode of outbreak in the shortest time. The supersaturation for nucleation is higher than crystal growth. Growth units spread to the surface of nuclei, deposit, and then grow up; the same growth process is conducive to the formation of roughly uniform nanoparticles [22].

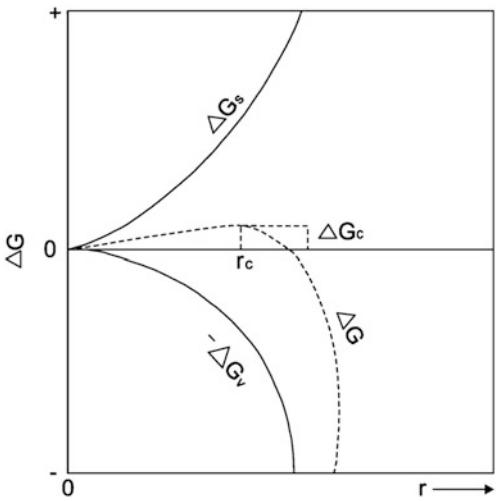

Fig. 4 The relation of crystal nucleus radius and free energy change in the system (According to Chen Jingzhong 2001)

In this experiment, the initial reaction temperature is low, which can't meet the nucleation and growth condition of mineral crystal. So it deposits to obtain the insoluble precursors merely. When the supersaturation increases, the driving force to form solid phase appears. As the temperature improves at the second stage, the supersaturation breaks through the threshold of nucleation, and a lot of mineral crystals nucleate simultaneously. The degree of supersaturation reduces with the continuous reaction, and nanocrystals begin to grow. Since a large number of Fe_3S_4 nuclei are formed simultaneously, reactants are depleted or conditions are changed; Fe_3S_4 nanocrystals can't grow up. Thus, many spherical nanocrystals with similar size and shape can form. In this growth stage, if the supersaturation of a certain region exceeds the threshold of nucleation once again, the secondary nucleation occurs. Double or multiple nucleations will cause the inconsistency of growth time of colloidal particles, which may lead to difference in particle sizes.

4.2 Stability Research on the Fe_3S_4 Nanocrystals

Wilkin and Barnes [24] observed that the solid-state reaction of greigite to pyrite requires the outward diffusion of iron, the reduction of ferric iron, and the oxidation of sulfide to disulfide. They presented strong evidence for a solid-state transformation (Eq. 2).

$$Fe_3S_4 \xrightarrow{-2e^-,\,-Fe^{2+}} 2FeS_2 \tag{2}$$

On the basis of previous studies, Hunger et al. [25] discussed the parameters that control the stability of Fe_3S_4 through hydrothermal experiments. He found greigite

was as an intermediate phase from 125 °C to 200 °C and proposed in theory that greigite can form on the pathway to pyrite as an intermediate in the reaction between mackinawite and excess sulfur (Eq. 3) or via an iron loss pathway (Eq. 4).

$$3FeS \xrightarrow[+S^{2-}]{-2e^-} Fe_3S_4 \xrightarrow[+2S^{2-}]{-4e^-} 3FeS_2 \tag{3}$$

$$4FeS \xrightarrow[-Fe^{2+}]{-2e^-} Fe_3S_4 \xrightarrow[-Fe^{2+}]{-2e^-} 2FeS_2 \tag{4}$$

Experimental results show the temperature and the heating time can affect the formation and transformation of Fe_3S_4. Pure Fe_3S_4 nanocrystals were prepared under the conditions of 200 °C, $t = 30$ h, pH = 4–5. When the heating time increased, the reaction would conduct more fully and be conducive to the formation of pyrite.

In the Fe–S binary system phase diagram [26], Fe_3S_4 mainly keeps stable below 100 °C. At a higher temperature, $Fe_{1-x}S$ (mpo/hpo) and FeS_2 exist symbiotically. The experimental result which is marked in Fe–S phase diagram (Fig. 5) broadens the steady range of Fe_3S_4.

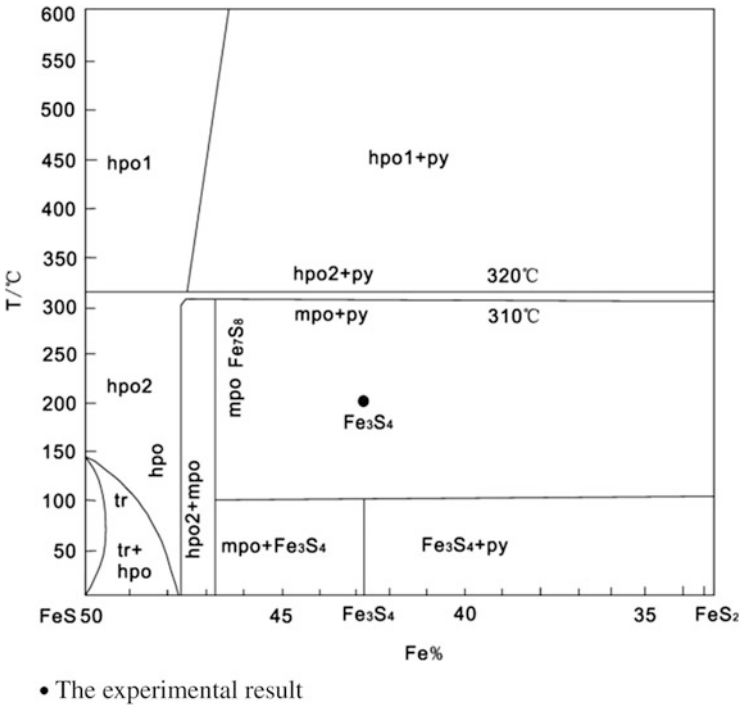

Fig. 5 The Fe–S binary system phase diagram (According to Chen Zheng, 1990)

5 Conclusions

1. Pure Fe_3S_4 nanocrystals were prepared under the conditions of 200 °C, $t = 30$ h, pH = 4–5. Its morphology is mainly spherical granular and structure belongs to cubic system.
2. Fe_3S_4 is mainly stable at 200 °C, 30 h. When the heating time increased, the reaction would conduct more fully and be conducive to the formation of pyrite.
3. The stable temperature and evolution direction of Fe_3S_4 defined by the experiments under thermal and humid conditions broaden the steady range of Fe_3S_4 in the Fe–S binary phase diagram.

Experimental results have typomorphic significance on the natural geological conditions and provide a scientific basis for the preparation of Fe_3S_4 nano-magnetic materials.

References

1. Kiner BJ, Erd RC, Grimaldi FS (1964) Greigite: the thio-spinel of iron, a new mineral. Am Mineral 49:543–555
2. Andrew PR, Richard LR, Kenneth LV et al (1996) Environmental magnetic implications of greigite (Fe_3S_4) formation in a 3 m. y. lake sediment record from Butte Valley, northern California. Geophys Res Lett 23(20):2859–2862
3. Wang Z, Chen Z, Gu J (2005) Occurrence and environmental implications of magnetic iron sulfides in stiff muds from the continental shelf of the East China Sea. Geo-Mar Lett 25 (5):300–305
4. Blanchet CL, Thouveny N, Vidal L (2009) Formation and preservation of greigite (Fe_3S_4) in sediments from the Santa Barbara Basin: implications for paleoenvironmental changes during the past 35 ka. Paleoceanography 24(2):1–15
5. Stephen M, Nicholas HCS, Frankel RB et al (1990) Biomineralization of ferrimagnetic greigite (Fe_3S_4) and iron pyrite (FeS_2) in a magnetotactic bacterium. Nature 343(6255):258–261
6. Andrew PR, Gillian MT (1993) Diagenetic formation of ferrimagnetic iron sulphide minerals in rapidly deposited marine sediments, South Island, New Zealand. Earth Planet Sci Lett 115 (1–4):257–273
7. Daniel A, Dobson J (1996) Magnetic investigations of framboidal greigite formation: a record of anthropogenic environmental changes in eutrophic Lake St Moritz, Switzerland. The Holocene 6(2):235–241
8. Hu S, Appel E, Hoffmann V et al (2002) Identification and magnetic significance of greigite in lake sediments. Sci China Ser D Earth sci 32(3):234–238
9. Yanzhe F, von Dobeneck T, Franke C et al (2008) Rock magnetic identification and geochemical process models of greigite formation in quaternary marine sediments from the Gulf of Mexico (IODP Hole U1319A). Earth Planet Sci Lett 275(3–4):233–245
10. Kasama T, Mihály P, Chong RKK et al (2006) Magnetic properties, microstructure, composition, and morphology of greigite nanocrystals in magnetotactic bacteria from electron holography and tomography. Am Mineral 91(8–9):1216–1229
11. Andrew PR, Chang L, Christopher JR et al (2011) Magnetic properties of sedimentary greigite (Fe_3S_4): an update. Rev Geophys 49(1):1–46
12. Jeffrey CC, John WM (1987) The characterization of iron sulfide minerals in anoxic marine sediments. Mar Chem 22(2–4):193–206

13. Saulwood L, Morse FW (1991) Sulfate reduction and iron sulfide mineral formation in Gulf of Mexico anoxic sediments. Am J Sci 291:55–89
14. Gu L, Vokes FM et al (1990) Melnikovite in the South China type massive sulfide deposits and its annealing. Acta Petrol Mineral 9(4):351–356
15. Zeng P, Pei R, Hou Z et al (2005) The Dongguashan deposit in the Tongling mineralization cluster area, Anhui: a large-sized superimposition-type copper deposit. Acta Geol Sin 79 (1):106–113
16. Berner RA (1984) Sedimentary pyrite formation: an update. Geochim Cosmochim Acta 48:605–615
17. Schoonen MAA, Barnes HL (1991) Reactions forming pyrite and marcasite from solution: II. Via FeS precursors below 100 °C. Geochim Cosmochim Acta 55(6):1505–1514
18. Stanjekl H, Fassbinder JWE, Vali H et al (1994) Evidence of biogenic greigite (ferrimagnetic Fe_3S_4) in soil. Eur J Soil Sci 45(2):97–103
19. Dong J, Zhang S, Ganqing J et al (2013) Greigite from carbonate concretions of the Ediacaran Doushantuo formation in South China and its environmental implications. Precambrian Res 225:77–85
20. Snowball I, Thompson R (1988) The occurrence of greigite in sediments from Loch Lomond. J Quat Sci 3(2):121–125
21. Bian W, Deng J et al (2004) Comprehensive analysis of electron diffraction pattern application. J Chin Electron Microsc Soc 23(4):426
22. Feng Y, Ma T, Liu L et al (2009) Insights into shape control and growth mechanism of inorganic nanocrystals. Sci China Ser B Chem 39(9):864–886
23. Jingzhong C (2001) Chemical theory and method of modern crystal. Higher Education Press, Beijing, pp 126–128
24. Wilkin RT, Barnes HL (1996) Pyrite formation by reactions of iron monosulfides with dissolved inorganic and organic sulfur species. Geochim Cosmochim Acta 60(21):4167–4179
25. Hunger S, Benning LG (2007) Greigite: a true intermediate on the polysulfide pathway to pyrite. Geochem Trans 8(1):1–20
26. Chen Z (1984) On mineral sequence and mineral paragenesis. J Chengdu Inst Geol 03:1–15

Antarcticite: A Phase Change Material for Thermal Energy Storage—Experiments and Simulation

Xiaobin Gu, Jingjing Niu, and Shan Qin

Abstract Antarcticite, $CaCl_2 \cdot 6H_2O$, is an ideal phase change material (PCM) due to its high-energy storage density and good thermal conductivity. In this chapter, supercooling and subsequent solidification behavior of antarcticite are studied based on the cooling curve method and DSC measurement. The results show that the minor $SrCl_2 \cdot 6H_2O$ as the nucleator and carboxymethyl cellulose as the thickening agent could significantly reduce supercooling and partly restrain the phase separation. Moreover, we incorporated antarcticite as PCM into building envelopes in four different cases, and the simulation of the heat transfer processes showed that the temperature fluctuation could be reduced to about 2 °C in the best case.

Keywords Antarcticite • Phase change material • Supercooling • Simulation

1 Introduction

The continuous increase in the level of gas emissions and the rise in fuel prices are the main driving forces which stimulate the better utilization of various sources of renewable energy. Energy storage plays important roles in conserving renewable energy and improving its utilization, because most renewable energy sources are intermittent in nature. Solar energy, one of the most promising energy sources, is only available during the day, and hence its application requires efficient thermal energy storage (TES) so that the excess heat collected during sunshine hours may be stored for later use during the night. As a result, the TES using latent heat of phase change material (PCM) has become more and more popular [1–4]. Antarcticite, a mineral with composition $CaCl_2 \cdot 6H_2O$ and structure P321 [5], is an ideal PCM due to its high-energy storage density, good thermal conductivity, and characteristics to store heat at a constant temperature (29 °C, the melting point). However, the supercooling and phase separation would weaken its longevity and

X. Gu • J. Niu • S. Qin (✉)
Key Laboratory of Orogenic Belts and Crustal Evolution, MOE, School of Earth and Space Sciences, Peking University, No. 5 Yiheyuan Road, Beijing, People's Republic of China
e-mail: sqin@pku.edu.cn

F. Dong (ed.), *Proceedings of the 11th International Congress for Applied Mineralogy (ICAM)*, Springer Geochemistry/Mineralogy,
DOI 10.1007/978-3-319-13948-7_14

thermal properties and then hinder its application. Some efforts to lower the supercooling of antarcticite have been made. For example, Liu and Chung [6] have investigated the effect of different nucleators on supercooling, giving a supercooling of 8 °C which looks too large to be used in thermal storage. Voelker et al. [7] did a good job of suppressing the supercooling on antarcticite; however, the nucleator they applied is toxic. Although some authors [8–10] have found good nucleators of antarcticite which could reduce supercooling to less than 2 °C, most of the authors haven't investigated its effect on application via simulation. The work to find more suitable nucleators for antarcticite and to test its effect on application through simulation is very significant in the application.

To assess the performance of the PCM integrated in the wall, the numerical method is effective and essential, and lots of achievements via simulations have been made. Kuznik et al. [11] optimized the thickness of PCM in wallboard and found that a 1 cm wallboard allowed a doubling of the thermal inertia of the building, prevented building rooms from overheating during hot days, and increased the minimum air temperature by releasing energy during night. Ahmad et al. [12] studied three types of wallboards containing PCM by experimental and numerical methods, and the results revealed that PVC panels filled with PEG 600 were compatible with the objective of a light envelope having high heat capacity storage. Alawadhi's paper [13] presented the thermal analysis of a building brick containing PCM used in hot climates; the results indicated that the heat gain was significantly reduced when the PCM was incorporated into the brick and that increasing the quantity of the PCM had a positive effect. And PCM cylinders located at the centreline of the bricks had the best performance.

Therefore, the aims of this study are (1) to investigate the impact of possible nucleators and thickening agents on the supercooling and solidification behavior of antarcticite based on the cooling curve method and DSC measurement and (2) to examine the performance of the PCM which is incorporated into the building envelopes by ANSYS [14] simulation.

2 Experiment and Simulation

2.1 Material

Antarcticite ($CaCl_2 \cdot 6H_2O$, purity >99 %), which was the target material, was produced by Kang Pu Hui Wei Technology Co., Ltd. (Beijing, China). Strontium chloride hexahydrate ($SrCl_2 \cdot 6H_2O$, purity >99 %) from Xilong Chemical Co., Ltd. (Guangdong, China) and carboxymethyl cellulose (CMC, AR with high viscosity of 300–800 m Pa · s in 20 g/L aqueous solution) from Sinopharm Chemical Reagent Co., Ltd. (Shanghai, China) were used as the nucleator and thickening agent, respectively.

2.2 Experimental Method

Though the supercooling and phase separation would weaken the longevity and the thermal properties of antarcticite, the modification is made possible by additives. Many studies have been carried on to approve the thermal characteristic of antarcticite; from a number of potential candidates, $SrCl_2 \cdot 6H_2O$ was chosen. All of the specimens were weighted in the precision balance and set in a glass beaker. Next, the specimens were heated to about 50 °C in thermostat water bath, and then the melted specimen was cooled to room temperature in air. As shown in Fig. 1, during the melting–freezing process, the solidification behavior of the specimen was monitored by the change in temperature measured by thermocouples that were set into the center of the solution, and in the meantime, the paperless recorder was employed as the data acquisition apparatus. PCMs with and without $SrCl_2 \cdot 6H_2O$ as nucleator were prepared to evaluate the effect on the supercooling. Also, PCMs with different weight percentage of CMC (0, 1, 1.5, 2) were prepared to examine the influence on the incongruent melting and to decide the optimum ratio of CMC (i.e., the one can best restrain the phase separation).

2.3 Thermal Analysis

Differential scanning calorimeter (DSC, TA Q100 America) was used to measure the thermal properties of antarcticite. The analyses were carried out under a constant stream of nitrogen with a heating rate of 5 °C/min. The specimens of 1.55 mg in mass were set in a crucible, and the temperature interval of the measurement is 10–50 °C. From the thermal analyses of antarcticite with DSC, as shown in Fig. 2, we could confirmed that its melting point is about 29.6 °C. However, the specimens didn't crystallize during the cooling process until the temperature decreased to −5 °C, which means antarcticite has the supercooling

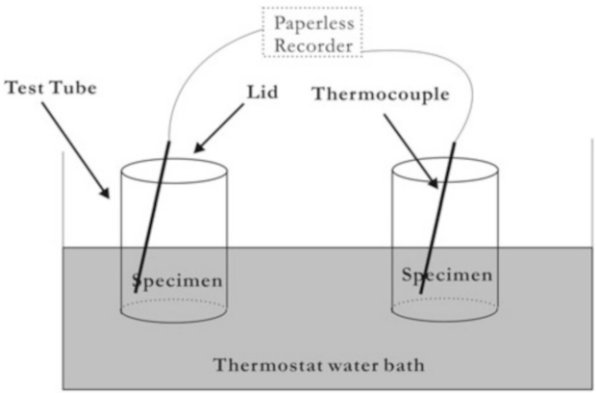

Fig. 1 Schematic view of experimental apparatus

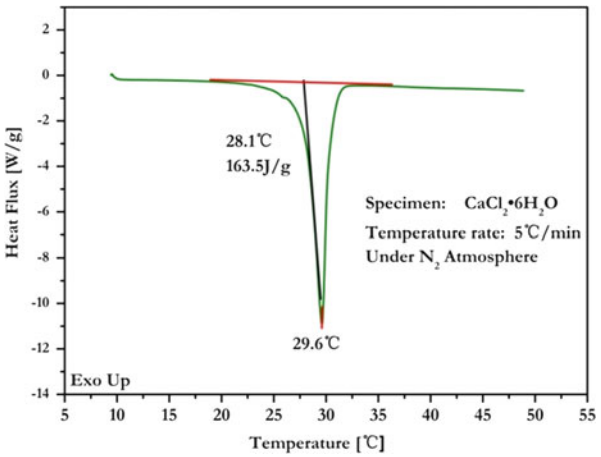

Fig. 2 DSC curve of antarcticite ($CaCl_2 \cdot 6H_2O$)

of more than 30 °C under this condition. According to the DSC data, we deduced that the latent heat is 163.5 $J \cdot g^{-1}$ from the area of the endothermic peak, which is higher than Shi and Zhang's result [9], but lower than that of Zalba et al. [15], and the specific heat is 2.26 and 3.35 ($J \cdot g^{-1} \cdot k^{-1}$) for liquid and solid phases, respectively, from the slope of the tangent line.

2.4 Numerical Scheme

In order to compare the heat insulation ability of PCM, we designed four cases of the building walls as shown in Fig. 3. All the designed walls basically consist of two layers of 15 mm thick oriented strand board (OSB) and one layer of polystyrene (PS). The total 165 mm thick wall contains a 40 mm thick antarcticite layer, but the layer position is different. No antarcticite layer is incorporated in case A, which is only used for comparison purpose.

In the simulation, conductive heat transfer through the walls is generally supposed to be unidirectional. The thermal expansion of PCM, OSB, and PS is neglected, and the effect of the natural convection of liquid PCM is not accounted in the computations either. The convection between the wall and the air, as well as the radiation, is also ignored for simplification. Under the above assumptions, the problem we studied becomes a solution of unidirectional thermal conductivity. To evaluate the capacity of the thermal insulation, the amplitude of the thermal fluctuation of interior and exterior faces of the wall in cases of the models is shown in Fig. 3. The exterior temperature is set equal to the environmental temperature, which could be simulated by a sine-exponential model as shown in Fig. 4.

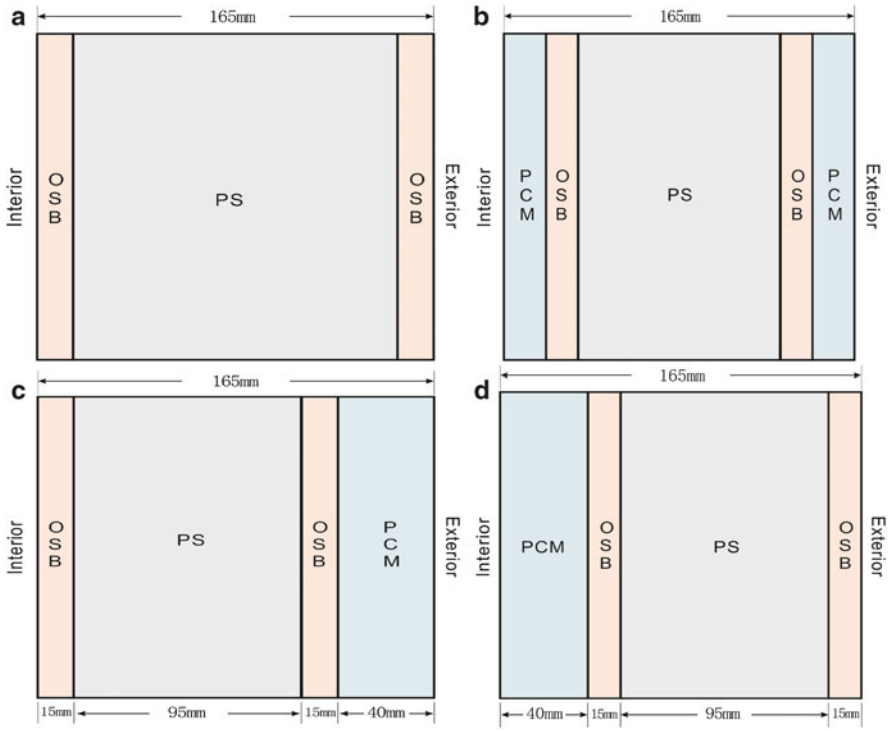

Fig. 3 Four designed wallboard schematics

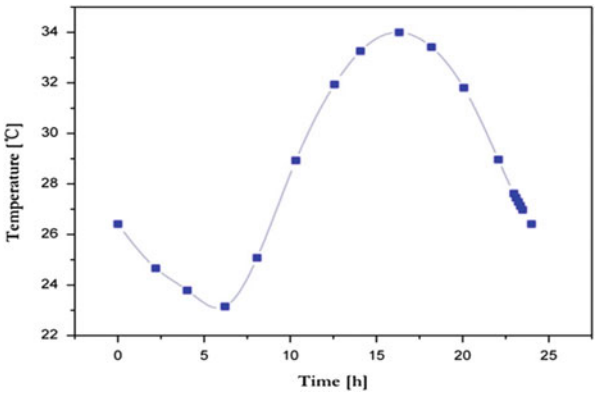

Fig. 4 The temperature variation in 1 day

The finite element method is employed to simulate the heat transfer along the wallboards with the software ANSYS. The phase change process, which is highly no-liner, can be taken into account in the heat equation using either the effective heat capacity method or the enthalpy method. In our work, enthalpy method is used. Figure 5 shows an experimental enthalpy–temperature curve measured by DSC,

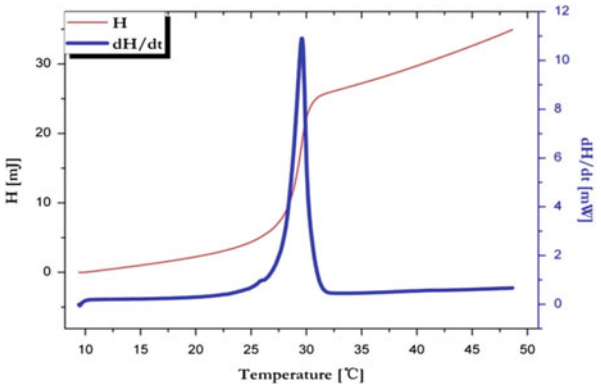

Fig. 5 The DSC results and enthalpy–temperature curve

Table 1 The parameters used in the simulations

Material	Density [kg/m^3]	Thermal conductivity [W/(m • K)]	Specific heat [J/(kg • K)]	References
OSB	465	0.108	1,760	[15]
PS	100	0.047	1,386	[16]
PCM	1,562 (liquid, 32 °C)	0.540 (liquid, 38.7 °C)	2,260 (solid)	[17]
	1,802 (solid, 24 °C)	1.088 (solid, 23 °C)	3,550 (liquid)	

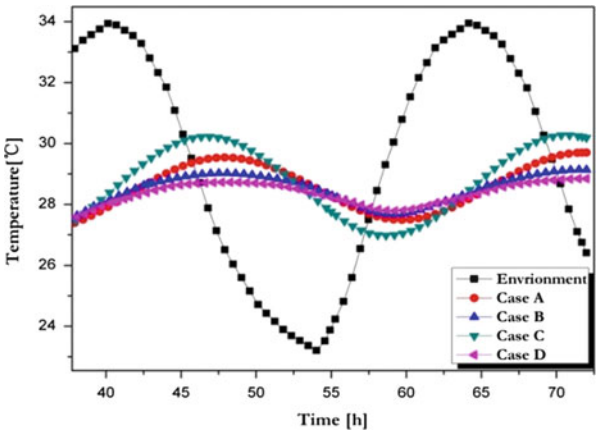

Fig. 6 Interior temperature variation from 40 to 72 h

where the enthalpy–temperature data sets are chosen. The other parameters used in the simulation are listed in Table 1 [15–17].

The interior temperature of the board is set same as the environmental temperature at time $t = 0$. We set up a 3-day (72 h) process. Grids are divided automatically by the software, and the step is sized as 2,000 s. Because the data in the first day are not at balance, we choose the 40–72 h as the observing period, as shown in Fig. 6.

3 Result and Discussion

3.1 Experimental Result

Supercooling, also known as undercooling, is the process of lowering the temperature of a liquid or a gas below its freezing point without it becoming a solid. As shown in Fig. 7, the temperature variation of the PCM with and without $SrCl_2 \cdot 6H_2O$ revealed the effect of the nucleators on the degree of the supercooling. We can see from the result that the specimen without $SrCl_2 \cdot 6H_2O$ doesn't crystallize until at about 10 °C with a supercooling of over 18 °C. In comparison, the one with $SrCl_2 \cdot 6H_2O$ as nucleator could significantly restrain the supercooling, which can decrease the supercooling to about 2 °C. It is obvious that the addition of $SrCl_2 \cdot 6H_2O$ would significantly reduce the degree of supercooling, which makes it possible for the application of the PCM. The mechanism of nucleator reducing the supercooling could be explained by the theory of heterogeneous nucleation [18]. In the present case, the nucleator $SrCl_2 \cdot 6H_2O$ adopts the P321 structure, the same as that of antarcticite; the difference of the lattice constants [19, 20] is less than 4.2 % [21]. So during the experiment, $SrCl_2 \cdot 6H_2O$ became the perfect heterogeneous nucleus for antarcticite, which made it easier for the nucleation of antarcticite. As a result, supercooling of antarcticite was significantly reduced.

In the process of melting–freezing, phase separation of PCM is very common. For antarcticite, due to its unstablility under low temperature, $CaCl_2 \cdot 6H_2O$ is easily transformed to calcium chloride tetrahydrate ($CaCl_2 \cdot 4H_2O$). And then the undesired lower hydrate will settle at the bottom of the container and will not convert to the higher hydrate phase even if conditions change and the higher hydrate becomes thermodynamically the stable modification. Experimentally this

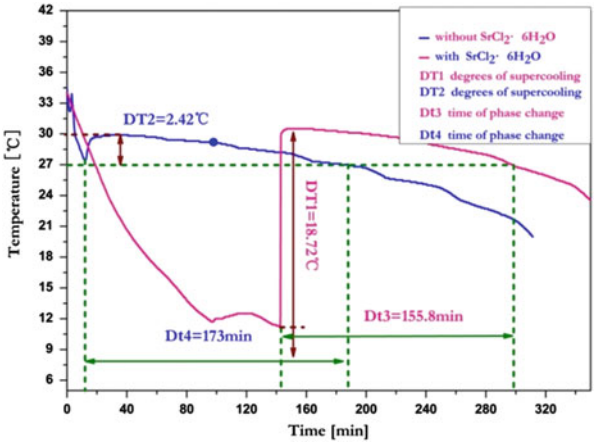

Fig. 7 Cooling curve of antarcticite with and without $SrCl_2 \cdot 6H_2O$

stratification shows up as a decrease in the heat absorbed on melting and released on crystallization [22]. Therefore, we tried to use thickening agents to restrain phase separation of antarcticite. Figure 8 shows the performance of the four recipes, in which the different ratios of CMC were added. The corresponding data for the degree of supercooling and time of discharge were listed in Table 2. As we can see, the specimen with 2 % CMC had the least degree of supercooling, but its heat storage is too low. The specimen with 1 % CMC not only further decreased the degree of supercooling but also possessed higher heat storage capacity. In conclusion, the use of CMC could partly increase the stability of liquid antarcticite without obvious decline of the heat storage. The use of thickening agent will increase the liquid viscosity and then slow the rate of crystal growth, which makes for the existence of a larger number of small crystals; as a result, the stabilization of the solution will be partly improved. Further, the CMC can keep the crystals localized so even if by mischance the undesired tetrahydrate were formed, it would re-melt at approximately its original position and not cause stratification during the heating process [22]. What calls for special attention is that the heating temperature shouldn't reach over 50 °C, for the performance of CMC would significantly decrease under the condition of high temperature during the experiment.

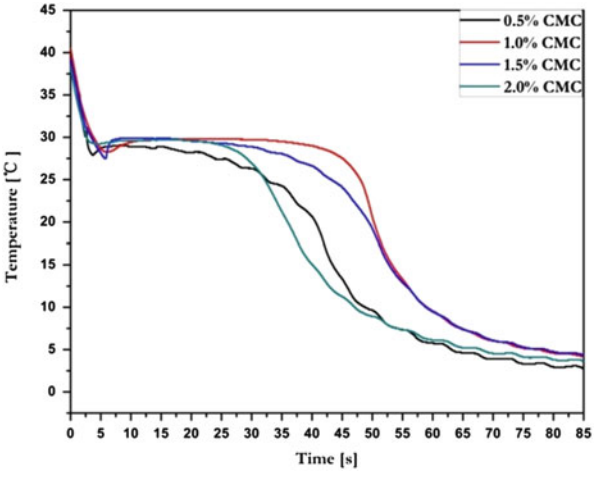

Fig. 8 Cooling curve of antarcticite with 0.5, 1.0, 1.5, 2.0 wt% CMC

Table 2 Properties of antarcticite with different mass fraction CMC (0.5 %, 1.0 %, 1.5 %, and 2.0 %)

Mass fraction [%]	0.5	1.0	1.5	2.0
Degree of supercooling [°C]	1.92	1.62	2.42	0.62
Time of discharge [min]	195	399	327.7	264.5

3.2 Numerical Results

The simulation results show that in all the cases (Case A–D) the thermal fluctuation can be reduced. We list the highest and the lowest temperatures for every case in Table 3. It is interesting to see that the location of PCM layer affects apparently the performance of the board. Case D, whose amplitude is 0.9 °C, is the best design, whereas case C is the worst one. PCM in board does not prevent the temperature increasing compared with SIP. Compared with cases D and C, we find that the place where PCM layer located is of vital importance. PCM with the same thickness of 40 mm, which is put in the exterior wall, could not exert a significant effect on the temperature increasing or decreasing.

Figures 9 and 10 show the temperature distribution in the wallboard, in which four nodes, i.e., the exterior face, 1/2 thickness of PCM, 1/2 thickness of PS, and the interior face, are picked up and recorded. In both cases, the temperature distribution in PCM layer appears to be uniform, and no temperature gradient is observed. This is because the thermal conductivity of PCM is much higher than the PS, and the temperature gradient is not easily built under ambient conditions. A 40 mm-thick PCM layer put in the exterior wall (case C) cannot absorb all the heat when the environmental temperature increases. In case D, PS prevents some of the exterior heat transferring into the interior face, which makes the temperature amplitude decrease to about 6 °C; at the same time, antarcticite also lowers the temperature

Table 3 The highest and the lowest temperature in four cases

	Environment	Case A	Case B	Case C	Case D
Highest T (°C)	34.0	29.5	29.0	30.2	28.7
Lowest T (°C)	23.1	27.5	27.7	27.0	27.8
ΔT (°C)	9.9	2.0	1.3	3.2	0.9

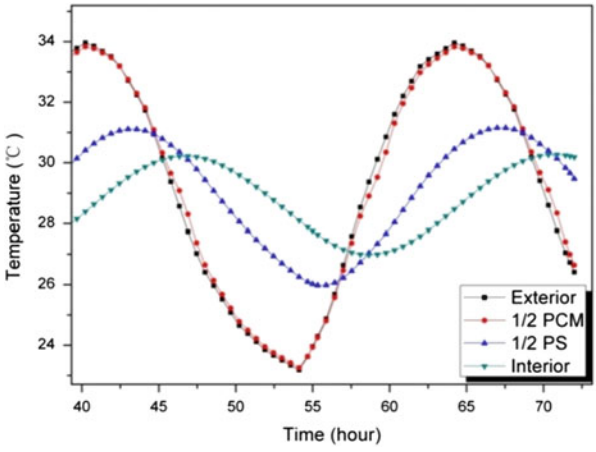

Fig. 9 The temperature distribution in case C

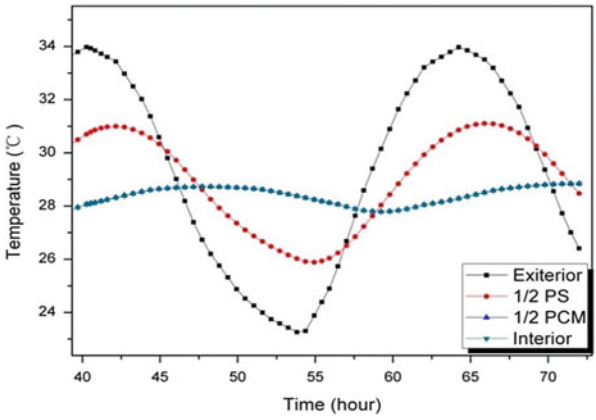

Fig. 10 The temperature distribution in case D

amplitude due to its good thermal storage; as a result, the temperature amplitude at interior face is down to 0.9 °C. The simulation results indicate that PCM is not a good heat-insulation material for its higher thermal conductivity compared with PS, but is better at adjusting the temperature, especially near the phase change temperature on account of its high phase change latent heat.

4 Conclusions

Based on the cooling curve method and DSC measurement, we investigated the supercooling and solidification behaviour of antarcticite. The heat insulation effect of antarcticite as a PCM incorporated into the wallboard was also studied in four typical cases. The results are summarized as follows:

1. As the nucleator from a number of potential candidates, $SrCl_2 \cdot 6H_2O$ with an addition of 2 wt% could significantly reduce the supercooling to 2–3 °C, which makes it possible for the application of antarcticite as PCM.
2. Also we selected CMC as the thickening agent. The addition of 1 % CMC could not only partly restrain the phase separation of antarcticite during the freezing–melting process but also further decrease the supercooling.
3. PCM integrated into the wallboard can reduce the thermal fluctuation compared with SIP or other advanced light building wallboard, but an optimization must be considered. In this work, we found that PCM layer put in interior face has a minimum amplitude of temperature fluctuation in four case studies.

Acknowledgment This work is financially supported by Beijing Nature Science Foundation (2132024).

References

1. Zhang Z, Shi G, Wang S, Fang X, Liu X (2013) Thermal energy storage cement mortar containing n-octadecane/expanded graphite composite phase change material. Renew Energy 50:670–675
2. Nomura T, Tsubota M, Oya T, Okinaka N, Akiyama T (2013) Heat storage in direct-contact heat exchanger with phase change material. Appl Therm Eng 50(1):26–34
3. Waqas A, Din ZU (2013) Phase change material (PCM) storage for free cooling of buildings—A review. Renew Sustain Energy Rev 18:607–625
4. Anisur MR, Mahfuz MH, Kibria MA, Saidur R, Metselaar IHSC, Mahlia TMI (2013) Curbing global warming with phase change materials for energy storage. Renew Sustain Energy Rev 18 (C):23–30
5. Torii T, Ossaka J (1965) Antarcticite: a new mineral, calcium chloride hexahydrate, discovered in Antarctica. Science 149(3687):975–977
6. Liu Z, Chung DDL (2001) Calorimetric evaluation of phase change materials for use as thermal interface materials. Thermochim Acta 366(2):135–147
7. Voelker C, Kornadt O, Ostry M (2008) Temperature reduction due to the application of phase change materials. Energy Build 40(5):937–944
8. Liu D, Xu YL (2007) Thermoproperties research on nucleators-$CaCl_2 \cdot 6H_2O$ composites under distinctive systems. Acta Energ Sol Sinica 28(7):732–738
9. Shi MM, Zhang XL (2010) Preparation of phase-change material for natural cool energy storage and its characteristics. Chem Eng China 38(9):82–85
10. Lane GA (1992) Phase change materials for energy storage nucleation to prevent supercooling. Sol Energy Mater Sol Cells 27(2):135–160
11. Kuznik F, Virgone J, Noel J (2008) Optimization of a phase change material wallboard for building use. Appl Therm Eng 28(11):1291–1298
12. Ahmad M, Bontemps A, Sallée H, Quenard D (2006) Experimental investigation and computer simulation of thermal behaviour of wallboards containing a phase change material. Energy Build 38(4):357–366
13. Alawadhi EM (2008) Thermal analysis of a building brick containing phase change material. Energy Build 40(3):351–357
14. Moaveni S (2003) Finite element analysis: theory and application with ANSYS. Pearson Education, India
15. Zalba B, Marín JM, Cabeza LF, Mehling H (2003) Review on thermal energy storage with phase change: materials, heat transfer analysis and applications. Appl Therm Eng 23(3):251–283
16. Yang QX (1992) Theoretical approach to the thermal property of wood: thermal conductivity and diffusivity of wood. J Fujian Coll Forest 12(2):182–188
17. Liu YN (2007) Energy conservation research of composite PCM wallboard applied in the north residential building. Doctoral dissertation, Beijing, North China University of Technology
18. Mullin JW (2000) Crystallization, 3rd edn. Heinemann, Butterworth
19. Leclaire A, Borel MM (1977) Le dichlorure et le dibromure de calcium hexahydrates. Acta Crystallogr Sect B: Struct Crystallogr Cryst Chem 33(9):2938–2940
20. Abrahams I, Vordemvenne E (1995) Strontium dibromide hexahydrate. Acta Crystallogr Sect C: Cryst Struct Commun 51(2):183–185
21. Telkes M (1952) Nucleation of supersaturated inorganic salt solutions. Ind Eng Chem 44 (6):1308–1310
22. Feilchenfeld H, Sarig S (1985) Calcium chloride hexahydrate: a phase-changing material for energy storage. Ind Eng Chem Prod Res Dev 24(1):130–133

Illite–Smectite Mixed-Layer Minerals in the Alteration Volcanic Ashes Under Submarine Environment

Hanlie Hong, Wenpeng Gao, Ke Yin, Zhaohui Li, and Chaowen Wang

Abstract The clay mineralogy of the clay intervals interbedded with siliceous mudstones across the Permian–Triassic boundary (PTB) in Pengda, Guiyang, Guizhou province, was investigated by X-ray diffraction (XRD) and high-resolution transmission electron microscopy (HRTEM). The clay mineral assemblages of the sediments are mainly I/S clays and minor smectite, kaolinite, and illite as revealed by XRD analyses. The peak-shaped parameters BB1 and BB2 of I/S clays of the representative clay bed PL-01 are 4.7° and 4.4°, respectively, and the peak position of the low-angle diffraction is at 6.5° 2θ (13.6 Å), suggesting that the I/S clays have a IS type of ordering. However, multi-order diffractions and their intensities are different from those of completely ordered 1:1 mixed-layer I/S clay rectorite, indicating that I/S clays of the Pengda section have partially ordered IS structures. HRTEM observations show that most of the I/S clays exhibit a IS stacking ordering. However, in some areas within a IS particle, smectite layer is observed in doublets, triplets, and quartets, which are interstratified by various amounts of illite layers, suggesting the presence of other irregular stacking in addition to the major 1:1 IS-ordered stacking. Transformation of smectite layer into illite layers is also observed in the I/S clays, suggesting that the Pengda I/S clays are derived from smectite illitization, in good agreement with the clay mineral assemblage. The I/S clays of the Pengda section contain up to 45–95 % smectite layer, the notably higher contents of smectite layer relative to those of other PTB stratigraphic sets in south China can be attributed to the difference in alteration and smectite illitization processes due to different sedimentary environments.

Keywords Permian–Triassic boundary (PTB) • High-resolution transmission electron microscopy (HRTEM) • Clay minerals • Mixed-layer illite–smectite

H. Hong (✉) • W. Gao • K. Yin • C. Wang
Faculty of Earth Sciences, China University of Geosciences, Wuhan, Hubei 430074, People's Republic of China
e-mail: hongh18311@yahoo.com.cn

Z. Li
Faculty of Earth Sciences, China University of Geosciences, Wuhan, Hubei 430074, People's Republic of China

Geosciences Department, University of Wisconsin—Parkside, Kenosha, WI 53141-2000, USA

F. Dong (ed.), *Proceedings of the 11th International Congress for Applied Mineralogy (ICAM)*, Springer Geochemistry/Mineralogy,
DOI 10.1007/978-3-319-13948-7_15

1 Introduction

The Permian–Triassic boundary (PTB) mass extinction is considered as the most serious biotic crisis in the history of life, in which both marine and terrestrial biota suffered near annihilation [1, 2]. The causes for this biotic crisis are still debated [3]. However, the pronounced and worldwide negative carbon isotope excursion at the PTB is indicative of a strong disruption in carbon reservoirs [2, 4], related to prominent volcanic events of the Siberian Traps [3, 5, 6]. In the PTB stratigraphic set in south China, there occur several clay intervals with a thickness of mainly 2–20 cm interbedded within carbonate sediments that encompass mass extinction. These intervals were recognized as products of alteration of volcanic ashes based on the associated heavy minerals and clay mineral composition. Previous studies on the PTB clay intervals were focused mainly on mineral composition, clay morphology, and their provenance [7–11]. The identification of clay minerals from XRD measurement suggests that mixed-layer I/S clays dominantly comprise the clay sediments, but the stacking structures of the mixed-layer I/S clays are still not well known [11–14], making it difficult to reveal the formation of clays in the sediments due to alteration and transformation between clay minerals during diagenesis.

XRD measurement provides usually the information on average layer stacking of mixed-layer I/S clays within crystallites based on Markovian statistics, while HRTEM analysis gives structural information on layer stacking in local regions within a crystallite. For investigation of the transformation mechanisms of I/S clays during diagenesis, HRTEM methods have been utilized to determine the structures of mixed-layer I/S minerals [15–17]. The clay beds within the PTB stratigraphic set in south China provide an opportunity to study the formation of mixed-layer I/S minerals resulted from the alteration of volcanic ashes under submarine environment. However, only rare HRTEM study was undertaken to investigate their transformation mechanisms. In this study, we investigated the one-dimensional structure images of mixed-layer I/S minerals using HRTEM analysis in combination with XRD analyses to obtain a better understanding of clay mineralogical characteristics and formation mechanisms of I/S minerals from the alteration of volcanic ashes under submarine environment.

2 Materials and Methods

2.1 Sample Preparation

The Pengda section (26.37°N, 106.59°E) is located at Dangwu town, Guiyang city, Guizhou province, southeastern China. A general map of the study area around Guiyang is shown in Fig. 1. In the PTB stratigraphic set, there are eight clay layers each with a thickness of 3–12 cm interbedded with siliceous mudstones, based on their distinctive color, texture, and composition. The siliceous mudstones are

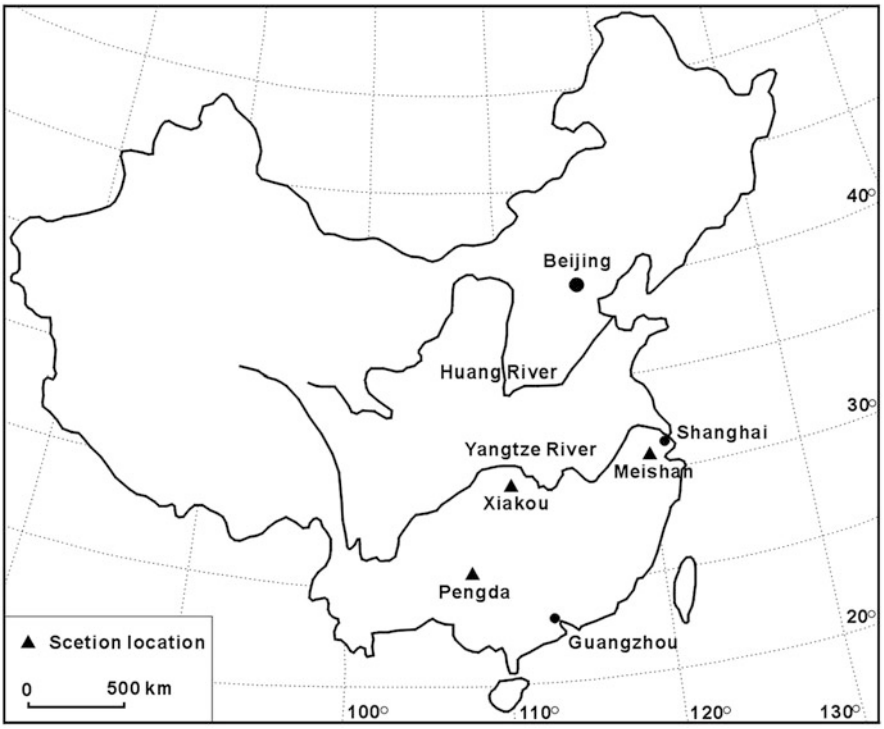

Fig. 1 A generalized map showing the location of the PTB sections

considered as neritic deposits according to the occurrence of Radiolaria fossils [18]. Representative clay samples, weighing around 500 g, were collected from each of the eight interbedded clay layers across the PT boundary according to their distinctive color, texture, and composition.

2.2 XRD Analysis

Bulk clay samples were air dried and then crushed and ground to powder with a pestle and mortar, and the clay–mineral fraction was obtained by the sedimentation method as described by Jackson [19]. Oriented clay samples were prepared by carefully pipetting the clay suspension on a glass slide and were air dried at ambient temperature. Ethylene glycol saturated clays were prepared by vapor treatment method. The oriented clay samples were placed on the shelf of a desiccator with about 1 cm depth of ethylene glycol in the base, which was then placed in an oven and saturated at 65 °C for about 4 h. The XRD patterns were recorded from 3° to 65° 2θ at a scan rate of 4° 2θ/min using a Rigaku D/MAX-IIIA diffractometer, with

Ni-filtered Cu Kα radiation (1.5404 Å) and 1° divergence slit, 1° anti-scatter slit, and 0.3 mm receiving slit.

Clay species were identified by their characteristic diffractions, as discussed by Moore and Reynolds [20]. Illite was identified using its 001 diffraction of 10 Å spacing. Smectite was identified by the 15-Å diffraction at air-dried conditions. Mixed-layer illite–smectite has the basal 001 spacing of 10–15.5 Å, and was further identified by their glycolated samples. The basal 001 diffraction of glycolated chlorite is 14 Å and the 001 and 002 diffractions of kaolinite are 7.15 and 3.57 Å, respectively.

The relative proportions of clay minerals in the sample were estimated using the weighting factor method [21, 22]. Semiquantitative calculation of the clay phases was undertaken in the air-dried sample, for the 001 diffraction of I/S clays separates into two peaks with varied intensity ratios among the samples after glycolated treatment, due to the difference in illite and smectite layer contents between the I/S clays. The weighing factors were adopted from Hong et al. [14] and Schwertmann and Niederbudde [23], which are 7.5, 5.0, 1.0, 1.0, and 1.3 for I/S clay, illite, smectite, kaolinite, and chlorite, respectively. The detection limits were 1 % for kaolinite, smectite, and chlorite, 3 % for illite, and ~5 % for mixed-layer I/S.

Percentages of smectite layers in I–S were estimated using the reciprocal vector method [12], which was calculated using the formula: $1/d001(I/S) = \alpha/d001(I) + \beta/d001(S)$, where d001(I/S) is the d-spacing of the 001 diffraction of the mixed-layer I/S, and d001(I) and d001(S) are those of the 001 diffractions of illite and smectite, with *d* values of 10 and 15.5 Å, respectively, and α and β represent the layer content of illite and smectite in the mixed-layer I/S with the relation $\alpha + \beta = 1$.

2.3 HRTEM Analysis

A clay fraction separated from bed PL-01 was selected as the representative sample in our HRTEM analysis. The air-dried clay fraction was embedded in M-bond 610 resin and was then placed between two Si slides and allowed to solidify in an electric oven at 80 °C for ~2 h. The resin-solidified clay sample was cut vertically so that the (001) planes of clay particles were perpendicular to the cut surface. The thin slices were further thinned to ultrathin sections with a thickness <50 nm using ion-beam thinning techniques. HRTEM analysis was performed on a Philips CM12 high-resolution transmission electron microscope equipped with an EDAX9100 X-ray energy-dispersive detector (EDS), which was operated at an accelerating voltage of 120 kV and a beam current of ~20 nA. The lattice-fringe images of clay minerals were taken under over-focus conditions [24], for this condition usually gives the best contrast effect of the mixed-layer clay minerals. The point and line resolutions were 0.34 nm and the 0.20 nm respectively.

3 Results

3.1 Clay Mineralogy of the Pengda Clay Beds

The XRD patterns of the air-dried and glycolated clay fractions are shown in Fig. 2. Most of the air-dried samples display a strong peak of 11–15 Å, and some of the samples exhibit two peaks, one has the *d*-value of ~15 Å and another has the *d*-value of 12–14 Å. Glycolated treatment of the air-dried samples with a strong peak produces two separate peaks in this region, one at ~16.7 Å and one at 9.0–9.5 Å. Ethylene glycol saturation of the air-dried samples with two peaks produces three separate peaks at 16.7, ~13.6, and ~9.3 Å, respectively. These suggest that smectite and I/S clays are the dominant clay components in the samples. The weak 7.15 Å peak is present in all samples, indicating that kaolinite occurs as a minor component in all the clay sediments.

Samples PL-02 and PL-03 are composed dominantly of I/S clays and minor kaolinite, while samples PL-01, PL-04, PL-05, and PL-06 consisted of mainly I/S clays and contain small amounts of smectite and kaolinite. In addition, the XRD profiles reveal that chlorite is only present in sample PL-07 as a minor component, which is not detected in other samples. Calculations from the XRD patterns of the air-dried clay fractions show that the I/S clays contain varying amounts of smectite layers. I/S clays of Layer PL-02 contain up to 95 % smectite layers, while PL-06 has only 45 % smectite layers.

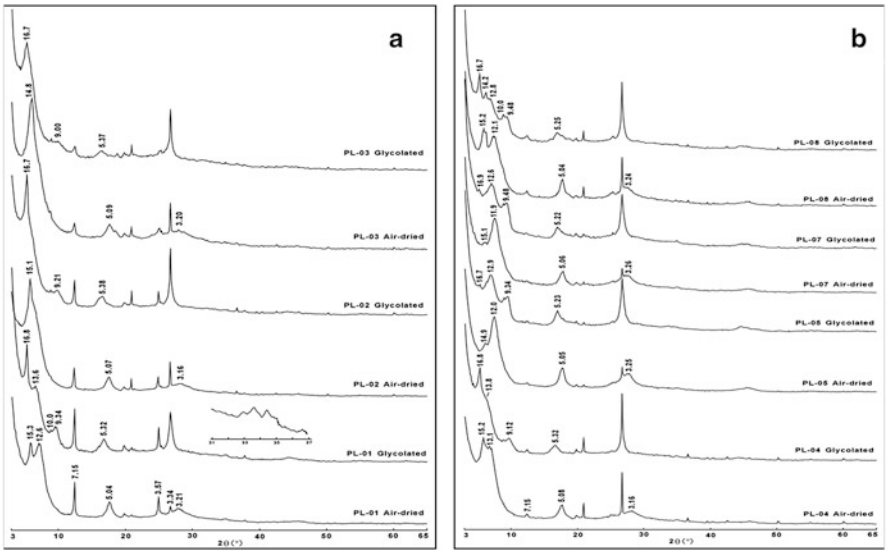

Fig. 2 XRD patterns of air-dried and glycolated clays from the Pengda section. (**a**) Beds PL-01–PL-03; (**b**) Beds PL-04–PL-07

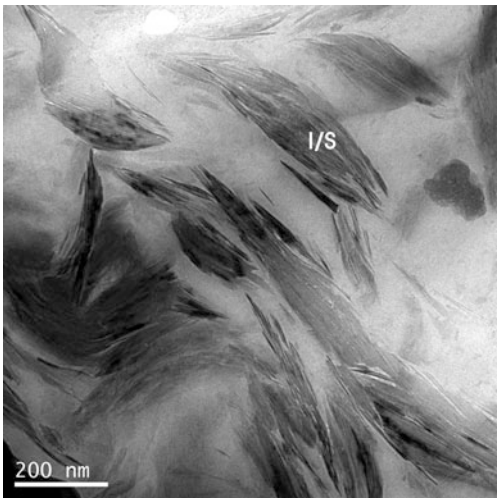

Fig. 3 The HRTEM image shows the typical wave-shaped morphology of the Pengda I/S clays

3.2 Layer Stacking of I/S Clays

Observations on the air-dried samples showed that most clay particles exhibit typical wave-shaped morphology with only trace in straight outline (Fig. 3), suggesting that clay minerals are mainly I/S clays and smectite [25], in agreement with the results from XRD analysis. In general, crystal boundaries of the clay particles could be readily recognized and the lattice fringes bent but well defined.

The I/S clays are characterized by lattice-fringe spacings of interstratified 10 and 12 Å under HRTEM observation. Some wave-shaped particles appear to have 12 Å fringes only, without or with only few interstratified 10 Å layers, while in most of the clay particles the lattice fringes consist of mainly 10 Å layers and minor 12 Å layers (Fig. 4a–c). The former may be interpreted as smectite phase and the latter as I/S clays, for the 15 Å smectite lattice-fringe spacing collapsed to 12 Å under the electron beam [26]. In most particles, the interstratified illite/smectite sequences are ordered and exhibit a layer proportion of 1:1 (Fig. 4a). In some particles, the 10 Å illite layers are interstratified with 12 Å smectite layers, and the illite/smectite sequences are disordered. Smectite layer is present in units of doublets, triplets, and quartets, which are interstratified by various amounts of illite layers (Fig. 4b). In some regions of the lattice-fringe image, one smectite layer laterally split into two illite layers (Fig. 4c), suggesting the transformation of smectite into I/S clays.

In some small particles, the lattice fringes are straight and are all 10 Å thick (Fig. 4a), indicative of illite mineral. The EDS analyses of clay particles show that their elemental composition consists of mainly Si, Al, and minor K, Ca, Na, Mg, and Fe. However, the areas with mainly 12 Å lattice-fringe spacings contain more Na and Mg, confirming the presence of a smectite mineral, while the areas with mainly 10 Å lattice-fringe spacings have more K but less Ca and Mg, indicating the presence of an illite mineral.

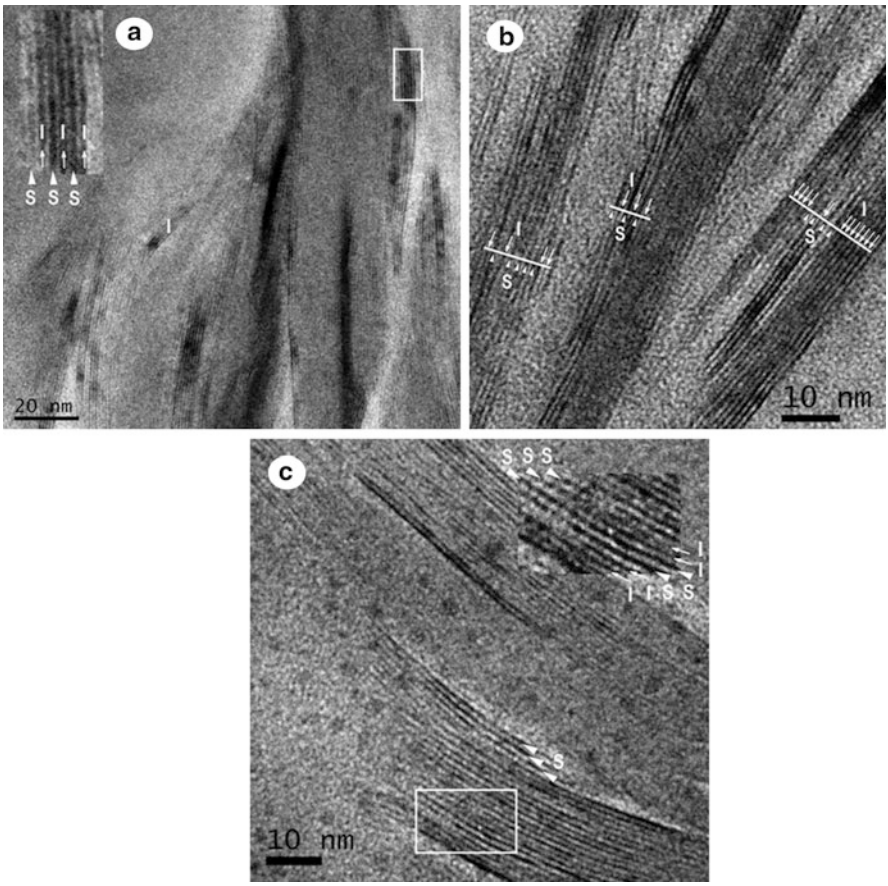

Fig. 4 Lattice-fringe images of the I/S clays. (**a**) 1:1 IS stacking ordering; (**b**) smectite layer in doublets, triplets, and quartets, interstratified by various amounts of illite layers; (**c**) the lateral transition S → I. *I* illite layer, *S* smectite layer

4 Discussion

4.1 Characteristics of Pengda I/S Clays

The characteristic diffraction of the air-dried I/S clay is 12.6 Å and that of its glycolated product is 13.6 Å, which are quite similar to the ordered 1:1 mixed-layer I/S clay rectorite [27, 28]. The structure of I/S clays could be determined using the two noncoincident mixed-layer diffractions at 6–8° and 33–35° 2θ [29]. The peak-shaped parameters BB1 (angle width of the complex 10 Å diffraction) and BB2 (angle width of the diffraction at 33–35°) measured from the XRD pattern of glycolated sample are 4.7° and 4.4°, respectively, which are larger than the criteria value of >4.0° for ordering IS clay, suggesting that the I/S clay in layer PL-01 of the

Pengda section has an IS type of ordering. This is also confirmed by the peak position of the low-angle diffraction at 6.5° (the criteria value of <7.5°) [29].

The ordering types of I/S clays are also correlated with the smectite contents of the I/S minerals. For I/S clays with ~50 % smectite layers, their interstratification structures vary from completely random to maximum IS ordered, and change in content of smectite layer will favor the occurrence of partially ordered IS structures [30]. For the perfectly ordered 1:1 mixed-layer I/S clay rectorite and its glycolated product, almost all theoretically multi-order diffractions of 001 could be observed in their XRD patterns. However, unlike those of rectorite, only 12.6, 5.05, 3.17, 2.57, and 1.99 Å diffractions of the air-dried sample and 13.6, 9.34, 5.32, 3.33, 2.56, and 2.03 Å diffractions of the glycolated sample could be observed in their XRD patterns of the Pengda I/S clay. The peaks are relatively broad and their intensities are relatively weak. Again, at the low-angle side of 2.56 Å peak there is a diffuse band at ~33° 2θ, suggesting the occurrence of certain amounts of random interstratification I/S clays [29]. Therefore, the I/S clay of layer PL-01 in the Pengda section consists of mainly IS ordering mineral and randomly interstratified I/S mineral as indicated by the XRD analysis.

Illitization process and the crystal chemistry of I/S depend on environmental conditions, such as temperature, compositions of fluid and rock and water/rock ratio, as well as geological time. Variability in the inherited characteristics of smectite formed during earlier periods of alteration may also influence later illitization during burial diagenesis. HRTEM observations show that most of the I/S clays exhibit an IS stacking ordering, in agreement with the results of XRD analysis. However, in local regions within a crystallite, the IS layer stacking sequences are irregular. Smectite layers are observed in layer-doublets, layer-triplets, and layer-quartets, which are interstratified by various amounts of illite layers. These suggest that the stacking of Pengda I/S clay consists of various types of the subunits, in addition to the 1:1 IS-ordered stacking, and the smectite illitization can be described by a systematic change in the type and proportion of the subunits constituting crystallites [31]. Transformation of the smectite layer into illite layers in HRTEM observations reinforces the hypothesis that the Pengda I/S clays are derived from smectite illitization.

4.2 Formation of Clay Beds in the Pengda Section

In diagenesis processes, discrete clay minerals are little changed and the main change in clay mineralogy is an increase in the amounts of illite layers together with the increasing degree of ordering of I/S clays [32, 33]. However, in the Pengda section, the I/S clays containing a large amount of smectite layers (Beds PL-02 and PL-03) are interbedded with those having relatively smaller amount of smectite layers (Beds PL-01 and PL-04). The transformation of smectite to illite often takes place at the temperature of oil formation during burial diagenesis [34]. The PTB

stratigraphic set in south China is mature for oil generation [35]. It would be expected that the I/S clays in the Pengda have undergone smectite illitization and an increase in ordering in the layer-type distribution. However, these clay beds occur only within 3 m thick sediments, the difference in amount of smectite layer in the I/S clays should not be attributed to different burial temperatures. Variation in the amount and type of discrete clay minerals between the clay beds can be attributed to different parent materials and the environment conditions of the episode of volcanism.

Though the clay sediments are recognized as an alteration product of volcanic ashes, and in one case as a mixture of volcaniclastic and continental alteration materials [14], the sedimentary environment and the redox conditions may be different between the volcanism episodes, as suggested by the differences in color, texture, and mineralogical characteristics of the clay sediments. The variation in color from pale yellow to dark gray may probably reflect increasingly reducing conditions, and changes in texture and clay mineral composition may be derived from sedimentation rate and chemical composition of the parent volcanic ashes. Thus, variations in the amount of smectite layers in the I/S clays of the clay sediments could be due to different parent materials [36]. The occurrence of chlorite and illite, in association with larger amount of I/S clays in the clay beds, is indicative of a mixture of terrigenous and volcanic sources, similar to those found in other PTB stratigraphic sets elsewhere in south China [14].

Kaolinite is usually considered as a result of intense chemical weathering [37]. However, authigenic kaolinite could also be formed in early diagenesis in a relatively acid environment. The PTB stratigraphic set at Pengda consists of mainly siliceous mudstones with interbedded clay beds; in early diagenesis, the contact with acid siliceous deposits could have caused the removal of alkali elements in solution and resulted in the formation of kaolinite [38]. The interbedded pure smectite beds in marine sediments are usually derived from marine alteration of volcanic ashes [25, 39–41], and the major mineral I/S could represent a major smectitic volcanogenic component that was converted to I/S by alteration [25, 40, 42, 43]. XRD results show that clay beds in the Pengda section are composed of mainly I/S clays, smectite, and minor kaolinite and illite, which are considered as alteration products of volcanic ashes in marine environment in association with the alteration of burial diagenesis. Dong et al. [16] suggested that smectite illitization produces mainly I/S clays with small proportions of smectite and illite. The major mineral I/S clays in association with minor smectite and illite in the Pengda section may probably reflect the transformation of smectite to illite, as is confirmed by HRTEM observations.

Clay mineral assemblages of the Pengda clay beds are mainly I/S clays, smectite, and kaolinite, and the I/S minerals in this section contain up to 45–95 % smectite layers (Table 1). However, clay minerals of the Meishan section consist mainly of I/S clays, illite, and kaolinite, with 27–50 % smectite layers within the I/S clays, and clay minerals of the Xiakou section are composed of only I/S clays, with only 15–31 % smectite layers [14]. The smectite layer contents of I/S clays in the Pengda section are significantly higher than those in the Xiakou, Meishan, and many other

Table 1 Clay mineral compositions of clay intervals in the Pengda PTB stratigraphic set (vol%)

Layer	Color and texture	I/S	Smectite	Kaolinite	Illite	Chlorite	S content in I/S (%)
PL-01	Grayish white, loose	78	8	9	5	–	58
PL-02	Grayish white, condensed	93	–	4	3	–	95
PL-03	Light gray to pale yellow, condensed	90	–	3	7	–	91
PL-04	Dark gray, loose	81	11	3	5		67
PL-05	Grayish yellow to grayish green, loose	87	3	1	9	–	47
PL-06	Grayish yellow to grayish green, loose	88	2	2	8	–	45
PL-07	Dark gray, condensed with lamination	62	9	3	16	10	49

sections [10, 14]. Unlike the Pengda section formed in neritic sea environment, the Meishan sediments formed in an intraplatform depression between an uplift and a platform, and the Xiakou deposits formed in an open continental-shelf sedimentary environment [44, 45]. Variations in clay assemblage and smectite layer content of the I/S clays among the PTB stratigraphic sets can be attributed to different sedimentary environment, which may have resulted in differences in redox and weathering conditions and in alteration processes during burial diagenesis.

5 Conclusions

The clay intervals with siliceous mudstones across the PT boundary in the Pengda section consist mainly of I/S clays with minor kaolinite, smectite, and illite. Chlorite only occurs in layer PL-07, though the peak-shaped parameters BB1 and BB2 of I/S clays of layer PL-01 are 4.7° and 4.4°, respectively, suggesting that the I/S clays has an IS type of ordering, as is also confirmed by the peak position of the low-angle diffraction at 6.5°2θ (13.6 Å). The presence of multi-order diffraction and their intensities is different from those of completely ordered 1:1 mixed-layer I/S clay rectorite, suggesting that I/S clays of the Pengda section have partially ordered IS structures.

Most of the I/S clays exhibit an IS stacking ordering under HRTEM observations. However, in some areas within an IS particle, smectite layer is present as units of doublets, triplets, and quartets, which are interstratified by various amounts of illite layers. These reinforce that the stacking of Pengda I/S clays consists of various types of the subunits, in addition to the major 1:1 IS-ordered stacking, in good agreement with the results of XRD analysis. Transformation of the smectite layer into illite layers is also observed under HRTEM observations, confirming that

the Pengda I/S clays are derived from smectite illitization. I/S clays of the Pengda section contain up to 45–95 % smectite layers, which are notably higher than those of other sections in south China, such as the Meishan section (27–50 %) and the Xiakou section (15–31 %). Variations in smectite layer content of the I/S clays among the PTB stratigraphic sets may reflect the differences in alteration and smectite illitization processes due to the different sedimentary environments.

Acknowledgment This work was supported by the Natural Science Foundation of China (41272053 and 41072030) and the Specialized Research Fund for the Doctoral Program of Higher Education of China (20110145110001). The authors wish to thank Jiang H. S. for sample preparations, Dr. Liu X. W. for HRTEM observations, and Dr. Yu J. S. for XRD analyses, and especially Prof. Dong F. Q. and Zhao X. Q., the Guest Editors, and two anonymous reviewers for their insightful reviews, valuable comments, and suggestions.

References

1. Erwin DH (1994) The Permo-Triassic extinction. Nature 367:231–236
2. Jin YG, Wang Y, Wang W, Shang QH, Cao CQ, Erwin DH (2000) Pattern of marine mass extinction near the Permian-Triassic boundary in south China. Science 289:432–436
3. Korte C, Kozur HW (2010) Carbon-isotope stratigraphy across the Permian-Triassic boundary: a review. J Asian Earth Sci 39:215–235
4. Holser WT, Schölaub HP, Attrep M, Boeckelmann K, Klein P, Magaritz M, Orth CJ, Fenninger A, Jenny C, Kralik M, Mauritsch H, Pak E, Schramm JM, Stattegger K, Schmöler R (1989) A unique geochemical record at the Permian/Triassic boundary. Nature 337:39–44
5. Wignall PB (2001) Large igneous provinces and mass extinctions. Earth Sci Rev 53:1–33
6. Knoll AH, Bambach RK, Payne JL, Pruss S, Fischer WW (2007) Paleophysiology and end-Permian mass extinction. Earth Planet Sci Lett 256:295–313
7. Wu SB, Ren YX, Bi XM (1990) Volcanic material and origin of clay rock near Permo-Triassic boundary from Huangshi, Hubei and Meishan of Changxing county, Zhejiang. Earth Sci J China Univ Geosci 15:589–594
8. Lu Q, Lei XR, Liu HF (1991) Genetic types and crystal chemical classification of irregular illite/smectite interstratified clay minerals. Acta Mineral Sin 11:97–104, Chinese text with English abstract
9. Yin HF, Huang SJ, Zhang KX, Hansen HJ (1992) The effects of volcanism on the Permo-Triassic mass extinction in South China. In: Sweet WC, Yang ZY, Dickins JM, Yin HF (eds) Permo-Triassic events in the eastern Tethys. Cambridge University Press, Cambridge, pp 146–157
10. Zhang SX, Yu JX, Yang FQ, Peng YQ, Yin HF, Yu JS (2004) Study on clayrocks of the neritic, littoral and marine-terrigenous facies across the permiantriassic boundary in the eastern Yunnan and western Guizhou, south China. J Mineral Petrol 24:81–86, Chinese text with English abstract
11. Yu KP, Han GM, Yang FL, Mansy JL, Xu CH, Zhou ZY, Cheng XR, Liu ZF, Fu Q (2005) Study on clay minerals of P/T boundary in Meishan section, Changxin, Zhejiang province. Acta Sedimentol Sin 23:108–112, Chinese text with English abstract
12. Lu Q, Lei XR, Liu HF (1993) Study of the stacking sequences of a kind of irregular mixed-layer illite-smectite (I/S) clay mineral. Acta Geol Sin 67:123–130, Chinese text with English abstract
13. Wang SL (1998) The stacking type of I/S clays in the Permian-Triassic boundary stratigraphic sets of south China—a review. Northwestern Geol 19:14–19, Chinese text with English abstract

14. Hong HL, Xie SC, Lai XL (2011) Volcanism in association with the prelude to mass extinction and environment change across the Permian–Triassic boundary (PTB), southern China. Clays Clay Miner 59:478–489
15. Altaner SP, Ylagan RF (1997) Comparison of structural models of mixed-layer illite/smectite and reaction mechanisms of smectite illitization. Clays Clay Miner 45:517–533
16. Dong H, Peacor DR, Freed RL (1997) Phase relations among smectite, R1 illite-smectite, and illite. Am Mineral 82:379–391
17. Bauluz B, Peacor DR, Ylagan RF (2002) Transmission electron microscopy study of smectite illitization during hydrothermal alteration of a rhyolitic hyaloclastite from Ponza, Italy. Clays Clay Miner 50:157–173
18. Guizhou Bureau of Geology and Mineral Resources (1987) Regional Geological Annals of Guizhou Province. Beijing: Geological Publishing House, pp 698
19. Jackson ML (1978) Soil chemical analyses. Authors' publication University of Wisconsin Madison
20. Moore DM, Reynolds RC (1989) X-ray diffraction and the identification and analysis of clay minerals. Oxford University Press, Oxford, p 332
21. Islam AKME, Lotse EG (1986) Quantitative mineralogical analysis of some Bangladesh soils with X-ray, ion exchange and selective dissolution techniques. Clay Miner 21:31–42
22. Bronger A, Winter R, Sedov S (1998) Weathering and clay mineral formation in two Holocene soils and in buried paleosols in Tadjikistan: towards a Quaternary paleoclimatic record in Central Asia. Catena 34:19–34
23. Schwertmann U, Niederbudde EA (1993) Tonminerale in Böden. In: Jasmund K, Lagaly G (eds) Tonminerale und Tone, Struktur, Eigenschaften, Anwendung und Einsatz in Industrie und Umwelt. Steinkopff, Darmstadt, pp 212–265
24. Guthrie GD, Veblen DR (1989) High-resolution transmission electron microscopy of mixed-layer illite/smectite: computer simulations. Clays Clay Miner 37:1–11
25. Deconinck JF, Chamley H (1995) Diversity of smectite origins in late Cretaceous sediments: example of chalks from northern France. Clay Miner 30:365–379
26. Nieto F, Ortega-Huertas M, Peacor DR, Arostegui J (1996) Evolution of illite/smectite from early diagenesis through incipient metamorphism in sediments of the Basque-Cantabrian Basin. Clays Clay Miner 44:304–323
27. Brindley GW (1956) Allevardite, a swelling double-layer mica mineral. Am Mineral 41:91–103
28. Hong HL, Zhang XL, Wan M, Hou YJ, Du DW (2008) Morphological characteristics of K, Na-rectorite from Zhongxiang rectorite deposit, Hubei, central China. J China Univ Geosci 19:38–46
29. Środoń J (1984) X-ray powder diffraction identification of illitic materials. Clays Clay Miner 32:337–349
30. Schultz LG (1982) Mixed-layer illite/smectite and other minerals in shale, bentonite, and concretions in the Montana Disturbed Belt: Prog. Abst. 19th Annual Meeting, The Clay Minerals Society, Hilo, Hawaii, 1982, p 82 (abstract)
31. Murakami T, Inoue A, Lanson B, Meunier A, Beaufort D (2005) Illite-smectite mixed-layer minerals in the hydrothermal alteration of volcanic rocks: II. One-dimensional HRTEM structure images and formation mechanisms. Clays Clay Miner 53:440–451
32. Hower J, Eslinger EV, Hower ME, Perry EA (1976) Mechanism of burial metamorphism of argillaceous sediment: 1. Mineralogical and chemical evidence. Geol Soc Am Bull 87:725–737
33. Pearson MJ, Small JS (1988) Illite–smectite diagenesis and palaeotemperatures in northern North Sea Quaternary to Mesozoic shale sequences. Clay Miner 23:109–132
34. Reynolds RC, Hower J (1970) The nature of interlayering in mixed-layer illite-montmorillonite. Clays Clay Miner 18:25–36
35. Wang ZY (1998) Permian sedimentary facies and sequence stratigraphy in Daxiakou section, Xingshan county, Hubei province. J Jianhan Petrol Inst 20:1–7, Chinese text with English abstract

36. Chamley H (1989) Clay sedimentology. Springer, Berlin, p 623
37. Millot G (1970) Geology of clays. Springer, Berlin, p 499
38. Dera G, Pellenard P, Neige P, Deconinck JF, Pucéat E, Dommergues JL (2009) Distribution of clay minerals in Early Jurassic Peritethyan seas: Palaeoclimatic significance inferred from multiproxy comparisons. Palaeogeogr Palaeoclimatol Palaeoecol 271:39–51
39. Nadeau PH, Reynolds RC Jr (1981) Burial and contact metamorphism in the Mancos Shale. Clays Clay Miner 29:249–259
40. Pellenard P, Deconinck JF, Huff WD, Thierry J, Marchand D, Fortwengler D, Trouiller A (2003) Characterization and correlation of Upper Jurassic (Oxfordian) bentonite deposits in the Paris Basin and the Subalpine Basin, France. Sedimentology 50:1035–1060
41. Do Campo M, del Papa C, Nieto F, Hongn F, Petrinovic I (2010) Integrated analysis for constraining palaeoclimatic and volcanic influences on clay–mineral assemblages in orogenic basins (Palaeogene Andean foreland, Northwestern Argentina). Sediment Geol 228:98–112
42. Pearson MJ (1990) Clay mineral distribution and provenance in Mesozoic and Tertiary mudrocks of the Moray Firth and northern North Sea. Clay Miner 25:519–541
43. Meunier A, Lanson B, Velde B (2004) Composition variation of illite-vermiculite-smectite mixed-layer minerals in a bentonite bed from Charente (France). Clay Miner 39:317–332
44. Yin HF, Zhang KX, Tong JN, Yang ZY, Wu SB (2001) The global stratotype section and point (GSSP) of the 142 Hong et al. Clays and Clay Minerals Permian-Triassic boundary. Episodes 24:102–113
45. Wang GQ, Xia WC (2004) Conodont zonation across the Permian-Triassic boundary at the Xiakou section, Yichang city, Hubei province and its correlation with the Global Stratotype Section and Point of the PTB. Can J Earth Sci 41:323–330

The Occurrence of Sc, Co, and Ni in Lithiophorite-type Manganese Ore

Qiuyang Hong, Lili Zhang, and Bo Li

Abstract The lithiophorite in manganese ore is rich in aluminum, and actually it is a generic name for the multi-mineral aggregates mixed by silicon, aluminum, and iron, which is quite different from ordinary psilomelane. There is no Sc, Ni, or Co mineral in this ore, and more than 98 % of Co, Ni, and Sc exist in lithiophorite and a little pyrolusite. The distribution of Co, Ni, and Sc in lithiophorite is further studied by EPMA and the results indicate that Co and Sc in lithiophorite are sparse and have scattered distribution, while Ni mostly distributes in the argillaceous lithiophorite and is local enrichment. Reduction-sulfuric acid leaching tests show that Co and Sc dissolve before Mn and the dissolution rate of Co and Sc is almost equal, which is significantly higher than that of Mn. However, the dissolution rate of Ni is extremely low with the dissolution of Mn, which indicates that Ni is hard to dissolve and its dissolution rate obviously lags behind that of Mn, Sc, and Co. The initial conclusions can be drawn that Co and Sc exist in the lithiophorite as interface adsorption while Ni exists in the clay (kaolinite) mixed up with lithiophorite as interface adsorption.

Keywords Manganese ore • Scandium • Cobalt • Nickel • Occurrence

1 Introduction

Manganese ore is an important strategic mineral resource, especially the high-grade and high-quality ore, which has been classified as scarce minerals by China. China's manganese resources have the characteristics including imbalanced distribution, small-scale deposits, low-grade and high-impurity content, fine valuable minerals, many gangue minerals, complex ore texture that brings great difficulties for the processing, and utilization of manganese ore, especially low-grade manganese ore. Besides, China's manganese resources are usually associated with the

Q. Hong (✉) • L. Zhang • B. Li
Department of Mineral Processing Engineering, Guangzhou Research Institute of Non-ferrous Metals, 363 Changxing Road, Guangzhou, Tianhe District, Guangdong, People's Republic of China
e-mail: hongqy456@163.com

F. Dong (ed.), *Proceedings of the 11th International Congress for Applied Mineralogy (ICAM)*, Springer Geochemistry/Mineralogy,
DOI 10.1007/978-3-319-13948-7_16

valuable elements such as Ag, Pb, Zn, Co, Ni, Sc, etc., which should be comprehensively recovered during beneficiation. In order to develop the limited manganese resources efficiently, study on process mineralogy, especially the occurrence of valuable elements, should be strengthened. Only adopting appropriate beneficiation process based on the studies can a breakthrough in the technology and reduction of cost be achieved possibly. In this chapter, the process mineralogy study is carried out for a lithiophorite-type manganese ore. Based on identifying the occurrence of Mn, Co, Ni, and Sc, the efficiency of comprehensively recovering valuable elements is evaluated through hydrometallurgical exploratory tests.

2 Materials and Methods

2.1 Major Element Chemical Composition of Ore

The results of major elements chemical compositions of ore are as follows (%): Mn 23.18, Fe 8.5, Co 0.073, Ni 0.21, Sc 0.013, Al_2O_3 21.67, SiO_2 15.53, CaO 0.28, MgO 0.11, As 0.029, and Li_2O 0.082.

2.2 Mineralogy Composition of Ore

The mineralogy composition of ore is determined by optical microscope and electron microprobe ("EPMA" for short) combined with X-ray diffraction analysis. According to the results given in Table 1, manganese minerals of this ore are mainly lithiophorite, followed by pyrolusite. The ratio of lithiophorite (including clay mixture) to pyrolusite is 5 to 1. The lithiophorite is mixed with a lot of clay and limonite, so it means sensu lato lithiophorite; in this chapter it is a generic name for the mixture.

Table 1 Mineralogy composition of ore

Mineral	Lithiophorite (including clay)	Pyrolusite	Limonite	Pyrite
Content %	66.67	14.02	8.36	Traces
Mineral	Kaolinite	Quartz	Sericite	Total
Content %	6.06	4.38	0.10	100.00

3 Results

3.1 Ore Structure and Texture

3.1.1 Ore Structure

It is an eluvial and accumulation type manganese deposit. The ore is massive or clay-like and has the characteristics of weathering mineralization. The texture and structure of ore are complex and the ore structure is as follows: (1) porous-cellular drusitic structure that is the typical structure of weathered ore. The soluble ingredients of ore are taken away because of weathering and leaching while the insoluble lithiophorite, clay, and limonite form skeleton as irregular porous, regular cellular, or drusitic structure if the hole is a little large with pectinate lithiophorite growing on the wall of hole. (2) Earthy-arenaceous brecciated structure: the mixture of lithiophorite, clay, and limonite occurs in the secondary abundance zone as earthy, arenaceous, or brecciated because of the weathering and leaching. The grit in arenaceous structure is composed of earthy manganese so it has a high content of manganese while the cement has a high content of silicon as well as iron and low content of manganese. (3) Pisolitic crumb structure: the oxides of manganese, iron, and aluminum are in the state of colloidal solution. When they are transported by surface water, lithiophorite, kaolinite, and limonite as gel will precipitate from colloidal solution and form pisolitic or crumb structure because of the role of electrolyte and humus and colloid with opposite charges. There is manganese pisolite, limonite pisolite, etc., in the ore. (4) Vein structure is formed by infilling in postmineralization. Most veins are pyrolusite; sometimes there is secondary lithiophorite on the wall of vein.

3.1.2 Ore Texture

In this ore, lithiophorite has many forms of texture including pelitomorphic texture, arenaceous texture, aphanitic texture, flaky texture, foliaceous texture, cement texture, catablastic texture, etc. Limonite and kaolinite are mostly pelitomorphic texture. Quartz and kaolinite in lithiophorite have an inclusion texture.

3.2 Occurrence of Valuable Elements in the Ore

Manganese minerals, limonite, and gangue minerals are separated, purified, and determined by the content of Mn, Co, Ni, and Sc in chemical analysis. According to the distribution of Mn, Co, Ni, and Sc given in Table 2, more than 98 % of Mn exists as lithiophorite and pyrolusite, while the Mn contained in the limonite and gangue minerals accounts for less than 1 %; about 98 % of Co exists as lithiophorite and pyrolusite, while Co contained in the limonite and gangue minerals accounts for

Table 2 Distribution of Mn, Co, Sc, and Ni

Mineral	Mineral content %	Grade of valuable metals %				Distribution %			
		Mn	Co	Sc	Ni	Mn	Co	Sc	Ni
Lithiophorite and pyrolusite	80.69	27.18	0.0930	0.0190	0.260	99.73	98.04	98.33	99.39
Limonite	8.77	0.52	0.0130	0.0030	0.011	0.21	1.44	1.67	0.47
Gangue minerals	10.54	0.12	0.0039	0	0.026	0.06	0.52	0.00	0.14
Total	100.00	21.99	0.0765	0.0156	0.211	100.00	100.00	100.00	100.00

about 2 %; more than 99 % of Ni exists as lithiophorite and pyrolusite, while the Ni contained in the limonite and gangue minerals accounts for less than 1 %; more than 98 % of Sc exists as lithiophorite and pyrolusite, while the Sc contained in the limonite and gangue minerals accounts for less than 2 %.

3.3 Occurrence of Co, Ni, and Sc in the Manganese Minerals

According to the distribution of Co, Ni, and Sc, there is no Co, Ni, or Sc minerals and about 98 % of Co, Ni, and Sc exist in the manganese minerals that are dominant by lithiophorite. In order to learn more about how the valuable metals exist in the lithiophorite and provide detailed data for hydrometallurgy, the occurrence of Co, Ni, and Sc is studied by EPMA and Reduction-sulfuric acid leaching tests.

3.3.1 Surface Scan Analysis by Wavelength Dispersive Spectrometer of EPMA

The distribution of major elements in the pisolitic manganese minerals is detected by EPMA-1600, and the scanning images are shown in Fig. 1. Figure 1b shows that Mn is distributed unevenly in the ore; the pisolite is richer in Mn than in cement while Mn has a dotted distribution in the limonite. Figure 1c doesn't show the Co-rich area, which indicates Co has a scattered distribution in the ore. Figure 1d shows that Ni is local enrichment and that Ni in the pisolite is a little poor while Ni in the cement is slightly rich and is locally dense in the earthy manganese cement. In order to identify whether the Ni-rich area is also rich in Co and whether Ni exists as nickel sulfide, the Ni-area is magnified and compared with the characteristic X-ray of Co and S. According to Figs. 1e–g, the Ni-area is not rich in Co, and Co is distributed sparsely and evenly; the Ni-area is poor in S, which means Ni doesn't exist as nickel sulfide; Ni is not closely related to Co and mainly rich in the cement in the form of non-uniform adsorption. Figure 1h shows that Sc has a scattered distribution in the pisolitic manganese minerals.

3.3.2 Reduction-Sulfuric Acid Leaching Tests

The EPMA analysis shows that Co and Sc are sparsely and scatteredly distributed in the pisolitic manganese minerals, while Ni is locally enriched in the cement. Reduction-sulfuric acid leaching tests are carried out to further explore the dissolution relationship among Co, Ni, Sc, and Mn. 100 g sample is added to sulfuric acid with the concentration of 10 %; the ratio of solid to liquid is 1 to 9 and some sodium sulfite is also added as reductant. According to the dissolution rate with time changing given in Table 3, after 20 min, the reductant still doesn't work; Mn is almost not dissolved while Co and Sc have reached a high dissolution rate. In the whole process, the dissolution rate of Co and Sc is nearly equal and faster than that

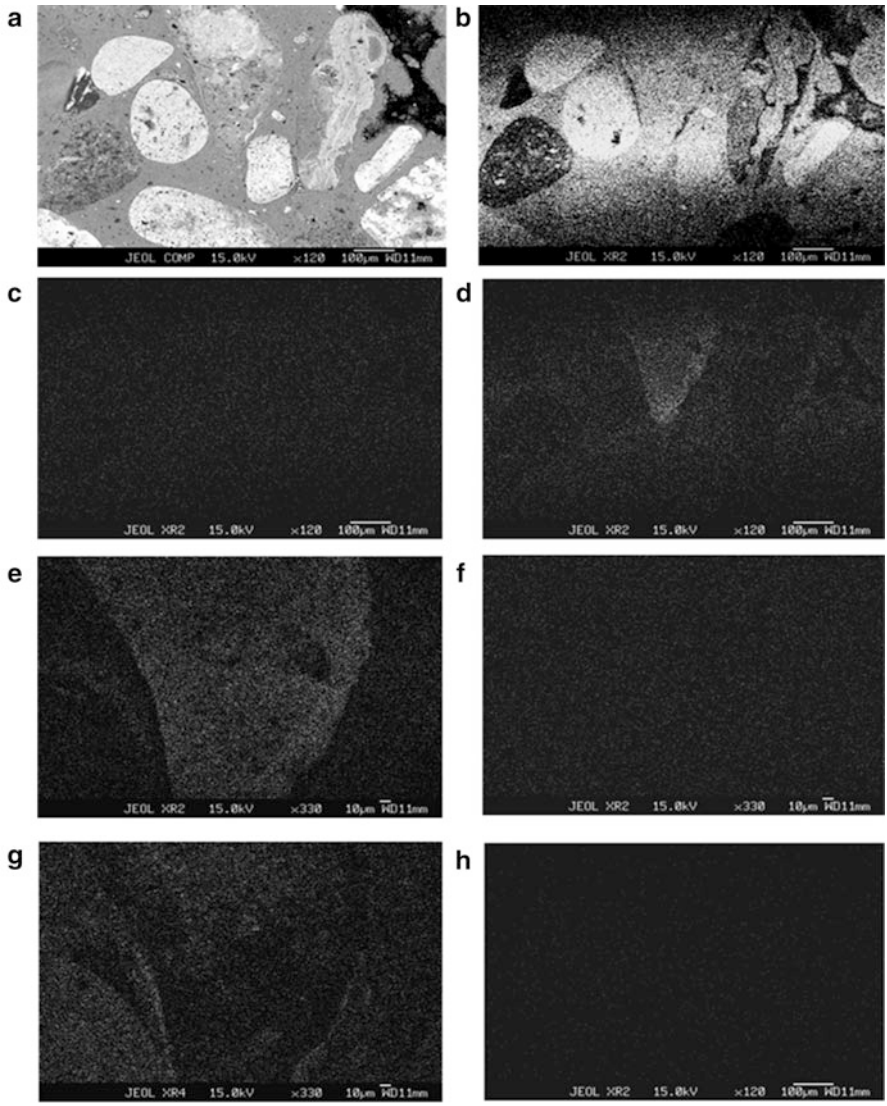

Fig. 1 Scanning image by EPMA. (**a**) Backscattered image by EPMA, pisolitic lithiophorite, and the cement that is made up of lithiophorite, clay, and limonite; (**b**) Mn Kα scanning image; (**c**) Co Kα scanning image; (**d**) Ni Kα scanning image; (**e**) Ni Kα scanning image, the magnified image of Ni-rich area; (**f**) Co Kα scanning image, the magnified image of Ni-rich area; (**g**) S Kα scanning image, the magnified image of Ni-rich area; (**h**) Sc Kα scanning image

of Ni significantly. The dissolution of Co and Sc happens before Mn. With the dissolution of Mn, the dissolution rate of Co and Sc is always faster than that of Mn. However, the dissolution rate of Ni is very slow, which indicates Ni is hard to dissolve and its dissolution rate obviously lags behind that of Mn, Co, and Sc. The dissolution rate of Mn is more than 50 %, while that of Ni is only 20 %.

Table 3 The dissolution rate of Mn, Co, Ni, and Sc with time changing

	Dissolution rate %			
Leaching time (min)	Mn	Co	Ni	Sc
20	1.27	34.25	0.00	15.38
40	17.49	41.10	4.17	38.46
60	21.35	45.21	8.33	46.15
80	22.07	47.95	8.33	46.15
100	32.17	50.68	8.33	53.85
120	36.42	56.16	8.33	53.85
140	42.49	56.16	12.50	53.85
160	45.71	63.01	16.67	61.54
180	53.65	64.38	20.83	61.54

The hydrometallurgical exploratory tests show that the final dissolution rate of Ni also can be more than 90 %, but its indissolvableness is shown in this test.

4 Discussion

The distribution of Co and Sc in the manganese minerals and reduction-sulfuric acid leaching tests indicate that Co and Sc is unevenly and scatteredly distributed in the lithiophorite and dissolve before Mn in sulfuric acid. Based on the above, one can draw a conclusion that Co and Sc exist in the lithiophorite crystals as interface adsorption and report to solution because of desorption. In the structure of lithiophorite, the octahedron $[Mn^{4+}O_6]$ layer and octahedron $[(Al, Li)(OH)_6]$ layer are alternate stacking in the direction perpendicular to the C-axis. The Li and Al distribution in the octahedron $[(Al, Li)(OH)_6]$ is disordered. The octahedron $[(Al, Li)(OH)_6]$ has unsaturated charges so is easy to adsorb cations such as Co, Sc, etc. Obviously, Co and Sc are dissolved before the structure of lithiophorite is damaged because of their interface adsorption.

Ni is unevenly distributed in the lithiophorite and generally has a little higher content in the cement of pisolitic lithiophorite. The Ni area is also rich in Si and Al (excluding the Al of lithiophorite). The reduction-sulfuric acid leaching tests indicate that the dissolution of Ni is very slow with the dissolution of Mn. Natural clay can adsorb Ni from $NiSO_3$ solution; in other words, Ni exists in the interlayer of clay in the form of Ni^{2+} ion adsorption. The adsorptive capacity depends on the acidity, concentration, and volume of solution. Therefore, the conclusions can be drawn that Ni exists in the clay (kaolinite) mixed up with lithiophorite as interface adsorption. Although Ni also can desorb from the clay layers, the dissolution rate is very slow because clay is indissolvable in the acid solution.

5 Conclusions

1. The manganese minerals of this ore are mainly lithiophorite, followed by pyrolusite. The ratio of lithiophorite (including clay mixture) to pyrolusite is 5 to 1.
2. The occurrence of Mn, Co, Ni, and Sc indicates that more than 98 % of Mn, Co, Ni, and Sc exist in the lithiophorite and pyrolusite.
3. The EPMA analysis and leaching tests indicate that Co and Sc exist in the lithiophorite crystals as interface adsorption while Ni exists in the clay (kaolinite) mixed up with lithiophorite as interface adsorption. These results indicate that Co and Sc can dissolve before Mn with a high dissolution rate, while Ni also can desorb from the clay layers and dissolve, but the dissolution rate is very slow because clay is indissolvable in the acid solution.

Cytotoxicity of Quartz and Montmorillonite in Human Lung Epithelial Cells (A549)

Tingting Huo, Faqin Dong, Mingcui Wang, Shiyong Sun, Jianjun Deng, Qingbi Zhang, and Siwang Yu

Abstract In this study, A549 cell viability, extracellular activities of lactate dehydrogenase (LDH), and tumor necrosis factor (TNF)-α and interleukin (IL)-6 levels were investigated after incubation with quartz (KWC-Q4 and KWC-Q3), Nano-SiO_2, and KWC-M; the micronucleus test and comet assay were carried out to evaluate the genotoxicity. The results showed there were significant differences in the cell death rate and extracellular LDH activities compared with the control group, and showed a good linear relationship in certain concentration range. All mineral particles tested can induce the increase of TNF-α after incubation with mineral powders at 200 μg/mL for merely 3 h and also induce significant increase of IL-6 for 24 h; the results indicated that inflammatory reaction can be triggered by the exposure of KWC-Q4, KWC-Q3, Nano-SiO_2, and KWC-M. The results of micronucleus test showed FMN (Frequency of micronucleus number) listed as Nano-SiO_2>KWC-Q3>KWC-Q4. There was no significant FMN increase of KWC-M compared with the control group, which maybe resulted from its high cell mortality at low concentration. The comet assay confirmed the genotoxicity of all tested samples, and the DNA damage: KWC-M>Nano-SiO_2>KWC-Q4>KWC-Q3.

Keywords Quartz • Montmorillonite • A549 • Cytotoxicity

T. Huo • F. Dong (✉) • M. Wang • S. Sun
Key Laboratory of Solid Waste Treatment and Resource Recycle, Ministry of Education, SWUST, 59 Qinglong Road, Mianyang, Sichuan, People's Republic of China
e-mail: fqdong@swust.edu.cn

J. Deng
The Mianyang 404 Hospital, 56 Yuejin Road, Mianyang, Sichuan, People's Republic of China

Q. Zhang
Luzhou Medical College, 319 Zhongshan Road, Luzhou, Sichuan, People's Republic of China

S. Yu
Department of Chemical Biology, School of Pharmaceutical Science, Peking University Health Science Center, 38 Xueyuan Road, Haiding District, Beijing, People's Republic of China

F. Dong (ed.), *Proceedings of the 11th International Congress for Applied Mineralogy (ICAM)*, Springer Geochemistry/Mineralogy,
DOI 10.1007/978-3-319-13948-7_17

1 Introduction

More evidences concerning mortality, increased asthma morbidity, and other respiratory disorders with increased concentrations of airborne fine particulate matters whose aerodynamic diameter was less than 2.5 μm have attracted the public attention. Experiments in vitro and in vivo all have revealed that the exposure can result in pulmonary inflammation, airway hyperreactivity, cell impairment, and epithelial permeability increase. For their small diameter, they can be transported deeply to the alveolar in the lungs, even involved in the blood circulation [1], and there is no effective clearance mechanism. The relationship between them is obviously.

As for the airborne particles, researches can be classified into three kinds: (1) the whole particle, it may attach some organics or adsorb heavy metals around the nucleus; (2) leachate of airborne particles, it often contains the soluble components of the particle itself as well as the attachments on its surface; (3) particles after leaching, it is always called as a bare nucleus. It is revealed that different fractions of particle stir the toxic behaviors to different extent, but the mechanisms are still uncertain [2, 3]. Although it has been ignored for a long time, as one important part of airborne particles, mineral particle counted for a half of the total mass [4]. According to the phase analysis of particles captured during the sandstorm, silicate minerals counted for 60 % approximately. In the normal daily life, clay and digenetic minerals also play a vital role in the air. Researches focus on the safety assessment of airborne particles, especially the particles attached with organics and heavy metals, and there are some pathogenesis mechanisms being developed. However, the complex composition of particles limits the real reasons that stir the blasting fuse. In this chapter, we focused on the natural mine particles (including silica and montmorillonite) and exposed lung epithelial cells to particles of different size fractions (<5 μm and <2.5 μm). The particles were analyzed for size, mineral phase, and element composition. The experiment aimed to investigate the cytotoxic and genotoxic potential of natural mine particles to lung epithelial cells and to analyze how the various physicochemical properties were related to chemokine release. The study also aimed to examine whether information on physicochemical characteristics could be used to predict the biological effects of stone quarry particles.

2 Materials and Methods

2.1 Reagents

3-(4,5-dimethylthiazol-2-yl)-2,5-diphenyltetrazolium bromide (MTT), dimethyl sulfoxide (DMSO), RPMI 1640 medium with L-glutamine, penicillin–streptomycin, and fetal bovine serum (FBS) were purchased from Hyclone, American. LDH

Detection Kit, TNF-α Detection Kit, and IL-6 Detection Kit were bought from Nanjing Jiancheng Bioengineering Institute, Nanjing city, China. All other reagents and solvents used were of analytical grade. All solutions were prepared with deionized water from a Milli-Q purification system.

2.2 Cell Culture and Treatment

A549 cell line was obtained from the experimental center of the Affiliated Hospital of Luzhou Medical School which was purchased from the American Tissue Type Culture Collection (ATCC, Rockville, MD, USA). It is one of typical epithelial cells of lung adenocarcinoma and is considered as a good model to study the interaction between allogenic material and the respiratory system because of its typical characteristics of II type alveolar epithelial cells in the cultivating process. Besides as a mechanical barrier, lung epithelial cells also act as the first line of breathing defense system and contain important pathogen recognition system of transmembrane and intracellular pathogens. This research aims at elaborating the toxicity effect of A549 cells incubated with different size quartz powder and nature montmorillonite mineral power (Table 1).

Cells were maintained in RPMI1640 medium containing 10 % fetal calf serum (FBS) and 1 % penicillin/streptomycin at 37 °C with 5 % of CO_2 prior to exposure. The cell line was split with 0.25 % trypsin and the medium was changed the day after.

2.3 Particle Preparation and Analysis Method

Silica rock was obtained from Erlangmiao quarry in Jiangyou, Sichuan. Rocks were firstly crushed into fragments by horizontal planetary ball mill and then milled with deionized water in the ball mill. Particles were grinded through 200 mesh sieve after dehydration in the air dry oven, finally. Because Quartz milling has different median diameters at different times, the powders' size distributions within the

Table 1 The experiment design

Test item	Concentration (μg/mL)	Time (h)
MTT-cell viability	0, 50, 100, 200, 400, 800	24
LDH-cell membrane damage	0, 50, 200, 800	24
TNF-α	0, 50, 200, 800	3, 6, 8, 24
IL-6	0, 50, 200, 800	24
Comet assay	0, 50, 100, 200, 400	24
Micronucleus test	0, 50, 100, 200, 400	24

<5 μm and <2.5 μm fractions were labeled as KWC-Q3 and KWC-Q4, respectively.

Montmorillonite was obtained from Altai, Xinjiang, which appeared light yellow powder. It was first soaked in distilled water for 3 days before removing the floating and suspending debris and then stirred for 3 days with the pulp density of 2 wv%. Granularity of the particle suspension was determined by Laser Particle Analyzer after removing the top supernatant liquid and stood out for 24 h. The suspension was then dehydrated in the air dry oven and grinded through 200 mesh sieve oven finally. The particle size distribution of purified montmorillonite within 10 μm was labeled as KWC-M.

All the dried mineral powders were dispersed in the cultural medium and sonicated for 30 min prior to size distribution analysis by Laser Particle Analyzer again. Besides, mineral phases were determined using X-ray diffraction (XRD) analysis (X'pert PRO PHILIPOS); semiquantitative element was analyzed by X-ray fluorescence (XRF, Magix, PANalytical); particle surface morphology character was measured by scanning electron microscope (SEM, TM-1000, HITACHI).

2.4 MTT Proliferation Assay

Cell viability was measured by the MTT assay, performed according to kit manual. Briefly, 20 μL of MTT solution (5 mg/mL) per well was incubated with cells (about 2.0×10^5 cells) for further 4 h at 37 °C, 5 % CO_2 after the incubation experiment already described above. Then the wells were drained, cells were washed with PBS, and 200 μL of DMSO was added to dissolve the intracellular crystalline formazan product for 30 min at room temperature. The optic density at 490 nm was read spectrophotometrically using a Microplate Reader (Multiskan GO, THERMO) immediately. The results were expressed as a percentage of the absorbance of control cells, called relative proliferation rate (ω), following the equation:

$$\omega \times 100\% = \frac{\mathrm{OD}_{\mathrm{expos.c}} - \mathrm{OD}_{\mathrm{cont.m}}}{\mathrm{OD}_{\mathrm{cont.c}}} \times 100\% \quad (1)$$

where $\mathrm{OD}_{\mathrm{expos.c}}$ stands for the well optic density of cells incubating with different mineral samples, $\mathrm{OD}_{\mathrm{cont.m}}$ for the well optic density of mineral suspensions without cells, and $\mathrm{OD}_{\mathrm{cont.c}}$ for the cells of negative group without exposing to the mineral suspensions or others.

2.5 LDH Activity Assay and Cytokines Release

Cells were incubated with different concentrations (50, 200, and 800 μg/mL) of quartz and montmorillonite in six-well plates at 37 °C for 24 h. Subsequently,

culture media were collected and centrifuged in two steps (first at 250 g aiming to remove cells and then at 2,500 g to remove the remaining particles). The final supernatants were stored at −80 °C. LDH, IL-6, and TNF-α levels were determined using enzyme-linked immunosorbent assay (ELISA) according to the manufacturers' guides. Absorbance was measured and quantified by the Microplate Reader.

2.6 Micronucleus Assay

To assess the chromosomal damage of particles to A549 cells, the micronucleus (MN) assay was performed as follows. Briefly, cells were seeded in a 12-well chamber slide at a density of 1×10^5 cells/well and grown for 24 h. Cells were treated with 0, 50, 100, 200, and 400 μg/mL powder suspensions with 2 vv% FBS in RPMI1640 for 24 h. Cyclophosphamide (CP, 300 μg/mL, 24 h, Sigma) was used as a positive control. Each sample was run in duplicates. After incubation with different mineral suspensions at 37 °C or 24 h, medium was removed and cells were fixed with 1 mL stationary liquid (with methanol and formaldehyde volume ratio is 3:1, precooled at −20 °C until staining and evaluation) for 30 min. To stain the cells, stationary liquid was aspired and cells were stained for 10 min with Wright-Giemsa stain (Baso Diagnostics Inc.) after drying in room temperature and washed twice with phosphate buffer for 3 min. Finally, cells were analyzed by the oil lens of microscope (CX21, Olympus), 1×10^3 cells/slide. Results were shown as the frequency of micronucleated cells (FMN) per slides.

$$\mathrm{FMN} = \frac{N_{\mathrm{MN}}}{\mathrm{TN_{CC}}} \times 1000\,\% \tag{2}$$

where NMN stands for the number of micronucleated cells in one slide and TNCC for the total number of the cells in the slides.

2.7 Comet Assay

A549 cells were seeded in 12-well plates at 5×10^5 cells/mL 1 day before treatment. Cells were exposed to 50, 100, 200, and 400 μg/mL of particles with 2 vv% FBS in RPMI1640 for 24 h. After the exposure, the media were removed; cells were washed once by PBS gently and harvested using PBS with the cell concentration at 4×10^5. 30 μL of the cell suspension which was mixed with 70 μL 0.5 wv% low-melting agarose (Roth, Karlsruhe) warmed in 37 °C before. 90 μL agarose cell solution was applied to microscope slides, covered with coverslip, and fixed 10 min in refrigerator at 4 °C. 90 μL agarose (Roth, Karlsruhe) was added on the surface of the first agarose, fixed 10 min in refrigerator at 4 °C again, and then covered with coverslip. The cell coverslip was removed before putting the slides

into lysis solution (2.5 M NaCl, 100 mM Na_2EDTA, 10 mM Tris-1 HCl, 1 % Na-Sarcosinate, pH 10; 1 vv% Triton-X-100, and 10 vv% DMSO were added before use) for 2.5 h. Slides were then put into a horizontal electrophoresis tray containing the alkaline electrophoresis buffer (0.3 M NaOH, 1 mM Na_2EDTA) precooled at 4 °C allowing the unwinding of the DNA for 20 min. Electrophoresis (25 V, 300 mA) was performed for 30 min. Slides were neutralized in Tris–HCl buffer (0.4 M Tris–HCl, pH 7.5), rinsed in H_2O, dehydrated in 99 % ethanol, and dried overnight. DNA was stained with fluorochrome (20 μg/mL) and comets were analyzed by using a Leica ×2500 microscope with a blind camera. 50 comets chosen randomly were analyzed per slide by the software "CASP."

2.8 Statistic Analysis

All experiments were repeated three times. The data were presented as the means ± standard deviation (S.D.) of three independent experiments. They were analyzed by using the software of statistical package for the social sciences (SPSS) Version 11.0. The statistical difference between groups was determined with a one-way ANOVA. The minimum level of significance was considered to be $p < 0.05$.

3 Results

3.1 Mineral Analysis

Mineral samples used in this study were analyzed by XRD, XRF, and SEM, and the results showed that the SiO_2 content of quartz samples (KWC-Q4 and KWC-Q3) was above 97 %, and the main mineral phase was quartz. The content of SiO_2 in Nano-SiO_2 was 97 % of amorphous structure. The purity of montmorillonite was 96 % by semiquantitative analysis. The SEM images of particle samples were listed in Fig. 1.

3.2 Cell Viability

As illustrated in Fig. 2, exposure to 50, 100, 200, 400, and 800 μg/mL quartz, Nano-SiO_2, and montmorillonite for 24 h all induced a statistical significant decrease in the number of viable A549 cells compared with the control group. The figure showed that KWC-Q4 and KWC-Q3 samples caused a concentration-dependent decrease in cell viability. As to the particles in different size range, there was

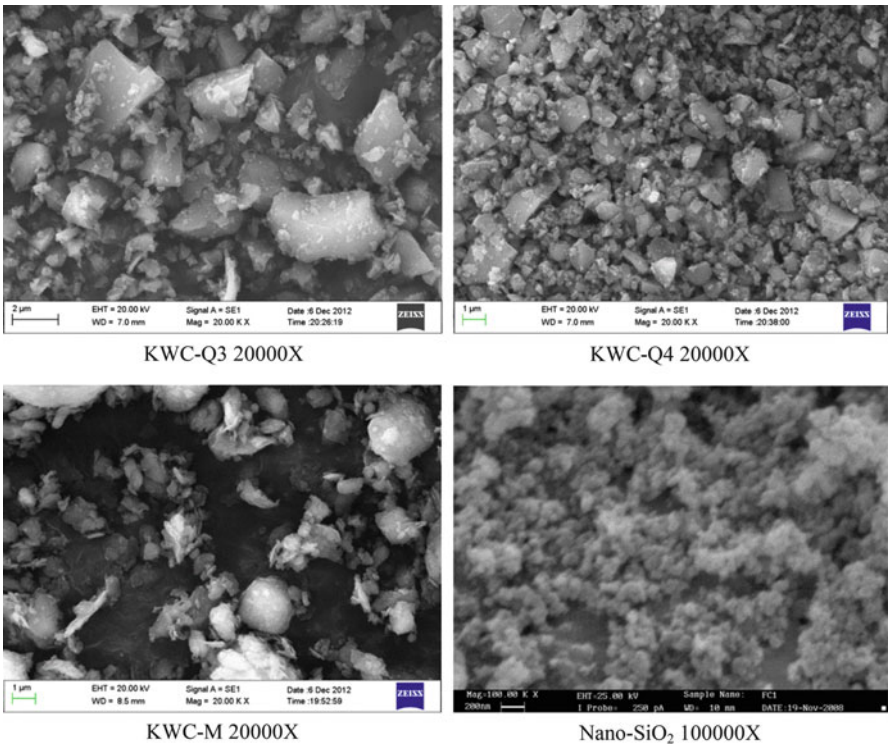

Fig. 1 SEM of mineral samples

significant difference between KWC-Q4 and KWC-Q3. From low concentration to high concentration, the cell toxic effect induced by KWC-Q3 was significantly higher than KWC-Q4.

The cell viability of Nano-SiO_2 group and KWC-M decreased sharply as the increase of concentration. The dose–effect curve of Nano-SiO_2 from 50 μg/mL to 200 μg/mL was $y = -0.252x + 93.753$, with a correlation coefficient of 0.8695, while decreased to $(5.05 \pm 1.01)\,\%$, as the powder concentration was 400 μg/mL. KWC-M has the same cell toxic tendency as Nano-SiO_2; the cell viability of KWC-M was $(53.22 \pm 7.94)\,\%$ at the powder concentration of 50 μg/mL and decreased to $(18.74 \pm 8.46)\,\%$ as the concentration was 200 μg/mL.

3.3 Effects on Plasma Membrane Permeability

As exposed to mineral powder, there was a continuous interaction between the cell membrane and the mineral surface, resulting in the increase of intracellular LDH enzyme leakage in the medium which reflects the damage of the membrane-

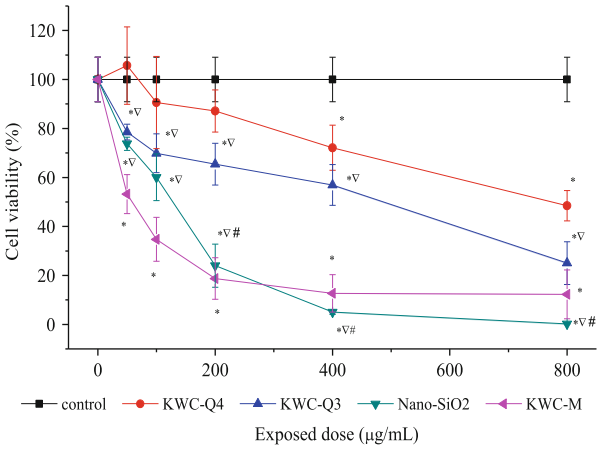

Fig. 2 Cell viability of A549 after incubation with different doses of mineral suspensions for 24 h. Note: *Asterisk, triangle, hash* $p \leq 0.05$, as compared to the control, the 50 and 200 μg/mL exposure group of the same kind of powder, $n = 3$

damaged extent. In this study, extracellular LDH was used as an indicator of the cell membrane integrity. Figure 3 shows that all kinds of powders lead to significant increase of extracellular LDH activity compared with the control group. The leakage of A549 cell LDH indicated a dose–effect relationship after exposure to different concentrations. Low dose (50 μg/mL) powder suspension can lead to significant increase of LDH activity, which was two to three times higher than the control. KWC-Q4, KWC-Q3, Nano-SiO_2, and KWC-M all resulted in significant increase of the activity of LDH at the exposure concentration of 800 μg/mL. LDH activity was increased by approximately 754.4 % and 686.9 %, 896.6 %, and 845.6 %, respectively, as compared with controls. Besides, there was a good linear relationship between LDH release and cell viability. The increase of extracellular LDH indexed the membrane permeability change and the membrane damage.

3.4 Cytokine Release

The content of extracellular TNF-α of A549 after incubation with powder for 8 h was shown in Fig. 4. The content of TNF-α of control group was at (30.69 ± 1.00) ng/L, while the contents of TNF-α of all exposure groups were approximately at 30 ng/L, with no significant difference with the control, or between the two concentrations of the same kinds of samples. Therefore, the TNF-α content of A549 cell incubation with powder suspensions for 3 h, 6 h, and 24 h at 200 μg/mL was measured. Figure 5 shows the change of TNF-α in the A549 cell medium after exposure to the mineral particle suspensions for 3 h, 6 h, and 24 h. The TNF-α content of control group was at (26.48 ± 1.08) ng/L for 3 h and increased to (31.39 ± 1.31) ng/L 3 h later but had no significant difference among the contents of TNF-α for 24 h, 6 h, and 8 h. The contents of extracellular TNF-α of all samples suspensions were triggered and increased for 3 h, compared with the control group,

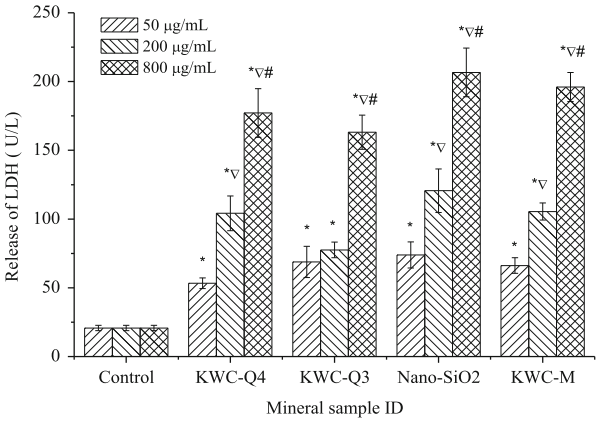

Fig. 3 Extracellular LDH activities of A549 cells after incubation with KWC-Q4, KWC-Q3, Nano-SiO_2, and KWC-M. Note: *Asterisk, triangle, hash* $p \leq 0.05$, as compared to the control, the 50 and 200 μg/mL exposure group of the same kind of powder, $n = 3$

but the difference disappeared when the time was stretched to 6 h and maintained stability for 8 h or long. Experiments showed no visible time or dose–effect relationship.

The secretion of IL-6 of A549 cells exposed to different powder suspensions was shown in Fig. 6. Results showed the addition of quartz, Nano-SiO_2, and montmorillonite powder caused the IL-6 secretion of A549 cells to increase significantly compared with the control group. The content of extracellular IL-6 was 1.61 and 1.40 times of the control group, when the exposure concentrations of montmorillonite and Nano-SiO_2 were 50 μg/mL. However, the levels of IL-6 show a declining trend when the exposure concentration continued to increase, which may result from their high and instant toxic effect on cells. The secretion of IL-6 of A549 exposed to KWC-Q4 and KWC-Q3 of the relative low concentration was increased with the concentration. But there was no significant difference of the IL-6 secretion between the neighboring concentrations of all mineral powders. From the figure, KWC-M has a great influence on the secretion of IL-6 of all the mineral suspensions at low exposure dose (50 μg/mL). KWC-Q4 was the only sample that showed a dose–effect relationship in the test concentration range. The experiment indicates that all samples tested can promote the release of IL-6 and trigger the inflammation reaction of A549 cells.

3.5 Micronucleated Cell Test

The cells' micronucleus rate exposed to different mineral suspensions for 24 h was shown in Fig. 7. The micronucleus rate of negative control group cells (−) cultivated with culture solution only was (5.667 ± 1.528)‰ at 24 h; with 300 μg/mL of cyclophosphamide (CP) as a positive control, the micronucleus rate was (21.667 ± 1.528)‰. All the micronucleus rates of mineral exposure groups had significant difference compared with negative control group, except for

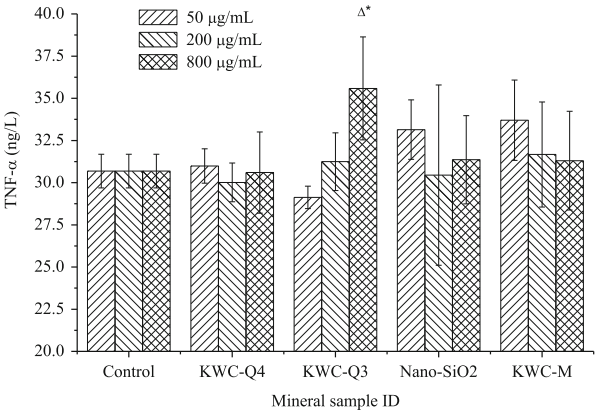

Fig. 4 Change of TNF-α in the A549 cell medium supernatant after incubation with mineral suspensions for 8 h. Note: *Triangle, asterisk, hash* $p \leq 0.05$, as compared with control, 50 μg/mL, 200 μg/mL of same mineral sample, $n = 3$

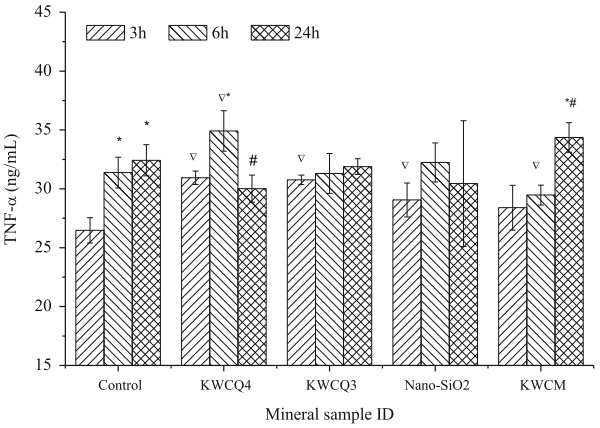

Fig. 5 Concentration change of TNF-α in A549 cell culture medium supernatant after incubation with mineral suspensions at 200 μg/mL. Note: *Triangle, asterisk, hash* $p \leq 0.05$, as compared with control, 3 h, 6 h exposure group of the same mineral sample, $n = 3$

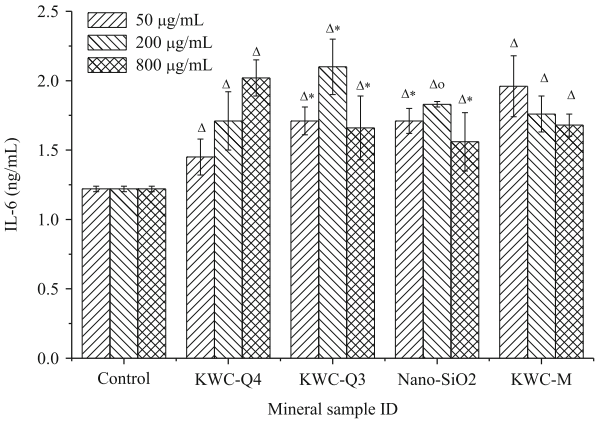

Fig. 6 Change of IL-6 in the A549 cell medium after incubation with mineral particle suspensions. Note: *Triangle, asterisk, circle* $p \leq 0.05$, as compared with negative control group, KWC-Q4, KWC-Q3 exposed group, respectively, $n = 3$

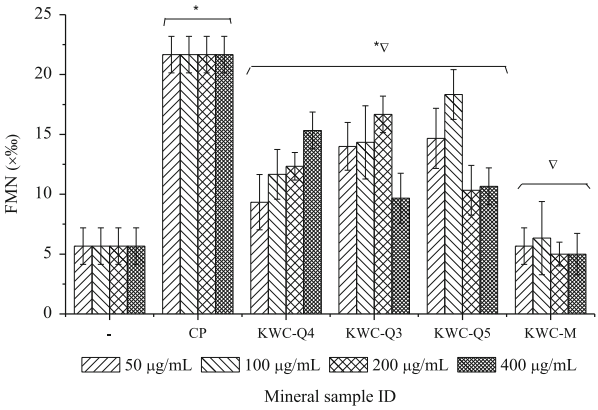

Fig. 7 Micronucleus test of A549 cells after incubation with KWC-Q4, KWC-Q3, Nano-SiO_2, and KWC-M for 24 h. Note: *Asterisk, triangle* $p \leq 0.05$, as compared with negative control (−) and positive control (CP) respectively, $n = 3$

montmorillonite. Cells' micronucleus rate of low concentration groups (50 μg/mL and 100 μg/mL) is as follows: Nano-SiO_2>KWC-Q3>KWC-Q4. KWC-Q3 and KWC-Q4 mineral suspensions caused an increasing trend of cell micronucleus rate with the concentration when the exposure concentration was lower than 200 μg/mL. While the addition of montmorillonite led to higher cell mortality by lessening cell adhesion quickly even at a low concentration of 50 μg/mL, it was meaningless to measure the cell micronucleus rate when the cell mortality was 50 % approximately. The micronucleus test results showed the quartz samples, the Nano-SiO_2, can lead to the increase of cell micronucleus rate, namely the mineral can cause damage to cell's chromosomes, and lead to chromosome aberration; A549 cell micronucleus rate shows a tendency to rise with the increase of exposure concentration, within the condition of low cell mortality.

3.6 Comet Assay

Comet assay is a sensitive test to detect the genotoxicity of allogenic materials. In this chapter, Olive Tail Moment (OTM) was taken as the main indicators analyzed by the CASP software.

The cells of negative control group have no obvious DNA migration, cells appeared bright round head with regular shape, and distinguished difference in background. Cells incubated with different mineral samples exhibited a dose-dependent increase in DNA migration with their tails stretched and rounded out and heads smaller and brighter. The cells became badminton shaped as the DNA was damaged to a great extent. Comet cells OTM is a comprehensive index of cell DNA damage. The box plot of A549 cells comet OTM after incubation with KWC-Q4, KWC-Q3, Nano-SiO_2, and KWC-M powders for 24 h was shown in Fig. 8. The negative control group cell OTM was 2.589 ± 1.706. Quartz, Nano-SiO_2, and montmorillonite powder produced significant difference compared with

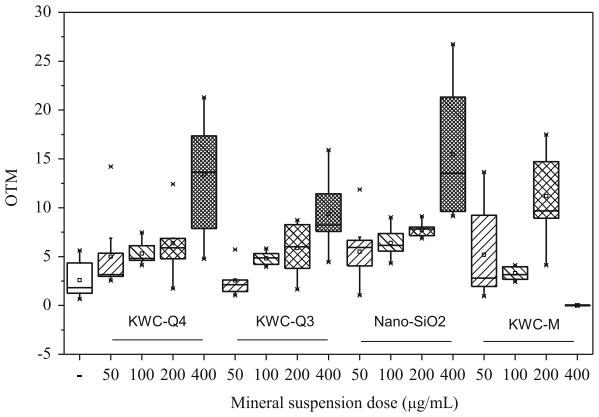

Fig. 8 Box plot of A549 cells comet OTM after incubation with KWC-Q4, KWC-Q3, Nano-SiO_2, and KWC-M powders for 24 h

control group as the exposure dose was more than 100 μg/mL and appeared an increase trend with the concentration, but no significant difference between the neighboring concentration groups.

4 Discussion

This study focuses on the cytotoxicity of quartz with two different particle sizes, Nano-SiO_2, and montmorillonite. Its results showed the toxic effect of Nano-SiO_2 on A549 cells was obviously higher than that of KWC-Q3 and KWC-Q4, which was in accordance with results of Donaldson [5]. The toxic effect of nanoparticles were significantly higher than that of micron particles, especially when the particle size was smaller than 100 nm, for the biological activity of nanoparticles increased sharply with the decrease of the particle size, which can cause more damage to the lung tissue. For different size range of quartz particles, the toxicity of KWC-Q3 on A549 was more larger than that of KWC-Q4. The toxicity of montmorillonite sample was almost same to Nano-SiO_2 and led to a higher mortality at low dosage. All the test samples showed the cell viability was inversely related to the concentration of treatment in cells.

LDH was a cytoplasm enzyme and leaked into the culture medium with the permeability increasing or the damage of cell membrane. So the extracellular LDH was often analyzed as an index of the membrane integrity [6]. Results showed the extracellular LDH concentration: Nano-SiO_2>KWC-Q3>KWC-Q4 with the same amount of exposure; the leakage of LDH increased with the exposure dosage; there appeared a concentration-dependent relationship which is consistent with the relationship between mortality rate and the exposure dosage.

IL-6 and TNF-α were the main cytokines that mediated the inflammatory reaction, cells will synthesize and secrete the cytokines by the real time of being stimulated by factors which were identified as the ideal indicators to evaluate the

ability of materials to inducing inflammatory response [2, 7]. As one typical II alveolar epithelial cell, A549 cells had been analyzed as the test body, and exhibits a dose-dependent relationship between the inflammatory cytokines secretion and the exposure dosage in Zhang's study [8, 9]. In this experiment, all test samples stimulated the secretion of IL-6, but not all of them exhibited a dose-dependent relationship in the test concentration range. The mineral samples caused the increase of TNF-α in culture medium for 3 h compared with the control group, but the difference disappeared when the exposure time extended to 8 or 24 h. The experiments testified the ability of mineral samples to cause the secretion of inflammatory cytokines and then triggered the inflammatory action. The micronucleus assay and the comet assay also deveined the genotoxicity of quartz, Nano-SiO_2, and montmorillonite.

The montmorillonite sample in the experiment showed a different cytotoxic effect compared with the others' results, which may link with its strong adsorption to promote the interaction with cell membrane and accelerate the cell membrane damage, or the micron nanoquartz particles mixed in the suspension. The mechanism of why the montmorillonite produced a lager effect to the A549 cells and the interaction with cells need further study.

Acknowledgements This study was supported by grants from the National Natural Science Foundation of China (No. 41130746).

References

1. Wei A, Meng Z (2006) Evaluation of micronucleus induction of sand dust storm fine particles (PM) in human blood lymphocytes. Environ Toxicol Pharmacol 22:292–297
2. Qu F, Ding W, Yi S, Zhang F (2010) Cytotoxicity of $PM_{2.5}$ in typeIIalveolar epithelial cells (MLE-12). J Toxicol 24:19–24
3. Maurizio G, Johan Ø, Jørn AH (2010) Differences in cytotoxicity versus pro-inflammatory potency of different PM fractions in human epithelial lung cells. Toxicol in Vitro 24:29–39
4. Per ES, Ragna BH, Magne R, Marit L, Rune B (2002) Mineral composition other than quarts is a critical determinant of the particle inflammatory potential. Int J Hyg Environ Health 204:327–331
5. Donaldson K, MacNee W (1998) The mechanism of lung injury caused by PM. In: Hester RE, Harrison RM (eds) Issues in environmental science and technology, vol 10. Royal Society of Chemistry, London, pp 21–32
6. Geng H, Meng Z, Zhang Q (2005) Effects of blowing sand fine particles on plasma membrane permeability and fluidity, and intracellular calcium levels of rat alveolar macrophages. Toxicol Lett 157:129–137
7. Ovrevik J, Myran T, Refsnes M (2005) Mineral particles of varying composition induce differential chemokine release from epithelial lung cells: importance of physic-chemical characteristics. Ann Occup Hyg 49:219–231
8. Zhang W, Qi Q, Xu D (2003) Study on inflammation cytokines of alveolar epithelial cells induced by ambient fine particles $PM_{2.5}$ in two cities of China. J Lab Med 5:325–330
9. Annarica C, Stefania M, Manuela M (2004) Fine environmental particulate engenders alterations in human lung epithelial A549 cells. Environ Res 95:82–91

Assessment and Characterization of REE Minerals from an Alkali-Carbonatitic Complex

Juliana Lívi Antoniassi, Daniel Uliana, Henrique Kahn, M. Manuela M. Lé Tassinari, and Carina Ulsen

Abstract The demand for rare earth elements (REE) in high technology industries has been intensified and coupled with the fact that China accounts for about 95 % of world production and is actually creating trade restrictions for these elements; the search for new resources has been encouraged in several countries. This chapter presents a methodology for characterizing an earth rare mineralized sample, which occurs in association with alkali-carbonated complexes and with fine-grained monazite. The procedure was conducted by an automated image analysis system, besides physical separations and selective comminution by scrubbing, thereby evaluating the possibility of enrichment of rare earth bearing minerals in the attained products. Monazite is the main REE bearing mineral, counting for 40 % of the total content; it usually occurs in aggregates with micrometric crystals often with cerianite intergrowth. Monazite is mostly associated with anatase and Fe-oxy-hydroxides presenting a very poor liberation (34 wt% on average for material grinded below 0.30 mm). Both mineral separations and selective grinding by scrubbing did not succeed to obtain products with significant enrichment in REE.

Keywords Rare earth elements • Applied mineralogy • Automated mineralogy • Monazite

1 Introduction

New attention has been given to rare earth minerals resources over the last years. The trade restrictions recently imposed by China and the growing demand for rare earth elements (REE) in high technology industries have motivated the Brazilian Government to encourage new projects by inserting the exploitation of REE in the National Mining Plan, which deals with industry strategic issues in the country and

J.L. Antoniassi (✉) • D. Uliana • H. Kahn • M.M.M.L. Tassinari • C. Ulsen
Mining and Petroleum Engineering Department, Polytechnic School, University of Sao Paulo, Av. Prof. Mello Moraes, 2373 Sao Paulo, SP, Brazil
e-mail: juliana@lct.poli.usp.br

F. Dong (ed.), *Proceedings of the 11th International Congress for Applied Mineralogy (ICAM)*, Springer Geochemistry/Mineralogy,
DOI 10.1007/978-3-319-13948-7_18

helps to reduce current importation. The incentives can be in the choice of future targets for mineral exploration and for the development of laboratory studies and pilot scale processing tests [1, 2].

Although in Brazil there is almost no large-scale exploitation of rare earth minerals, the existing resources are significant and occur mainly in association with alkali-carbonatitic complexes. In these deposits there are several rare earth bearing minerals and monaziteis, the one that has greater resources and potential for exploitation, usually present at extremely fine grain sizes [3, 4].

Because of textural features, fine grain sizes, and complex associations, the technological feasibility of REE depends primarily on the detailed applied mineralogy studies, focus on better understanding of the ore characteristics, processing limitations, and possible stages of physical concentration [5, 6].

This chapter presents a typical and recent applied mineralogical study, developed on a lateritic rare earth ore sample from Brazil, aiming to determinate the mineralogical composition and associations, liberation degree, partition of the rare earth oxides (REO), and its potential recovery, defined by SEM-based automated image analysis (MLA) [7], providing support and parameters for the mineral beneficiation process. Physical separations by density and magnetic susceptibility, as well as selective comminution by scrubbing were also developed, thereby evaluating the possibility of enrichment of rare earth bearing minerals in the attained products.

2 Materials and Methods

2.1 Studied Sample

The studies were performed on a low-grade lateritic rare earth mineralized sample from one of the alkali-carbonatitic complexes in Minas Gerais State, Brazil.

2.1.1 General Characterization Studies

The experimental procedure was adopted for the characterization studies, which comprises:

Homogenization and sampling;
Desliming of a representative aliquot through a 25 mm hydrocyclone (estimated cut off in 0.008 mm) to remove the natural fines from sample;
Grinding of deslimed fraction below 0.30 mm in a rod mill, followed by a second desliming to remove the generated fines by grinding;
Sieve size analyzed by wet screening with screen apertures of 0.21, 0.15, 0.074, 0.037, and 0.020 mm;
Chemical analyses at sieve fractions and in the bulk sample;

Detailed mineralogical studies were conducted by SEM-based automated image analysis and by X-ray diffraction.

2.1.2 Exploratory Mineral Separations and Selective Comminution by Scrubbing

Mineral separations were conducted by a Davis Tube magnetic separator followed by heavy liquid separation (di-methylene iodide—3.30 g/cm^3), aiming to obtain products enriched in rare earth minerals. These assays were performed in all fractions size above 0.008 mm and obtained in general characterization studies. Additionally, selective comminution by scrubbing tests was held on not comminuted aliquots as described below.

Desliming of a representative aliquot through a 25 mm hydrocyclone coupled with two stages (estimated cut off in 0.008 and 0.005 mm) to remove the natural fines from sample;
Scrubbing of material above 0.008 mm in a Denver D12 1,0L cell, considering a 50 % of solids, during 10 min at 1,200 rpm; this assay was followed by a second desliming to remove the fines generated by scrubbing;
Sieve size analysis by wet screening with screen apertures of 0.60, 0.30, 0.15, 0.074, 0.037, and 0.020 mm;
Chemical analyses at sieve fractions and in the bulk sample;
To repeat the desliming and sieve size analysis for a not scrubbed aliquot.

The proposed method is based on the strong and natural tendency of the monazite to break up easily and consequently to concentrate in the finest size fraction, as discussed by Tassinari et al. [4].

2.2 Methods for Assessment and Analysis

2.2.1 Chemical Analysis (X-ray Fluorescence)

Quantitative chemical analysis were carried out by X-ray fluorescence (XRF) in fused pellets, by means of Axios Advanced spectrometer (PANalytical) with determination of CeO_2, La_2O_3, Nd_2O_3, and Pr_2O_3 (REO), besides Nb_2O_5, P_2O_5, CaO, SiO_2, Al_2O_3, Fe_2O_3, MgO, TiO_2, BaO, MnO, and SO_3. Loss on ignition (LOI) was also performed by sample calcinations in a muffle furnace at 1,050 °C for 1 h.

2.2.2 X-ray Diffraction

The mineralogical analysis by X-ray diffraction (XRD) was performed by the powder method in X-ray diffractometer X'Pert PRO with X'Celerator detector (PANalytical). The identification of crystalline phases was obtained by comparing

the diffraction patterns with the database ICDD—International Centre for Diffraction Data.

2.2.3 SEM-Based Automated Mineralogy

The study by scanning electron microscopy (SEM) was carried out in polished sections, previously coated with a carbon film. The qualitative and semi quantitative evaluation of chemical elements presented in the several minerals was accomplished by Stereoscan 440 microscope (LEO) with energy dispersive spectrometer (EDS, Oxford) with an SDD detector and INCA microanalysis system (Oxford). The mineralogical composition of the samples and the partition of the main elements in the bearing minerals were performed through automated image analysis software (Mineral Liberation Analyzer—MLA) coupled with a scanning electron microscope Quanta 600 FEG (FEI) with EDS (Bruker) and microanalysis system Esprit (Bruker). The automated search routine was held by XBSE mode, considering such the atomic number contrast as the chemical composition of each mineral phase (backscattered electrons images and characteristic X-ray spectra by EDS). The chemical and morphological variability of the bearing rare earth minerals was also obtained, taking into account X-ray mapping of the main chemical elements and detail images (1,000–15,000 times magnification).

3 Results

3.1 Chemical Composition

The chemical composition of the sample is presented in Table 1 and the REO total grade is 1.25 wt% (0.63 % of CeO_2, 0.40 % of La_2O_3, and 0.22 % of Nd_2O_3).

High grades of Fe_2O_3 and TiO_2 reach 35.8 and 30.7 wt% respectively, while the SiO_2 content is 15.7 wt%. In minor amounts are the grades of CaO (4.35 wt%), Al_2O_3 (3.65 wt%), P_2O_5 (1.50 wt%), MgO (1.32 wt%), BaO (0.49 wt%), MnO (0.58 wt%), and Nb_2O_5 (0.11 wt%), besides 3.34 % of LOI.

3.2 Particle Size Analysis

Particle size cumulative distribution curves for weight, REO, P_2O_5, SiO_2, Fe_2O_3, and TiO_2 are presented in Fig. 1 for the material comminuted below 0.30 mm.

The fraction size above 0.008 mm represent 83 wt% of the total mass, while 15.8 wt% is relative to the natural fines below 0.008 mm and 1.2 wt% to the fines generated on comminuting process.

Table 1 Bulk sample chemical composition

REO	CeO_2	La_2O_3	Nd_2O_3	Pr_2O_3	Nb_2O_5	P_2O_5	CaO	SiO_2	Al_2O_3	Fe_2O_3	MgO	TiO_2	BaO	MnO	SO_3	LOI	REO/P_2O_5	CaO/P_2O_5
1.25	0.63	0.40	0.22	<0.10	0.11	1.50	4.35	15.7	3.65	35.8	1.32	30.7	0.49	0.58	<0.01	3.34	0.83	2.90

REO Sum of rare earth oxides (CeO_2, La_2O_3, Nd_2O_3, Pr_2O_3)

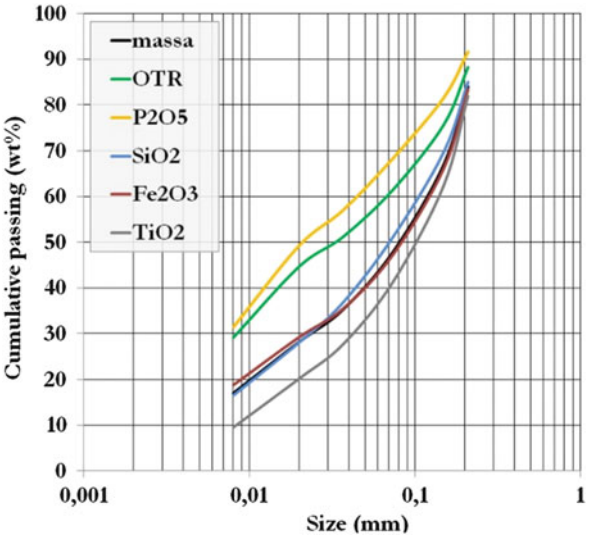

Fig. 1 Weight and main elements distributions by size

REO grades vary from 0.93 to 1.76 wt% above 0.008 mm, increasing to the fine fractions, whereas in the natural fines, this value is 2.18 wt% (27 % of REO total contained in the sample) and reach 2.28 wt% on generated fines (2.1 % of REO total contained).

Among the REO total content, the CeO_2 values are the highest which ranging from 0.50 to 1.17 wt%; the La_2O_3 grades are between 0.28 and 0.66 wt%, the Nd_2O_3 between 0.14 and 0.50 wt%, while the Pr_2O_3 vary between 0.10 and 0.17 wt % in the fractions below 0.037 mm and is less than 0.10 wt% above.

3.3 Mineral Modal Composition

The mineralogical composition of the sample (total -0.30 mm) is represented in the Fig. 2. The major constituents are iron oxy-hydroxides (31 wt%; goethite, hematite and magnetite), anatase (21 wt%), quartz (13 wt%), ilmenite (11 wt%), as well as perovskite (9.0 wt%), clay minerals (8.7 wt%; gibbsite and kaolinite), and Al-phosphates (3.4 wt%; gorceixite–goyazite).

Monazite represents 0.9 wt% of sample with proportions varying between 0.2 and 1.2 wt% in fractions sizes above 0.008 mm and reaching 2.4 and 2.8 wt% in the passing natural and generated material, respectively. Other minerals are also presented with proportions below 1 wt% like Mn-oxide, apatite, zirkelite–zirconolite, baddeleyite, titanite, vermiculite, dolomite, cerianite, and Ba-phosphate.

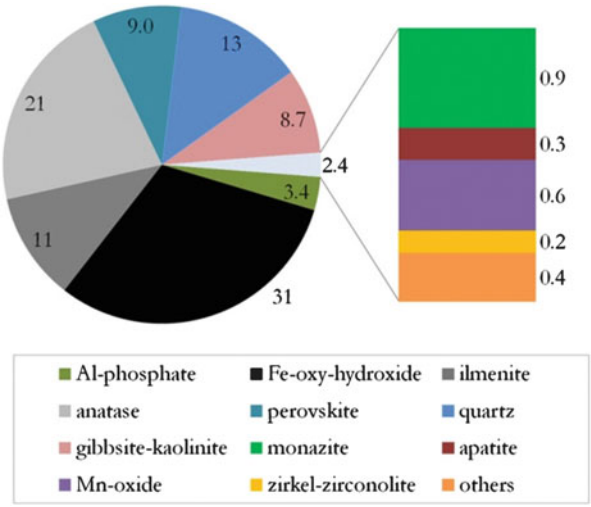

Fig. 2 Mineralogical composition of the studied sample

3.4 Monazite Liberation and Associations

Monazite is the main REO bearing mineral in the sample; usually occurs in aggregates of monazite often with cerianite intergrowth and shows micrometric crystals. These aggregates may present as massive aspects, colloform, or as acicular crystals.

Monazite is mostly associated with anatase and Fe-oxy-hydroxides and shows some compositional variability ($(Ce,REE)PO_4$) and apparently also some hydration (monazite-rhabdophane group), being possible to identify the intergrowth of two predominant types: one richer in lanthanum and another in cerium; this differentiation is not focused in this study.

Monazite aggregates are reached on average 34 wt% of liberation degree by area (particles with >95 % of monazite), varying from 0 to 65 wt% in fractions sizes, gradually increasing towards the fines—Fig. 3. In terms of exposed perimeter (or "free surface" as referred in MLA), the liberation degree is slightly lower due to the trend of gangue minerals concentrating at the border of the locked particles.

It was noticed also the occurrence of submicron inclusions of monazite is preferably associated with anatase and perovskite. The differentiation of these phases depending on the size of these associations sometimes became infeasible for the MLA software to perform a proper mineral classification. So it is expected that the results of monazite quantification may have been slightly underestimated, as well as cerianite and eventually other REO bearing minerals with sub micrometric dimensions may have been added as monazite; on the other side the monazite liberation data are overestimated.

The main features observed for the monazite aggregates are illustrated in Photomicrographs 1 and 2, obtained by SEM/EDS and by elemental mappings.

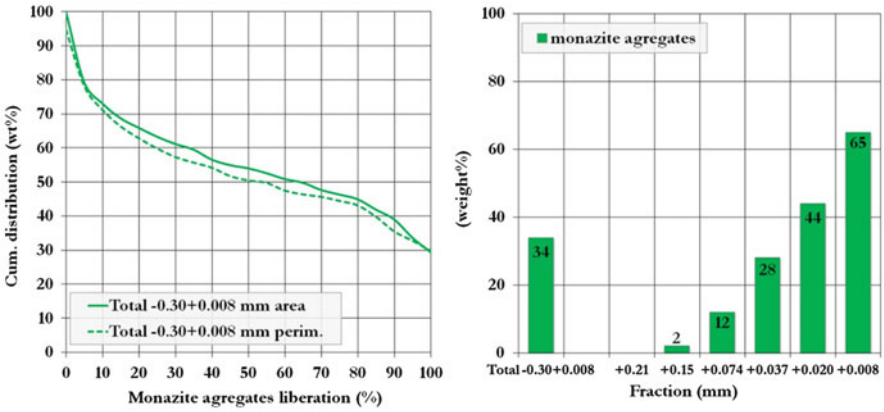

Fig. 3 Liberation degree for the monazite aggregates

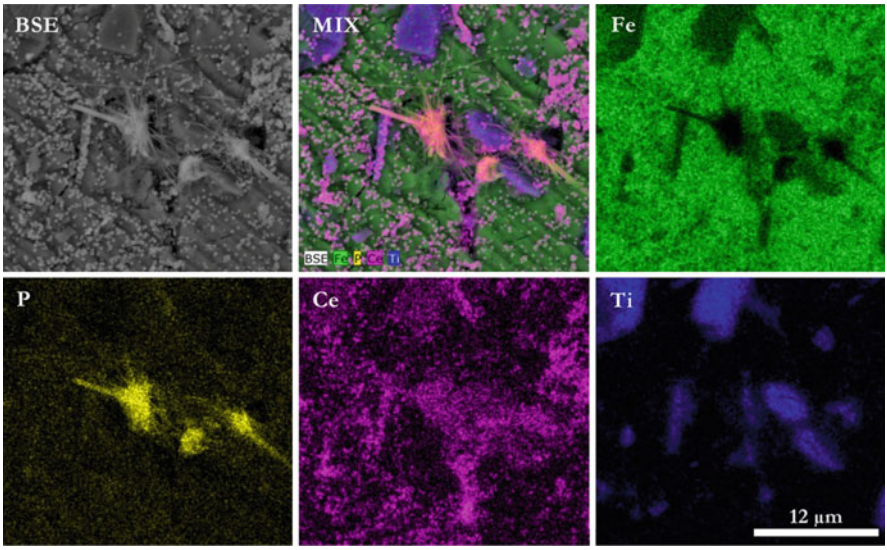

Photomicrograph 1 X-ray elemental mapping obtained by SEM/EDS. Monazite aggregates showing acicular aspect and cerianite as submicron crystals (rounded and porous) associated with Fe-oxide and Ti-oxide

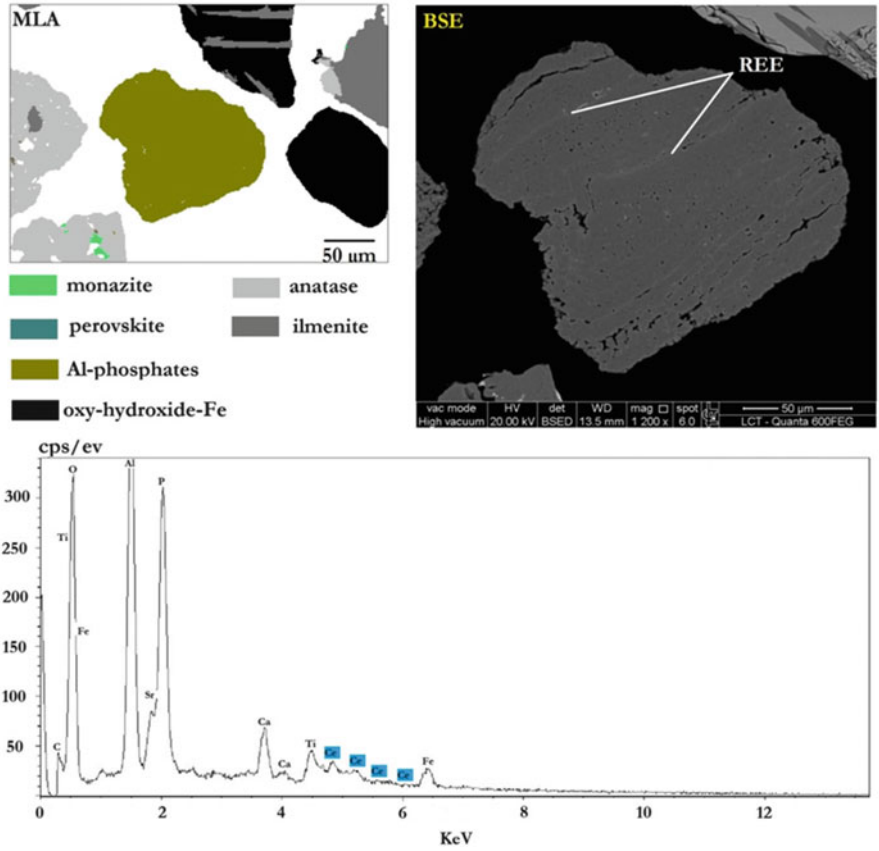

Photomicrograph 2 Free Al-phosphate particle classified by MLA image analysis—gorceixite/goyazite series. Note the presence of veins enriched in REE on the EDS spectrum (not differentiated by MLA in this study)

3.5 Elemental Distribution

The distributions of REO, P_2O_5, CaO, Fe_2O_3, and TiO_2 on bearing minerals are shown in Fig. 4.

Among the REO total content (sum of CeO_2, La_2O_3, Nd_2O_3, and Pr_2O_3), 40 wt% is presented as monazite and cerianite, 4 wt% as Al-phosphates, 1 wt% as zirkelite-zirconolite, 31 wt% is associated with anatase, 11 wt% with iron oxy-hydroxides, 10 wt% with perovskite and 3 wt% with gibbsite–kaolinite. These high contents of REO associated with anatase, iron oxy-hydroxides, perovskite, and others can be also justified by the unclassified submicron REO phases and presented like inclusions as previously mentioned.

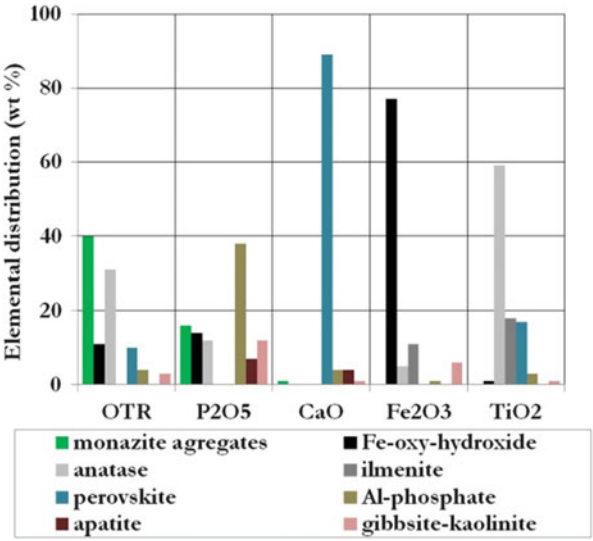

Fig. 4 Distribution of REO-total, P_2O_5, CaO, Fe_2O_3 and TiO_2 among the bearing minerals

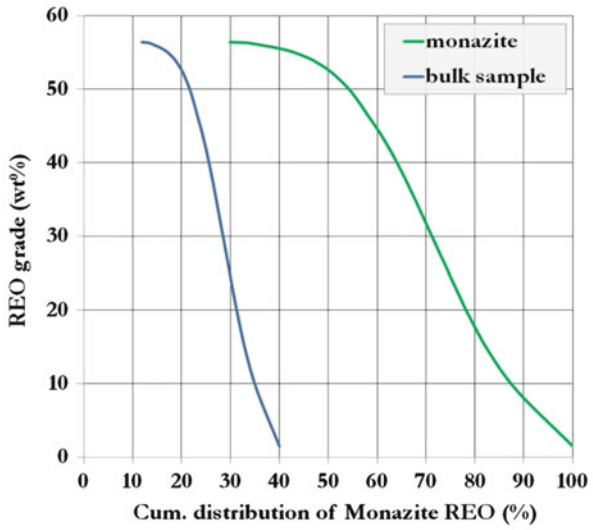

Fig. 5 Distribution of REO-total, P_2O_5, CaO, Fe_2O_3 and TiO_2 among the bearing minerals

3.6 REO Grade Versus Monazite Aggregates Distribution

Considering only the REO is contained in monazite aggregates, the REO grades versus cumulative distribution curves are shown in Fig. 5, indicating a potential recovery of 54 wt% of monazite with a 50 wt% REO grade for the material grinded in 0.30 mm.

As monazite responding for only 40 wt% of REO total content in the sample (−0.30+0.008 mm), considering a product with the same REO grade in monazite aggregates (50 wt%), the potential recovery of REO is 22 wt% for the bulk sample.

3.7 Mineral Separations

Mineral separation results presenting mass distribution and grades and distribution for REO, P_2O_5, CaO, SiO_2, Al_2O_3, Fe_2O_3, and TiO_2 are summarized in Table 2 for the total fraction size −0.30+0.008 mm.

The results indicated no possibility of obtaining products with significant enrichment in REO through physical separations. The nonmagnetic sink product above 0.008 mm corresponds to 41.6 wt% of the sample and presents 1.73 wt% of REO grade (59.6 % recovery relative to the bulk sample); A high concentration of TiO_2 (53.5 wt%; 72 % of the total present in the sample), Fe_2O_3 (22.5 wt%), and CaO (8.70 wt%; 84.5 % of the total present in the sample) remains associated with this product, besides 2.11 wt% of Al_2O_3, 1.53 wt% of P_2O_5, 0.77 wt% of BaO, 0.74 wt% of MnO, 0.27 wt% of Nb_2O_5, and loss on ignition of 3.36 %.

3.8 Selective Comminution by Scrubbing

Cumulative distribution curves for weight, REO, P_2O_5, SiO_2, Fe_2O_3, and TiO_2 are presented in Fig. 6, considering particle size distributions of the original sample and after the scrubbing (selective scrubbing).

Despite increasing the weight to the fine fractions, the REO content in the fines generated after 10 min of scrubbing is almost the same with the natural fines (below 0.008 mm) with no proper evidence of a selective comminution of the monazite aggregates.

Table 2 Summary of the mineral separation results

Product/assay	Fraction (mm)	Weight (wt%)	Grades (wt%)							Distribution (wt%)					
			REO	P_2O_5	CaO	SiO_2	Al_2O_3	Fe_2O_3	TiO_2	REO	P_2O_5	CaO	Al_2O_3	Fe_2O_3	TiO_2
Bulk sample	Total −0.30	100.0	1.25	1.50	4.35	15.7	3.65	35.8	30.7	100.0	100.0	100.0	100.0	100.0	100.0
Float ($d < 3.30$ g/cm^3)	−0.30 +0.008	20.4	0.51	1.92	1.10	56.5	4.39	14.0	13.8	8.5	24.6	5.2	24.2	8.0	9.0
Magnetic (Davis Tube)		21.0	0.15	0.25	1.43	...	0.44	79.3	13.8	2.7	3.4	7.0	2.6	46.9	9.4
Sink ($d > 3.30$ g/cm^3)		41.6	1.73	1.53	8.70	...	2.11	22.5	53.5	59.6	40.6	84.5	24.5	26.3	72.0
Fines	−0.008 natural	15.8	2.18	2.87	0.67	14.7	11.40	41.6	15.0	27.0	29.6	2.5	47.6	18.0	7.8
	−0.008 generated	1.2	2.28	2.33	2.69	15.2	3.42	22.3	44.9	2.1	1.8	0.7	1.1	0.7	1.8

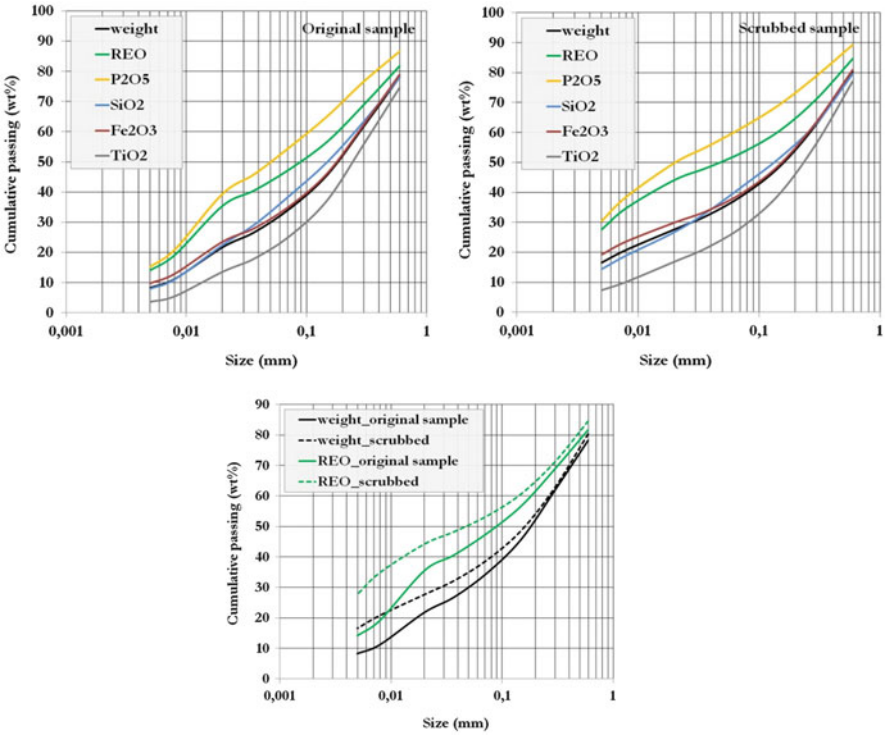

Fig. 6 Weight and main elements distributions by size, considering the original sample and the same scrubbed

4 Final Considerations

The studied sample founded in a Brazilian alkali-carbonatitic complex presents 1.65 % of REO wt%, being 70.8 % presented above 0.008 mm fraction. Monazite aggregates are the main REO bearing mineral and show a poor liberation above this fraction (only 34 wt%); due to monazite associations, mineral separations were not effective in obtaining products with higher enrichments in rare earth oxides. Because fractions below 0.008 mm, even with grinding and scrubbing assays, the grades of REO did not exceed 2.2 wt% in the fine products generated. The only remaining alternative is to evaluate hydrometallurgical tests by sulphuric acid leaching at low temperatures.

Acknowledgments The authors acknowledge the financial support of FAPESP—Sao Paulo Research Foundation, process 2009-54007-0 to carry out this research.

References

1. Guerra R (2013) Comitê define prioridades para aplicar orçamento do setor mineral. MCTI—Ministério da Ciência, Tecnologia e Inovação, Brasil
2. Rocio MAR, Silva MM, Carvalho PSL, Cardoso JGR (2012) Terras raras: situação atual e perspectivas. Banco Nacional do desenvolvimento, Brasil. BNDES setorial: Mineração 35:369–420
3. Kahn H, Tassinari MMML, Ulsen C, Uliana D (2012) Terras Raras—Monazita associada a complexos alcalino-carbonatíticos. Revista ABM Metalurgia, Materiais & Mineração 38:125–129
4. Tassinari MMML, Kahn H, Ratti G (2001) Process mineralogy studies of Córrego do Garimpo REE ore, Catalão-I alkaline complex, Goiás, Brazil. Miner Eng 14(12):1609–1617
5. Mariano AN (1989) Economic geology of rare earth minerals. In: Lipin BR, McKay GA (eds) Geochemistry and mineralogy of rare earth elements, vol 21. Reviews in Mineralogy, pp 309–337
6. Viera EV, Lins FAF (1997) Concentração de minérios de terras-raras: uma revisão. Rio de Janeiro: CETEM/CNPq. Série Tecnologia Mineral 73, p 53
7. Fandrich R, Ying G, Debra B, Kurt M (2007) Modern SEM-based mineral liberation analysis. Int J Miner Process 84:310–320

Study on Influencing Factors and Planning Model of Mining Quantity About Mineral Resources in Open Pit

Lihua Ke and Jie Chen

Abstract According to the particularity of the open pit, the main influencing factors of mining quantity about mineral resources have been summarized systematically in life cycle, and the structured hierarchical relation of its influencing factors has been constructed. In the light of the production process of open pit, the functional relationships between investment, mining cost, and mining quantity have been defined based on the process of mining and loading so that the relation of the life-cycle cost and mining quantity can be set up. And what's more, in order to obtain the maximum economic profit of mining enterprises in life cycle, the planning model of mining quantity has been established based on the life-cycle cost. The rational distribution of mining quantity is found on the condition of obtaining optimal solution about the planning model so as to determine scientifically the production scale of mining enterprises from the point of view of the sustainable development.

Keywords Open pit • Mining quantity • Life-cycle cost • Planning model

1 Introduction

Planning the mining quantity in an open pit is to set up a rational distribution of mining quantity changing with time and then determine the production scale of mining enterprise. The work is a basis of determining the extraction speed of mineral resources and achieving maximum economic benefits in life cycle. At the same time, determination of the extraction speed is an important basis for laying down the production scale and production planning scientifically.

The production scale of mining enterprise can affect the organization of production, which determines the configuration of staff, materials, and equipment and determines investment and production cost [1]. Production costs and sales revenue vary with the production scale, which leads to the change of the mine's annual net

L. Ke (✉) • J. Chen
College of natural resource and environment engineering, Wuhan University of Science and Technology, 947 Heping Road, WUHAN, Hubei, People's Republic of China
e-mail: 413404880@qq.com

F. Dong (ed.), *Proceedings of the 11th International Congress for Applied Mineralogy (ICAM)*, Springer Geochemistry/Mineralogy,
DOI 10.1007/978-3-319-13948-7_19

income and eventually determines the total economic profit of mining enterprises in life cycle. So it is important to lay down rationally the mining quantity in the light of the market situation, mining conditions, and the level of organization and management conditions, which can provide decisions and suggestions about the production scale of mining enterprises.

In this chapter, the main influencing factors of mining quantity about mineral resources have been summarized systematically in life cycle according to the particularity of the open pit and a planning model of mining quantity about mineral resources has been established based on the maximum economic profit of mining enterprises in life cycle.

2 The Particularity of Production in Open Pit

Compared with the general industrial enterprises, the special nature of open pit is that production and life cycle are uncertain and vary with the condition of mining resources and the abundance degree of mineral resources. So the reserve in resources and the total mining quantity vary largely, and the investment and production costs in open pit change with the variation so that life-cycle costs are different based on different technical and economic conditions. And what's more, the particularity of an open pit is also that mining ore and stripping rock are carried out simultaneously in the production process. Therefore, the life-cycle cost of an open pit has a special implication. It is important to analyze the composition of life-cycle cost and its influencing factors in order to obtain the maximum economic profit of mining enterprises.

3 The Main Influencing Factors on Mining Quantity

It is important to analyze the composition of life-cycle cost and its influencing factors in order to obtain the maximum economic profit of mining enterprises.

3.1 The Structured Hierarchical Relation of Influencing Factors on Mining Quantity

The influencing factors on production scale of mining enterprise are mining technical conditions, prices of the mineral resources, reserves in mineral resources, and so on [2]. From the perspective of production process in an open pit, there are several influencing factors about mining quantity such as occurrence conditions of ore body and its grade, mining technical conditions , equipment configuration,

production organization, market demand, the prices of the mineral resources, investment and production costs, and so on. Factors affecting sales revenue and mining costs in an open-pit mine must be analyzed based on maximum economic benefits of mining enterprise.

Among the above factors, the grade of mineral resources, market demand, and the price determine the sales revenue of mining enterprise, which are the external factors of determining the mining quantity in an open pit. The production cost can be classified into the cost of mining ore and the cost of stripping rock in the light of the special production process of open pit. The occurrence conditions of ore body, the mining technical conditions, and the equipment configuration influence the production cost including the cost of mining ore and that of stripping rock when the mining boundary of open pit has been determined. At the same time, the mining technical conditions and the equipment configuration influence investment. So life-cycle cost is the internal factor of determining the mining quantity and constituted the investment and production cost. Therefore, the hierarchy structure relation of main influencing factors on mining quantity in an open-pit mine is shown in Fig. 1.

3.2 *Relationships Between Mining Quantity and Its Influencing Factors*

The influencing factors of mining quantity are classified into sales revenue and life-cycle cost from the perspective of utility. The mining quantity increases with the improvement of sales revenue and the reduction of life-cycle cost. Relationships between mining quantity and its influencing factors have been analyzed as follows according to the production process of open pit and Fig. 1.

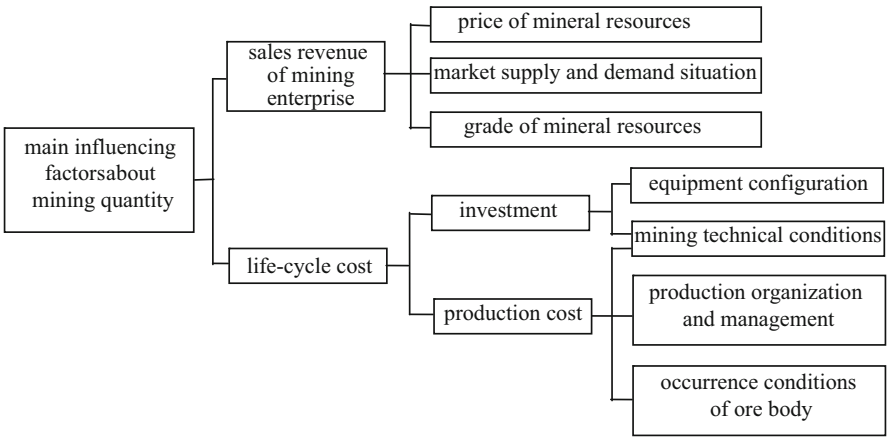

Fig. 1 The structured hierarchical graph of the main influencing factors on mining quantity

3.2.1 Grade of Mineral Resources

Grade of mineral resources means the abundance of useful components in the ore. Production cost decreases and sales revenue increases with the addition of the abundance of useful components. So the mining quantity increases when grade of mineral resources is larger.

3.2.2 Condition of Market Demand and Supply

Occurrence of mineral resources is determined by the long-term geological conditions which can provide the basic material conditions for socioeconomic development. The supply quantity of mineral resources varies with the demand quantity of mineral resources. The mining quantity increases with the addition of supply quantity of mineral resources which improves the exploitation rate of mining enterprise.

3.2.3 Price of the Mineral Resources

Most of the mineral resources are competitive with each other, and the total demand quantity of mineral resources is much larger than every single mining enterprise. The exploitation of every single mining enterprise is not enough to affect the market price of the mineral resources. However, the prices of the mineral resources influence the scale of mining enterprises indirectly [3, 4]. Under normal circumstances, mining quantity of an open pit increases with the increasing of the mineral resources and mineral extraction increases if prices of mineral resources are higher than the life cycle cost.

3.2.4 Occurrence Conditions of Ore Body

The difficulty of mining is reflected by some information of occurrence features about the deposit by which the stripping methods and the mining procedures can be determined. Therefore, production cost varies with the difficulty of mining. Mining quantity of an open pit increases with the reduction of the mineral resources.

3.2.5 Organization and Management of Production Process

The production process of an open pit is a complex system, including the main process such as drilling and blasting process, mining and loading process, transporting process, and rock dumping. It is important for mining enterprise to

manage staff, equipment, and materials. The rational allocation of production personnel and equipment is indemnification of the mine production capacity. Scientific organization and management effectively improve production efficiency and reduce the cost of mining process so as to affect mining quantity.

3.2.6 Mining Technical Conditions

The mining technology and equipment in open pit are also improving with the development and interdisciplinary of technology, especially the introduction of new techniques. Not only technological progress in mining field improves production capacity but also reduces the production cost and investment. So the life-cycle cost is reduced based on the increase of production profit and mining quantity.

3.2.7 Equipment Configuration

From the perspective of technical feasibility, production capacity of mining enterprise determines the type and quantity of equipment so as to determine the investment of equipment. Life-cycle cost of an open pit grows with the equipment investment from the perspective of economy, which can reduce the rate of extraction and mining quantity of mineral resources.

The several external factors demand the mineral resources and price of the mineral resources, while the internal factors are mining technical conditions, equipment configuration, production organization, and investment and production costs. Mining quantity of mineral resources increases when mining cost and investment can be controlled with rational organization of production, scientific configuration, and the improvement of production technology.

4 Planning Model of Mining Quantity About Mineral Resources

Annual mining quantity of mineral resources can be decided according to the life of the mine when the total quantity of mineral resources has been determined within the mining boundary. Investment and production costs and sales revenue change with annual mining quantity which decreases with the longer life cycle. Therefore, planning model of mining quantity about mineral resources in an open pit can be set up based on life-cycle cost.

4.1 Sales Revenue of Open Pit

P_t is defined as market price of mineral resources in year t. X_t is defined as mining quantity of mineral resources in year t. The rate of sales tax in year t is denoted by p_t. So sales revenue S_t in year t can be shown in Eq. (1).

$$S_t = P_t(1 - p_t)X_t \tag{1}$$

4.2 Determination of Investment and Cost in Life Cycle

In the production process of an open pit, ore is being mined, while rock is being stripped. Mining ore, stripping rock, and preparation of new level are three essential engineering projects in the construction period and production one. The three major engineering projects include the main processes such as drilling and blasting process, mining and loading process, transporting process, and rock dumping. Therefore, the life-cycle cost is classified into investment in the construction period and production cost in the production period. The investment includes investment of equipment and that of basic engineering projects. The production cost is classified into the cost of mining ore and that of stripping rock.

M is defined as the investment of equipment. In general, the selection of equipment and its quantity are determined in the light of the annual mining capacity and technology. The core process is mining and loading process whose equipment is important. The equipment of other processes should match with that of the core one in order to achieve the production capacity. Considering matching relationships among process equipments, the function can be established to describe the relation of the total equipment investment and mining quantity shown in Eq. (2) based on the equipment investment of mining and loading process.

$$M = (1 + \alpha)f_1(X_t) \tag{2}$$

where α is equipment investment coefficient of other processes and $f_1(X_t)$ is a function reflecting the relationship between mining quantity and the cost of mining and loading equipment investment.

It is defined as the investment of basic engineering projects in year t, which means cost of excavating ditch in pioneering system. The main processes of excavating ditch are drilling and blasting, mining and loading, and transporting and rock dumping. The investment of basic engineering project changes with the development of mining procedure. Mining and loading process is the core process and the cost of excavating ditch changes with the mining quantity. So the function can be established to describe the relation of investment about basic engineering projects and mining quantity shown in Eq. (3) based on the basic engineering projects' investment of mining and loading process.

$$I_t = (1 + \beta_1 + \delta_1 + \eta_1) f_2(X_t) \tag{3}$$

where β_1 is the cost coefficient of drilling and blasting processes, δ_1 is cost the coefficient of transporting processes, η_1 is the cost coefficient of rock dumping, and $f_2(X_t)$ is a function reflecting the relationship between mining quantity and the cost of mining and loading equipment investment.

C_t is defined as production cost in year t, which includes the cost of drilling and blasting process, mining and loading process, transporting process, and rock dumping. Mining and loading process is the core process and the cost of mining and loading process changes with mining quantity. So the function can be established to describe the relationship between production cost and mining quantity shown in Eq. (4) based on the cost of mining and loading process.

$$C_t(1 + \beta_2 + \delta_2 + \eta_2) f_3(X_t) \tag{4}$$

where β_2 is the cost coefficient of drilling and blasting processes, δ_2 is the cost coefficient of transporting processes, η_2 is the cost coefficient of rock dumping, and $f_3(X_t)$ is a function reflecting the relationship between mining quantity and the production cost of mining and loading process.

4.3 Model of Mining Quantity

Considering the time value of funds, the total present value of mineral resources is shown in Eq. (5).

$$V = \sum_{t=1}^{T} \frac{S_t - C_t - I_t}{(1 + r)^t} - M \tag{5}$$

Here r is discount rate.

In order to obtain the maximum profit, the total present value of mineral resources should be the largest in life cycle of an open pit. At the same time, the mining quantity of mineral resources reduces gradually because the mineral resources are nonrenewable. So reserve in mineral resources and the mining quantity should satisfy the following conditions shown in Eq. (6).

$$\begin{cases} Q_{t+1} - Q_t = -X_t \quad (t = 1, 2, T) \\ Q_0 = R(0) \end{cases} \tag{6}$$

where Q_t is the reserve in mineral resource in year t and $R(0)$ is the initial reserve.

In summary, considering the actual situation of production in an open pit, the model of mining quantity has been established based on life-cycle cost in an open pit shown in Eq. (7).

$$V = \max\left[\sum_{t=1}^{T} \frac{S_t - C_t - I_t}{(1+r)^t} - M\right]$$
$$\text{s.t.}\begin{cases} Q_t - Q_{t+1} = X_t \\ Q_t > 0 \\ t = 1, 2, \ldots, T \end{cases} \tag{7}$$

The influence of life-cycle cost on mining production efficiency has been considered in the above model. The optimal solution of the model can be obtained if the functions of equipment investment, investment of engineering project, and production cost have been determined. The optimal solution of the model can reflect the rational distribution of annual mining quantity changing with time, on which the production scale of mining enterprises can be determined scientifically from the point of view of the sustainable development.

5 Conclusions

1. In this chapter, the main influencing factors of mining quantity about mineral resources have been analyzed such as occurrence conditions of ore body and its grade, mining technical conditions, equipment configuration, production organization, market demand, price of the mineral resources, investment and production costs, and so on. And what's more, the structured hierarchical relation of its influencing factors has been constructed according to the particularity of the open pit.
2. Combined with the production process of an open pit, the relationships between the mining quantity and its influencing factors have been summarized so as to provide decisions and suggestions about the control measures for the mining quantity.
3. From the perspective of the production process, the composition of the life-cycle cost has been analyzed. The functional relationships between investment, mining cost, and mining quantity have been defined based on the process of mining and loading so that the relation of the life-cycle cost and mining quantity can be set up.
4. The planning model of mining quantity has been established based on the life-cycle cost combined with the constraints of resource consumption in the light of the maximum economic profit of mining enterprises in life cycle. This model can be used for determining annual mining quantity so as to decide scientifically the production scale of mining enterprises from the point of view of the sustainable development.

Acknowledgments This work was supported by the National Natural Science Foundation of China under Grant No.51204127.

References

1. Wang WJ, Lu HJ (2008) Application of grey multi-objective decision-making in optimization of mining scale from surface into underground. Min Metall 17(1):8–9, 29
2. Zhang JS, Wang XL (2007) Study on influential factors of coal mining scale and its model. Energy Technol Manag 5:68–71
3. Yu RC (2009) Handbook of mining engineering, vol 3. Metallurgical Industry Press, Beijing, p 250
4. Zhang ZM, Cai QX, Zhou W, Wang BW, Wei H (2011) Scale model to determine the open pit production. Metal Mine 11:5–8, 68

Effect of Temperature upon Fe–Mg Composition of Garnet in Pelitic System

Ying Li, Jianguo Du, Chao Xie, and Zhihua Zhou

Abstract The Effects of pressure and temperature on Fe–Mg compositions of garnet in natural pelitic system were studied experimentally at temperatures of 700–780 °C and pressures from 21 to 29.4 kbar. The concentrations of FeO and MgO of garnet in the run products show linear relationships with experimental temperatures. The result determined the Fe–Mg partition trend with temperature in a natural rock with complex chemical compositions, which favors the identification of metamorphic temperature for pelitic rocks in eclogite facies.

Keywords Fe–Mg partition • Garnet • Pelite • Geothermometer

1 Introduction

Garnet is an essential phase in a wide range of rocks from different metamorphic grades. Ratios of Fe and Mg concentrations in garnet have been widely used as a geothermometer for the crystallization, cooling rate, and tectonic uplift rate because garnets in natural rocks always show a variety of Fe–Mg compositional partitions. Garnet can preserve memory of the thermal and growth histories of the minerals because the Fe–Mg exchange equilibrium between garnet and its coexisting minerals is very sensitive to metamorphic temperature [1]. Coexisting with garnet, many minerals such as biotite, clinopyroxene, cordierite, hornblende, chlorite, olivine, and so on have been identified to be thermometer minerals in rocks occurring in a wide variety of geological environments [2]. Normally, Fe–Mg concentrations of natural garnets vary widely and the Fe–Mg exchange reactions usually occur in a complex chemical system. Studies on the behavior of Fe–Mg contents in different chemical systems have indicated that the ions or components in the rock, like Ca, Mn, Fe^{3+}, and H_2O, seriously affect the P–T conditions under

Y. Li (✉) • J. Du • C. Xie
Institute of Earthquake Science, China Earthquake Administration, CEA Key Laboratory of Earthquake Prediction, 63 Fuxing Road, Beijing, People's Republic of China
e-mail: subduction6@hotmail.com

Z. Zhou
China Earthquake Networks Center, 5 Sanlihe East Road, Beijing, People's Republic of China

F. Dong (ed.), *Proceedings of the 11th International Congress for Applied Mineralogy (ICAM)*, Springer Geochemistry/Mineralogy,
DOI 10.1007/978-3-319-13948-7_20

which Fe and Mg exchange in garnet [2–4]. Consequently considerable uncertainties exist in the P–T conditions for Fe–Mg equilibrium reaction in a wide range of bulk compositions of natural rocks. This chapter aims at investigating experimentally the temperature effect upon Fe–Mg partition between coexisting garnet and the whole pelitic system (Na_2O–K_2O–CaO–MgO–FeO–Al_2O_3–MnO–SiO_2–TiO_2–H_2O). The results would strive to provide useful data to model the variation of Fe–Mg contents with temperature in primarily ferromagnesian garnets in the crust.

2 Material and Methods

2.1 Starting Materials

Pelites are the most widely distributed rocks in the crust. A metapelite LS26 from the Lu-Shan, central China, was used as the starting material (Table 1). The protolith of the selected rock could be pelitic (more illite and chlorite) and less carbonatic (or carbonate free) and may represent a mixture of greywackes and pelagic clays. The chemical composition is close to the average composition of the upper continental crust which has been previously taken as representative for subducted sediments [5, 6]. The pelite was ground with ethanol submersed in an agate mortar into particles less than 200 mesh. Subsequently, the powders were heated at 1,300 °C for 3 h in a high-frequency electromagnetic oven with argon gas inflow. The resulting glass attained was ground again into particles less than 200 mesh and analyzed by X-ray powder diffraction to make sure that no crystalline mineral phase remained. The glass powder mixed with about 7–10 wt% distilled H_2O was utilized as the starting material for the high-pressure experiments.

Table 1 Phases in the starting material and high-pressure experimental run products

Sample number	*P* (Kbar)	*T* (°C)	*t* (h)	Minerals (Microprobe and XRD)
LS26[a]	Starting material			Qz, Chl, Ms, Ilm, Ab
G17	21.0	720	351	Qz, Grt, Amp, Ms, Rt
G12	24.0	710	351	Qz, Grt, Amp, Jd, Ms
G4	28.2	750	301	Qz, Grt, Jd, Ms, Ky, Rt
G19	29.2	700	356	Qz, Grt, Jd, Ms, Rt, St
G16	29.4	780	382	Coe, Grt, Ms, Ky, Rt, Melt

[a]Chemical composition of starting material [10]: SiO_2—63.31, TiO_2—0.63, Al_2O_3—17.89, FeO—7.00, MnO—0.09, MgO—1.50, CaO—0.60, Na_2O—1.60, K_2O—2.85, P_2O_5—0.10, ignition loss—4.28.

Mineral abbreviations: *Qz* quartz, *Chl* chlorite, *Ms* muscovite, *Ilm* ilmenite, *Ab* albite, *Grt* garnet, *Amp* amphibole, *Rt* rutile, *Jd* jadeite, *Ky* kyanite, *St* staurolite

2.2 High-Pressure and High-Temperature Experiment

The experiments at high-pressure and high-temperature were carried out with an end-loaded piston-cylinder apparatus in the Institutfür Mineralogie und Kristallchemie, Universität Stuttgart, Germany. The apparatus has a WC core containing a pressure chamber is 1.27 cm in diameter and 5.2 cm in length. A low-friction NaCl cell [7] was employed for the cell assembly (Fig. 1). A golden capsule with 2 mm in diameter and about 10 mm in length was used as the sample container. About 20 mg samples were loaded into the capsule and sealed by arc welding. The temperature was measured with mantled chromel–alumel thermocouples. The 2σ uncertainties in P and T have been calibrated to be ±1 % and ±2 %, respectively [8]. Five high-pressure experiments under different conditions were conducted (Table 1). The P–T conditions can be held to be constant by the apparatus, but they were recorded each 2 h, respectively, and the average values were taken as the experimental conditions due to a relative longer experimental duration. The phases in the run products were examined under a polarizing microscope and by X-ray powder diffraction. The chemical composition of each phase was analyzed by an electron microprobe (Cameca SX-100) equipped with energy-dispersive spectrometer.

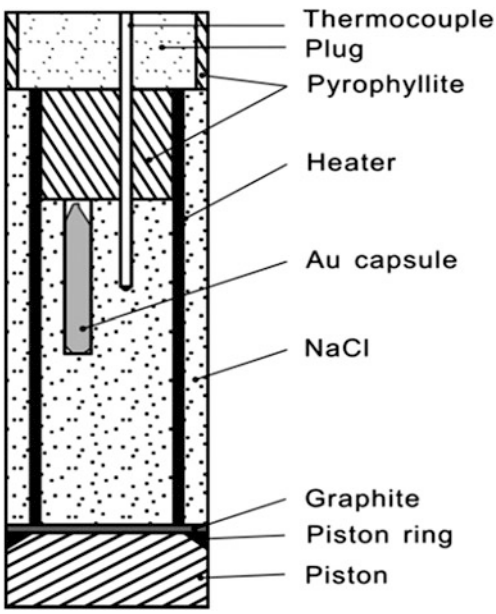

Fig. 1 Setup of the cell for high-pressure and high-temperature experiment

3 Results

Phase transition occurred in all experiments. The mineral phases in the run products show a typical eclogitic assemblage within the experimental P–T range (Table 1, Fig. 2). In the run products, garnet and muscovite formed as stable phases. Amphibole was present above 21 kbar but disappeared when pressure was higher than 24 kbar. Jadeite is additionally present at 24 kbar and 710 °C, but it breaks down with increasing pressure and temperature. Jadeite disappeared at about 29.4 kbar and 780 °C. Kyanite as a stable phase was present in the run products of G4 and G16 at higher experimental temperature. Staurolite appeared in sample G19 and coesite occurred in sample G16 (Table 1). No melt has been observed in the run products. The electron microprobe analysis shows that the garnet grains are homogenous in chemical composition and show no compositional zoning (Fig. 2). Therefore, 5 garnet crystals were selected for each run product and their chemical compositions were given in Table 2. The garnets were mainly characterized by magnesian and ferreous compositions. Pyrope (Prp) and almandine (Alm) represent more than 88 wt% of the garnet particles analyzed, whereas grossular (Grs) and spessartine (Sps) were present as less than 12 wt% (Table 2). The average of the compositions of five garnet particles was taken as representative for each pressure and temperature. FeO concentration of the garnets in the run products increased with rising temperature, but MgO concentration decreased, and it appears

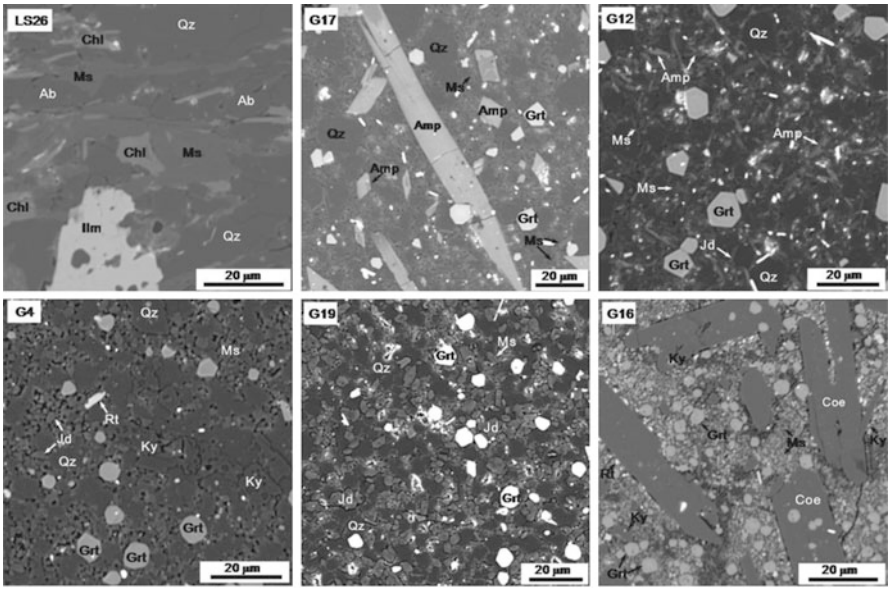

Fig. 2 Backscattered electron images of the starting material and run products. Mineral abbreviations are the same as in Table 1

Table 2 Selected electron microprobe analyses of garnet in high-pressure experimental run products

Sample	SiO_2	TiO_2	Al_2O_3	FeO	MnO	MgO	CaO	Na_2O	Total	Grswt%	Pypwt%	Almwt%	Spswt%
G17	36.45	0.74	20.29	35.44	1.88	2.53	2.64	0.12	100.10	8	10	78	4
	36.86	0.59	21.25	35.11	0.53	4.08	1.50	0.15	100.07	4	16	78	1
	36.79	0.40	21.03	35.40	0.61	4.02	1.37	0.24	99.86	4	16	79	1
	37.05	0.58	20.86	35.36	0.47	3.96	1.53	0.23	100.03	4	16	79	1
	36.78	0.99	20.79	35.47	0.91	2.96	2.36	0.14	100.40	7	12	79	2
G12	36.65	0.39	21.30	34.80	1.03	3.17	2.28	0.18	99.80	7	13	78	2
	36.50	0.91	21.08	35.13	1.48	3.06	1.97	0.17	100.30	6	12	78	3
	36.85	1.31	21.09	35.52	0.84	2.83	2.15	0.21	100.80	6	11	80	2
G4	36.44	0.76	21.26	34.96	1.44	3.00	2.15	0.19	100.20	6	12	78	3
	36.59	0.39	21.04	35.03	1.64	2.88	2.03	0.17	99.77	6	11	78	4
	36.75	0.61	21.04	33.25	0.64	5.23	0.93	0.29	98.74	3	21	74	1
	36.68	1.11	20.84	33.05	0.66	5.31	0.93	0.31	98.89	3	21	73	1
	36.62	0.59	20.84	33.54	0.67	5.37	1.06	0.23	98.92	3	21	73	2
	40.33	0.50	21.47	30.99	0.68	6.35	1.01	0.39	101.71	3	25	69	2
	37.17	0.47	21.18	32.57	0.73	6.18	0.90	0.26	99.46	3	24	70	2
G19	36.24	0.61	20.63	36.52	1.35	2.64	1.28	0.22	99.49	4	11	81	3
	36.90	0.50	20.90	35.10	0.76	4.02	1.14	0.16	99.47	3	16	78	2
	36.19	0.59	20.48	36.72	1.44	2.58	1.30	0.11	99.42	4	10	82	3
	35.87	0.59	20.60	36.34	1.41	2.66	1.30	0.14	98.91	4	11	82	3
	36.61	0.50	20.75	36.29	0.77	3.61	1.04	0.08	99.65	3	14	80	2
G16	35.90	0.92	20.58	32.38	1.62	3.96	2.71	0.09	98.18	8	16	72	4
	36.15	0.77	20.87	32.44	0.81	6.07	1.31	0.27	98.68	4	24	69	2
	40.81	0.57	20.22	30.38	0.50	7.00	0.85	1.50	101.83	2	27	62	1
	40.63	0.30	19.57	27.09	0.17	7.35	0.54	0.49	96.14	2	31	64	0
	37.91	0.56	20.63	31.14	0.51	7.33	0.99	0.24	99.31	3	29	66	1

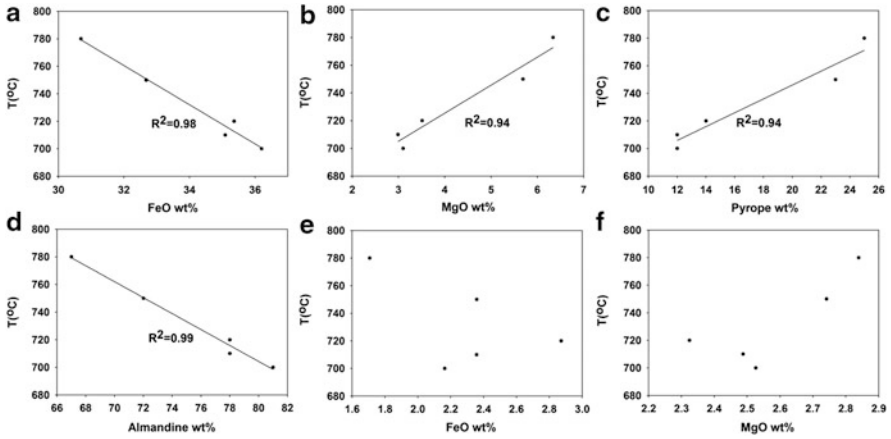

Fig. 3 Variations of FeO and MgO contents in garnets (**a**–**d**) and muscovites (**e**–**f**) with temperature

that the contents of pyrope and almandine varied linearly with the experiment temperatures (Fig. 3a–d).

4 Discussion

The Fe–Mg exchange reaction between garnet and a coexisting mineral phase has been widely studied [2]. FeO and MgO contents in garnet and the coexisting phase normally have a linear relation with temperature. This is caused by the diffusion coefficients (D) of Fe^{2+} [D(Fe)] and Mg^{2+} [D(Mg)] between garnet and the coexisting mineral in a certain system, expressed by Arrhenian relation, $D = D0\exp\{-[Q(1\ \text{bar}) + P\Delta V+]/RT\}$, where D0, Q, and $\Delta V+$ are the constant diffusion coefficient, activation energy, and activation volume, respectively. T and P are the temperature and pressure of exchange reaction. Muscovite was the only phase that coexisted with garnet in all run products. However, the FeO and MgO concentrations of muscovite did not show any linear relation with temperature (Fig. 3e and f), which indicates that muscovite is not the pair phase with garnet in Fe–Mg partition. Consequently, it can be concluded that the partition of FeO and MgO occurred between garnet and the remaining phases of the whole pelitic system during the crystallization of garnet. Therefore, it is reasonable to interpret the variation of garnet composition with temperature because the primary FeO–MgO partition is dominated by the spontaneous intermingling properties and can be characterized by a diffusion equilibrium process of Fe and Mg between garnet and the residual phases in pelitic system.

However, in this study, the FeO–MgO partition was preceded in a more complex chemical system than the various sets of minerals in earlier studies, such as pyrope-almandine garnets [9], aluminosilicate garnets [1], and Ca–Mg–Fe–Mn garnets

[4]. Of course, factors like the presence of Ca^{2+}, Mn^{2+}, H_2O, and fO_2 (oxygen fugacity) in the system have some effects on the Fe–Mg exchange equilibrium. The Ca/Mn effect is believed to be due to a combination of nonideal Ca–Mg and Mn–Fe substitutions in the garnet [3, 4]. H_2O and fO_2 are able to change the activation of cations and the ionizations. We have no experimental evidence to discuss the effect of fO_2, but the fO_2 effect can be expected to have been essentially the same in all experiments. However, as already mentioned, the pelite was melted under the protection of inert gas; the fO_2 in the HP experiment remained originally and same for each sample. Therefore, the variation of Fe–Mg content with temperature in garnets attained in the pelitic system was dominated by temperature but simultaneously affected by the factors mentioned above. We are unable to discuss the thermodynamic process of the Fe–Mg diffusion in the pelitic system due to not only the nonexistence of a satisfactory standard activity-composition model addressing the enthalpies, entropies, and volumes of mixing for the garnets but also the disagreement regarding interpretations of the significance of the experimental data. Currently, the problem of Fe–Mg exchange equilibrium in garnet has been stagnating and no coherent conclusion has been proposed since the last century [9]. The contribution of this study is establishing a temperature-dependent Fe–Mg diffusion trend of garnet in a natural and complex rock system, providing the data for the building of a reliable standard model describing the Fe–Mg geothermometer principle.

5 Conclusions

This study indicates that the concentrations of FeO and MgO of garnets in pelitic system follow a linear relation with experimental temperature in which FeO concentrations of the garnet products are increasing with rising temperature, but MgO concentrations are decreasing. Certainly, our results provided experimental evidence of Fe–Mg partition trend with temperatures in a more complex natural rock and therefore improve our confidence in the determinations of metamorphic temperature calculated by garnet geothermometer. Although the accurate geological application of our results requires knowledge of the effects of other components upon [D(Mg)] and [D(Fe)] which are at present largely unknown currently, the relation between FeO–MgO contents and temperature appears to be a promising indicator. The data presented in this study suggest it might be helpful for the estimation of the temperature of metamorphic crystallization in rocks of politic composition.

Acknowledgments This work is financially supported by the project of the National Natural Science Foundation of China (grant No. 41273073).

References

1. Chakraborty S, Ganguly J (1991) Compositional zoning and cation diffusion in aluminosilicate garnets. In: Ganguly J (ed) Diffusion, atomic ordering and mass transport, Advances in physical geochemistry. Springer, Berlin, pp 121–175
2. Spear FS (1993) Metamorphic phase equilibria and pressure-temperature-time paths. Mineralogical Society of America, Troy, NY, p 350
3. Ellis DJ, Green DH (1979) An experimental study of the effect of Ca upon garnet-clinopyroxene Fe-Mg exchange equilibria. Contrib Mineral Petrol 71:13–22
4. Berman RG (1990) Mixing properties of Ca-Mg-Fe-Mn garnets. Am Mineral 75:328–344
5. Li Y, Massonne HJ, Willner W, Tang HF, Liu CQ (2008) Dehydration of clastic sediments in subduction zones: theoretical study using thermodynamic data of minerals. Island Arc 17:577–590
6. Li Y, Du JG (2010) Thermodynamic calculation on the phase transformation and water release of subducted sediment from 10 to 35 kbar. J Phys Chem Solid 71:1077–1083
7. Mirwald PW, Getting IC, Kennedy GC (1975) Low- friction cell for piston-cylinder high-pressure apparatus. J Geophys Res 80:1519–1525
8. Massonne HJ, Schreyer W (1986) High-pressure syntheses and X-ray properties of white micas in the system K_2O-MgO-Al_2O_3-SiO_2-H_2O. Neues Jb Mineral Abh 153:177–215
9. Ganguly J, Cheng WJ, Chakraborty S (1998) Cation diffusion in aluminosilicate garnets: experimental determination in pyroxene-almandine diffusion couples. Contrib Mineral Petrol 131:171–180
10. Tang HF, Liu CQ (2000) Mass transfer and element mobility of rocks during regional metamorphism—a case study of metamorphosed pelites from the shuangqiaoshan group in Lushan. Geol Rev 46:245–254, in Chinese

An Overview of Process Mineralogy of Tungsten and Its Associated Elements

Dongyun Liang, Qiuyang Hong, Bo Li, and Lili Zhang

Abstract China produces much tungsten metal every year. The tungsten deposits in China usually are low grade and have a complex mineralogy composition as well as many associated valuable elements. The associated elements include Sn, Mo, Bi, Cu, Pb, Zn, Sb, Be, Co, Au, Ag, Nb, Ta, Re, Sc, REE, Li, As, S, and P and the nonmetallic minerals such as quartz, fluorite, feldspar, etc. Therefore, only when the tungsten ore dressing is done in accordance with the ore properties based on a detailed and complete process mineralogy study can the valuable elements be reasonably and fully recovered and the maximization of resource utilization as well as environment-friendly technology be achieved eventually. This chapter summarizes the status quo of process mineralogy of tungsten and its associated elements in China, focusing on the process mineralogy studies on major types of tungsten ore including tungsten–molybdenum-associated ore, tungsten–tin polymetallic ore, and tungsten–copper polymetallic ore, suggesting the future process mineralogy research on tungsten and its associated elements.

Keywords Tungsten ore • Associated ore • Process mineralogy

1 Introduction

The abundance of tungsten in the Earth's supracrust is only 2 ppm [1]. It is found in almost all types of rocks, but the abundance is generally very low. It needs special metallogenesis to enrich and form into deposits. It has an extremely uneven spatial distribution in the Earth's crust. Tungsten reserves are concentrated in China, Russia, Canada, and the United States [2]. China's tungsten deposits usually are low grade and have a complex mineralogy composition as well as many associated valuable elements. The associated elements include Sn, Mo, Bi, Cu, Pb, Zn, Sb, Be, Co, Au, Ag, Nb, Ta, Re, Sc, REE, Li, As, S, and P and the nonmetallic minerals

D. Liang (✉) • Q. Hong • B. Li • L. Zhang
Department of Mineral Processing Engineering, Guangzhou Research Institute of Non-ferrous Metals, 363 Changxing Road, Guangzhou, Tianhe District, Guangdong, People's Republic of China
e-mail: gzldy2012@163.com

F. Dong (ed.), *Proceedings of the 11th International Congress for Applied Mineralogy (ICAM)*, Springer Geochemistry/Mineralogy,
DOI 10.1007/978-3-319-13948-7_21

such as quartz, fluorite, feldspar, etc. Therefore, only when the tungsten ore dressing is done in accordance with the ore properties based on a detailed and complete process mineralogy study can the valuable elements be reasonably and fully recovered and the maximization of resource utilization as well as environment-friendly technology be achieved eventually.

2 Status Quo of Process Mineralogy Study of Tungsten and Its Associated Elements

Process mineralogy is developed with the development and utilization of resources. The process mineralogy study of tungsten and its associated elements also has been greatly developed with the scientific research and technological innovation of tungsten industry in recent years. Traditionally, the measurement of mineralogy parameters employed the tools of an optical microscope and/or a semi-automated SEM. These methods are time-consuming, too much influenced by workers, and cannot produce complete and accurate results. The modern SEM-based quantitative mineralogy tool-MLA has solved those problems and brings revolutionary advances for the process mineralogy study of low-grade tungsten ore and its associated elements. Fast, accurate, and quantitative results of mineralogy composition and liberation make beneficiation workers know the ore characteristics before tests which have a great benefit to think and design separation process for the ore.

Nowadays the development and utilization of tungsten resources have turned to scheelite deposits, wolframite associated with scheelite deposits, old tailings, and associated tungsten resources. These resources have the characteristics of low-grade, poor nature, and complex mineral association that give new challenges to process mineralogy study. Process mineralogy not only provides basic information on the ore characteristics for beneficiation fast and accurately but also properly assesses the occurrence and separability of associated components as well as the recoverability of nonmetallic resources.

3 Process Mineralogy of Major Types of Tungsten Ore

3.1 Process Mineralogy of Tungsten Ore Associated with Molybdenum

The chemical composition of several ores is given in Table 1. Tungsten ore associated with molybdenum (referred as “tungsten–molybdenum associated ore” in this chapter) can be divided into porphyry, porphyry, and skarn transition and skarn in accordance with ore genesis. In terms of chemical composition, the valuable metals are dominant by tungsten and the molybdenum grade is variable; both the content of tungsten and molybdenum reach to minimum mining grade;

Table 1 The chemical composition of the tungsten ore associated with molybdenum

	Chemical composition %					
Ores	Xingluokeng, Fujian	Xianggelila, Yunnan	Qingyang, Anhui	Huangshaping, Hunan	Haihaigang, Tibet	King Island, Australia
Type of ore	Porphyry	Porphyry	Skarn	Skarn	Skarn	Skarn
WO_3	0.230	0.200	0.270	0.220	0.250	1.340
Mo	0.018	0.300	0.074	0.150	0.092	0.035
Cu	0.013	0.045	0.006	0.032	0.046	0.059
Zn	0.060	0.015	0.048	0.110	0.064	0.001
Fe	1.800	1.810	7.940	10.950	15.670	13.110
$CaCO_3$	2.180	0.270	7.961	9.020	0.850	8.650
CaF_2	0.740	0.005	1.580	7.100	2.940	2.920
SiO_2	73.780	72.800	47.970	35.950	44.950	36.480
Al_2O_3	12.450	7.830	8.330	7.680	4.620	4.850

sometimes the grade of molybdenum is even higher than that of tungsten, for example, a tungsten–molybdenum ore from Xianggelila, Yunnan Province; sometimes tungsten is dominant and the molybdenum content only meets the grade requirements of comprehensive recovery, for example, a tungsten ore associated with molybdenum from Xingluokeng, Fujian Province. Molybdenum is the most important associated element in this tungsten ore; meanwhile, the determination and recovery of expensive rare element rhenium should be considered. For example, the molybdenite of a skarn molybdenum–tungsten deposit from Luanchuan, Hennan Province, that is rare in the world contains Re 10–20 ppm [3] and has a great economic value due to the huge reserves of Re.

Tungsten–molybdenum associated ore has the following characteristics of mineralogy composition: (1) tungsten minerals are scheelite as well as wolframite, and tungstite usually exists in the hypergene deposits. The ratio of wolframite to scheelite depends on the concentration of cations including Fe^{2+}, Mn^{2+}, Ca^{2+}, etc., in the ore-forming solution. Scheelite is dominant and wolframite is rare or even absent in most ores. (2) Scheelite in this type of tungsten ore is mostly euhedral and well formed with the grain size ranging from 0.02 to 0.32 mm that is appropriate for flotation. In the lattice of scheelite, W can be substituted by Mo. Scheelite in this tungsten ore generally contains Mo with the MoO_3 content being 1–10 %. However, some scheelite has altered into scheelite-Mo (means the scheelite containing high content of Mo) because it contains too much Mo and the highest MoO_3 content is up to 57 %. The scheelite-Mo is harder to concentrate than ordinary scheelite due to the poor floatability of MoO_3. (3) Molybdenum mineral is only molybdenite and other sulfide minerals generally have a small number but a great variety. The sulfide minerals usually include pyrite, pyrrhotite, bismuthinite, sphalerite, galena, etc., except molybdenite, in which pyrrhotite and sphalerite usually have a large number and should be recovered. The metallic sulfide minerals will impact on Mo cleaner significantly especially the easy-floating minerals including galena, chalcopyrite, monoclinic pyrrhotite, etc. (4) Gangue minerals are different in different types of ore. The gangue minerals of porphyry tungsten–molybdenum-associated ore include a lot of quartz and feldspar, so the tailings can be used as raw materials of ceramics while the gangue minerals of skarn ore include a large number of weakly magnetic Ca-rich silicate minerals such as garnet, diopside, tremolite, etc., and other Ca-rich gangue including fluorite, calcite, apatite, etc., in which fluorite and garnet can be recovered and utilized.

3.2 Process Mineralogy of Tungsten–Tin Polymetallic Ore

The genesis of tungsten–tin polymetallic ore is complex and it can be divided into two types: one is quartz vein wolframite ore with the paragenetic association of wolframite-cassiterite-sulfide which is one of China's famous geochemical types of quartz vein wolframite ore [4]; the other is greisen, greisen combined with skarn, or the superposition of multiple mineralization activities. In terms of chemical

composition, it changes greatly and the content of tungsten as well as tin is quite different; there are associated metals including Mo, Bi, Ag, Fe, etc.; the nonmetallic elements depend on the type of ore; quartz vein and greisen ore are rich in Si while skarn ore is rich in Ca and Mg.

Tungsten–tin polymetallic ore has the following characteristics of mineralogy composition: (1) in the quartz vein ore, generally wolframite is the only tungsten mineral and sometimes wolframite is metasomatized by scheelite; wolframite crystals are coarse and well formed that are appropriate for gravity separation. In greisen or greisen combined with skarn ore, both wolframite and scheelite exist with the grain size appropriate for floatation; hypergene ore often has tungstite and limonite that contains tungsten or tin. Pseudomorphous scheelite formed from scheelite metasomatizing wolframite usually exists in this ore. According to the studies of Jun Chen [5] from Beijing General Research Institute of Mining and Metallurgy, feldspar alters into muscovite in the process of greisenization with much H^+ consumption, which makes the acidic environment become alkaline; the generated wolframite of vein rock changes into scheelite (that is called pseudomorphous scheelite) because of the replacement by calcium ions evolved in the process of greisenization; meanwhile, the excess iron and manganese ions form into oxidized minerals including magnetite, etc. The reaction formula is:

$$6(\mathrm{Mn,Fe})\mathrm{WO_4} + 6\mathrm{Ca(OH)_2} + 7\mathrm{O_2} \rightarrow 6\mathrm{CaWO_4} + 2\mathrm{Fe_3O_4} + 6\mathrm{MnO_2} + 8\mathrm{H_2O} \quad (1)$$

Pseudomorphous wolframite is also found when we study a tungsten polymetallic ore from Xitian, Hunan Province. It is formed from wolframite metasomatizing scheelite and has the scheelite crystal shape (Figs. 1 and 2). In the deuteric tectonic activities, ore-forming solution becomes acidic because of many sulfides from fault zone and contains a lot of iron and manganese ions. So the eogenetic scheelite alters into wolframite due to the metasomatization of iron and manganese; meanwhile, gysum is generated. The reaction formula is:

$$2\mathrm{Ca}\,[\mathrm{WO}]_4 + \mathrm{FeSO_4} + \mathrm{MnSO_4} \rightarrow 2(\mathrm{Fe,Mn})[\mathrm{WO}]_4 + 2\mathrm{CaSO_4} \quad (2)$$

(2) Tin minerals are cassiterite, stannine, and sometimes malayaite with chemical formula $CaSn[SiO_4]O$. (3) Sometimes there are metallic sulfide minerals including chalcopyrite, sphalerite, etc., or associated silver minerals. (4) The gangue minerals of greisen ore are a lot of mica and quartz while the gangue minerals of greisen combined with skarn ore include a lot of weakly magnetic silicate minerals such as garnet, diopside, tremolite, etc., and Ca-rich gangue such as fluorite, calcite, apatite, etc., except quartz and mica.

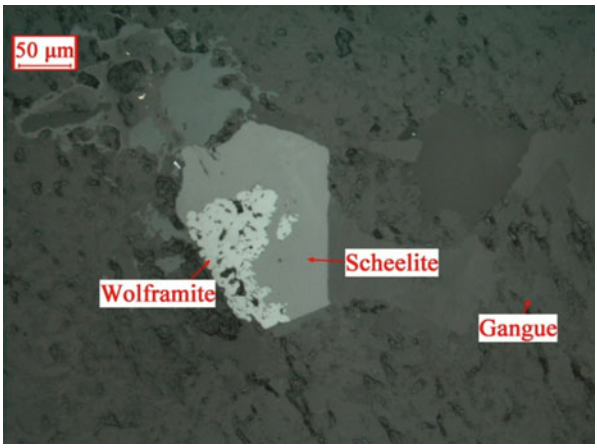

Fig. 1 Optical microscope, reflected light, to magnify 320 times. Wolframite metasomatizes scheelite, in the tungsten–tin ore from Xitian, Hunan

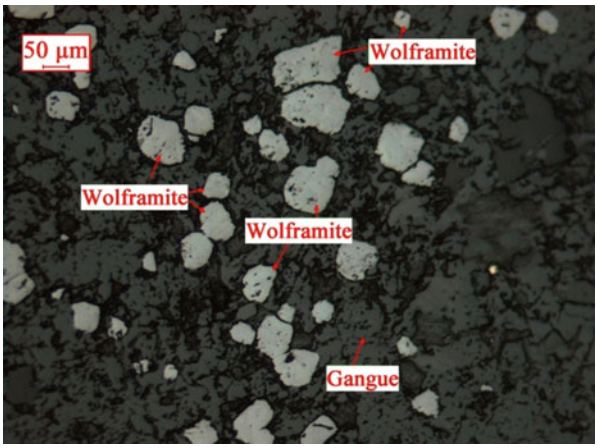

Fig. 2 Optical microscopes, reflected light, to magnify 160 times. Pseudomorphous wolframite that is in the scheelite crystal shape occurs in the tungsten–tin ore from Xitian, Hunan

3.3 Process Mineralogy of Tungsten–Copper Polymetallic Ore

In China, the number of associated tungsten in the copper–sulfur deposits or copper–lead–zinc deposits accounts for 19.4 % of tungsten reserves. The tungsten–copper polymetallic ore is mostly skarn with low-to-moderate-temperature hydrothermal alteration. Tungsten–copper polymetallic ore usually contains a lot of Ca-rich gangue minerals including garnet, diopside, tremolite, etc., that will impact on the scheelite cleaner and the different floatability of pyrrhotite will also have a great influence on copper–sulfur separation. Take a tungsten–copper ore from Jiangxi Province as an example. The major element composition of this ore is as follows: WO_3 0.75 %, Cu 0.15 %, Pb 0.011 %, Zn 0.033 %, Bi 0.036 %, Fe 11.34 %, $CaCO_3$ 5.68 %, CaF_2 6.35 %, SiO_2 53.96 %, Al_2O_3 4.55 %. Its mineralogy

composition is as follows: scheelite 0.86 %, wolframite 0.05 %, tungstite 0.02 %, chalcopyrite 0.40 %, bismuthinite 0.04 %, pyrrhotite 12.02 % and a lot of skarn minerals including diopside, tremolite, actinolite, garnet, etc. The scheelite crystals are well formed and have an even grain size distribution with the main size range of 0.04–0.5 mm. A small amount of scheelite grains is closely intergrown with pyrrhotite, but they can be liberated through grind while most scheelite has a good dissociation. Removing the magnetic minerals including pyrrhotite, garnet, diopside, and tremolite by high-intensity magnetic separation will simplify beneficiation process and optimize indexes.

4 Future and Trends of Process Mineralogy of Tungsten Ore

1. Establish mineralogy database using the advanced quantitative mineralogy tool. There are laboratories for chemical analysis in most mines, but the simple chemical analysis data are not enough to assess and characterize the complex physical and chemical properties of ore. Ore is composed of elements from microscopic point of view while it is made up of different minerals from macroscopic point of view. There is a contact but also great difference between elements and minerals. Beneficiation is a process of separating and concentrating the minerals so as to achieve the enrichment of a metal. Therefore, the process mineralogy information including mineralogy composition, mineral content, occurrence, grain size, etc., has a great effect on the beneficiation efficiency. Especially for tungsten and other rare metal ore that has a complex mineralogy composition and low content of valuable minerals, process mineralogy results are particularly important for the research and optimization of technical process. It is extremely necessary to establish mineralogy database for each tungsten mine, organize the information on the material composition as well as characteristics of different mines and different types of ore, and make the complex ore properties digitalization and pictorialization which has a great significance to develop an economic and reasonable beneficiation process, realizing modern management, reaching maximization of resource utilization and nonpolluting emissions, and achieving sustainable development of China's tungsten mines eventually.
2. Monitor the associated low-grade metals that easily result in pollution. Most tungsten ore is associated with the metals including Pb, Zn, As, Hg, etc. The associated metals are usually low content and do not meet the grade requirements for comprehensive recovery. Currently the bargh-own detection technology is low level and the information on the mineralogy composition of ore, occurrence of each valuable and bad element, sources and generation of pollutants, and the mineralogy data on feed to tailings cannot be known by managerial and technical personnel. So the associated metals (especially the metals cause

pollution) are not recovered in the beneficiation process and report to the tailings. For example, there is sphalerite in most of China's tungsten ore. Zinc is not contaminated, but the dispersed element Cd usually exists in the sphalerite as isomorphous substitutes. The loss of sphalerite will result in the loss and pollution of Cd. Therefore, detection and monitoring from the point of view of process mineralogy should be carried out for China's tungsten mines using high-tech tools. This work can give guidance for comprehensively recovering the associated metals that don't reach the minimum mining grade and are easily result in environment pollution while recovering major metals.

3. Study on the occurrence of colloidal tungsten in the ore. Recent hypergene tungsten deposit is one of the five genetic types. Also the tungsten resource is still not utilized nowadays because tungsten is scattered in the colloidal iron and manganese minerals and can't be separated and concentrated in physical methods. These tungsten resources have always been ignored. Therefore, it is very necessary to study the occurrence and properties of colloidal tungsten so as to give guidance for its separation and concentration by beneficiation and metallurgy.

With the depletion of mineral resources, the development and utilization of refractory low-grade polymetallic tungsten ore and the increasing requirements of comprehensively utilizing resources, process mineralogy has a closer relationship with mineral processing and plays a more important role because of its own progress. In future, process mineralogy not only serves for studying beneficiation process but also serves for monitoring and optimizing the production process of bargh, so as to promote the ordinal, normative, and sustainable development and utilization of mineral resources.

References

1. Han YW (2003) Geochemistry. Geology Press, pp 46–47
2. Shen JX (1999) The exhaustion of wolframite resource of our country and its countermeasure, cemented carbide
3. Wu X, Li LP, Zhang WZ (2008) The characters and resource distribution of rhenium. Express Inf Min Ind 11:67–69
4. Tan YJ (1992) Ore of geochemical types of vein wolframite deposits on evaluation of ore resources. Min Geol 6:142–147
5. Chen J (1993) Mineralization and processing characteristics of tungstenic minerals occurring in zone III of Shizhuyuan, Nonferrous Metals

Light Absorption Characteristics of Multi-morphology FeS_2 Granular Synthesized Under Hydrothermal Conditions

Jia Liu, Fei Huang, Guanglu Li, Lin Meng, Haoran Yu, Yinghua Chen, Weifeng Wang, Shang Gao, and Wenyuan Gao

Abstract This chapter examines granular FeS_2 synthesized under hydrothermal conditions of 220 °C, with a Fe/S ratio of 1:3. SEM and XRD characterize its morphology, composition, and structure. Measurement of the absorption spectrum within the range of 200–2,000 nm was performed using Cary 500 UV–Vis–NIR spectrophotometer. The band gap was calculated according to the band gap (eV) formula. The results showed that the samples were granular pyrite in the form of cube and octahedron, with a particle size of about 2–5 μm, and include a certain amount of pyrrhotite ($Fe_{1-x}S$). The absorption peak was about 1,879 nm, with the intrinsic absorption edge (λ_0) and band gap values of 1,885 nm and 0.6578 eV, respectively. Through the relationship between semiconductor conversion efficiency and band gap, we obtained a limiting conversion efficiency which can achieve to about 15 %. We present a brief analysis of the vacancy affection to the band gap of pyrite.

Keywords FeS_2 granular • Light absorption characteristics • Hydrothermal • Band gap • Limiting conversion efficiency

1 Introduction

Pyrite ($E_g = 0.95$ eV) is being developed as a solar energy material due to its environmental compatibility and its very high light absorption coefficient [1]. A. Ennaoui [2] studied the feasibility of pyrite thin films in solar cells and its development. Wang Xiuhong [3] studied the light absorption characteristics of natural

Funds: Supported by National Natural Science Foundation (Grant No.:40872045;41172047); The Opening Project of Key Laboratory of Solid Waste Treatment and Resource Recycle (SWUST), Ministry of Education (12zxgk01).

J. Liu • F. Huang (✉) • G. Li • L. Meng • H. Yu • Y. Chen • W. Wang • S. Gao • W. Gao
College of Resources and Civil Engineering, Northeastern University, Wenhua Road, Shenyang, Liaoning, People's Republic of China
e-mail: huangfei@mail.neu.edu.cn

F. Dong (ed.), *Proceedings of the 11th International Congress for Applied Mineralogy (ICAM)*, Springer Geochemistry/Mineralogy,
DOI 10.1007/978-3-319-13948-7_22

pyrite, containing Co, Ni impurities, which resulted in a lower band gap and conversion efficiency. Due to structure defects in natural pyrite, the photovoltaic performance of pyrite is inefficient. Researchers have studied the pyrite under different conditions to improve the photovoltaic performance. Dahman H [4] measured the band gap of pyrite by iron coating, which is about 1.35 eV. A.S. Aricò [5] studied the performance of natural pyrite after heating. Formation of a heterostructure composed of FeS_2 and Fe_2O_3 phases is considered to be a promising method for the development of low-cost devices for the direct conversion of solar energy. PL Antonucci et al. [6] studied the photovoltaic performance of pyrite prepared by screen printing; the band gap of pyrite containing pyrrhotite is 1.1 eV. Xu Jinbao [7] demonstrated that the larger the thickness and grain size, the wider the band gap. They believed that crystal grain size, defect density, and crystalline quality are important factors that affect the light absorption properties. However, the effects of changes due to the crystal type and internal defects are less well known.

In order to make a detailed study of the absorption properties, this chapter analyzed the FeS_2 synthesized under hydrothermal conditions and characterized its morphology, composition, and structure. We then measured the absorption spectrum of the samples and analyzed the effect of band gap on the photoelectric conversion efficiency. The discussion of the relationship between structure and properties of different minerals can provide a scientific basis for the development of low-cost photovoltaic material.

2 Sample Sources and Characterization

2.1 Sample Sources

The experimental conditions: the concentration of iron and sulfur source 0.5 mol/L, ratio of Fe/S 1:3, and heat for 24 h at the temperature of 220 °C. A SSX-550 scanning electron microscope and a multi-crystal X-ray diffraction (XRD) were used to characterize the morphology, composition, and structure of the samples.

2.2 Methods for Assessment and Analysis

2.2.1 Scanning Electron Microscope

Scanning electron microscope (SEM) of Northeastern University is SSX-550. Resolution: 3.5 nm; magnification: 20–300,000; acceleration voltage: 0.5–30 kV; EDS energy resolution: 144 eV; element: C-U; and the minimum range: <1 μm.

2.2.2 X-Ray Powder Diffraction

X-Ray Powder Diffraction (XRD) of Northeastern University is PW3040/60X. Test conditions: CuKα target ($\lambda = 0.154056$ nm); continuous scan range: 5°–90°; step size: 0.033°; and the consecutive scan time: approximately 7 min. Crystal diffraction patterns were drawn using OriginPro8.5 software.

2.2.3 Cary 500 UV–Vis–NIR Spectrophotometer

The obtained sample powder was coated on the ITO conductive glass (to eliminate the impact of the measurement process on the substrate). Measure the absorption spectrum of the samples within the range of 200–2,000 nm by using Cary 500 UV–Vis–NIR spectrophotometer.

3 Results

As seen in Fig. 1, sample crystal morphology comprised cubic and octahedron poly-shaped granular morphology, with a particle size of about 2–5 μm.

As shown in Fig. 2, the sample prepared under experimental condition is mainly pyrite and pyrrhotite. FWHM was small, with the (220) and (311) crystal faces of pyrite, and the (228) and (224) crystal faces of pyrrhotite being well developed.

The measured absorption is shown in Fig. 3. As seen in Fig. 3, the sample has an obvious absorption band of small spectral range and the absorption peak has a wavelength of about 1,879 nm.

4 Calculations and Analysis of the Band Gap

4.1 Calculation of the Band Gap

Optical, electrical, and other properties of the crystal are related to the electron energy band position; calculation of the energy band of the crystal is the key to understanding the properties of the crystal [8].

Band gap energies of common iron sulfides are shown in Table 1.

The intrinsic absorption is the crystal's absorption caused by transition of electrons between the valence band and the conduction band electrons which determines the optical properties of the semiconductor. The most obvious feature is the fundamental absorption edge (where the absorption coefficient increases steeply).

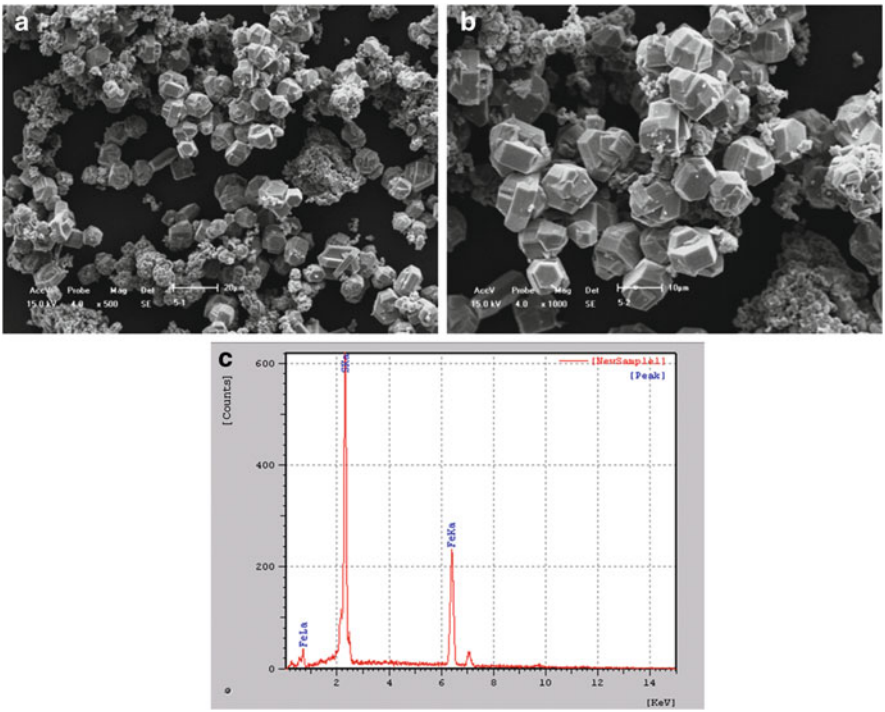

Fig. 1 Granular iron sulfide synthesized in hydrothermal conditions
Note: (**a**) and (**b**) are the SEM micrographs; (**c**) is EDS spectrum

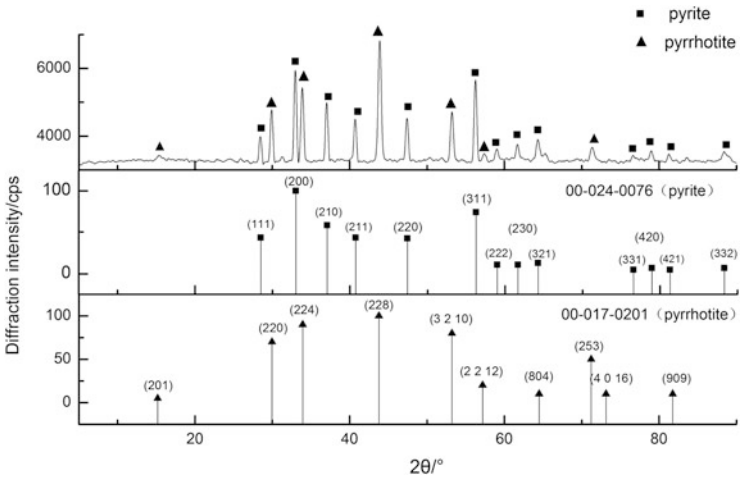

Fig. 2 XRD patterns of the samples synthesized under hydrothermal conditions

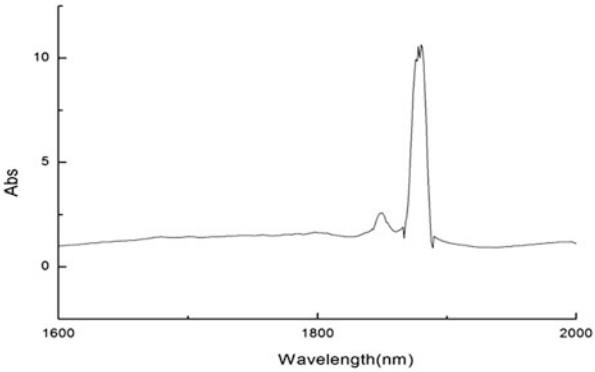

Fig. 3 The absorbance spectrum of the granular crystals synthesized under hydrothermal conditions

Table 1 Band gap of common iron sulfides

Chemical formula	Band gap /eV	Sources
FeS_2 (pyrite)	0.95	[9]
FeS_2 (marcasite)	0.34	
Fe_3S_4	0.00	
FeS	0.04	
$Fe_{1-x}S$	0.37	[10]

We can determine the intrinsic absorption edge from Fig. 3, which is about 1,885 nm. From the band gap (eV) Eq. (1), the absorption edge wavelength was used to calculate the band gap energy of 0.6578 eV.

$$E_g = {}^{1240}/_{\lambda_0} \tag{1}$$

The band gap determines the ideal photoelectric conversion efficiency. The band gap value is related to the crystal structure and the binding properties of the atoms. The binding force caused by valence bond in pyrite is larger than that caused by pyrrhotite. From Table 1, the band gap value of the sample is between the theoretical value of pyrite and pyrrhotite.

4.2 Discussion

The studies of Chen Jianhua et al. [11] have shown that the conduction bands of pyrite are mainly composed of the 3*p* orbitals of the sulfur atom and the 3*d* orbitals of iron atoms, whereas the conduction bands of pyrrhotite are mainly composed of the 3*p* orbitals of the sulfur atom and the 3*d* orbitals of iron atoms; the density of states near the Fermi level is mainly constituted by the 3*d* orbitals of the iron atoms.

The narrowing of the optical band gap with increasing temperature is the result of grain coarsening, defect density, and crystalline quality [12]. The increase in

grain size and the decrease of grain boundary increase the impurity content, which would affect its band gap. Huang Liuyi [12] found that with increasing curing temperature, the band gap changes from high to low.

A high concentration of point defects will lead to a decrease in band gap energy: the higher the concentration, the lower the band gap [13, 14]. The formation of crystal defects includes the presence of some trace components and the lack of lattice anion and cation [15]. Due to the different nature of the impurities and the imbalance caused by the vacancy defects, the properties of pyrite were changed. The presence of pyrite and pyrrhotite in the sample prepared at 220 °C resulted in an intermediate band gap value.

By means of the CASTEP module in Material Studio 4.2, we calculated the band structure of perfect pyrite based on the first principles (e.g., "Fig. 4"). The results show that the ideal pyrite has an indirect band gap structure with a band gap of 0.553 eV, which is lower than the reported value (0.95 eV) [16]. Combined with the band structure of pyrite with sulfur of vacancy [15], we determined that sulfur vacancies contribute to a reduction in cell volume and play a greater role in the band structure near the Fermi level. The new level caused by the vacancy results in the increase of band gap from 0.553 to 0.6578 eV.

The emergence of pyrrhotite with pyrite results from the absence of sulfur anion; this is the positively charged defect. In the absence of sulfur ions, the energy of the electrons is reduced, which means that the binding of the iron ions near the vacancies is tighter (e.g., "A in Fig. 5a"). When a crystal was exposed to light, the bound electrons (e.g.. "A in Fig. 5b") excited into the conduction. Due to these point defects, an additional donor or acceptor level formed in the band gap of FeS_2, which decreased the band gap value relative to the theoretical value.

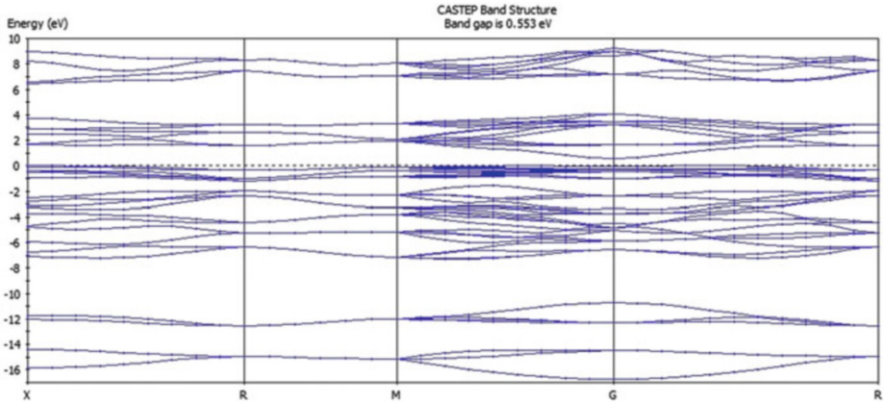

Fig. 4 Band structure of perfect pyrite

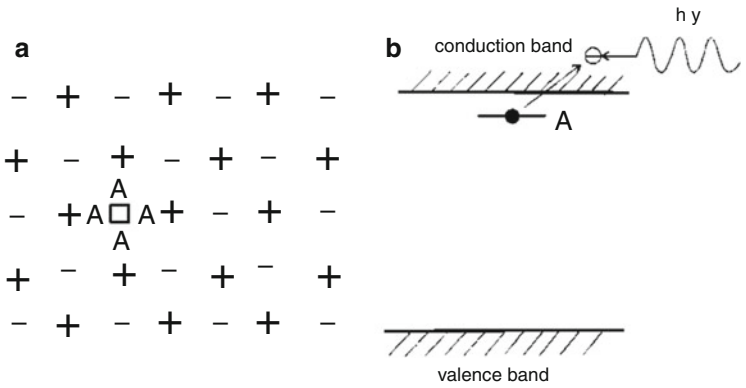

Fig. 5 The bound levels caused by anion absence. (Modified according to Xie Xide, 1962 [17])

5 Optical Properties Evaluation

Calculation of the photoelectric conversion efficiency is given by Eq. (2):

$$\eta = \frac{\mathrm{FF} I_{\mathrm{sc}} V_{\mathrm{oc}}}{P_{\mathrm{in}}} \tag{2}$$

where η is the photoelectric conversion efficiency,
I_{sc} is the photocurrent,
V_{oc} is the open voltage,
FF is the filling factor, and
P_{in} is the incident light intensity.

The band gap determines the ideal photoelectric conversion efficiency. On the one hand, the band gap has a direct impact on the photocurrent. Due to the different energies of photon emitted by the sun, only those with energy greater than the band gap can generate "electron–hole" pairs in the semiconductor to form a photocurrent. The larger the E_{g}, the smaller the number of photons; so, I_{sc} will decrease. From Eq. (2), we know that the smaller the I_{sc}, the smaller the photoelectric conversion efficiency, but it is not good if E_{g} is too small, which would reduce the utilization of photon energy. On the other hand, the band gap impacts the value of V_{oc}, which is inversely related to the current I_0: the bigger the band gap, the smaller the I_0, and the larger the value V_{oc}. From Eq. (2) we can see that the larger the V_{oc}, the bigger the utilization of photon energy.

The relationship between semiconductor conversion efficiency and band gap is shown in Fig. 6. The band gap of the sample was 0.6578 eV and the limiting conversion efficiency was about 15 %. From this study we find that the photoelectric conversion efficiency of the sample is larger than natural pyrite with Co, Ni impurities [3]. Formation of a heterostructure composed of FeS_2 and $Fe_{1-x}S$ phases is considered to be a promising method for the development of low-cost devices in the direct conversion of solar energy.

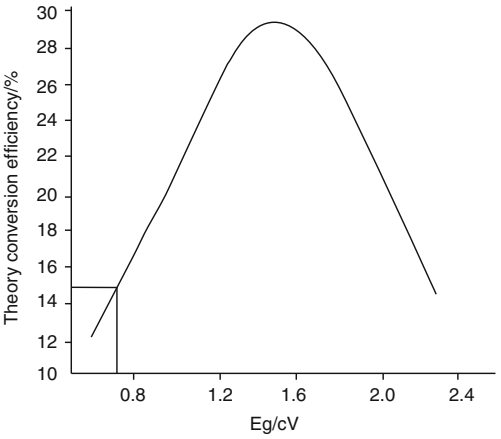

Fig. 6 The relationship between semiconductor conversion efficiency and band gap

6 Conclusions

1. The samples were cube, with a combination of octahedral and cubic granular pyrite, with a particle size of about 2–5 μm, and include a significant proportion of orthorhombic pyrrhotite ($Fe_{1-x}S$).
2. The band gap of the sample was 0.6578 eV with a limiting conversion efficiency of about 15 %. The emergence of pyrrhotite resulted from an absence of sulfur, which produces the acceptor level and leads to a decrease in the band gap.
3. Formation of a heterostructure composed of FeS_2 and $Fe_{1-x}S$ phases is considered to be a promising method for the development of low-cost devices for the direct conversion of solar energy.

References

1. Ennaoui A, Tributsch H (1986) Energetic characterization of the photoactive FeS_2 (pyrite) interface. Sol Energy Mater 14(6):461–474
2. Ennaoui A, Fiechter S, Pettenkofer C, Alonso-Vante N, Buker K, Bronold M, Hopfner C, Tributsch H (1993) Iron disulfide for solar energy conversion. Sol Energy Mater Sol Cells 29 (4):289–370
3. Wang XH, Huang T, Huang F, Zhang SN, Wang Y, Gao C (2011) Light absorption characteristics of nature pyrite. Spectrosc Spectr Anal 31(09):2508–2511
4. Dahman H, Khalifa M, Brunel M, Rezig B (1996) Iron pyrite films prepared by sulfur vapor transport. Thin Solid Films 280(1–2):56–60
5. Aricò AS, Antonucci V, Giordano N (1991) Photoelectrochemical behavior of thermally activated natural pyrite-based photoelectrodes. Mater Chem Phys 28(1):75–87
6. Pl A, Aricò AS, Giordano N, Antonucci V (1995) Polycrystalline iron sulphide based semiconductors for solar energy conversion. Adv Perform Mater 2(2):145–159
7. Xu JB, Zheng YF, Li J, Sun YF, Wu R (2004) The structural optical and electrical properties of films prepared by screen print. Acta Phys Sin 53(9):3229–3233

8. Yan Ji M, Zhang QY (1982) Structure characteristics of electronic energy bands about molecular crystal. Acta Chim Sin 40(9):774–789
9. Cyrus W, Yue W, Sheraz G, Steven Volkman K, Guo JH, Paul Alivisatos A (2009) Surfactant-assisted hydrothermal synthesis of single phase pyrite FeS2 nanocrystals. Chem Mater 21 (13):2568–2570
10. Kashyout AB, Aricò AS, Monforte G, Crea F, Antonucci V, Giordano N (1995) Electrochemical deposition of ZnFeS thin film semiconductors on tin oxide substrates. Sol Energy Mater Sol Cells 37(1):43–53
11. Chen JH, Zhong JL, Li YQ, Chen Y, Guo J (2011) Electronic structures and floatability of pyrite, marcasite and pyrrhotite. Chin J Nonferrous Metals 21(7):1719–1727
12. Huang LY (2011) Preparation and optoelectronic properties of FeS_2 and FeS_2/TiO_2 composite films Zhejiang University. Dissertation, Zhejiang University
13. Ferrer IJ, Cballero F, Cdelas H, Sánchez CJ (1994) Preparation of n-type doped FeS_2 thin films. Solid State Commmun 89(4):349–352
14. Ferrer IJ, Cballero F, Cdelas H, Sánchez CJ (1995) The effect of Ni impurities on some structural properties of pyrite thin films. Phys Condens Matter 7(17):2115–2121
15. Li YQ, Chen JH, Chen Y (2010) Electronic structures and flotation behaviour of pyrite containing vacancy defects. Acta Phys Chim Sin 26(5):1435–1441
16. Schlegel A, Wachter P (1976) Optical properties, phonons and electronic structure of iron pyrite (FeS_2). J Phys C Solid State Phys 9(17):3363–3369
17. Xie XD, Fang JX (1962) Solid physics, 2nd edn. Scientific and Technical Publishers, Shanghai, pp 112–116

Bolshetagninskoe Deposit Microcline–Pyrochlore Ore Process Mineralogy

Liudmila Azarnova

Abstract Bolshetagninskoe deposit is one of the most valuable potential Russian niobium resource. It contains challenging pyrochlore ore that in the pre-feasibility study stage has been divided into a few geological–metallurgical units by metallurgical–geological mapping (in general, it is adequate to geometallurgy field). The microcline–pyrochlore ore is the predominant and most challenging metallurgical unit at the deposit. To optimize this unit ore processing flowsheet, broad-view process mineralogy approach was applied. It was shown that preliminary processing of the microcline–pyrochlore ore by radiometric separation stabilizes floatation feed ore grade by decreasing gangue mineral content and content of pyrochlore grain of size less than 10 μm. Comparing pyrochlore grain size and liberation of it in the ore, comminuted by both conventional ball mill and innovative impact centrifuge mill, some grounds of dramatically increased floatation concentrate grade and recovery have been discovered. The fine-grained ore-forming pyrochlore (the mineral average weighted grain size is 61 μm in the radiometric separated ore) has a relatively low liberation degree in the grinding ore (63 %) that, in addition to close association of the mineral with microcline, causes reduced content of Nb_2O_5 (29.9 %) and high content of SiO_2 (22.8 %) in the floatation final product. SiO_2 is concentrated by microcline that is definitely needed for an intensive hydrometallurgy processing flowsheet to produce ferroniobium from the product.

Keywords Bolshetagninskoe • Microcline–pyrochlore ore • Challenging rare-metal ore • Liberation degree • Niobium • Geological–metallurgical mapping • Geometallurgy

L. Azarnova (✉)
All-Russian Scientific Research Institute of Mineral Recourses named after N.M. Feodorovsky, VIMS, 31 Staromonetny Street, Moscow 119017, Russia
e-mail: lazarnova@mail.ru

F. Dong (ed.), *Proceedings of the 11th International Congress for Applied Mineralogy (ICAM)*, Springer Geochemistry/Mineralogy,
DOI 10.1007/978-3-319-13948-7_23

1 Introduction

Rare-metal (RM) ore process mineralogy has been developed in Russia since 1950–1960. The main results were covered by A. I. Ginzburg, I. T. Aleksandrova, and L. B. Chistov' publications and summarized in 1991 monograph [1]. The approach was widely integrated in complex geological and mining projects that helped metallurgists to develop robust processing flowsheets of challenging domestic RM ores.

VIMS has grown to become the leader of RM ore mineralogy, geology, and metallurgy by planning and coordinating Soviet RM ore exploration programs, and Giredmet (State Research Institute of RM industry) has been one of the leaders of RM ore processing flowsheet development. 2008–2012 pre-feasibility study of the Bolshetagninskoe niobium deposit is an example of a current approach, taken by VIMS in cooperation with Giredmet to metallurgical assessment of challenging RM ore in early exploration stage.

Bolshetagninskoe deposit is one of the most important Russian niobium resource. It is confined to carbonatite complex of the same name that is situated in the Sayan Mountains, Eastern Siberia. Ores contain 1.0 % Nb_2O_5 and are unique in that the economic pyrochlore mineralization is concentrated in alkaline metasomatic rocks but not in carbonatites [2–4]. In 1988 pre-feasibility study of the deposit was commenced. The result was that preliminary orebody reserve assessment and processing flowsheet was developed in general. In 2008 the pre-feasibility study has been continued and successfully completed in 2012. As economic viability of the deposit ore was confirmed, the niobium ore reserves were applied by Russian State Committee on Mineral Reserves.

To get orebody knowledge and assess its variability, the method of so-called geological–metallurgical mapping (GMM) was used. The base of this approach, developed since 1940–1950 in Russia, is an integration of complex mineralogical, chemical, and metallurgical investigation of a large number of small-scale samples and traditional bulk sample testwork [5]. It is vital that a few domestic standards and instructions formalize GMM methodology depending on exploration stage and ore deposit type. Generally, GMM conforms to reinvented field of "geometallurgy." The latter involves geometallurgical mapping and modeling, based on orebody mineralogy study, and integrates ore characteristics with the mine plan and processing [6].

The current pre-feasibility study of the Bolshetagninskoe deposit ore involves drilling nine holes. A total of 1,998 m of core was extracted for the purpose of sampling and GMM for the project. To perform GMM, 47 small-scale samples were selected based on core logging and analytical data. The samples were analyzed with process mineralogy techniques and partly (26 samples) were roughly floated. Mineralogical, analytical, and metallurgical data were interpreted with mathematical statistic methods [7].

Table 1 Selected average chemical (XRF) and mineral (OMA) composition of geological–metallurgical units of Bolshetagninskoe deposit (including all of the Nb-minerals), wt%

Geological–metallurgical units	Nb_2O_5	P_2O_5	Pcl	Clb	Mi	Bi	Crb	Py + Po	Pcl locked Mi (rl%)
Microcline–pyrochlore	1.0	3.6	1.4	0.1	62	6	12	4.6	52
Carbonate–pyrochlore	0.7	4.5	1.5	0.1	11	31	30	4.8	13
Biotite–columbite–pyrochlore	1.2	3.8	1.4	0.7	10	56	10	6.2	6

Analyzed in volumetric samples materials, grounded by wet-ball milling to 125 μm
Pcl pyrochlore, *Clb* columbite, *Mi* microcline, *Bi* biotite, *Crb* carbonates, *Py + Po* pyrite + pyrrhotite

Three geological–mineralogical and metallurgical ore types were determined by GMM at the Bolshetagninskoe deposit: microcline–pyrochlore (MP), biotite–columbite–pyrochlore (BCP), and carbonate–pyrochlore (CP) (Table 1).

Three represented ore-type volumetric samples have been tested by commissioned flowsheet (radiometric separation → milling → selective floatation → pyrochlore leaching → ferroniobium) to verify different processability of the ore types and deliver viable processing flowsheets. To develop the robust flowsheets, process mineralogy methods were integrated into laboratory testworks.

The most important Bolshetagninskoe deposit ore type is the MP one, as it will be mined and processed at first 10 years of the mining project life cycle. BCP and CP ore types are deep mined and their processing is more straightforward; therefore results from them are not discussed in this chapter.

MP ore consists of microcline (59–70 wt%) with minor carbonates, apatite, sulfides, and goethite. Pyrochlore, the essential ore niobium mineral (94 % of a total ore Nb content), occurs as fine grains. It is indicated by GMM; a few geometallurgical variables of the feed MP ore impact pyrochlore' rougher floatation grade and recovery: content of Nb_2O_5, P_2O_5, share of liberated pyrochlore and the locked one in apatite particles.

Since the MP ore pyrochlore grains are fine and friable, viable grinding ore coarseness and device were assigned by metallurgists as a key instrument to optimize pyrochlore concentrate grade and recovery. While primary ore processing by radiometric separation is effective to remove about 30 % waste material, it was also important to evaluate its impact of it on floatation feed grade. And an additional challenge was final float pyrochlore concentrate that contained 22.8 % SiO_2. The necessary information has been provided by process mineralogy approach that was the main objective of this research.

2 Materials and Methods

In order to characterize the mineral composition and liberation of the MP ore processing products, seven samples were collected: two samples represented radiometric separation products (tails, RT1, and concentrate, RC1), another two samples were collected from grinding by ball and impact mill ore, and three samples were selected from final floatation concentrate and its scavenging floatation products. To analyze pyrochlore grain size, thin sections were made of the 37 MP ore fragments, which were selected from 150 fragments of the ore fraction size −30 + 50 mm. The latter were preliminarily studied by X-ray radiometric method involving Nb concentration characterization and divided into a few groups by the metal content.

Mineral composition and liberation, as well as pyrochlore grain size, were analyzed by traditional expert-mineralogist-driven optical microscopy. As control methods X-ray powder diffraction and X-ray fluorescence spectroscopy were used.

Traditional expert-mineralogist-driven optical microscopy analyses (OMA) were performed by optical microscope Olympus BX 51 in accordance with national branch instructions that formalize semiquantitative optical mineralogical and geometrical analysis.

X-ray powder diffraction (XRD) analyses were obtained in X'pert Pro PANalytical equipment, with CuKα radiation using inclusive standard method and X'pert High Score software with a PDF2 database.

X-ray fluorescence spectroscopy analyses were performed by PANalytical MagiX PRO instrument. The domestic branch standard was entered in the analytical procedure.

To obtain analyses by XRD and XRF, sample material was comminuted in laboratory disk-mill to particle grain size less than 40 μm.

3 Results and Discussion

3.1 Radiometric Separation Impact on Floatation Feed Ore Grade

The first stage of the MP ore treatment is radiometric separation. At this stage, the preliminary crushed ore is separated by threshold content of 0.2 wt% Nb_2O_5 into waste product (about 30 % of a total ore, radiometric tails, RT1) and concentrate. The latter one is integrated with the ore non-separated fraction (less than 30 mm) and this product («radiometric concentrate», RC1, later) is a feed of the floatation circuit.

Data of the Table 2 characterized mineral composition and liberation degree in radiometric separation feed ore and products.

The MP ore separated by radiometric separator (RT1) contains not only more pyrochlore (1.87 wt%, +44 rl%), but also apatite (11 and 9 wt% accordingly) and

Table 2 Mineralogical composition (wt%) and pyrochlore liberation degree (rl%) of microcline–pyrochlore ore[a] and products of the ore radiometric separation (mineralogical analysis were performed with optical microscopy methods)

Mineral	RT1	RC1	MP ore[b]
Liberated microcline	34	60	50
Microcline with Fe hydroxides, hematite	15	3	8
Carbonates	8	1	4
Biotite	25	10	16
Apatite	6	11	9
Fe hydroxides >> hematite	10	12	11
Liberated pyrochlore	0.22	1.19	0.81
Pyrochlore with microcline	0.19	0.68	0.49
SUM pyrochlore	0.41	1.87	1.30
Pyrochlore liberation degree, −0.125 + 0.07 mm	11	26	20
Pyrochlore liberation degree, −0.125 + 0.01 mm	46	57	53

[a]Volumetric sample material of oxidized microcline–pyrochlore ore products was analyzed (grounding by laboratory ball mill to 125 μm)
[b]The MP ore characterization was calculated using data of it radiometric separation products analysis (RT1 and RC1)

microcline (63 and 58 wt% accordingly) have been grown; then the separation waste material is characterized by higher contents of biotite (25 and 16 wt% accordingly) and carbonates (8 and 4 wt% accordingly) (Table 2). It can be explained by pyrochlore's close association with microcline (the mineral forms disseminated fine grains and thin veins) and apatite (apatite–pyrochlore veins in microcline matrix), whereas carbonate and biotite aggregates usually don't contain the mineral. Another important radiometric separation result, as seen in Table 2, is that the content of liberated pyrochlore has been increased in RC1 to 1.19 wt% (+38 rl% in comparison with the feed ore); then in the RT1 content of it is only 0.22 wt%.

The data of pyrochlore grain size analysis in the MP ore can clarify this result (Table 3).

To interpret pyrochlore grain size composition data right, it firstly should be mentioned that to study the MP ore floatation and grinding variables the ore was grounded by different devices to 125 μm or 200 μm (basing on pyrochlore grain friable and average size of it 54 μm, Table 3). Thus this grinding coarseness prevents the significant pyrochlore losses with slim fraction, which determines that pyrochlore grain of size less than 16 μm will be mostly locked in the comminuted ore (so-called "hard-liberated" pyrochlore) and lost at rough floatation tails.

As seen in Table 3, more than a half pyrochlore grain of the MP ore is a size less than 32 μm, and 37.8 rl% of it is distributed in the floatation hard-liberated size fraction −16 μm. If ore fragments' content is less than 0.2 wt% Nb_2O_5 to delete (as operated by radiometric separation), then pyrochlore grain size composition smoothly changes: content of pyrochlore of well-liberated size fraction +32 μm increases from 38.2 to 44.8 rl% and it declined from 37.8 to 31.8 rl% in the fraction

Table 3 Pyrochlore grain size composition (optic geometrical analysis results) of the microcline–pyrochlore ore and some radiometric concentrates of it, predicatively calculating by different Nb_2O_5 content threshold

Size fraction (mm)	MP ore fragment group (by content of Nb_2O_5 from–to, %)								A total ore	Predictive radiometric concentrate by different Nb_2O_5 content threshold		
	4.2–6.7	2.1–3.8	1.7–1.8	1.1–1.5	0.7–1.0	0.4–0.7	0.2–0.4	<0.2		0.2	0.4	0.7
Amount of ore fragments and analyzed thin sections	5	19	8	8	14	31	38	27	150	123	85	54
	7	4	2	4	5	5	4	6	37	31	27	22
−0.25 + 0.125	26.9	44.6	0.0	62.5	24.5	0.0	0.0	0.0	12.2	14.8	21.5	33.8
−0.125 + 0.064	25.3	24.0	9.8	19.2	31.3	0.0	18.7	0.0	13.1	16.0	14.7	23.2
−0.064 + 0.032	28.2	16.2	14.7	8.9	12.5	9.5	16.3	8.0	12.9	14.0	13.0	15.0
−0.032 + 0.016	7.1	10.8	32.7	4.6	21.9	27.9	30.6	26.7	24.0	23.4	20.1	15.7
−0.016 + 0.008	11.1	3.3	33.1	4.1	8.0	53.8	24.0	51.1	29.9	25.2	25.9	9.8
−0.008	1.4	1.1	9.7	0.7	1.8	8.8	10.4	14.2	7.9	6.6	4.8	2.5
SUM	100.0	100.0	100.0	100.0	100.0	100.0	100.0	100.0	100.0	100.0	100.0	100.0
Pyrochlore grain average size (μm)	91	135	28	141	87	18	36	19	54	61	72	104

size −16 μm. The pyrochlore grain average weighted size increases from 54 to 61 μm in the example.

To dramatically change pyrochlore grain size distribution, as shown in Table 3, ore fragments containing less than 0.7 wt% Nb_2O_5 should be deleted from the MP ore by radiometric separation that is unviable. A product which contains only 12.3 rl% of pyrochlore of hard-liberated fraction size will be obtained by the operation and pyrochlore grain average weighted size will be increased to 104 μm in the floatation feed ore (Table 3).

3.2 Preferential Ore Comminution Method

As early mentioned, a comminution circuit development is vital to the MP ore processing. To grind the ore, two comminution devices have been tested: conventional wet ball mill and dry impact centrifuge mill [8]. To test the first one, the ore has been grounded to particle size less than 125 μm. Dry impact milling performance has been studied by grinding the ore to particle size less than 200 μm, while preliminary optical mineralogical analysis was identified earlier pyrochlore liberation by this comminution device in comparison with the ball mill.

Both pyrochlore and microcline liberation degrees are essential to floatation selectivity and its final product grade and recovery, while non-liberated pyrochlore is locked in microcline and the latter is the main MP ore gangue mineral. Therefore increasing microcline liberation degree from another gangue minerals and pyrochlore has positive impact on the ore floatation selectivity.

Although the impact mill product has coarser content than the ball mill one (51 % less than 74 μm and 66 % less than 74 μm, respectively), the products pyrochlore (63 and 70 rl% accordingly) and microcline (90 and 82 rl% accordingly) liberation degrees are similar (Table 4).

Liberated pyrochlore average weighted grain size is larger in impact mill product (32 μm and 25 μm in ball mill product accordingly) that improves floatation characteristics of the ore. Another impact grinding device advantage is declined content of fine-liberated pyrochlore particle of size less than 10 μm (17 rl% and 35 rl% of the liberated ore in the ore grinding by impact and ball mill accordingly), which is hard extracted by conventional floatation technique.

MP ores grounded by both devices have been tested by commissioned floatation circuit. The best floatation results have been obtained from the impact mill product in comparison with ball mill one due to preferential pyrochlore liberation and fresh surfaces of mineral particles: the concentrate grade and recovery increased to 11 and 25 % of Nb_2O_5 relatively [8].

Table 4 Pyrochlore and microcline liberation in microcline–pyrochlore ore grounding by different methods (optic mineralogical analysis results)

Grinding method and size	Liberated pyrochlore weighted average grain size (μm)	Share of liberated pyrochlore in size fraction (%)		Liberation degree (rl%)	
		−40 + 10 μm	−10 μm	Pcl	Mi
Wet ball milling, 66 % less than 74 μm	25	59	35	70	82
Dry impact milling, 51 % less than 74 μm	32	71	17	63	90

Table 5 Pyrochlore and microcline liberation characterization of floatation final product and its scavenging products (optic mineralogical analysis results, content of Nb_2O_5 is obtained by XRF)

Floatation product	Content of (wt%)			Pyrochlore liberation (rl%)			Microcline liberation from pyrochlore grain degree (rl%)
	Nb_2O_5	Pcl	Mi	Liberated	Middling	Locked	
Final product	29.9	53	26	75	18	7	24
Final product scavenging "concentrate"	39.5[a]	67	20	92	5	3	30
Final product scavenging waste material	20.7[a]	35	38	51	35	14	17

[a]It is calculated by pyrochlore average content of 59 wt% Nb_2O_5

3.3 Floatation Final Product Grade Assessment

Floatation final product grade is low (29.9 wt% Nb_2O_5, 22.8 wt% SiO_2), as pyrochlore liberation degree from microcline in the comminuted MP ore is not high enough (63 rl%, Table 4) to float the niobium mineral more selectively.

To investigate the feasibility of increasing floatation selectivity, the final product was scavenged. As shown in Table 5, the scavenging final product has higher pyrochlore liberation degree than the feed product (75 and 92 rl% accordingly) that positive impacts niobium content (39.5 wt% of Nb_2O_5), but a lot of microcline particles still have contained pyrochlore impurities (microcline liberation degree from pyrochlore is smoothly increased from 24 rl% in the final product to 30 rl% in the scavenging final product).

As seen in Table 5, the final product scavenging waste material is characterized by reduced values of pyrochlore and microcline liberation degree (51 and 17 rl% accordingly), but it still contains too much pyrochlore (35 wt%), the tails to consider.

The obtained data have shown that the final product scavenging could not be recommended, while the middling product contains a lot of pyrochlore and

scavenging concentrate still has been too low grade to process it viably by pyrometallurgy in order to produce ferroniobium. It is much more preferable to achieve higher pyrochlore recovery in this nonconventional product and process it by modern hydrometallurgy techniques with further ferroniobium production.

4 Conclusions

The Bolshetagninskoe deposit microcline–pyrochlore ore is the new Russian challenging niobium resource. It can be viably processed by complex flowsheet that involves preliminary radiometric separation, grounding to 200 μm by impact centrifuge mill, selective floatation, pyrochlore concentrate leaching, and finally ferroniobium production. To deliver the robust processing flowsheet, the domestic RM process mineralogy approach was integrated into laboratory testwork.

By the process of mineralogy study, some essential problems of the MP ore processing were covered.

1. The positive radiometric separation impacts on the floatation feed ore characteristics have been shown. Due to radiometric preliminary processing, the content of gangue minerals in the floatation feed ore is declined and pyrochlore grain size distribution is smoothly corrected to increase the mineral average grain size from 54 to 61 μm. The result is increasing floatation sustainability and selectivity, declining losses of hard-treated and hard-liberated pyrochlore.
2. Compared with wet ball mill, using dry impact mill to ground the MP ore helps to prepare it to flotation processing better due to earlier pyrochlore liberation and coarser size of liberated pyrochlore particle. In addition to fresh surfaces of mineral particles, dramatically increased floatation recovery (+25 % of a total ore Nb_2O_5) and grade (+11 wt% Nb_2O_5) are determined.
3. Pyrochlore liberation is 75 rl% and microcline liberation (from pyrochlore) is 24 rl% in the analyzed final float pyrochlore concentrate. There is 18 rl% of middling pyrochlore and 7 rl% of the locked one (in microcline) in the concentrate that determines its inadequate quality (29.9 wt% Nb_2O_5, 22.8 wt% SiO_2). By pyrochlore and microcline liberation analyses, it has been shown that the further concentrate scavenging could not be viable: thus pyrochlore losses are increased significantly by the operation, and the content of microcline (mineral-concentrator of SiO_2) too smoothly declined, to process this product by pyrometallurgy in order to produce ferroniobium. It is much more preferable to achieve higher pyrochlore recovery in this nonconventional pyrochlore product and process it by modern hydrometallurgy techniques with further ferroniobium production.

Acknowledgements The author has taken a part in the Bolshetagninskoe deposit pre-feasibility study as a mineralogist-member of multidisciplinary specialist team and would like to acknowledge colleagues from VIMS and Giredmet institutes for the complex research effort performing.

A. V. Temnov, the head of the project, and N. J. Stenin, the project chief-metallurgist, are gratefully thanked for their assistance and discussion, contributed to this paper.

References

1. Sidorenko GA, Aleksandrova IT, Petrova NV (1991) Process mineralogy of rare-metal ores (in Russian). Nauka, Saint-Petersbourg, p 236
2. Pozharitskaja LK, Samoilov VS (1972) Petrology, mineralogy and geochemistry Eastern Siberia carbonatites (in Russian). Nauka, Moscow, p 268
3. Azarnova LA, Temnov AV, Chistjakova NI, Naumova IS (2010) Kalipyrochlore from weathered ore at Bolshetagninskoe deposit (in Russian). Razvedka i ohrana nedr 3:33–37
4. Azarnova L, Temnov A (2010) Pyrochlore from metasomatic rocks at Bolshetagninskoe niobium deposit (Russia, Eastern Siberia). In: Proceedings of the 20th general meeting of the IMA, Budapest. Acta Mineral Petrogr. Abstr. Ser., vol 6. Department of Mineralogy, Geochemistry and Petrology, University of Szeged, Szeged, p 564
5. Kotz GA, Chernopjatov SF, Shmanenkov IV (1980) Metallurgical sampling and mapping of ore deposits (in Russian). Nedra, Moscow, p 288
6. Dunham S, Vann J, Coward S (2009) Beyond geometallurgy—gaining competitive advantage by exploiting the broad view of geometallurgy. In: Proceedings of the first AusIMM international geometallurgy conference, Brisbane, QLD, Australia, 5–7 September, 2011, pp 131–140
7. Stenin NJ, Azarnova LA, Belousova EB, Temnov AV (2011) Bolshetagninskoe deposit microcline niobium ore comminution method selection and assessment of its impact on floatation processing grade (in Russian). In: Proceedings of the international conference "Plaksinskie chtenija-2011" of scientific council for problems of mineral processing of RAN, Verhnaja Pishma, Russia, 19–24 September 2011, pp 101–105
8. Stenin NJ, Azarnova LA, Temnov AV, Kushparenko JS, Goeorgiady EK, Belousova EB (2010) Determination of metallurgical types of Bolshetagninskoe deposit niobium ore (in Russian). In: Proceedings of the international conference "Plaksinskie chtenija-2010" of scientific council for problems of mineral processing of RAN, Kazan', Russia, 13–18 September 2010, pp 518–521

The Roughness on Polished Gemstone Surfaces

Angela V. Nadur, Rainer A.S. Gütller, Sheila S. Carmo, and H. Kahn

Abstract Gemstone cutting is a useful process to create shapes on rocks and minerals. This is done through sawing, grinding, faceting, and polishing, thus providing better light reflection in the pavilion with specific angles for each translucent mineral; brightness of the surface, aesthetic appreciation, and their use in the jewelery industry. This process aims to decrease the abrasive grain size in each step, providing the gemstone surface with less roughness and flatness. In this article we present a detailed study about the variation of roughness through four kinds of polishing materials used, combined with six kinds of gemstone samples that are currently used in the jewelery industry. Each mineral has its specific crystallography structure, chemical composition, and hardness, when in contact with another polishing material with the same characteristics and variation of grain size in the three-body abrasive wear process (gem, polishing material, and flat disk), which can result in a particular surface for each gem.

The quality of surfaces was characterized through the roughness with equipments, Confocal Microscope Leica DCM3D and Surface Roughness Measuring Instrument Kosakalab Surfcorder SE1700α, and through light reflection with the equipment Reflectivity Meter Presidium, which is dependent on the grain size and the kind of material used. The aim of this process is to find ways to define roughness patterns that are acceptable for each polished material and type of gemstone.

Keywords Gemstone cutting • Tribology • Roughness • Quality of surface

1 Introduction

Gemstone cutting is a two-body and three-body abrasive wear process with lubrication by water or oil.

A.V. Nadur (✉) • R.A.S. Gütller
Geosciences Institute, University of São Paulo, São Paulo, Brazil
e-mail: angelavnadur@usp.br

S.S. Carmo • H. Kahn
Laboratory by Technological Characterization, University of São Paulo, São Paulo, Brazil

F. Dong (ed.), *Proceedings of the 11th International Congress for Applied Mineralogy (ICAM)*, Springer Geochemistry/Mineralogy,
DOI 10.1007/978-3-319-13948-7_24

The rough gems are studied under the focus by light to analyze the best translucent part, without fractures, inclusions, color zoning, and ideal size and shape by lapidary. To display this, the gemstones are fixed on a stick with compound wax and it is cut, ground, faceted, and polished. The cut excludes inappropriate parts or divides the rough material, with a thin saw of 1 mm, resulting in the surface being highly roughened.

In the next process all steps by grinding are made with vertical wheels and the aim is to get the shape of the gem, decreasing the abrasive grain size in each step, providing smoothness of surface. The aim is to put the determined angle for pavilion and crown, depending on the project design. The next step is to create the facets on pavilion and crown, using a flat disk with a diamond compound on the top, which enables the process to create surfaces sufficiently smooth to receive the polish. The polishing process happens in a three-body abrasive wear process, which uses a flat disk of lead and tin, the powder polish, and the gemstone [1]. The materials used in this process were based on the Brazilian gemstone cutting process.

Throughout the course of the history of human beings, men rub materials against each other to give shapes and to use as ornaments. Over the course of the time, the use the gemstones such as jewelery is increasing and the industry has a necessity to search for perfection when analyzing the best polishing material, with chemical composition and grain size to a specific mineral.

2 Materials and Methods

2.1 General

The chosen gemstones have been studied through the orientation of crystallographic axes and their cleavage plans. It was organized following the order of the group of silicates, in the sequence; garnet, topaz, beryl, tourmaline, spodumene, and quartz. The garnet almandine ($Fe_3Al_2Si_3O_{12}$) belongs to nesosilicate group and cubic crystal system. The surface analyzed by garnet was polished randomly as regards the crystallographic axes, because their atomic organization is equal (isometric) in all directions. The imperial topaz ($Al_2SiO_4(F,OH)_2$) belongs to nesosilicate group and orthorhombic crystal system with three different axes, *a*, *b*, and *c*, of which the surface analyzed was perpendicular to the *c* axis. The beryl ($Be_3Al_2Si_6O_{18}.nH_2O$) belongs to cyclosilicates and hexagonal crystal system. The hexagonal crystal system has four axes, of which a_1, a_2, $a_3 \neq c$; ergo the distances interatomics between axes are not the same, because of that, the analyzed surface was polished perpendicular to the *c* axis. Tourmaline with its complex structure $(Na, Ca)(Li, Mg, Al)_3(Al, Fe, Mn)_6(BO_3)_3(Si_6O_{18})(OH)_4$ belongs to cyclosilicate group and trigonal crystal system, following the same pattern as hexagonal axes. The analyzed surface was polished perpendicular to the *c* axis. The spodumene hiddenite ($LiAlSi_2O_6$), with clear green color, belongs to inosilicates group and

monoclinic crystal system, which has three different axes such as their distances interatomics. Their analyzed surface was polished between the axes *a* and *b*, on bisectrix, parallel to the one of cleavage plans. Finally, quartz (SiO_2) belongs to tectosilicates group and hexagonal crystal system. Our analyzed random surface as regarding the crystallographic axes, because their mineral is largely used to lapidaries and industry without orientation and we needed to understand this surface without orientation [2].

The polishing materials used in this article are generally used by lapidaries that polish colored gemstones in Brazil. The most common is chromium oxide (Cr_2O_3) and the powder by diamond (C) is used only in special cuts; another two powders are aluminum oxide (Al_2O_3) and cerium oxide (Ce_2O_3). In the process of polishing with this material, specific fluids are added to each one. The chromium oxide uses only water, the diamond powder uses soybean oil, the aluminum oxide uses water with soup, and the cerium oxide uses only water. The mineral surfaces react in different ways for each polishing material due to the chemical composition and grain size.

2.2 Methods for Assessment and Analysis

2.2.1 General

First, four groups with six mentioned gemstones were prepared through all steps by lapidation, which lasts 5–10 min working time and 500 rpm by velocity in each one. In the last step, the polishing, the samples were divided into four groups, each one with polishing powder to simulate the current process of cutting.

The polished samples were characterized with three equipments. The Reflectivity Meter Presidium used in the gemmological area to identify the type of gem through the absorption (index of refraction) and reflection by light. In addition, the Surface Roughness Measuring Instrument Kosakalab Surfcorder SE1700α was used, which through one diamond tip stylus measures surface roughness and waviness, with calibration in *X* and *Z* directions, of which measure resolution is 0.01 μm or 10 nm. Finally, the Confocal Microscope Leica DCM3D constructs image information with sample scanning vertically in predefined steps during which every point on the surface passes through the focus level, with resolution down to 0.1 nm.

2.2.2 Reflectivity Meter Presidium

The polished samples were prepared with acetone solution placed in a beaker for 10 min vibrating with ultrasonic equipment. They were analyzed three consecutive times in different regions on the sample and the arithmetic mean was calculated with the results—Table 1. For the garnet sample, the best result was Al_2O_3 featuring

Table 1 Selected results by reflectivity meter presidium

Gemological minerals	Aluminum oxide	Cerium oxide	Chromium oxide	Diamond
Garnet	39.66	36.66	38.00	38.33
Topaz	27.33	39.00	28.00	27.66
Beryl	23.66	25.00	25.33	24.66
Tourmaline	28.33	26.33	29.00	28.00
Spodumene	29.33	29.33	30.00	30.33
Quartz	22.33	23.00	22.66	23.33

the reflection index of 39.66. For the topaz, the best result was with Ce_2O_3 and reflection index by 39.00. For the beryl, tourmaline, and spodumene the best material was Cr_2O_3 with the numbers 25.33/29.00/30.00, respectively. Finally, the quartz showed best results with diamond powder with 23.33.

The numbers of reflection are related with the refraction index by each mineral. For presenting a high number of reflection, it is necessary to have high refraction index, following it by gemstone minerals: garnet (1.72–1.756), topaz (1.61–1.643), beryl (1.565–1.602), tourmaline (1.614–1.666), spodumene (1.660–1.681), and quartz (1.544–1.553) [3].

2.2.3 Confocal Microscope Leica DCM3D

In these steps by analysis, the samples didn't need preparation; it's necessary only to be cleaned. The aim was to generate 3D surfaces images and rough graphics. The polished samples were characterized and compared with each other through the numeration by Ra, which represents the average roughness defined by the arithmetic mean of the absolute values of the average profile departures (peaks and valleys) [4]. The lower Ra numbers provide the smooth surface and consequently lower angle bend by light reflection. When the surfaces have many peaks and valleys, the path covered by light reflection can be changed in many different angles, providing leakage by light and where the surface is smooth the light reflection can be altered, without changing the angles by reflection. Table 2 shows the roughness results about the arithmetic mean between three consecutive measurements in three different places on the sample. Figures 1 and 2 show images of polished spodumene with diamond powder, oil, and lead and tin disk, created in confocal microscope Leica DCM3D.

The polished samples were analyzed by Kosakalab Instrument affixed on hard plastic clay, which ensures a fixed surface and no movement. The slope of equipment was adjusted on *Z* axes, the cutoff specific for the range of polished plans, such as 0.08 and 0.25 for Ra < -0.02 and 0.02–0.1, respectively. The distance covered by diamond tip will depend on the cutoff configured, lower roughness, lower distance covered, and high resolution. The diamond tip velocity is 0.1 mm/s with 4,800 registers (Filter Profile GAUSS). Table 2 shows the measurement (arithmetic mean between three measures) which the diamond powder presented a better

Table 2 Results about Ra numbers (μm) ISO 4287

Gemological minerals	Aluminum oxide	Cerium oxide	Chromium oxide	Diamond
Garnet	0.002	0.005	0.003	0.030
Topaz	0.024	0.049	0.003	0.002
Beryl	0.011	0.017	0.002	0.003
Tourmaline	0.023	0.019	0.019	0.005
Spodumene	0.006	0.041	0.002	0.005
Quartz	0.003	0.005	0.013	0.015

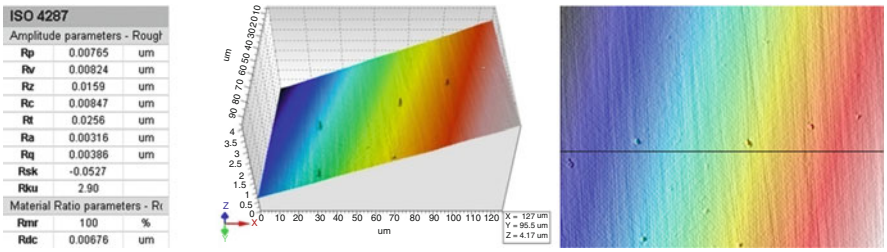

Fig. 1 *Left* to *right*, Table about analyses by Spodumene roughness, 3D images, 2D images about point by roughness analyses

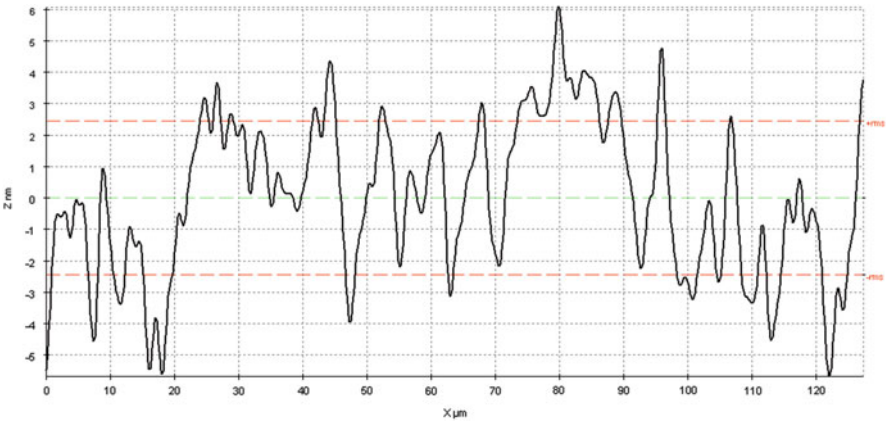

Fig. 2 Roughness graphic by spodumene polished with diamond powder, soybean oil, and lead and tin disk. Surface Roughness Measuring Instrument Kosakalab Surfcorder SE1700α

quality of surface. The figure below shows one graphic generated with the software OriginPro with the data by Kosakalab instrument on the garnet polished surface with four kinds of polishing materials. The first graphic on the left shows the roughness profile with x axes (0–240 μm) and the second graphic on the right is the same measurements but with short scale on *x* axes (70–90 μm) (Fig. 3).

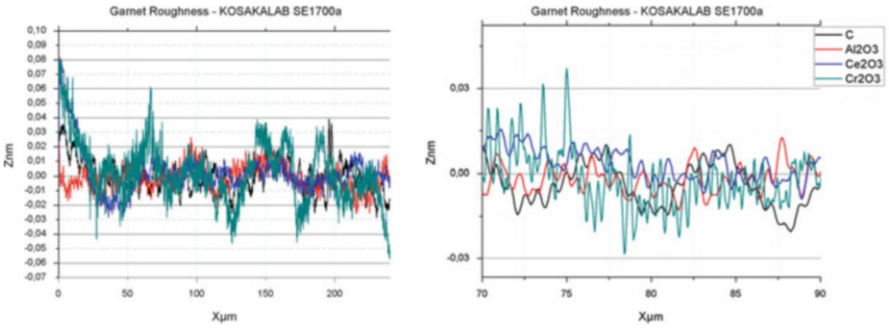

Fig. 3 Garnet roughness surface. *Left* complete graphic with *x* scale (0–240) and *right x* scale (70–90)

Table 3 Results about Ra numbers (μm)—KOSAKALAB SE1700α

Gemological minerals	Aluminum oxide	Cerium oxide	Chromium oxide	Diamond
Garnet	0.010	0.009	0.020	0.009
Topaz	0.010	0.010	0.031	0.006
Beryl	0.009	0.008	0.024	0.007
Tourmaline	0.019	0.030	0.018	0.007
Spodumene	0.017	0.017	0.012	0.010
Quartz	0.012	0.006	0.011	0.012

3 Results

As already mentioned in the essays above, the results are variant. For analysis realization, the same samples were used in three pieces of equipment, of which the aim was to define the best polishing powder for each mineral. Therefore, observations (e.g., "Tables 1, 2, and 3") presented outline results. The first essay on Reflectivity Meter needs to be analyzed singly, because their results are altered by the index refraction. In addition, the essays of results of roughness were characterized among two pieces of equipment with possible interpretation and discussion. The microscope Leica DCM3D created layered images through optical means and another Kosakalab instrument through physical means. Second, specifications provided by the Leica DCM3D have 0.1 nm resolution and Kosakalab Surface Roughness has measurement 10 nm resolution.

4 Discussion

First of all, the analyses on Reflectivity Meter enable discussions about the comparison among the same minerals with different polishing materials. The recognition of the column on table that presents high value represents the best polishing

material. Therefore, the same cannot be done with analysis by roughness; the results from two pieces of equipment and samples have discrepancies. It is necessary to take the scale into consideration by analyses in nanometers and variations can occur up to 10 %. To obtain more information about the surface, we should receive results from a Scanning Electrical Microscopy and observe the flatness on surfaces to compare with the previous results.

5 Conclusions

To provide concise conclusions, the analyses show us that polished surfaces have scales on tenths of nanometers related to polishing materials, kind of minerals, and kind of lubricants. Preferably to identify the best quality surface by which the reflection of the light on surface can be obtained, use the Reflectivity Meter. Therefore, complementary studies need to be done.

References

1. Sinkankas J (1984) Gem cutting–a lapidary's manual. Van Nostrand Reinhold, New York
2. Klein C, Hurlbut CS Jr (1993) Manual of mineralogy. After James D. Dana. Wiley, New York
3. Schulmann W (2002) Gemas do Mundo. Tradução por Mario Del Rey. 9. ed. ampl. e atual. Ao Livro Técnico, Rio de Janeiro
4. Hutchings IM (1992) Tribology–friction and wear of engineering materials. Butterworth-Heinemann, Cambridge

Minerals of Bauxites and Residues: Problems of Processing and Enrichment (Russia)

Olga Kotova, Galina Gasaleeva, and Aleksandr Vakhrushev

Abstract The complex of mineralogical methods was developed to obtain reliable data about mineral composition of bauxites and new crystal-chemical information (the whole cycle of used chemical elements, methods of residue utilization, and position of residue tails in dump pits). Natural and technogenic structures were studied as sources of necessary chemical elements and useful properties. Four main mineral types of bauxites (Vezhayu-Vorykvinskoe deposit) were studied. X-ray amorphous phase was determined in all bauxite types except kaolinite–boehmite types. The morphometric analysis of fine component of Vezhayu-Vorykvinskoe bauxites was developed and tested by using the method of small-angle scattering, which allowed defining the morphometric features of mineral grains of submicron size and their aggregational character.

New data on the composition of fine classes of bauxite minerals and their residues have been received. For example, mineral gold and tellurium were found in bauxites of Middle Timan. It is shown that fine component of hematite–shamosite–boehmite and kaolinite–boehmite bauxites (Vezhayu-Vorykvinskoe deposit, Russia) is formed by predominant mineral particles with sizes from 20 to 40 nm. Morphostructural characteristics of mineral grains allow predicting ore behavior in technological processes and the loss of aluminum during enrichment. Innovative experiments in the area of adsorbophysical fields during raw processing and enrichment were presented. The influence of laser irradiation on mineral substance of bauxite was studied. A new method of ore preparation for low-ferriferous bauxite enrichment was presented. This innovation can be applied for bauxite processing. It results in concentration of titanium and formation of corundum phases. This method increases efficiency and completeness of bauxite processing. Currently rare earth elements are extracted from bauxites apart from aluminum.

The processing of bauxites into alumina results in the formation of considerable residues—more than one million tons in every aluminum production in Russia.

O. Kotova (✉) • A. Vakhrushev
Institute of Geology, Komi SC UB RAS, 54 Pervomayskaya Street, Syktyvkar, Russia
e-mail: kotova@geo.komisc.ru

G. Gasaleeva
OJSC Uralmekhanobr, 87 Khokhryakov Street, Ekaterinburg, Russia

F. Dong (ed.), *Proceedings of the 11th International Congress for Applied Mineralogy (ICAM)*, Springer Geochemistry/Mineralogy,
DOI 10.1007/978-3-319-13948-7_25

The bauxite residues show considerable amount of amorphous structures (floccules) including ferriferous minerals. The material composition of the residues shows the prospection of iron extraction technologies, especially considering surface physics of extracted particles.

Keywords Mineral bauxites • Mineral residues • Processing and extraction of bauxites and residues

1 Introduction

Traditionally bauxites are observed as the source of aluminum. The basic idea of the paper is the revival of interest for fundamental concepts—a mineral as the carrier of chemical elements and useful properties, but at the new predictive (informative) level of high instrumental technologies and progress of experiment in the processes of ore preparation and enrichment of minerals and products of their processing by the example of bauxites. For successful commercialization of bauxites, the deep study of bauxite ores with modern methods of mineralogical studies, involving all the mineral substances, expansion of the list of produced useful components, and products with new properties is necessary.

The fundamental problems of detection, mineralogical-geochemical estimation, and recovery of fine components of bauxite ore and residues, which are not utilized at present, have been observed.

2 Materials and Methods

Mineral types of bauxites were studied during field works in Vezhayu-Vorykvinskoe deposit (Russia) by the classical methods including Mossbauer spectroscopy.

Applying X-ray small-angle scattering method to bauxites, we showed that the rocks include fine particles with linear size equal to 40 nm. To prove the data of small-angle scattering, we tested the samples of hematite–boehmite bauxites from the Vezhayu-Vorykvinskoe deposit with the help of electron microscopy. Thus, the results of small-angle scattering comply with electron microscopy results [1].

The method of Mossbauer spectroscopy gives a unique possibility to study the phase composition (including phase definition of nanosize grains) and crystal-chemical features of ferriferous minerals in bauxites with information from other methods as the basis for interpretation of Mossbauer spectra.

By the quantitative distribution in ferriferous phases, the series of the studied bauxite samples is divided into predominantly oxide and silicate types of iron localization. The areas of Mossbauer spectra well correlate with contents of iron oxides according to chemical analysis data.

The bauxite residues of aluminum production from Nikolaev and Ural (NAP and UAP) were studied. The magnetic separation of source residues and residues with dehydroxylated surface was carried out.

3 Results

Hematite. Our data testify to that hematite from Vezhayu-Vorykvinskoe deposit is characterized by isomorphic replacement of iron by aluminum in all the studied samples. The quantity of isomorphically hematite-embedded aluminum does not decrease lower 7 at.% from quantity of iron. All hematite in the deposit is represented by Al-hematite variety.

In hematite–chamosite–boehmite bauxites, the major part of iron is embedded into Al-hematite, the content of which is 11.9 %; the content of isomorphic aluminum is at 12 % from quantity of iron (Table 1).

It means that about 2 % from total aluminum is included in hematite structure and will be lost during processing of bauxites.

The kaolinite–boehmite bauxites contain Al-hematite less 1.3 %, isomorphous aluminum at 13 % (Table 1); aluminum losses make less 0.3 %. In hematite–boehmite bauxites Al-hematite makes 17.4 %. Aluminum losses make more 2.8 %.

Goethite. The novelty of our studies is in determining significant amounts of goethite (6–7 %) in the content of mineral types of bauxites from Vezhayu-Vorykvinskoe deposit by the Mossbauer method.

All the investigated samples along with a goethite always present haematite. All the goethite-containing samples present isomorphic replacement of iron by aluminum in goethite. The goethite is subdivided into two varieties: magnetic and superparamagnetic (Table 1). The magnetic goethite predominates. The superparamagnetic goethite is characterized by small size of particles <20 nm.

The diffractograms do not represent goethite due to the small size of particles. The thermograms represent discernible endopeaks in (between) 80–100 °C and 310–330 °C which are characteristic for fine-disperse goethite and hydrogoethite.

Chamosite. Our studies demonstrated that certain mineral types of bauxites in the deposit largely (to 6–7 %) present X-ray amorphous goethite (Table 1). According to X-ray diffraction data all the chamosite-containing samples show two polymorphic varieties of chamosite: monocline and rhomboid.

Kaolinite. Kaolinite in bauxites is usually considered as originated debauxitization. In the content of X-ray amorphous phase of hematite–boehmite bauxites a mineral is found with the structure close to kaolinite. In kaolinite–boehmite bauxites the kaolinite part makes 19 %. By the Mossbauer method it is determined that half of iron in these bauxites is a part of kaolinite with predominance of bivalent iron.

Among four studied mineral types of bauxites from Vezhayu-Vorykvinskoe deposit (hematite–boehmite, hematite–chamosite–boehmite, chamosite–boehmite, kaolinite–boehmite), hematite–boehmite and hematite–chamosite–boehmite types

Table 1 Mossbauer spectra of bauxite mineral varieties

Hematite–chamosite–boehmite bauxite

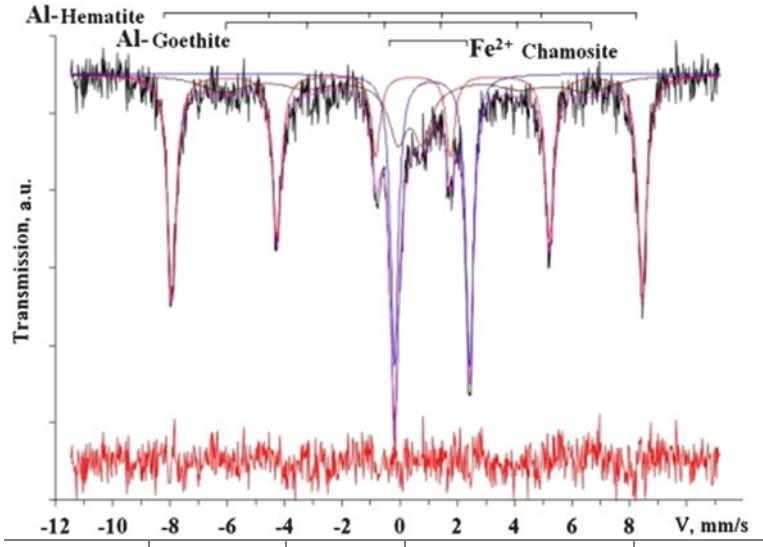

Kaolinite–boehmite bauxite

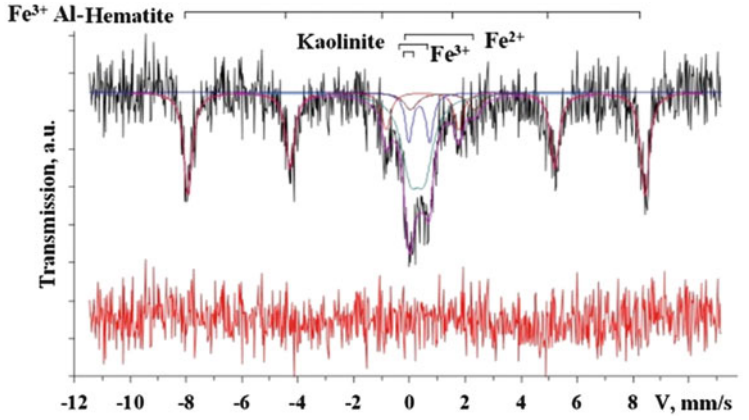

QS (mm/s)	IS (mm/s)	S (a.u.)	Position Fe	Fe^{2+}/Fe^{3+}	QS (mm/s)	IS (mm/s)	S (a.u.)	Position Fe	Fe^{2+}/Fe^{3+}
−0.21	0.37	46.31	Al-hematite (12 at.% Al)	–	−0.21	0.37	50.59	Al-hematite (13 at.% Al)	–
−0.28	0.37	17.48	Al-goethite (m)	–	0.75 (6)	0.36 (3)	9.41	Al-goethite(s)	–
0.85 (4)	0.37 (2)	11.00	Al-goethite (s)		2.3 (8)	1.2 (4)	6.4	Fe^{2+}VI, kaolinite	0.19
2.620 (5)	1.133 (3)	25.21	Fe^{2+}VI(M2), chamosite	>8	0.5 (2)	0.3 (1)	33.59	Fe^{3+}VI, kaolinite	

Hematite–boehmite bauxite

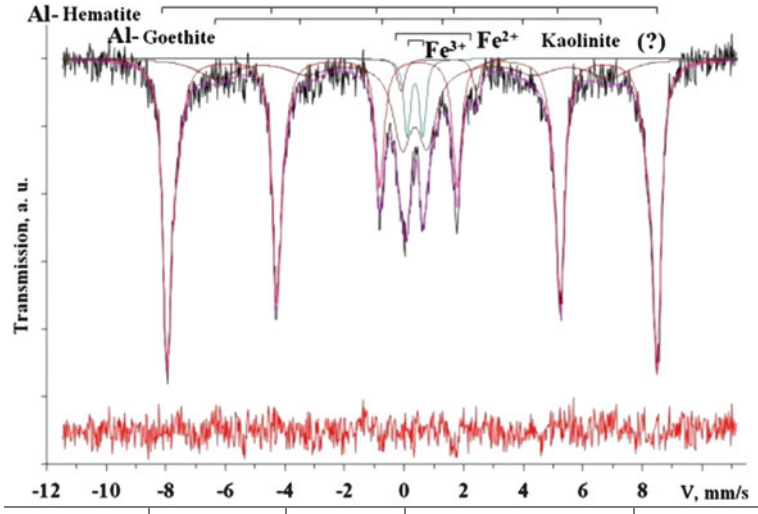

Chamosite–boehmite bauxite

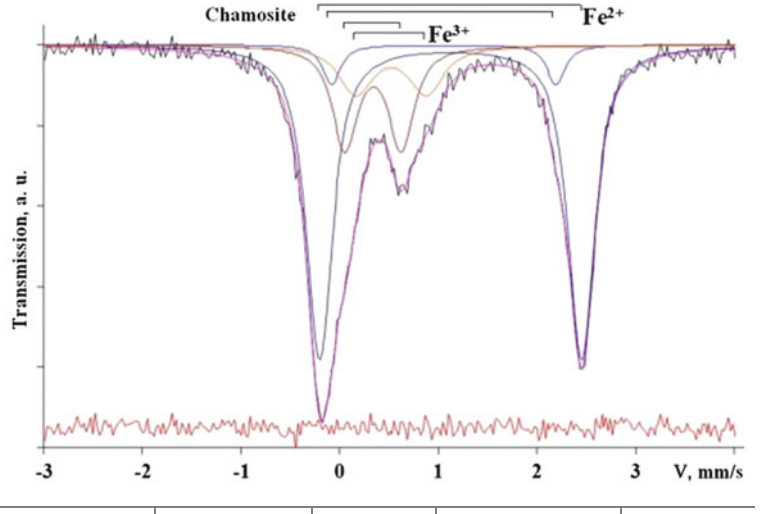

QS (mm/s)	IS (mm/s)	S (a.u.)	Position Fe	Fe^{2+}/Fe^{3+}	QS (mm/s)	IS (mm/s)	S (a.u.)	Position Fe	Fe^{2+}/Fe^{3+}
−0.21	0.37	43.04	Al-hematite (9 at.% Al)	–	2.654 (3)	1.124 (1)	62.8	Fe^{2+}VI(M2), chamosite	2.15
−0.22	0.38	23.18	(>16 at.% Al)		2.28 (2)	1.057 (9)	5.5	Fe^{2+}VI(M1), chamosite	
−0.25	0.40	13.90	Al-goethite (m)	–	0.57 (1)	0.341 (6)	19.5	Fe^{3+}VI chamosite	
0.83 (4)	0.35 (2)	12.82	Al-goethite (s)		0.71 (2)	0.52 (2)	12.2	Fe^{3+}VI, chamosite	
0.52 (4)	1.16 (2)	2.33	Fe^{2+}VI, “kaolinite”	0.50					
0.53 (2)	0.36 (7)	4.7	Fe^{3+}VI, “kaolinite”						

contain significant amount of goethite (6–7 %), whose essential part (not less than 38–48 %) is in X-ray amorphous conditions.

Hematite and goethite in bauxites of Vezhayu-Vorykvinskoe deposit contain the isomorphic admixture of aluminum (not less than 2–3 % from total aluminum) which is lost during Bayer processing [1].

4 Discussion

4.1 Method of Preliminary Preparation of Bauxites for Extraction

To prepare low-quality bauxites for the Bayer processing, various methods of extraction are used.

It is necessary to take into account the difference of properties of basic ore minerals for ore preparation.

Bauxites are complex, thin, and ultradisperse on valuable components and hard-to-enrich ores. Considerable "diffusion" of mineral concentration practically always results in economical inexpediency of their developments by the existing methods and demands special technological solutions to process them.

The method of laser processing of kaolinite–boehmite bauxites which results in redistribution of matter with the agglomeration of titanium minerals and formation of new phases, accessible for classic processing methods, was developed. According to statistical interpretation of microprobe scanning data, the content of titanium increased on average 1.7 times. The crystallization of a new phase (possibly corundum) was observed.

4.2 Utilization of Bauxite Residues

Bauxite processing to alumina results in the formation of significant amount of wastes—bauxite residues. About 200 million tons of the given products were accumulated in Russia. From aluminous department of factories, the residues in the form of pulp arrive to residue storages which contaminate environment and increase costs of basic products. Research works on residue processing were held by research institutes both in Russia [2] and in other countries, including China [3]. Their studies observed two basic approaches of processing—pyro- and hydro-metallurgical, and also their combinations. By the first method the basic stage after drying is regenerative electrical melting, or annealing in mine furnaces, or fluid-bed furnaces. The hydrometallurgical method is characterized by essentially smaller capital and operational expenses than the pyrometallurgical one. Here the acid

methods of mineral recovery are implemented. However, both processes are low and nonprofitable.

Concentrating operations are relatively low cost. The gold recovery method from bauxite residues was studied in Ukraine. The residues from the Nikolaev aluminum production showed free gold with the content 0.2 g/t. The basic mineral phases of ferruginous residues from the Nikolaev production are in decreasing order: goethite, hydrogoethite, hematite, and magnetite. Two alternatives schemes were developed for concentration: gravitational-magnetic and magnetic-gravitational. The first scheme, the lowest cost, resulted in the concentrate containing gold, zircon, and rutile with yield 1.56–2.1 % which was then re-cleaned by dry magnetic separation. Besides, by this scheme the ferruginous product composition hematite–goethite–hydrogoethite (Fetotal—51 %, yield—35 %) product was received, which was considered as the analogue of brown ore, and also zircon and rutile concentrates were obtained. The given technology is profitable [4].

4.3 Influence of Chamosite on the Process of Residue Concentration

According to the phase analysis, the bauxites of Timan deposit (Vezhayu-Vorykvinskoe site) and Northern Ural bauxite mine considerably differ from each other both in chemical and phase composition. Their major difference consists in the increased content of chamosite in Timan bauxites which makes 17.2 % against 8.8 % in bauxites from the mine, and which on average is 15 %.

The mineralogical composition of the residues from the Ural production sharply differs from the mineralogical composition of residues from Nikolaev aluminum production by the low content of hematite, the presence of chamosite, increased content of carbonate rocks, and alumosilicate. The NAP residues are represented by goethite, hydrogoethite, and hematite (87.4 %) which are well extracted by high gradient magnetic separation with yield of ferrous concentrate with Fetotal = 52.1 %.

From the X-ray diagram [4] it follows that the basic iron-ore minerals in Ural residues are hematite, chamosite, and goethite. Iron is also in magnetite (less than 0.1 %), in hard dissoluble silicates related to amphibole group, and in free state. The main part of nonmetallic minerals is represented by calcite and sodium hydroaluminosilicates. Apart from these minerals, quartz, diaspore, perovskite, glauconite, and illite were found.

The total content of iron minerals in the studied samples of Ural residues makes only 53 % (at 1.65 times lower than in NAP residues). At that 15 % are represented by chamosite, the formula of which is $Fe_4Al[AlSi_2O_{10}(OH)_6]$. The iron content in chamosite fluctuates from 25 to 28 % by reference data [4]. The actual study

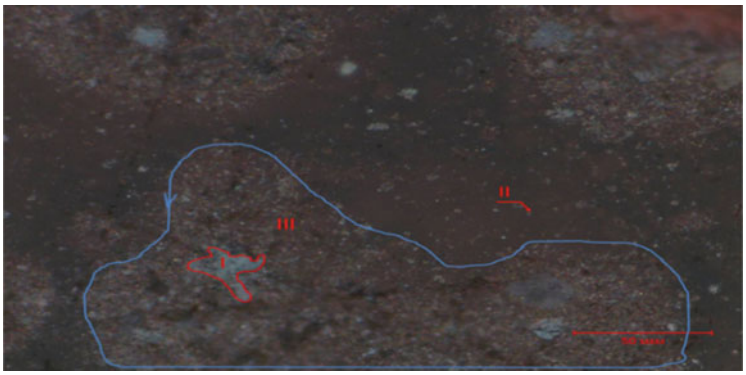

Fig. 1 Initial probe of bauxite residues of sample 1. The hematite aggregate (I) surrounded by micrograins of ore and nonmetallic minerals (III). II—free micrograins of minerals. Polished section, reflected light, without the analyzer, 500×

demonstrates its content as only 18 % which is resulted from the fact that in crystal lattice it is substituted partially by other elements (Mn and Mg).

The structure of minerals was determined during the study of polish sections under a microscope with software "Mineral–7." Figure 1 presents the image of structural elements of the initial sample of residues.

The image in Fig. 1 confirms the presence of amorphous formations (flocculas) with grains of ferruginous minerals. It is necessary to perform preliminary disaggregation of initial residue samples.

The physical methods were chosen as basic methods of extraction of residues (magnetic and gravitational methods) as well as the physical-chemical methods—attritioning of product in rotary-pulse device with processes of cavitation and chemical processes of surface processing by hexametaphosphate for floccula dispergation.

Surface physics. The distribution of minerals in extraction products was studied. The final concentrate contains general iron from 46.3 to 50.6 %. The hematite content makes 38–46 %, and chamosite—26–30 % accordingly. Thus, by their magnetic properties these two minerals are not partitioned but concentrated in magnetic products evenly. Both minerals have close magnetic receptivity.

Figures 2 and 3 present curves of distribution of chamosite and hematite content in enrichment products. They show considerable difference of results of magnetic and gravitational methods of extraction. The gravitational method is much more effective. Conclusion: without surface modification chamosite and hematite possess almost equal magnetic properties and are not effectively partitioned by magnetic methods of extraction. At that chamosite considerably decreases the quality of iron concentrate due to low iron content in it. Gravitation for chamosite separation is a preferential operation, as it allows achieving the content of chamosite in tails and intermediate product of concentration table 49–52 % against 43 % by results of magnetic separation. It has been explained by more considerable differences between chamosite and hematite on gravity (3.0–3.4 g/cm^3 against 4.9–5.4 g/cm^3

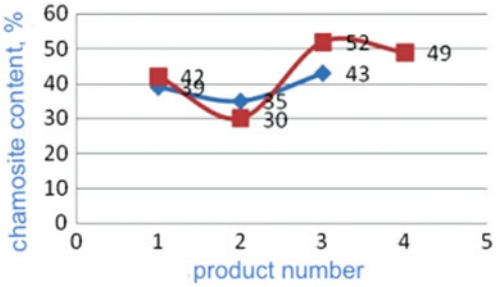

Fig. 2 Chamosite distribution in extraction products of magnetic separation (*blue*) and gravitational method (*red*)

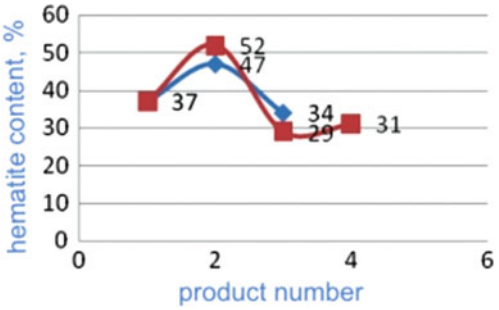

Fig. 3 Hematite distribution in extraction products of magnetic separation (*blue*) and gravitational method (*red*)

accordingly). With increasing size the hematite content decreased and chamosite content increased, that is, hematite is concentrated in finer fractions, and chamosite—in larger fractions. Thus, it is possible to divide these minerals by size.

According to the final scheme of concentration, the summary magnetic concentrate was obtained with the content of iron 46.3–50.64 % and yield 6.3 %. The mineralogical composition of final concentrates was studied.

Their separation by magnetic methods is not efficient. Increasing the efficiency of separation by magnetic methods is possible by the directional change of surface properties of partitioned minerals at the break of structure of hydroxyl cover [5]. Such approach is promising for small particles. The samples of residues form Ural aluminum production were studied. The magnetic separation of initial residues and residues with dehydroxylated surface was carried out.

After separation and dehydroxylation of I type OH groups the chemical composition of products was insignificantly different from each other [6]. The changes occurred in the yield and mineral composition of dehydroxylated products. So the nonmagnetic fraction of the product with dehydroxylated surface increased in comparison with source at 22 %. Diffractograms of source products were insignificantly different from each other; and the products with modified surface present redistribution in mineral composition. Two basic minerals—chamosite and hematite—are diagnosed in the bauxite residues. The intensity of main peak of chamosite in the nonmagnetic product with modified surface is much lower than in the initial product, and vice versa, the sample of magnetic product with modified

surface shows considerable increasing intensity. After withdrawal of I type OH groups the magnetic features of chamosite are changed and the ratio of magnetic and nonmagnetic fractions is modified. Thus, due to change of surface properties, it is possible to increase the efficiency of specific valuable product.

5 Conclusions

The fine-disperse component of hematite–chamosite–boehmite and kaolinite–boehmite bauxites of Vezhayu-Vorykvinskoe deposit are predominated by mineral particles with sizes from 20 to 40 nm that influence physical and chemical properties during processing and concentration.

Hematite and goethite in bauxites of Vezhayu-Vorykvinskoe deposit contain the isomorphic impurity of aluminum (not less than 2–3 % from total aluminum), which is lost at repartition of bauxites to alumina by Bayer method.

Aggregation processes (concentration of useful component in the bauxite matrix at laser influence) can become alternative methods of increasing efficiency of utilization of mineral raw contrary to dispergation.

1. The material composition of bauxite residues from UAP was studied:
   - total content of iron minerals in the studied samples makes 53 % (at 1.65 times lower than in bauxite residues form Nikolaev aluminum production); at that 15 % from them are represented by chamosite with iron content at 18 %;
2. Perspective directions of concentration of residues from UAP-RUSAL:
   - magnetic separation in weak field—for magnetite recovery;
   - high gradient magnetic separation for recovery of hematite, chamosite, and goethite;
   - gravitational concentration on a concentration table for preparation of magnetic products;
   - selective flocculating of tails with subsequent recovery of iron concentrates (perspective direction).
3. The considerable influence of chamosite's presence on a magnetic separation toward efficiency drop is demonstrated. The gravitational concentration demonstrated considerably higher results of separation. Also there is a dependence of the content of chamosite and hematite from the size of initial bauxite residues.
4. The influence of surface condition on redistribution of minerals in magnetic and nonmagnetic fractions was demonstrated.

Acknowledgment The work is executed within the Project 12-M-35-2055 Development of scientific principles of flotation recovery of valuable minerals from hard-to-enrich mineral raw on the basis of creation of selectively acting reagents and new technological solutions of ore concentration and 12-5-6-016-ARKTIKA.

References

1. Vakhrushev AV, Kotova OB (2011) Timan bauxites: distribution, composition, industrial application (Komi Republic, Russia), Proceedings of ICAM, pp 741–748
2. Smirnov DI, Molchanova TV, Vodolazov LI, Peganov VI (2002) Methods of enrichment of bauxite residues. Nonferrous Met 8:64–69
3. Wanchao L, Yang J, Xiao B (2009) Review on treatment and utilization of bauxite residues in China. Int J Miner Process 93:220–231
4. Gazaleeva GI et al (2012) Chamosite influence on extraction of bauxite residues. International Congress, Ekaterinburg, pp 210–214
5. Kotova OB (2004) Surface processes in fine disperse mineral systems. UB RAS, Ekaterinburg
6. Kotova OB (2000) Adsorbophysical methods of enrichment of fine mineral raw. Nauka, Saint-Petersburg, p 80

Effects of Sintering Temperature on Crystallization Behavior and Performance of Glass Ceramics from Coal Fly Ash

Tongjiang Peng, Chao Cao, and Hongjuan Sun

Abstract The glass ceramics were prepared from coal fly ash, limestone, and Na_2CO_3 by sintering processes. Effects of the crystallization temperature (850–1,100 °C) on crystallization behavior, microstructure, sintering character, and chemical stability of the glass-ceramics samples were analyzed by the means of DTA, XRD, SEM, and other analytical methods. The results show that the main crystalline phase of as-prepared glass ceramics after crystallization treatment is gehlenite ($Ca_2Al_2SiO_7$). The species of crystalline phases remain the same; however, the main crystalline intensity, line shrinkage rate, and bulk density increase first and then decrease with the increasing of heat treatment temperature. Water absorption of the samples was reduced as the heat treatment temperature rises. The glass ceramics display high-performance crystallization properties and chemical stability. The optimized glass ceramics with desired sintering character and chemical stability were obtained by crystallization at 1,050 °C.

Keywords Coal fly ash • Glass ceramics • Crystallization • Sintering

1 Introduction

Glass ceramics are a kind of fine-grained polycrystalline materials with dual characteristics of glass and ceramics, which are prepared from glasses of suitable compositions after heat-treated and controlled crystallization [1]. It has been widely used in architectural ornament, machine, chemical industry, electronics and

T. Peng (✉) • H. Sun
Key Laboratory of Solid Waste Treatment and Resource Recycle, Ministry of Education, Mianyang 621010, China

Institute of Mineral, Materials and Application, Southwest University of Science and Technology, Mianyang 621010, China
e-mail: tjpeng@swust.edu.cn

C. Cao
Key Laboratory of Solid Waste Treatment and Resource Recycle, Ministry of Education, Mianyang 621010, China

F. Dong (ed.), *Proceedings of the 11th International Congress for Applied Mineralogy (ICAM)*, Springer Geochemistry/Mineralogy,
DOI 10.1007/978-3-319-13948-7_26

electrical engineering, and spaceflight because of its excellent performances on mechanical properties, chemical stability, thermal stability, and insulativity [2].

A huge amount of coal fly ash (CFA) was generated from thermal power plant. As in China, more than two billion tons of stockpiling coal fly ash has been accumulated over the years [3]. CFA has been widely used as a supplementary cementitious material in Portland cement concrete, as mineral admixture in blended cements, and as soil conditioner for many years [4, 5]. However, most of the CFA is mainly deposited in the slag plants without utilization. Therefore, it is important to develop a novel method to utilize the industrial waste. Previous studies showed that CFA is mainly composed of SiO_2, Al_2O_3, CaO, and Fe_2O_3 [6]; it is feasible to use coal fly ash as a raw material to prepare glass matrices. The major phases of glass ceramics of wollastonites, feldspars, and pyroxenes have been prepared in the use of CFA as a raw material in ceramic products. Numerous scientists focused on the formula, crystal behavior, and mechanical properties of the glass ceramics while ignoring their chemical stability and sintering character over the years [7–12]. The key factor of heat treatment influences the properties of glass ceramics such as the composition and quantity of crystalline phase, the microstructure, morphological structure, porosity, etc. Consequently, in-depth research should pay attention to heat treatment effects.

This chapter discusses how coal fly ash with a certain amount of limestone and Na_2CO_3 has been used to prepare glass ceramics with routine sintering process. The phase composition and microstructure of the glass ceramics were characterized by XRD and SEM. Furthermore, the physicochemical properties such as shrinkage, bulk density, water absorption, and chemical resistance were measured. The effects of sintering temperatures on the properties of the glass ceramics were also discussed.

2 Experimental Procedure

Coal fly ash used in this research is collected from the thermal power plant located in Jiangyou of Sichuan province, China. The samples of limestone are from Ma Jiaoba in Sichuan, China. The chemical composition of CFA and limestone was determined by XRF (Axios, PANalytical B.V.). The chemical compositions of the raw materials are given in Table 1. It was clear that the main constituents of CFA were SiO_2, Al_2O_3, Fe_2O_3, and CaO. The chemical composition analysis indicated that CFA was typical high aluminum powder coal ash. Fe_2O_3 and TiO_2 can be used as nucleating agents which enhance crystallized process [13]. Since CFA contains Fe_2O_3 and TiO_2, there is no need to add other nucleating agents. Na_2CO_3 (analytically pure) is utilized to reduce the melting temperature and the melting viscosity. These raw materials were mixed together in agate pot by ball mill.

Well-mixed powder samples were melted in alumina crucible for 90 min in an electrically heated furnace at 1,400 °C to ensure homogeneity of the melts. The melts were rapidly poured into water to form parent glasses. The parent glass grain

Table 1 Chemical composition of raw materials (mass fraction, %)

Raw materials	SiO_2	Al_2O_3	Fe_2O_3	MgO	CaO	Na_2O	K_2O	TiO_2	L.O.I.
Coal fly ash	53.10	26.67	8.05	2.06	5.23	0.80	1.76	1.39	0.48
Limestone	0.15	0.16	0.09	0.40	55.70	–	–	–	43.51

Table 2 Chemical composition of the parent glasses (mass fraction, %)

Oxide	SiO_2	Al_2O_3	CaO	Fe_2O_3	MgO	Na_2O	K_2O	TiO_2
Content (wt%)	36.34	18.20	28.85	5.49	1.63	7.20	1.20	0.95

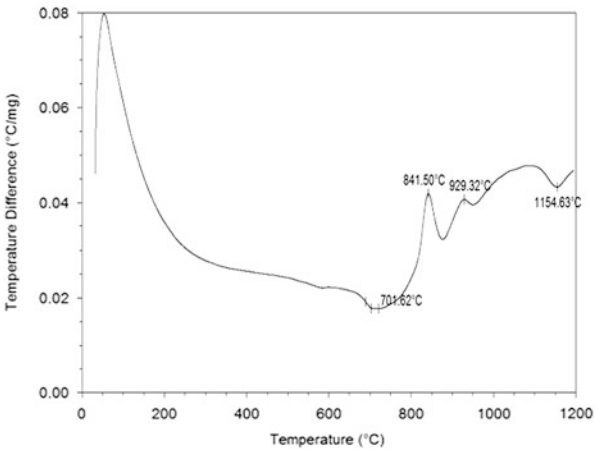

Fig. 1 DTA curve of the parent glass sample

is dried and then milled in a high-speed porcelain ball mill until the particle size becomes <74 μm. Chemical compositions of the parent glasses are given in Table 2. The glass powders are mixed with 5 % polyvinyl alcohol solution in the scale of 25:1. Columned parent glasses samples with 25 × 5 mm dimensions are prepared in the mold by uniaxial pressing (6 MPa).

Differential Thermal Analysis (DTA, heating rate 10 °C/min in nitrogen, from room temperature to 1,200 °C) is used to determine the heat treatment of the parent glass. From DTA curve of the parent glass sample (Fig. 1), the vitrification processes occurred around at $T_g = 702$ °C. The melting temperature of the glass sample is around $T_m = 1{,}155$ °C. Previous studies showed that the optimum nucleation temperature usually occurred in the range from 50 to 100 °C above the glass transition temperature [14, 15]. In our study, the nucleation temperature of the parent glass sample we chose is 760 °C. Prepared samples were heat treated at the nucleation temperature (T_g) at the holding time of 1.5 h and then heated at the rate of 5 °C/min to four different temperatures (850 °C, 900 °C, 950 °C, 1,000 °C, 1,050 °C, and 1,100 °C) at the holding time of 2 h, respectively.

The phase of the blast-furnace slag and obtained glass ceramics was examined by X-ray diffraction (XRD) (X' Pert PRO, PANalytical B.V.). The samples' surfaces were polished and corroded in HF (5 vol.%) for 20 s and then observed by scanning electron microscopy (SEM) (S440, LEO, Britain). The density of the samples was measured by the Archimedes method. Water absorption is measured according to the ISO standard 10545-3, 1995. Referring to GB/T 9966.3-2001, the chemical resistance of glass-ceramics samples corroded in the 10 % H_2SO_4 and 10 % NaOH solutions for 24 h and then the residual rate was calculated. Linear shrinkage was determined with an electronic digital caliper as the dimension difference between the green (L1) and the fired material (L2) by using Eq. (a): $L_s = 100 \times (L1 - L2)/L1$.

3 Results and Discussion

3.1 Crystallizing Phases

The sintering treatments at the crystallization temperature are effective, for all samples, to produce glass ceramics. The results are shown in Fig. 2. It showed different tendencies toward crystallization as a function of thermal treatment temperatures. The major phase of all the glass-ceramics samples was gehlenite ($Ca_2Al_2SiO_7$) ($d = 4.21$ Å, 3.87 Å, 3.29 Å, 3.02 Å, and 2.91 Å), and nepheline was the minor crystalline phase. In Fig. 2, there were notable differences in the peak intensity due to the different crystallization temperatures. As the crystallization temperature increases from 850 °C to 1,000 °C, the peak intensity of gehlenite strengthens gradually. When the crystallization temperature is up to 1,050 °C, the peak intensity weakens, which indicates that the crystalline phases are remelted because of the high temperature [16]. With an increase in temperature during crystallization treatment, the intensities of nepheline decreased. This phenomenon indicates that the higher crystallization temperature can convert nepheline to gehlenite.

3.2 Microstructural Characteristics

After crystallization processes in different temperatures, as shown in Fig. 3, spherical grains formed in the samples obviously. As the crystallization temperature rises, the spherical grains grew up gradually; in addition, the amount of the grains increased. As a result, the structures of the samples tend to be compact. Under the heat treatment of $T_c = 1{,}050$ °C for 2 h, the spherical grains become equirotal and

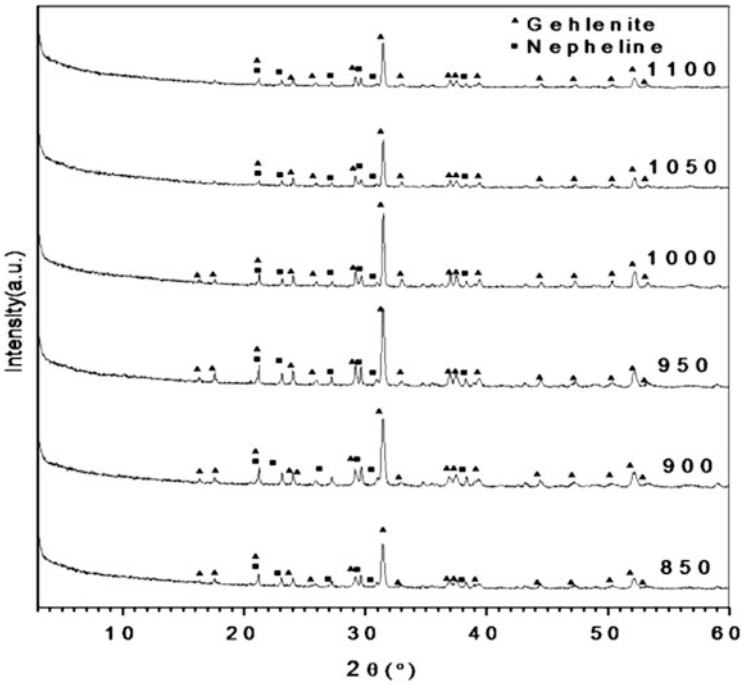

Fig. 2 XRD spectra of the glass-ceramics samples by crystallizing treatment at various temperatures

aswarm, the microstructure of glass ceramics becomes the most compact. When the crystallization temperature rises to 1,100 °C, as shown in Fig. 3f, part of the crystals begins to melt and agglomerate. These results are in agreement with XRD analysis.

3.3 The Physical and Chemical Properties

3.3.1 Linear Shrinkage and Bulk Density

The variation in linear shrinkage and bulk density with crystallization temperature is shown in Fig. 4. Samples show an increase in the linear shrinkages with firing temperature and reach a maximum value at 1,000 °C and then slightly decrease with the temperature increase. Bulk density depicts a similar trend to that of the linear shrinkage. Research shows that bulk density mainly depends on its pore structure and crystallinity. Glass ceramics with lower porosity and higher crystallinity show higher bulk density [12]. With increasing firing temperature in the range 850–1,000 °C, firing at crystallization temperature range results in a decrease in a constant shrinkage due to transformation of glass to well-crystallized gehlenite. Simultaneously, at temperatures higher than the glass transition temperature,

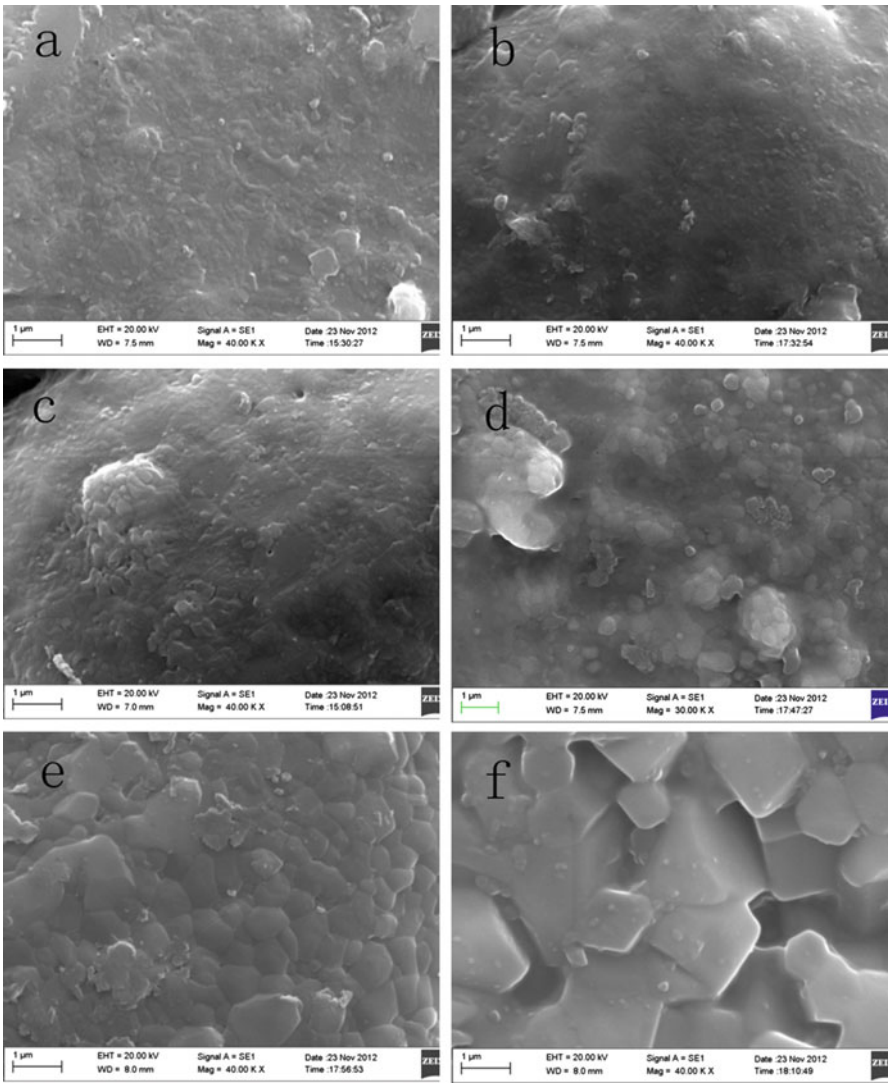

Fig. 3 SEM morphologic image of the glass-ceramics samples by crystallizing treatment at various crystallization temperature, (**a**) 850 °C; (**b**) 900 °C; (**c**) 950 °C; (**d**) 1,000 °C; (**e**) 1,050 °C; (**f**) 1,100 °C

softened glass resides at the grain boundaries of particulate solid pulls the particles together and leads to high shrinkage. As a result, the bulk density of samples increases gradually. Density decreases with increasing firing temperature up to 1,050 °C. The possible explanation is that expansion of the entrapped gases (such as CO_2 and N_2) leads to the decrease in density [17].

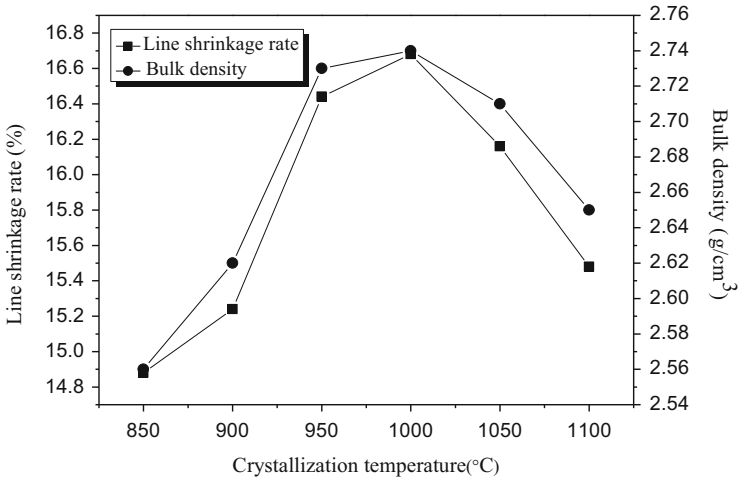

Fig. 4 Linear shrinkage of the glass-ceramics samples at various crystallization temperature

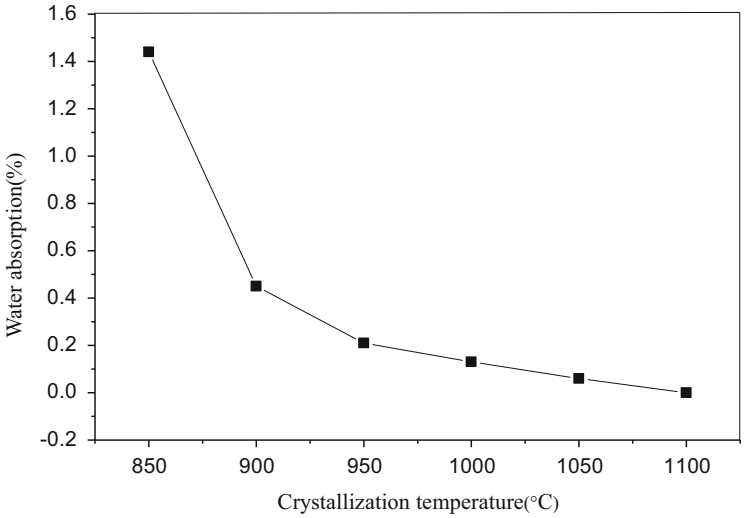

Fig. 5 Water absorption of the glass-ceramics samples at various crystallization temperature

3.3.2 Water Absorption

Water absorption as a function of firing temperatures is shown in Fig. 5. After crystallization treatment, water absorption of samples reduced significantly. As the crystallization temperature increased, water absorption decreased constantly. Water absorption is closely related to apparent porosity in theory [18]. As the firing treatment temperature rises with the increase of crystallization degree, the more

Table 3 Chemical stability of the glass ceramics

Crystallization temperature (°C)	850	900	950	1,000	1,050	1,100
Acid loss (%)	1.06	0.73	0.28	0.17	0.15	0.29
Alkali loss (%)	0.01	<0.01	<0.01	<0.01	<0.01	0.01

dense crystalline structure could be formed and the pore space between crystals gradually decreases. As a result, the apparent porosities of the samples reduce as well. The high crystallization degree caused a reduction of the open porosity so that the glass-ceramics material showed better water resistance when the fire temperature reached 1,100 °C.

3.3.3 Chemical Stability

The chemical resistance of samples was shown in Table 3. The chemical stability of glass-ceramics materials is directly associated with the composition and structure of the glass ceramics. Through the analysis of XRD, SEM, and water absorption, after crystallization treatment, it found that gehlenite is also generated besides nepheline in samples. Nepheline is easily dissolved in acid. The sample with firing temperature at 850 °C performs worst acid resistance because of its highest nepheline content as well as its lower compact structure. The increase of crystallization temperature caused the occurrence of more gehlenite phase and less nepheline phase in glass ceramics which causes samples to become more stable in stronger acid solution. The sample crystallization temperature at 1,050 °C with the highest crystallization degree and fine microstructure showed the most resistance to strong acid solution. When firing temperature is up to 1,100 °C, acid resistance of the sample decreased as part of gehlenite remelted and glass phase increased.

The glass-ceramics samples in this study showed good stability in NaOH solution. According to the Ginsberg method, the proper mixture ratio of oxides in raw material predicted optimized glass-ceramics formation. The glass phase, gehlenite crystals, and nepheline crystals, which are constituted by the basic units of silicon oxygen tetrahedron in the glass ceramics, have remarkable stability in alkaline environment [14].

4 Conclusions

This chapter discusses how the predominated amount of as-prepared glass-ceramics samples shows gehlenite ($Ca_2Al_2SiO_7$) phase, with a little amount of ($K(Na, K)_3Al_4Si_4O_{16}$) crystalline phase. The results show that the gehlenite phase increased with rising crystallization temperature and reached a maximum value at

1,000 °C and then decreased with rising temperature up to 1,050 °C. The nepheline phase transits to gehlenite phase with crystallization temperature over 1,000 °C.

As the heat treatment temperature is lower, the increase of crystallization temperature benefits the sintering of coal fly ash glass ceramics. Line shrinkage and bulk density were decreased along with the increase of crystallization temperature. Surface crystallization is a benefit for the water resistance of the glass-ceramics samples.

Coal fly ash glass ceramics show a good alkali resistance. The acid resistance property is comprehensively influenced by composition, the content of crystalline phase, and microscopic structure. The increase of gehlenite in fly ash glass ceramics can enhance its acid resistances, while nepheline crystalline phase decreases its acid resistances.

The optimized processes for preparing glass ceramics with desired liner shrinkage, bulk density, and acid corrosion resistance properties by heat treatment are first nucleating temperature of 780 °C and then crystallization treatment of 1,050 °C.

References

1. Astm D75-97 (1997) Standard practice for sampling aggregates. American Society for Testing & Materials, West Conshoshocken, Annual Book of ASTM Standards (04.03): Soil and rock, building stones, geotextiles, pp 16–20
2. Rawlings RD, Wu JP (2006) Boccaccini A R. Glass–ceramics: their production from wastes-a review. J Mater Sci 41(3):733–761
3. Barbieri L, Karamanov A, Corradi A et al (2008) Structure, chemical durability and crystallization behavior of incinerator-based glassy systems. J Non-Cryst Solids 354(2–9):521–528
4. Liu ZN, Zhao XC (2007) Actuality and countermeasure analysis of coal fly ash resource utilization as a low-cost absorbent. J Xi'an Univ Arch Tech (Nat Sci Ed) 39(5):690–694
5. Lu AX, Wang Y, Xiao ZH (2008) Effects of alkalis on crystallization and properties of MgO-Al_2O_3-SiO_2 system glass ceramics. Cent South Univ (Sci Technol) 39(1):42–47
6. Bian BX, Li Z (2005) Separation and utilization technology of fly ash. China University of Mining and Technology Press, Xuzhou, pp 123–151
7. Han HQ, Jiang TD (2001) Technology of using fly ash. Chemical Industry Press, Beijing, pp 10–11
8. Erola M, Gencb A, Ovecoglu ML (2000) Characterization of a glass-ceramic produced from thermal power plant fly ashes. Eur Ceram Soc 20:2209–2214
9. Park YJ, Moon SO, Heo J (2003) Crystalline phase control of glass ceramics obtained from sludge fly ash. Ceram Int 29:223–227
10. Qian GAR, Song Y (2006) Diopside-based glass-ceramics from MSW fly ash and bottom ash. Waste Manag 26:1462–1467
11. Furlani E, Bruckne S, Minichelli D (2008) Synthesis and characterization of ceramics from coal fly ash and incinerated paper mill sludge. Ceram Int 34:2137–3142
12. Ikeda K, Kinoshita H (2011) Production of high-strength glass-ceramics from industrial wastes using phase equilibrium diagram of CaO-Al_2O_3-SiO_2 system. J Solid Mech Mater Eng 5:209–218
13. Luan JD, Li AM, Su T et al (2010) Synthesis of nucleated glass-ceramics using oil shale fly ash. J Hazard Mater 173:427–432
14. Liu HY, Lu HX (2009) Preparation and properties of glass–ceramics derived from blast-furnace slag by a ceramic-sintering process. Ceram Int 35:3181–3184

15. Luan JD, Li AM, Cui XB et al (2010) Effect of nucleation and crystallization time on characteristics of glass ceramics from oil shale fly ash. Trans Mater Heat Treat 31(7):1–4
16. Cheng TW, Tu CC, Koa MS et al (2011) Production of glass–ceramics from incinerator ash using lab-scale and pilot-scale thermal plasma systems. Ceram Int 37:2437–2444
17. Li Y, Feng ZY, Yang H et al (2008) Crystallization of glass-ceramics with oil shale residue. Chin J Nonferrous Met 18(4):676–681
18. Maity S, Sarka BK (1996) Development of high-strength whiteware bodies. Eur Ceram Soc 16:1083–1088

The Oxidation–Reduction Mineralogical Features of Graphite Deposit in Pingdu, Shandong

Lang Qin and Xiuyun Chuan

Abstract The oxidation–reduction mineralogical features of graphite deposit in Pingdu Shandong province were studied by field researches, polarization microscope, X-ray diffraction (XRD), and SEM. The results show that the major rocks of the reduction graphite zone are graphite–quartz anorthosite and gabbro. The major rocks of the oxidation graphite zone are marble with graphite, biotite granite, and monzogranite. The main minerals of the reduction zone are plagioclase, pyroxene, quartz, pyrite, etc. The graphite is aphanitic graphite appearing as dense massive, layered, and spherical aggregates. The main minerals of the oxidation zone are calcite, quartz, K-feldspar, biotite, amphibole, chlorite, etc. The graphite is flake graphite uniformly dispersed in the loose and strongly eroded rocks. A large number of rocks in the area have suffered chloritization and regional metamorphism, indicating that the formation of the graphite deposit should be related with gabbro melting. The carbon source in the lower part was taken into the mine and then experienced regional metamorphism.

Keywords Graphite • Oxidation–reduction deposit • Mineralogical feature • Pingdu, Shandong

1 Introduction

Graphite is a kind of nonmetallic mineral with excellent physical and chemical properties: excellent electrical conductivity, excellent heat conductivity, and plasticity. It has good performance to withstand high temperatures. Other properties such as lubricity and coating properties are also outstanding.

Graphite is divided into aphanitic graphite and flake graphite. Flake graphite means natural crystalline graphite, while aphanitic graphite can be called amorphous graphite. Previous researches show that the better the crystallinity of graphite, the bigger the flake scale, the higher the carbon content, and the less the

L. Qin • X. Chuan (✉)
School of Earth and Space Science, Perking University, 5th Yiheyuan road, Beijing, China
e-mail: xychuan@pku.edu.cn

F. Dong (ed.), *Proceedings of the 11th International Congress for Applied Mineralogy (ICAM)*, Springer Geochemistry/Mineralogy,
DOI 10.1007/978-3-319-13948-7_27

impurities contains, the mineral properties and process performance are better. In the metallurgical industry, flake graphite is used to manufacture crucible, mold coating, etc. In the electrical industry, graphite is used to produce electrode, electrical brusher, etc. In the chemical industry, flake graphite is used to make acid and base resistance apparatus and high-temperature resistant and high-pressure resistant apparatus, while aphanitic graphite is used to manufacture coating materials, pencil leads, battery carbon rods, and high-temperature resistant material [1].

Graphite is mainly mineralized through metamorphism, which can be divided into contact metamorphism and sedimentary metamorphism [2]. The former kind is formed in the shale containing coal and other carbon-rich minerals that have gone through thermal metamorphism or carbonate decomposition; the latter one is formed in the sedimentary rocks that have suffered regional metamorphism and is distributed widely [3–7]. A wide range of formation conditions are for graphite with the changes of temperature and pressure. The carbon source can be organic or inorganic [8].

The graphite deposit is located to the east of the Yishu fault, at the boundary of Jiaolai basin and Jiaonan mountains. The main rocks contain graphite gneiss, including graphite marbles and even granite [9–15].

In this research, we discussed the forming conditions, such as temperature, pressure, and carbon source and the mineralogical characteristics and features of the graphite deposit. That's why we think this article is of significance to the study of graphite mines in this area.

2 Materials and Methods

2.1 General

More than 300 were samples collected from Liugezhuang, Zhougezhuang, Mencun of Pingdu graphite deposit, which can be divided into oxidation graphite and reduction graphite (Table 1). Polarization microscope (Nikon ECLipse LV100POL), X-ray powder diffraction (XRD Rigaku RINT 2000), SEM, and C-S analyzer (C-S-500) are used in our research. With all these methods, we figured out the different mineralogical features between the oxidation graphite and the reduction graphite.

The ore in the reduction zone is primary ore. Thickness of layer graphite ore body ranges from a few meters to tens of meters, even as thick as several 100 m. The dominant sulfur mineral in the ore is pyrite, which indicates high crystallization. Graphite, which is mostly agglomerated, layered, or spherical aggregated, featured with high carbon sequestration, is thin graded.

Graphite ore in oxidation zone mainly consists of gneiss and gneissic graphite marble. Graphite mainly contains carbonate, aluminosilicate, and mica, which are likely to be hydrolyzed to kaolinite and hydromica. Pyrite is easy to transform into ferrous sulfate or other sulfides after oxidation and is also easy to leach under

Table 1 Location and lithology of samples

Samples	Location	Field description	Lithology
PDMC-7-2	N: 36°48′49.6″ E: 119°52′00.1″	White, granular texture; the main mineral is quartz	Anorthosite with graphite and quartz
PDMC-9-1	N:36°48′49.9″ E:119°52′01.8″	Gray, short prismatic structure, silky luster	Gabbo
PD-26-1	N:36°48′49.7″ E:119°52′02.7″	Gray, fine particle structure; the main mineral is calcite, graphite is dispersed inside	Graphite marble
PDMC-21	N:36°48′49.7″ E:119°52′2.3″	Gray, fine particle structure; the light-colored minerals: Quartz, calcite. The dark-colored minerals: biotite and graphite	Gneissic graphite marble
PD-ZJS-1	N: 36°49′10.4″ E: 119°55′45.7″	Light gray, fine particle structure; the main minerals: plagioclase, quartz, and amphibole	Biotite granite
PD-BS-1	N: 36°57′38.5″ E: 119°55′18.7″	Gray-red colored, fine particle structure, the main mineral: K-feldspar, plagioclase, quartz, and biotite	Adamellite

weathering condition. Ferrous sulfate is likely to be further oxidized and hydrolyzed to hydrous iron oxide (e.g., goethite, hydrogoethite, limonite) or form hematite. Thus, graphite deposit oxidation zone in Pingdu appears to be reddish brown, containing gossan-like deposit. The graphite in oxidation zone shows loose structure with fine-scale structure that can be well preserved and few sulfur minerals that affects the quality of graphite.

2.2 Methods for Assessment and Analysis

2.2.1 Optical Characteristics of Minerals

Optical thin slices were prepared in Peking University, and the most representative samples which could be used as evidences to show the characteristics of the oxidation and reduction deposit were analyzed with polarizing microscope. Polarizing microscope (Nikon ECLipse LV100POL) with eyepiece magnification is 10×, while the objective lens magnification ranged from 5 to 100×. Orthogonal polarization, single polarization, and reflection light were all used.

The main rocks of the reduction are anorthosite (containing graphite and quartz) and gabbro. Fine flake graphite or graphite aphanitic makes up the vast majority with appearance of massive, layered, or spherical. Reduction zone hardly contacts with air. The surrounding rocks are of great density, mostly block structured and hard. The main types of the oxidation are marble, granite, and biotite granite. Minerals are partially oxidized by oxygen. The graphite in oxidation zoom mostly is mostly large scale and finely crystallized. Oxidation deposits in contact with the

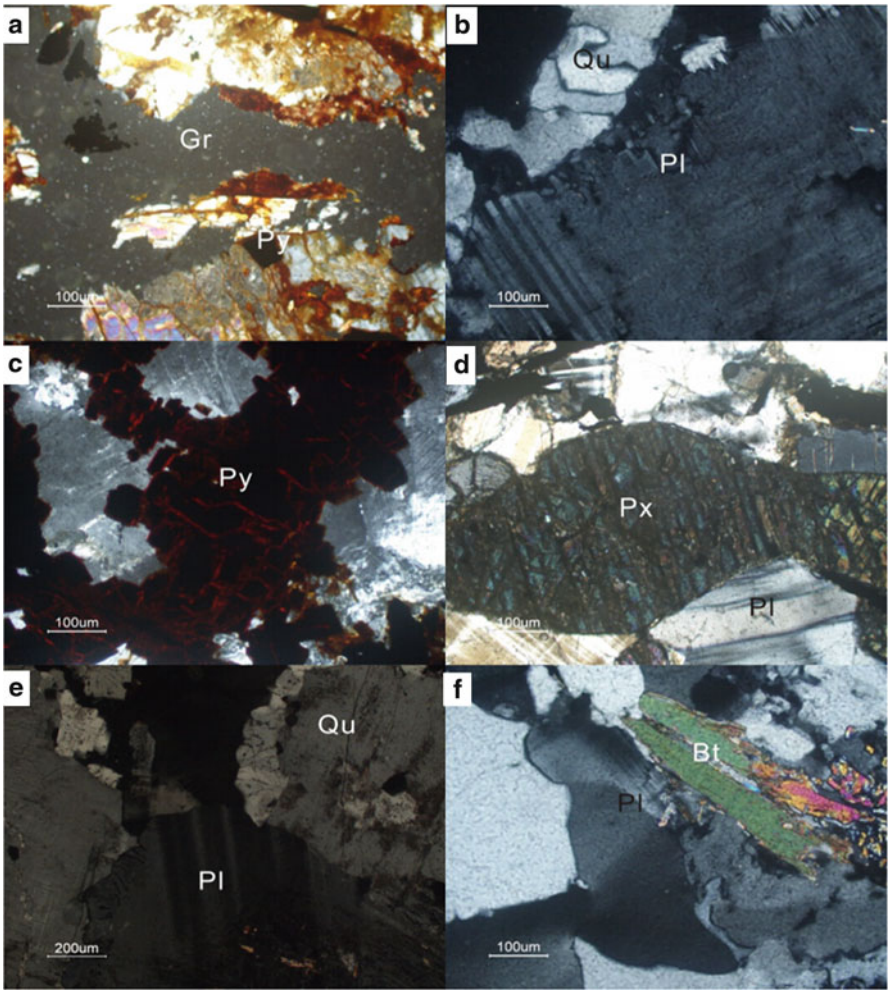

Fig. 1 Photographs of the reduction of graphite deposit. (**a**) Photo of graphite and quartz; (**b**) image of quartz and plagioclase; (**c**) pyrite; (**d**) pyroxene in Gabbro; (**e**) quartz and plagioclase in Gabbro; (**f**) plagiclase and biotite in Gabbro; *Gr* graphite, *Pl* plagioclase, *Py* pyrite, *Px* pyroxene, *Bt* biotite

external environment could be easily corroded, and the loose surrounding rocks contain large number of detritus.

Minerals containing graphite researching by optical methods should pay more attention to the reflectance, because graphite is black opaque mineral (Fig. 1). One of the most important means to research graphite under the microscope is to measure the reflectance. According to Mo Rujue [16], the percentage of the reflected light intensity (I_r) and the incident light intensity (I_i) can be called the mineral reflectance (R); this can be expressed as:

$$R = \frac{I_r}{I_i} \times 100\% \quad (1)$$

The reflectance depends on the mineral's natural characteristics, particle binding types, the absorption of light, and the index of refraction. Furthermore, it also can be influenced by the incident light or other factors. Graphite has a law reflectance, which has direct proportion relationship with the degree of crystallization.

There are two main graphite ore in the graphite deposit in Pingdu: graphite-bearing quartz anorthosite and gabbro. Graphite under single polarization light presents as dark opaque mineral, while it shows livid under reflected light (Fig. 1a).

Quartz shows gray interference color under orthogonal polarization microscope and extinction. Pyrite presents as quadrate or irregularly granular opaque mineral and shows off-white under reflected light and presents maroon on the edge (Fig. 1c). Pyroxene under the orthogonal polarization microscope presents secondary interference color, inclined extinction, and two groups of cleavage, and the particle size is about 0.3 mm. The size of quartz in gabbro (Fig. 1e, f) under the orthogonal polarization microscope is 0.5–1.0 mm.

The oxidation zone of graphite deposit in Pingdu area mainly consist of gneissic graphite marble, biotite granite, and monzonitic granite. Photographs of minerals are shown in Fig. 2. The particle size of pyrite is about 0.5 mm (Fig. 2a).

Flake graphite in gneissic graphite scatters in calcite with grain size of 0.2 mm (Fig. 2b) and shows light gray under reflected light, of which grain size is about 0.1 mm. Under the polarized light, biotite grain size about 0.1 mm (Fig. 2d). Biotite adjoins to the hornblendes under the polarized light, and the biotite is clearly to be observed, a group of cleavage along with the long axis has length between 0.1 and 0.3 mm. Rhombic hornblendes surround the biotite with the length of 0.05 mm. Chlorites and K-feldspars are in adamellite (Fig. 2f) under the polarized light; the particle size of K-feldspars is about 0.5 mm.

2.2.2 X-ray Powder Diffraction

On the research of the oxidation–reduction characteristics of graphite deposit, the X-ray diffraction is a significant method to analyze the mineral composition. Samples from the deposit were grounded into particles less than 30 μm.

For X-ray powder diffraction (XRD) (Model: X'Pert Pro MPD; Manufacturer: PANalyticalB.V. Company), the conditions required are as follows: copper target; voltage: 40 kV; Current: 100 mA; Scan step width: 0.02°; slit system; scanning speed of 2 (°)/min, scan range 3–80°.

In Fig. 3a, it can be easily figured out that the quartz and biotite are the major minerals in oxidation deposit. Small section partially chlorite minerals imply that the oxidation ore containing graphite is derived from the clay, semi clay, and carbonate mixed with mafic volcanics. Figure 3b indicates that the reduction ore is mainly composed of pyroxene, hornblende, calcite, and some clay minerals.

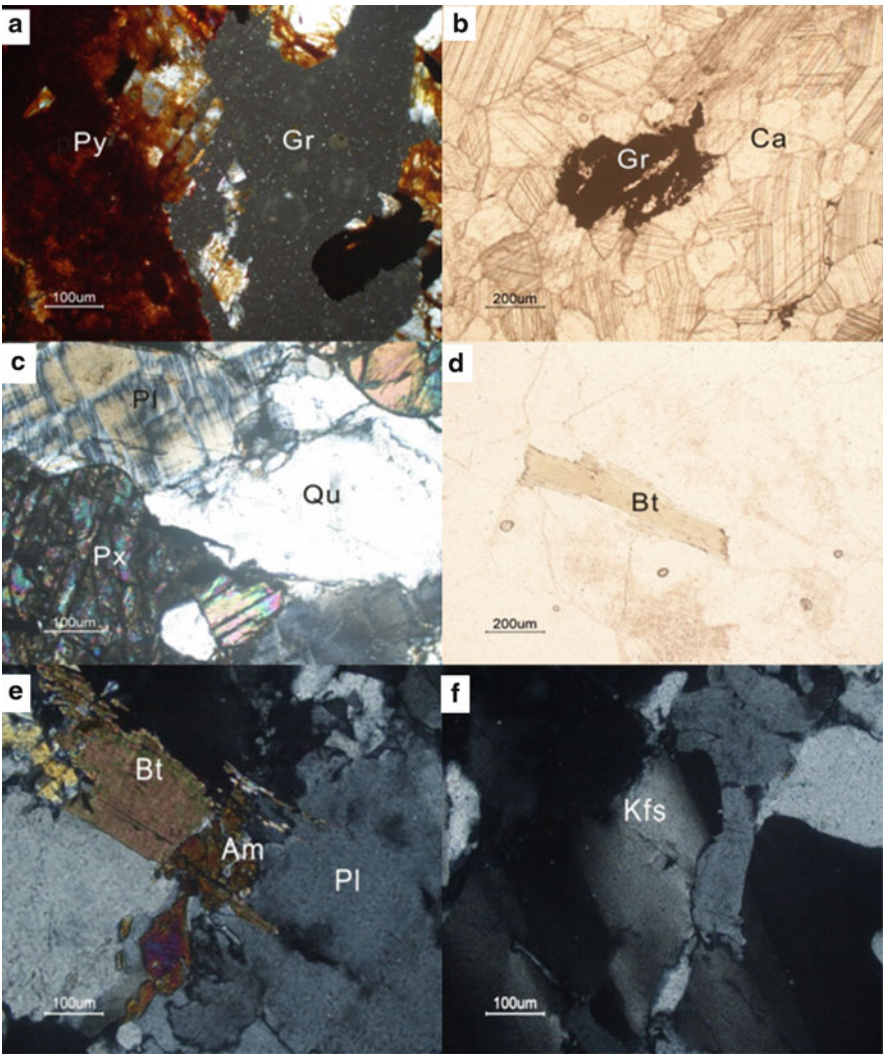

Fig. 2 Photographs of the oxidation of graphite deposit. (**a**) Pyrite and calcite; (**b**) graphite and calcite; (**c**) plagioclase and quartz; (**d**) biotite; (**e**) biotite, plagioclase, and amphibole; (**f**) potassium feldspar; *G* graphite, *Py* pyrite, *Ca* calcite, *Qu* quartz, *Pl* plagioclase, *Bt* biotite, *Am* amphibole, *Kfs* potassium feldspar

According to the minerals and ore compositions, we can speculate that the reduction has the same protolith.

According to Bragg equation: $2d\sin\theta = \lambda$, $\lambda = 0.15406$ nm, in the XRD diffraction pattern of the oxidation ore (Fig. 3a) the (002) peak can be observed clearly where $d = 3.3481$ ($2\theta = 26°$). In reduction ore XRD diffraction pattern (Fig. 3b), the

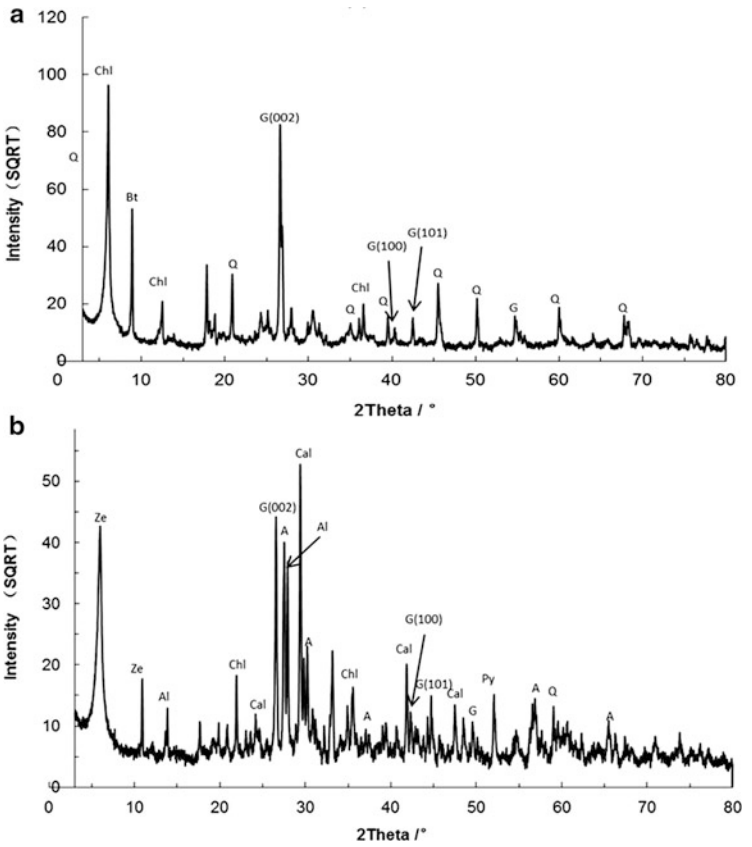

Fig. 3 The X-ray diffraction of the graphite mine of Pingdu district of Shandong province. (**a**) The X-ray diffraction of oxidation of graphite deposit. (**b**) The X-ray diffraction of reduction graphite deposit, *Chl* Chlorite, *Cal* calcite, *Q* quartz, *Bt* biotite, *Gl* Glaucophane, *A* augite, *Al* albite, *Py* pyrite, *Ze* zeolite

(002) peak was calculated $d = 3.3534$ $(2\theta = 26^\circ)$. Furthermore, the peaks at $d = 1.68$ and $d = 1.23$ can clearly identified in both oxidation and reduction.

2.2.3 Scanning Electron Microscope Analysis

We take advantage of the polarizing microscope (Nikon ECLipse LV100POL) and scanning electron microscope (QUANTA-650FEG) to analyze the particle size and graphitization grade of the graphite in oxidation and reduction deposits. The scanning electron microscopy (SEM) images were taken with a QUANTA-650FEG microscope equipped with a cold field emission gun operating at 20 kV, and all SEM images were captured by CCD (charge-coupled device) cameras. The specimen was mounted on SEM mount with a carbon tape.

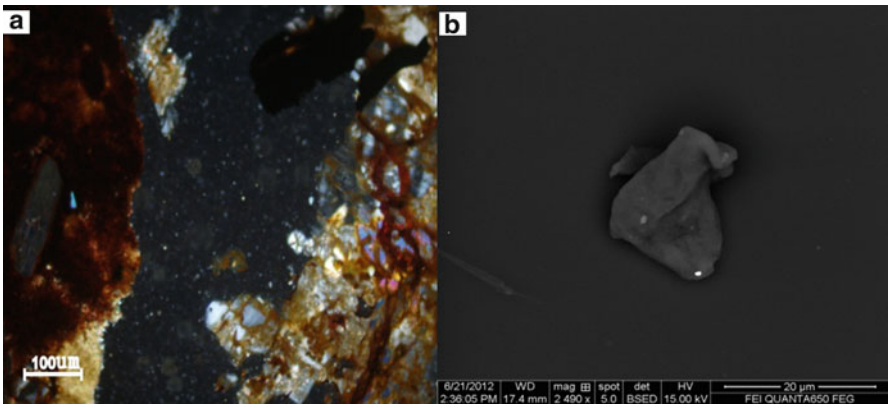

Fig. 4 Graphite of oxidation and reduction, (**a**) photo of the oxidation graphite, (**b**) SEM photo of the reduction graphite

The graphite flakes of the oxidation deposit are larger than those in the reduction deposit. These flakes can be identified by eyes. Analyzing the oxidation samples under the polarizing microscope (Fig. 4a), the particle size of flakes is between 0.5 and 3.0 mm. Microcrystalline graphite occupies the predominant position in the reduction deposit and the particle size is below 30 μm (Fig. 4b).

2.2.4 Carbon–Sulfur Analysis

The sulfur content of the oxidation graphite samples and reduction graphite samples was studied by infrared absorption of carbon and sulfur analyzer (CS-600, Leco company USA) (Table 2). All the particle graphite samples were sent to test in the Powder Central of the Central South University. The results showed that the average sulfur content of the sample of reduction is 350 ppm, and the average sulfur content of the graphite samples of oxidation is 139 ppm.

2.2.5 Results

Graphite in reduction zone is aphanitic crystallized graphite or fine flake graphite. Characterized by small grain size and low crystallization, the low reflectivity of graphite indicates a low degree of metamorphism in graphite. Residual and replacement textures are common in microscope observation. Earlier minerals like plagioclase and biotite are metasomated by the later minerals (e.g., quartz and microcline) which indicates typical features of amphibolite facies, suggesting that the metamorphic facies of reduction zone in Pingdu area is amphibolite facies.

Flake graphite occupies dominate position in the oxidation graphite ore. The flakes lie aligned along with the direction of the gangue minerals. A secondary-stage

Table 2 Sulfur content of graphite samples

Samples of the oxidation deposit	Sulfur content (ppm)	Samples of the reduction deposit	Sulfur content (ppm)
O-1	138	R-1	425
O-2	161	R-2	289
O-3	162	R-3	375
O-4	175	R-4	311

mineralization is easily observed on the surface of massive graphite. While albite suffered calcification, microcline turned into orthoclase; it indicated that the metamorphic phase in oxidation zone was also the amphibolite facies. Another characteristic of the oxidation zone is obvious migmatization. It's usually found that the migmatite consists of graphite marble, gneiss, and amphibolite.

Under XRD, compare to $d = 3{,}534$ at the peak (002), the reduction that $d = 3.3481$ is a bit lower at the same peak of the oxidation ore. According to the relationship between the distance in carbon layers of graphite and the degree of metamorphism, the number of d decreases, while the distance of peak (100) and peak (101) increases, which can be explained that the sample has a higher graphitization, higher metamorphic grade, lower distance between two carbon layers, and higher degree of order.

As the XRD analyzing shows, the distance between peak (100) and peak (101) of the oxidation sample is longer than that of the reduction one, indicating that the graphite of the oxidation deposit has higher metamorphic grade and higher degree of order and less volatile and hydrogen.

From the SEM figures, we can observe that the graphite flakes in reduction deposit are mostly fine flake graphite or amorphous graphite. These kinds of graphite suffered low graphitization and low metamorphism.

Graphite in oxidation deposit has larger flakes and can be identified by eyes. Furthermore, some secondary crystallization can be observed around the graphite in oxidation ore.

It is obvious that the average sulfur content of the graphite sample of oxidation is much lower than the sample of reduction. The sulfur content is an important index of the quality of the graphite mine, and the sulfur in the graphite mainly derives from the FeS_2 according to the obvious results. The FeS_2 can be transformed to ferric sulfur due to the oxidation if the FeS_2 is exposed to air for a long time, and the sulfur content of the graphite samples of oxidation decreases when the ferric sulfur is dissolved in water.

3 Discussion

Based on the previous studies [16], the δC^{13} (PDB value) ratios of light and heavy carbon stops possessed by the large flake graphite that located in the oxidation zone range between −14.7 and 25.9‰ that are close to the organic carbon proportion. However, δC^{13} ratios possessed by the aphanitic-ultrafine graphite in the reduction zone range between 1.5 and −2.7‰, which indicates the carbon source in this area belongs to biocarbon. Migmatization and stress action in later period have no significant influence on the δC^{13} ratio.

Graphite ore in Pingdu Shandong is crystalline basement and is formed by regional metamorphism at the temperature between 600 and 800 °C in amphibolite facies. So we can infer that in a certain period the temperature in Pingdu area exceeded that for gabbro alteration (about 600 °C) and was consistent with the temperature for graphitization. Gabbros and other rocks were raised by stress function after melting which brought the surrounding carbon substances together. Then influent graphite sources were formed after series of metamorphisms [17–19].

Graphite ores in oxidation zone were obviously pulled up, thus being arranged linearly, which indicates tectonic stress action worked on the oxidation zone. The oxidation zone is mostly red with loose texture and high degree of mineral oxidation. Structures similar to "gossan" also exist. Here are the concrete reaction formulas:

$$2FeS_2 + 7O_2 + 2H_2O = 2FeSO_4 + 2H_2SO_4$$
$$4FeSO_4 + 2H_2SO_4 + O_2 = 2Fe_2(SO_4)_3 + 2H_2O$$
$$Fe_2(SO_4)_3 + 6H_2O = 2Fe(OH)_3 + 3H_2SO_4$$
$$2Fe(OH)_3 + nH_2O = Fe_2O_3 \bullet nH_2O$$

Sulfur content in the oxidation zone is lower than that in the reduction zone, mainly because the former one was in contact with the air for a long time, thus leading to the transformation of common pyrite to ferric sulfate and sulphuric acid which are taken away when resolved in surface water. The formula is given below:

$$4FeS_2 + 15O_2 + 2H_2O = 2Fe_2(SO_4)_3 + 2H_2SO_4$$

By researching the features of the oxidation zone and reduction zone of Pingdu, Shandong province, we can see the graphite ores should be treated differently according to their special types. We should exploit and produce them separately to cut the exploiting and producing cost, as well as to make full use of the large flake graphite recourses and to earn more economic benefits. At the same time it contributes to changing the current extensive exploiting pattern for recourses.

4 Conclusion

This chapter studied the graphite ore collected from the oxidation zone and the reduction zone in Pingdu, Shandong province, with optical properties, XRD, FESEM, and carbon–sulfur analyzer methods. The conclusions are showed below:

1. Graphite ore in Pingdu Shandong is crystalline based and is formed by regional metamorphism. It's located in the ancient metamorphic rocks which were formed in early Precambrian. Then the ore-bearing rock body generally consists of gneiss, amphibolites, and chroismite. Intense magmatism leads to universal migmatization. The graphite ore was formed in amphibolite facies, and the carbon source in this area belongs to biocarbon.
2. Characteristics of graphite ore in Pingdu Shandong mainly located in the oxidation zone and reduction zone are obvious zonation and definitely fine limit. Graphite produced in the reduction zone is mainly aphanitic–ultrafine and that in the oxidation zone is mainly orientated arrangement flake graphite. Graphite located in the oxidation zone crystallizes better with higher degree of order, and its flakes are bigger. Besides, obvious secondary crystallization exists. On the contrary, graphite in the reduction zone has lower crystallization and degree of order with special shapes such as spherality and bulk graphite gathering.
3. Graphite produced in this area is easy to sort preserving big flake ones with low sulfur content. While in reduction zone, graphite is low crystallized, has small grain size, and has high sulfur content. Studying the functions of graphite from the two zones pertinently contributes to make full use of graphite resources and reduce wastes, thus increasing the commercial benefits.

References

1. Mo J (1986) Graphite minerals in China and their applications in industry. Bull Mineral Petrol Geochem (4):160–162
2. Zhu YS (2007) China's main metallogenic region (belt) metallogenic geological characteristics and metallogenic spectrum. Geological Publishing House, Beijing
3. Qin CJ, Qiu YZ, Wen HJ et al (2009) The discovery of graphite deposit in Baiyunebo and its geological significance. Acta Mineral Sin 29(s1):234–235
4. Wang FR, Xue JQ (2010) Geological characteristics and genesis of Beizi crystal graphite deposit in Lushan, Henan province. Miner Explor 01(3):248–253
5. Zhang BC (2005) Geological features and genesis of the Guangyi graphite deposit of Muling County. Jilin Geol 24(4):47–53
6. Chuan XY, Morihara N, Ying B et al (2012) Orbicular graphite in Oshirabetsu, Hokkaido, Japan. Acta Geol Sin 86(2):241–246
7. Cao FF, Wang XL, Geng TS (2012) Geological characteristics and genesis analysis of Wuliliang graphite mine in Xichuan. China Non-metallic Miner Ind (1):43–44
8. Chuan XY (2001) Carbon materials applied in environmental engineering. Acta Petrol Mineral 20(4):507–510
9. Ren JC, Wang JL (1994) A study on the selection process of Nanshu graphite ore. Multipurp Util Miner Resour (4):18–20

10. Wang KQ (1990) A study on the structure of graphite crystals in nanshu graphite deposit, Shandong province. Acta Mineral Sin 10(2):106–114
11. Yan LY, Chen JY, Du HZ et al (2012) Geological characteristics and prospecting criteria of Liugezhuang graphite deposit in Pingdu city of Shandong province. Shandong Land Resour 28 (2):11–14
12. Zhang XL, Chuan XY (2010) Crystallographic characteristics and environmental significance of the six squares columnar calcite in Pingdu, Shandong. Acta Mineral Sin (s1):107–108
13. He QX (1992) The natural flaky graphite in Hongshan No. 3 graphite mine in Pingdu, Shandong. New Carbon Mater (1):4
14. Wang Q, Yan TF (1990) A study on the produce of high-carbon graphite through the flotation of gneiss crystalline graphite. Multipurp Util Miner Resour (5):18–20
15. Lin HA (1996) Study on the processing of a weathered graphite ore. Multipurp Util Miner Resour (4):15–16
16. Mo JR, Liu SB, Huang CR et al (1989) Geological graphite deposit in China. China Building Industry Press, Beijing
17. Qin L (2011) Bachelor Thesis, Perking University, pp 11–32
18. John DB, Dan DE (1993) Carbon-carbon, materials and composites. Noyes Publications, Park Ridge, p 121
19. Miyashiro AR (1964) Oxidation and reduction in the earth's crust with special reference to the role of graphite. Geochim Cosmochim Acta 28:717–729

Study on the Effect and Mechanism of Calcination of Asbestos Tailings Mixed with Ammonium Sulfate

Bei Song, Chao Liu, Shuilin Zheng, Tongtong Wang, and Jian Zhao

Abstract The research involves the calcination of SiChuan ShiMian asbestos tailings with ammonium sulfate in order to extract magnesium. This chapter studies the effect of different calcination conditions on the magnesium extraction rate and the mechanism of calcination of asbestos tailings mixed with ammonium sulfate. The results are characterized by XRD, TGA, and elemental analysis. The results show that as the temperature rises the magnesium extraction rate first increases and then decreases. Optimal experimental conditions are 600 °C of calcination temperature and 1 h of calcination time, by means of which a magnesium extraction rate of 68.56 % can be achieved.

Keywords Asbestos tailings • Calcination • Extraction rate

1 Introduction

Asbestos tailing is a kind of hazardous waste, which is stripped down from asbestos ore in the beneficiation process. The main mineral component is serpentine, and it also contains a small amount of non-serpentine family coexisting minerals, such as magnesium stone, magnetite, quartz, chlorite, and talc [1, 2]. The theoretical chemical composition is $Mg_6[Si_4O_{10}](OH)_8$, and its main chemical compositions are magnesium oxide and silicon [3]. A lot of accumulation of Asbestos tailings poses a major threat to the environment and human health. It contains a large number of non-elected small staple fibers, which are pathogenic substances to human and animals. Long-term inhalation of asbestos dust can result in workers' suffering from asbestosis, lung cancer, and other diseases [4–8].

Asbestos tailings calcined with ammonium sulfate simplify the process of extracting magnesium from asbestos tailings. And the generated ammonia can be absorbed by water, which can be used as the raw material for producing magnesium

B. Song • C. Liu • S. Zheng (✉) • T. Wang • J. Zhao
School of Chemical and Environmental Engineering, CUMTB, 11 Xueyuan Road, Haidian, Beijing, People's Republic of China
e-mail: shuilinzh@sina.com

F. Dong (ed.), *Proceedings of the 11th International Congress for Applied Mineralogy (ICAM)*, Springer Geochemistry/Mineralogy,
DOI 10.1007/978-3-319-13948-7_28

hydroxide. This chapter studies the effect of different calcination temperature and time on the extraction rate of magnesium from asbestos tailings, as well as its mechanism.

2 Materials and Methods

2.1 Materials

Asbestos tailings used in the experiments are from the Sichuan Shimian. The major chemical composition is MgO and SiO_2. The main chemical composition is shown in Table 1. Asbestos tailings XRD spectra are shown in Fig. 1 and its phase compositions are shown in Table 2. As can be seen in Table 2, the major mineral component of asbestos tailings is Lizardite-1 T.

Table 1 Elemental analysis of parent sample

Chemical composition	SiO_2	MgO	Fe_2O_3	Al_2O_3	FeO	CaO	K_2O	Na_2O	L.O.I.
Wt%	41.09	34.37	5.78	3.68	1.29	1.24	0.32	0.30	11.50

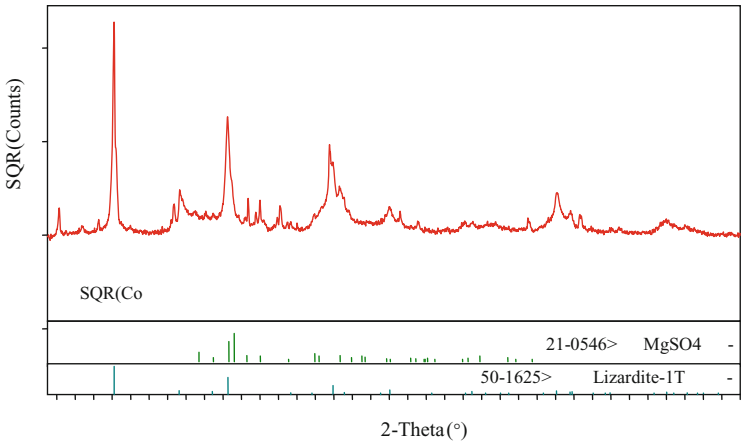

Fig. 1 XRD pattern for asbestos tailings

Table 2 Elemental analysis of parent sample

Phase composition	Lizardite-1 T	Magnetite	Chlorite	Feldspar	Mica	Quartz	Dolomite
Wt%	66.4	4.4	14.7	6.7	3.7	2.1	2.0

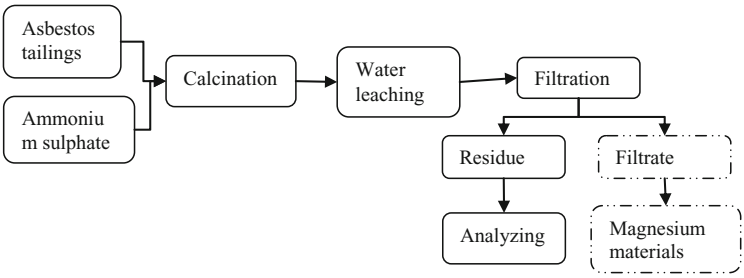

Fig. 2 Experiment technical routes

2.2 Methods

Asbestos tailings mixed with ammonium sulfate are calcined in different calcination conditions. Calcined sample in accordance with a predetermined ratio of solid to liquid is leached in water bath. After leaching it is filtered by vacuum filtration machine and then the chemical and mineral compositions of the water leaching residue are analyzed. And the filtrate will be used to produce magnesium materials. The main technical route is shown in Fig. 2.

2.3 Characterization

The chemical compositions of residue are analyzed by DHF82 multi-element analyzer, Xiangtan City Instrument Co., Ltd. The phase compositions of residue are analyzed by Xpert X-ray diffractometer, Netherlands PHILIPS. The thermal gravimetric analysis of sample is analyzed by Q5000 thermo gravimetric analyzer, TA instruments.

3 Results and Discussion

3.1 Effects of Calcination Temperature on the Extraction Rate of Magnesium from Asbestos Tailings

With reference to the experiment conditions of serpentine calcined with ammonium sulfate, the base conditions of the experiment of asbestos tailings calcined with ammonium sulfate are set as follows: the mass of asbestos tailings is 50 g, the mass ratio of ammonium sulfate and asbestos tailings is 3:2, and the calcination time is 1 h [9]. A single-factor experiment is performed under the base conditions, and the calcination temperature was selected as 400, 500, 600, 700, and 800 °C to carry out calcination temperature single-factor experiment.

The extraction rate of magnesium from asbestos tailings is calculated by the analysis of the chemical compositions of water leaching residue. The formula as below:

$$\text{Extraction rate of Mg} = \frac{M1 \cdot \omega 1 - M2 \cdot \omega 2}{M1 \cdot \omega 1} \times 100\% \quad (1)$$

$M1$ Mass of asbestos tailings
$M2$ Mass of water leaching residue
$\omega 1$ The percentage content of magnesium of asbestos tailings
$\omega 2$ The percentage content of magnesium of water leaching residue

The results of the experiment are shown in Table 3.

According to the data of Table 2 and the formula of extraction rate of Mg, the effects of calcination temperature on the extraction rate of magnesium are shown in Fig. 3. When the calcination temperature is below 600 °C, the extraction rate of magnesium increases as the temperature rises. When the calcination temperature is 600 °C, the extraction rate of magnesium reaches to a maximum of 68.75 %. When the calcination temperature is higher than 600 °C, the extraction rate of magnesium decreases as the temperature is rising. In summary, the optimal calcination temperature is 600 °C.

Table 3 The results of the experiment

Calcination temperature (°C)	400	500	600	700	800
$M2$	32.039	33.855	33.352	33.323	32.771
$\omega 2$	18.21	17.02	16.00	16.78	18.01

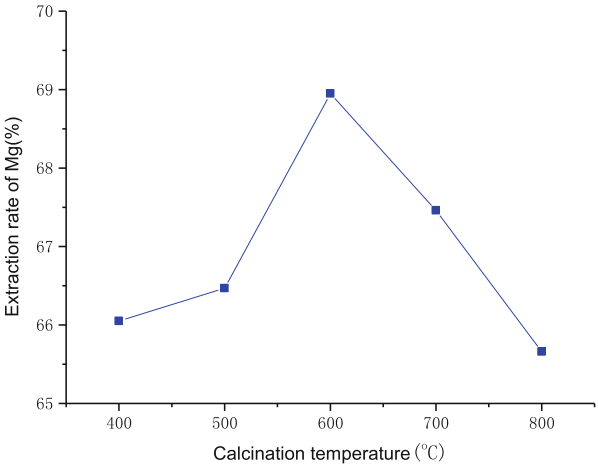

Fig. 3 The extraction rate of magnesium at different calcination temperatures

3.2 *Effects of Calcination Time on the Extraction Rate of Magnesium*

A single-factor experiment was performed under such conditions as the mass of asbestos tailings is 50 g, the mass ratio of ammonium sulfate and asbestos tailings is 3:2, and the calcination temperature is 600 °C. The calcination time was selected as 1, 1.5, 2, 2.5, and 3 h to carry out calcination time single-factor experiment. The experimental results are shown in Fig. 4. It can be seen that as the calcination time rises, the extraction rate of magnesium increases too. Theoretically, with the rise of calcination time, the ammonium sulfate and asbestos tailings react. But the extraction rate of Mg requires 3 h of calcination, which is only 0.33 % higher than 1 h of calcination. Taking the energy consumption into account, the optimal calcination time is determined as 1 h.

3.3 *Mechanism of Calcination of Asbestos Tailings Mixed with Ammonium Sulfate*

In order to further analyze the mineral compositions of the calcined product of water leaching residue, the XRD spectra of residue at different temperatures are shown in Fig. 5.

As can be seen in Fig. 5, there are strong and sharp Lizardite-1 T diffraction peaks. And as the temperature rises, the characteristic peaks are essentially unchanged. That illustrates Lizardite-1 T structure is not destroyed under the conditions of 400 and 500 °C, which explains why the extraction rate of magnesium is rather low in such conditions. When the calcination temperature is higher than 600 °C, Lizardite-1 T characteristic diffraction peak intensity declines, and a strong

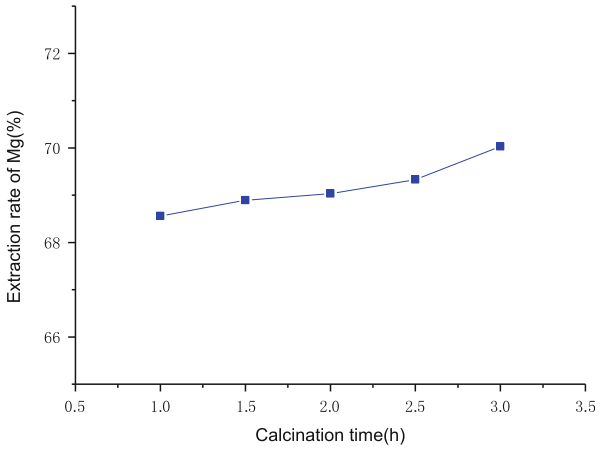

Fig. 4 The extraction rate of magnesium at different calcination time

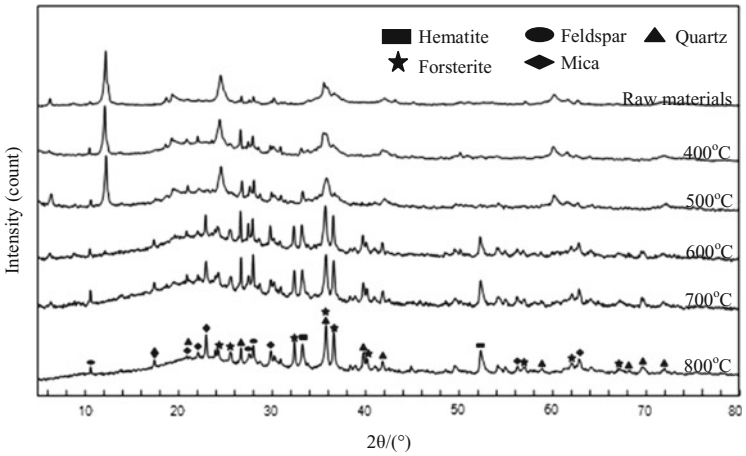

Fig. 5 XRD spectra of residue at different temperatures

characteristic diffraction peak of Mg_2SiO_4 appears. That means as the temperature rises Lizardite-1 T gradually is transformed into forsterite. But when the calcination temperature is higher than 600 °C, the characteristic diffraction peak of residue essentially has no change, which means that in the condition of 600 °C the reaction was essentially complete.

In order to further study the mechanism of reaction of asbestos tailings with ammonium sulfate at high temperatures, thermal gravimetric analysis is made under such conditions as the mass ratio of ammonium sulfate and asbestos tailings is 3:2, the calcination temperature is 600 °C, and the calcination time is 1 h. The TGA curve of asbestos tailings calcined with ammonium sulfate is shown in Fig. 6:

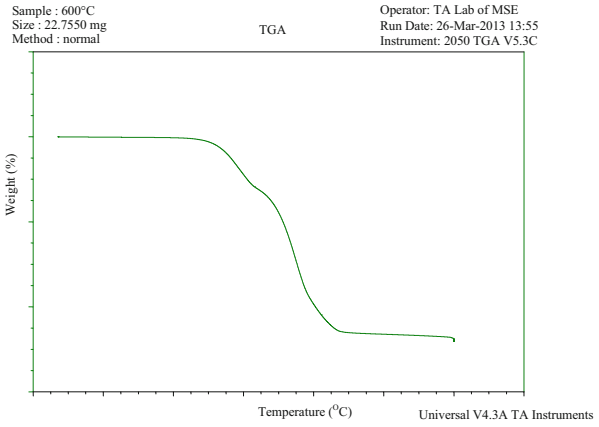

Fig. 6 TGA curve of asbestos tailings calcined with ammonium sulfate

It can be seen in Fig. 6, the mass of mixture of asbestos tailings and ammonium sulfate begins to decrease at temperature of 250 °C and the mass of mixture begins to stabilize until temperature reaches 450 °C. The reason of mass decrease of mixture is that ammonia and water are released in the reaction process of asbestos tailings with ammonium sulfate. From Figs. 5 and 6 it can be concluded that at the stage of 250–450 °C the reaction may be as follows:

$$Mg_6Si_4O_{10}(OH)_8 + 6(NH_4)_2SO_4 \rightarrow \underset{\uparrow}{Mg_6Si_4O_8(SO_4)_6} + 12NH_3\uparrow + 8H_2O \quad (2)$$

When the temperature is at the stage of 450–600 °C, the reaction may be as follows:

$$Mg_6Si_4O_8(SO_4)_6 \rightarrow 6MgSO_4 + 4SiO_2 \quad (3)$$

When the temperature increases at 600 °C, the reaction has essentially been completed.

4 Conclusions

The optimal conditions of calcination of asbestos tailings with ammonium sulfate are 600 °C of calcination temperature and 1 h of calcination, by means of which a magnesium extraction rate of 68.56 % can be achieved.

The mechanism of the calcination of asbestos tailings with ammonium sulfate is the reaction starts at 250 °C. When the temperature is at the stage from 250 to 450 °C, the reaction of the intermediate produces Mg_6Si4O_8 $(SO_4)_6$ and releases ammonia and water. When the temperature is at the stage from 450 to 600 °C, it is the reaction of the soluble magnesium sulfate. When the temperature increases to 600 °C, the reaction has essentially been completed.

References

1. Zhou XY, Fan JP (1998) Production of precipitated silicon dioxide from asbestos tailings. Chem Prod Technol 4:38
2. Su QP, Long XL (2009) On the approach for comprehensive utilization of asbestos tailing. Multipurp Util Miner Resour 1:009
3. Zhu TJ, Peng CJ, Xian HY, Zhong J, Wu S, Tang JY (2012) Preparation of basic magnesium sulfate from chrysotile asbestos tailing. Non-metallic Mines 1:013
4. Xu LR (2011) Asbestos tailings as aggregates for asphalt mixture. J Wuhan Univ Technol (Mater Sci Ed) 26(2):335–338
5. Holmes E (2012) Effects of weathering on the surface and chemical properties of chrysotile asbestos: implications for management of naturally occurring asbestos and carbon dioxide sequestration in ultramafic mine tailings. University of British Columbia, Vancouver
6. Vignaroli G et al (2011) Linking rock fabric to fibrous mineralisation: a basic tool for the asbestos hazard. Nat Hazards Earth Sci Syst 11:1267–1280
7. Koumantakis E et al (2009) Asbestos pollution in an inactive mine: determination of asbestos fibres in the deposit tailings and water. J Hazard Mater 167(1):1080–1088
8. Zhu P et al (2013) Investigative studies for inert transformation of toxic chrysotile tailing. J Mater Cycles Waste Manage 15(1):90–97
9. Dai R (2012) The research on a new green process to comprehensively utilize serpentine. China University of Mining & Technology, Beijing

Heavy-Ion Radiation Stability of $Gd_2Zr_2O_7$-Pyrochlore Glass-Ceramic Wasteforms Doped by Simulated Actinides

Sijin Su, Faqin Dong, Xirui Lu, Jingyou Tang, and Xiaoli Wang

Abstract To research the structure radiation stability of simulated $Gd_2Zr_2O_7$-pyrochlore glass-ceramic wasteforms, Nd^{3+} and Ce^{4+} were selected as the simulated nuclides of An^{3+} and An^{4+} radionuclides, respectively. A series of compounds with the general formula $Gd_{2-x}Nd_xZr_{2-x}Ce_xO_7$ ($0.0 \leq x \leq 2.0$) were prepared by high-temperature sintering method at 1,623 K for 48 h in air atmosphere. The heavy-ion irradiation experiments were done at room temperature and atmospheric pressure. The structure and microscopic morphology of $Gd_{2-x}Nd_xZr_{2-x}Ce_xO_7$ ($0.0 \leq x \leq 2.0$) glass-ceramic wasteforms before and after irradiation experiments were investigated by the X-ray diffraction and scanning electron microscopy. The results showed that $Gd_{2-x}Nd_xZr_{2-x}Ce_xO_7$ ($0.0 \leq x \leq 2.0$) glass-ceramic wasteforms exhibited pyrochlore phase within the scope of the wholly solid solution. With the added amount of analog nuclides increasing, the X-ray diffraction peak of wasteforms had a trend of moving in the direction of the small angle. XRD patterns and SEM photos suggested the series of wasteforms containing both crystalline phase and glass phase. The structure and microscopic morphology of wasteforms didn't change significantly before and after irradiation according to the XRD spectra and SEM photos. The $Gd_2Zr_2O_7$-pyrochlore glass-ceramic wasteforms showed a good radiation stability.

S. Su
School of Environmental Resource and Engineering, SWUST, 59 Qinglong Road, Mianyang, Sichuan, People's Republic of China

National Defense Key Discipline Laboratory of Nuclear Waste and Environmental Safety, SWUST, 59 Qinglong Road, Mianyang, Sichuan, People's Republic of China

F. Dong (✉)
School of Environmental Resource and Engineering, SWUST, 59 Qinglong Road, Mianyang, Sichuan, People's Republic of China
e-mail: fqdong@swust.edu.cn

X. Lu • J. Tang
National Defense Key Discipline Laboratory of Nuclear Waste and Environmental Safety, SWUST, 59 Qinglong Road, Mianyang, Sichuan, People's Republic of China

X. Wang
China Academy of Engineering Physics, Mianyang, Sichuan, People's Republic of China

F. Dong (ed.), *Proceedings of the 11th International Congress for Applied Mineralogy (ICAM)*, Springer Geochemistry/Mineralogy,
DOI 10.1007/978-3-319-13948-7_29

Keywords $Gd_2Zr_2O_7$-pyrochlore • Glass-ceramic • Radiation stability • Wasteforms

1 Introduction

The processing of high-level radioactive waste (HLW) is the emphasis and difficulty of the radioactive waste. 239Pu, 240Pu, 241Pu, 241Am, 243Am, and other actinides are the main radionuclides in it, and they have a high degree of radioactivity, high toxicity, long decay cycle, and high rate of heat release and are strongly acidic and corrosive [1, 2]. And the decay of actinide may lead to changes in the structure of the wasteforms, so the treatment and disposal technology of HLW are complex, difficult, and expensive. Vitrification, glass-ceramic, and synrock curring are the most commonly used methods for HLW [3]. Vitrification technology has been developed maturely, but the wasteforms will dissolute in high temperature and humid conditions, which causes leaching rate to rise rapidly and makes the safety performance of wasteforms to be questioned. In contrast, synroc-wasteforms has high density, resistance to leaching performance, radiation-resistant properties, chemical stability, and other characteristics. It is widely regarded as the second generation of solidified high-level waste and still in the research stage.

We found in the study that gadolinium zirconium pyrochlore ceramic wasteforms were prepared successfully with the conditions of 1,500 °C by high-temperature solid-phase method. However, when the sintering temperature reduced to 1,350 °C, the sintered wasteforms formed the glass-ceramic phase ranging between the crystalline phase and glass phase. It had unique properties such as chemical and mechanical stability [4, 5]. In this chapter, we present the ion-beam irradiation data on the solid solution of $Gd_{2-x}Nd_xZr_{2-x}Ce_xO_7$ ($0.0 \leq x \leq 2.0$) in order to evaluate the radiation stability of glass-ceramic wasteforms. The behavior of pyrochlores as wasteforms for the immobilization of actinides can be simulated by the incorporation of Nd and Ce because of the similarity in the ionic size and oxidation state of Nd and Am and Ce and Pu, respectively.

2 Materials and Methods

2.1 General

Powdered samples of $Gd_{2-x}Nd_xZr_{2-x}Ce_xO_7$ ($x = 0.0, 0.2, 0.4, 0.6, 0.8, 1.0, 1.2, 1.4, 1.6, 1.8, 2.0$) were prepared by sintering mixtures of ZrO_2 (AR, 99.99 %), CeO_2 (AR, 99.99 %), Gd_2O_3 (AR, 99.99 %), and Nd_2O_3 (AR, 99.99 %) powders in air at 1,623 K for 48 h.

The actinide produces α particles, recoil nuclei, and γ rays in the decay process. Compared to α particles, low-energy heavy recoil nucleus is the main factor that

lattice causes atom displacement damage of solidified body. Therefore, this thesis uses low-energy heavy ions produced by accelerator to simulate the long-term irradiation effects of recoil nuclei in wasteforms [6]. Using SRIM 2011 program for simulation, we obtain the range of the incident ions in the target material and the amount of displacement atoms generated on an Å in damage peak area. Irradiation damage rate R (irradiation displacement atoms in unit time) was calculated by the following formulas.

$$R = F \cdot \overline{v} \tag{1}$$

$$F = \frac{I \times 10^{-9}}{ne} \cdot \frac{4}{\pi D^2} \tag{2}$$

$$\overline{v} = v \times 10^8 / N \tag{3}$$

$$N = \frac{\rho}{M} \cdot A \tag{4}$$

In the formulas, F: the ion circulation (ions/cm^2·s); I: ion-beam intensity (nA); D: the beam spot diameter (cm); e: electronic charge (1.602×10^{-19} C); n: the number of incident ion charge; M: atomic weight of materials grams; ρ: density of the material; $\overline{v}$: the number of displacement atoms producing an incident ions in the unit volume of material per unit area; A: Avogadro constant (6.023×10^{23}).

A 300 KeV Xe ion irradiation was performed at room temperature using LAPECRZ facility at the Institute of Modern Physics, Chinese Academy of Sciences. High-pressure range: 5–320 kV. The beam intensity: 200 nA. Beam spot: 1 cm^2. The calculated dose and irradiation time were showed in Table 1.

2.2 Materials and Mix Designs

The raw materials were dried in oven at 100 °C for 2 h. The corresponding quality of Gd_2O_3, ZrO_2, Nd_2O_3, CeO_2 powder measured by standard chemical was weighed accurately. Put raw materials into an agate mortar, adding appropriate amount of anhydrous ethanol; then grind and mix them thoroughly for 30 min. The mixed samples would be placed in oven and dried for 30 min, and then were tabulated under the pressure of 10 MPa forming wafers with a diameter of 10 mm and a thickness of 2 mm approximately. The press-formed prefabricated blocks, named N0–N10, were put on the ceramic pieces in turn. And then put the ceramic into the box-type resistance furnace, conducting high-temperature synthesis in accordance with the established conditions. The process curve was showed in Fig. 1.

Table 1 Radiation dose and irradiation time of samples

Target compounds	Radiation dose (dpa)	Irradiation time (s)
$Gd_{1.8}Nd_{0.2}Zr_{1.8}Ce_{0.2}O_7$	0.2, 0.5, 0.8, 1.0	22.4, 56.0, 89.6, 112.0
$Gd_{1.6}Nd_{0.4}Zr_{1.6}Ce_{0.4}O_7$	0.2, 0.5, 0.8, 1.0	22.4, 56.0, 89.6, 112.0
$Gd_{1.4}Nd_{0.6}Zr_{1.4}Ce_{0.6}O_7$	0.2, 0.5, 0.8, 1.0	22.4, 56.0, 89.6, 112.0
$Gd_{1.2}Nd_{0.8}Zr_{1.2}Ce_{0.8}O_7$	0.2, 0.5, 0.8, 1.0	22.4, 56.0, 89.6, 112.0
$Gd_{1.0}Nd_{1.0}Zr_{1.0}Ce_{1.0}O_7$	0.2, 0.5, 0.8, 1.0	22.4, 56.0, 89.6, 112.0
$Gd_{0.8}Nd_{1.2}Zr_{0.8}Ce_{1.2}O_7$	1.0, 2.0, 3.0, 4.0	112.0, 224.0, 336.0, 448.0
$Gd_{0.6}Nd_{1.4}Zr_{0.6}Ce_{1.4}O_7$	1.0, 2.0, 3.0, 4.0	112.0, 224.0, 336.0, 448.0
$Gd_{0.4}Nd_{1.6}Zr_{0.4}Ce_{1.6}O_7$	1.0, 2.0, 3.0, 4.0	112.0, 224.0, 336.0, 448.0
$Gd_{0.2}Nd_{1.8}Zr_{0.2}Ce_{1.8}O_7$	1.0, 2.0, 3.0, 4.0	112.0, 224.0, 336.0, 448.0

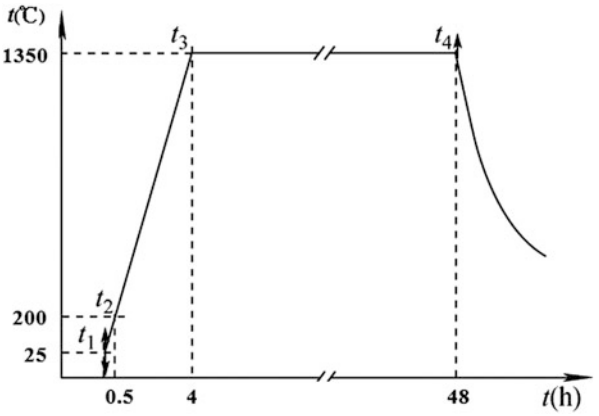

Fig. 1 Process curve of sintering samples

2.3 Methods for Assessment and Analysis

The morphology of the samples was examined by scanning electron microscope (SEM, TM-1000, Hitachi Ltd., Japan). The pattern of the samples was identified by an X-ray powder diffractometer (XRD, X'pert PRO, Panake, Holland) using Cu K α radiation ($\lambda = 1.54178$ Å).

3 Results

Figure 2 shows the XRD patterns of $Gd_{2-x}Nd_xZr_{2-x}Ce_xO_7$ (x = 0.0, 0.2–2.0). The patterns show that there are strong diffraction peaks at the degree ($2\theta = 29.367°$, 8.903°, 8.074°), which is in line with the standard card (PDF01-080-0471). Compared with the standard pattern of $Gd_2Zr_2O_7$, the X-ray diffraction peaks of samples prepared are wider and shorter. Further, the peaks have a trend of movement to small angle with the addition of simulated actinides into pyrochlore structure.

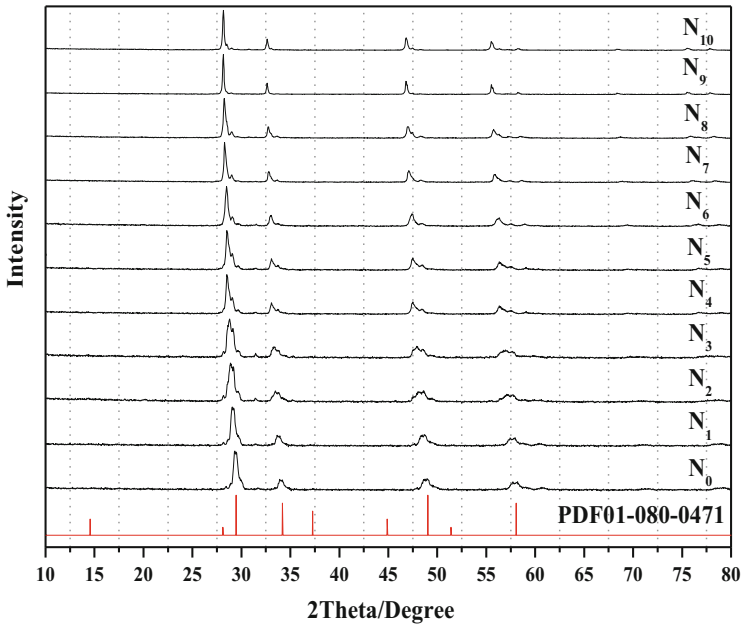

Fig. 2 X-ray diffraction patterns of $Gd_{2-x}Nd_xZr_{2-x}Ce_xO_7$ ($x = 0.0$, 0.2–2.0)

All the samples keep pyrochlore phase after the different doses of irradiating, which is shown in Fig. 3. The intensity of X-ray diffraction peaks decreases, the width is slightly larger, and the degree of crystallinity decreases, when compared with samples before irradiating. There was little change with the dose increasing. Figure 4 shows that with the increase in the amount of dopant, the position, intensity, and width of X-ray diffraction peaks of samples after the same dose of irradiation almost have no change. Figure 5 shows some SEM photographs of the portion of the samples before and after irradiation, and the magnification is 20,000–30,000. There is no defect or fault on the face of samples after irradiation. The samples keep crystalline and glassy mixed morphology.

4 Discussion

The X-ray diffraction peaks of samples prepared are wider and shorter; therefore, the wasteforms contain both glass phase and crystal phase. The trend of movement to small angle of peaks with the addition of simulated actinides into pyrochlore structure is caused by the different ionic radius between Nd^{3+} (0.098 nm) and Gd^{3+} (0.094 nm) and Ce^{4+} (0.087 nm) and Zr^{4+} (0.072 nm). When Nd^{3+} and Ce^{4+}, which have larger ionic radius to substitute Gd^{3+} and Zr^{4+} respectively, are used, the lattice parameters and unit cell sizes of $Gd_2Zr_2O_7$ increase and result in the

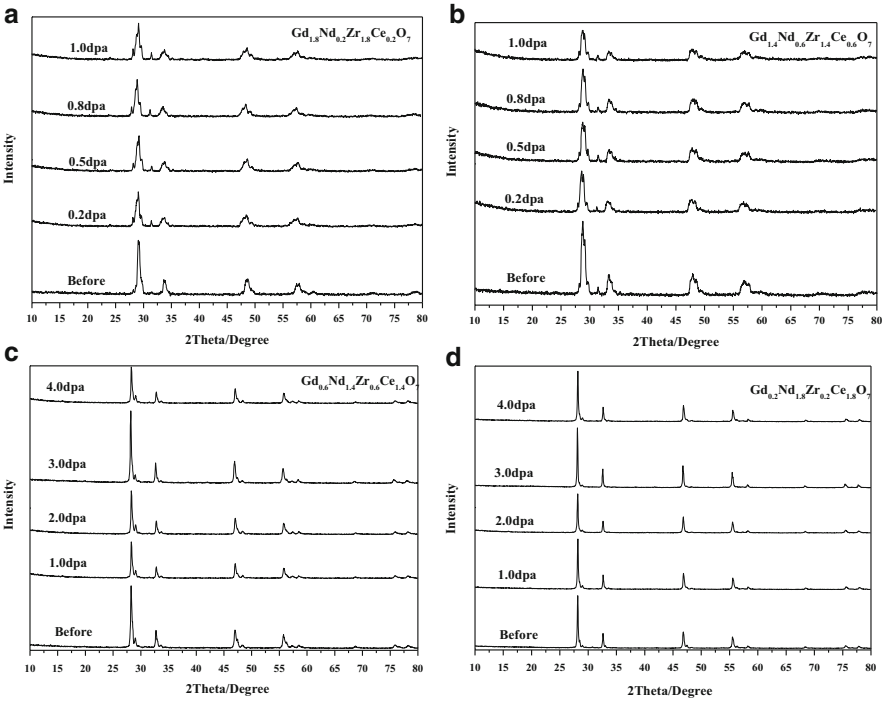

Fig. 3 XRD patterns of some samples after different doses of Xe irradiation. (**a**) $Gd_{1.8}Nd_{0.2}Zr_{1.8}Ce_{0.2}O_7$; (**b**) $Gd_{1.4}Nd_{0.6}Zr_{1.4}Ce_{0.6}O_7$; (**c**) $Gd_{0.6}Nd_{1.4}Zr_{0.6}Ce_{1.4}O_7$; (**d**) $Gd_{0.2}Nd_{1.8}Zr_{0.2}Ce_{1.8}O_7$

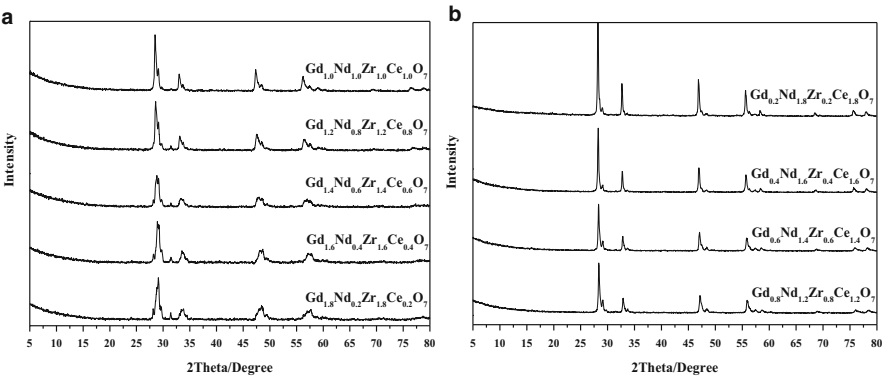

Fig. 4 XRD patterns of samples after the same dose of Xe irradiation. (**a**) XRD patterns of N1–N5 absorbed dose of 0.2 dpa; (**b**) XRD patterns of N6–N9 absorbed dose of 1 dpa

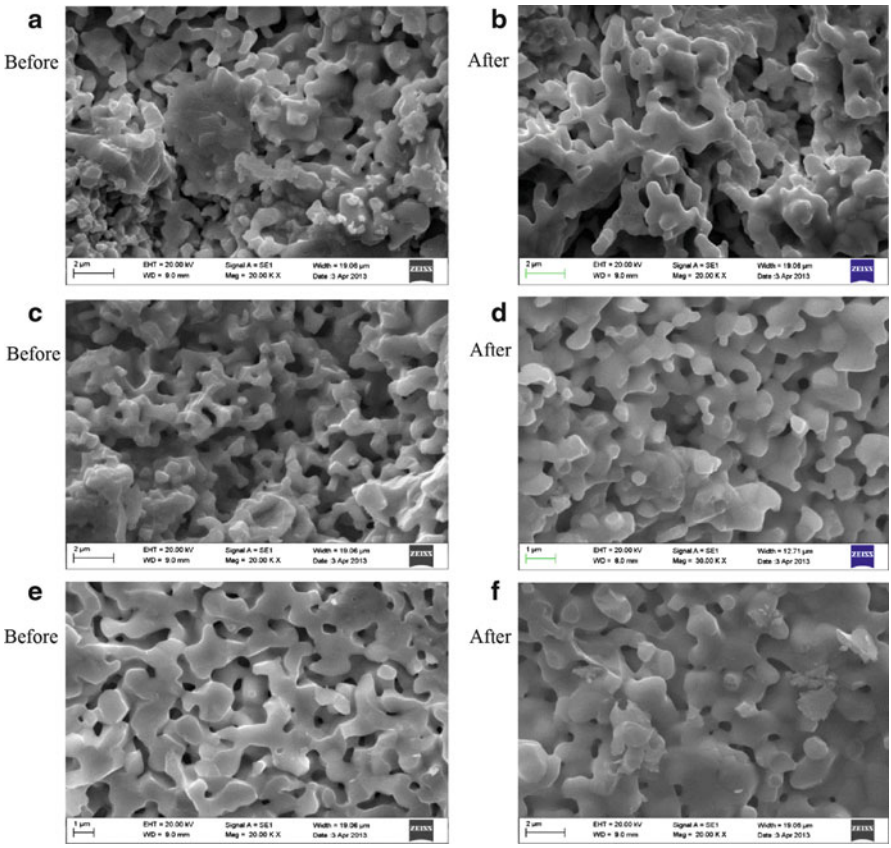

Fig. 5 SEM images of some samples before and after irradiation. (**a**), (**b**) $Gd_{1.8}Nd_{0.2}Zr_{1.8}Ce_{0.2}O_7$; (**c**), (**d**) $Gd_{1.4}Nd_{0.6}Zr_{1.4}Ce_{0.6}O_7$; (**e**), (**f**) $Gd_{0.6}Nd_{1.4}Zr_{0.6}Ce_{1.4}O_7$

movement of peaks. There was little change with the radiation dose increasing in the XRD patterns of wasteforms. And the added amount of dopant has little influence on the irradiated stability of the samples, because with the increase of it, the position, intensity, and width of X-ray diffraction peaks of samples after the same dose of irradiation almost have no change. The SEM photos show the samples prepared form both crystalline portion and glassy portion and have no change before and after irradiation, which is in line with the results of XRD patterns. In summary, the cured body showed a good radiation stability after the radiation of heavy ions.

5 Conclusions

$Gd_2Zr_2O_7$-pyrochlore glass-ceramic wasteforms doped by simulated actinides were prepared in this experiment and the characterizations were tested and analyzed with the help of XRD and SEM before and after the heavy-ion irradiation experiments. The results are as follows: (1) the prepared wasteforms maintained the pyrochlore phase in the full degree of solid solution, and the X-ray diffraction peaks of the samples had a trend of movement to small angle with the addition of simulated actinides into pyrochlore structure; (2) XRD patterns and SEM photos showed that the series of samples were glass-ceramic wasteforms containing both crystalline and glass phase; (3) after irradiation experiments with different doses of Xe^{20+}, the XRD spectra and SEM photos of wasteforms did not change significantly. The cured body showed a good radiation stability.

The performance of glass-ceramic solidified should be evaluated from many aspects such as the physical properties and chemical stability. We are still carrying out relative research, and the results will continue to be published in paper.

References

1. Lang M, Zhang FX, Zhang JM et al (2010) Review of A2B2O7 pyrochlore response to irradiation and pressure. Nucl Inst Methods Phys Res B 268:2951–2959
2. Patwe SJ, Tyagi AK (2006) Solubility of Ce^{4+} and Sr^{2+} in the pyrochlore lattice of $Gd_2Zr_2O_7$ for simulation of Pu and alkaline earth metal. Ceram Int 32:545–548
3. Stanek CR, Uberuaga BP, Scott BL (2012) Accelerated chemical aging of crystalline nuclear waste forms. Curr Opin Solid State Mater Sci 16:126–133
4. Zhang JM, Livshits TS, Lizin AA et al (2010) Irradiation of synthetic garnet by heavy ions and a-decay of 244Cm. J Nucl Mater 407:137–142
5. Sengupta P (2012) A review on immobilization of phosphate containing high level nuclear wastes within glass matrix-present status and future challenges. J Hazard Mater 235–236:17–28
6. Todorov IT, John AP (2006) Simulation of radiation damage in gadolinium pyrochlores. J Phys 18:2217–2234

Veins, Dikes, and Pods of the UAE Mantle Peridotites: Possible Industrial Raw Materials

Sulaiman Alaabed

Abstract The northern extension of the Semail ophiolite in the UAE is dominated by tectonic mantle peridotites and gabbros. The peridotites are mostly harzburgite with little lherzolites and contain various intermittent veins, dikes, and pods. These veins, dikes, and pods can be divided into three rock categories: the ultramafic group that includes dunites, chromitites, and pyroxenites; the granitic dikes; and carbonate veins. Occurrences of these bodies are explicit and ubiquitous, but their distribution is not consistent throughout the sequence. Pyroxenites, chromitites, and granites occur in the upper half of the sequence, but more pronouncedly and dominantly close to the transition zone. Dunites pods and carbonate veins can be found at different stratigraphic levels. Magmatic signatures and monomineralic forms of the three ultramafic varieties are observed. Where it occurs, chromite-rich variety is always enveloped in olivine-rich pods. Coarse-grained mica-rich granites and pegmatites are well developed below and within the transition zone. Carbonates, and occasionally serpentine materials, impregnate through fractures and structures.

These rocks and their host peridotites offer a range of probable industrial raw materials that can be exploited accordingly. Carbonates, e.g., magnesite and dolomite, are important in refractory protection and cupellation process. The resistant property of granites to mechanical and chemical weathering has made them favored from other alternative rocks in multiple uses such as landscaping, road base and concrete aggregates, wall and floor tiles, raw building stones, and so on. The ultramafic bodies and their host peridotites mainly occur at the eastern part of the country. In addition to their use as foundation materials and some like chromitites as metallic commodity, they have recently become efficiently and environmentally preferred in iron and steel industry and in probable CO_2 sequestration.

Keywords Olivine • Magnesite • Mantle peridotite • Semail ophiolite • Industrial minerals

S. Alaabed (✉)
Department of Geology, College of Science, United Arab Emirates University, 15551, AlAIN, UAE
e-mail: s.alaabed@uaeu.ac.ae

F. Dong (ed.), *Proceedings of the 11th International Congress for Applied Mineralogy (ICAM)*, Springer Geochemistry/Mineralogy,
DOI 10.1007/978-3-319-13948-7_30

1 Introduction

The UAE section of the Oman Mountains includes an integral part of the northern Semail ophiolite (Fig. 1). The mantle sequence of the Semail ophiolite represents oceanic upper mantle tectonic peridotites of mainly harzburgites with little lherzolites and various types of intrusions. The entire Semail succession is about 15 km thick. The base of the succession is sedimentary rocks of the Arabian shield, not part of the ophiolite, on which the oceanic plate was pushed and obducted.

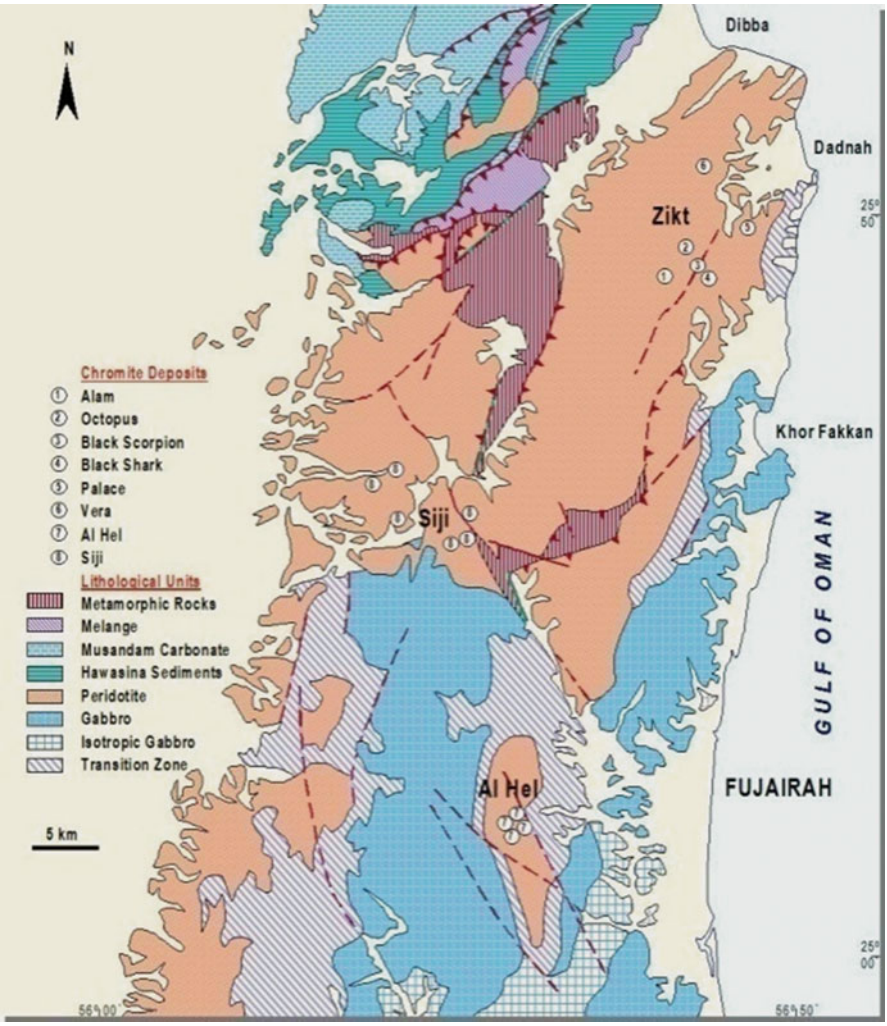

Fig. 1 Geological map of the Semail ophiolite section in the UAE and its major lithological units. The mantle sequence unit is the largest [1]

Semail rocks consist of two complete sequences. The ultramafic mantle sequence, at the lower part, is mostly made of harzburgitic peridotite (olivine and enstatite), with various dike-like and sill-like intrusives, and dunite. The mafic crustal sequence consists of layered to uniform gabbros, sheeted diabasic dikes, and basic volcanics above. Gabbros (mostly plagioclase and clinopyroxene-augite) are capped by dikes and volcanic basalts (pillow lava erupted on the ocean floor). The mantle sequence is seismically and petrologically separated from the crustal sequence by a transition zone (Moho). The base of the complex is floored by a metamorphic sole.

All ophiolite unites are presented in the Semail complex; however, the uppermost part of the complex (diabase basaltic dikes and Pillow lavas) is very limited or disappears in UAE Semail section, while mantle peridotites and crustal gabbros are ubiquitous. This work mainly aims to generally review the mantle peridotite inclusions (dikes, veins, lens, pods, etc.) as potential raw materials for the current and near future industrial applications.

2 Veins, Dikes, and Bodes Rock Types

The dike, veins, lens, and pods that are hosted in the mantle peridotites can be categorized into three groups:

First Group: Carbonate Veins
Second Group: Granitic Dikes
Third Group: Ultramafic Bodies, namely, dunites, chromitites, and pyroxenites

Occurrences of these intrusions are explicit and ubiquitous, but their distribution throughout the sequence is not consistent. Pyroxenites, chromitites, and granites occur in the upper half of the sequence but are more dominantly close to the transition zone. Dunite pods and carbonate veins can be found at different stratigraphic levels.

The upper mantle peridotite is generally uniform in composition with slight diversity in places. Cr/Al ratio of chromite increases down section. Mg# of olivine is high reaching 92.5 %, whereas in chromite (of chromitite) it is low to average 46 %. Ultramaphic bodies were formed either by early partial melting of the host peridotite or as invading melt that interacted with host. Granitic dikes show higher K compared to the crustal sequence dikes. They may have sedimentary protolith, syn-tectonically intruding the peridotites. Carbonate and serpentine are alteration products of the host minerals most likely obtained during emplacement process.

3 Carbonate Veins

Carbonates, and occasionally serpentine materials, impregnate through fractures and structures. They are mainly magnesite and dolomite with some calcite. Some carbonate bodies show distinct microstructures, e.g., oolites, and others depict serpentine fragments in carbonate matrix.

Carbonates occur in the mantle peridotites as fillings of the opening fractures and fault planes (Fig. 2). They are also found as replacement veins, indicating an exchange action of invading water (Fig. 3). The carbonated water takes Mg from the host rock to form dolomite ($(Ca, Mg)_2CO_3$) or magnesite (Mg_2CO_3). The source of the replacing water could be meteoritic water, hydrothermal water, or metamorphic water. The filling spaces and replacement activity can also be inferred from the thin-section micrograph image (Fig. 4), where a specific microstructure could be

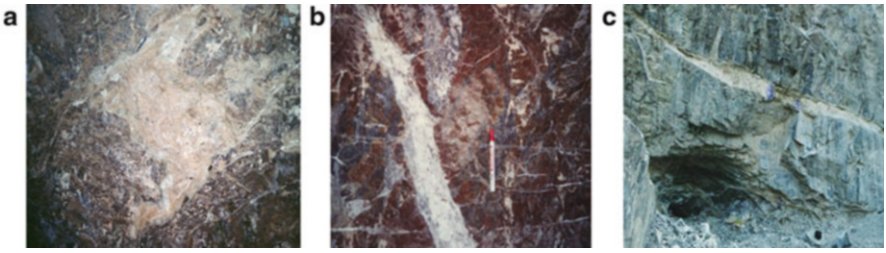

Fig. 2 Occurrence examples of the carbonate bodies as fillings of opening fracture (**a**, **b**) and along fault planes (**c**)

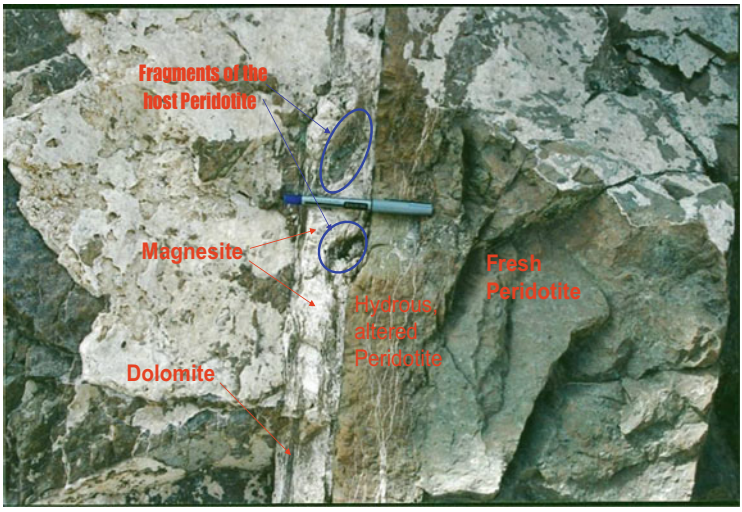

Fig. 3 The exchange action of the invading water is manifested by the hydrated border; magnesite and dolomite and host fragments exist within the carbonate veins

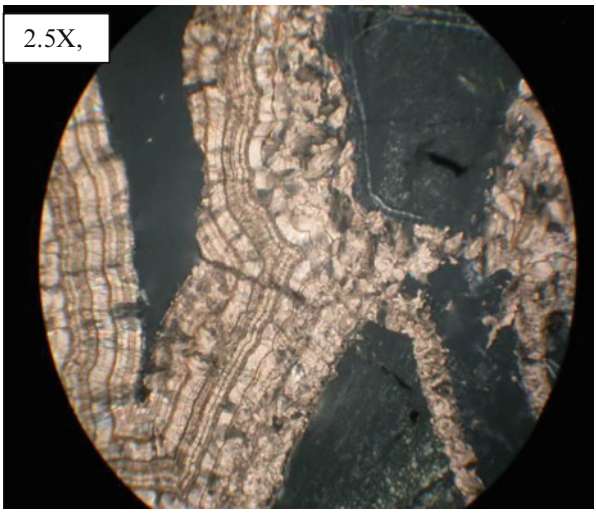

Fig. 4 Micrograph photo of a carbonate microstructure indicating an energetic shallow water environment

developed at an energetic shallow water environment that may point to a syn- or post-deformation origin.

Carbonates have many industrial applications. One of the major uses is the production of the quicklime. Lime is one of the greatest commercial products that have numerous diversities of usage applications indicated by many authors [4, 3, 6, 12–14, 17].

Although much use of carbonates is based on the limestone availability, magnesite is important in many other industrial applications. It is used as a slag in steelmaking furnaces, combined with lime. Quicklime and magnesite are introduced for refractory protection, neutralizing the alumina and silica separated from the metal, and assist in the removal of sulfur and phosphorus from the steel. Similar to the production of lime, magnesite can burn in the presence of charcoal to produce MgO, periclase, an important product in refractory materials. It can also be used as a catalyst and filler in the production of synthetic rubber and in the preparation of magnesium chemicals and fertilizers. Another application is the use in a metallurgy refining process called cupellation, where ores or alloyed metals are treated under high temperatures and controlled operations to separate noble metals, like gold and silver, from base metals like lead, copper, zinc, arsenic, antimony, or bismuth, present in the ore [5, 7]. The process is based on the principle that precious metals do not oxidize or react chemically, unlike the base metals; so when they are heated at high temperatures, the precious metals remain apart, while others react forming slags or other compounds [6]. Finally, magnesite is dyed to make beads and also used as a binder in flooring material.

4 Granitic Dikes

Granites are plutonic felsic rocks with a general mineral composition of quartz, feldspar, and mica. Existence of these felsic intrusions is not coherent with the mantle sequence composition, but their formation is likely related to the ophiolite emplacement. Granitic bodies at the Semail mantle sequence mostly show a dike-like pattern with a width range from 10 cm to about 1.5 m (Fig. 5), but the thickness becomes much bigger for some occurrences close to or at the transition zone.

Most of the dikes are foliated with alignment of the mineral grains parallel to the magmatic foliation, but deformation-related foliation is also observed. The grains are aligned parallel to the contact indicating shear flow direction in a single-surge dike (Fig. 6).

Many intrusions are coarse-grained mica-rich granites and granodiorites (Fig. 6a). However, tourmaline-bearing modes are also present (Fig. 6b). These are observed close to the transition zone at AlBedyah, Dhadnah-Zikt, and AlFiqaat areas. Black prismatic crystals (schorl) are well observed in the field (Fig. 6b). Under microscope, tourmaline is zoned probably indicating pneumatolytic stage of alteration or "tourmalinization" (Fig. 7). In this, boron attacks granitic minerals to form tourmaline, which in turn demonstrates the sedimentary source of tourmaline formation.

The small ledges or veins show composite and multiple surges/generations (Fig. 8).

Fig. 5 A granitic dike (*white*) intruding the ultramafic rocks of the mantle sequence at AlFiqaat area

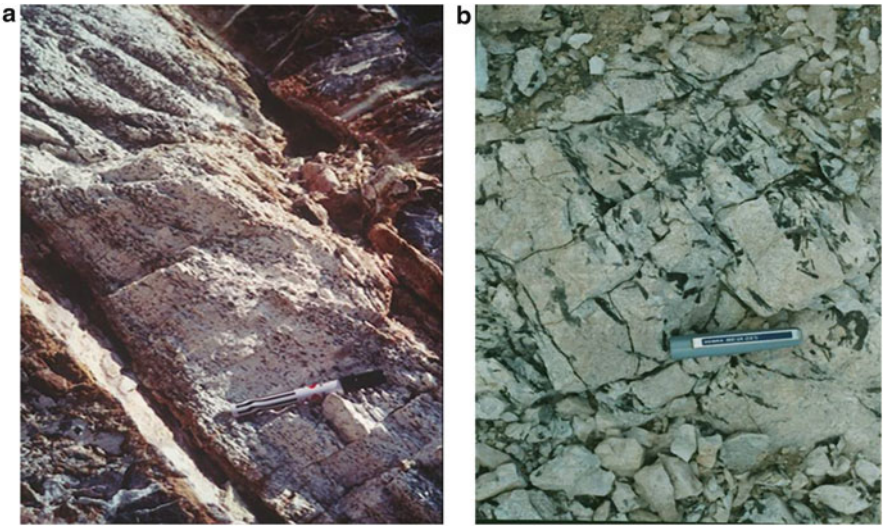

Fig. 6 (**a**) Biotite–mica granite intrusion showing biotite grains are aligned parallel to the contact, particularly at the borders, indicating shear flow direction in a single-surge dike (Zikt Area). (**b**) Tourmaline prismatic black grains (schorl) are well developed in tourmaline-bearing granitic rock (Dhanah area)

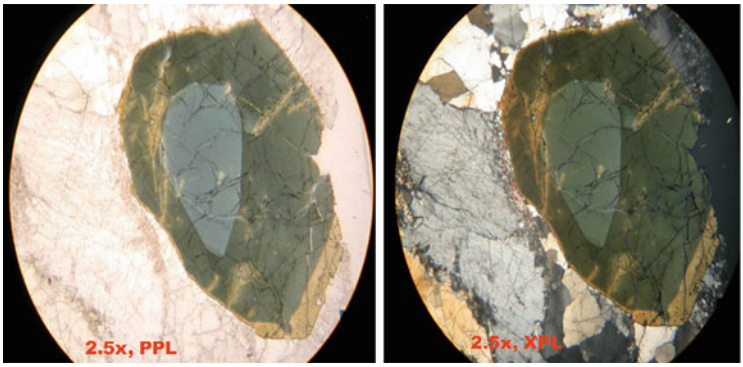

Fig. 7 (First two, *left*): Photomicrograph taken under microscope showing evidence of "tourmalinization." A zoned tourmaline indicates pneumatolytic stage of alteration, where boron attacks granitic minerals to form tourmaline

In areas, unusual composition and inclusions are found. For example, some mica granitic dikes consist of andalusite and cordeirite (Fig. 9), and others include chromitite fragments (Fig. 10).

Andalusite is formed in the granitic dike probably due to the retrograde metamorphism during a deformation episode. Chromitite fragments are not related to the granite composition, but may be brought from depth during the rising up of the intrusion.

Fig. 8 (Second two, *right*): The small ledges or veins show (**a**) composite and (**b**) multiple surges

Fig. 9 Large crystals of andalusite in granitic pegmatite. Some show chiastolite structure, and tourmaline also occurs in the same dike (AlFiqaat Area)

The contrasted mineralogy of granite (e.g., white quartz, light color feldspar, and dark mica) and its high resistivity to mechanical and chemical weathering make it more preferable to a direct utilization as building materials. Its uses include floor tile, landscaping, road base, concrete aggregate, stone facings, monuments, sculpture, countertops, and wall tile. However, the minerals of granite (e.g., quartz, feldspar, mica, tourmaline, andalusite, etc.) largely broaden the industrial importance of the granitic intrusions. Other than the use as gem, precious, or ornamental stones, each of its mineral has many manufacturing and commercial applications that cannot be covered in this chapter.

Fig. 10 A big granitic dike showing a sharp border with country ultramafic rocks and including chromitite exotics (Chromite open pit—Zikt)

5 Ultramafic Bodies

The ultramafic bodies found in the mantle sequence have three types: dunite, pyroxenite, and chromitite rocks. They occur as lenses, pods, veins, and dikes. Magmatic signatures and monomineralic form of the three ultramafic varieties are observed. Several pyroxenite dikes can be found at Zikt Area, vertically intruding the mantle harzburgite (Fig. 11a).

In places, they are cut by shear faulting probably during post-emplacement deformation episode, and the fault plan may be occupied by carbonate veins (Fig. 11b). Some pyroxenites have been partially or completely altered to amphibolites (Fig. 12b) and discordant with the mantle flow. Some are found to include chromite grains (Fig. 12).

Dunites are the most widespread that show concordant and discordant structural signatures with the mantle tectonic foliation (mantle flow). Although chromite grains are common accessories in the mantle harzburgite, chromite-rich variety (chromitite) is always enveloped in olivine-rich pods (dunite pods/lenses) or otherwise alternative with dunite layers (Fig. 13). Chromite rocks vary from disseminated to massive chromitites. Rhythmic layering, nodular, and anti-nodular (e.g., grape-shot) are regular structures in this rock (Fig. 14). Chromitites in the area were

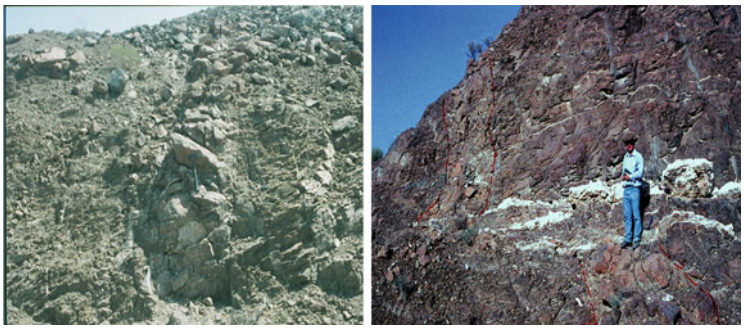

Fig. 11 (First two, *left*): Pyroxenite dikes intruding the mantle harzburgite at Zikt Area. The second photo (*left*) shows that the pyroxenite dike was cut by shear faulting, and the fault plan was invaded by carbonate (magnesite) veins

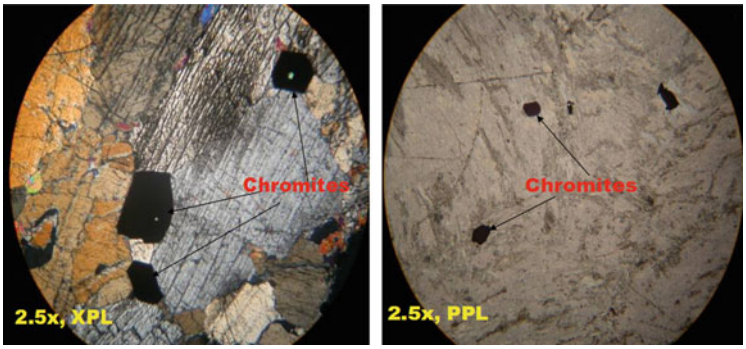

Fig. 12 (Second two, *right*): Two photo micrographs taken under microscope for a pyroxenite. The first one (*left*) under cross-polarized light (XPL) showing large pyroxenes with chromite inclusions. The second one (*right*) under plan-polarized light (*right*) showing amphiboles (after pyroxenes) with chromite inclusions

mined by Derwent Company from the beginning to the end of 1990s; the mined ores were exported through Fujairah harbor. However, not all were mined and the area is still fertile with deposit and capable of more exploration and mining.

Rather than building materials, the high-temperature minerals of the ulteramaphic rocks, peridotite, dunite, and pyroxenite, are preferred in several industrial applications.

They are used as flux, dolomite being a major MgO source in sintering and in iron and steel industry. Especially, olivine has become more favored over dolomite in slag conditioning of the iron and steel manufacturing. The high MgO content of olivine gives several preferences such as eliminating the preheat treatment, reducing energy and coke consumption, reducing slag volume, and lowering CO_2 emissions. The presence of higher amount of silica in dunite leads to lower sinter basicity (i.e., CaO/SiO_2) at around 2.5 than 3.5 of dolomite and the phases in sinter

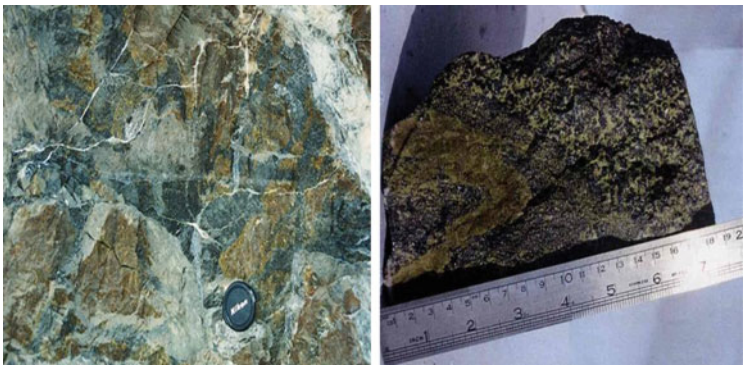

Fig. 13 (First two, *left*): Examples of the coexistence of dunite and chromitite as pods, lenses, or alternating layers. (**a**) Chromitite (*black*) impregnates through dunite (*brown*) in a large pod. Dunite is a green rock, but *brown* color due to serpentinization or alteration process. (**b**) Four folded layers: massive chromitite, dunite, massive chromitite, and disseminated chromitite

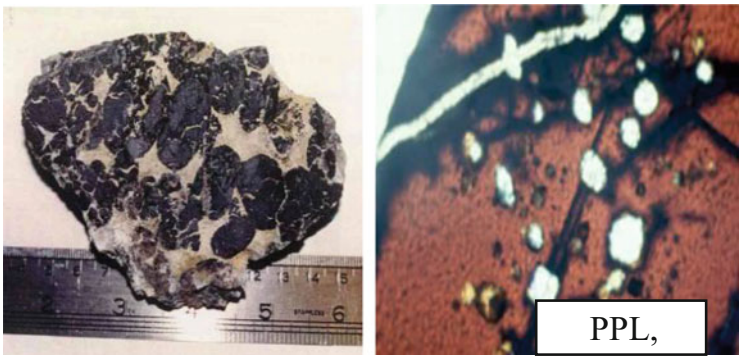

Fig. 14 (Second two, *right*): (**a**) Nodular form of chromitite showing a grape-shot structure, where the rounded massive chromitite nodules are surrounded by dunite (SE Dhadnah area). (**b**) Photo micrograph of chromite grain under plan-polarized light showing the ordinary *red-brown* color of chromite with few silicate inclusions

change to those having better reducibility. The net result is a reduction in the resistance of the cohesive zone to gas flow in the blast furnace leading to drop in fuel rate and higher productivity [8].

Emission of the greenhouse gas, CO_2, has become a critical environmental syndrome throughout the world due to the high emission of this gas from many sources and its effects on the rising global warming. Several recent studies on the ultramafic rocks, e.g., dunite, show the potential of these rocks in the sequestration of CO_2 by weathering or replacement reaction. The high-temperature minerals of the ultramafic rocks, particularly olivine, are very sensitive to the effect of water at low temperature (alteration) and so are easily metasomatized than the minerals of other rocks [2]. Köhler's research group [11] reported that carbon sequestration

technique by artificially enhanced silicate weathering via the dissolution of olivine would not only operate against rising temperatures but also oppose ocean acidification, because it influences the global climate by the carbon cycle. Several research groups in the United States (e.g., the Earth Institute at Columbia University, 2008; University of Tennessee at Knoxville, 2010; Kansas State University, 2012) have conducted separate projects to test the absorption of CO_2 by mafic or ultramafic rock through weathering interaction and then store the CO_2 in a rock format [9, 15, 16]. A study on Oman Mountains [10] found that underground carbonates bodies were formed much earlier than the surface veins in the ultramafic rocks probably by carbonated water or moisture penetrating through the mantle peridotite. They inferred that Oman ophioltic peridotite may be used to sequestrate a large volume of emitted CO_2. If the method outcome is achieved, a similar technique can be applied in all areas of large ultramafic occurrences.

Finally, the pervasive serpentinization of the mantle sequence may provide the commercial serpentine, asbestos, as natural source in the rock wool industry.

6 Conclusions

Veins, dikes, and pods of the UAE mantle peridotites can be generally divided into three groups: carbonate veins, granitic dikes, and ultramafic bodies.

The carbonates are mainly magnesite and dolomite in composition. Most granitic dikes are mica-quartz granite and granodiorite, sometimes including tourmaline and andalusite minerals, and few are pegmatitic. The ultramafic bodies occur as pods, lenses, or dikes of pyroxenite, dunite, and chromitite. However, dunites are the largest bodies hosted in the mantle peridotite, where sometimes they become envelopes of chromitites.

These various rocks provide a wide range of building materials, ornamental stones, and industrial applications.

Volume and quantity assessment of these resources is outside the magnetite of this chapter. Nevertheless, the ultramafic bodies and their hosts provide large volumetric occurrences that can be easily accessed. Moreover, the preferred use of the ultramafic minerals in the iron and steel industry, and their expected potentiality in sequestration of the emitted CO_2, put them in the crucial lead for near future industry.

References

1. Alaabed S (2000) Petrogenesis of chromite and associated minerals in the upper mantle peridotite of the northern Semail ophiolite (UAE). PhD thesis, The Ohio State University, Columbus, OH, USA
2. Alaabed S (2011) Rocks mineralogy controls the metasomatic activities: an indication from water/rock ratio modeling. Arab J Geosci 4(1–2):283–289

3. Bob B (1993) The standards for the use and disposal of sewage sludge. USEPA, 40CFR, p 257
4. Boynton R (1988) The Chemistry and technology of lime and limestone, 2nd edn. Wiley, New York
5. Bayley J, Rehren T (2007) Towards a functional and typological classification of crucibles. In: LaNiece S, Craddock P (eds) Metals and mines. Studies in archaeometallurgy. Archetype Books, Westminster, pp 46–55
6. Bayley J (2008) Medieval precious metal refining: archaeology and contemporary texts compared. In: Martinón-Torres M, Rehren T (eds) Archaeology, history and science: integrating approaches to ancient materials. Left Coast Press, Walnut Creek, CA, pp 131–150
7. Craddock PT (1995) Early metal mining and production. Edinburgh University Press, Edinburgh
8. Government of India, Ministry of Mines, Indian Bureau of Mines (2011) Indian Minerals Yearbook (2011): Part- II, 50th edition: dunite & pyroxenite (advance release), vol 33. Government of India, Ministry of Mines, Indian Bureau of Mines, Nagpur, pp 2–8
9. Kansas State University (2012) Geologists testing aquifer rocks as containers to permanently trap carbon dioxide. ScienceDaily. http://www.sciencedaily.com/releases/2012/07/120709121319.htm. Retrieved 5 Jan 2013
10. Kelemen P, Matter J (2008) In situ carbonation of peridotite for CO_2 storage. Proc Natl Acad Sci U S A 105(45):17295–17300
11. Köhler P, Hartmann J, Wolf-Gladrow DA (2010) Geoengineering potential of artificially enhanced silicate weathering of olivine. Proc Natl Acad Sci U S A 107(47):20228–20233
12. Landsberg VD (1992) The history of lime production and use from early times to the industrial revolution. Cement Lime Gypsum 8
13. Nicholas GP (1995) Hoover's water supply and treatment, vol 211. National Lime Association, Washington DC, pp 94–99
14. Robert NJ (1996) Use of lime water in Germany to solve handling and water quality concerns related to lime addition. In: The national conference on integrating corrosion control and other water quality goals
15. The Earth Institute at Columbia University (2008) Rocks could be harnessed to sponge vast amounts of carbon dioxide from air. ScienceDaily. http://www.sciencedaily.com/releases/2008/11/081105180813.htm. Retrieved 6 Jan 2013
16. University of Tennessee at Knoxville (2010) Storing carbon dioxide deep underground in rock form. ScienceDaily. http://www.sciencedaily.com/releases/2010/06/100617102402.htm. Retrieved 6 Jan 2013
17. World Health Organization (1995) Bactericidal effect of hydrated lime in aqueous solution. Carlos Munoz, Grupo Bertran, Mexico City, in Pan America, Report No. 5, p 52

Dissolution Characteristic Study on Dustfall in Citric Acid

Jun Tang, Faqin Dong, Qunwei Dai, Yuequan Deng, Shiping Zhou, and Wu Chen

Abstract In this chapter, the aim of our study is to evaluate dustfall's physical and chemical changes in acid conditions. pH and conductivity variation of reaction solution are measured by time. FTIR, SEM, and ICP analysis is applied to analyze the residuum and filtrate after the experiment. The results of conductivity variation show that the conductivity increases quickly in the first 10 min, then decreases slowly. pH of reaction solution keeps increasing in the first 4 h. Both the pH and conductivity become stable after 4 h. The combined analysis of XRD and FTIR spectrum of residuum and initial sample indicates that calcite and dolomite in dustfall are dissolved completely in the 0.05 M citric acid solution in 2 days. Besides, metal cations are extracted, including Ca^{2+}, K^{+}, Mg^{2+}, Fe^{3+}, Al^{3+}, and Si. In general, after the dissolution of dustfall in citric acid, minerals are dissolved in different degrees, and metal elements are extracted. Carbonate minerals are almost dissolved completely, and the structures of silicate minerals change with the extraction of elements.

Keywords Dustfall • Citric acid • Dissolution • Characteristic analysis

1 Introduction

The compositions of atmospheric particle are complex [1]. As the main source of dustfall is surface loose particles of earth's. It is reported by research groups of DONG Faqin and SHAO Longyi [2–4] that the main compositions of dustfall are

J. Tang • Q. Dai • S. Zhou
Key Laboratory of Solid Waste Treatment and the Resource Recycle, Ministry of Education, Southwest University of Science and Technology, Mianyang, Sichuan, China 621010

School of Environment and Resource, Southwest University of Science and Technology, Mianyang, Sichuan, China 621010

F. Dong (✉) • Y. Deng • W. Chen
Key Laboratory of Solid Waste Treatment and the Resource Recycle, Ministry of Education, Southwest University of Science and Technology, Mianyang, Sichuan, China 621010
e-mail: fqdong@swust.edu.cn

F. Dong (ed.), *Proceedings of the 11th International Congress for Applied Mineralogy (ICAM)*, Springer Geochemistry/Mineralogy,
DOI 10.1007/978-3-319-13948-7_31

minerals including quartz, albite, dolomite, calcite, gypsum, etc. It is also reported that minerals are with strong chemical activities, which may lead to diseases through physical appearances, interface chemistry properties, and particle sizes after entering human body. Previous researches [5–8] of the harm of atmospheric particles mainly focused on species concentration level and seldom concerned the changes of dustfall in human body. Minerals such as quartz, silicate, and carbonate minerals can dissolve in aqueous solution, and the existence of organic acid can greatly promote the dissolution process. As a result, many heavy metal elements are extracted, including toxic Al, Fe, Si, etc. Metabolism process as well as food taking can bring in a wide variety of organic acids in human body and make the body acidic. This paper discusses the physical chemistry variation by analyzing the initial sample, residuum, and solution and proving an important significance for exploring the harm mechanism of atmosphere particles.

2 Materials and Methods

2.1 Materials

Atmosphere dustfall used in this experiment was collected in the west of Xining city in May (2012), when sandstorm occurred frequently. And the sample was collected with wool brush on the roofed windowsill of citizens, which were seldom cleaned for a long time. Importantly, in order to prevent the influence of impurity, sample sites were all at least 1.5 m higher than road surface. Collections were sieved through 200 BS (0.074 mm) to eliminate the large particle and floccule.

Citric acid in this experiment was analytically pure from Tianjin Fuchen chemical reagents factory.

2.2 Experiment Methods

Experiments with dustfall were performed in conical flask. The experiment temperature was 37 °C, the rotating speed was 160 rad/min, and the solid–liquid ratio was 1:100. Dustfall was reacted for 2 days with 0.05 mol/L citric acid. During the reaction, pH and conductivity were measured at fixed time. After the experiment, the reaction solution was centrifuged to obtain filtrate and residuum. The residuum and filtrate were used for XRD, FTIR, SEM, and ICP analysis, respectively.

pH and conductivity were measured with the pH/conductivity/iron general-purpose tester [Mettler Toledo instrument company (Shanghai)]. Phase determination was performed with Multi-functional X-ray diffractometer (X'Pert PRO, PANalytical B.V.). Functional group was analyzed by Fourier transform infrared (FTIR) spectrometer (Nicolet-5700, Thermo Nicolet Corporation). Morphology

was observed by scanning electron microscope (EVO 18, Carl Zeiss Company). Extracted cations were analyzed by plasma emission spectrometer (iCAP6500, Thermo Fisher Company).

3 Results and Discussion

3.1 pH/Conductivity

The pH and conductivity are monitored in situ during the experiment, and the results are shown in Fig. 1. The conductivity increases quickly in the first 10 min, from initial 4.31 ms/cm to 5.61 ms/cm. After 4 h it becomes stable at 5.32 ms/cm. pH gradually increases from initial 1.74 to 1.90 in the first 4 h, and then pH of reaction solution no longer increases. According to X-ray crystallography results, the compositions of dustfall are quartz, calcite, dolomite, albite, and small amount of mica and chlorite group. The dissolution of minerals in organic acid depends on the ionized H^+. It is the consumption of H^+ that leads to the increase of pH and the extraction of cations which makes the conductivity go up. The balance of pH after 4 h is ascribed to the step-by-step process of citric acid's ionization. The consumption of H^+ promotes further ionization of citric acid, and the latter ionized H^+ compensates the consumption before dustfall, which makes the pH no significant variation. The stability of conductivity can be ascribed to the following aspects [9, 10]: on the one hand, as the experiment proceeds, cations exchange processes are complete. A new layer of residuum is formed with the proceeding of experiment, hindering the contact between H^+ and minerals. On the other hand, soluble minerals such as calcite and dolomite dissolved earlier; only quartz and albite were left, which were all difficult to dissolve [11].

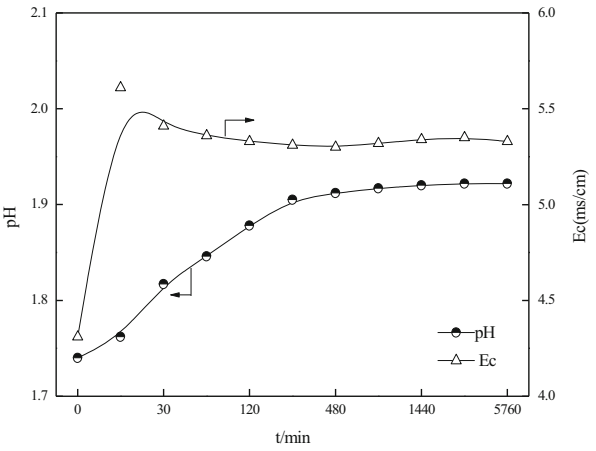

Fig. 1 pH/conductivity variation during the dissolution process

3.2 XRD Analysis

XRD spectra of initial and residuum are depicted in Fig. 2. It should be noted that only quartz, albite, and muscovite are detected. Minerals such as calcite ($2\theta = 23.093°$, $29.455°$, $36.061°$, $47.191°$, $43.219°$, $47.625°$) and dolomite ($2\theta = 30.986°$, $37.405°$,$41.182°$, $44.978°$, $50.605°$) detected in initial sample are not detected in residuum. It indicates that these kinds of minerals dissolve completely after leaching experiment. Besides, the full width at half maximum (FWHM) of the residual minerals such as muscovite increases ($2\theta = 8.890°$, $28.000°$). It can be explained with the theory of PENG Tongjiang et al. [12] that after H^+ exchanges with interlayer cations, and as the radius of H^+ is smaller than cations, the interlayer spacing becomes smaller. Ultimately, the grain size becomes smaller.

3.3 FTIR Analysis

The infrared spectrum of residuum and initial sample in 400–4,000 cm^{-1} is displayed in Fig. 3. Clearly there are several bands observed among 500–400 cm^{-1}, 1,100–900 cm^{-1}, and 1,160–1,300 cm^{-1}. According to previous research results, the bands in 3,800–3,000 cm^{-1} are assigned to the constitution water and interlayer water [13]. The affiliations of main adsorption bond are as follows: wave numbers 1,100–900 cm^{-1}, 770–800 cm^{-1}, and 694 cm^{-1} are attributed to Si–O bond, while between 1,430 and 877 cm^{-1} are assigned to CO_3^{2-} units. Bonds at 650 cm^{-1} and 471 cm^{-1} are assigned to feldspar and mica, respectively [14].

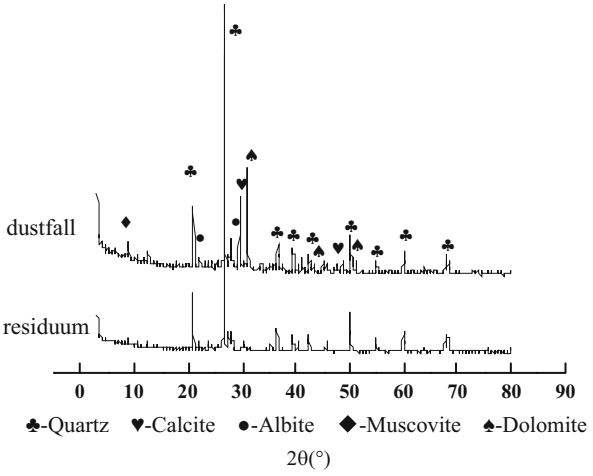

Fig. 2 XRD spectra of initial sample and residuum after reacting in citric acid

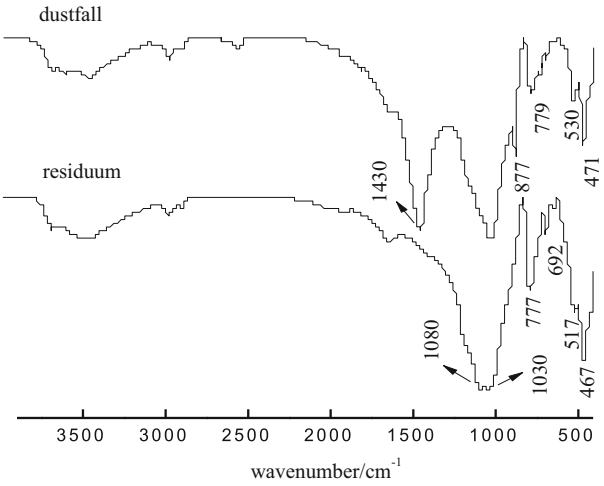

Fig. 3 FTIR spectra of initial sample and residuum after reacting in citric acid

The specific peaks at 1,430 and 877 cm^{-1}, which are assigned to CO_3^{2-} units, disappeared compared with initial sample, indicating that calcite and dolomite are completely dissolved in citric acid. This result is consistent with the results of composition analysis. A new peak is split out at 1,080 cm^{-1} in residuum compared with initial sample as the decrease of symmetry of silica tetrahedron caused by the leaching of citric acid.

3.4 Extracted Element Analysis

After 2 days' dissolution experiment, filtrate is prepared for elemental analysis with ICP analyzer, and the results are shown in Table 1. Compared with the concentration of extracted element in different solution, the extracted mass of cations in citric acid is apparently higher than that in ultrapure water, which indicates that citric acid has an effective acceleration on the dissolution of dustfall. The amount of extracted Ca^{2+} in citric acid and water is very large, 711.627 mg/L and 253.49 mg/L, respectively. The enhancing multiples of cation extraction in citric acid are listed as follows: Fe: 479.5, Al: 88.8, Mg: 13.1, Si: 10.0, Ca: 2.8, K: 1.7.

Comparing the metal element–Si ratio in filtrate and initial dustfall, it can be noted that the ratio in filtrate is apparently higher than that in dustfall. This reflects the nonsynchronous dissolution of elements in dustfall. It is because the composition of dustfall is complex, and different minerals have their own dissolution law and mechanism. The mass of extracted elements depends on their positions in structure, not on their percentages in chemical composition. It is well reported that Si mainly exists in silica tetrahedron, which exists in lattice and is difficult to

Table 1 Extracted cations of dustfall after reacting with citric acid

Extracted element		Ca	Si	Al	Fe	K	Mg
Leaching amount/mg. L^{-1}	Pure water	253.49	7.81	0.54	0.15	11.98	16.00
	Citric acid	711.63	77.84	47.88	70.96	20.68	209.00

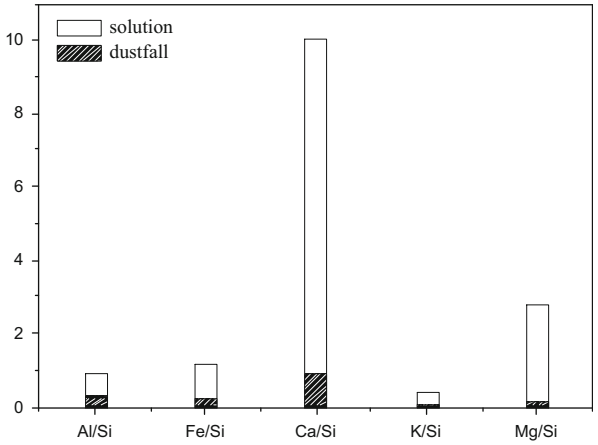

Fig. 4 Element/Si ratio in dustfall and filtrate residuum initial sample

break, while K, Ca, Mg, and Fe mainly exist at crystal edges and corners or between layers, formed by ionic bond, and are feasible to break which lead to more extracted mass of K, Ca, Mg, Fe, etc. Fig 4

3.5 Morphology Analysis

The morphology of initial sample and residuum is shown in Fig. 5. The particle size range varies from several to tens of microns. The compositions of dustfall are complex, including smoke, smoke aggregate, mineral aggregate, and biomass etc., which makes its multifarious morphology. After disposal with citric acid, the residuum is more ordination. There is less substance on particle surface. This may be ascribed to dissolution of some minerals as well as the extraction of impurity adsorbed on dustfall by citric acid. The rest of the minerals in residuum are primarily quartz, albite, mica, etc., which are difficult to be dissolved.

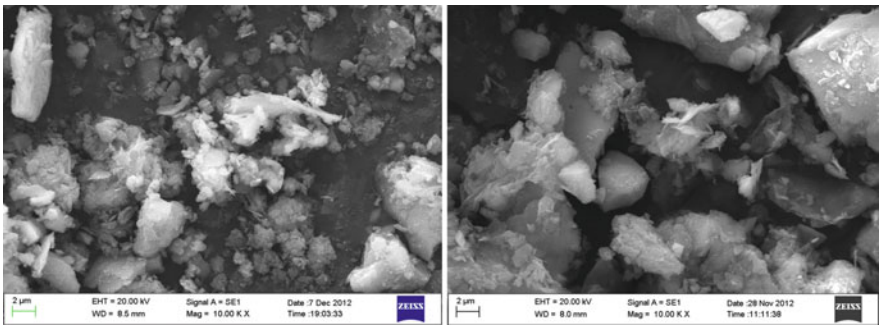

Fig. 5 Morphology analysis of dustfall and residual solid

4 Conclusions

With the extraction of cations, pH and conductivity vary obviously. In the frontier period of dissolution between dustfall and citric acid, pH and conductivity of reaction solution increase quickly, and both become stable after 4 h.

Insoluble minerals such as calcite and dolomite completely dissolved after 2 days' dissolution in citric acid; only quartz, albite, and muscovite were left.

Organic acid has an obvious acceleration in dissolution of dustfall. Compared with water, the enhancing multiples of cation extraction in citric acid are listed as follows: Fe: 479.5, Al: 88.8, Mg: 13.1, Si: 10.0, Ca: 2.8, K: 1.7.

After dissolution, dustfall becomes more tactic, with less impurity.

Acknowledgments This research is conducted as a part of study on the repercussion between inhalable particles and microbe, which is funded by National Natural Science Foundation of countries (No.41130746).

References

1. Hu GR, Yu RL et al (2013) Assessment of toxicity of heavy metal contaminated dustfall in Quanzhou city by toxicity characteristic leaching procedure. Acta Miner Sin 33(01):1–9
2. Dong FQ, He XC et al (2005) Study on the basic characteristics of several atmospheric dusts in the northern China. J Mineral Petrol (25, 03):114–117
3. Zheng N, JI A et al (2009) Mineralogical study on inhalable particles during the haze period in winter Beijing. Acta Sci Nat Univ Pekin (2):89–96
4. Xiao ZH, Shao LY et al (2009) Mineralogical characteristics of PM10 collected before and during dust storm episode in Lanzhou city, northwestern China. Bull Mineral Petrol Geochem 28(02):177–182
5. Cama J, Ganor J (2006) The effects of organic acids on the dissolution of silicate minerals: a case study of oxalate catalysis of kaolinite dissolution. Geochim Cosmochim Acta 70 (9):2191–2209

6. Teir S et al (2007) Dissolution of natural serpentinite in mineral and organic acids. Int J Miner Process 83(1–2):36–46
7. Oelkers EH et al (2011) Do organic ligands affect calcite dissolution rates? Geochim Cosmochim Acta 75(7):1799–1813
8. Hellmann R, Daval D, Tisserand D (2010) The dependence of albite feldspar dissolution kinetics on fluid saturation state at acid and basic pH: progress towards a universal relation. Compt Rendus Geosci 342(7–8):676–684
9. Bickmore BR et al (2006) The effect of Al(OH)4− on the dissolution rate of quartz. Geochim Cosmochim Acta 70(2):290–305
10. Bickmore BR et al (2008) Reaction pathways for quartz dissolution determined by statistical and graphical analysis of macroscopic experimental data. Geochim Cosmochim Acta 72 (18):4521–4536
11. Ptáček P et al (2011) Mechanism and kinetics of wollastonite fibre dissolution in the aqueous solution of acetic acid. Powder Technol 206(3):338–344
12. Peng TJ, Liu FS et al (2005) The acid corrosion mechanism and the soak-out substances after treating phlogopite-vermiculite interstratification minerals with hydrochloric acid. Acta Petrol Mineral 24(06):622–628
13. Hudson PK et al (2008) Coupled infrared extinction spectra and size distribution measurements for several non-clay components of mineral dust aerosol (quartz, calcite, and dolomite). Atmos Environ 42(24):5991–5999
14. Liu Gk, Peng WS (1983) Quantitative infrared spectroscopic analysis of calcite, feldspar and quartz in loess. Acta Mineral Sin (01):63–67

Graphite and Graphite-Like Materials from Black-Shale and Magmatic Ores: Raman Spectroscopy Data

Tatyana Moroz, Victor Ponomarchuk, Sergey Goryainov, Konstantin Kovalev, and Nadezhda Palchik

Abstract The graphite and graphite-like samples from many gold-ore deposits of the black-shale formation and magmatic ore deposits of Russia and Kazakhstan are investigated by means of micro-Raman spectroscopy technique with near-ultraviolet excitation. The results showed different Raman spectral variations of carbonaceous materials (CM) with metamorphic grade: the well-ordered graphite from magmatic rocks, more ordered, and the disordered less graphitized CM from black-shale ores. For the first time in the world's practice, the Raman spectroscopy technique has been applied to determine the temperature of graphitizing for CM at gold-ore deposits of the black-shale formation. The temperatures obtained from carboniferous substance for the gold deposits range from 405 to 280 °C. Temperature of CM formation from Pt-low sulfide ores of the Talnakh deposit ranges from 4,700 to 6,500 °C. It showed that the carbon-rich phases from black-shale and magmatic rocks have various degrees of graphitization and different carbon forms.

Keywords Carbonaceous material • Graphite • Raman spectroscopy • Gold-ore deposits • Black-shale formation

1 Introduction

Graphite and graphite-like materials now exist widely in black shales and magmatic ores. The nature of these carbon materials (CM) is multifarious. What causes a mineralization that connected with carbon? A great number of parameters, namely, the temperature, the pressure, the shear stress, the catalytic species, the host-rock lithology, the time, etc., have an influence on the graphitization process. Accumulations of gold and platinum group elements in black graphite shale and extraction of these metals from rocks depend on considerable degrees from structural

T. Moroz (✉) • V. Ponomarchuk • S. Goryainov • K. Kovalev • N. Palchik
Institute of Geology and Mineralogy, Siberian Branch Russian Academy of Science, 630090 Novosibirsk, Russia
e-mail: moroz@igm.nsc.ru

F. Dong (ed.), *Proceedings of the 11th International Congress for Applied Mineralogy (ICAM)*, Springer Geochemistry/Mineralogy,
DOI 10.1007/978-3-319-13948-7_32

properties of CM [1–3]. Raman spectroscopy has been widely applied for the study of various carbon modifications, including nanostructuring materials [4, 5]. The nano- and microstructures carbons in natural magmatic rocks are of great interest [6]. Natural carbons with nanostructured formations in graphite globules of igneous rocks are much like nanostructures synthesized under strictly controlled conditions. SR XRF applied to graphite globules revealed high amounts of Fe and Pt, which are potential catalysts for the decomposition of carbon-containing gases. The model of chemical deposition in the vapor phase can only explain the formation of nanotubes in graphite globules [7–9]. Raman microspectroscopy analysis of the CM can contribute to resolving various questions in the field of earth sciences. The first- and second-order Raman spectra have been correlated with changes in the structure of graphite. There is a linear relationship between temperature and Raman $R2$ and $R1$ parameter (derived from the area and intensity of the defect band (D) relative to the ordered graphite band (G), respectively) [10–18]. A comparison shows that these parameters depend on the use of excitation [12, 17–19]. $R2$ ratio with a laser wavelength of 532 nm was systematically larger than that of a 514.5 nm laser [20]. The intensity ratio $R1$ decreases with increasing UV excitation in all forms of carbon, with a faster decrease in more ordered carbons, which is generally small for UV excitation [18, 19]. But in many cases, ultraviolet excitation successfully yielded fluorescence-free Raman spectra [21]. The purpose of this study is about characterizing the rocks and CM from carbon-rich rocks of gold-ore deposits of the black-shale formation and magmatic ore deposits using micro-Raman spectroscopy technique with near-ultraviolet excitation and applying this technique for determining the temperature of graphitizing for CM.

2 Materials and Methods

2.1 General

The graphite and graphite-like samples from Malomyr and Talnakh ore deposits of Russia and from Suzdal deposit of Kazakhstan are investigated. Raman spectroscopy is useful for the characterization of CM and rocks [23, 24]. Knowledge of specific minerals and CM for different types of rocks allows us to reconstruct geological processes. The reported results showed that different Raman spectral variations of carbonaceous materials have metamorphic grade [11, 13–16, 20, 23–26]. Such method of vibrational spectroscopy as IR spectroscopy is important in the characterization of reducing carbon-bearing rocks [27, 28]. Three groups of samples are studied: firstly, unusual graphite shapes (needles and spiked structures within globules) have been found in thin sections of globular leucogabbro of the Verhnetalnahskaya trap layered intrusion on the Siberian platform, Talnakh, Russia [7–9] and, secondly, from black-shale gold deposit, the Malomyr, found in Russia and Suzdal, Kazakhstan.

2.2 Materials and Mix Designs

CM from carbon-rich rocks of gold-ore deposits of the black-shale formation (Malomyr—M1, M2, M3, and M4 and Suzdal—S1, S2, S3, and S4 samples) and Talnakh magmatic ore (T1–T4 samples) are from different sites. Pt-low sulfide ores of the Talnakh deposit are located on Siberian Platform, Russia. Unusual graphite shapes (needles and spiked structures within globules) have been found in thin sections of globular leucogabbro of the Verhnetalnahskaya trap layered intrusion [9, 29]. The Malomyr gold deposit is located in Amyr region, Russia [22]. The Suzdal gold deposit is located in the Western Kalba gold-ore belt, Eastern Kazakhstan. The geological setting of the Suzdal deposit is described in [30] its references.

2.3 Methods for Assessment and Analysis

The composition and structure of the rock and graphite-like materials from carbon-rich rocks of gold-ore deposits of the black-shale formation and magmatic ore deposits are studied by means of micro-Raman spectroscopy with near-ultraviolet excitation, X-ray powder diffraction, and infrared spectroscopy methods. XRD patterns are recorded by means of ARL X'TRA Thermo X-ray powder diffraction. CuKα radiation was used as the X-ray source. Recorded diffraction lines were indexed with JSPDS powder data file. Infrared spectra were recorded on the Bruker FT-IR VERTEX 70 spectrophotometers. Samples of 1.8 mg were embedded in spectro-pure KBr. The Raman spectra were measured by using micro-Raman spectroscopy technique (Horiba Jobin Yvon LabRam spectrometer). Near-ultraviolet excitation was performed with 325 nm (3.8 eV) line of He–Cd laser. The Raman spectra were measured also in backscattering geometry which was used in the Horiba Jobin Yvon's spectrometer T64000 with triple monochromator. Excitation was performed with 514.5 nm (2.41 eV) line of Ar ion laser [24]. The laser power falling onto the sample, 2–3 mW, was chosen to be enough low to prevent the laser-induced heating of the sample. The Raman spectra with near-infrared excitation 1,064 nm (1.17 eV) were recorded on Bruker RFS100 FT-Raman spectrometer.

3 Results and Discussion

The Raman spectra obtained from CM of the Talnakh unusual graphite shapes (needles and spiked structures within globules) showed same results with 514.5 nm and 325 nm excitation (Figs. 1 and 2, Tables 1 and 2). All the structures of samples were organized compactly. Raman spectrum of crystalline graphite should consist of a strong line at 1,582 cm^{-1}; for disordered carbons additional bands appear in

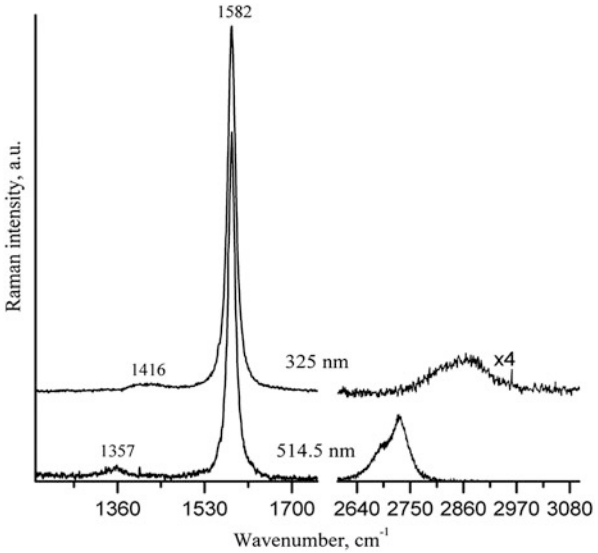

Fig. 1 Raman spectrum T1 Talnakh sample. *Top curve*—325 nm excitation, *bottom*—514.5

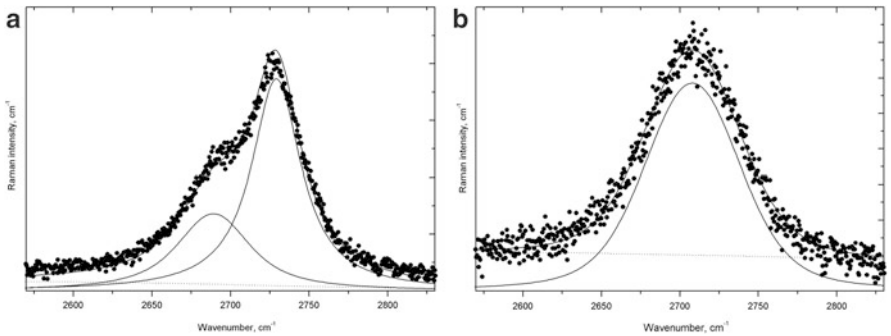

Fig. 2 Fitting of Raman spectrum with 514.5 nm T1 (**a**) and T4 (**b**) Talnakh samples in region 2,400–3,000 cm^{-1}

1,355 cm^{-1} ($D1$-band), ~1,620 cm^{-1} ($D2$), and ~1,560 cm^{-1} ($D3$). The second-order Raman bands are assigned to obtain scattering at ~2,695 and ~2,735 cm^{-1} ($2D1$ and $2D2$) merged into a single band ~2,710 cm^{-1} with increasing disorder (Fig. 1, bottom curve). Defect bands of first and second order strongly depend on the energy of excitation (Fig. 1, top curve, Table 1). Raman $R2$ and $R1$ parameters are derived from the area and intensity of the defect band (D) relative to the ordered graphite band (G), respectively. The intensity ratio $R1 = I(D1)/I(G)$ at ~0.01 to −0.02 confirms the highest degree of structural organization in these unusual graphites. SEM images of these samples were shown in [7–9]. Raman spectra of samples from Talnakh with different excitation lines (514.5 nm and 325 nm) may

Table 1 Results of Raman spectral analysis

Sample	*G* center (cm^{-1})	%	*D*1 center (cm^{-1})	FWHM (cm^{-1})	*R*2 (I(D2)/I(G))	*R*1 (I(D1)/I(G))	*T* (°C)	2*D*1 (cm^{-1})	2*D*2 (cm^{-1})	2*D*/*GI*
T1	1,583	15.3	1,359.8	26.9	0.041	0.024	623	2,689	2,729	0.18
T2	1,583.1	17.8	1,358.3	53.1	0.192	0.08	556	2,695	2,727	0.2
T3	1,582.3	20.3	1,356.98	66.4	0.2385	0.107	535	2,696	2,724	0.23
T4	1,580.2	24.5	1,355.6	64.9	0.3069	0.186	504.5	2,708		0.32
T1	1,582.6	19.0	1,416.5	82	0.076	0.018	607	2,819	2,864	0.021
T2	1,583.7	14.8	1,421.9	34.5	0.022	0.0047	631	2,810	2,881	0.015
T3	1,583.7	18.9	1,393.0	46	0.046	0.014	620.5	2,806	2,868	00.16
T4	1,584.25	22.7	1,390.3	36	0.1	0.049	596	2,858		0.013

Table 2 Results of Raman spectral analysis

Sample	*G* center (cm^{-1})	%	*D* center (cm^{-1})	FWHM (cm^{-1})	*R*2 (I(D2)/I(G))	*R*1 (I(D1)/I(G))	*T* (°C)
S1	1,603.3	49.80	1,389.5	153.7	0.53	0.470	405
S2	1,602.0	49.76	1,782.0	98.0	0.60	0.840	297
S3	1,602.7	46.40	1,377.6	123.9	0.53	0.420	405
S4	1,591.4	73.00	1,383.5	143.0	0.57	0.680	386
M1	1,576.7	35.00	1,385.6	112.0	0.46	0.270	436
M2	1,579.2	25.00	1,397.4	91.0	0.38	0.160	473
M3	1,580.2	29.05	1,385.0	84.7	0.63	0.605	359
M4	1,580.7	40.03	1,396.0	185.0	0.69	0.480	335

be used for estimation of difference between *R*2 parameter and temperature correlations. You can see that *R*2 ratio using excitation of Ar^+ laser line is significantly larger at 514.5 nm than at 325 nm. For the use of Raman spectroscopy data as geothermometer, any coefficient is necessary.

The composition and structure of the rock and graphite-like materials from carbon-rich rocks of gold-ore deposits of the black-shale formation are studied by means of micro-Raman spectroscopy with near-ultraviolet excitation, X-ray powder diffraction, and infrared spectroscopy methods.

According to IR spectroscopy and X-ray diffraction data, samples from Malomyr black-shale ores have as the main component phengite type mica (dioctahedral 2 M muscovite with parameter $a = 5.212$, $b = 9.043$, $c = 19.99$, $\beta = 96.017$, $V = 937.04$) [1].

IR spectra show a small amount of ankerite. Raman spectra show similar Raman spectrum of samples from Sykhoi Log giant gold deposit (Siberian, Russia) [31] picture, with different peak position OH group of muscovite for samples M1–M4 (Figs. 3 and 4).

The intensity ratio $R1 = I(D1)/I(G)$ at ~0.2 to −0.6 indicates the high degree of structural organization in these samples. Attempts to register Raman spectra at 1,064 for Malomyr and Talnakh samples are met with failure. Only 325 nm excitation allowed us to record good quality of Raman spectra (Fig. 5).

Raman and IR spectra showed a considerable amount of calcite in Suzdal samples, but only these samples have good Raman spectra with near-infrared excitation at 1,064 nm. Fragment of the spectra in region—1,200–1,800 cm^{-1} can seen in Fig. 6 (bottom curve). According to X-ray powder diffraction patterns, different minerals like quartz, carbonates, Fe-chlorite, feldspars, muscovite in mineral composition, and bitumen component are determined in samples of Suzdal gold-ore deposit (Fig. 7). There is large fluorescence background in Raman spectra of Suzdal samples with 325 nm excitation (Fig. 8).

The results show that samples from Suzdal gold-ore black-shale formation are less graphitized, and the disordered matter in comparison with Malomyr ores is graphitized for CM at gold-ore deposits of the black-shale formation. The temperatures obtained from carboniferous substance for the gold deposits range from 400 to 280 °C (Fig. 9). Estimation of temperature may be from more stable

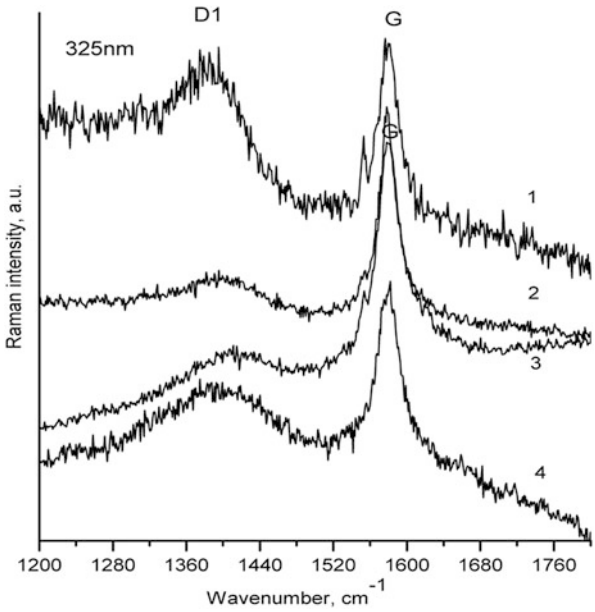

Fig. 3 Fragment of Raman spectra of Malomyr sample in region 200–1,200 cm^{-1} and 3,400–3,800 cm^{-1} (*insert*) 1—M2 sample, 2—sample from Syxoi log black-shale deposit, *center curve*—rruff.info data [32]

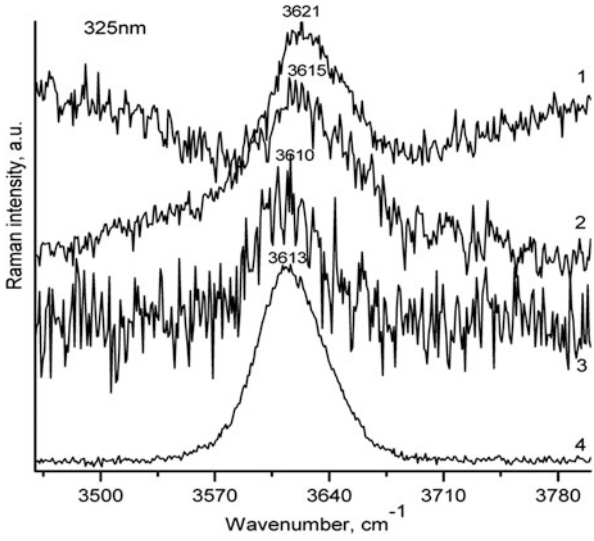

Fig. 4 Fragment of Raman spectra of Malomyr samples in region 3,460–3,800 cm^{-1}. 1—M1, 2—M4, 3—M3, 4—M2 sample

parameters, Raman spectra and position band G [17–19]. Temperature of CM formation from Pt-low sulfide ores of the Talnakh deposit ranges from 4,700 to 6,500 °C. It showed that the carbon-rich phases from black-shale and magmatic rocks have various degrees of graphitization and different carbon forms.

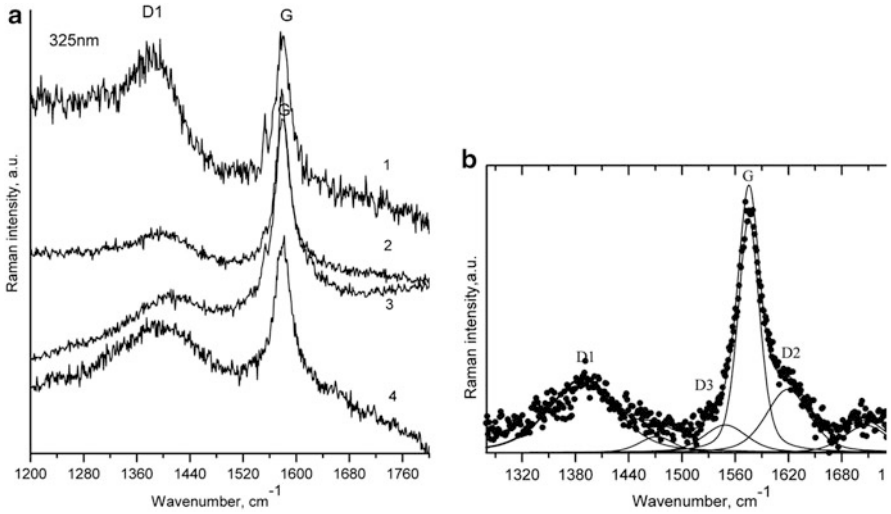

Fig. 5 Fragment of Raman spectra of Malomyr samples in region 1,200–1,800 cm^{-1}. (**a**) 1—M3, 2—M2, 3—M1, 4—M4 samples, (**b**) fitting spectra

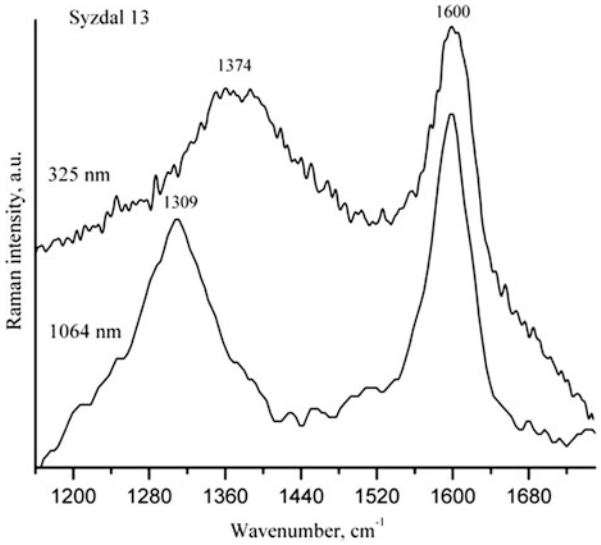

Fig. 6 Raman spectra S3 Suzdal sample. *Top curve*—325 nm excitation, *bottom*—1,064 nm

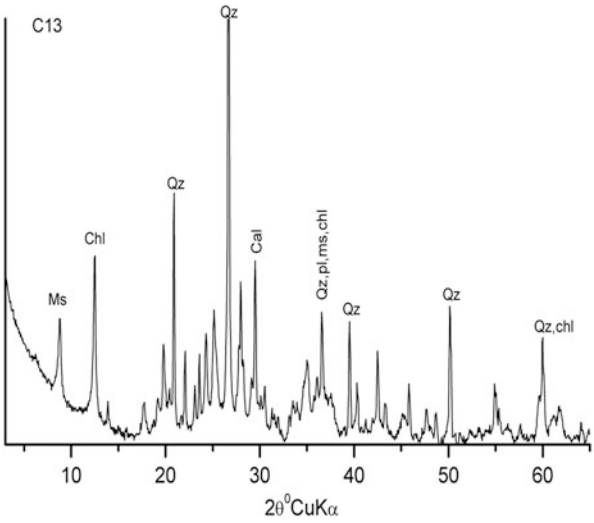

Fig. 7 X-ray powder diffraction Suzdal samples S3

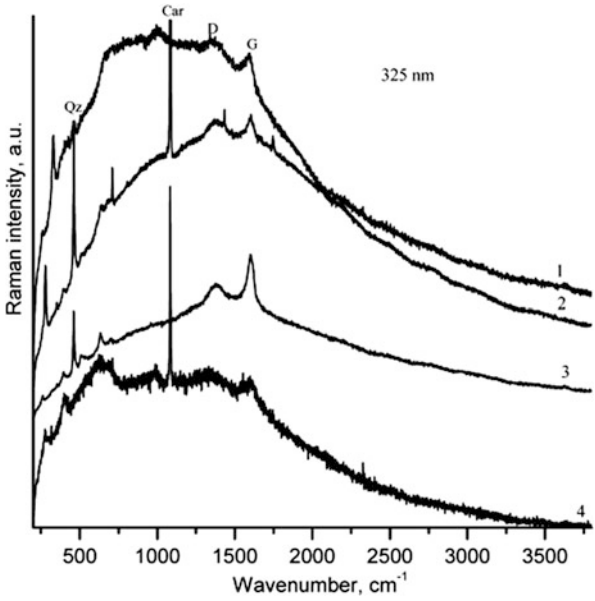

Fig. 8 Raman spectra S3 Suzdal sample. *Top curve*—325 nm excitation, *bottom*—1,064 nm

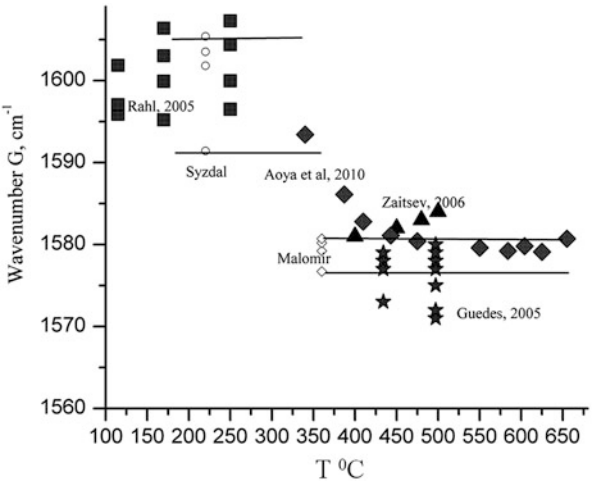

Fig. 9 Relation between *G* band position and *T* °C at literature data [20, 25, 26]

4 Conclusions

The results showed different spectral variations of CM with metamorphic grades. The well-ordered graphites are registered in magmatic rocks, more ordered in Malomyr black-shale ores, and the disordered less graphitized matter in samples from Suzdal gold-ore deposit. The Raman spectroscopy technique has been applied to determine the temperature of graphitizing for CM at gold-ore deposits of the black-shale formation. The temperatures obtained from carboniferous substance for the gold deposits range from 405 to 280 °C. The temperature of CM formation from Pt-low sulfide ores of the Talnakh deposit ranges from 4,700 to 6,500 °C. It showed that the carbon-rich phases from black-shale and magmatic rocks have various degrees of graphitization and different carbon forms.

Acknowledgements We thank Dr. Yu. Chesalov of the Institute of Catalysis, Novosibirsk, Russia, and Dr. V. Volodin from Novosibirsk State University, Russia, for technical assistance with the Raman spectrometer. The support of RFBR Foundation (No. 12-05-01040a and No. 13–05) is gratefully acknowledged.

References

1. Van Deventer JSJ, Tan H, Feng D, Lukey GC (2005) The behaviour of carbonaceous matter in gold extraction. Treatment of gold ores. In: Proc. 44th annual conf. of metallurgists, CIM, Montreal pp 111–125
2. Tan H, Feng D, Lukey GC, van Deventer JSJ (2005) The behaviour of carbonaceous matter in cyanide leaching of gold. Hydrometallurgy 78:226–235
3. Zavodinsky VG, Khanchuk AI, Mikhalenko EA (2012) Towards to extraction of nanodispersed noble metals from natural black graphite shales. Eur Researcher 16:12–19

4. Moroz TN, Fedorova EN, Zhmodik SM, Mironov AG, Rilov GM, Ragozin AL, Afanasiev AD, Zaikovskii VI (2000) Investigation of various carbon modifications by means of Raman spectroscopy. Chem Sustain Dev 8:43–47
5. Ryabenko AG, Kiselev NA, Hutchison JL, Moroz TN, Bukalov SS, Mikhalitsyn LA, Loutfy RO, Moravsky AP (2007) Spectral properties of single-walled carbon nanotubes encapsulating fullerene. Carbon 45:1492–1505
6. Jaszczak JA, Dimovski S, Hackney SA, Robinson GW, Bosio P, Gogotsi Y (2007) Micro- and nanoscale graphite cones and tubes from Hackman Valley, Kola Peninsula, Russia. Can Mineral 45:379–389
7. Ponomarchuk VA, Kolmogorov YP, Ryabov VV, Titov AT, Moroz TN, Semenova DV, Pyryaev AN, Ponomarchuk AV (2013) SR XRF study of carbon from igneous rocks. Bull Russ Acad Sci Phys 77:203–206
8. Ponomarchuk VA, Semenova DV, Moroz TN, Titov AT, Ryabov VV (2011) 250-Ma old nature carbon nanostructuring materials and nanotubes in intrusive rocs. Mineral Mag 75:1659
9. Ryabov VV, Ponomarchuk VA, Titov AT, Semenova DV (2012) Micro and nanostructures of carbon in Pt-low sulphide ores of the Talnakh deposit (Siberian platform). Dokl Earth Sci 446:556–560
10. Tuinstra F, Koenig JL (1970) Raman spectra of graphite. J Chem Phys 53:1126–1130
11. Pasteris JD, Wopenka B (1991) Raman spectra of graphite as indicators of degree of metamorphism. Can Mineral 29:1–10
12. Profeta M, Mauri F (2001) Theory of resonant Raman scattering of tetrahedral amorphous carbon. Phys Rev B 63:245415
13. Wopenka B, Pasteris JD (1993) Structural characterization of kerogens to granulite-facies graphite: applicability of Raman microprobe spectroscopy. Am Mineral 78:533–557
14. Buseck P, Huang B-J (1985) Conversion of carbonaceous material to graphite during metamorphism. Geochim Cosmochim Acta 49:2003–2016
15. Beyssac O, Goffe B, Chopin C et al (2002) Raman spectra of carbonaceous material in metasediments: a new geothermometer. J Metamorph Geol 20:859–871
16. Beyssak O, Rouzaud JN, Goffe B, Brunet F, Chopin C (2002) Graphitization in a high-pressure, low-temperature metamorphic gradient: a Raman microspectroscopy and HRTEM study. Contrib Mineral Petrol 143:19–31
17. Ferrary A, Robertson J (2000) Interpretation of Raman spectra of disordered and amorphous carbon. Phys Rev B 61:14095–14107
18. Ferrari AC, Robertson J (2001) Resonant Raman spectroscopy of disordered, amorphous, and diamondlike carbon. Phys Rev B 64:075414
19. Ferrari AC, Robertson J (2004) Raman spectroscopy of amorphous, nanostructured, diamond-like carbon, and nanodiamond. Philos Trans R Soc London A 362:2477–2512
20. Aoya M, Kouketsu Y, Endo S, Shimizu H, Mizukami T, Nakamura D, Wallis S (2010) Extending the applicability of the Raman carbonaceous-material geothermometer using data from contact metamorphic rocks. J Metamorp Geol 28:895–914
21. Shoute LCT, Schmidt KJ, Hall RH, Webb MA, Rifai S, Abel P, Arboleda PH, Savage A, Bulmer JT, Loppnoe GR (2002) UV Raman spectroscopy of oilsands-derived bitumen and commercial petroleum products. Appl Spectrosc 56:1308–1313
22. Ozhogin DO, Orlova NI, Vlasov NG, Dubinchuk VT, Shuvalova YN (2008) Vertical mineralogical zonation of gold-sulphidic metallization of the deposit Malomyr. Razvedka i oxrana nedr 8:16–21 (in Russian)
23. Jehlicka J, Urban O, Pokorny J (2003) Raman spectroscopy of carbon and solid bitumens in sedimentary and metamorphic rocks. Spectrochim Acta A 59:2341–2352
24. Moroz TN, Zhmodik SM, Mironov AG, Volodin VA (2012) Raman spectra of the carbonaceous materials from Ospa-Kitoy ultrabasic massif and Botogol graphite deposit (the East Sayan, Russia). In: Georaman Xth. 10th international conference on Raman spectroscopy applied to earth sciences—Sensu Lato, Nancy, France, 11–13 June 2012, pp 127–128

25. Guedes A, Noronha F, Prieto AC (2005) Characterisation of dispersed organic matter from lower Palaeozoic metasedimentary rocks by organic petrography, X-ray diffraction and micro-Raman spectroscopy analyses. Int J Coal Geol 62:237–249
26. Rahl JM, Anderson KM, Brandon MT, Fassoulas C (2005) Raman spectroscopic carbonaceous material thermometry of low-grade metamorphic rocks: calibration and application to tectonic exhumation in Crete, Greece. Earth Planet Sci Lett 240:339–354
27. Pitcairn IK, Roberts S, Teagle DAH, Craw D (2005) Detecting hydrothermal graphite deposition during metamorphism and gold mineralization. J Geol Soc 162:429–432
28. Zeng Y, Wu C (2007) Raman and infrared spectroscopic study of kerogen treated at elevated temperature and pressure. Fuel 86:1192–1200
29. Ryabov VV, Shevko AY, Gora MP (2000) Magmaticheskie obrazovaniya Noril'skogo raiona (Magmatic Buildups of Norilsk District), vol 2, Atlas magmaticheskikh porod (Atlas of Magmatic Rocks). Nonpareil, Novosibirsk
30. Kovalev KR, Kalinin YA, Naumov EA, Pirajno F, Borisenko AS (2007) A mineralogical study of the Suzdal sediment-hosted gold deposit, Eastern Kazakhstan: implications for ore genesis. Ore Geol Rev 35:186–205
31. Wood BV, Popov NP (2006) The giant Sukhoi Log gold deposit Siberia. Russ Geol Geophys 47:315–341
32. Downs RT (2006) The RRUFF project: an integrated study of the chemistry, crystallography, Raman and infrared spectroscopy of minerals. In: Program and abstracts of the 19th general meeting of the international mineralogical association in Kobe, Japan, O03-13

Analysis of Impurity Density in the Structure of Arsenopyrite of the Panimba Deposit

Victor V. Onufrienok and Maarten A.T.M. Broekmans

Abstract Based on the comprehensive analysis of the crystal structure and chemical and phase composition of natural arsenopyrite of the "Panimba" deposit (Krasnoyarsk region), an analytical expression for calculating the impurity density in the structure of minerals like marcasite is received.

Calculation of impurity density in crystal structure of natural arsenopyrite of various chemical compounds is made and compared with the gold content in samples. As a result of theoretical calculations, the analysis of X-ray spectra, a chemical composition by electron-probe micro-analysis (EPMA), the dependence of the concentration of impurity atoms in the crystal structure from various chemical compound of arsenopyrite, and the gold content in the rock is established. The maximum content of gold corresponds to arsenopyrite in which ratio $((S + As)/Fe) > 2$. The chemical formula for content representation of the minerals like marcasite containing crystal structure atoms distinct from atoms of a forming matrix is offered.

Keywords Impurity density • Arsenopyrite • Chemical compound • Crystal structure • Theoretical calculations

1 Introduction

In mineralogy textbooks, the chemical composition of arsenopyrite is usually presented in an idealized form by the formula FeAsS (see e.g. entry in [1]). However, most natural arsenopyrites have a substantial content of chemical impurities, notably cobalt Co, but also minor quantities of copper Cu, zinc Zn, nickel Ni, silver Ag, and gold Au are all known to replace Fe. The arsenic As and sulfur S in

V.V. Onufrienok (✉)
Institute of Mineralogy, Geology and Mining, Siberian Federal University, Krasnoyarsky's rabochy av. 95, Krasnoyarsk, Russian Federation
e-mail: VOnufriynok@yandex.ru

M.A.T.M. Broekmans
Department of Industrial Minerals and Metals, Geological Survey of Norway, PO Box 63125, 7491 Sluppen, Trondheim, Norway

F. Dong (ed.), *Proceedings of the 11th International Congress for Applied Mineralogy (ICAM)*, Springer Geochemistry/Mineralogy,
DOI 10.1007/978-3-319-13948-7_33

the As-S dianions may be partly replaced by minor amounts of antimony Sb, Selenium Se, and/or tellurium Te. The chemical composition of arsenopyrite may differ in detail from one deposit to another, from one deposition stage to another in a given deposit, and even from the outer parts of a single grain towards its interior [2]. Thus, for real-world arsenopyrite samples, it is more realistic to present the composition formula as $Fe_{1-x}[Co,Cu,Zn,Ni,Ag,Au]_{\Sigma=x}[AsS]_{1-y}[Sb,Se,Te]_{\Sigma=y}$.

Let's take Boliden (Sweden) which is Europe's largest ore field as an example. Boliden ore field is rich in gold and arsenopyrite. It is not completely extracted by mechanical enrichment that despite it location at a country which has the high economic level. But the ore field is so important not only to the Sweden but also to the EEC. The purpose of this work is:

1. To analyze the concentration of point defects of different nature in the structure of Panimba arsenopyrite mine;
2. Based on the algorithm for calculating the impurity atoms, to obtain formulas for the density of impurity atoms of the monoclinic structure of arsenopyrite;
3. Calculate the density of the proposed formulas of the atoms in the applicable arsenopyrite structure;
4. On the basis of the numerical values of the density of various kinds of impurity atoms, to establish trends in their preferential location in the structure of the samples with different ratios (As + S)/Fe.

2 Materials and Methods

2.1 General

Glocker [3] made a laudable first attempt to classify arsenopyrite and put it in a different group than marcasite. Buerger [4] reclassified arsenopyrite together with marcasite and gudmundite (FeSbS) based on Weissenberg X-ray diffraction. The structural classification of Strunz and Nickel [5] places arsenopyrite in class 02. EB.20 together with marcasite, gudmundite, paxite ($CuAs_2$), ruarsite (RuAsS), and osarsite ([Os,Ru]AsS). Arsenopyrite may contain up to 9 wt% Co, and the structure of glaucodot ([Co,Fe]AsS) is indeed closely related. Crystal structure and chemical aspects of pyrite-, marcasite-, arsenopyrite-, and löllingite-type minerals were discussed in detail by Morimoto and Clarke [6], Nickel [7], Brostigen and Kjekshus [8], and Tossell et al. [9]. The crystal structure of arsenopyrite was refined by Fuess et al. [10].

2.2 Materials and Mix Designs

Samples of arsenopyrite were acquired from the Panimba mine located in the Rybnaya-Panimba volcanic belt in the Krasnoyarsk region in SE Siberia, operated

by OJSC Polyus Gold. The deposit is located about 200 km NNE of Krasnoyarsk and about 100 km SSE of the cities of Teya and Severo-Eniseyskiy.

In the ore, arsenopyrite (FeAsS) occurs in association with pyrrhotite (FeS_{1-x}), stibnite (Sb_2S_3), pyrite (cubic FeS_2), scheelite ($CaWO_4$), berthierite ($FeSb_2S_4$), gudmundite (FeSbS), aurostibite ($AuSb_2$), jamesonite ($Pb_4FeSb_6S_{14}$), tetrahedrite ($Cu_6Cu_4[Fe,Zn]_2[Sb,As]_4S_{13}$), galena (PbS), sphalerite (ZnS), chalcopyrite ($CuFeS_2$), bismuthinite (Bi_2S_3), marcasite (orthorhombic FeS_2), magnetite ($FeFe_2O_4$), ilmenite ($FeTiO_3$), main gangue minerals quartz, and carbonate [11,12].

2.3 *Methods for Assessment and Analysis*

2.3.1 X-ray Powder Diffraction

Samples were studied in the laboratory for X-ray diffraction (XRD) of the Institute of Mining, Geology and Geotechnology of the Siberian Federal University at Krasnoyarsk. Purified arsenopyrite sample material was prepared for analysis by precrushing in a percussion mortar to pass a 400 μm sieve. About 6.5 g of grit was fed to a McCrone Micronizing Mill with synthetic polycrystalline corundum grinding elements and ground for 10 min in 10 mL isopropanol, poured out in a Petri dish, covered, and allowed to dry overnight at 50 °C. The dry powder was recovered from the dish, homogenized, and stored in a polyethylene vial.

For analysis, arsenopyrite powder was mounted in a dimpled alumina sample holder and finished with an object carrier glass for microscopy to obtain a smooth specimen surface. Thus prepared specimens were analyzed in a Shimadzu MAXima_X XRD-7000 S diffractometer instrument operated at 40 kV and 40 mA. Diffractograms were recorded using (nonmonochromated) Ni-filtered CuKα radiation with wavelength $\lambda = 1.541840$ Å, from 5-80°2θ at 0.05°2θ increments and 6 s counting time per step, resulting in an overall scan time of 2 h 30 min. Raw data were processed using proprietary instrument software and ICDD PDF 2/4 card files for reference. With above procedures for sample/specimen preparation and analysis, net lower limits of detection (LLD) for possible trace mineral species present are around 1–2 wt%.

2.3.2 Mineral Compositions by Electron-Probe Micro-analysis

Mineral compositions at microscale were determined using the facilities provided by the Analytical Center of the Institute of Geology and Mineralogy SB RAS, located in Novosibirsk. Specimen for analysis were first dimensioned to fit the instrument sample holder, then lapped in a number of successive steps of increasing fineness, and finally polished with 0.25 μm diamond paste on cloth. The polished specimen was then sputter coated in vacuum with carbon C of ~30 nm thickness to prevent charging under the incident electron beam. Thus, prepared specimens were

mounted on a sample holder and loaded to the analytical instrument via a load lock maintaining chamber vacuum at 10-5 Torr (~0.001 Pa) or better.

The Cameca Camebax-Micro instrument is equipped with five wavelength-dispersive spectrometers (WDS), plus a single energy-dispersive spectrometer (EDS) cooled with liquid nitrogen. The instrument was operated at 20 kV and 22 nA with beam focus to 1 μm, acquisition time per spot was set to 60 s, and live-time of the EDS detector was always kept >60 %. Element species were assigned to specific detectors by the instrument control software as follows: A, B (WDS-LIF1), C, D (WDS-LIF2), X, Y (WDS-PET1), Z, U (WDS-PET2), V, W (WDS-TAP), and K, L, M (EDS). The instrument was internally calibrated against a custom set of natural minerals (mostly sulfides) of known composition from Structure Probe Inc. (SPI Supplies), as follows: element species A, B, and C on mineral1, D and U on mineral2, W and Z on mineral3, V on mineral4, Y on mineral5, X on mineral6, K and L on mineral7, and M on mineral8. Raw analytical data were corrected using a ZAF-algorithm implemented in the instrument software.

Final data in weight percent (wt%) were recalculated to mineral compositions in atoms per formula unit (apfu) following the protocol outlined in e.g., Deer et al. [13]. With procedures and instrumentation, as specified above in detail, net LLD values are on the order of 0.01 wt% for most element species. Applicable LLD values are listed per element in the data tables.

2.3.3 Methods of Calculating the Defect

The analysis of the projection of marcasite structure along [010] (Fig. 1) shows that it can be obtained from the structure of the type NiAs by an ordered removal of half of the positions of the atoms involved in nickel arsenide, nickel atoms ($z = o$ and $z = 1/2$), and the subsequent relaxation of the provisions of the remaining atoms [14].

Since, as noted above, the structure of marcasite and arsenopyrite has crucial similarities, all of the above applies to the arsenopyrite. In fact, half of the S atoms replaced by atoms of As in arsenopyrite which results indicate the “pseudo-vacancies” in arsenopyrite electrically neutral, since the trivalent As atom and the electrons induced by ferric ions, and are collected for the covalent bonds.

The calculation of the density of impurity atoms in the structure of arsenopyrite was determined on the basis of the algorithm proposed in [15]. The formulas obtained by Onufrienok for structures such as NiAs and arsenopyrite for having a different crystal structure were not fit, so they made appropriate changes, and made a new formula for calculating the density of impurity atoms in the structure such as arsenopyrite.

In general, for minerals arsenopyrite containing cations with an atomic weight M_k and anions with an atomic weight $M1,2$, the maximum percentage of interstitial atoms with their full filling of all pseudo-vacant positions in the structure can be calculated by the formula:

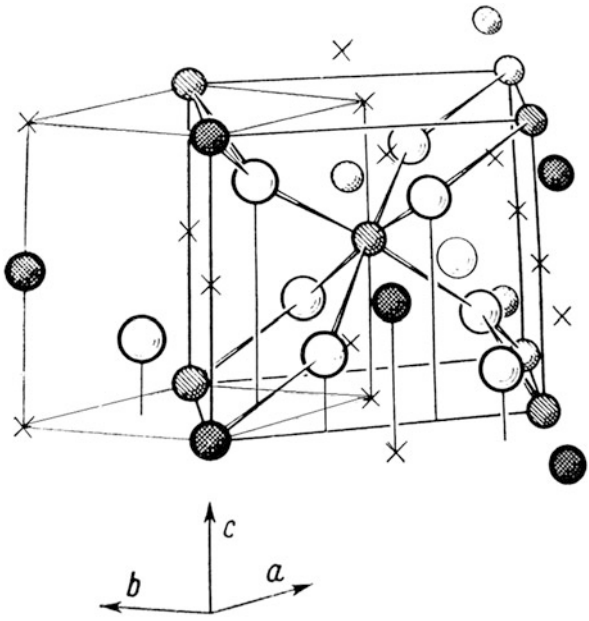

Fig. 1 The relation between the structures of marcasite (FeS_2) and nickel arsenide (NiAs). The *crosses* marked the atoms to be removed from the structure of NiAs to get the structure of marcasite after adjusting the atomic positions

$$\varphi = \frac{(5x_1x_2 - 2x_2 - 2x_1)y10^2}{(M_1 + M_2)x_1x_2 + 2M_\kappa(x_1 + x_2) + (5 - x_1 - x_2)y} \tag{1}$$

where y is the atomic weight cations introduction, $x_1 = A_1/K$, $a\ x_2 = A_2/K$ (A_1–S, A_2–As, $a\ K$–Fe)

On the basis of the analysis of a chemical compound of natural minerals follows that atoms of introduction not usually occupy all pseudo-vacant positions but only a certain part of them. Then for calculation of concentration of atoms of introduction, it is necessary to know the mass percent of the introduced elements defined in minerals by laboratory methods (α).

In this case, density of atoms of introduction (i.e., the number of atoms having an average of one unit of a crystal lattice) can be calculated by the formula:

$$\beta = \alpha \times (2.5 - 1/x1\ - 1/x2)/\varphi(x1\ x2) \tag{2}$$

3 Results

Based on a comprehensive analysis of the crystal structure, the chemical and phase composition of the analytical expressions which for calculate the impurity density in the arsenopyrite are received. The algorithm for calculating the impurity density structures such as NiAs was proposed by Onufrienok [15]. To calculate the density, impurities into arsenopyrite were amended. The impurity density for the impurity atoms cobalt Co, copper Cu, nickel Ni, and gold Au is calculated separately. Studies

Table 1 Selected results of calculations of the density impurity atoms in the structure of arsenopyrite (α) on the basis of the chemical compound (β)[a]

Cobalt Co		Nickel Ni		Copper Cu		Gold Au			(S + As)/Fe	Sum of defect	
β (10^{-2})	α, mas (%)	β (10^{-2})	α, mas (%)	β (10^{-3})	α, mas (%)	α, mas (%)	β (10^{-3})	g/t	$X_1 + X_2$	α, mas (%)	β (10^{-2})
0.547	0.166	0.069	0.021	–	–	0.002	0.026	0.1	1.9627	0.189	0.620
0.613	0.186	–	–	0.216	0.007	0.061	0.792	0.1	1.9467	0.282	0.715
0.996	0.302	0.251	0.076	–	–	0.011	0.142	0.1	1.9328	0.411	1.260
0.597	0.181	0.009	0.003	0.124	0.004	0.048	0.620	0.1	1.9387	0.237	0.681
0.504	0.153	0.013	0.004	–	–	0.002	0.025	0.1	1.9198	0.183	0.520
0.621	0.188	0.019	0.006	–	–	0.045	0.592	0.1	1.9690	0.253	0.700
0.578	0.175	0.039	0.012	0.433	0.014	0.007	0.091	0.1	1.9552	0.226	0.670
2.746	0.832	0.053	0.016	1.795	0.058	0.008	0.105	0.5	1.9866	0.932	2.990
1.716	0.520	–	–	0.588	0.019	0.040	0.521	0.5	1.9646	0.585	1.830
1.694	0.513	1.444	0.436	0.527	0.017	0.027	0.361	0.5	2.0020	1.041	3.230
1.714	0.519	1.391	0.421	–	–	–	–	0.5	2.0139	1.021	3.110
0.832	0.252	1.086	0.328	–	–	–	–	0.5	2.0106	0.604	1.920
0.954	0.289	0.692	0.209	–	–	–	–	0.5	2.0157	0.552	1.650
0.564	0.171	0.066	0.002	–	–	0,013	0.169	1.2	1.9532	0.186	0.588
2.740	0.829	0.043	0.013	0.994	0.032	0.104	1.427	0.9	2.0592	1.016	3.030
2.058	0.623	0.175	0.053	0.838	0.027	0.05	0.678	0.9	2.0447	0.781	2.390
1.586	0.480	0.116	0.035	0.589	0.019	0.03	0.407	3.5	2.0264	0.590	1.800
2.835	0.858	0.225	0.068	–	–	0.051	0.699	3.5	2.0469	0.997	3.130
1.658	0.502	0.162	0.049	0.931	0.03	0.088	1.194	3.5	2.0263	0.674	2.030
1.678	0.508	0.129	0.039	–	–	0.021	0.281	3.5	2.0021	0.568	1.840

[a]Accuracy of the results of chemical analysis was ~10^{-3} (XRS and XRD), respectively; theoretical calculations were performed with an accuracy up to ~10^{-4}

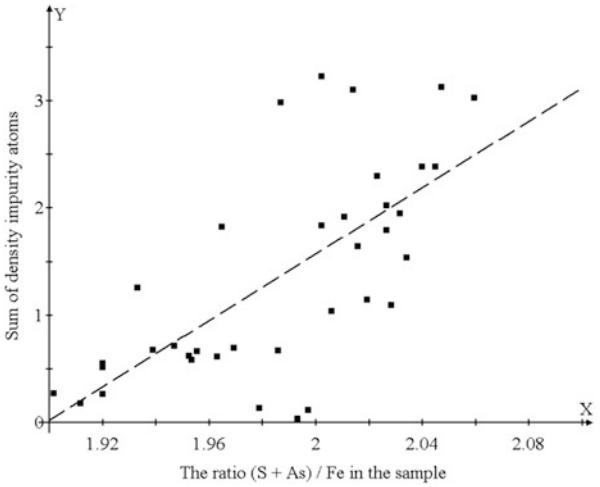

Fig. 2 The tendency of changes in the density of impurity atoms in the structure of arsenopyrite of various compositions

have been conducted on ~65 samples from different mines. One such series is presented in Table 1.

Though the experimental points are scatter, but it can express a tendency. (Fig. 2). As it is shown in Fig. 2, the tendency to increase the density impurities with increasing nonstoichiometry is installed. Stoichiometric composition should be considered when the ratio (As + S)/Fe is equal to two. Decreasing this ratio, impurity density tends to decrease. Statistical analysis of all samples (~65) confirmed the findings.

Particular interest is in the behavior of the density of impurity atoms of different nature in the structure of arsenopyrite of different composition. These features are shown in Fig. 2. Fig. 2 and Table 1 show that the atoms of the noble metals-Cu and Au, is almost identical to penetrate into the crystalline arsenopyrite—the differences are minimal, while the cobalt and nickel atoms occupy the position of "pseudo-vacancy" effectively increases their density in the structure. Preference should be given to, of course, cobalt, ionic radius of which is as close to the gland.

4 Discussion

The presence of gold Au in (the crystal structure of) arsenopyrite has been investigated in great detail with a variety of techniques [16–19]. There is general consensus that gold in arsenopyrite can be present as metallic native gold in small clusters down to a few nanometers in size or as individual Au atoms replacing Fe in the structure. Recently, nanoparticles of gold telluride were identified in As-free pyrite [20]. The predominant bond type (of gold) in arsenopyrite is covalent with a subordinate ionic character [17]. However, it appears that the exact position of Au is not identical with the Fe it replaces, which may be a combined effect of

both (partial) valence and size. According to the published literature, unit cell parameters for chemically pure synthetic arsenopyrite are slightly smaller than for natural arsenopyrite containing chemical impurities, and there seems a correlation with the impurities sum total versus the cell parameters.

To explain the results requires a detailed analysis of the structure of arsenopyrite. Crystal system monoclinic with arsenopyrite (oP12), show unit cell parameters $a = 5.74$ Å, $b = 5.67$ Å, $c = 5.78$ Å, $\alpha = \gamma = 90°$, $\beta = 112.2°$, and $Z = 4$. These parameters appear to vary the concentration of impurity atoms, but in the literature, this information is missing (C18).

A typical example of a C18-type structure is marcasite. The structure of marcasite (space group oP6) iron atoms occupies the nodes of the amount of centered orthorhombic lattice, and sulfur atoms are arranged in such a way that it is surrounded by iron atoms in octahedral coordination ($2 \cdot 2.235$ Å; $4 \cdot 2.255$ Å). It is known that the structures $FeSb_2$, FeS_2, $FeTe_2$, and $CoTe_2$ have no plane of symmetry, and the metal atoms are not exactly in the centers of octahedra of the dianions. The unit cell parameters marcasite are $a = 4.445$ Å; $b = 5.425$ Å; $c = 3.388$ Å; and $Z = 2$.

The structure of arsenopyrite is a triclinic distorted form of marcasite structure—atoms As and sulfur (S) are occupied in (in an orderly manner) the position of the atoms of sulfur (S) in marcasite. The chain of octahedra of atoms S and As, the surrounding atoms of Fe and having common edges (alternating S=S and As–As), go through the entire structure along the [101]. In this direction, the atoms of Fe pairs are shifted towards each other, so that the Fe–Fe distance through the edges of S–S are equal to 2.79 Å and through the edges of As–As—3.53 Å [14].

The crystal structure of arsenopyrite FeAsS, as well as the structure of marcasite FeS_2, is based on a two-layer closest packing, with the only difference being that it does not form a sulfur atom, as in marcasite, and two kinds of atoms—As and S. Taking as reference a cell composed of four unit cells of marcasite and replacing half of the S atoms with As, see that the set of all elements of holohedric orthorhombic space group symmetry of marcasite to arsenopyrite structure preserved only its monoclinic subgroup. Although all atoms (Fe, As and S) are in general positions and their coordinates are comparable to the atomic coordinates of a highly symmetric structure of marcasite.

From the above studies, it follows that many of the properties of arsenopyrite can be applied to marcasite and vice versa. Thus, we can assume that the structure of arsenopyrite as well as the structure of marcasite has "pseudo-vacancies." Their presence explains the high concentration of impurity atoms—they occupy a position "pseudo-vacancies," just as in the structure of pyrrhotite impurity atoms occupy vacant cation positions. Let us consider in more detail the concept of "pseudo-vacancy." If a structure can be obtained from the other by a systematic removal of atoms from certain positions, formal structure thus can be obtained, free of vacancies. The nodes of the crystal structure of which the cations are removed will be called "pseudo-vacancies."

From the presented scheme of calculation of point defects follows that any connection can be written in a form of the chemical formula:

$$KA_1A_2$$

where A_1, A_2, and K are respectively represent anions and cations of the main crystal matrix.

Researches of gold in the rock pattern revealed its increase with increasing ratio of (S + As)/Fe in the samples. Since this ratio is related to the density of "pseudo-vacancies," we can conclude that if arsenopyrite in rock contains a higher density of "pseudo-vacancies," then the gold content in the rock increases. This phenomenon has already been noted for the pyrrhotite deposit "Blagodatny" with the only difference being that in pyrrhotite the density of cation vacancies is analyzed [15]. Thus, the properties of the "pseudo-vacancies" in many respects are similar to the properties of cationic vacancies.

5 Conclusions

An analytical expression for calculating the density of impurity atoms is in the structure of arsenopyrite.

It is the calculation of the density of impurity atoms in the crystal structure of natural arsenopyrite of different chemical composition and is associated with the gold content in the samples. The concentration of point defects was calculated separately for the impurity atoms—Co, Ni, Cu, and Au.

The dependence of the density of impurity atoms in the crystal structure of the gold content in the rock was amended. The maximum corresponds to the arsenopyrite gold content, which has the highest ratio (S + As)/Fe.

References

1. Anthony JW, Bideaux RA, Bladh KW, Nichols MC (1990) Elements, sulfides, sulfosalts, vol 1, 1st edn, Handbook of mineralogy. Mineral Data Publishing, Tucson, p 28
2. Choi SG, Youm SJ (2000) Compositional variation of arsenopyrite and fluid evolution at the Ulsan deposit, southeastern Korea: a low-sulfidation porphyry system. Can Mineral 38:567–583
3. Glocker EF (1847) Ordo VI. Pyritae. Pyrite. III. Pyritae arsenopyritoidei. 10. Arsenopyrites. In: Generum et Specierum Mineralium, Secundum Ordines Naturales Digestorum. Synopsis. Apud Eduardum Anton, Halae Saxonum (Halle in Saxony), pp 34–43
4. Buerger MJ (1936) The symmetry and crystal structure of the minerals of the arsenopyrite group. Z Krist 95:83–113
5. Strunz H, Nickel EH (2001) Strunz' mineralogical tables, 9th edn. Schweizerbart'sche Verlagsbuchhandlung (Nägele und Obermiller), Stuttgart, p 870
6. Morimoto N, Clark LA (1961) Arsenopyrite crystal-chemical relations. Am Mineral 46:1448–1469

7. Nickel EH (1968) Structural stability of minerals with the pyrite, marcasite, arsenopyrite and löllingite structures. Can Mineral 9:311–321
8. Brostigen G, Kjekshus A (1970) On the relationship between the structure types pyrite, marcasite and arsenopyrite. Acta Chem Scand 24(8):2983–2992
9. Tossell JA, Vaughan DJ, Burdett JK (1981) Pyrite, marcasite, and arsenopyrite type minerals: crystal chemical and structural principles. Phys Chem Miner 7:177–184
10. Fuess H, Kratz T, Töpel-Schadt J, Miehe G (1987) Crystal structure refinement and electron microscopy of arsenopyrite. Z Krist 179:335–346
11. Genkin AD, Lopatin VA, Savel'ev RA, Safonov YG, Sergeev NB, Kerzin AL, Tsepin AI, Amshtutz K, Afanas'eva ZB, Wagner F, Ivanova GF (1994) Gold ores of the Olimpiada deposit (Enisei Range, Siberia). Geol Ore Deposits (Geologiya Rudnykh Mestorozhdenii) 36:101–123
12. Khiltova VYA, Pleskach GP (1997) Chapter 16 Yenisey fold belt. In: Rundqvist DV, Gillen C (eds) Precambrian ore deposits of the East European and Siberian Cratons, vol 30, Developments in economic geology. Elsevier Science, Oxford, pp 289–316
13. Deer WA, Howie RA, Zussman J (1992) An introduction to the rock forming minerals, 2nd excerpted student edn. Longman, Burnt Mill, pp 696
14. Pearson WB (1972) The crystal chemistry and physics of metal and alloys. Wiley, New York, p 826
15. Onufrienok VV, Sazonov AM, Terehova AV (2012) Influence of the phase composition of pyrrhotites on gold content in rocks. In: Broekmans MATM (ed) Proceedings of the 10th international congress for applied mineralogy (ICAM). Springer, Berlin, pp 487–495
16. Bindi L, Moëlo Y, Léone P, Suchaud M (2012) Stoichiometric arsenopyrite, FeAsS, from La Roche-Balue quarry, Loire-Atlantique, France: crystal structure and Mössbauer study. Can Mineral 50:471–479
17. Cabri LJ, Newville M, Gordon RA, Crozier ED, Sutton SR, McMahon G, Jiang DT (2000) Chemical speciation of gold in arsenopyrite. Can Mineral 38:1265–1281
18. Fleet ME, Mumin AH (1997) Gold-bearing arsenian pyrite and marcasite and arsenopyrite from Carlin-trend gold deposits and laboratory synthesis. Am Mineral 82:182–193
19. Vaughan DJ, Craig JR (1978) Mineral chemistry of metal sulfides, 1st edn. Cambridge University Press, Cambridge, p 493
20. Ciobanu CL, Cook NJ, Utsunomiya S, Kogagwa M, Green L, Gilbert S, Wade B (2012) Gold-telluride nanoparticles revealed in arsenic-free pyrite. Am Mineral 97:1515–1518

Research on Preparation and Influencing Factors of High Calcium High Sulfate Ash to Autoclaved Aerated Concrete

Jun Wan and Shaohui Jia

Abstract In this chapter, a high calcium high sulfate ash is chosen as the main material, added with fly ash, lime, cement, gypsum, and some modifiers, to prepare autoclaved aerated concrete. The products comply with the technical requirements of GB/T11968-2006. This chapter also studies the influence of the physical methods and water ratio on autoclaved aerated concrete by high calcium high sulfate ash-aerated concrete. The best ratio of water and Grinding time was found in experimental study.

Keywords High calcium high sulfate ash • Autoclaved aerated concrete • Ratio of water • Lime densification

1 Introduction

High calcium high sulfate ash is generated by 850–950 °C combustion of coal in the circulating fluidized bed boiler, a new coal-fired technology with advantages of wide adaptability, low emission, and high efficiency [1–3]. However, the combustion temperature of this boiler is between 850 and 950 °C, and adding a lot of $CaCO_3$ in the combustion process leads to the result that the CaO, SO_3, and loss of the fly ash are higher than that of general fly ash, so the fly ash is called high calcium high sulfate ash. Because of various compositions, there is a great influence on the ability and the durability of the building materials with the high calcium high sulfate ash. Using it to produce autoclaved aerated concrete has preferably environmental, economic, and social benefits, a practical significance, and long-term significance of sustainable development in environmental protection and power

J. Wan (✉)
Guizhou Institute of Building Materials Scientific Research and Design, 13 South Shachong Road, Guiyang, Guizhou, People's Republic of China
e-mail: 275204598@qq.com

S. Jia
Guizhou Engineering Technology and Research Center for the Comprehensive Utilization of Industrial Waste (Materials), 13 South Shachong Road, Guiyang, Guizhou, People's Republic of China

F. Dong (ed.), *Proceedings of the 11th International Congress for Applied Mineralogy (ICAM)*, Springer Geochemistry/Mineralogy,
DOI 10.1007/978-3-319-13948-7_34

plants. The breakthrough of high calcium high sulfate ash comprehensive utilization of the bottleneck is very necessary.

In this chapter, we used high calcium high sulfate ash as the main material, adding general fly ash, cement, lime, and some modifiers. The production complies with the technical requirements of GB/T11968-2006 "autoclaved aerated concrete blocks."

2 Materials and Methods

2.1 Raw Materials

High calcium high sulfate ash was supplied by Guizhou Huadian Bijie Thermal Power Co. Ltd., and its chemical compositions of raw materials are shown in Table 1, while XRD and SEM are shown in Fig. 1.

Lime: from Xiuwen Guizhou;
Aluminum paste: bought in market;
Cement: P.C32.5;
Modifier: made in our lab.

In Table 1, we can see, compared with general fly ash, high calcium high sulfate ash is lower in SiO_2 and Al_2O_3 while higher in f-CaO and SO_3, which contributes to the important reason why the high calcium high sulfate ash cannot be largely used in the building materials. In addition, although the combustion temperature of high calcium high sulfate ash is lower, there are some spherical compositions in high calcium high sulfate ash calcium ash vitreous material, which evident increase through 10 min ball milling (Table 2).

2.2 Test Method

The slurry was poured into mould (10 cm × 10 cm × 10 cm) after being mixed, and then the bread head was cut after maintenance 4 h in 40 °C. Maintenance system: the pressure increasing and heating phase lasted for 2 h, the constant pressure and temperature phase lasted for 10 h, and the decreasing and cool phase lasted for 2 h.

Test methods of dry density, intensity, dry shrinkage, freeze–thaw cycle, and thermal conductivity are in accordance with GB/T11969-2008 "Test methods of autoclaved aerated concrete."

Table 1 Chemical composition of raw materials %

Sample	SiO_2	CaO	MgO	Fe_2O_3	Al_2O_3	SO_3	Loss	f-CaO
High calcium high sulfate ash	32.33	24.57	0.81	7.84	16.14	10.06	8.24	11.23
Fly ash	44.64	2.96	1.23	8.79	26.38	0.69	11.69	–
Modifier	92.68	1.21	0.18	0.12	2.19	–	1.88	–

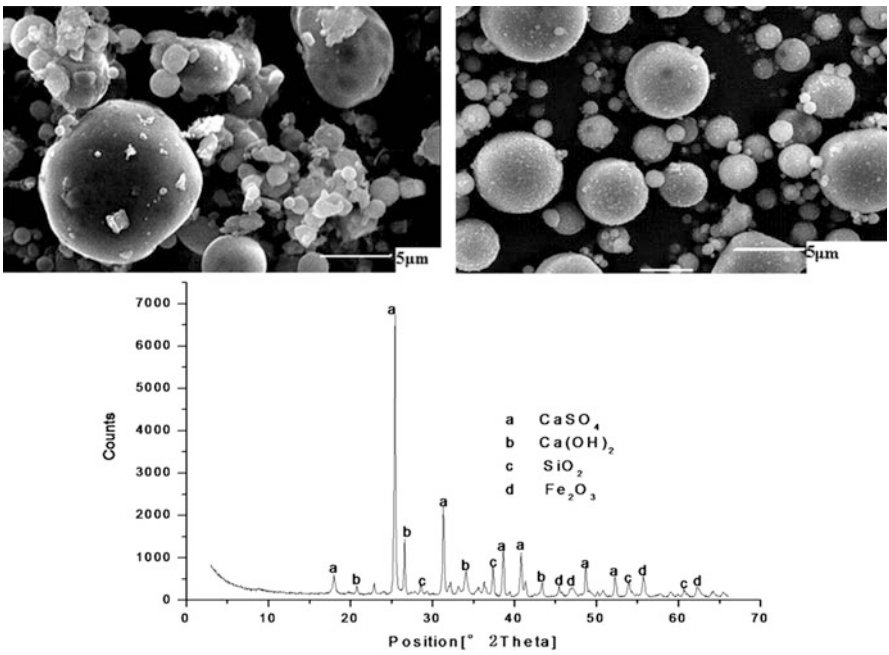

Fig. 1 SEM and XRD of the high calcium high sulfate ash. (**a**) SEM of high calcium high sulfate ash; (**b**) SEM of high calcium high sulfate ash after milling 10 min; (**c**) XRD patterns of high calcium high sulfate ash

Table 2 Properties of lime

A(CaO + MgO)	Digestion time (min)	Digestion temperature (°C)	MgO (%)
75.2	13	82	3.5

2.3 Test Plan

Because of the characteristics of low silicon and high calcium of high calcium high sulfate ash, it's difficult to meet requirements of autoclaved aerated concrete, so we need to add some general fly ash, testing plan as shown in Table 3.

Table 3 Test plan

	High calcium high sulfate ash (%)	Fly ash (%)	Lime (%)	Cement (%)	Modifier (%)	Gypsum (%)	Water–powder ratio (%)	Aluminum paste (‰)
A	30	45	15	7	0	3	0.52	0.8
B	35	35	15	7	5	3	0.54	0.8
C	40	30	15	7	5	3	0.56	0.8
D	45	20	15	7	10	3	0.58	0.8
E	50	15	15	7	10	3	0.58	0.8
F	55	10	15	7	13	0	0.60	0.8
G	60	5	15	7	13	0	0.60	0.8

3 Results and Discussion

3.1 Impact of Grinding Time on Activity of High Calcium High Sulfate Ash

The requirement of fineness of materials used in autoclaved aerated concrete is very high; we can improve the specific surface area and activity through grinding. In this chapter, the ratio of materials is 40 % of high calcium high sulfate ash, 30 % of general fly ash, 5 % of modifier, 15 % of lime, 7 % of cement, and 3 % of gypsum. The grinding time of high calcium high sulfate ash is 0, 5, 10, and 15 min. Then the relation between properties of autoclaved aerated concrete and grinding time is analyzed.

It is seen in Table 4 that intensity of product is the highest after being grinded 10 min. So we can see that appropriate grind can make slurry with good consistency and liquidity, even good for hardening of body and development of intensity. But if the fineness of materials is too large, the intensity of product is increased a little, or even lower, and the drying shrinkage and natural shrinkage increase greatly. This is because when the fineness of raw materials is too large, the grain crystal of hydrated calcium silicate by the reaction is too small and without aggregate to support intensity of product.

3.2 Impact of Water–Powder Ratio on Adaptability Between Gas Evolution of Aluminum Paste and Densification of Lime

This experiment selects sample C as the research object, by adjusting water–powder ratio to study adaptability between gas evolution of aluminum paste and densification of lime, and the results are shown in Table 5.

Table 4 Relation between properties of aerated concrete and grinding time

Grinding time (min)	0	5.00	10	15
Screen residue (%)	9.80	7.20	5.90	3.50
Intensity (MPa)	4.08	4.67	5.02	4.80
Dry density (kg/m^3)	629	618	612	606

Table 5 Adaptability between gas evolution of aluminum paste and densification time of lime

Water–powder ratio (%)	Pouring temperature (°C)	Densification time (min)	Phenomena
0.52	40	10	Densification is too fast
0.54	40	12	Densification is a little fast
0.56	40	18	Densification preferably
0.58	40	25	Surface cracking
0.60	40	30	Densification is slow

In Table 5, we can see that the slurry densification is too fast and hard to pour when the water–powder ratio is lower than 0.56 %, adaptability between gas evolution of aluminum paste and densification of lime is best when water–powder ratio equal to 0.56 %, the slurry is too watery, and densification is slow.

3.3 Impact of Water Consumption on Property of Product

Select sample C as the research object and four different water–powder ratios to test the dry density and intensity; the results are shown in Figs. 2 and 3.

It is seen that dry density of product decreases with the increasing water–powder ratio, but the dry density of product increases when water–powder ratio is over 0.56 %, because of adaptability between gas evolution of aluminum paste and densification of lime is best when water–powder ratio is 0.56 %. When the water–powder ratio changes between 0.52 and 0.56, the intensity of product increases with the increasing water–powder ratio. But when the water–powder ratio is over 0.56 %, the slurry densification decreases with the increasing water–powder ratio and body hardening speed slows down and will not be able to support the expansion of gas evolution, so the intensity decreases.

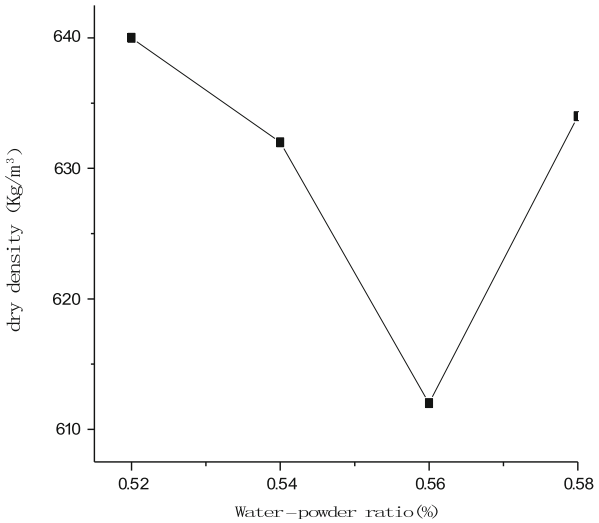

Fig. 2 Impact of *w*/*p* on dry density of product

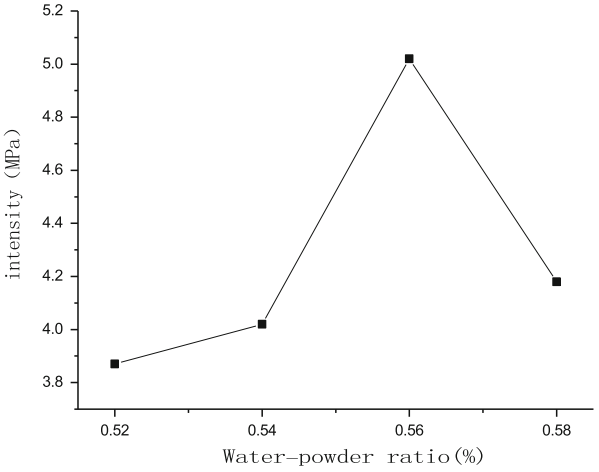

Fig. 3 Impact of *w*/*p* on intensity of product

4 Conclusions

1. Contents of SiO_2 and Al_2O_3 in high calcium high sulfate ash are lower and contents of f-CaO and SO_3 are higher than general fly ash, and the high calcium high sulfate ash used in building materials is restricted in that it needs to add some general fly ash to product aerated concrete.
2. Because the active substance in high calcium high sulfate ash is little, we need to improve the activity of high calcium high sulfate ash by grinding. The results show that the properties are best when grinding 10 min.

3. The results show that the best sample is 40 % of high calcium high sulfate ash, 30 % of general fly ash, 5 % of modifier, 15 % of lime, 7 % of cement, and 3 % of gypsum.
4. Because the fineness of high calcium high sulfate ash is great, water requirement is big; thus the properties of aerated concrete are best when the water–powder ratio is 0.56 %.

References

1. Chen B, Liu HB, Wan J (2012) Research on use of high calcium desulfurization ash in autoclaved brick. Brick-Tile 7:5–6
2. Chen B, Zhong J, Wang D (2012) The successful application of high calcium and solid sulfate fly ash in autoclaved aerated concrete. China Sci Technol Inf 16:113–113
3. Pei YL, Wei CD, Yang DF, Yang TD, Li JP (2006) Study on characteristics and comprehensive utilization of circulating fluidized bed ash. Fly Ash Compr Util 5:14–16

Preliminary Discussion on Comprehensive Utilization of Tailings

Fudong Wang, Xiaoqing Zhu, Zhonggang Wang, Tao Han, Zengsheng Li, Xiaohui Sun, and Kunyue Ling

Abstract The study on the tailings' comprehensive utilization is mainly concentrated in minerals in the past, which means we need to use all kinds of research methods and results that we use in the mineralogy nowadays. Maybe we can break away from the research bondage of the modern mineral technology, tracing back to the genesis of the mineral deposits from the genesis of mineral formation, especially some sedimentary deposits, which we can call "natural metallurgical field," so that we can probably get some new technologies and methods of the tailings' comprehensive utilization. On the other hand, after re-understanding of the varieties of deposit types and the occurrence states of metal elements, we can select the corresponding technology to recover associated components according to different types of deposits tailings, which will maximize the recovery rate of associated components.

Keywords Tailings • Comprehensive utilization • Mineral • Deposit genesis • Element occurrence

1 Introduction

Tailings produced in a concentration plant are the discharges of solid wastes after grinding ore into size and select useful components in the specific economic and technological condition. According to statistics, for the mining of metal ore, nonmetallic ore, coal, clay, etc., the production of tailings in the world is up to

This study was supported jointly by the National Basic Research Program of China (Grant No. 2007CB411401) and the Special Fund of State Key Laboratory of Ore Deposit Geochemistry and the National Natural Science Foundation of China (Grant No. 40773035) and the Southwest University of Science and Technology Doctoral Fund. (11zx7125)

F. Wang
Southwest University of Science and Technology, Mianyang, Sichuan 621010, China

X. Zhu (✉) • Z. Wang • T. Han • Z. Li • X. Sun • K. Ling
State Key Laboratory of Ore Deposit Geochemistry, Institute of Geochemistry, Chinese Academy of Sciences, Guiyang, Guizhou 550002, China
e-mail: zhuxqcas@sohu.com

F. Dong (ed.), *Proceedings of the 11th International Congress for Applied Mineralogy (ICAM)*, Springer Geochemistry/Mineralogy,
DOI 10.1007/978-3-319-13948-7_35

100 million tons per year. The number of existing tailing piles is 12,718 in China, of which the construction ones is 1,526, accounting for 12 % of the total. And the closed tailing piles is 1,024, accounting for 8 %. As in 2007, the national total tailings accumulation is 8.046 billion tons [1]. The nonferrous metal mining is one of the largest discharges of solid wastes industries because of its low comprehensive recovery rate. For example, the beneficiation and recovery rate of nonferrous metal mine is from 50 to 60 % in China, which is lower 10–15 % than developed countries, and the associated nonferrous metal recovery rate is 40 %, which is lower 20 % than developed countries. The utilization of duns is 90–100 % in Poland and is followed by United States, Australia, France, Canada, Belgium, and other countries, while China is only about 20 %. The utilization of fly ash is 100 % in Japan and Denmark, 65 % in France, 55 % in UK, and just 45 % in China [2–4]. Quantities of waste rock, waste slag, and wastewater have occupied land, destructed vegetation, and deteriorated the soil and water quality, causing land subsidence, landslides, mud-flow, and other geological disasters. Therefore, the comprehensive utilization of resources is the right choice of mining sustainable development, environment protection, resource conservation, and economic and social development.

There is a notable feature that the "the number of comprehensive deposits is much bigger than single mineral resource deposits in China." For example, over 85 % nonferrous metal deposits are comprehensive deposits [5]. Because of weak concept of utilization, lack of the constraints with policies and regulations, artificial separation of underground resources and driven by short-term interests, confined by the deposit theory and level of technology, as well as paying less attention to the ecological and environmental protection, people have taken up extensive development and production for underground resources, which leads to a great wastage of a large number of symbiotic and associated minerals; most of resources have been discarded in the tailings piles. As a result, the awareness of various types of deposits and associated components is needed to be raised (shown in Table 1). In the process of mining and recycling, we need to focus on the associated components of such minerals particularly, take corresponding favorable technology to comprehensively salvage the associated components, and change the tailings known as "artificial ore" into the actual meaning of "mine." Besides the types of deposits mentioned above, it needs to show that new types of nontraditional deposits have been found, such as rare earth elements ion-adsorption ore discovered in southwest China in recent years, lateritic gold, and basalt-type copper; these types of deposits formed under supergene geological condition; their metallogenic mechanisms have a certain similarity of the long-term accumulation process of tailings, from which some lessons can be drawn for the comprehensive utilization of tailings.

Table 1 The deposit types and their associated components

Deposit types	Associated components
Iron ore deposit	V, Ti, Cr, Ni, Cu, Co, PGE, Au, REE, Nb
Manganese ore deposit	Co, Ni, B
Copper deposit	Mo, Au, Ag, Co, Se, Te, PGE, Pb, Zn, S
Lead–Zinc deposit	Ag, Ge, Ga, In, Cd, Tl, Se, Te, Au, Cu, S, W
Mercury–Antimony deposit	Au, S, Se, Te, Fluorite, Barite
Tungsten–Tin deposit	Bi, Mo, Nb, Ta, Be, Li, Rb, Sc, Cu, Pb, Zn, Re, Fluorite, Rock quartz, Muscovite, Feldspar
Molybdenum deposit	Re, Cu, Fe, W, Zn, Ag, S
Rare metal deposits	Nb, Ta, Be, Li, Rb, Cs, Sc, Fluorite, Rock quartz, Muscovite, Feldspar
Rare earth element deposit	Nb, Ta, P, Ba, S c, P, Fluorite, Barite
Gold deposit	Ag, PGE, W, Sb
Aluminum ore deposit	Ga, Sc, Nb, Ta, Ti, Li
Phosphorite deposit	REE, Co, V, Ti, Fe
Salt deposits	K, Na, Li, Rb, Cs, B, Cl, Br, I, Gypsum, Glauber salt
Coal deposit	Ge, S, Clay, Bentonite, Aluminum-bauxite, Diatomite

2 The Inspiration of Deposits Genesis for Tailings Comprehensive Utilization

At the present stage, the study on the tailings' comprehensive utilization is mainly concentrated in minerals; it means we need to use all kinds of research methods and results that we use in the mineralogy nowadays to solve the problems we have met in the mineral utilization study. This study particularly points to the compositions of the ore minerals, the technology of object minerals, as well as the occurrence of harmful and beneficial elements, the different behaviors of the object minerals under different technologies, and the possible mineralogical factors that would affect the metallurgical process indicators. Maybe we can break away from the research bondage of the modern mineral technology, tracing back to the genesis of the mineral deposits from the genesis of mineral formation, especially some sedimentary deposits, which we can call "natural metallurgical field," so that we can probably get some new technologies and methods of the tailings' comprehensive utilization.

As to the tailings, its source is based on the physical and chemical properties of the different minerals in the ore. Grinding ore reduction makes all kinds of symbiosis minerals which are useful apart from each other as much as possible, removing or reducing harmful impurities in order to obtain the target that the content is the lowest part of the remaining useful components after smelting or other industrial. While the process of extracting useful components is approximated

to the formation of certain sedimentary deposits, such as weathering deposits or we can say that the formation process of weathering deposits is essentially a "naturally smelting process."

A common understanding is that the weathering deposits, the residual materials of rocks, or ores were formed mostly in modern times, which had experienced the chemical weathered process. The detail procedures are stated as follows: soluble contents were migrated out by surface water or groundwater; insoluble contents interacted with each other in situ, or precipitated out from the solution to form the insoluble minerals on surface in situ, or transport downward to groundwater table to free sedimentation or by water–rock interaction. The air, water, and biological in weathering process are similar to the crushing and grinding in metallurgical process, and the natural environments, especially the different physical and chemical conditions, make the mineral assemblage or chemical composition change, and these changes were caused by rocks or ores destruction. This procedure equivalent to nature selected the different metallurgical methods during weathering process and finally formed different types of weathering deposits. The residual deposits that come from more stable minerals were the results of "the gravity separation, flotation, and magnetic separation" of the weathering. And the illuvial type deposits were caused by the materials which dissolved in surface water and ore-forming fluid precipitated due to the "electrochemistry" and other difficult geological processes. However, we need to focus on the tectonic movement and metamorphism in later period during "natural metallurgical process," because it can make the metal redistribution and re-enrichment on ore-bearing sediments. That is the superimposed mineralization and precisely the "over-check" in geological processes.

It is worth noting that the "natural metallurgical deposits" during weathering processes have two types of deposits, namely, residual deposit and illuviated deposit, respectively. The first type mainly included residual clay deposits (kaolinite and montmorillonite), residual bauxite, residual iron deposits, residual manganese deposits, residual REEs deposits, laterite gold deposits, and so on. Another one included illuviated nickel deposits, illuviated uranium deposits, and ion-adsorption type REEs deposits. Metallogenic mechanism research on these deposits may help to explore the new technology and new method of the process mineralogy, thereby inverting the comprehensive utilization of tailings.

3 The Research Progress of Elements Occurrence

Comprehensive utilization of tailings must be mastered in the existing forms of the useful elements in raw materials and thus can be targeted to select the separation and extraction methods and the technology process. That is to say the availability of raw material not only depends on the abundance of useful elements but also on the mode of occurrence of elements.

In recent years, high-resolution and nondestructive electronic micro-beam technology was used in the mode of occurrence of elements researched. The electronic micro-beam technology that based mainly on electron microprobe was the earliest development of micro-analysis tools. In recent years scanning electron microscopy (SEM) and transmission electron microscopy (TEM) have emerged, which have had the nanometer spatial resolution and perfect scan function. It also can know the element contents, distribution, structure, and other information. The development of these technologies encourages people to study the mode of occurrence of elements from nanoscale.

In addition, we need to point out that study on occurrence states of material is important. The traditional view shows that the associated components occur as independent of minerals, isomorphic, and microscopic inclusions in the useful components, but recently, geologists have found that useful components and associated components still exist in the adsorption between each other, so adsorption states of associated components are another form of mineral occurrence. In particular, scientists found the nanomaterials in various geological bodies (Figs. 1 and 2), which set up another mode of occurrence states and migration form of materials. For example, the nanoparticles size fractions of metal minerals were found in Carlin-type gold, red clay-type gold deposits, ocean floor manganese nodules, copper concretion, the materials of earth air, volcanic gas, the meteorite, and the loess [6, 7].

4 Understanding

Tailing is the solid material that comes from the dehydrated of tailing slurry, which is the ore residues that had selected the useful elements. It usually consists of ore, gangue, and a variety of minerals in country rocks. Furthermore, it often has silicates, carbonates, and many other elements. The traditional sailing

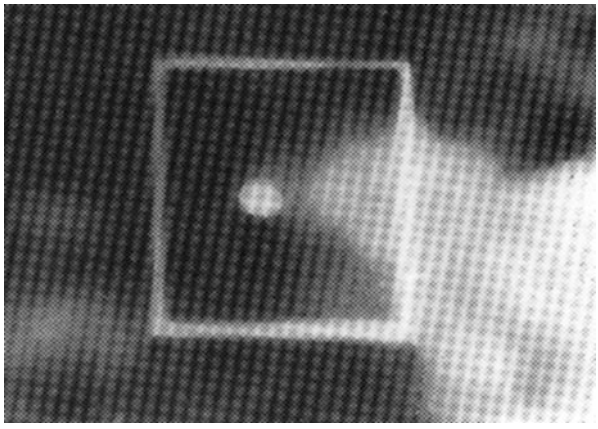

Fig. 1 EPMA image: the native gold particle (90 nm) distributed in the binding site of the limonite and quartz

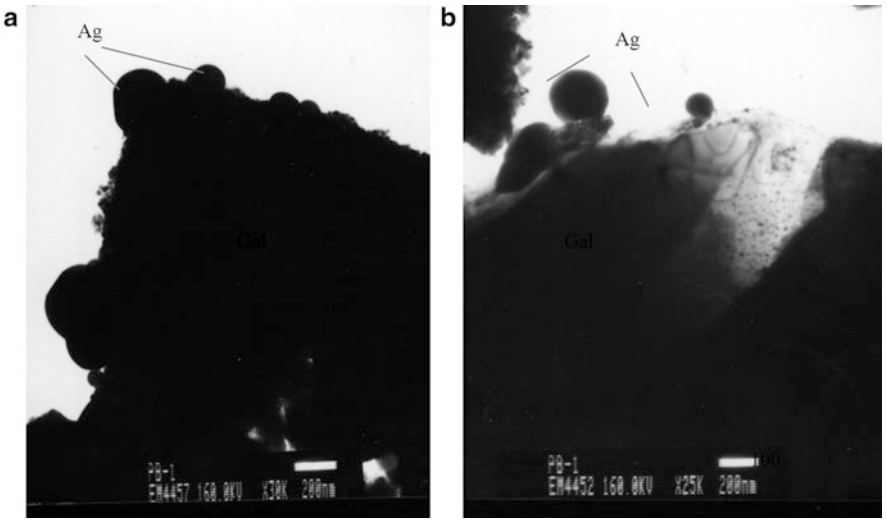

Fig. 2 SEM images show nano-silver particles are adsorbed on surface of galena (Gal) crystal (**a**) and a perfect spherical silver particle (**b**) (×40,000), Excerpted from [6]

comprehensive utilization research was concentrated in process mineralogy, but it is difficult to extract the useful components from those minerals which have complicated mineral assemblages and chemical compositions. Maybe we turned to study the genesis of minerals, especially the genesis of the ore deposit, to resolve these difficulties. It will also be able to explore the new ways and methods of tailing comprehensive utilization and have the great significance to study "the place of Natural analogue comprehensive utilization"—weathering deposits.

Furthermore, after re-understanding of the varieties of deposit types and the occurrence states of metal elements, we can select the corresponding technology to recover associated components according to different types of deposits tailings, which will maximize the recovery rate of associated components, such as the comprehensive utilization of dispersed elements: Germanium, gallium, indium, cadmium, thallium, rhenium, selenium, and tellurium, for their abundances, are very low in the earth crust, which are captured by some of the common minerals as form of isomorphic or adsorbed state. It is not easy to form their own separate deposits, so their production is usually from the recycling of dressing and smelting other metals. Ge is extracted from the zinc ore and coal dust, recycled from electronic or optical waste, and its price is \$1,000 kg^{-1}. Ga is a by-product of bauxite, which is recycled from the zinc smelting residue and industrial waste, and its price is \$550 kg^{-1}. Re is extracted from molybdenite and industrial waste, its price being \$1,100 kg^{-1}; Se and Te are recovered from the anode sludge of copper, industrial waste. and the coal, their prices being \$8 and 40 kg^{-1} respectively; Tl is recovered from smelting process of the copper, lead, and zinc ore, its price being \$1,200 kg^{-1}.

References

1. Xiao M (2010) The special planning of metal tailings utilization (2010–2015). Land Resour People's Repub China (5):1 (in Chinese)
2. Zhang QH, Su RH (1996) The resources of non-ferrous metal mine tailings. Multipurp Util Miner Resour (4):27–30 (in Chinese)
3. Xu H, Ki X (2006) Accelerate the development and utilization of China's nonferrous metal mine tailings. China Nonferrous Met (10):49–51 (in Chinese)
4. Xu FP, Zhou X, Hu TX (2007) Current situation of using tailing resource in our country and some suggestions. Yunnan Metall 36(4):25–27 (in Chinese)
5. Yang BJ, Li YK (2010) The practices and recommendations of tailings resource utilization. Chin J Min Geol (volumes up):197—200 (Metallurgical Industry Press) (in Chinese)
6. Zhu XQ, Zhang ZG, Jiang ZC (1998) Experimental studies on the origin of the Carlin-type gold deposits in southwestern Guizhou. Chin Sci Bull 43(22):2431–2433 (in Chinese)
7. Wang FD, Zhu XQ, Han T (2011) An experimental study on genesis of emeishan basalt-related native copper deposit in the Sichuan-Yunnan-Guizhou area. Acta Mineral Sin 31(3):322–327 (in Chinese)

Study on the Thermal Conductivity of Compacted Buffer/Backfill Materials

Maoli Wang, Facheng Yi, Zhe Wang, Zhongyan Wan, Chong Wang, and Jianwei Wang

Abstract The thermal property is one of the key properties for the design of the high-level radioactive waste (HLW) repository. In this study, the thermal properties transient automatic tester (HPP-F) is used to study the thermal conductivity of multiphase composite buffer/backfill material including the type B–Z and B–Z–P (here B, Z, and P represents bentonite, zeolite, and pyrite, respectively, the same as the following) in different dry density and moisture conditions. The results show that thermal conductivity of specimens increases as the dry density (moisture content) increases for the same moisture content (dry density). As a result, the type B–Z–P which is highly compacted of 1.8 g/cm^3 in dry density and 17.65 % in moisture content performs well; it meets the requirements of the IAEA and is easy to be compacted, so it may be recommend as an alternative material of high-level radioactive waste disposal repository buffer/backfilling material.

Keywords High-level radioactive waste • Compacted buffer/backfill materials • Thermal conductivity • B–Z • B–Z–P

1 Introduction

As the gap between the waste container and surrounding rock and the cracks or pores in near-field rock, buffer/backfill material plays an important role in radiant heat conductor [1]. Therefore, good thermal conductivity and thermal stability performance of buffer/backfill material are required.

In order to research the influencing factors of sand–bentonite mixture's heat transfer properties, Xie Jingli et al. [2] use transient plane source method to determine thermal conductivity and thermal diffusivity of sand–bentonite mixed

M. Wang (✉) • F. Yi • Z. Wang • C. Wang • J. Wang
Fundamental Science on Nuclear Wastes and Environmental Safety Laboratory, SWUST, 59 Qinglong Road, Mianyang, Sichuan, People's Republic of China
e-mail: 765978620@qq.com

Z. Wan
Geothermal Geological Brigade, The Tibet Bureau of Geology and Exploration, 96 Jinzhu West Road, Lhasa, Tibet, People's Republic of China

F. Dong (ed.), *Proceedings of the 11th International Congress for Applied Mineralogy (ICAM)*, Springer Geochemistry/Mineralogy,
DOI 10.1007/978-3-319-13948-7_36

material under different compacted density and moisture content. The experimental results show that the thermal conductivity and thermal diffusivity of sand–bentonite mixture increase significantly with the increase of compacted density and the moisture content of the sample. As an additive, quartz sand makes the thermal conductivity and thermal diffusivity properties of the hybrid material improve significantly. CUI Yu et al. [3] have studied that what dry density, moisture content, and saturation have effects on the thermal conductivity of the United States MX80 bentonite and have found that the volume of the pore gas has a linear relationship with thermal conductivity. J. Pacavsky [4] has studied the thermal conductivity of RMN bentonite mixed with quartz and graphite, and the experimental results show that the temperature has little effect on the thermal conductivity, while the density and water content have obvious influence on it. Anh-Minh Tang et al. [5] have used a hot-wire method to determine the thermal conductivity of compacted bentonite MX80. The experimental results show that the mineral composition, moisture content, dry density, hysteresis, saturation, and volume fraction of the components have a certain impact on the thermal conductivity, and a linear correlation to predict the thermal conductivity of compacted bentonite has been put forward.

On the basis of the determined integrated BZP type buffer/backfill material (B:Z:P = 63:27:10) in precious work [6], which has good radionuclide block performance and engineering performance, further development of thermal conductivity of BZP and BZ-integrated buffer/backfill material has been studied in this paper, so as to lay the foundation to develop high-performance buffer/backfill material for high-level radioactive waste disposal.

2 Experiment

2.1 Experimental Materials

Raw materials used in this experiment include: Xinjiang Altai bentonite, zeolite in Xinjiang, and pyrite in Sichuan Jiangyou. Among them, Xinjiang Altai sodium bentonite works as the base material, zeolite in Xinjiang works as auxiliary material, and pyrite in Jiangyou works as additive.

Xinjiang Altai bentonite's alkaline and its chemical composition mainly includes SiO_2, Al_2O_3, and Fe_2O_3, and its physical and chemical properties are shown in Table 1. We can see from Table 1 that the Xinjiang Altay bentonite has a good colloidal nature and it's sodium bentonite. Not only it has good cation exchange capacity and high montmorillonite content but also good swelling resistance and plasticity. However, its thermal conductivity is low, which primarily relates to smectite content, water content, and compacted density. Therefore, Xinjiang bentonite can be used as a candidate material of composite minerals, but need to add other ingredients to improve its thermal conductivity, compaction and retardation of radionuclides and other related performance.

Table 1 Physical and chemical engineering indicators of Xinjiang Altai bentonite [6]

Glial price (mL/15 g)	Capacity expansion (mL/1 g)	The swelled value (mL/3 g)	pH value	Blue absorption capacity (Meq/100 g)	CEC (Meq/100 g)	Liquid limit (%)	Plastic limit (%)
>100	28	42	6.4	115	82	82.3	27
Air-dried water content (%)	Bulk density (g/cm^3)	Proportion	Dry density (g/cm^3)	Porosity (%)	Void ratio	Plastic index	Thermal conductivity ($W \cdot m^{-1} \cdot k^{-1}$)
14.47	2.23	2.52	1.89	24.10	0.32	51.1	0.107

Table 2 Physical and chemical engineering indicators of zeolite in Xinjiang [6]

Glial price (mL/15 g)	Capacity expansion (mL/1 g)	The swelled value (mL/3 g)	pH value	Blue absorption capacity (Meq/100 g)	CEC (Meq/100 g)	Liquid limit (%)	Plastic limit (%)
47	<5	10	8.62	22.1	97.97	46.3	31.8
Air-dried water content (%)	Bulk density (g/cm^3)	Proportion	Dry density (g/cm^3)	Porosity (%)	Void ratio	Plastic index	Thermal conductivity ($W \cdot m^{-1} \cdot k^{-1}$)
7.20	1.63	2.52	1.54	38.89	0.64	14.5	0.113

Chemical composition of zeolite in Xinjiang mainly includes SiO_2, Al_2O_3, H_2O, and alkaline earth metal, and its physical and chemical properties are shown in Table 2. From Table 2 we know that the cation exchange adsorption performance of zeolite has an obvious advantage over that of Xinjiang Altay bentonite, but it has the characteristic of porosity and poor impermeability, so we choose it as the auxiliary material in this paper.

Pyrite powder is mainly composed of FeS_2, containing a small amount of quartz and dolomite. Engineering barrier environment should be reductive environment, which helps the body of waste containers and waste solidification have a good chemical stability, so this paper tries to add a small amount of pyrite powder, in order to create a reductive environment. In addition, research results of literature [7] show that the pyrite has a certain block performance so that it can play a certain role on easing the migration of uranium. Moreover, pyrite has high thermal conductivity, so this paper tries to join a small amount of pyrite to increase the thermal conductivity of the mixed material.

2.2 Experiment

In the BZP mixture, the ratio of bentonite, zeolite and pyrite is 63:27:10. Mix and fully stir bentonite, zeolite, and pyrite; then prepare a total of 16 samples with initial water content of 11.11 %, 14 %, 17.65 %, and 20 % and dry density of 1.3 g/cm^3, 1.5 g/cm^3, 1.7 g/cm^3, and 1.8 g/cm, respectively. The sample number is respectively B7ZP-1 to B7ZP-16, where B, Z, and P represent bentonite, zeolite, and pyrite respectively, and the subscript 7 means that the mass of bentonite accounts for 70 % of the total mass of bentonite and zeolite.

In the BZ mixture, the ratio of bentonite, zeolite is 63:27. Mix and fully stir bentonite and zeolite; then prepare a total of 16 samples which with initial water content of 11.11 %, 14 %, 17.65 %, and 20 % and dry density of 1.3 g/cm^3, 1.5 g/cm^3, 1.7 g/cm^3, and 1.8 g/cm, respectively. The sample number is respectively B7Z-1 to B7Z-16, where B and Z represent bentonite and zeolite, respectively, and the subscript 7 means that the mass of bentonite accounts for 70 % of the total mass of the mixture.

2.2.1 Drying of Material

Before the experiment, bentonite, zeolite and pyrite should firstly be grinded through a 200-mesh sieve firstly, then dried at 105 °C with an oven.

2.2.2 Preparation of Specific Water Content

The predetermined water content of the experiment is respectively 11.11 %, 14 %, 17.65 %, and 20 %, and the predetermined compacted dry density is respectively 1.3 g/cm, 31.5 g/cm^3, 1.7 g/cm^3, and 1.8 g/cm^3. After mixing powder of bentonite, zeolite, and pyrite in accordance with the predetermined ratio (i.e., B:Z: P = 63:27:10 or B:Z = 7:3), add a certain amount of distilled water to prepare samples with different water content. Put the mixture into sample bags after stirring the sample evenly and then place the sample bags in desiccators for 48–72 h.

2.2.3 Compaction of Samples

The soil should be compacted with different water content to the desired dry density through the press machine. After compaction, release the sample from the mold slowly, and record the quality and thickness of the compacted sample, in order to calculate the actual dry density of the compacted samples; then you should immediately test its thermal conductivity. When being compacted the sample with dry density of 1.8 g/cm^3 and the one with water content of 20 % and the dry density is relatively higher, which are more difficult to prepare. And it is particularly difficult when in the suppression of BZ mixture; the maximum dry density can only reach about 1.7 g/cm^3. Figure 1 shows the compacted samples.

2.3 Test Methods of Thermal Conductivity

In this experiment, SHT-F thermal properties transient automatic tester (as Fig. 2), which is based on the theory of one-dimensional semi-infinite plane heat transfer model (as Fig. 3), is used to measure the thermal conductivity of the samples. It has two measuring methods including pulse method and constant current method, and it fits to measure the thermal conductivity of various solid sheets by using either of the measuring methods. The so-called pulse method is the one to heat with a plane constant heating pulse; after a certain temperature increase of the cold surface, stop heating and continue to measure temperature increase of the cold surface and temperature drop of the hot surface, and thus calculate the thermal properties of a specimen under test. While constant current method is to use plane heat source to heat a specimen under test with a constant heat flux intensity flowing through the interface between plane heat source and the main test piece, and end the measurement until enough data are collected; then directly use the temperature increase curves of cold and hot surface to calculate the thermal properties of the specimen under test. Abovementioned plane heat source refers to the effective heating area; it's a circular plane of 60 mm.

Fig. 1 Compacted samples

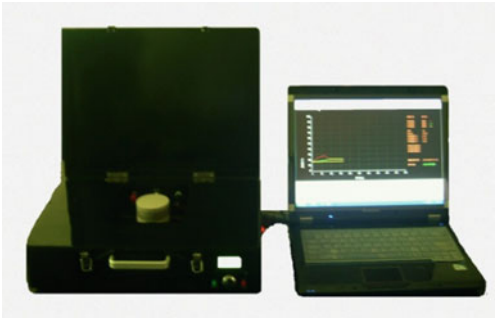

Fig. 2 SHT-F thermal properties transient automatic tester

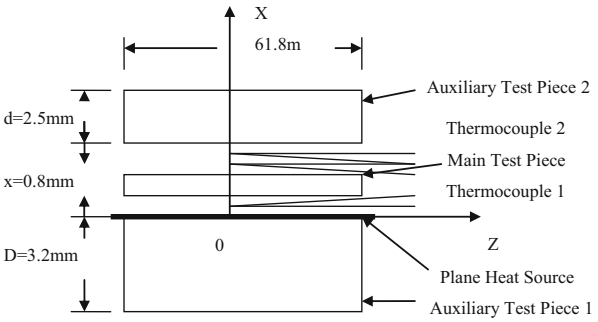

Fig. 3 Schematic of the planar one-dimensional semi-infinite heat transfer model

SHT-F thermal properties transient automatic tester consists of two parts including operating system and data processing system. The specifications and main technical indicators of this instrument are the following: Main Test Piece: $\Phi 60 \sim 120$ mm $\times$ X mm, 1 mm $\leq$ X mm ≤ 5 mm; Auxiliary Test Piece 1: $D \geq 30$ mm; Auxiliary Test Piece 2: $d \geq 20$ mm. Thus, in this experiment, diameter of main Test Piece, Auxiliary Test Piece 1, and Auxiliary Test Piece 2 are all 61.8 mm, and heights of those are 0.8 mm, 3.2 mm, and 2.5 mm, respectively.

When measuring, first the compacted sample is placed in the groove of the instrument according to the layout of Fig. 2 and then the plane heat source and thermocouple are connected. After that, the measuring method and the sampling

time interval, the preheating current and the heating measurement is selected to calculate the thermal conductivity of the samples by monitoring the relationship between the time under specific current and temperature. In this experiment, the measuring method is selected as pulse method, the sampling interval is set as 1,000 ms, and the heating current is set as 0.455 A.

3 Experimental Results

Thermal conductivity of compacted BZP and BZ mixture of different water content and dry density is shown in Figs. 2 and 3.

3.1 The Effects of Dry Density and Water Content on Thermal Conductivity

As what we see from Figs. 2 and 3, for the same water content, as the dry density increases, thermal conductivity of compacted BZP and BZ mixture increases. And as can be seen in Figs. 4 and 5, for the same dry density, as the water content increases, the thermal conductivity of the sample gradually increases. Among them, compacted BZP and BZ samples with water content of 20 % and dry density of 1.8 g/cm^3 are more difficult to be compacted. When the dry density is 1.7 g/cm^3, and the water content is 17.65 % and 20 %, respectively, the thermal conductivity of the BZP mixture is, respectively, 0.82 Wm^{-1} k^{-1} and 0.88 Wm^{-1} k^{-1}. When dry density is 1.8 g/cm^3, and the water content is 17.65 %, the thermal conductivity of BZP mixture reaches 0.96 Wm^{-1} k^{-1}. The thermal conductivity of the above three can all meet the recommended values of the International Atomic Energy Agency (IAEA) 0.8 Wm^{-1} K^{-1}.

3.2 The Effects of Pyrite on Thermal Conductivity

The compositions of the compacted BZ buffer/backfill material are bentonite and zeolite in a ratio of 7:3. While the compositions of BZP buffer/backfill material are bentonite, zeolite, and pyrite, in which the ratio of bentonite and zeolite remains 7:3. And the difference between compacted BZ and BZP buffer/backfill material studied in this paper is only that whether pyrite was added or not. Therefore, we can study the pyrite's effect on the thermal conductivity of compacted buffer/backfill material by comparing the thermal conductivity of compacted BZ and BZP mixture under the conditions of same water content and dry density.

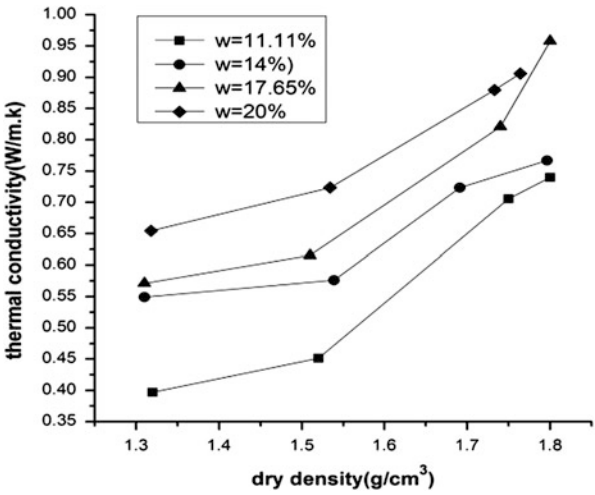

Fig. 4 Curves of dry density and thermal conductivity of compacted BZP mixture

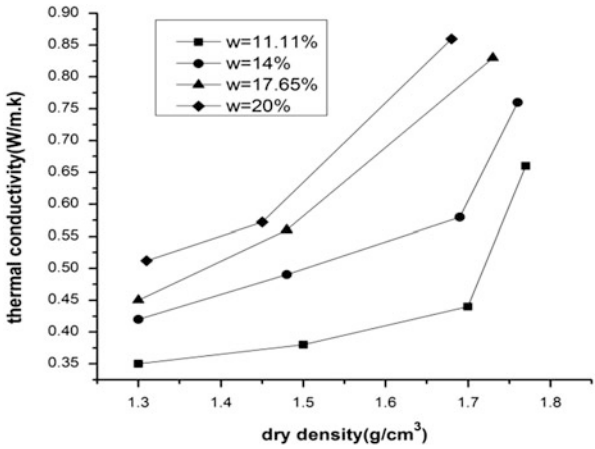

Fig. 5 Curves of dry density and thermal conductivity of compacted BZ mixture

Fig. 6a–d shows respectively curves of thermal conductivity of compacted BZP and BZ mixture under the same water content conditions. From Figs. 4, 5, 6, and 7, we can clearly see that the curves of the BZP mixture are all above BZ mixture, which indicates that pyrite can improve the thermal conductivity of the buffer/backfill material to a certain extent

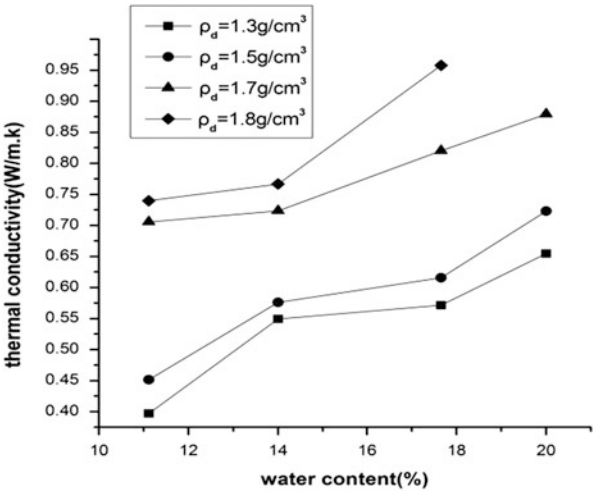

Fig. 6 Curves of water content and thermal conductivity of compacted BZP mixture

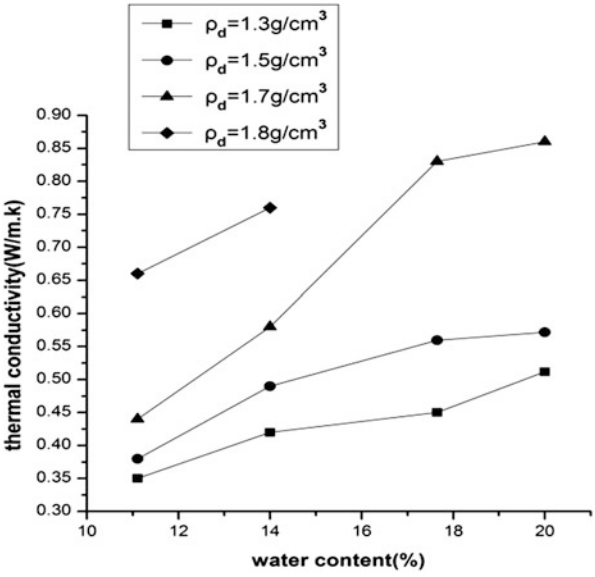

Fig. 7 Curves of water content and thermal conductivity of compacted BZ mixture

4 Discussions

In the pressing process, the samples with higher dry density and higher water content are more difficult to prepare. And it is particularly difficult when pressing BZ mixture, for which the maximum dry density can only reach about 1.7 g/cm^3. We can analyze the reasons for this phenomenon from the two aspects as follows. On one hand, because of the higher density and water content, the pores of the samples decrease or are filled with water; thus it's more difficult to suppress

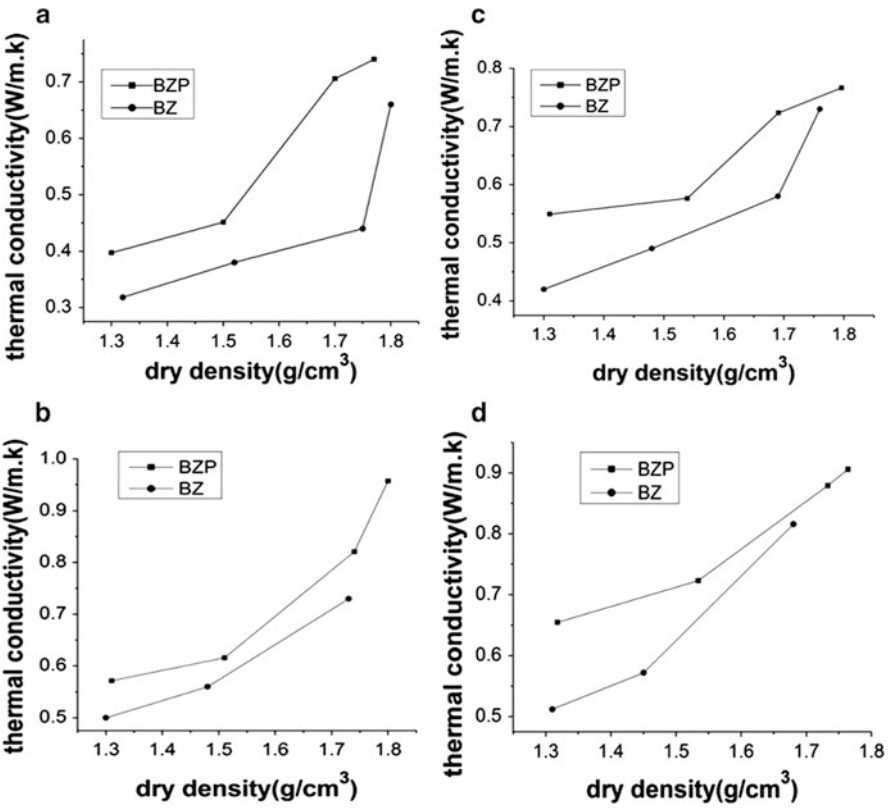

Fig. 8 Curves of thermal conductivity of compacted BZP and BZ mixture under different water content and dry density. (**a**) water content of 11.11 %, (**b**) water content of 14 %, (**c**) water content of 17.65 %, (**d**) water content of 20 %

samples with higher dry density or water content. On the other hand, bentonite in the samples is easy to expand when meeting water, so as that the water content increases, the expansion of the samples increases and the corresponding samples are more difficult to be compacted. While under the conditions of same water content and dry density, bentonite content of the BZ mixture is higher than that of BZP mixture, so the former is more difficult for compaction compared to the latter (Fig. 8).

As dry density increases, thermal conductivity of both compacted BZP and BZ mixture increases. The main reason is that during the sample preparation process voids inevitably exist, and these voids are filled with air. As dry density increases, the voids in the sample are gradually filled by the sample particles. And the thermal conductivity of bentonite, zeolite, and pyrite is much higher than that of air; therefore, the increase of dry density leads to the reduction in the amount of air within the samples, resulting in the thermal conductivity of the samples increase.

Under the condition of same dry density, thermal conductivity of compacted BZP and BZ mixture increases with the water content increasing. The reason for which is that when the water content of samples increase, hydration expansion capability of bentonite increases as well, so that the voids between the bentonite powder may be filled, causing the void ratio of the samples to reduce and the thermal conductivity to increase in the end.

5 Conclusions

The experimental results show that the water content, dry density, and pyrite all have an impact on the thermal conductivity.

For compacted BZ mixture, when the dry density is 1.7 g/cm^3, and the water content is 17.65 % and 20 %, respectively, the thermal conductivity of the BZ mixture is, respectively, 0.81 Wm^{-1} k^{-1} and 0.86 Wm^{-1} k^{-1}. And for compacted BZP mixture, when the dry density is 1.7 g/cm^3, and the water content is 17.65 % and 20 %, respectively, the thermal conductivity of the BZP mixture is, respectively, 0.82 Wm^{-1} k^{-1} and 0.88 Wm^{-1} k^{-1}. When the dry density is 1.8 g/cm^3, and the water content is 17.65 %, the thermal conductivity of the BZP mixture reaches 0.96 Wm^{-1} k^{-1}. The thermal conductivity of the above BZ and BZP mixture can all meet the recommended value of the International Atomic Energy Agency (IAEA) 0.8 Wm^{-1} K^{-1}.

According to the experimental results, combined with the degree of difficulty for compaction, the compacted BZP (B:Z:P = 63:29:10) mixture with dry density of 1.8 g/cm^3 and water content of 17.65 % is recommended as an alternative material for high-level radioactive waste geological repository in buffer/backfill material.

Acknowledgments This work was financially supported by the Open Project of State Key Laboratory Cultivation Base for Nonmetal Composites and Functional Materials (11zxfk06), Defense Basic Research Projects, Science and Technology Support Program of Sichuan Province for Technology Research on the Preparation of Multiple Integrated Buffer/Backfill Materials (2012GZ0021) and Young Science Fund Projects of Department of Education of Sichuan Province (07ZB092).

References

1. Liu YM, Chen ZR (2001) The feasibility of GAOMIAOZI bentonite from Inner Mongolia working as backfill material for high-level radioactive waste repository. J Miner 21(3):541–543
2. Xie JL, Liu YM, Zhou HW (2010) A study of heat transfer characteristics on sand-bentonite mixture. In: The third waste underground disposal symposium proceedings. Research Institute of Geology for Beijing Nuclear Industry, Beijing, pp 439–444
3. Cui YJ, Chen B (2006) New progress for high-level nuclear waste in geological disposal of engineered barriers research. J Rock Mech Eng 25(4):842–847

4. Pacovsky J (2002) Some results from geotechnical research on bentonite. In: Konvalinka P, Lxemburk F (eds) CTU reports–experimental investigation of building materials and technologies, Burges, pp 107–116
5. Tang AM, Cui YJ, Le TT (2008) A study on the thermal conductivity of compacted bentonites. Appl Clay Sci 41:181–189
6. Fan X (2007) Engineering properties study on buffer/backfill materials. Southwest University of Science and Technology, Mianyang
7. Liu Y (2007) Study on the block performance of buffer/backfill material against uranium. Southwest University of Science and Technology, Mianyang

Study on Performances of the Concrete Pavement from Zincilate

Yong Wang and Ya'nan Yan

Abstract The zincilate production of concrete pavement brick uses industrial solid waste, both protecting the environment and promoting energy efficiency; there are huge comprehensive benefits. Based on the Guizhou Bijie zincilate, as the main raw material preparation from concrete pavement brick, the main factor which influences the quality of the products was investigated. The test results show that concrete pavement brick compressive strength at 28 days with zinc slag volume increases; zinc slag admixture is 40 %; 28 days compressive strength is more than 32 MPa.

Keywords Zincilate • Concrete pavement brick • Compression strength

1 Introduction

Zincilate is waste residue after the refining zinc in zinc-smelting plant by dry or wet method [1]. In China, some areas have a history of hundreds of years of zinc production. Due to not being used efficiently, storing up a lot of zinc tailings, occupation of land resources and pollution environmental are seriously.

According to nonferrous Association statistics, China's annual discharge ismore than about 60,000,000 t of zincilates [2]. After investigation, Guizhou province starts with the disorderly discharge; storage involves 15 villages and 61 villagers group, piling up a total of about 30,000,000 t covering an area of 18,000 acres including 24.86 % of arable land, 69.86 % barren ravine and depression, and 5.28 % river.

Y. Wang (✉)
Guizhou Engineering Technology, Research Centre for the Comprehensive Utilization of Industrial Waste (Materials), 13 South Shachong Roads, Guiyang, Guizhou, People's Republic of China
e-mail: 109815556@qq.com

Y. Yan
Guizhou Institute of Scientific Research and Design of Building Materials, 13 South Shachong Road, Guiyang, Guizhou, People's Republic of China

F. Dong (ed.), *Proceedings of the 11th International Congress for Applied Mineralogy (ICAM)*, Springer Geochemistry/Mineralogy,
DOI 10.1007/978-3-319-13948-7_37

From literature we can see that using zinc slag to produce concrete paving brick has not been reported in China so far. One is the large number waste residues are not available; the other is the production of concrete brick that consumes a large amount of natural sandstone; it goes against the rational use of resources. Therefore, it is important to use Zinc slag to product concrete paving brick.

In terms of XRD patterns, there is quartz, hematite, and mullite stone in zinc slag.

2 Materials and Methods

2.1 Materials

1. Zinc slag. The zinc slag was from Bijie with the dross loose bulk density: 965 kg/m^3, closely packed density: 1,118.5 kg/m^3, apparent density calculation: 2,075.5 kg/m^3, the loose voids rate: $V = 53.51$ %, and closely packed the porosity: $V = 46.11$ %; its chemical composition results are shown in Table 1, radionuclide limited test results are shown in Table 2; zinc slag material phase analysis is shown in Fig. 1, and the particle size distribution analysis is shown in Table 3.
2. Sand. Sand particle size distribution is shown in Table 3.
3. Cement. P.O 42.5.

2.2 Test Methods

1. Preparation of raw materials

   The zinc slag stacking spare after crushing and screening; the ordinary sand by sieving coarse sand more than 5 mm and the unsifted ordinary sand with a ratio of 2:3 mix.
2. Preparation of the concrete pavers from zinc slag

Table 1 Chemical composition of zinc slag (%)

Raw material	SiO_2	Fe_2O_3	Al_2O_3	CaO	MgO	Loss	K_2O	Na_2O	SO_3	f-CaO
Zinc slag	50.74	13.31	18.15	0.76	2.48	11.45	1.10	0.77	0.58	None

Table 2 Radionuclide limited test results

Raw material	Internal exposure index (IRa)	External exposure index (Ir)
Zinc slag	0.4	0.6

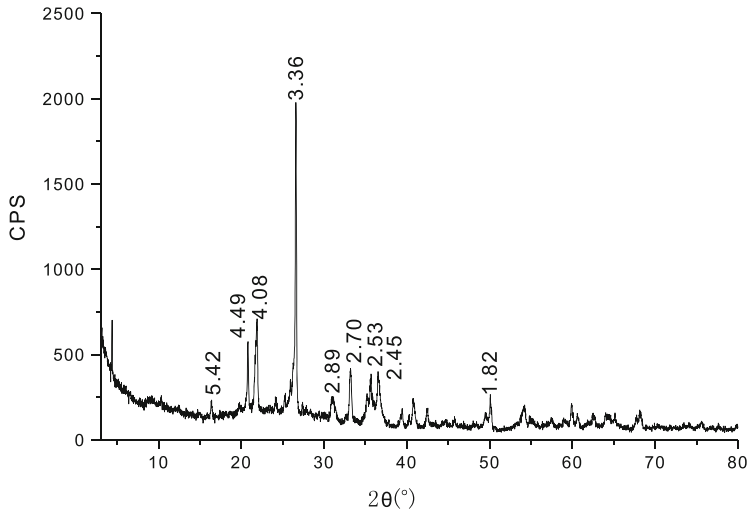

Fig. 1 X-ray diffraction (XRD) patterns of zinc slag

Zinc slag ordinary unburned preparation process: mixing aggregate and adjunct by stirring and natural curing to product. The zinc smelting the tailings ordinary brick ratio of raw materials for the solid material (100 %) accounts for 30–60 % in the aggregate, cement accounts for 15–20 %, sand 20–25 %; the specific test formulations are shown in Table 4 (each 18 kg powder forming a group).

2.3 Performance Test

The Zincilate concrete pavement bricks on performance testing of JCT446-2000 Standard detection.

3 Results and Discussion

It was seen in Table 5 that the strength requirements of the Formulations 1, 2, and 5 meet the concrete solid brick (GBT21144-2007). It can be seen, from the results, that the cement content was under the same circumstances, as Zinc slag increased. The strength of concrete pavement bricks decreases; bulk density along with reduced water absorption is gradually increasing. When the amount of Zinc slag is from 30 to 60 %, 28-day compressive strength of concrete pavement bricks will

Table 3 Grain composition of zinc slag and sand

Grade (mm)		>4.75	4.75–2.36	2.36–1.18	1.18–0.60	0.60–0.30	0.30–0.15	<0.15
Content (%)	Zinc slag	2.44	23.88	11.18	15.24	18.39	9.04	19.82
	sand	12.93	27.23	15.91	15.15	13.99	10.74	4.00

Table 4 The Zinc slag concrete pavement brick test formulation

Number	Cement (%)	Zinc slag (%)	Ordinary sand (%)	Coarse sand (%)	Water consumption (kg)
1	20	30	30	20	2.860
2	20	40	24	16	3.105
3	20	50	18	12	3.245
4	20	60	12	8	3.345
5	15	30	33	22	2.520

Table 5 The performance of concrete brick road from zinc slag

Number	Compression strength (MPa)		Bulk density (kg/m^3)	Water absorption (%)
	7d	28d		
1	27.2	36.8	3040	7.5
2	25.3	32.9	2920	7.9
3	21.9	29.8	2700	11.0
4	17.3	21.5	2350	12.8
5	26.5	31.6	2820	7.3

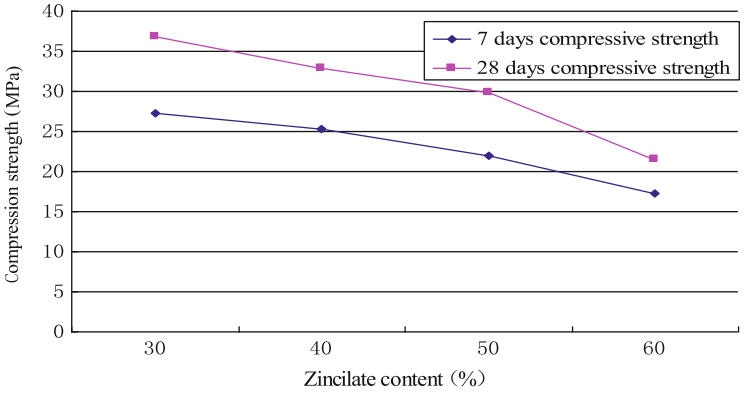

Fig. 2 Effect of mixing amount of zinc slag on compressive strength of concrete paving bricks

reduce from 36.8 to 21.5 MPa, which reduced by 41.6 %, while the water absorption increases by 5.3 %. The effects of the amount of Zinc slag on strength of concrete pavement bricks are shown in Fig. 2; the effect of the amount of Zinc slag on bulk density of concrete pavement bricks are shown in Fig. 3; the effects of the amount of Zinc slag on water absorption of concrete pavement bricks are shown in Fig. 4. According to the formula, the greater amount of Zinc slag requires a corresponding increase in water consumption.

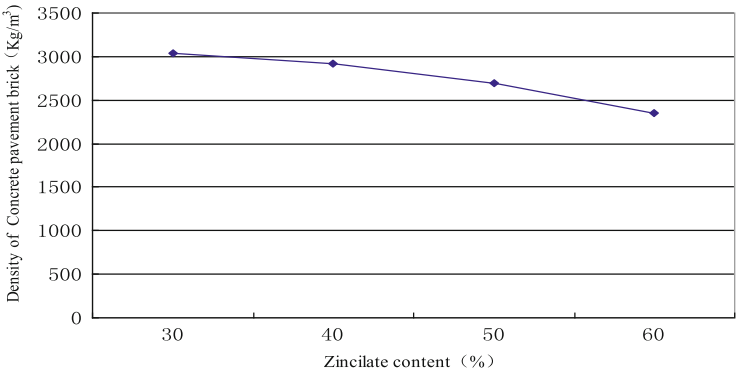

Fig. 3 Effect of mixing amount of zinc slag on bulk density of concrete paving bricks

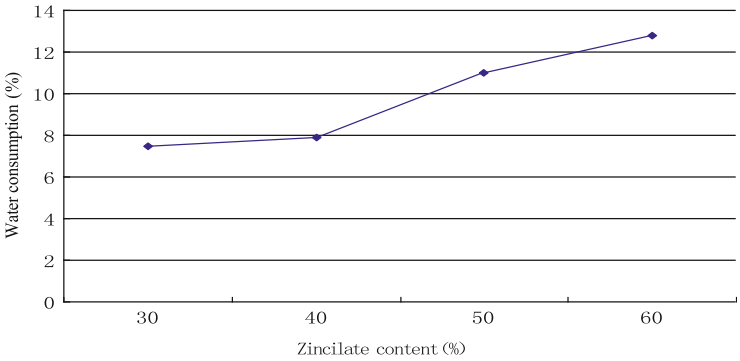

Fig. 4 Effect of mixing amount of zinc slag on water consumption of concrete paving bricks

4 Conclusions

1. The maximum mixing amount of zinc slag can reach 40 % when using it to produce concrete paving brick and the properties of brick are very good.
2. The 28d compressive strength and bulk density of brick decrease and water absorption increases while mixing amount of zinc slag is increasing and mixing amount of cement is unchanged.
3. The intensity of brick is reduced while mixing amount of zinc slag is decreasing and cement is unchanged.
4. The water consumption increases while mixing amount of zinc slag is increasing and mixing amount of cement is unchanged.

References

1. Wang WG (1996) Research and application of comprehensive utilization of zinc slag. Mining Metall 5(1):74–80
2. Xiao Z, Wang X, Huo C, Song L, JinSong X, Junping G, Wenyi W (2009) The Influence on properties of cement using zinc slag from Jiaozuo as mixed material. Guangdong Build Mater 10:22–25

Preparation of Carbon-Coated Tourmaline and the Degradation of Methylene Blue

Yuesong Wang, Xiuyun Chuan, Lin Li, and Dubin Huang

Abstract An attempt was made to prepare carbon-coated tourmaline by mixing tourmaline powders and polyvinyl alcohol (PVA), followed by heat treatment in argon atmosphere. All samples were characterized by powder X-ray diffraction, high-resolution transmission electron microscopy, and UV diffuse reflectance spectroscopy. Results showed that the residual carbon content was influenced by heat treatment temperature and the amount of PVA. The degradation of methylene blue by carbon-coated tourmaline was also studied. The experiments pointed out that the carbon-coated effects were best when the heating temperature was 900 °C and the weight content of PVA was 70 %. And the tourmaline prepared under 900 °C in the oxidation atmosphere has the best degradation efficiency. The results also proved that the infrared radiation of tourmaline had no effect in the degradation progress.

Keywords Tourmaline • Carbon coated • Methylene blue • Degradation

1 Introduction

Tourmaline is a kind of silicate mineral with complex components and structures. Its chemical formula is ordinarily $XY_3Z_6(BO_3)_3Si_6O_{18}(OH)_4$, in which X represents K^+, Na^+, Ca^+; Y Fe^{2+}, Mg^{2+}, Al^{3+}+Li^+, Fe^{3+}, Mn^{3+} and Z Al^{3+}, Fe^{3+}, Cr^{3+} [1–3].

The spontaneous electrical polarity of tourmaline has been found by previous studies [4–6]. Afterward it was widely used in dealing with the wastewaters and gases [7–9]. Meanwhile, tourmaline has several special functions, such as piezoelectric effect, thermoelectric effect, far-infrared radiation, anion release property, bioelectric property, and so on. All these characteristics make tourmaline extensively useful in a large number of regions [10–14].

Because of the uncoupled electrons in tourmaline's components, the electron spins between the particles are not counteracted, thus forming permanent magnetic distance. The magnetic mineral processing for tourmaline based on this property is

Y. Wang (✉) • X. Chuan • L. Li • D. Huang
School of Earth and Space Science, Key Laboratory of Orogenic Belt and Crust Evolution, Peking University, Beijing 100871, China
e-mail: wys_0816@163.com

F. Dong (ed.), *Proceedings of the 11th International Congress for Applied Mineralogy (ICAM)*, Springer Geochemistry/Mineralogy,
DOI 10.1007/978-3-319-13948-7_38

used to work on [15, 16]. And, previous studies show that tourmaline after being processed under different temperatures would improve its ability of far-infrared radiation and the infrared emission function efficiently [17–20]. At the same time, the magnetic property for different kinds of tourmalines was studied [21]. However, reports including how the magnetic function can be effected by the thermal processing, whether it can be improved together with the far-infrared radiation and the infrared emission ability, and can then be used on the environment protection and the health care were relatively fewer [22]. This paper works on the aphrizite from Yingkou, Liaoning. The aphrizites were first thermally dealt with under different temperatures and then tested for the magnetic susceptibility contrastively before and after being processed to learn the effects of the thermal treatment on the phase transition and the magnetic capabilities of the aphrizites, thus conducting ore dressing and exploiting.

1.1 The Harm of the Methylene Blue

Methylene blue (MB) is also named methylthionine chloride, which is one of the typical pollutants in the dyeing effluent and the crucial harnessed object. This kind of effluent has not only dark color but also low light transmission that affects the quality of water and decreases the photosynthesis of water plants. Most of the dyes are poisonous and responsible for cancers, distortions, and mutations. Methylene blue is an important organic chemically synthesized cationic dye used widely in industries such as dyeing linen, natural silk textiles and paper, coloring bamboo or wood, chromosome staining for organisms and bacteria tissues, producing inks and lakes, etc. The extensive usage of methylene blue leads to serious pollution of pure waters. Presently, the methods to deal with such wastewater mainly include biological process, coagulation method, hydrocarbonylation, adsorption method, membrane separation, and so on.

1.2 The Function of Tourmaline in Effluent Treatment

The spontaneous polarization and anion release features of tourmaline make it react with water generating $OH^{-}(H_2O)n$ molecules with surface activities, which can saturate, disperse, and dissolve organics [23] and therefore decompose the methylene blue [24]. When tourmaline is used to deal with Argazol Blue BF-BR wastewater, together with the oxidant H_2O_2 at the same time, the decolorization result is perfect. Besides, tourmaline works well in degradation of other organic water pollutants, such as ethyl violet and ethylenediaminetetraacetic acid.

2 Experiments

2.1 Carbon Coating Experiments

The tourmaline was ground and sieved by a 200-mesh sieve. Add polyvinyl alcohol, denoted as PVA, into the tourmaline and then the mixture was heat treated under argon atmosphere from room temperature to the target temperature at a heating rate of 5 min^{-1} and then kept for 3 h in order to complete the carbonization. The target temperature and quality ratio of PVA of each experiments are described as Table 1.

2.2 Degradation of Methylene Blue

Add 2 g carbon-coated tourmaline separately prepared under 500, 700, 900 °C into 200 ml methylene blue solution (20 mg/L). Input the tourmaline samples prepared under corresponding temperature without adding PVA as contrast experiments. Then 2 g analytically pure H_2O_2 was added into each beaker and stirred with magnetic stirring apparatus.

When the begin of reaction, sampled and centrifuged the samples regularly. Then the light absorption value of the supernatant, $\lambda = 610$ nm, was determined by the UV–vis Diffuse Reflectance Spectroscopy.

In another series of experiments, the carbon-coated tourmaline was prepared under the temperature of 900 °C with the PVA weight ratio of 70, 30, and 20 %.

2.3 Characterization

The chemical component of tourmaline samples was analyzed by X-ray fluorescence spectrometry (ADVANT′XP+, Airline Rotables Limited Co., Switzerland).

Table 1 The heating temperature and the abbreviation

No.	Temperature (°C)	The weight content of PVA (wt%) (%)
Tour		
T500-1-1	500	50
T600-1-1	600	50
T700-1-1	700	50
T800-1-1	800	50
T900-1-1	900	50
T900-3-7	900	70
T900-7-3	900	30
T900-8-2	900	20

The mineral composition was determined by the X-ray diffraction (DMAX-2400, Rigaka, Japan). Scanning electron microscope (S-3400, Nicolet, America) was used to observe the effect of carbon coating on the surface of tourmaline. The infrared radiation was analyzed by Fourier transform infrared spectrometer (5DX, NICOLET, America) and its emissivity analyzing accessory (JD-1, Jilin University, China). The concentration of MB was analyzed by UV–vis Diffuse Reflectance Spectroscopy (HP8453, Agilent, America).

3 Results and Discussions

3.1 The Mineralogy Properties of Tourmaline

The chemical component of tourmaline was described in Table 2. The data show that the tourmaline of the working region has a high content of Al, Mg, and Fe. In the meanwhile the K-Na isomorphism supersede can be figured out.

The XRD data showed that the tourmaline sample had a complex mineral composition. Figure 1 showed that the tourmaline was mainly composed by dravite (Na $(Mg,V)_3Al_6(BO_3)_3Si_6O_{18}(OH)_4$) and schorl ($NaFe_3Al_6(BO_3)_3Si_6O_{18}(OH)_4$).

3.2 The Carbon-Coated Effect

The morphology of the carbon-coated tourmaline was observed by SEM and the element content was studied by EDS. The result was described in Fig. 2.

The study showed that the carbon-coated effect was better under higher temperature. The C element was not detected on the surface of tourmaline prepared under 500 and 600 °C. The C element was detected when the heating temperature rose to 700 °C and the atomic percent was 12.23 %. As the heating temperature kept rising to 800 and 900 °C, the content of C increased to 22.5 and 25.8 %.

The results demonstrated that PVA was not fully carbonized under low temperature. The C content increased as the PVA ratio increases. The carbon layer was not fully coated on the surface of the tourmaline when the weight ratio of PVA was 20 and 30 % and the atomic content of carbon was only 18.44 %. The carbon layer got thicker as the ratio of PVA increased. The atomic content of carbon was 92.68 % for the samples concluding 70 % PVA.

Table 2 The chemical constituent (wt%) of the black tourmaline of Liaoning province

Chemical composition	CO_2	Al_2O_3	K_2O	Na_2O	MgO	SiO_2	Fe_2O_3	CaO	P_2O_5	V_2O_5	TiO_2	Cr_2O_3	MnO	CoO	ZnO
Wt%	3.44	20.3	0.10	1.44	7.32	32	11.3	2.74	0.318	0.118	0.719	0.0173	0.0358	0.0222	0.0159

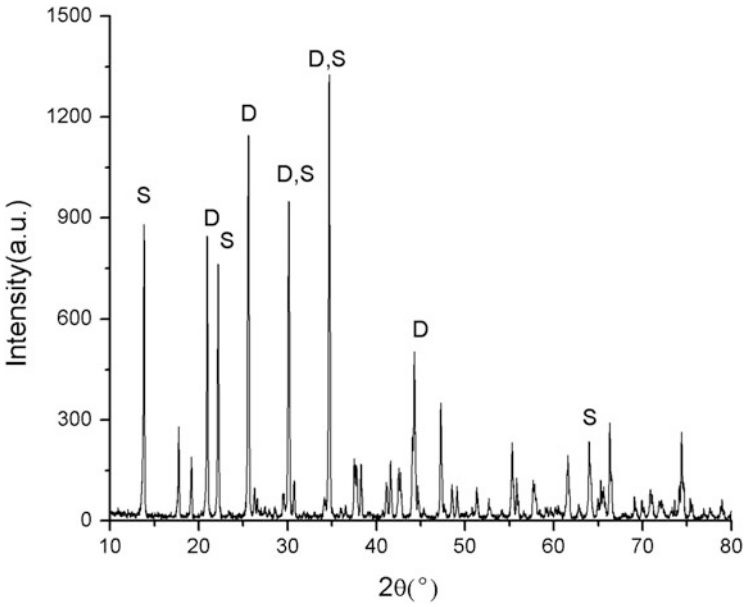

Fig. 1 X-ray powder diffraction patterns of tourmaline samples of Liaoning. *D*-Dravite, *S*-Schrol

3.3 The Degradation Effect of Different Tourmaline Samples

The MB solution was in accord with Bouguer–Lambert–Beer's law when the concentration was in the range of 1–10 mg/L. The regression equation was

$$A = 0.0313C + 0.0017(R2 = 0.9992) \quad (1)$$

A Absorbance value of the solution
C Concentration of MB solution
R Regression coefficient

Degradation rate of the MB solution was figured out by the absorbance using this equation (Tables 3 and 4).

3.4 Infrared Radiation of Carbon-Coated Tourmalines

The infrared radiation of carbon-coated tourmalines prepared with different PVA weight contents was analyzed by fourier transform infrared spectrometer and its emissivity analyzing accessory (Tables 5 and 6).

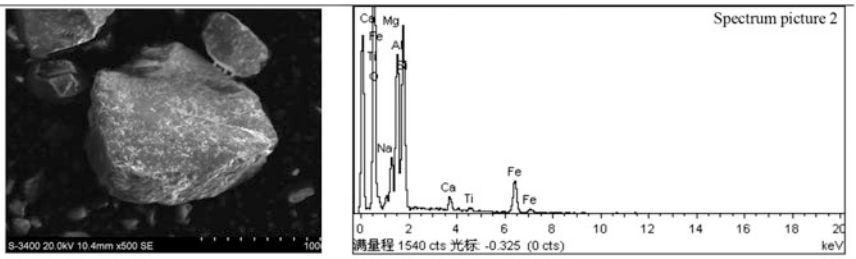

T500-1-1

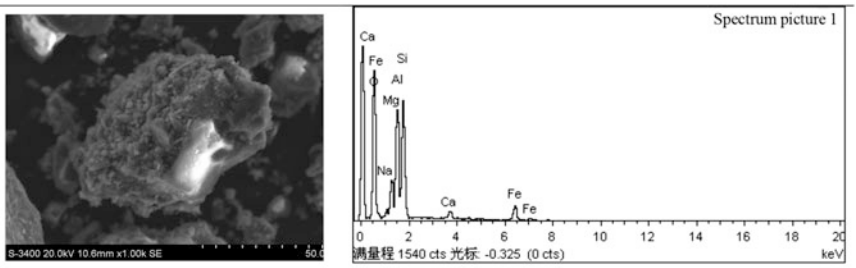

T600-1-1

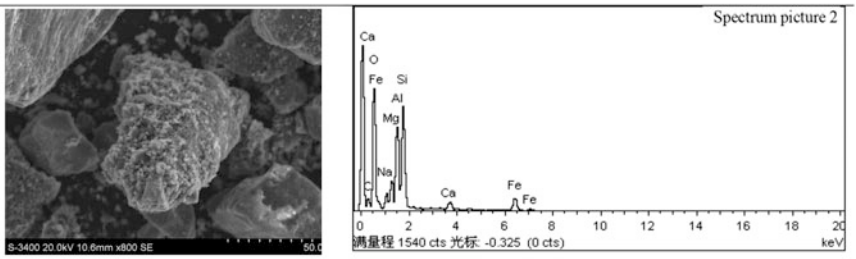

T700-1-1

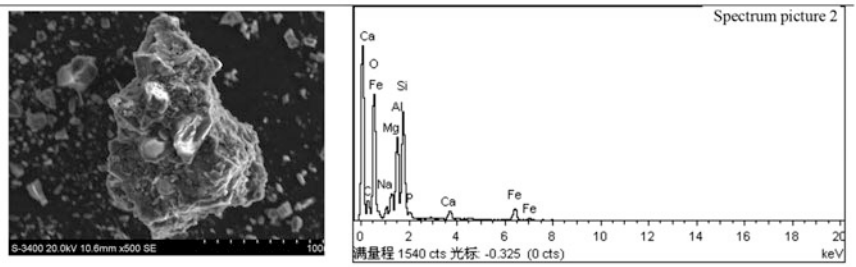

T800-1-1

Fig. 2 (continued)

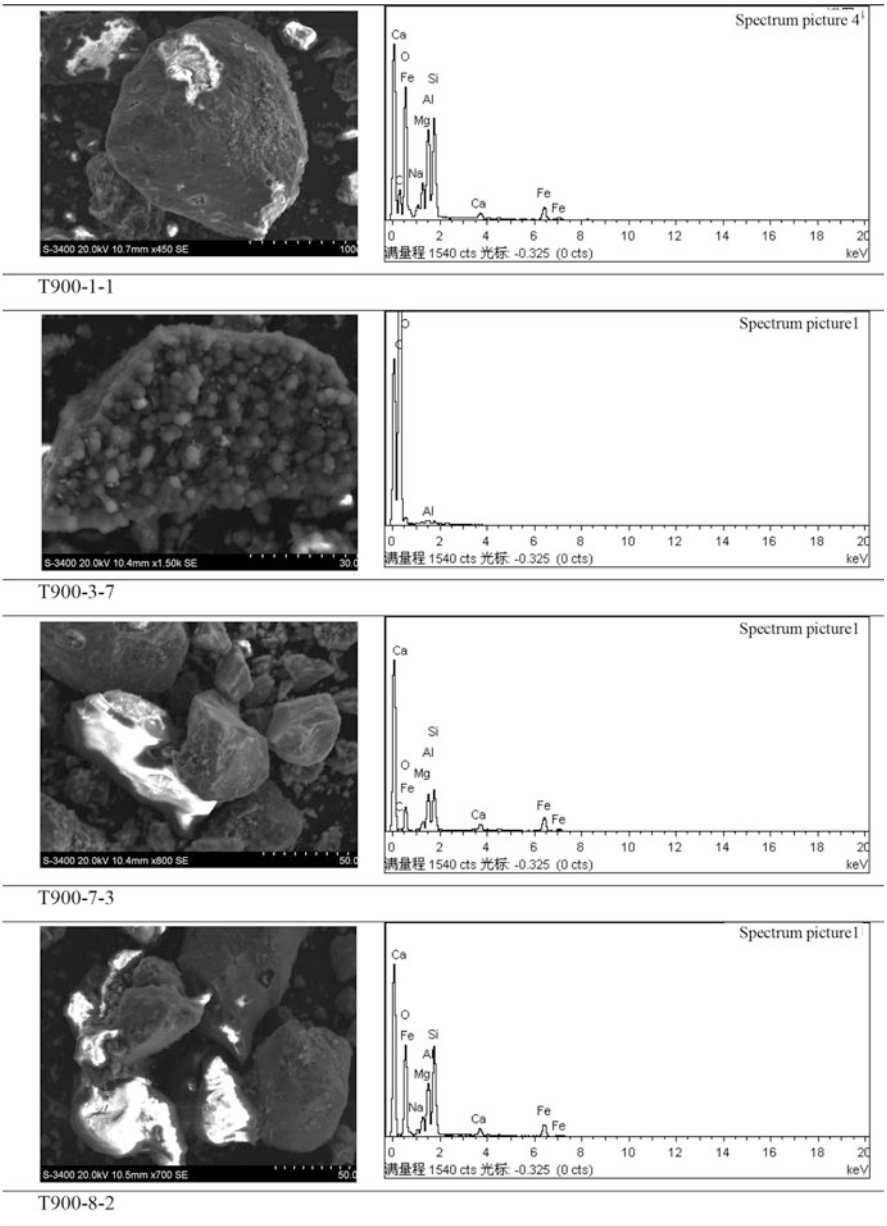

Fig. 2 The micromorphology and EDS results of carbon-coated tourmaline

Table 3 Concentration of MB solution of carbon-coated tourmaline prepared under different temperatures

Reaction time	Concentration of MB solution (mg/L)						
	Tour	T500	T500-1-1	T700	T700-1-1	T900	T900-1-1
0 min	20	20	20	20	20	20	20
20 min	17.36	17.69	18.47	17.87	17.87	17.28	17.54
40 min	16.58	16.84	17.06	16.47	16.45	16.33	16.17
60 min	15.21	15.58	15.35	15.25	15.03	14.46	14.85
4 h	14.24	14.16	14.82	14.02	14.68	12.03	14.66
8 h	13.62	12.90	14.21	12.14	14.12	10.51	14.01
12 h	12.75	11.23	13.73	10.35	13.44	9.38	13.56
24 h	12.03	10.06	13.62	9.02	13.28	8.10	13.34
36 h	11.47	9.34	13.45	8.41	13.23	7.40	13.28
48 h	11.02	8.05	13.36	7.38	13.21	6.65	13.25

Table 4 The removal rates of MB solution

Reaction time	Removal rates of MB solution (%)						
	Tour	T500	T500-1-1	T700	T700-1-1	T900	T900-1-1
0 min	0	0	0	0	0	0	0
20 min	13.20	11.55	7.65	10.65	10.65	13.60	12.30
40 min	17.10	15.80	14.70	17.65	17.75	18.35	19.15
60 min	23.95	22.10	23.25	23.75	24.85	27.70	25.75
4 h	28.80	29.20	25.90	29.90	26.60	39.85	26.70
8 h	31.90	35.50	28.95	39.30	29.40	47.45	29.95
12 h	36.25	43.85	31.35	48.25	32.80	53.10	32.20
24 h	39.85	49.70	31.90	54.90	33.60	59.50	33.30
36 h	42.65	53.30	32.75	57.95	33.85	63.00	33.60
48 h	44.90	59.75	33.20	63.10	33.95	66.75	33.75

Table 5 Concentration of MB solution of carbon-coated tourmaline prepared with different PVA weight content

Reaction time	Concentration of MB solution (mg/L)		
	T900-3-7	T900-7-3	T900-8-2
0 min	20.00	20.00	20.00
20 min	18.25	17.42	17.53
40 min	17.13	16.67	16.62
60 min	15.94	15.30	15.22
4 h	15.54	14.23	14.45
8 h	14.77	14.13	14.17
12 h	14.32	13.65	13.54
24 h	13.87	13.39	13.41
36 h	13.63	13.30	13.32
48 h	13.47	13.23	13.24

Table 6 The Removal rates of MB solution of different carbon-coated tourmaline prepared with different PVA weight content

Reaction time	Removal rates of MB solution (%)		
	T900-3-7	T900-7-3	T900-8-2
0 min	0	0	0
20 min	8.75	12.90	12.35
40 min	14.35	16.65	16.90
60 min	20.30	23.50	23.90
4 h	22.30	28.85	27.75
8 h	26.15	29.35	29.15
12 h	28.40	31.75	32.30
24 h	30.65	33.05	32.95
36 h	31.85	33.50	33.40
48 h	32.65	33.85	33.80

Tourmaline was once used to adsorb and degrade methylene blue in previous studies. The results showed the obvious synergistic reaction between tourmaline and H_2O_2. The mechanism for Fenton Reaction is that H_2O_2 produces hydroxyl by catalyzing iron ions. By comparing the processing effects of tourmalines with different iron components, aphrizite with high iron components reacts fast and does well in dealing with the methylene blue. During the reaction, iron dissolves out, so we can infer it may be Fenton-like process. In addition, tourmaline increases the amount of oxide dissolved in water according to other researches. What's more, the function of increasing oxide content could be used on fish farm. A fish pond without any oxygen equipment, if dealt with tourmaline, will keep more than 7.5 mg/L of dissolved oxygen. On the other hand, dissolved oxygen is a significant fact for the degradation of organics (Fig. 3).

Researches show that with the temperature of thermal treatment rising under oxidative circumstances, the texture and phase of tourmaline change. When the temperature gets to 800 °C, dravite and schorl peaks decrease, while new phases of anorthite ($CaAl_2Si_2O_8$) and hematite (Fe_2O_3) emerge. When the dealing temperature reaches 900 °C, dravite peak decreases more, which indicates at 800 °C tourmaline crystal structure is destroyed, and then all components react with each other, resulting in crystal transition and new phase formation as a result. When the temperature gets 800 and 900 °C, sintered layer forms on the surface of the sample whose ingredient is proved to be anorthite and hematite (Fig. 4).

The reason for the new phases is that at high temperature the boron particles start to separate from the crystal lattice to result in the destruction of BO_3 triangle and the further collapsing of cyclic Si_6O_{18} tetrahedrons. The previous studies prove that B_2O_3 helps decrease the synthesis temperature of anorthite. So at 800 °C, anorthite appears and Fe^{2+} transforms into hematite meanwhile after being oxidized.

Based on the experiments we can see that tourmalines synthesized in oxidized circumstances are superior in degradation. By the way, its degradation capability is more powerful along with the dealing temperature being increasing. This is regarded as the result of heating with oxidation. During this process, Fe^{2+} is oxidized to Fe^{3+} which has more efficient catalysis effects on H_2O_2. The result

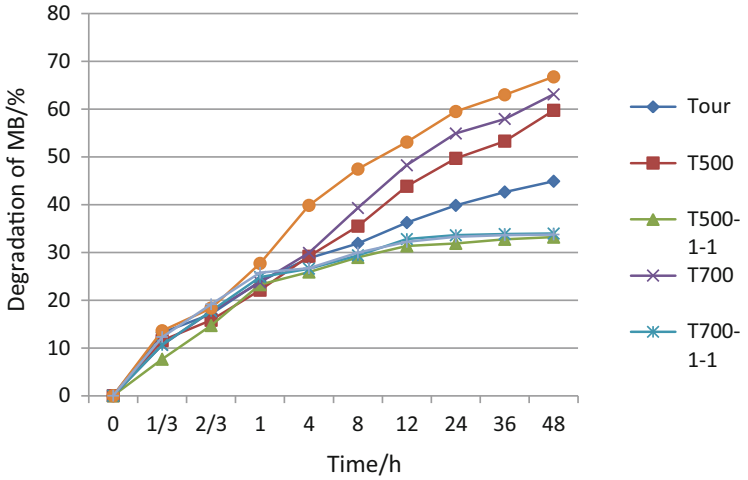

Fig. 3 Degradation rate of MB with different tourmaline samples

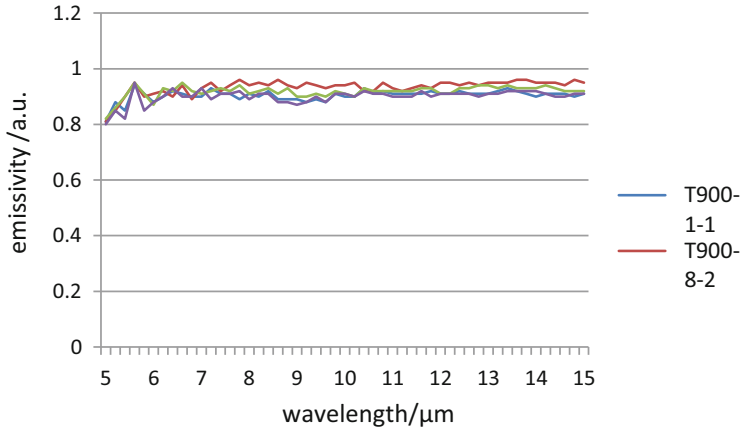

Fig. 4 Infrared radiation of carbon-coated tourmalines of different carbon-coated tourmalines prepared with different PVA weight content

also proves tourmaline/H_2O_2 system works on methylene blue based on Fenton Reaction.

Because of the absence of void structure in the surface carbon floor cladding around tourmaline, methylene blue was not adsorbed. Moreover, the existence of the carbon floor cuts down the contact area between the two samples, thus cutting down the degradation effects compared with those crude tourmalines without being processed.

Meanwhile, previous studies show the reaction of tourmaline/H_2O_2 system is complex, which may be caused by the special functions of these minerals, such as

permanent spontaneous polarity characteristic and far-infrared radiation abilities [25]. However, based on this paper we can see that at the same temperature tourmalines crabbed by carbon in different mass ratio vary in the far-infrared radiation abilities. While the tourmaline/H_2O_2 system makes little difference on degrading methylene blue. As a result, we think that far-infrared radiation ability does not work directly on the methylene blue degradation.

4 Conclusions

1. 900 °C is the optimum temperature for carbon crabbing around the tourmaline.
2. When the processing temperature is permanent, the crabbing result would be the best with the mass ratio between tourmaline and PVA reaching 3:7.
3. The appropriate circumstance for the methylene blue degradation experiment is 900 °C with oxidized environment. What's more, there are no apertures generating in the surface carbon floor cladding around tourmaline which restrains the methylene blue degradation.
4. The far-infrared radiation ability of tourmaline has nothing to do with the methylene blue degradation.

References

1. Guo Y, Sang WB, Wang RC (2008) Cluster analysis of Mossbauer spectra of tourmaline crystals. J Funct Mater 39(12):2113–2116
2. Hawthorne FC, Henry DJ (1999) Classification of the minerals of the tourmaline group. Eur J Mineral 11:201–215
3. Kubo TJ (1989) Interface activity of water given rise by tourmaline. Solid State Phys 24 (12):279–285
4. Barton RJ, Donnay G (1968) Absolute orientation of tourmaline by arcomalous dispersion of X-rays (abst). Geol Soc Am 101:12–13
5. Barton RJ (1969) Refinement of the crystal structure of buergerite and absolute orientation of tourmaline. Acta Crystallogr B25:1524–1533
6. Zhan J, Ge BH, Wang P et al (2009) Study on the microstructure of natural tourmaline and mechanism of its influence on PH value of water. J Funct Mater 40(4):556–559
7. Li L, Chuan XY (2008) Microstructure, properties and application of tourmaline. China Non-metallic Miner Ind 71:33–37
8. Dong FQ, He DL, Yuan CL (2005) The environmental functional property and trends of application of tourmaline. J Funct Mater 36(10):1485–1488
9. Liu LB, Zhang YS, He DL (2012) Kinetic study on photocatalysis degradation of phenol by using tourmaline/TiO_2 system as catalyst. J Funct Mater 43(4):512–515
10. Zhan J, Wang ZY, Wang P et al (2010) The influence of natural mineral tourmaline on water cluster. J Funct Mater 41(1):159–161
11. Wang Y, Yeh JT, Yue TJ et al (2006) Influence of tourmaline on negative air ion emitting property of poly(ethylene terephthalate). J Macromol Sci, Phys 43:1749–1756
12. Nashi Y, Yazawa A, Oguri K (1996) pH self-controlling induced by tourmaline. J Intell Mater Syst Struct 7(3):260–263

13. Mashi Y (2001) Physiology effects when wearing AP fiber cloth containing special tourmaline crystal powder. J Int Soc Life Inf Sci 19(1):73–74
14. Fox GW, Fink GA (1934) The piezoelectric properties of quartz and tourmaline. Physics 5:302–306
15. Zhang H, Xu XP (2004) Purification of taltalite by magnetic separation. Min Metall Eng 4:38–40
16. Ren F, Han YX, Yin WZ (2005) Investigation on schorl purification by wet high-intensity magnetic separation. Metal Mine 5:31–33
17. Ji ZJ, Liang JS, Jin ZZ et al (2002) Structure change of dravite-schorl after heat treatment. Acta Mineral Sin 22(3):281–284
18. Liang JS, Meng JP, Zhu DB (2008) Effect of heat treatment of Hesur tourmaline powders. J Chin Ceram Soc 36(2):258–260
19. Zhang LJ, Guo XH, Yang H et al (2009) Effects of heat treatment on far-infrared emissivity of tourmaline. J Ceram 30(3):286–289
20. Liao CC, Liao LB, Shen L (2011) Influence of heat treatment on the intrinsic influence of heat treatment on the intrinsic. Acta Mineral Sin 31(1):108–112
21. Li WW, Zhang XH, Wu RH (2007) Piezoelectricity and magnetic properties of diverse tourmalines. Bull Chin Ceram Soc 26(6):1116–1120
22. Zhou WW, Chuan XY, Wang SQ (2011) Infrared emission function and its influencing factors of Yingkou serpentine jade. Acta Mineral Sin 31(4):750–756
23. Cao HL, Zhang L, Lu GY et al (2007) Absorption and degradation of organic dyestuff like methylene blue by tourmaline. Guangdong Chem 1(34):30–34
24. Xu HY, Wang P, Mao GJ et al (2007) Novel application of tourmaline in environmental field: treatment of argazol blue BF-BR dyeing waste water. Chin J Environ Eng 1(4):65–69
25. Lu T, Li HY, Zhang HM (2009) Study on degradation of methylene blue by tourmaline/H_2O_2 system. Non-Metallic Mines 32(2):64–67

Raman Spectroscopic Core Scanning for Iron Ore and BIF Characterization

M.A. Wells and E.R. Ramanaidou

Abstract The application of Raman spectroscopy, utilizing a HyLogging™ automated core-scanning platform, to map the iron ore and gangue mineralogy in banded iron formation drill core and hematite-rich, detrital iron deposit ore was tested as a demonstration of the potential of this technique for rapid, in situ mineralogical mapping. The common iron ore Fe-oxide mineral hematite as well as gangue minerals, such as quartz and Fe^{2+}-carbonate, shows distinct Raman spectra, which enabled these phases to be readily detected and mapped in situ. Despite also exhibiting a distinct Raman spectrum, detection of magnetite was problematic and is now the focus of ongoing research to optimize the Raman scanning conditions to enhance detection of the common iron ore and BIF mineralogy.

Coupling to the HyLogger™ platform clearly extends and augments the utility of Raman spectroscopy for routine characterization of iron ore mineralogy and delivers a step change to current characterization methods that underpin strategies to best manage and process existing Australian iron ores (e.g., BID and CID), as well as the newly developed MID ores.

Keywords Raman spectroscopy • Iron ore • Bedded iron-derived deposits • BID • Drill core • HyLogging

1 Introduction

With reserves of premium high-grade (i.e., >64 % Fe and <0.07 % P) iron ore in decline in Australia (i.e., Brockman ores) and worldwide over the past 5–10 years (e.g., [1]), iron ore producers have increased their utilization of lower Fe-grade ore with higher gangue element contents (e.g., P, Al, and Si) [2]. Driven mainly by the increased demand from Chinese steel mills, Australian iron mining companies have increased their usage of channel iron deposit (CID) and bedded iron deposits (BID)

M.A. Wells (✉) • E.R. Ramanaidou
CSIRO Mineral Resources Flagship (MRF), Australian Resources Research Centre,
PO Box 1130, Bentley, WA 6102, Australia
e-mail: Martin.Wells@csiro.au

F. Dong (ed.), *Proceedings of the 11th International Congress for Applied Mineralogy (ICAM)*, Springer Geochemistry/Mineralogy,
DOI 10.1007/978-3-319-13948-7_39

and have sought to develop the newly emerging BIF-derived magnetite iron deposits (MID) [3].

Efficient utilization of lower-grade iron ores requires a detailed understanding and better characterization of ore mineralogy and geochemistry to improve the resource management of iron ore. Application of reflectance spectroscopy over the 400–2,500 nm, visible to near-infrared wavelength range, is now an established technique for mineral analysis in exploration and mining and is being increasingly used to characterize the iron oxide and clay mineralogy of a number of deposits. For example, the technique can quantify the hematite: goethite ratio in ore deposits (e.g., [4]). More recent work has seen the use of this technique to characterize the iron ore oxide mineralogy of BID-derived iron ores in India [5] and Brazil [6], and in characterizing the color of Australian soils in general [7].

Application of semi-automatic or automatic core-scanning techniques with large-scale, rapid, and routine identification and near-quantitative characterization of iron ore is now well established in the minerals industry. For example, recent application of CSIRO's HyLogging™ system was used to aid resource modeling of the Rocklea Dome CID [8]. Importantly, the common iron ore (e.g., goethite, hematite, and magnetite) and gangue minerals (e.g., carbonates, silicates, and quartz) are all Raman active (e.g., [9]). Recent work by [3] and [2] demonstrated the value of Raman spectroscopy in characterizing better the economic and gangue mineralogy of BID-derived iron ore. The main iron oxide minerals of economic interest in iron ore, goethite and hematite, are well known sinks of a range of minor and trace elements, particularly Al which can replace Fe in the structure of both goethite and hematite (e.g., [9]). Earlier work in our laboratory demonstrated that shifts in the main phonon lines of goethite and hematite varied systematically with Al content and can provide an estimate of the Al substitution in goethite or hematite [10].

Combining the discriminatory power of Raman spectroscopy with the potential of the core-scanning technique offers large-scale (volumetric) characterization of iron ore that will be of great value not only to the existing BID and CID ore types but also to the newly emerging magnetite iron deposits (MID). In this chapter we describe the application of Raman spectroscopy utilizing a HyLogging™ platform to map the iron ore and gangue mineralogy in banded iron formation drill core, as a demonstration of the potential of this technique for rapid, in situ mineralogical mapping.

2 Materials and Methods

2.1 Iron Ore Samples

Drill core, approximately 60 mm in diameter, of banded iron formation (BIF) and a hematite-rich iron ore (detrital iron ore, DID), representative of the Pilbara region,

Western Australia, were selected for analysis. Encased in polyvinyl tubing, the BIF drill core sample was cut longitudinally in half using a diamond saw to obtain a smooth surface for analysis. The DID sample was also cut to obtain a smooth surface for scanning. The half-core BIF sample presented for analysis had final dimensions of 240×60 mm, whereas the DID sample was approximately 80×60 mm in size (Fig. 1). In this chapter sample locations were not considered important as the samples were chosen to demonstrate the potential of the technique.

2.2 Spectroscopic Analysis

2.2.1 Reflectance Spectroscopy and HyLogging™

Reflectance spectroscopy measures light as function of wavelength as it is scattered or reflected from a solid surface. Absorption effects in the visible to near-infrared wavelength range of the electromagnetic spectrum (e.g., 400–1,000 nm) result from crystal field and charge transfer effects, whereas absorption features at longer wavelengths (1,000–2,500 nm) are overtones or combination tones of longer-wavelength, fundamental, OH-group bending and stretching vibrations (e.g., [9]). An innovative core logging system, the HyLogger™, measures reflectance spectra using an Analytical Spectral Device (ASD) FieldSpec Pro instrument over the 400–2,500 nm wavelength range. Reflectance spectra are measured from a small spot (6–8 mm in diameter) focused at the sample (drill core, chips, or pulps) surface, which is placed on a robotic, X–Y translation stage that moves under the detector. Further details regarding instrumental setup and scanning conditions of the HyLogger™ are provided by [9].

2.2.2 Raman Spectroscopy

Raman spectroscopy is a technique named after one of its discoverers and Nobel Prize winner, Sir Chandrasekhara Venkata Raman [11] and is based on the inelastic scattering of monochromatic light, typically a laser source. The technique examines molecular vibrational and rotational modes within a system from the very small proportion of incident photons that undergo inelastic scattering and a change in frequency upon interaction with a sample surface. A detailed discussion of Raman theory and its general applications is made in the review by [12], with a more general discussion regarding the application of the method to iron ore characterization by [3].

Fig. 1 Samples representative of a banded iron formation. BIF (*left*) prepared as half-core and a detrital iron deposit, DID, iron ore (*right*), presented to the HyLogger™ scanner for reflectance spectroscopic and Raman analyses. The *yellow line* down the center of the BIF half-core section and DID sample represents the path along which measurements of reflectance and Raman spectra were made

2.2.3 Spectroscopic Analysis

For this study the selected BIF half-core and DID iron ore samples were fixed to a wooden base to ensure a level surface and to maintain a constant height between the sample surface and the HyLogger™ and Raman optic sensors. Reflectance spectra were measured over the 400–2,500 nm wavelength range with samples scanned at 3 mm intervals or steps along the longitudinal center, using quartz halogen lamps to maintain a source of constant illumination. The ASD spectrometer was calibrated against a 99 % reflectance standard Spectralon (compressed polytetrafluoroethylene, PTFE). High-resolution, digital images of the half-core samples were collected simultaneously. Raman spectra were measured using an EZRaman-1 spectrometer mounted to the HyLogger™ frame. The spectrometer is a fully integrated lab-based or portable unit, using a 785 nm wavelength, frequency stabilized, narrow line width laser, operating at a power output of 300–400 mW. Raman spectra were measured over the 100–2,150 cm^{-1} wavelength range at a spectral resolution of ≈6 cm^{-1}, with spectra also collected at 3 mm intervals along the longitudinal center at the sample surface from spot measurements of area ≈2–5 μm^2.

Processing and visualization of calibrated spectra were performed using the purpose built program the Spectral Geologist (TSG™)-Core version 7.1.0.055 software (e.g., [13]) using the method of [14].

3 Results and Discussion

A screen image captured from the (TSG™)-core graphical user interface (GUI) presents both the reflectance and Raman spectra measured at a single spot for the DID ore sample (Fig. 2). The reflectance spectrum shows the main iron oxide absorption feature centered at about 915 nm indicating the goethite-rich nature of the sample at the point of measurement (Fig. 2).

The Raman spectrum of a spot collected within the area from which the reflectance spectrum was measured shows excitation lines detected at 222, 289, 409, and 611 cm^{-1} confirming the presence of hematite (Fig. 2). This is consistent with Raman spectra reported for hematite (e.g., [3, 9]). In addition, detection of an excitation line at 463 cm^{-1} confirmed the presence of quartz (Fig. 2) consistent with other reported Raman spectra of quartz detected in iron ore-related material [3]. It must be noted that the measured reflectance spectrum is representative of a much larger area (about 50 mm^2) compared to the measurement area for Raman spot analysis (2–5 μm^2). Hence, it is conceivable that the Raman spectrum may be representative of only a few grains at the sample surface, whereas the reflectance spectrum is "averaged" from many more grains of a predominantly goethite-rich mineralogy and explains why hematite was not detected in the reflectance spectrum (Fig. 2).

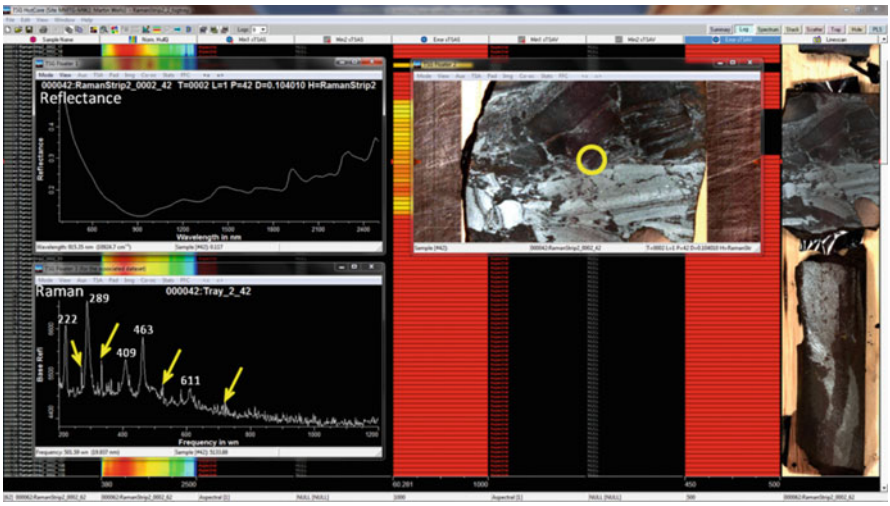

Fig. 2 Measured reflectance spectra over the 300–2,500 nm wavelength range and Raman spectra over the 200–1,200 cm^{-1} wavelength range for the area circled (*yellow*) in the digital inset image of the detrital iron ore (DID) sample scanned in the far-right column. Wavelength (cm^{-1}) positions of the main peaks in the Raman spectrum are labeled (e.g. 289), whereas "spikes" (*yellow arrows*) are noise. The Raman spectrum was measured over a much smaller area, ≈2–5 μm^2, within the area (*yellow circle*) focused for reflectance spectroscopic analysis

Reflectance and Raman spectra for the scanned BIF core are presented as screen captured images from the (TSG™)-core GUI in Figs. 3, 4, and 5. Positioned over an approximately 5 mm wide, buff-colored band in the BIF sample, the reflectance spectra shows a very strong Fe^{2+} absorption feature centered at ≈ 1,200 nm, with a longer wavelength feature at about 2,340 nm, consistent with the presence of a ferrous-bearing carbonate (Fig. 3). The associated Raman spectra confirmed the presence of carbonate from the strong excitation lines at 280 and 1,083 cm^{-1} (Fig. 3), consistent with the presence of siderite [15]. Quartz was also detected from the two main excitation lines detected at 199 and 463 cm^{-1} consistent with reported occurrences of quartz in BIF (e.g., [3]).

Positioned over a narrow, 5–6 mm wide, oxidized band as evidenced by the visible, red-brown discoloration (Fig. 4), the strong Fe^{2+}-related absorption feature in the reflectance spectrum was similar to that shown in Fig. 3, whereas the strong, longer wavelength absorption features at 1,404 and 2,341 nm indicate the presence of a Mg-OH-bearing phase, likely of the amphibole group (Fig. 4). The Raman spectrum for the area measured in Fig. 4 was similar to that for the area measured in Fig. 3, with the presence of both quartz and a ferrous-bearing carbonate (i.e., siderite) being detected (Fig. 4). In addition, a weak excitation line at 293 cm^{-1} (Fig. 4) identified the presence of hematite (e.g., [3]).

Spectroscopic measurements of one of the conspicuous, dark (i.e., black) magnetite bands present in the BIF sample are shown in Fig. 5. The reflectance spectrum for this location was very similar to that measured in Fig. 4. However, the

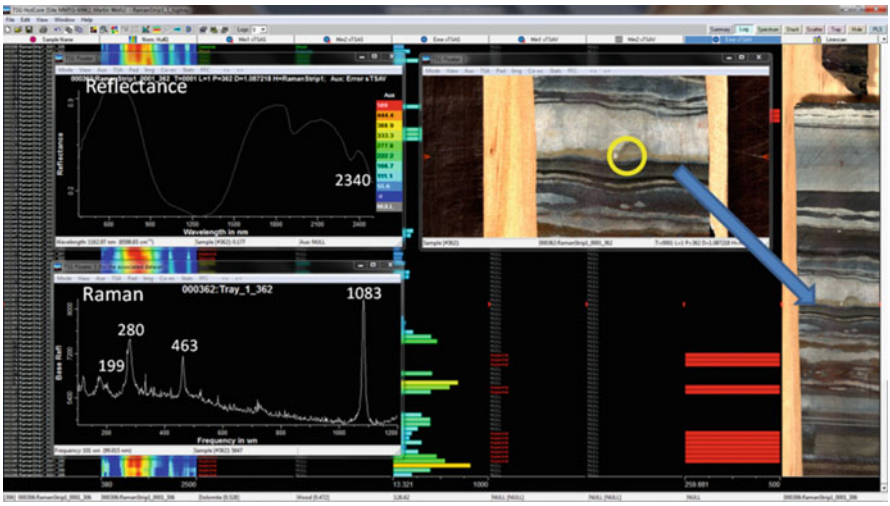

Fig. 3 Measured reflectance spectra over the 300–2,500 nm wavelength range and Raman spectra over the 200–1,200 cm^{-1} wavelength range for the area circled (*yellow*) in the digital inset image of the BIF half-core section scanned in the far-right column. Wavelength (cm^{-1}) positions of the main peaks in the Raman spectrum are labeled (e.g., 280). The Raman spectrum was measured over a much smaller area, 2–5 μm^2, within the area (*yellow circle*) focused for reflectance spectroscopic analysis

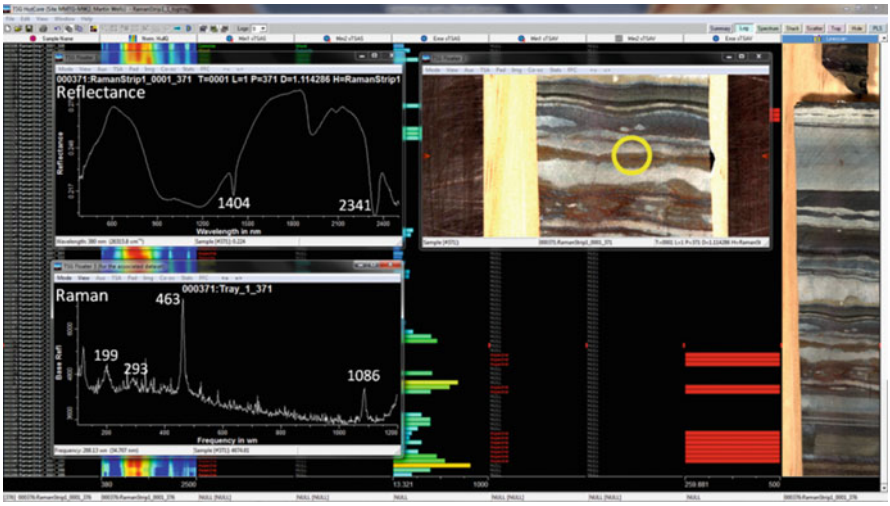

Fig. 4 Measured reflectance spectra over the 300–2,500 nm wavelength range and Raman spectra over the 200–1,200 cm^{-1} wavelength range for the area circled (*yellow*) in the digital inset image of the BIF half-core section scanned in the far-right column. Wavelength (cm^{-1}) positions of the main peaks in the Raman spectrum are labeled (e.g., 463). The Raman spectrum was measured over a much smaller area, 2–5 μm^2, within the area (*yellow circle*) focused for reflectance spectroscopic analysis

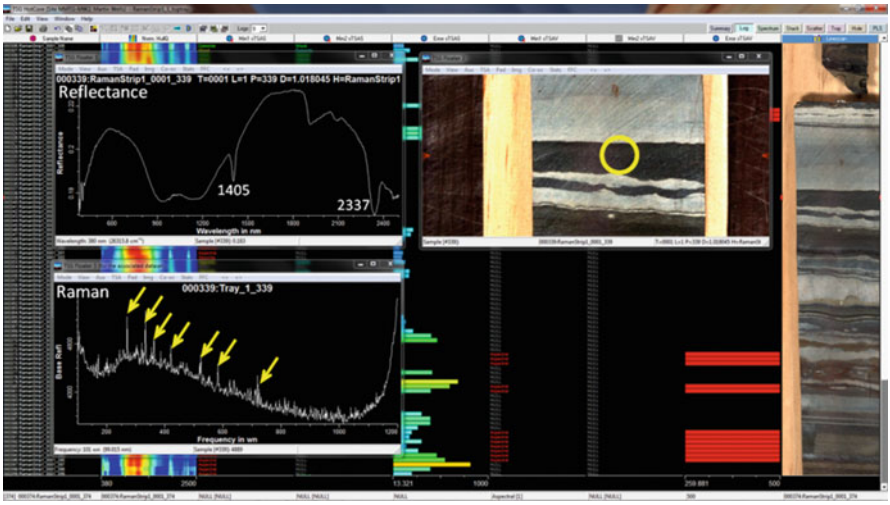

Fig. 5 Measured reflectance spectra over the 300–2,500 nm wavelength range and Raman spectra over the 200–1,200 cm^{-1} wavelength range for the area circled (*yellow*) in the digital inset image of the BIF half-core section scanned in the far-right column. Spikes in the Raman spectrum (*yellow arrows*) are noise. The Raman spectrum was measured over a much smaller area, 2–5 μm^2, within the area (*yellow circle*) focused for reflectance spectroscopic analysis

corresponding Raman spectrum for the location in Fig. 5 was unexpectedly noisy (i.e., "spikes") with no excitation lines being detected, particularly for magnetite. Reasons for this are unknown. Magnetite theoretically displays five phonon lines with typically only the three strongest modes at 666, 538, and 306 cm^{-1} being detected [16]. However, for magnetite in BIF examined by [3] only the main line at 666 cm^{-1} was detected. Relative enhancement (or suppression) of individual bands, depending on orientation or polarization effects of single grains, can occur, but this would be less of a problem for multigranular grains [9] as expected for the BIF core scanned in this study. A contributing factor may be the very small spatial resolution (i.e., 2–5 μm^2) of the laser spot for Raman analysis compared to the sample grain size, which may result in a "hit-or-miss" situation in the area selected for analysis. Further work is ongoing in our laboratory to optimize the Raman scanning conditions for application to the HyLogger™ platform to enhance the detection of CID ore, BIF-derived ore, and BIF mineralogy.

4 Conclusions

Using representative samples of Pilbara Province BIF and detrital iron deposit (DID) iron ore, this study has, for the first time, demonstrated the potential of Raman spectroscopy for rapid, in situ, mineralogical mapping. Raman analysis of a half-core section of BIF and of a DID ore easily detected the presence of hematite,

quartz, and a Fe^{2+}-bearing carbonate (i.e., siderite). Detection of magnetite in BIF was problematic. Further work is ongoing in our laboratory to continue development and optimization of the Raman scanning conditions for application to the HyLogger™ platform to enhance the detection of the common BIF and iron oxide mineralogy in iron ore. This may include a slight "defocusing" of the laser beam to increase the spatial "footprint" of the laser for spot analysis.

Coupling to the HyLogger™ automated, core-scanning platform clearly extends the utility of Raman spectroscopy for routine characterization of iron ore oxide (i.e., hematite) and gangue (i.e., quartz, carbonate) mineralogy. The integrated approach tested here provides a step change to augment current characterization methods that underpin strategies to best manage and process existing iron ores (e.g., BID and CID), as well as the newly developed MID ores.

Acknowledgments The authors would like to acknowledge the assistance of Martin Schodlok and Lew Whitbourn (CSIRO, North Ryde) in the operation of the HyLogger™ for reflectance and Raman spectroscopic scanning.

References

1. Das SK, Das B, Sakthivel R, Mishra BK (2010) Mineralogy, microstructure, and chemical composition of goethites in some iron ore deposits of Orissa, India. Miner Process Extr Metall Rev 31:97–110
2. Wells MA, Ramanaidou ER (2012) Raman spectroscopic characterisation of Australian banded iron formation and iron ore. In: Geophysical research abstracts, EGU general assembly 2012, vol 14, Vienna, 23–27 April 2012, EGU2010-6847
3. Ramanaidou ER, Wells MA (2011) Raman I Do–Raman spectroscopy for the mineralogical characterisation of banded iron formation and iron ore. In: Iron ore 2011 conference, The Australasian Institute of Mining and Metallurgy, Perth, 11–13 July 2011, pp 345–349
4. Cudahy TJ, Ramanaidou ER (1997) Measurement of the hematite: goethite ratio using field spectrometry in the channel iron deposits, Western Australia. Aust J Earth Sci 44:411–420
5. Thangavelu M, Shanmugam S, Bhattacharya AK (2011) Hyperspectral radiometry to quantify the grades of iron ores of Noamundi and Joda mines, Eastern India. J Indian Soc Remote Sens 39(4):473–483
6. Da Costa GM, Barrón V, Ferreira CM, Torrent J (2009) The use of diffuse reflectance spectroscopy for the characterization of iron ores. Miner Eng 22:1245–1250
7. Viscarra Rossel RA, Bui EN, de Caritat P, McKenzie NJ (2010) Mapping iron oxides and the color of Australian soil using visible-near-infrared reflectance spectra. J Geophys Res 115: FO4031
8. Haest M, Cudahy T, Laukamp T, Gregory S (2012) Quantitative mineralogy from infrared spectroscopic data. II. Three-dimensional mineralogical characterization of the Rocklea channel iron deposit, Western Australia. Econ Geol 107:229–249
9. Ramanaidou ER, Wells M, Belton D, Verrall M, Ryan C (2008) Mineralogical and microchemical methods for the characterization of high-grade banded iron formation-derived iron ore. Soc Econ Geol 15:129–156
10. Ramanaidou ER, Tapley V, van Bronswijk W (1996) Determination of aluminium substitution in hematite and goethite by vibrational spectroscopy. In: Proceedings of the 2nd Australian conference on vibrational spectroscopy, Queensland University of Technology, 2–4 October 1996, pp 35–36

11. Raman CV, Krishnan KS (1928) The optical analog of the Compton effect. Nature 121:711
12. McMillan PF, Hofmeister AM (1988) Infrared and Raman spectroscopy. Rev Mineral 18:99–159
13. Berman M, Bischof L, Huntington J (1999) Algorithms and software for the automated identification of minerals using field spectra or hyperspectral imagery. In: Proceedings of the 13th international conference on applied geologic remote sensing, Ann Arbor Environmental Research Institute of Michigan, Vancouver, BC, pp 222–232
14. Cudahy T, Jones M, Thomas M, Laukamp C, Mike Caccetta M, Hewson R, Rodger A, Mike Verrall M (2008) Next generation mineral mapping: Queensland airborne HyMap and satellite ASTER surveys 2006–2008. CSIRO Exploration & Mining Report P2007/364, Perth, p 160
15. Rividi N, van Zuilen M, Phillipot P, Menez B, Godard G, Poidatz E (2010) Calibration of carbonate composition using micro-Raman analysis: application to planetary surface exploration. Astrobiology 10:293–309
16. Shebanova ON, Lazor P (2003) Raman spectroscopic study of magnetite ($FeFe_2O_4$): a new assignment for the vibrational spectrum. J Solid State Chem 174:424–430

Comprehensive Utilization and Purified Research on Kaolin Ores in Huichang

Caibin Wu and Guiming Shi

Abstract Kaolin ores in Huichang contain the minerals of quartz sand, kaolin, mica, and feldspars. In order to recover these valuable resources, some experiments of screening, classification, magnetic separation, grinding, and flotation are carried out on the basis of the kaolin ore properties. The test results indicate that quartz sand concentrate can be directly obtained when the size of vibrating screen is ten meshes. Materials that are smaller than the screen hole are injected to hydraulic cyclones of which the controlling classification size is 325 meshes; kaolin concentrate with the elements of Al_2O_3 above 33.70 % and Fe_2O_3 0.37 % can be well beneficiated from the overflow through magnetic separation with one stage which is rougher and cleaner to remove iron. On the other hand, the hydrocyclone spigot flow to grinding and flotation with one rougher stage and two scavengers, mica, and feldspar concentrate can be beneficiated in sequence. Therefore, comprehensive utilization of these valuable minerals of kaolin ores can be realized.

Keywords Kaolin ores • Comprehensive utilization • Classification • Magnetic separation • Flotation

1 Introduction

Kaolin is mainly composed of kaolinite cluster minerals that are smaller than two microns as tiny flake, tubular, and folded sheets. The appearance of mine ore is white and shallow ash; it is yellow, gray, or rosy with impurities. Other properties are also dense clumps or loose earthy, soft, satiny feeling, less than nails' hardness, relative density 2.4–2.6, high refractoriness that can reach 1,700–1,900 °C, low plasticity, and the caking property has small size, good insulation, and chemical stability. For these advantages, kaolin has been widely used in a lot of fields such as paint, coating, paper making, rubber, plastics, cables, ceramics, enamel, refractory, automobile, chemical, textile, cement, environmental protection, agriculture, and so on.

C. Wu (✉) • G. Shi
Jiangxi University of Science and Technology, Ganzhou, Jiangxi 341000, People's Republic of China
e-mail: wushirle@sina.com

F. Dong (ed.), *Proceedings of the 11th International Congress for Applied Mineralogy (ICAM)*, Springer Geochemistry/Mineralogy,
DOI 10.1007/978-3-319-13948-7_40

2 Materials and Methods

2.1 Materials

Samples were taken from Huichang kaolin mine of Jiangxi province in China. Mineral relative content is shown in Table 1 and multi-element analysis is shown in Table 2.

The results of Table 1 indicate that the main useful minerals of deposit are quartz sand, kaolin, mica, and feldspar which can all be comprehensively utilized. The results of Table 2 suggest that kaolin ore in Huichang is low in Al_2O_3 and high in Fe_2O_3 that is only suitable for porcelain of level 3. If directly used as porcelain, the valuable resources are not comprehensively utilized.

2.2 Methods

2.2.1 Dispersive Mixing

The undressed ore is crashed and dispersively mixed in the first place to make it broken, to prepare the appropriate fineness of kaolin slurry for the beneficiation production, and at the same time, to weed out the large particles of sand and gravel. In this experiment, the dispersant is sodium hexametaphosphate at a dosage of 0.3 % (relative to the sample weight).

2.2.2 Classification

The prepared pulp will be roughly graded firstly with vibrating screen of which the grading size is 10 meshes, and usually the oversize material can directly get quartz sand products. The undersize material will be hydraulically classified (325 meshes). The hydrocyclone spigot is settled into the ball mill and flotation, and meanwhile overflow is settled into the magnetic to remove iron. Sometimes the hydraulic classification overflow can be direct as the kaolin products with concentration and dehydration.

2.2.3 Magnetic Separation

Magnetic separation is the most effective method to remove iron. The magnetic field strength of magnetic separator is usually the main influence factors on the effects of removing iron. This experiment adopts the Slon-1w cycle and pulsating high gradient magnetic separator; magnetic separation process is one stage rougher and cleaner; its magnetic field intensity ranges from 1.0 to 1.3 T. Through the

Table 1 The relative contents of mineral (%)

mineral	Kaolinite	Quartz	Potassium feldspar	Sodium feldspar	White mica	Hydromuscovite	Protolithionite
Content	20	33	20		15	8	4

Table 2 Multi-element analysis of raw ore (%)

Component	SiO_2	Al_2O_3	Fe_2O_3	TiO_2	K_2O	CaO	Na_2O	MgO	Ignition loss	Whiteness
Content	68.42	18.65	1.20	0.01	4.02	0.36	0.58	1.20	1.24	74.2

magnetic separation in addition to removing iron, the purity and whiteness of −325 mesh kaolin products can be further improved.

2.2.4 Flotation

The oversize products of hydraulic cyclones mainly include the mica and feldspar. When the grinding particle size is about 70 % −200 meshes, the mica and feldspar will be flotated effectively. The flotation process of mica is one stage rougher, three cleaners and two scavengers. pH adjusting agent is sulfuric acid and of frother is 2# oil; 12 amine is collector; in the flotation of feldspar, hydrofluoric acid is activator, and 12 amine is collector.

3 Results

The granularity of sieve analysis and test results of undressed ore is shown in Table 3.

In the conditions with concentration of 20 %, agitator speed 250 r/min, and the mixing time for 30 min, the experimental results are shown in Table 4 in the condition of using 0.3 % sodium hexametaphosphate and sodium silicate, respectively, as a dispersant.

At the conditions that the magnetic separation process is a roughing and a selected, roughing magnetic field intensity is 1.0, 1.0, 1.3 T; the selected magnetic field intensity is 1.0, 1.3, 1.3 T; we get the test results shown in Table 5.

The test results of silicon reduction are shown in Table 6 on the different dosage of 12 amines which is the collector of mica flotation.

The tailings for mica flotation can realize the classification recycling of the feldspar. The test results of flotation are shown in Table 7.

4 Discussion

The results of Table 3 show that the distribution content of Al_2O_3 is increased as the particle size decreased in kaolinite and that of SiO_2 is contrary to the law. Therefore, quartz sand, kaolin, and other products can be separated according to the difference of granularity partial.

The results of Table 4 show that employing sodium hexametaphosphate as dispersion can obtain superior size distribution compared with sodium silicate. Therefore, odium hexametaphosphate is selected as dispersant on subsequent test.

The results of Table 5 show that when magnetic field intensity of roughing reaches 1.0 T and that of selection is 1.3 T, the effect of magnetic separation is the best. In this condition, the content of Fe_2O_3 in the concentrate is 0.47 %, that of

Table 3 The granularity analysis of raw ore (%)

Fraction (mesh)	+10	−10 + 16	−16 + 24	−24 + 60	−60 + 80	−80 + 140	−140 + 200	−200 + 325	−325	Total
Productivity	19.50	8.35	14.45	14.90	5.01	6.45	3.60	6.89	20.85	100.00
SiO_2	92.12	85.17	78.88	69.08	61.82	56.80	53.90	52.91	45.72	65.65
Al_2O_3	3.18	4.19	6.73	15.73	21.61	24.12	26.28	32.90	31.56	16.72
K_2O	0.67	2.10	2.76	4.81	5.86	5.03	5.09	2.41	2.53	2.92
Na_2O	0.40	0.47	0.37	0.43	0.64	0.96	0.92	0.43	0.34	0.46

Table 4 Contrast test of dispersant (%)

Dispersant	Sodium hexametaphosphate	Sodium silicate
Productivity of −325 mesh	21.1	14.2

Table 5 The test results and laboratory analysis of magnetic separation (%)

Test conditions	Products	Productivity	Al_2O_3	Fe_2O_3	SiO_2
Roughing: 1.0 T Selected: 1.0 T	1# concentrate	86.07	32.51	0.69	44.84
	1# tailings	13.93	32.04	1.52	44.14
Roughing: 1.0 T Selected: 1.3 T	2# concentrate	85.43	33.68	0.47	44.25
	2# tailings	14.57	33.18	3.25	44.18
Roughing: 1.3 T Selected: 1.3 T	3# concentrate	85.44	33.74	0.53	44.21
	3# tailings	14.07	31.90	3.24	44.82

Table 6 The flotation test results of silicon reduction

Dosage of 12 amine ($g \cdot t^{-1}$)	Concentrate/ SiO_2 %	Middlings/ SiO_2 %	Tailings/ SiO_2 %	Mica in the concentrate (%)
200	47.16	48.08	82.06	94.02
300	63.30	67.36	83.40	60.88
400	64.74	70.14	82.36	54.52

Table 7 The test results of flotation on feldspar /%

Dosage of 12 amine ($g \cdot t^{-1}$)	Feldspar concentrate			Feldspar tailings		
	Productivity	$K_2O + Na_2O$	SiO_2	Productivity	$K_2O + Na_2O$	SiO_2
400	50.21	12.78	68.21	49.79	0.49	82.57
600	53.36	13.34	69.26	47.53	0.42	83.39
800	78.05	13.02	72.97	30.93	0.46	83.94
1,000	82.03	12.94	72.54	29.56	0.50	83.37

Al_2O_3 is 33.68 %, and the whiteness of kaolin also reaches 88.6 %. The quality of kaolin can meet the requirements of TC-1 level kaolin products that are used in electronic components, optical glass, sand wheel, electric porcelain crucible, high-grade glaze, and blank.

The results of Table 6 show when the 12 amines dosage is 200 g/t; the concentrate with the content of 94.02 % mica can be beneficiated with 47.16 % SiO_2 which is closest to the theory mica grade (44–45 %).

The results of Table 7 show that sodium potassium feldspar concentrate with 69.26 % SiO_2 can be beneficiated when the dosage of 12 amines is 600 g/t. However, the tailing of flotation can be also low-grade feldspar concentrate.

5 Conclusions

The content of Al_2O_3 is 18.84 %, the content of Fe_2O_3 is 0.80 %, and the content of TiO_2 is 0.05 % in raw ore that directly fit the requirements of making porcelain with soft kaolin.

According to classification with 10 meshes for the products after mixing, quartz sand products with the yield of 19.50 %, the SiO_2 content of 92.12 %, and the Al_2O_3 content of 3.18 % can be directly obtained.

Kaolin concentrate with the content of 33.68 % Al_2O_3, of 44.25 % SiO_2, and of 0.47 % Fe_2O_3 is obtained when the magnetic separation process for −325 mesh hydraulic classification overflow is one thick, one fine process, and the magnetic field intensity is 1.0–1.3 T. The concentrate can satisfy the requirements of TC-1 kaolin products in ceramic industry.

Mica product and feldspar products are obtained through the grinding and flotation. Therefore, the comprehensive utilization of quartz sand, kaolin, mica, and feldspar can be realized by screening, hydraulic classification, magnetic separation, grinding, and flotation operation.

Using Goethite as a Heterogeneous Fenton Catalyst for the Removal of Tetracycline Hydrochloride: Effects of Its Adsorptive and Reductive Activities

Honghai Wu, Fenfen Jiang, Shaoyou Lu, Yufeng Guan, Dayi Deng, and Xiaoling Chen

Abstract The removal of the antibiotic compound tetracycline hydrochloride (TC) was investigated by using goethite/H_2O_2 as a heterogeneous Fenton reagent. At pH 3.0–4.0, although presenting the lowest adsorption capacity of TC to goethite, the TC removal can be still greatly promoted by the reductive transformation of Fe(III) to Fe(II) with TC in the solution over goethite. A rapid initial TC decay was observed at the first 5 min, followed by a much slower retardation stage. This reason was likely that the reductive transformation of Fe(III) to Fe(II) was inhibited with the proceeding of the Fenton reaction. However, all the goethite-catalyzed Fenton reactions responsible for the TC removal were well fitted to pseudo-first-order kinetics ($R^2 > 0.99$), and their apparent activation energy (E_a) for this Fenton-like reaction was 31.86 kJ·mol^{-1}. This low value of E_a was very consistent with the TC Fenton removal significantly enhanced with the temperature increase and simultaneously mediated by the surface-controlled homogeneous and heterogeneous reactions.

Keywords Goethite • Heterogeneous Fenton reaction • Tetracycline hydrochloride

H. Wu (✉) • F. Jiang • Y. Guan • D. Deng • X. Chen
School of Chemistry and Environment, SCNU, 55 Zhongshan Avenue West, Guangzhou, Guangdong, People's Republic of China

Key Laboratory of Theoretical Chemistry of Environment, Ministry of Education, SCNU, 55 Zhongshan Avenue West, Guangzhou, Guangdong, People's Republic of China
e-mail: whh302@163.com

S. Lu
Shenzhen Center for Disease Control and Prevention, Shenzhen, Guangdong, People's Republic of China

F. Dong (ed.), *Proceedings of the 11th International Congress for Applied Mineralogy (ICAM)*, Springer Geochemistry/Mineralogy,
DOI 10.1007/978-3-319-13948-7_41

1 Introduction

In the last decades, there had been growing concern focusing on the release of antibiotics in the environment [1]. Tetracyclines (TCs) were among broad-spectrum antibiotics extensively used for the disease control in human and animals due to their great therapeutic values. This good behavior made TCs to rank the second most in both output and usage globally [2] and thus led to high TCs residues in the environment [3–5]. Most of the used antibiotics were water soluble, and as much as 90 % of one dose can be excreted in urine and up to 75 % in animal feces, resulting in their frequent detection in surface, ground, and wastewaters [6]. Up to date, even though TCs presented just at trace levels in the environment, they had been characterized as "pseudo-persistence" due to their continuous introduction into the environment [7], posing potential hazard to public health [4]. Therefore, it was very important to develop a process to partially or totally eliminate these pollutants from the environment [7–10].

Due to their antibacterial nature, conventional biological methods and adsorption methods can't remediate antibiotic-contaminated waters effectively at low cost [11, 12]. In contrast, advanced oxidation methods were suitable alternatives for rapid degradation of recalcitrant and nonbiodegradable compounds in wastewater [13]. Compared to the homogeneous Fenton reaction, the heterogeneous Fenton reaction had its unique advantage since it can be efficiently operated in a wide range of pH values. The heterogeneous Fenton reaction process was preferred as a suitable treatment method for its capability of complete mineralization of organic compounds at ambient temperature and also its benefit from the easy separation of solid catalysts from treated wastewater [14, 15].

In the context, environmentally friendly iron oxides involving magnetite (Fe_3O_4), hematite (Fe_2O_3), goethite (α-FeOOH), and lepidocrocite (γ-FeOOH) had attracted much more concern because they were widespread in the natural environment and can be easily applied to in situ soil remediation processes [16]. Among iron minerals, goethite is the most abundant poorly crystalline mineral in natural environments, which has a low solubility ($pKsp = 14.7$), and it generally possesses huge surface areas. Using goethite as a heterogeneous Fenton catalyst had already received a great deal of attention due to its proven highly excellent catalytic reactivity toward H_2O_2 [17, 18]. Simultaneously, the goethite-catalyzed Fenton reaction had been found to be effective in aspect of oxidizing many kinds of organic compounds [19, 20]. Especially under acidic solution condition at pH below 4.0, there existed the potential for the combination of both heterogeneous and homogeneous Fenton reactions in the presence of goethite/H_2O_2 reagent, which may obviously promote the oxidative decomposition for those recalcitrant organic pollutants containing certain reductive active groups. For instance, tetracycline hydrochloride (TC) contained a reductive phenolic diketone moiety.

In addition, TCs used in common involve tetracycline (TC), oxytetracycline (OTC), and chlortetracyclines (CTC) [21, 22]. They were active against a range of organisms such as Myco-plasma and Chlamydia, as well as a number of gram-

positive and gram-negative bacteria. However, it should be noted that TCs generally have strong affinity to clay and oxide minerals, humic substances, and soils and sediments due to their highly hydrophilic nature [23–25]. Therefore, TCs' good adsorptive behaviors can somewhat enhance its Fenton removal rates over relevant iron minerals. However, unlike the well-characterized adsorptive interactions of TC with minerals, TC's Fenton decomposition had received less concern. So far, the TC degradation via the mentioned heterogeneous Fenton reaction by using goethite as a catalyst had not yet been reported in the literature, with the exception of the homogenous photo-Fenton reaction process [7]. Consequently, it was essential to develop an efficient treatment method to degrade TC via a heterogeneous Fenton process by utilizing the low cost and efficiently catalytic active goethite. In this study, the goethite-catalyzed heterogeneous Fenton process for TC removal from wastewater was investigated in detail via a series of batch experiments, with emphasis on the optimization of the TC Fenton oxidation process kinetic parameters and further the discussion of the Fenton reaction degradation mechanisms.

2 Materials and Methods

2.1 Chemicals and Materials

The antibiotic tetracycline (TC) was purchased from Alading Chemicals Co., Shanghai, China, and used without further purification. All other used chemicals, including hydrogen peroxide (H_2O_2, 30 %), sulfuric acid (H_2SO_4, 96 %), ferric nitrate ($Fe(NO_3)_3$, p.a.), ferrous sulfates ($FeSO_4 \cdot 7H_2O$, p.a.), potassium hydroxide (KOH, p.a.), and sodium hydroxide (NaOH, p.a.), were supplied by Guangzhou Chemicals Co., China. Duplicate-deionized water was used to make the dye solutions of desired concentration. Goethite was prepared in our laboratory based upon the synthesis methods reported by Wu et al. [16].

2.2 Characterization of Materials

The specific surface area (BET), pore size (BJH), and pore volume (V_p) of the catalysts were determined by the N_2 adsorption–desorption method at liquid nitrogen temperature (at 77 K) using an ASAP2020M apparatus (Micromeritics Instrument, USA). The XRD patterns of the samples were recorded on D-MAX 2200 VPC X-ray diffractometer equipped with Cu Kα radiation (Rigaku, Japan). The size and morphology of goethite were characterized by scanning electron microscopy (SEM) (ZEISS Ultra 55, Carl Zeiss of Germany).

2.3 Experimental Procedure for Fenton Reaction

All the experiments were conducted in a double glass cylindrical jacket reactor with a total volume of 0.5 L under dark. Before the reactions, TC solutions were adjusted to desired initial pH value (i.e., pH = 4.0) via the addition of NaOH or H_2SO_4 of 0.1 mol·L^{-1}. Next, catalyst of a given amount was added into 0.4 L of TC solution, which was equilibrated with goethite within 1 h (reaching over 80 % of adsorptive maximum), then the determination of its adsorption removal efficiencies for TC was done, followed by the addition of H_2O_2 into the TC and goethite mixed suspensions. Four constant temperatures in the range of 25–50 °C were obtained through a thermostat by using a magnetic stirrer to stir the suspensions during the reactions.

2.4 Analytical Methods

The aqueous concentration of TC was monitored by UV–vis spectrophotometer (Unico 3802; Shanghai instrument Co.) at a maximum absorption wavelength of 357 nm to determine the TC removal and decomposition. The TC's degradation was determined by a TOC analyzer (TOC-V, Shimadzu, Japan), and its products were determined by a high-performance liquid chromatography (HPLC, LC-20AT, Shimadzu, Japan). At regular time intervals, 2.5 mL solution samples were taken out and the solid was removed from the solution by using 0.45 μm cellulose acetate syringe membrane filter. TC's Fenton oxidative removal efficiencies were determined based on a calibration curve, which was obtained by a batch of standard TC solutions with defined concentrations. As such, the TC's Fenton oxidative removal efficiencies may be determined as Eq. 1:

$$\text{Removal efficiency}(E\%) = (C_0 - C_t)/C_0 \times 100\% \quad (1)$$

where C_t and C_0 were the solution TC concentrations at time t and initial time, respectively. The standard deviations (P) for the concentration measurement were small with most $P < 0.05$. The initial and final solution pH values were measured by a PHS-3C pH meter (Shanghai instrument Co., China).

3 Results

3.1 Characterization of Iron Oxide Catalysts

The XRD pattern of the as-synthesized goethite in this study (Fig. 1) well corresponded to the standard card for α-FeOOH (goethite, JCPDS No. 29-0713)

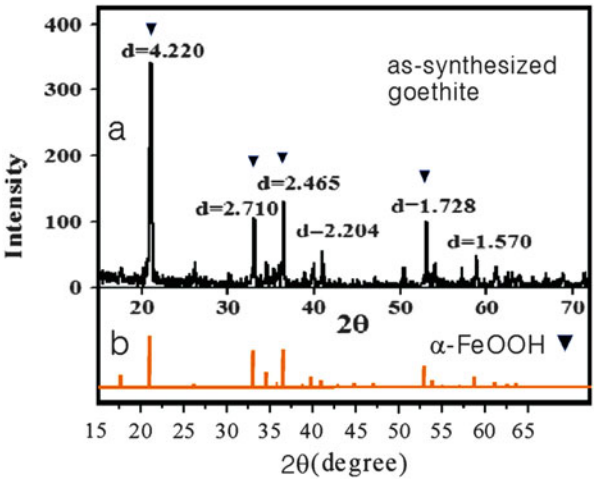

Fig. 1 X-ray diffraction (XRD) analysis of the as-synthesized goethite samples (**a**) compared to the reference diffractogram for α-FeOOH (**b**)

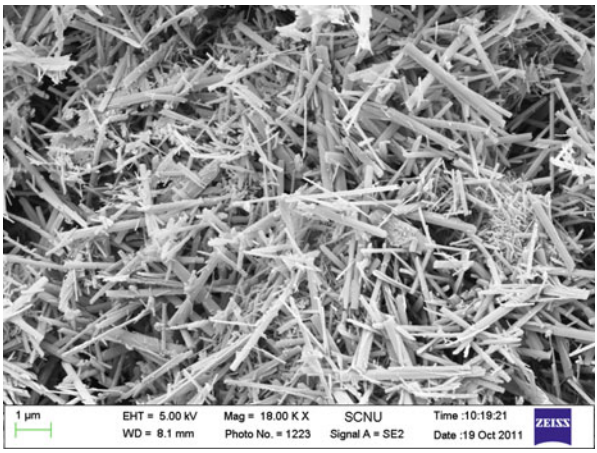

Fig. 2 The SEM patterns of the as-synthesized goethite images

[16], with the main reflection peaks at $2\theta = 21.23$, 33.28, and 36.67°. This confirmed that a highly purified α-FeOOH was obtained. An SEM image of goethite was shown in Fig. 2, revealing that the crystalline needle-like goethite was very small with typical lengths in the range of 1–5 μm and an average pore width around 10.0 nm. In addition, the BET surface area and pore volume of the as-synthesized goethite were 33.66 $m^2 \cdot g^{-1}$ and 0.078 $cm^3 \cdot g^{-1}$, respectively.

3.2 Effect of Initial pH

The effects of initial pH on the removal efficiency of TC were studied at an initial pH ranging from 3.0 to 10.0, and the results were shown in Fig. 3. At pH above 5.0,

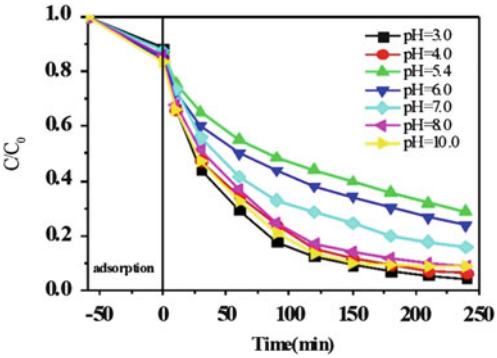

Fig. 3 Effect of initial pH values on the heterogeneous Fenton oxidation of TC (40 mg·L^{-1} TC, 20 mmol·L^{-1} H_2O_2, 1.0 g·L^{-1} α-FeOOH, 400 mL, $T = 35$ °C)

the removal rate of TC increased while the initial pH increased, and the final removal efficiency rose to over 95 % with an initial pH of 10.0 and a reaction time of 240 min. On the other hand, as the initial pH dropped below pH 4.0, the removal efficiencies of TC may also reach above 95 % within the same reaction time of 240 min, even though the TC adsorption capacity was relatively lower than at higher pH values. Our obtained results were very different from those of Wang et al. (2011) via an ultrasound-enhanced catalytic ozonation process by also using goethite as a catalyst (US/goethite/O_3) [8], where the removal rate of TC via oxidative degradation increased with the increase of initial pH in the pH range from 2.0 to 9.0. As a result, it can be concluded that at low pH 3.0–4.0, the Fenton degradation process presenting high TC's removal rates was mainly attributed to the aqueous homogeneous reactions related to dissolved iron species rather than the solid surface reactions, whereas at high pH around 8.0, the process was attributed mainly to the heterogeneous reactions occurring on the surfaces enhanced by the TC's strong adsorption besides the potential H_2O_2-enhanced adsorption able to benefit for the generation of $^{\bullet}OH$, which would be further discussed in detail later. On the other hand, at circumneutral pH (pH 5.5–7.4), the lower TC but higher Cl^- (chloride ion) adsorptions led to the relatively lower TC's removal rates. The Cl^- may inhibit the generation of $^{\bullet}OH$ over goethite. However, these processes were different from the decolorization of the azo dye Orange G using goethite as a Fenton catalyst [16].

3.3 Effect of the Catalyst Dosage

The effect of the initial dosage of goethite on Fenton oxidation of TC was investigated in the range of 0.4–1.2 g·L^{-1}. As clearly seen in Fig. 4, the removal efficiencies of TC gradually increased as the goethite dosage increased from 0.4 to 1.0 g·L^{-1}. This can be also explained by the heterogeneous generation processes of $^{\bullet}OH$ taking place directly at the goethite/water interface (Eqs. 7–9) [17]. The increase of goethite dosage may increase the amount of adsorption sites for TC as

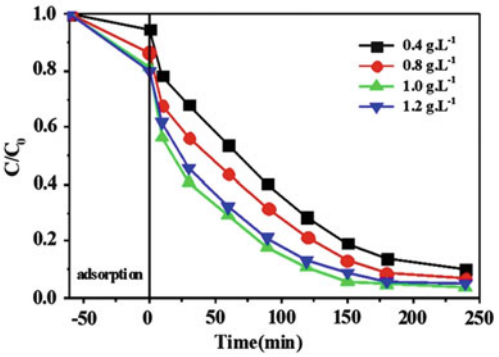

Fig. 4 Effect of goethite dosages on the heterogeneous Fenton oxidation rates of TC (40 mg·L^{-1} TC, 20 mmol·L^{-1} H_2O_2, 400 mL, pH 4.0, $T = 35$ °C)

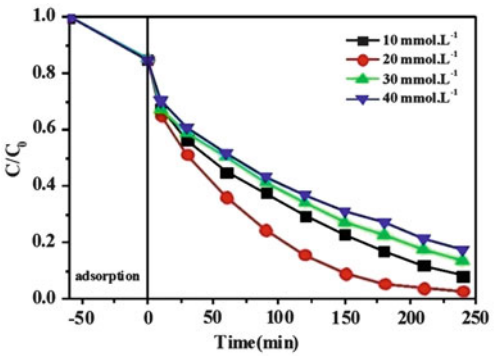

Fig. 5 Effect of H_2O_2 dosage on the heterogeneous Fenton oxidation of TC (40 mg·L^{-1} TC, 1.0 g·L^{-1} α-FeOOH, 400 mL, pH 4.0, $T = 35$ °C)

well as generating more hydroxyl radical. However, further increase of goethite dosage up to 1.2 g·L^{-1} can decrease the Fenton removal efficiency, potentially due to the proven "unproductive destruction of the reactant" effect [26]. This reason was that excessive goethite may catalyze H_2O_2 to produce more O_2 and less $^{\bullet}OH$, leading to an obvious decrease in the TC removal efficiency. Based on the observation in this study, the optimum goethite dosage was determined to be 1.0 g·L^{-1}.

3.4 Effect of the Hydrogen Peroxide Concentration

The influence of the H_2O_2 concentrations from 10 to 40 mmol·L^{-1} on the removal efficiency of TC decomposition via the heterogeneous Fenton processes was investigated and the results were present in Fig. 5. As the H_2O_2 concentrations increased from 10 to 20 mmol·L^{-1}, the TC removal efficiency displayed a slight increase from 91.8 to 97.2 % after 240 min owing to an enhancement in the quantum yield of formation of $^{\bullet}OH$. However, further increase of the H_2O_2 concentration caused an obvious decrease in the removal efficiency of TC, due to the scavenging effect of H_2O_2 as described in Eqs. 2 and 3 [27]:

$$H_2O_2 + \bullet OH \rightarrow H_2O + \bullet O_2H \quad (2)$$

$$\bullet O_2H + \bullet OH \rightarrow H_2O + O_2 \quad (3)$$

3.5 *Effect of the TC Concentration*

As can be seen in Fig. 6, the TC's initial concentrations substantially affect its removal rates. An increase in initial concentration led to a decrease in TC's removal rate. When the TC concentrations decreased from 60 to 10 mg·L^{-1}, its removal efficiencies relevantly increase from 35.7 to 92.3 % at the end of 30 min. But still, all the removal efficiencies can reach 98 %, providing enough reaction time.

3.6 *Influence of Reaction Temperature*

The impact of temperature on the removal of TC via the Fenton reaction process catalyzed by goethite was studied at 25, 30, 35, and 40 °C, respectively, and the obtained results were presented in Fig. 7. As shown in Fig. 7, reaction temperature

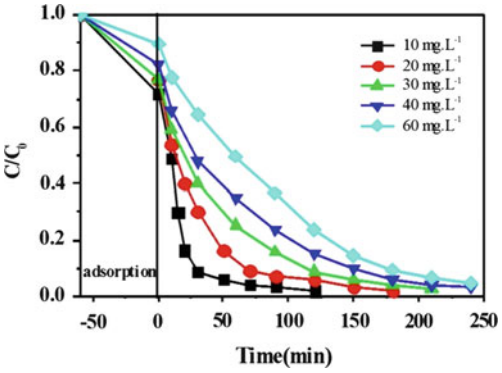

Fig. 6 Effect of initial concentration of TC on its heterogeneous Fenton oxidation (20 mmol·L^{-1} H_2O_2, 1.0 g·L^{-1} α-FeOOH, 400 mL, pH 4.0, $T = 35$ °C)

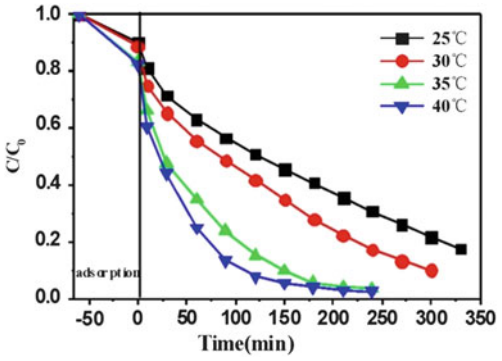

Fig. 7 Effect of temperature on the heterogeneous Fenton oxidation of TC (40 mg·L^{-1} TC, 20 mmol·L^{-1} H_2O_2, 1.0 g·L^{-1} α-FeOOH, 400 mL, pH 4.0, $T = 35$ °C)

has a significant influence on the TC Fenton removal rate. The TC's removal efficiencies increase from 49.2 to 92.1 % within 120 min when the reaction temperature rose from 25 to 40 °C. The results indicated that higher temperature favors the Fenton oxidation of TC, potentially due to the acceleration of Fenton's reaction with increasing temperature [28]. Higher temperature may also enhance the adsorption rates of both TC and H_2O_2 as well as the release rate of iron ions to some extent from goethite surfaces mainly through improving their interfacial diffusion rates at the goethite/water interface. Thus, increasing the temperature greatly improved the generation rate of the $^{\bullet}OH$ radical. Therefore, the removal rates of TC's Fenton oxidation were highly accelerated with increasing temperature, especially under the acidic condition at low pH 3.0–4.0.

4 Discussion

4.1 *Effects of Adsorptive Behaviors of Tetracycline to Goethite on the TC Fenton Removal*

TC has a p*K*ow of 1.19, indicating that TC is relatively hydrophilic as a result; the removal of TC mainly relies on its adsorption by goethite before the addition of H_2O_2, but the removal of TC by adsorption was below 20 % during the Fenton process as shown earlier. Tetracycline molecule presents very polar and has three proton-active groups, including a dimethylammonium, a tricarbonylamide group, and a phenolic diketone [23]. The distribution of tetracycline species depends upon solution pH conditions. These structural characteristics are favorable for its adsorption and oxidative degradation. On the other hand, the potential three different surface species, that is, $FeOH^{2+}$, $FeOH^0$, and FeO^-, on goethite can greatly mediate its surface adsorptive activities toward TC that is significantly controlled by the solution pH because these surface functional groups of goethite may transform subjected to the following two equations [8]:

$$\equiv FeOH^{2+} \rightarrow \equiv FeOH^0 + H^+, \quad pK_{a1} = 6.4 \tag{4}$$

$$\equiv FeOH^0 \rightarrow \equiv FeO^- + H^+, \quad pK_{a2} = 9.2 \tag{5}$$

Due to its pH_{pzc} (the point of zero charge) around 8.0, the goethite surface was presumably positively charged in acidic and neutral solution ($pH < pH_{pzc}$) and negatively charged in alkaline solution ($pH > pH_{pzc}$). Hence, it was deserved to especially note that goethite possesses a high surface-site density of Bronsted acid sites at the pH range of 3.0–4.0 that decrease adsorption of positively charged TC onto goethite for the reason of TC's strong protonation under the acidic low pH condition. For example, Tanis et al. [29] investigated the interactions of TC with goethite- or ferrihydrite-coated quartz and found that their maximum adsorption capacity for TC occurred at about pH 8.0, and the effect of ionic strength was of less importance. As such, previous studies indicated that the potential for TC strong

adsorption onto the minerals greatly depends upon TC's charge nature that is highly related to the protonation–deprotonation interactions of its three reactive surface functional groups [30–32].

The addition of H_2O_2 alone without goethite into the solution almost did not contribute to the removal of TC by direct oxidation. However, the strong adsorption of TC to goethite substantially enhanced the goethite-catalyzed heterogeneous Fenton oxidation in terms of TC's removal efficiency. There exist three different functional groups in TC molecule structure corresponding to its three different p*K*a values of 3.3, 7.7, and 9.7, and thereby TC may present varied predominant species of H_4TC^{2+}, H_3TC, H_2TC^-, and HTC^{2-} at pH 3, 6, 8, and 10, respectively. Hence, it should be noted that the four different species of TC can undergo protonation–deprotonation reactions depending upon aqueous solution pH value [33]. For this reason, electrostatic repulsion between TC and goethite surfaces both with similarly charged groups is much stronger at either lower pH value (positive–positive repulsion) or higher pH value (negative–negative repulsion).

However, especially in the case of pH value around 8.0, the interactions of TC with goethite surfaces may create a maximum electrostatic attraction. Hence, it was expected that there should exist a positive relationship between the increase in adsorption capacity of TC onto goethite and the relevant promotion of the TC removal as the pH values increased from 5.0 to 8.0. An the same time, it had been proven that H_2O_2 favors to be adsorbed onto the more negatively charged oxide surfaces because of its capability of forming strong complexes with those compounds with weak base properties [34]. As such, higher concentration of $^{\bullet}OH$ can be generated with the increase of the solution pH value. Moreover, the electrophilic $^{\bullet}OH$ radical will tend to attract negatively charged TC molecule with high electrical density on the ring system [35], thus leading to the enhanced Fenton catalytic activities in the alkaline conditions.

As a result, we can conclude that the alkaline pH condition (i.e., pH 8.0–10.0) was very favorable for the Fenton catalytic degradation of TC. On the contrary, the higher removal rate of TC also occurring at a low initial solution pH values (i.e., pH 3.0–4.0) was mainly due to the leaching of iron ions from goethite to the solution further to enhance the homogeneous Fenton oxidation in improving removal rate of TC mainly via raising the concentration of ferrous/ferric ions in the suspension. As acidic low pH values corresponded to the low adsorption of TC on to goethite, apparently it can not account for TC's displaying high removal rate from the suspension. This should be ascribed mainly to the homogeneous Fenton decomposition catalyzed by dissolved iron ions, which may be further explained in the following.

4.2 Effects of Reductive Behaviors of Tetracycline to Goethite on the TC Fenton Removal

The group of phenolic diketone in TC molecule was proven to benefit the iron ions to be released from goethite [19]. As shown in Fig. 8, the total iron concentration

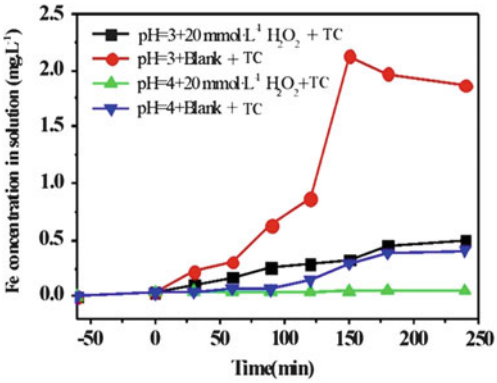

Fig. 8 The release of iron ions from goethite at different solution conditions

was obviously increased especially at pH 3.0, while TC was added into goethite containing suspension. As for blank suspension case with goethite only (not shown in the figure), the iron concentration below 0.5 $mg{\cdot}L^{-1}$ even cannot be detected at pH 4.0, so the leaching of iron to the suspension was negligible above pH 4.0.

Actually, the reductive activity of TC may improve the generation of ferrous ions either on the goethite surfaces or in the solutions prior to the addition of H_2O_2. Generally, the dissolved iron is expected to be much more released under acidic solution condition potentially due to existing three heterogeneous reaction processes at the goethite/water interface, namely, a proton-induced solubilization (Eq. 6), a reductive dissolution (Eqs. 7 and 8), and a non-reductive release [19]. A rapid initial TC decay observed at the first 5 min may be mainly ascribed to homogeneous Fenton reaction caused by high dissolution of iron in the suspension (Eq. 8), while the heterogeneous Fenton oxidation directly occurring over goethite (Eqs. 9–11) can be simultaneously strengthened by the reductive transformation of surface ferric ions caused by TC itself (Eq. 7) besides H_2O_2 (Eq. 9).

$$\equiv \mathrm{Fe(III)OH} + \mathrm{H^+} \rightarrow \mathrm{Fe^{3+}} + \mathrm{H_2O} \tag{6}$$

$$\equiv \mathrm{Fe(III)OH} + \mathrm{TC} \rightarrow \equiv \mathrm{Fe(II)OH} + \text{TC-oxidized products} \tag{7}$$

$$\equiv \mathrm{Fe(II)OH} + \mathrm{H^+} \rightarrow \mathrm{Fe^{2+}} + \mathrm{H_2O} \tag{8}$$

$$\equiv \mathrm{Fe(III)OH} + \mathrm{H_2O_2} \rightarrow \equiv \mathrm{Fe(HO_2)_{2^+}} + \mathrm{H_2O} \tag{9}$$

$$\equiv \mathrm{Fe(HO_2)_{2+}} \rightarrow \equiv \mathrm{Fe(II)OH} + \bullet\mathrm{HO_2} + \mathrm{H^+} \tag{10}$$

$$\equiv \mathrm{Fe(II)OH} + \mathrm{H_2O_2} \rightarrow \equiv \mathrm{Fe(III)OH} + \bullet\mathrm{OH} + \mathrm{OH^-} \tag{11}$$

4.3 Fenton Oxidation Kinetics

As can be seen in the aforementioned figures, a rapid initial TC decay was observed at the first 5 min, followed by a much slower retardation stage, which was likely because the reductive transformation of Fe(III) to Fe(II) by TC in the solution over goethite was inhibited with the Fenton reaction proceeding. However, the

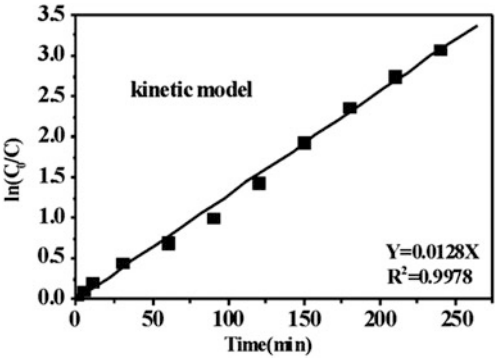

Fig. 9 The pseudo-first-order linear relationship for reaction kinetic curve (60 mg·L^{-1} TC, 20 mmol·L^{-1} H_2O_2, 1.0 g·L^{-1} α-FeOOH, 400 mL, pH 4.0, $T = 35$ °C)

surface-controlled Fenton oxidation reaction generally follows the Langmuir–Hinshelwood model [14], which was typically described as a second-order reaction. But in this study, as the TC concentration in the solution did not decrease quickly during the degradation, its instantaneous adsorbed amount can be assumed as constant, and the TC decomposition via the combination of both homogeneous and heterogeneous Fenton reactions can be described by the following pseudo-first-order equation [36]:

$$-\ln(C_t/C_0) = K_{app}\, t \tag{12}$$

where C_0 and C_t were the TC concentrations (mg·L^{-1}) at the initial time and reaction time t, K_{app} was the pseudo-first-order rate constant (min^{-1}), and t was degradation time (min). The K_{app} constant can be obtained from the slope of the straight lines by plotting $-\ln(C_t/C_0)$ as a function of time t, through regression. As can be seen in Fig. 9, the rate constant of TC decomposition, K_{app}, was found to be 0.0128 min^{-1} under the reaction conditions given in the figure caption. In addition, similar reasonable results can also be obtained for other cases as listed in Table 1. As seen, all the goethite-catalyzed Fenton-like reactions responsible for TC removal are greatly efficient under the optimal reaction conditions as described earlier, and in most situations they may be well fitted to the pseudo-first-order kinetics ($R^2 > 0.99$).

Based upon the apparent kinetic rate constants at different temperatures, the value of apparent activation energy for the TC Fenton removal can be computed with the Arrhenius equation. A good linear relationship was obtained in the Arrhenius plot of lnk versus $1/T$. The value of the activation energy (E_a) was determined to be 31.86 kJ·mol^{-1}. Since activation energy of ordinary thermal reactions was in general between roughly 60 and 250 kJ·mol^{-1} [37], apparently our obtained low value of E_a in this study was well in agreement with the given relevant higher removal rates measured in the Fenton-like reaction.

Table 1 Heterogeneous Fenton oxidation kinetic rate constants for the TC removal under different conditions

Performances	Variations	Constant conditions	k ($\times 10^{-2}$ min^{-1})	R^2
pH value	3.0	[α-FeOOH] = 1.0 $g{\cdot}L^{-1}$	1.65	0.991
	4.0	[H_2O_2] = 20 $mmol{\cdot}L^{-1}$	1.52	0.995
	5.4	[TC] = 40 $mg{\cdot}L^{-1}$	0.52	0.990
	6.0	T = 35 °C	0.58	0.991
	7.0		0.72	0.981
	8.0		1.46	0.991
	10.0		1.59	0.998
H_2O_2 ($mmol{\cdot}L^{-1}$)	10.0	[α-FeOOH] = 1.0 $g{\cdot}L^{-1}$	0.87	0.989
	20.0	[TC] = 40 $mg{\cdot}L^{-1}$	1.54	0.992
	30.0	pH = 4.0	0.73	0.987
	40.0	T = 35 °C	0.65	0.981
Goethite ($mg{\cdot}L^{-1}$)	0.4	[H_2O_2] = 20 $mmol{\cdot}L^{-1}$	1.08	0.996
	0.8	[TC] = 40 $mg{\cdot}L^{-1}$	1.12	0.990
	1.0	pH = 4.0	1.52	0.969
	1.2	T = 35 °C	1.34	0.978
Tetracycline ($mg{\cdot}L^{-1}$)	10.0	[α-FeOOH] = 1.0 $g{\cdot}L^{-1}$	8.27	0.989
	20.0	[H_2O_2] = 20 $mmol{\cdot}L^{-1}$	3.64	0.970
	30.0	pH = 4.0	1.85	0.966
	40.0	T = 35 °C	1.52	0.980
	60.0		1.28	0.998
Temperature (°C)	25.0	[α-FeOOH] = 1.0 $g{\cdot}L^{-1}$	0.52	0.971
	30.0	[H_2O_2] = 20 $mmol{\cdot}L^{-1}$	0.74	0.980
	35.0	[TC] = 40 $mg{\cdot}L^{-1}$	1.52	0.980
	40.0	pH = 4.0	1.89	0.979

4.4 Decomposition of TC

The UV–vis spectra of the TC removal evolution versus the reaction time were shown in Fig. 10, where the absorption spectra of TC in the aqueous solution were scanned in the range of 200–500 nm. As can be observed from these spectra, the absorbance of TC was characterized by two main wavelengths before the initiation of the heterogeneous Fenton-like oxidation. One band was located at 357 nm with a maximum absorption in the visible region, while another band was located at 275 nm with a relatively weaker absorption in the ultraviolet region. Moreover, the characteristic absorption peak at 357 nm decreased more rapidly as the reaction proceeded and essentially disappeared at the end of 240 min, whereas the later characteristic absorption peak at 275 nm decreased relatively slowly.

Since tert-butanol (TBA) is a strong radical scavenger, it can terminate radical chain reactions via generating inert intermediate radicals [8, 10]. As can be seen in Fig. 11, TBA can effectively inhibit the TC Fenton oxidation in the presence of

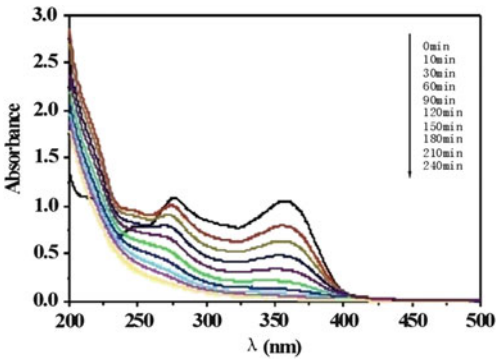

Fig. 10 UV–vis spectral changes of tetracycline oxidation decomposition as a function of reaction time ($C_0 = 40$ mg·L^{-1} of TC, 20 mmol·L^{-1} of H_2O_2, 1.0 g·L^{-1} of α-FeOOH, 400 mL, pH 4.0, and $T = 35$ °C)

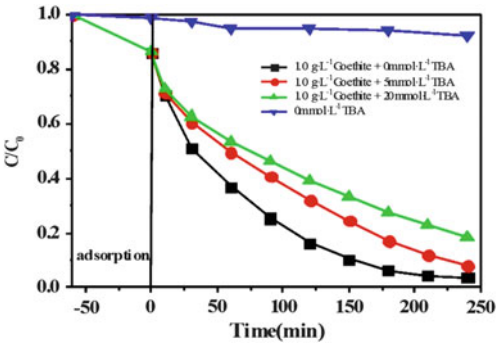

Fig. 11 Effect of i-PrOH on the removal efficiencies of TC oxidation ($C_0 = 40$ mg·L^{-1} of TC, 20 mmol·L^{-1} of H_2O_2, 1.0 g·L^{-1} of α-FeOOH, 400 mL, pH 4.0, $T = 35$ °C)

goethite/H_2O_2 reagent. And, hence, the TC removal efficiencies obviously exhibit the decrease to some extent with the increase of TBA concentrations in the range from 5 to 20 mg·L^{-1} in the solution. Consequently, the TC removal, which was mainly dependent upon the Fenton oxidation reaction with the requirement of $^{\bullet}$OH, clearly differed from the direct oxidation by H_2O_2 only. Furthermore, it had been determined that the peak at 275 nm was associated with aromatic ring A structure involving acylamino and hydroxyl in the molecule and that the peak at 357 nm was originated from aromatic rings B-D comprising the extended chromophores (Fig. 12). Hence, the progress of the TC Fenton decomposition can be easily monitored by the absorption peaks at $\lambda = 357$ and 275 nm. Very interestingly, our obtained result was very similar to a previous research report by Wang et al. (2011) using another advanced oxidation method (ultrasound-enhanced catalytic ozonation) [8].

4.5 Evaluation of the Mineralization of TC

The concentration of total organic carbon (TOC) is generally chosen as a mineralization index of the degradation. The TC mineralization catalyzed by goethite was monitored via TOC analyzer, and the obtained result was shown in Fig. 13. Please

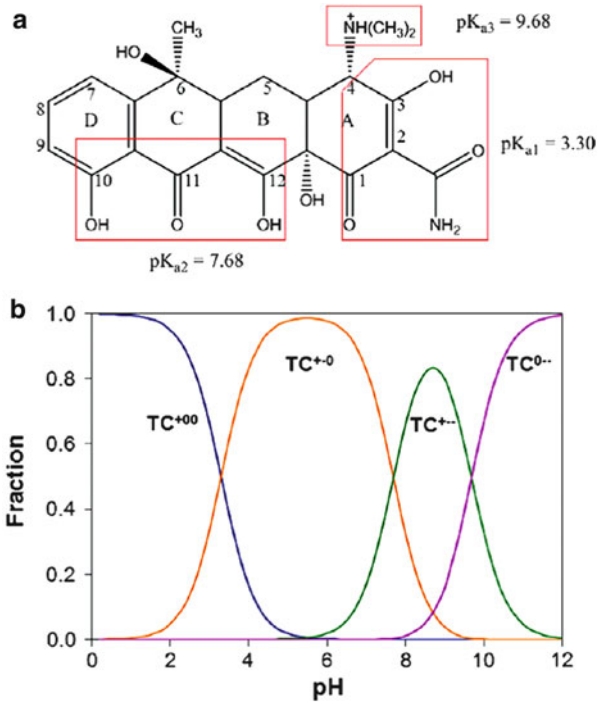

Fig. 12 Structure of TC (**a**) and pH-dependent molecular speciation distribution for TC (**b**)

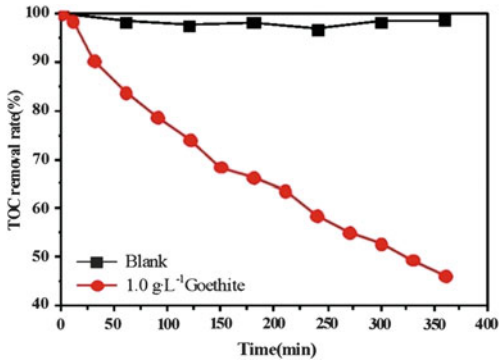

Fig. 13 TOC removal ratio on the heterogeneous Fenton oxidation of TC in the absence and presence of goethite (40 mg·L^{-1} TC, 20 mmol·L^{-1} H_2O_2, 1.0 g·L^{-1} α-FeOOH, 400 mL, pH 4.0, $T = 35$ °C)

note that the highest TOC removal efficiency for TC (just about 50 % TOC) after 240 min was much lower than its decomposition removal efficiencies (over 95 %), and this suggested that there still existed some intermediates in the solution. The HPLC chromatograms of the TC solution at varied reaction times were present in Fig. 14, where TC (R.T., 9.2 min) rapidly disappeared as the reaction progressed. This was well in agreement with the observation from the UV–vis spectra evolution. However, its degradation products need to be further tested by LC–MS analyses in future.

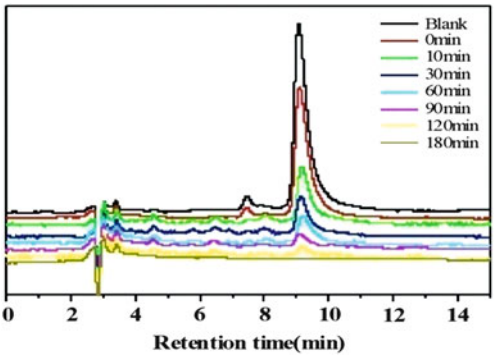

Fig. 14 HPLC–UV chromatograms measured for the TC degradation by-products in the solution

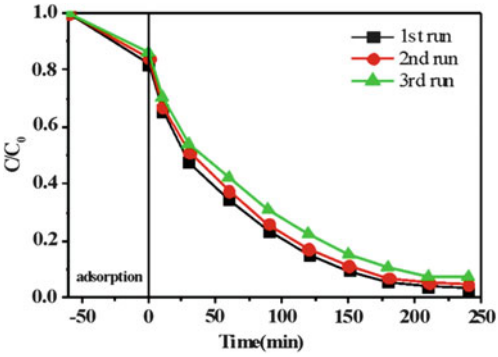

Fig. 15 Recycling properties of the as-synthesized goethite Fenton catalyst

4.6 Recycle of Goethite Catalyst

Numerous previous studies had clearly indicated that in a particular heterogeneous Fenton process using various small crystal size iron oxides as catalysts, the separation of these small particles from suspension after reaction may be very difficult for the recycle use [10]. Due to its relative larger size in micrometer scale, goethite mineral can be easily separated by simple filtration or even natural sedimentation at the end of the heterogeneous Fenton process.

To investigate the recyclability of the goethite particles, sample powders after TC Fenton reactions were collected by naturally settling and reused in the Fenton reaction for three times under the same conditions. As illustrated in Fig. 15, goethite displayed a good stability and maintained high removal rates during three reaction cycles, with removal efficiency at 96.5, 95.1, and 93.8 % after 240 min under the conditions employed (60 mg·L^{-1} TC, 20 mmol·L^{-1} H_2O_2, 1.0 g·L^{-1} α-FeOOH, and volume 400 mL, pH 4.0 and *T* 35 °C).

5 Conclusions

Goethite can be effectively applied for the degradation of tetracycline (TC) by the combination of both heterogeneous and homogeneous Fenton processes in a wide range of pH values. In addition, goethite may catalyze all the Fenton reactions responsible for TC removal following the pseudo-first-order kinetics ($R^2 > 0.99$) with a lower value of activation energy (31.86 kJ·mol^{-1}). More importantly, TC's good adsorptive and reductive activities for goethite were by far the predominant factors to TC's Fenton oxidation removal that can greatly promote the surface-controlled reactions involving the reductive dissolution and transformation of Fe (III) because they were highly consistent with the TC removal enhanced with the increase of temperature. Therefore, tetracycline may be effectively eliminated through the heterogeneous Fenton oxidative process with multimode reaction mechanisms by using the low-cost and efficient goethite.

Acknowledgment This work was funded by National Natural Science Foundation of China (Grant Nos. 41072034, 41372050 and 40773080).

References

1. Jones OAH, Voulvoulis N, Lester JN (2001) Human pharmaceuticals in the aquatic environment—a review. Environ Technol 22:1383–1394
2. Gu C, Karthikeyan KG (2005) Sorption of the antimicrobial ciprofloxacin to aluminum and iron hydrous oxides. Environ Sci Technol 39:9166–9173
3. Sarmah AK, Meyer MT, Boxall ABA (2006) A global perspective on the use, sales, exposure pathways, occurrence, fate and effects of veterinary antibiotics (VAs). Chemosphere 65:725–759
4. Kümmerer K (2009) Antibiotics in the aquatic environment—a review. Part I. Chemosphere 75:417–434
5. Kümmerer K (2009) Antibiotics in the aquatic environment—a review. Part II Chemosphere 75:435–441
6. Halling-Sørensen B (2001) Inhibition of aerobic growth and nitrification of bacteria in sewage sludge by antibacterial agents. Arch Environ Contam Toxicol 40:451–460
7. Bautitz IR, Nogueira RFP (2007) Degradation of tetracycline by photo-Fenton process—solar irradiation and matrix effects. J Photochem Photobiol A Chem 187:33–39
8. Wang Y, Zhang H, Chen L (2011) Ultrasound enhanced catalytic ozonation of tetracycline in a rectangular air-lift reactor. Catal Today 175:283–292
9. Chen WR, Huang CH (2011) Transformation kinetics and pathways of tetracycline antibiotics with manganese oxide. Environ Pollut 159:1092–1100
10. Hao R, Xiao X, Zuo XX, Nan JM, Zhang WD (2012) Efficient adsorption and visible-light photocatalytic degradation of tetracycline hydrochloride using mesoporous BiOI microspheres. J Hazard Mater 209–210:137–145
11. Chen Y, Hu C, Qu J, Yang M (2008) Photodegradation of tetracycline and formation of reactive oxygen species in aqueous tetracycline solution under simulated sunlight irradiation. J Photochem Photobiol A Chem 197:81–87
12. Zhang H, Liu F, Wu X, Zhang J, Zhang D (2009) Degradation of tetracycline in aqueous medium by electrochemical method. Asia Pac J Chem Eng 4:568–573

13. Hou LW, Zhang H, Xue XF (2012) Ultrasound enhanced heterogeneous activation of peroxydisulfate by magnetite catalyst for the degradation of tetracycline in water. Sep Purif Technol 84:147–152
14. Liang XL, Zhong YH, He HP, Yuan P, Zhu JX, Zhu SY, Jiang Z (2012) The application of chromium-substituted magnetite as heterogeneous Fenton catalyst for the degradation of aqueous cationic and anionic dyes. Chem Eng J 191:177–184
15. Zhong YH, Liang XL, Zhong Y, Zhu JX, Zhu SY, Yuan P, He HP, Zhang J (2012) Heterogeneous UV/Fenton degradation of TBBPA catalyzed by titanomagnetite: catalyst characterization, performance and degradation products. Water Res 46:4633–4644
16. Wu HH, Dou XW, Deng DY, Guan YF, Zhang LG, He GP (2012) Decolourization of the azo dye Orange G in aqueous solution via a heterogeneous Fenton-like reaction catalysed by goethite. Environ Technol 33:1545–1552
17. Lin SS, Gurol MD (1998) Catalytic decomposition of hydrogen peroxide on iron oxide: kinetics, mechanism, and implications. Environ Sci Technol 32:1417–1423
18. Hermanek M, Zboril R, Medrik I, Pechousek J, Gregor C (2007) Catalytic efficiency of iron (III) oxides in decomposition of hydrogen peroxide: competition between the surface area and crystallinity of nanoparticles. J Am Chem Soc 129:10929–10936
19. Ortiz de la Plata GB, Alfano OM, Cassano AE (2010) Decomposition of 2-chlorophenol employing goethite as Fenton catalyst. I. Proposal of a feasible, combined reaction scheme of heterogeneous and homogeneous reactions. Appl Catal B 95:1–13
20. Ortiz de la Plata GB, Alfano OM, Cassano AE (2010) Decomposition of 2-chlorophenol employing goethite as Fenton catalyst. II: reaction kinetics of the heterogeneous Fenton and photo-Fenton mechanisms. Appl Catal B 95:14–25
21. Hirsch R, Ternes TA, Haberer K, Mehlich A, Ballwanz F, Kratz KL (1998) Determination of antibiotics in different water compartments via liquid chromatography-electrospray tandem mass spectrometry. J Chromatogr A 815:213–223
22. Ma Y, Gao NY, Li C (2012) Degradation and pathway of tetracycline hydrochloride in aqueous solution by potassium ferrate. Environ Eng Sci 29:357–361
23. Zhao YP, Geng JJ, Wang XR, Gu XY, Gao SX (2011) Adsorption of tetracycline onto goethite in the presence of metal cations and humic substances. J Colloid Interface Sci 361:247–251
24. Li ZH, Schulz L, Ackley C, Fenske N (2010) Adsorption of tetracycline on kaolinite with pH-dependent surface charges. J Colloid Interface Sci 351:254–260
25. Chang PH, Li ZH, Jiang WT, Jean JS (2009) Adsorption and intercalation of tetracycline by swelling clay minerals. Appl Clay Sci 46:27–36
26. Pignatello JJ, Oliveros E, MacKay A (2006) Advanced oxidation processes for organic contaminant destruction based on the Fenton reaction and related chemistry. Crit Rev Environ Sci Technol 36:1–84
27. Chou S, Huang C (1999) Application of a supported iron oxyhydroxide catalyst in oxidation of benzoic acid by hydrogen peroxide. Chemosphere 38:2719–2731
28. Sun SP, Li CJ, Sun JH, Shi SH, Fan MH, Zhou Q (2009) Decolorization of an azo dye Orange G in aqueous solution by Fenton oxidation process: effect of system parameters and kinetic study. J Hazard Mater 161:1052–1057
29. Tanis E, Hannaa K, Emmanuel E (2008) Experimental and modeling studies of sorption of tetracycline onto iron oxides-coated quartz. Colloids Surf A Physicochem Eng Asp 327:57–63
30. Chen WR, Huang CH (2010) Adsorption and transformation of tetracycline antibiotics with aluminum oxide. Chemosphere 79:779–785
31. Essington ME, Lee J, Seo Y (2010) Adsorption of antibiotics by montmorillonite and kaolinite. Soil Sci Soc Am J 74:1577–1588
32. Chang PH, Li ZH, Jean JS, Jiang WT, Wang CJ, Lin KH (2012) Adsorption of tetracycline on 2:1 layered non-swelling clay mineral illite. Appl Clay Sci 67–68:158–163
33. Parolo ME, Savini MC, Vallés JM, Baschini MT, Avena MG (2008) Tetracycline adsorption on montmorillonite: pH and ionic strength effects. Appl Clay Sci 40:179–186

34. Wallace JG (1975) Hydrogen peroxide in organic chemistry. E.I. du Pont de Nemours, Wilmington
35. Khan MH, Bae H, Jung JY (2010) Tetracycline degradation by ozonation in the aqueous phase: proposed degradation intermediates and pathway. J Hazard Mater 181:659–665
36. Matta R, Hanna K, Kone T, Chiron S (2008) Oxidation of 2,4,6-trinitrotoluene in the presence of different iron-bearing minerals at neutral pH. Chem Eng J 144:453–458
37. Kasiri MB, Aleboyeh H, Aleboyeh A (2010) Mineralization of C.I. acid red 14 azo dye by UV/Fe-ZSM5/H_2O_2 process. Environ Technol 31:165–173

Palygorskite in the Late Miocene Red Clay Sediment from the Chinese Loess Plateau and Its Paleoclimatic Implications

Qiaoqin Xie, Gao Qiu, Tianhu Chen, Xiaochun Xu, Xiaoyong Wang, Huayu Lu, Huifang Xu, and Junfeng Ji

Abstract Palygorskite is the predominant component of the Red Clay sediment on the Chinese Loess Plateau. The morphological characteristics and microstructures of palygorskite in four sections of late Miocene Red Clay were investigated using power X-ray diffraction (XRD), scanning electron microscopy (SEM), and high-resolution transmission electron microscopy (HRTEM). The XRD results suggest that the clay minerals in the Red Clay are mainly illite, kaolinite, chlorite, and palygorskite with smectite. Two types of palygorskite microtexture were observed in the Red Clay sediment: (1) relatively straight, fibrous crystals in bundles or intertwined aggregates or in matted, felted masses on other minerals and silky aggregates radiating from platy minerals; and (2) single crystals scattering among or coating detrital particles. Based on SEM investigations, the first aggregate is considered to be the major type of microtexture. The occurrence of this type of microtexture supports the hypothesis that palygorskite developed through pedogenesis of the red clay deposits. The authigenic palygorskites are thought to be formed through the transformation of existing aeolian mineral (e.g., smectite) and direct

Q. Xie
School of Resource and Environmental Engineering, Hefei University of Technology, Hefei 230009, China

Radiogenic Isotope Laboratory, Center for Microscopy and Microanalysis, University of Queensland, St Lucia, QLD 4072, Australia

G. Qiu • T. Chen (✉) • X. Xu
School of Resource and Environmental Engineering, Hefei University of Technology, Hefei 230009, China
e-mail: chentianhu168@vip.sina.com

X. Wang • H. Lu
School of Geographical and Oceanographical Sciences, Nanjing University, Nanjing 210093, China

H. Xu
Department of Geoscience, and Materials Science Program, University of Wisconsin, Madison, WI 53706, USA

J. Ji
School of Earth Sciences and Engineering, Nanjing University, Nanjing 210093, China

F. Dong (ed.), *Proceedings of the 11th International Congress for Applied Mineralogy (ICAM)*, Springer Geochemistry/Mineralogy,
DOI 10.1007/978-3-319-13948-7_42

chemical deposition in soil pore solution. Consequently, the formation of palygorskite was largely controlled by the strength of the in situ pedogenesis process induced by the East Asian summer, and palygorskite can serve as an index mineral of arid and semiarid environment since the late Miocene for the Chinese Loess Plateau. These findings add to existing fundamental mineral data related to the climatic evolution of the northwest China arid region and of arid and semiarid zones in the Northern Hemisphere.

Keywords Chinese Loess plateau • Paleoclimatic implications • Palygorskite • Red clay sediment

1 Introduction

The Chinese Loess Plateau is located in arid and semiarid zones of the Northern Hemisphere. The windblown loess–red clay deposits consisting of Quaternary interbedded loess and paleosol units and late Miocene Red Clay sediment are valuable archives of paleoclimate in this region [1–3]. Studies on aeolian sequences have provided a wealth of information on regional climatic and environmental changes, the evolution of the East Asian monsoon, and the progressive aridification of the Chinese Loess Plateau since the Miocene was revealed by a number of proxy indicators, such as magnetic susceptibility, grain size, mineralogy, and pedogenic micromorphology [4–10]. In general, the alternations between loess and paleosols can be interpreted as a reflection of changing glacial and interglacial climates during the Quaternary [1]. The loess forms when the climate is cold and dry, resulting in relatively coarse-grained and weakly weathered dust accumulation, while the paleosols form when the climate is wet and warm, and pedogenesis is enhanced [11, 12]. This rhythm of Chinese loess/paleosol alternations was directly influenced by the alternating strengthening and weakening of the East Asian summer and winter paleomonsoons. The loess–paleosol sequence is underlain by Red Clay sediment, which may have accumulated under a relatively warm and stable climate [13]. The shift from the red clay to the loess–paleosol is interpreted as representing a shift in the regional climate from relatively warm and wet to alternating periods of cold and dry versus warm and wet climates [13]. A study on Qi'an loess deposits suggests that aeolian deposits were already present in the early Miocene [14]. Therefore, studies suggest that aridification in inland Asia began at approximately 22 Ma [14] with accelerated global aridification at 8–7 Ma and again at 3.6–3.2 and 2.6 Ma [3, 6, 15, 16]. In particular, mineralogy such as from magnetic and clay minerals has been used to retrieve the paleoclimatic signals recorded in the Chinese aeolian sequence [3, 12, 17–20].

Aeolian minerals (e.g., quartz and feldspar) in the loess–Red Clay sediments reflect the mineralogy of the source region including deserts such as the Gobi and piedmont alluvial fans of the arid region in northwest China [21, 22]. Aeolian minerals also record paleoclimate change in the source region. During the pedogenesis process, the degradation of detrital minerals is synchronous with the

deposition of new minerals, resulting in the formation of different minerals within different climatic environments [12]. Consequently, information on climate changes can be obtained through authigenic minerals in the Red Clay sediment.

Palygorskite is a clay mineral characterized by a fibrous morphology [23]. The formation and stability of palygorskite require alkaline conditions with high Si and Mg activity as well as an arid or semiarid climate with periodic evaporation of the water layer [24]. Given that palygorskite-containing soils occur almost exclusively in arid and semiarid areas of the world, it may be regarded as a proxy of a semiarid or arid paleoclimatic condition [23, 25–27].

Studies have examined the type, proportion, and crystallinity of clay minerals in the Chinese loess–red clay sequences as clues about the evolution of the Asian monsoon, and these clay minerals also provide information on the mineralogy of loess deposits and Red Clay sediment [12, 28, 29]. Little attention has been paid to typical arid minerals (e.g., palygorskite) in the aeolian sediments of northwest China. For first time, Xie et al. [30] reported that palygorskite was present in Lingtai Red Clay sediment and discussed its significance in terms of climate. The aim of this study is to investigate the morphological characteristics, genesis, and paleoclimatic significance of palygorskite in the Red Clay sediment through the Chinese Loess Plateau based on XRD, SEM, and HRTEM analysis.

2 Materials and Methods

2.1 Geological Setting and Samples

The Chinese Loess Plateau in northwest China can be divided into three zones: the North, Central, and South [1]. From northwest to southeast on the Loess Plateau, the present-day mean annual precipitation increases from less than 200 mm to approximately 600 mm, and the mean annual temperature increases from 8 to 14 °C. The Red Clay sediment that underlies the loess–paleosol sequences consists of highly developed soils and interbedded layers of less-weathered, loess-like materials, mainly reddish clay-to-silt-sized sediments. The Red Clay sediment is tens of meters to more than 100 m thick, with colors ranging from light to dark red. The Red Clay sediment contains carbonate layers, and magnetostratigraphic studies show that it began to accumulate at approximately 8.3–6.5 Ma [31, 32]. Recently, we finished a systematic investigation on the presence of palygorskite in the Red Clay sediment from the northernmost to southernmost parts of the Loess Plateau. Four Red Clay sediments, including Jiaxian, Xifeng, Luochuan, and Duanjiapo, were studied (Fig. 1).

At Jiaxian (38.16°N, 110.5°E), the mean annual temperature is 10 °C and the present annual precipitation is approximately 400 mm [33]. The Red Clay sediment is approximately 70 m thick and is overlain by approximately 20 m of loess [32, 33]. The Jiaxian Red Clay sediment has been subdivided into 18 units, which are

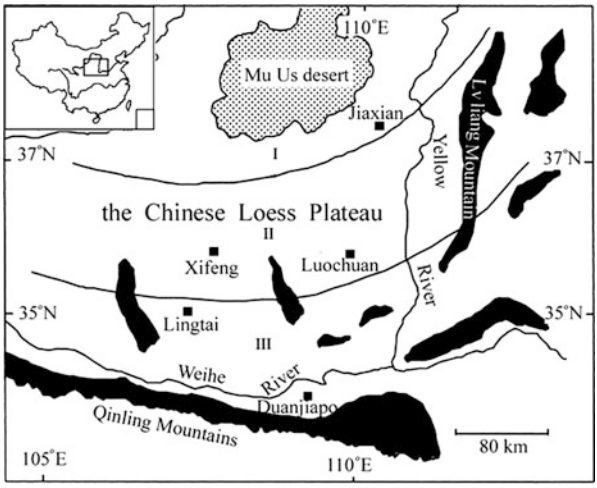

Fig. 1 Simplified map showing the zonation of loess and the locations of the studied sections on the Chinese Loess Plateau. Zone I = sandy loess; zone II = loess; zone III = clayey loess. Also shown are mountains (*black*) and the studied localities (*squares*). The *inset* diagram (the *upper-left* corner) shows a map of China (modified from [33])

designated consecutively as RC1–RC18. Each unit consists generally of two or more reddish pedogenic B and carbonate nodule horizons [33]. The magnetostratigraphy of the Jiaxian Red Clay deposit indicates that the accumulation of aeolian dust began approximately 8.35 Ma [32]. At Duanjiapo (34.2°N, 109.2°E), the mean annual temperature is 13.8 °C, and the mean annual precipitation is approximately 615 mm; the Red Clay sediment is approximately 50 m thick, overlain by a loess–paleosol sequence that is 130 m thick [34, 35]. This Red Clay sediment, which underwent relatively stronger pedogenesis, has a light red to deep red color and contains several tens of layers of carbonate nodules. The age of the lower surface of the Duanjiapo Red Clay sediment is approximately 7.3 Ma [35].

The Xifeng section (referred to here as the Zhaojiachuan section) (36.37°N, 107.6°E), which consists of the Red Clay sediment with a thickness of approximately 60 m and a Quaternary loess–paleosol sequence with a thickness of approximately 170 m [7, 36], is located in the mid-western part of the Loess Plateau, at the eastern margin of Liupan Mountain. The mean annual temperature is 8.3 °C, and the mean annual precipitation is approximately 560 mm. The Xifeng Red Clay sediment might have only experienced a weak pedogenesis process. Twelve light red paleosol complex units with Fe–Mn lamination coatings and granular structure can be recognized over the Red Clay section. Four carbonate layers with a thickness of 0.5–1 m are developed in the lower part of the section [35]. Based on magnetostratigraphic data, the lower boundary of the Red Clay has been dated to 7.6 Ma [37]. The lower part of the section, older than 6.2 Ma (representing a total thickness of approximately 220 m), has been reworked by fluvial processes [31]. The Luochuan section (35.48°N, 108.38°E) is located in the middle-eastern part of the Loess Plateau, in which the mean annual temperature is 9 °C, and the mean annual precipitation is 570 mm. The loess–paleosol sequence is approximately 135 m thick; it was one of the first loess sections studied in detail and has been the subject

of detailed stratigraphic studies using a variety of climate proxies [4, 34]. This Red Clay section is only approximately 14 m thick [38].

Samples of each profile were collected at intervals of 5 or 10 cm by digging a fresh profile in the sediment. Samples for SEM investigation were first selected at 50-cm intervals. Then, based on SEM observations, representative samples of microtexture in the matted aggregates (e.g., Fig. 3a, b) were selected for XRD analyses and TEM. In total, 200 samples were examined by SEM, 22 samples by XRD, and five samples by TEM.

2.2 XRD Analysis

The samples for XRD analysis were gently hand-ground to powder in an agate mortar. Prior to analysis, samples were repeatedly washed with deionized water to remove soluble compounds, and carbonates were removed with a 1 N solution of sodium acetate buffered at pH 5.0. The clay-sized fractions ($\leq$2 μm) were obtained using the sedimentation method according to Stokes and prepared as oriented mounts on glass slides using a pipette method [39]. The XRD patterns were recorded using a D/max-RB diffractometer with CuKα radiation for air-dried, glycol-saturated, and 550 °C-treated samples. The XRD analyses were carried out at the Structural Analysis Center of the Hefei University of Technology.

2.3 SEM Analysis

For SEM analysis, blocks or particles of intact samples were selected and then coated with Au. Images were obtained using a Sirion 200 SEM operated at an accelerating voltage of 30 kV housed at the Hefei National Laboratory for Physical Science at the Microscale, University of Science and Technology of China. The instrument is equipped with an INCA energy-dispersive spectrometer (EDS), which was used to examine the elemental composition of samples.

2.4 HRTEM Analysis

The TEM analysis was performed to investigate the morphological and structural characteristics of the fibrous crystal and related clay minerals. The $\leq$2 μm fraction was dispersed in deionized water with ultrasonic equipment for 20 min. Then, the mineral particles were collected with a copper grid and air dried. The TEM observation was performed with a JEM 2100 HRTEM equipped with an EDS system, with a resolution of 0.23 nm at 200 kV. TEM investigation was carried out at the Advanced Analysis Technology Center, Anhui University, P. R. China.

3 Results

3.1 XRD Analysis

The mineralogical identification is based on the criteria proposed by Brown and Brindley [40]. Quartz is identified from its 3.34 Å peak, kaolinite from its reflection both at 7.20 and 3.57 Å, illite from its strong reflection at 9.9 Å, and chlorite from its peak at 14 Å, which is unaffected by glycolation. The most intense peak of palygorskite occurs at approximately 10.5 Å. Some of the peaks for both smectite and kaolinite may overlap with those for chlorite. Thus, the glycol treatment is used to distinguish smectite from chlorite, and the heat treatment is applied to separate kaolinite from chlorite; additionally, the diffraction pattern of palygorskite is altered through heating.

Typical XRD patterns of the Red Clay samples from the Zhaojiachuan and Duanjiapo sections are illustrated in Fig. 2. The ≤2 μm clay fraction of the air-dried samples shows reflections corresponding to quartz at 3.34 and 4.25 Å; illite at 10.0, 5.0, and 3.33 Å; kaolinite at 7.20 and 3.58 Å; and chlorite at 14.24, 7.20, 4.73, and 3.53 Å. Glycol treatments caused a decrease in the reflection at 14.24 Å, with a concomitant increase at 17.15 Å and the disappearance of the reflection at 17.15 Å after the heat treatment (550 °C), which is indicative of smectite. In addition, the small peak with a d value of approximately 10.44 Å in air-dried and glycol-treated samples is apparent and probably related to

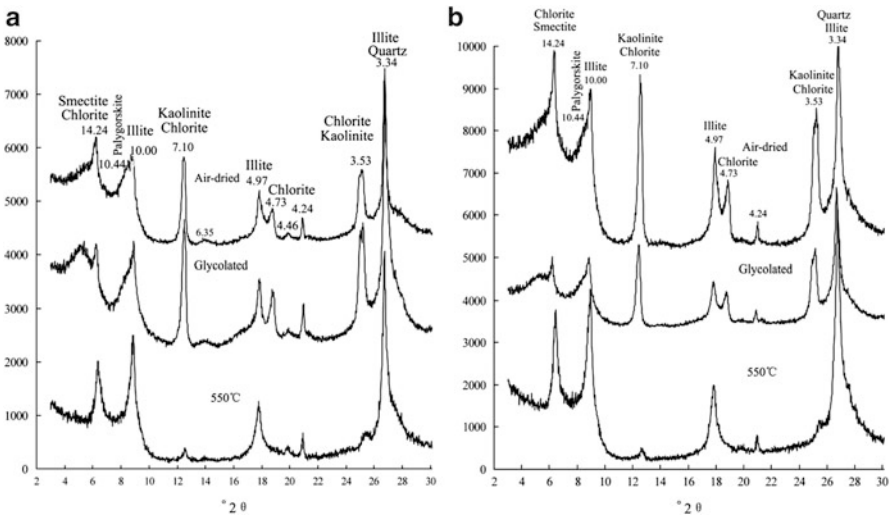

Fig. 2 Typical XRD patterns of the <2 μm fraction of Chinese Red Clay from the Xifeng (XFRC199) and Duanjiapo (DJPRC2702) profiles. (**a**) Oriented preparation of red clay sample XFRC199 from 199 m below the *S0*; (**b**) oriented preparation of red clay sample DJPRC2702 from 2702 cm below the base of L33

palygorskite. Heat treatment caused the disappearance of the 10.44 Å peak that resulted from the structural collapse of palygorskite [41]. However, the peak intensity is relatively weak, indicating a relatively low concentration of palygorskite and a possibly low degree of crystallization. The XRD patterns were similar for all samples examined, although the relative intensities of peaks for every mineral showed some variation.

3.2 SEM Analysis

SEM observations reveal fibrous crystals of palygorskite of indeterminate length due to intergrowth and show that palygorskite is a ubiquitous component of the samples examined from four sections on the Chinese Loess Plateau. The palygorskite has various micromorphologies and microtextures, including silky aggregates with a "net" appearance in void spaces (Fig. 3a) and mat aggregates consisting of the intergrowth or intertwining of silky crystals (Fig. 3b, c). In some cases, the silky palygorskite crystals are observed growing from the margins of a platy mineral (Fig. 3d), overlying dolomite crystals (Fig. 3e) or coating the surfaces of other mineral particles (Fig. 3f). Systemic SEM observations of the four sections studied indicate that the occurrences and microtextures of palygorskite are variable, as is the concentration from the base to the top layer in each profile. However, a "concentration" is only estimated through SEM analysis, and a quantitative mineralogical analysis of palygorskite using XRD was not performed. EDS analysis of the silky aggregates shows that their chemical composition consists of Si, Mg, Al, and minor amounts of Fe and K (Fig. 3g), which is consistent with the known composition of palygorskite.

3.3 TEM Analysis

The TEM images show obvious palygorskite fibers, indicating that the dispersive treatment did not damage the fibers. The single crystal exhibits a relatively straight fibrous morphology and is easily identified (Fig. 4a). In the TEM images, very finely dispersed platy minerals (possibly smectite) were very clear and common in the Red Clay sediment. Measurement of the fiber dimensions indicates a maximal length greater than 2 μm and widths of 20–30 nm (Fig. 4b). These fibers are comparable with the fibers of the crystals observed in the SEM. The SAED pattern from the fibrous crystals (the delicate, long crystals in the middle of Fig. 4a) shows 110, 040, and 400 powder diffraction rings (the lower-right corner of Fig. 4a) from a bundle of fibers. The EDS analysis (the lower-right corner of Fig. 4b) shows a similar chemical composition to that which is obtained by the SEM (Fig. 3g).

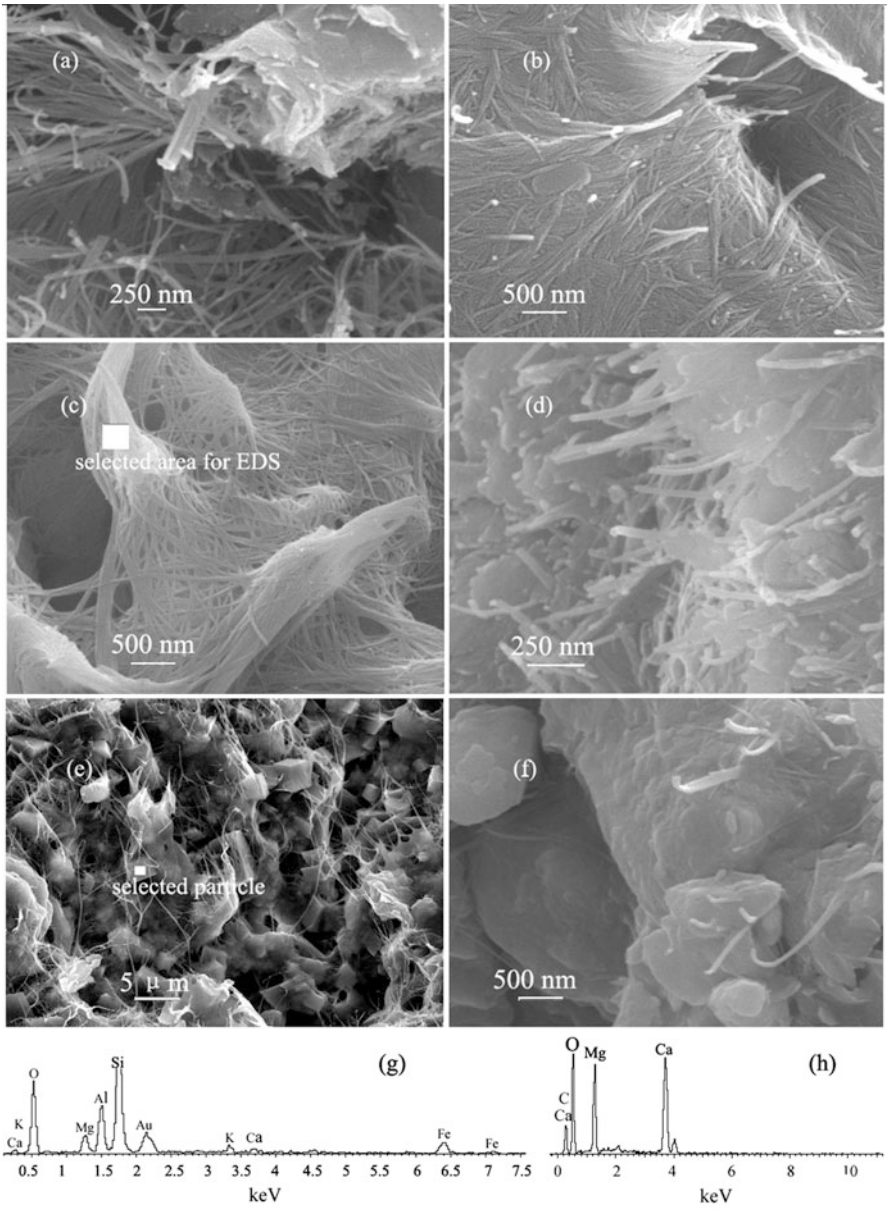

Fig. 3 SEM images of palygorskite occurrence in the red clay profiles. (**a**) Palygorskite in void spaces; (**b**) layer of randomly oriented fibers; (**c**) generally branched palygorskite fibers; (**d**) palygorskite fibers radiating from the margin of lath-like crystals; (**e**) palygorskite coating on the surface of a dolomite sample from XFRC199; (**f**) scattering palygorskite of detrital origin; (**g**) EDS spectrum obtained for fibrous palygorskite aggregates (*white square* in (**c**) for the selected EDS area), revealing the dominance of Si, Al, and Mg, with trace Fe, K, and Ca; and (**h**) EDS pattern of cube minerals showing the chemical composition of dolomite (*white square* in (**e**)), mainly consisting of Mg and Ca with a Mg-to-Ca ratio of 1:1. Samples examined in (**a–f**) are from

4 Discussion

4.1 Mineral Composition

The clay mineralogy of the Red Clay sediment was determined for the $\leq$2 μm size fraction samples and shows that the major clay minerals present are illite, kaolinite, chlorite, smectite, and also palygorskite (Fig. 2). Previous studies of the Red Clay of northwest China have clearly demonstrated the predominance of illite, kaolinite, smectite, and chlorite [12, 28, 42]. However, to the authors' knowledge, the present investigation is the first to report the widespread occurrence of palygorskite in these strata, as initially reported by Xie et al. [30]. The XRD results show that palygorskite is present in the fine clay fraction (Fig. 2). The SEM and TEM confirm the identification of the palygorskite in the Chinese Red Clay sediment.

Palygorskite and sepiolite are both fibrous clay minerals, and this has possibly led to their misidentification. Palygorskite has been reported to be a soil component worldwide, whereas the formation of sepiolite in soils is relatively rare because of its instability in soil [43, 44]. The intense peak of sepiolite is not present in Fig. 2, and the chemical composition of fibrous aggregates identified by EDS of the TEM is consistent with the known composition of palygorskite [45, 46]. Therefore, it is concluded that the Red Clay does not contain sepiolite. Thus, based on our studies, the clay minerals in Chinese Red Clay sediment consist of illite, kaolinite, chlorite, smectite, and palygorskite, which is a common mineral association in arid and semiarid soil.

4.2 Palygorskite Genesis

Palygorskite is present in several environments, including marine and lake sediments, arid soils, and areas of hydrothermal activity [47]. In many soils from semiarid regions of the world, palygorskite has been reported with increasing frequency. In these environments, two main mechanisms have been proposed to explain the presence of palygorskite: (1) a detrital origin [48, 49], i.e., the occurrence of palygorskite is attributed to palygorskite-bearing rocks, sediments, or soils, allochthonous or inheritance, and (2) an in situ pedogenic origin [24, 50, 51]. Allochthonous or inherited palygorskite provides insight into the evolution of the paleoclimate of the source area, whereas in situ authigenic palygorskite documents information on the paleoclimate of the depositional region. Consequently, whether palygorskite is inherited from the parent rock, transported by

Fig. 3 (continued) Duanjiapo (DJPRC349), Jiaxian (JXRC1451), Duanjiapo (DJPRC2702), Xifeng (XFRC199, 199), and Luochuan (LCRC690). The oriented preparation of samples is the same as in Fig. 2

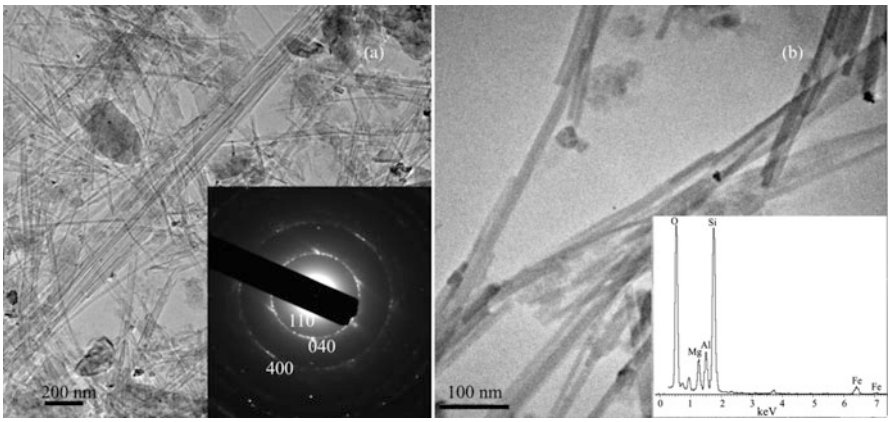

Fig. 4 TEM images of the fine clay fraction from JXRC361. (**a**) Palygorskite fibers are very apparent in the sample. (**b**) At a higher magnification, a single fiber with a diameter of approximately 30 nm can be examined. The SAED pattern (*insert*, the *lower-right* corner of (**a**)) from the delicate, longest fiber aggregate in (**a**) shows 110 and 400 diffraction rings. The EDS pattern of the single fiber (*insert*, the *lower-right* corner of (**b**)) shows that the palygorskite chemical composition is Si, Al, and Mg with trace Fe and K, and these findings are consistent with those obtained by SEM

wind from a distant source area, or formed authigenically in a soil environment during pedogenesis, it is important to determine the origin and genesis of palygorskite in soils and paleosols.

Many criteria have been used to discriminate authigenic palygorskite from windblown particles, including morphology and crystallinity [52]. Although palygorskite morphology is not diagnostic of its genesis, its occurrence as short, interlocking fibers is usually taken to indicate dust of detrital origin from a source area. In contrast, its occurrence as long, branched, or intertwined fibers, as observed in this study, suggests an authigenic origin, because such delicate morphologies would not be expected to survive transportation. The most convincing evidence of an authigenic origin, however, is the arrangement of palygorskite fibers in relation to other grains and pores. Palygorskite fibers radiate into the pore space, indicating in situ crystallization [53]. If the palygorskite fibers had originated elsewhere and been transported to their current position, it is more likely that the fibers would be oriented parallel to larger particles rather than being perpendicular [52, 54]. Thus, the genesis and origin of palygorskite can easily be determined from SEM observations.

The SEM observations reveal that palygorskite occurs as fibrous mats and bundles forming laminae and as interwoven fibrous mats and fibers as coatings, pore-fillings, and pore-bridging cements in the Red Clay. These microtextures (Fig. 3a–e) suggest an authigenic rather than detrital origin [52, 55]. The occurrence of fine, delicate, fibrous palygorskite in the Red Clay sediment is inconsistent with a detrital origin because it is difficult to envisage how such delicate fabrics could have been preserved during transport and deposition. Therefore, it is concluded that

palygorskite in the Chinese Red Clay is pedogenic in origin. Although some potential sediment basins may have provided palygorskite with the Red Clay sediment of the Chinese Loess Plateau [56], the mechanism of inheritance cannot adequately explain the genesis of palygorskite in the Chinese Red Clay sediment. The various samples investigated are widely distributed from the Red Clay sediment across the study area (Fig. 1).

Singer [57] suggested that the pedogenic palygorskite in modern soils is affected by fluctuating groundwater levels. In relation to groundwater, temporary waterlogged conditions or frequent wetting of calcareous pedon conditions are suitable for the neoformation of palygorskite [24]. In the Zhaojiachuan profile, Guo et al. [31] suggested that the lower part (>6.2 Ma BP) is a water-reworked deposit related to alluvial and slope processes and that the middle part (6.2–3.6 Ma) was significantly affected by groundwater-level oscillations. However, the pedogenic palygorskite is widely distributed in this profile and other sections studied, and the occurrence of palygorskite cannot be attributed entirely to groundwater oscillations. The palygorskite formed in situ, possibly through chemical precipitation from a Mg-rich pore solution, generally post-dating dolomitization [49, 57], or through the transformation of preexisting minerals (e.g., smectite or chlorite) related to chemical weathering processes controlled by the paleoclimate. The pedogenic palygorskite can serve as an index of paleoclimate change of the Chinese Loess Plateau.

4.3 Paleoclimatic Implications

Palygorskite is a common clay mineral in desert soils under arid and semiarid conditions [58–61] and is a reliable index mineral of such an environment [26, 57]. The present SEM observations reveal that palygorskite is a widespread component of the Red Clay sediment of the Chinese Loess Plateau. We identified two kinds of microtextures: (1) delicate fibrous aggregates or interwoven fibrous aggregate-forming fine laminae (Fig. 3a–e) and (2) single fibers in close association with other minerals. The main clay minerals in the Red Clay are illite, kaoline, chlorite, palygorskite, and smectite, which are the dominant clay minerals in arid and semiarid regions [61, 62], thereby indicating that the Red Clay formed in such an environment. In addition, the presence of palygorskite along with smectite suggests a hot (arid to semiarid) climate with some rainy intervals [53]. However, higher average concentrations of kaolinite in the Red Clay sediment are related to a more humid climate. Therefore, the mineralogy of the Red Clay indicates a steady warm–wet climate with alternation between successive dry and wet intervals.

The change from red clay to a loess–paleosol is interpreted to represent a shift in the regional climate from relatively warm and wet conditions to alternating periods of cold–dry and warm–wet conditions [13]. The accumulation of Red Clay on the Chinese Loess Plateau provides a record of the aridification of the interior Asian continent. The increasing aridity of the paleoclimate at approximately 3.6–3.2 Ma

is consistent with marine records [63] and with investigations of the Chinese Red Clay [30]. A rearrangement of atmospheric circulation in northern China occurred at ~2.6 Ma [5], leading to a change in the paleoclimate of the Chinese Loess Plateau and a change in mineralogy from the Red Clay to the loess sequence. In contrast to the Pleistocene climate that was characterized by frequent and large-amplitude fluctuations between cold–dry and warm–wet periods, the late Pliocene experienced a relatively steady and warm–dry climate compared with the present day [64–66]. Thus, the degree of aridity in north China increases from the red clay to the loess sediments.

This change in paleoclimate is also recorded by the proportions of various clay minerals in the Lingtai section. Relatively abrupt changes in the concentrations of smectite and kaolinite occur at the boundary between the red clay and the loess–paleosol, with the kaolinite concentration being higher in the Red Clay and the smectite concentration being higher in the loess–paleosol [12]. These trends reflect differences in source area [12] and differences in paleoclimate during pedogenesis. Kaolinite generally forms from intense chemical weathering under warm and wet conditions. A higher content of kaolinite indicates that the deposition region experienced intense weathering, possibly under tropical-like climate conditions, whereby abundant rainfall favors the transport of ions and pedogenesis. In contrast, smectite generally develops in terrestrial areas of low relief under seasonally warm climatic conditions.

The present analysis of red clay containing a high concentration of kaolinite indicates intense chemical weathering under high temperatures and abundant rainfall because the loess and red clay dust originated from the same source region [33]. The carbonate content in the Xifeng section increases from the top of loess sequence to the bottom of the Red Clay sediment, where the concentration is 50 % [67]. Carbonate minerals (calcite and dolomite) are the main components of the loess–Red clay sediment, which contains horizons of carbonate nodules that were formed from the recrystallization of Ca-bearing minerals (e.g., plagioclase) during weathering and dissolution under a seasonally arid paleoclimate that had high temperatures as well as heavy rainfall and evaporation. Indeed, one of the most striking features of the red clay sequences is the occurrence of numerous carbonate nodules [13].

The above results suggest that minerals in the Red Clay sediment were subjected to stronger pedogenic processes than the minerals in the overlying loess and that from the late Miocene to late Pliocene, the climate was characterized by a seasonally arid environment with relatively high rainfall and evaporation under a steady warm–wet climate in contrast to the frequent fluctuations between cold–dry and warm–wet periods experienced during the Quaternary. These environmental characteristics of the period of deposition and pedogenesis of the Red Clay sediment resulted in strong weathering, producing a fine grain-size distribution and a redder color than in the overlying loess as well as greater modifications to the mineralogy of the Red Clay. During weathering, the decomposition of detrital minerals and the formation of clay minerals occurred, forming different minerals in different climatic environments. Therefore, palygorskite in the Red Clay sediment is

considered to be a product of climate rather than oscillations in groundwater level and also a reliable mineralogical marker of arid conditions on the Chinese Loess Plateau since the late Miocene.

5 Conclusions

The loess–red clay sequences in north China are classic windblown dust sediments that provide a reliable archive of the paleoclimate from the East Asian Monsoon and that record a long-term aridification history in northwest China. This study examines the occurrence and detrital versus authigenic origin of palygorskite in the Red Clay sediment and its relevance to paleoclimate. The palygorskite in the Red Clay sediment from the arid and semiarid Chinese Loess Plateau is an authigenic mineral formed in situ during pedogenesis at the sites of dust deposition; it is not of detrital origin. The occurrence of delicate silky palygorskite in the Red Clay of northwest China is an indicator of paleoclimate and records a significant change in climate between the Red Clay deposition and the younger classic loess–paleosol sequences.

Acknowledgments This study was supported by the NSFC grants 41130206, 41172048, and 40072032. We are grateful to Professor Ray L. Frost for revising the manuscript.

References

1. Liu TS (1985) Loess and the environment. China Ocean Press, Beijing, p 251
2. Liu TS, Ding ZL (1993) Stepwise coupling of monsoon circulations to global ice volume variations during the late Cenozoic. Global Planet Change 7:119–130
3. Deng CL, Shaw J, Liu QS, Pan YX, Zhu RX (2006) Mineral magnetic variation of the Jingbian loess/paleosol sequence in the northern Loess Plateau of China: implications for quaternary development of Asian aridification and cooling. Earth Planet Sci Lett 241:248–259
4. Kukla G, Heller F, Liu XM, Xu TC, Liu T, An ZS (1988) Pleistocene climates in China dated by magnetic susceptibility. Geology 16:811–814
5. Ding ZL, Rutter NW, Sun JM, Yang S, Liu TS (2000) Rearrangement of atmospheric circulation at about 2.6 Ma over northern China: evidence from grain size records of loess–paleosol and red clay sequences. Quat Sci Rev 19:547–558
6. An ZS, Kutzbach JE, Prell WL, Porter SC (2001) Evolution of Asian monsoons and phased uplift of the Himalaya–Tibetan Plateau since Late Miocene time. Nature 411:62–66
7. Guo ZT, Peng SZ, Hao QZ, Biscaye PE, An ZS, Liu TS (2004) Late Miocene–Pliocene development of Asian aridification as recorded in the Red-Earth Formation in northern China. Global Planet Change 41:135–145
8. Vandenberghe J, Lu HY, Sun DH, Huissteden JK, Konert M (2004) The late Miocene and Pliocene climate in East Asia as recorded by grain size and magnetic susceptibility of the Red Clay deposit (Chinese Loess Plateau). Palaeogeogr Palaeoclimatol Palaeoecol 204:239–255
9. Ji JF, Chen J, Balsam W, Lu HY, Sun YB, Xu HF (2004) High resolution hematite/goethite records from Chinese loess sequences for the last glacial-interglacial cycle: rapid climatic

response of the East Asian Monsoon to the tropical Pacific. Geophys Res Lett 31, L03207. doi:10.1029/2003GL018975
10. Rutter NW, Ding ZL (1993) Paleoclimates and monsoon variations interpreted from micromorphogenic features of the Baoji paleosols, China. Quat Sci Rev 12:853–862
11. An Z, Kukla G, Porter S, Xiao J (1991) Magnetic susceptibility evidence of monsoon variation on the Loess Plateau of central China during the last 130,000 years. Quatern Res 36:29–36
12. Gylesjö S, Arnold E (2006) Clay mineralogy of a red clay-loess sequence from Lingtai, the Chinese Loess Plateau. Global Planet Change 51:181–194
13. Ding ZL, Xiong SF, Sun JM, Yang SL, Gu ZY, Liu TS (1999) Pedostratigraphy and paleomagnetism of a ~7.0 Ma eolian loess-red clay sequence at Lingtai, Loess Plateau, North-central China and the implications for paleomosoon evolution. Palaeogeogr Palaeoclimatol Palaeoecol 152:49–66
14. Guo ZT, Ruddiman WF, Hao QZ, Wu HB, Qiao YS, Zhu RX, Peng SZ, Wei JJ, Yuan BY, Liu TS (2002) Onset of Asian desertification by 22 Myr ago inferred from loess deposits in China. Nature 416:159–163
15. Nie J, King JW, Fang X (2008) Link between benthic oxygen isotopes and magnetic susceptibility in the red-clay sequence on the Chinese Loess Plateau. Geophys Res Lett 35, L03703. doi:10.1029/2007GL032817
16. Bai Y, Fang XM, Nie JS, Wang YL, Wu FL (2009) A preliminary reconstruction of the paleoecological and paleoclimatic history of the Chinese Loess Plateau form the application of biomarkers. Palaeogeogr Palaeoclimatol Palaeoecol 271:161–169
17. Chen TH, Xu HF, Xie QQ, Ji JF, Chen J, Lu HY (2005) Identification, characteristics and genesis of maghemite in loess-palaeosol sequences of China. Earth Planet Sci Lett 240:790–802
18. Chen TH, Xie QQ, Xu HF, Chen J, Ji JF, Lu HY (2010) Characteristics and formation mechanism of the pedogenic hematite in Quaternary Chinese loess and paleosols. Catena 81:217–225
19. Xie QQ, Chen TH, Xu HF, Chen J, Ji JF, Lu HY, Wang XY (2009) Quantifying the contribution of pedogenic magnetic minerals to magnetic susceptibility of loess and paleosols on Chinese Loess Plateau: paleoclimatic implications. J Geophys Res 114, B09101. doi:10.1029/2008JB005968
20. Jeong GY, Hillier S, Kemp RA (2011) Changes in mineralogy of loess-paleosol sections across the Chinese Loess Plateau. Quatern Res 75:245–255
21. Chen J, Li GJ, Yang JD, Rao WB, Lu HY, Balsam W, Sun YB, Ji JF (2007) Nd and Sr isotopic characteristics of Chinese deserts: implications for the provenances of Asian dust. Geochim Cosmochim Acta 71:3904–3914
22. Guan QY, Pan BT, Gao HS, Li N, Zhang H, Wang JP (2008) Geochemical evidence of the Chinese loess provenance during the Late Pletistocene. Palaeogeogr Palaeoclimatol Palaeoecol 270:53–58
23. Neaman A, Singer A (2004) The effects of palygorskite on chemical and physico-chemical properties of soils: a review. Geoderma 123:297–303
24. Singer A, Norrish K (1974) Pedogenic palygorskite occurrence in Australia. Am Mineral 59:508–517
25. Singer A (1979) The Paleoclimatic interpretation of clay minerals in soil and weathering: a review. Earth Sci Rev 15:303–326
26. Rodas M, Luque FJ, Mas R, Garzon MG (1994) Calcretes, palycretes and silcretes in the Paleogene detrital sediments of the Duero and Tajo basins, central Spain. Clay Miner 29:273–285
27. Tateo F, Sabbadini R, Morandi N (2000) Palygorskite and sepiolite occurrence in Pliocene lake deposits along the River Nile: evidence of an arid climate. J Afr Earth Sci 31:633–645
28. Kalm VE, Rutter NW, Rokosh CD (1996) Clay minerals and their paleoenvironmental interpretation in the Baoji loess section, Southern Loess Plateau, China. Catena 27:49–61

29. Ji JF, Chen J, Lu HY (1999) Origin of illite in the loess from the Luochuan area, Loess Plateau, Central China. Clay Miner 34:525–532
30. Xie QQ, Chen TH, Chen J, Ji JF, Xu HF, Xu XC (2008) Distribution and paleoclimatic interpretation of palygorskite in Lingtai profile of Chinese Loess Plateau. Acta Geol Sin 82:967–974
31. Guo ZT, Peng SZ, Hao QZ, Biscaye PE, Liu TS (2001) Origin of the Miocene-Plicene Red-Earth Formation at Xifeng in Northern China and implication for paleoenvironments. Palaeogeogr Palaeoclimatol Palaeoecol 170:11–26
32. Qiang XK, Li ZX, Powell CMA, Zheng HB (2001) Magnetostratigraphic record of the Late Miocene onset of the East Asian monsoon, and Pliocene uplift of northern Tibet. Earth Planet Sci Lett 187:83–93
33. Ding ZL, Sun JM, Yang SL, Liu TS (2001) Geochemisty of the Pliocene red clay formation in the Chinese Loess Plateau and implications for its origin, source provenance and paleoclimate change. Geochim Cosmochim Acta 65(6):901–913
34. Bloemendal J, Liu XM (2005) Rock magnetism and geochemistry of two plio–Pleistocene Chinese loess–palaeosol sequences—implications for quantitative palaeoprecipitation reconstruction. Palaeogeogr Palaeoclimatol Palaeoecol 226:149–166
35. Sun DH, Liu DS, Chen MY, An ZS (1997) Magnetostratigraphy and palaeoclimate of Red Clay sequences from Chinese Loess Plateau. Sci China (Ser D) 40(4):337–343
36. Liu XM, Liu TS, Xu TC, Liu C, Chen MY (1988) The Chinese loess in Xifeng, I. The primary study on magnetostratigraphy of a loess profile in Xifeng area, Gansu province. Geophys J 92:345–348
37. Sun DH, An ZS, Shaw J, Bloemendal J, Sun YB (1998) Magnetostratigraphy and palaeoclimatic significance of late Tertiary Aeolian sequences in the Chinese Loess Plateau. Geophys J Int 134:207–212
38. Wang XY, Lu HY, Ge SW, Deng CL (2006) Extension of the typical aeolian sequences at Luochuan, central Chinese Loess Plateau. Mar Geol Quat Geol 26(1):89–92 (Chinese text with English abstract)
39. Zhao XY, Zhang YY (1990) Clay minerals and analytical methods. Ocean Press, Beijing, pp 1–310 (in Chinese with English Abstract)
40. Brown G, Brindley GW (1980) X-ray diffraction procedures for clay mineral identification. In: Brindley GW, Brown G (eds) Crystal structures of clay minerals and their X-ray identification. Mineralogical Society, London, pp 305–360
41. Chen TH, Wang J, Qing CS, Peng SC, Song YX, Guo Y (2006) Effect of heat treatment on structure, morphology and surface properties of palygorskite. J Chin Ceram Soc 34(11):1406–1410
42. Peng SZ, Guo ZT (2007) Clay mineral composition of the Tertiary red clay and the Quaternary loess-paleosols as well as its environmental implication. Quat Sci 27:277–286
43. Singer A (1989) Palygorskite and sepiolite group minerals. In: Dixon JB, Weed SB (eds) Minerals in soil environments. Soil Science Society of America, Madison, pp 829–872
44. Singer A, Kirsten W, Bühmann C (1995) Fibrous clay minerals in the soils of Namaqualand, South Africa: characteristics and formation. Geoderma 66:43–70
45. Galan E, Carretero MI (1999) A new approach to compositional limits for sepiolite and palygorskite. Clays Clay Miner 47:399–409
46. Gionis V, Kacandes GH, Kastritis ID, Chryssikos GD (2007) Combined near-infrared and X-ray diffraction investigation of the octahedral sheet composition of palygorskite. Clays Clay Miner 55:543–553
47. Bouza PJ, Simón M, Aguila J, del Valle H, Rostagno M (2007) Fibrous-clay mineral formation and soil evolution in Aridisols of northeastern Patagonia, Argentina. Geoderma 139:38–50
48. Khademi H, Mermut AR (1998) Source of palygorskite in gypsiferous Aridisols and associated sediments from Central Iran. Clay Miner 33:561–578
49. Khademi H, Mermut AR (1999) Submicroscopy and stable isotope geochemistry of carbonates and associated palygorskite in Iranian Aridisols. Eur J Soil Sci 50:207–216

50. Elprince AM, Mashhady MS, Aba-Husayn MM (1979) The occurrence of pedogenic palygorskite (attapulgite) in Saudi Arabia. Soil Sci 128:211–218
51. Hiller S, Pharande AL (2008) Contemporary pedogenic formation of palygorskite in irrigation-induced, saline-sodic, shrink-swell soils of Maharashtra, India. Clays Clay Miner 56(5):531–548
52. Verrecchia EP, Le Coustumer MN (1996) Occurrence and genesis of palygorskite and associated clay minerals in a Pleistocene calcrete complex, SDE Boqer, Negev desert, Israel. Clay Miner 31:183–202
53. Daoudi L (2004) Palygorskite in the uppermost Cretaceous-Eocene rocks from Marrakech High Atlas, Morocco. J Afr Earth Sci 39:353–358
54. Wilson MD, Pittman ED (1977) Authigenic clays in sandstones: recognition and influence on reservoir properties and palaeoenvironmental analysis. J Sediment Petrol 47:3–31
55. Hassouba H, Shaw HF (1980) The occurrence of palygorskite in Quaternary sediments of the coastal plain of north-west Egypt. Clay Miner 15:77–83
56. Hong HL, Yu N, Xiao P, Zhu YH, Zhang KX, Xiang SY (2007) Authigenic palygorskite in Miocene sediments in Linxia basin, Gansu, northwestern China. Clay Miner 42:45–48
57. Singer A (1984) The paleoclimatic interpretation of clay minerals in sediments—a review. Earth Sci Rev 21:251–293
58. Abtahi A (1980) Soil genesis as affected by topography and time in calcareous parent materials. Soil Sci Soc Am J 44:329–336
59. Lee SY, Dixon JB, Aba-Hussein MM (1983) Mineralogy of Saudi Arabian soils: eastern region. Soil Sci Soc Am J 74:321–326
60. Gharaee HA, Mahjoory RA (1984) Characteristics and geomorphic relationships of some representative Aridisols in southern Iran. Soil Sci Soc Am J 48:115–119
61. Baghernejad M (2000) Variation in soil clay minerals of semi-arid regions of Fars Province, Iran. Iran Agric Res 19:165–180
62. Khormali F, Abtahi A (2003) Origin and distribution of clay minerals in calcareous arid and semi-arid soils of Fars Province. Clay Miner 38:511–527
63. Rea DK, Snoeckx H, Joseph LH (1998) Late Cenozoic eolian deposition in the North Pacific: Asian drying, Tibetan uplift, and cooling of the northern hemisphere. Paleoceanography 13:215–224
64. Ding ZL, Sun JM, Yang SL, Liu TS (1998) Preliminary magnetostratigraphy of a thick eolian red clay–loess sequence at Lingtai, the Chinese Loess Plateau. Geophys Res Lett 25:1225–1228
65. Anadón P, Burjachs F, Martín M, Rodriguez-Lázaro J, Robles F, Utrilla R, Vázquez A (2002) Paleoenvironmental evolution of the Pliocene Villarroya Lake, northern Spain. A multidisciplinary approach. Sediment Geol 148:9–27
66. Han JM, Fyfe WS, Gu ZY (2002) Assessment of the palaeoclimate during 3.0–2.6Ma registered by transition of Red Clay to loess-palaeosol sequences in central North China. Palaeogeogr Palaeoclimatol Palaeoecol 185:355–368
67. Sun YB, Xie QQ (2007) Genesis of the Carbonate in the Loess—Paleosol—Red Clay sequence of the Chinese Loess Plateau and its weathering phases. Bull Mineral Petrol Geochem 26:170–175 (In Chinese with English Abstract)

Preparation of Cristobalite and Its Thermal Characteristics

Ying Yan and Yongheng Zhou

Abstract Cristobalite is a crystalline form of silica and plays an important role in the application of casting industry, but it is rare in earth. Cristobalite has been manufactured by calcining fused silica ceramic in this work; the XRD, SEM, and thermal characteristics of the cristobalite have been tested. The result shows the formation of porous structure in the block cristobalite, and thermal linear expansion rate of the phase transition of β/α cristobalite reaches 0.5 % at the temperature range of 250–290 °C.

Keywords Cristobalite • Fused silica ceramic • Thermal expansion

1 Introduction

Silica has a series of polymorphs. The high-temperature phase of silica, namely, β-cristobalite, is stable between 1,470 °C and the melting point 1,728 °C, which has a significant transition to the low-temperature phase α-cristobalite when the temperature is below 275 °C [1]. It can be mentioned here that fused silica gradually transforms to crystalline state cristobalite when calcining above 1,000 °C [2]. The thermal expansion of the β/α-cristobalite phase transition can effectively compensate the unwanted shrinkage in model materials by thermal decomposition of the gypsum [3]; therefore cristobalite is an important material for the final dimension and surface roughness of casting [4].

Because cristobalite mine is rare in earth and formed only when high-temperature melt quickly erupts and cools, the cristobalite is usually manufactured by calcining quartz mine [5]. In the calcining process, phase transition of silica happened and resulted in large volume change; the thermal expansion rate of α-quartz/α-cristobalite reaches 15.5 %. Such a big volume change will make the ceramic to creak [6]. The cracked cristobalite is not suitable to measure the characteristic of thermal expansion. Hence the actual measurement results of

Y. Yan • Y. Zhou (✉)
Guangdong Engineering Research Center of Optoelectronic Functional Materials and Devices, South China Normal University, Guangzhou, Guangdong, P.R. China
e-mail: yhzhou@scnu.edu.cn

F. Dong (ed.), *Proceedings of the 11th International Congress for Applied Mineralogy (ICAM)*, Springer Geochemistry/Mineralogy,
DOI 10.1007/978-3-319-13948-7_43

cristobalite are hard to work out, and the data are available almost only by calculation based on its structural character [7].

This study was performed to test the thermal characteristic of cristobalite. The cristobalite was manufactured by calcining fused silica ceramic, and its thermal characteristic had been measured, which is very important to its application in casting.

2 Materials and Methods

2.1 Materials

A slurry was obtained by mixing fused silica powder (with SiO_2 content above 99.5 wt%), water, and the additives (PVA, lactate). After ultrasonic dispersion and vacuum degassing process, pour the slurry into plaster mold and dry it for 12 h at 90 °C and then sinter the temperature 1,300 °C for 4 h; fused silica ceramic sample was prepared. Finally block cristobalite was manufactured by heating the fused silica ceramic samples at the temperature 1,500 °C for 10 h.

2.2 Analysis

X-ray powder diffraction (X'Pert PRO X-ray diffractometer equipped with the copper Kα radiation $\lambda = 1.5418$ Å) was performed to identify the phase of fused silica ceramic and block cristobalite samples. The diffraction angle was scanned from 10° to 50° with the scanning speed of 0.02° per second.

The microstructures of the samples were examined by scanning electron microscopy SEM of Bruker Hitachi S-3400 M; the crisroblite sample was characterized by differential thermal analysis (DTA) (Beijing Hengjiu HCR-1) at the heating rate of 15 °C/min; the linear thermal expansion of the crisroblite sample was tested at the heating rate of 7 °C/min in the temperature range between 50 and 700 °C (ZRPY-1400 Hunan Xiangtan instrument Co, LTD).

3 Results and Discussion

3.1 The Characteristics of Cristobalite

The XRD patterns of the fused silica ceramic are shown in Fig. 1; it reveals that the ceramic is composed of glass phase and small amounts of quartz phase, which is drastically different from cristobalite. On the other hand, an intensity diffraction

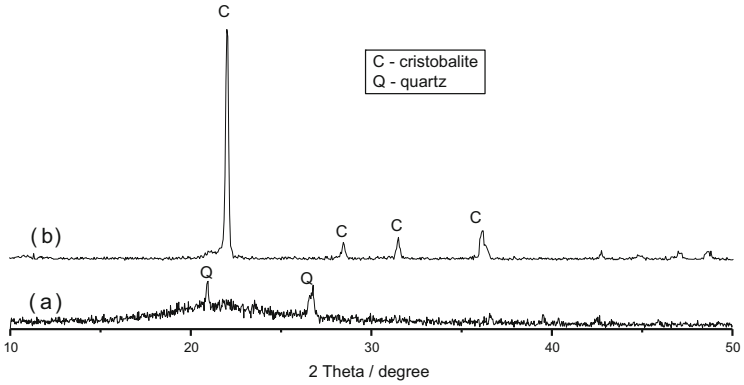

Fig. 1 XRD patterns of the samples. (**a**) Fused silica ceramic, (**b**) cristobalite made by calcining fused silica ceramic

peak appeared at $2\theta = 22°$ after the ceramic had been heated at 1,500 °C, consistent with the first peak of cristobalite SiO_2 crystal face (110). Other small peaks of 28°,31°, and 36° belong to the crystal faces of cristobalite (111), (102), (200), respectively. No other phases were shown in the XRD pattern; hence the cristobalite is of high purity. The results of XRD indicate that the fused silica has changed into cristobalite after calcining at 1,500 °C; the thermal expansion rate is 0.9 % occurring in the phase transition, which is too small to make the bulk material creak, so the cristobalite remains solid blocks.

The SEM photographs of fused silica ceramic and cristobalite are shown in Fig. 2. Silica glass particle size around 30 μm can be seen by dissolving in the ceramic matrix, and little pore exists on the surface of the sample. In contrast, the formation of porous structures is shown in the SEM micrographs of the cristobalite, which is caused by phase transition of the silica.

3.2 The Thermal Characteristics of the Cristobalite

The thermal analysis (DTA) of the cristobalite is shown in Fig. 3. A sharp endothermic peak around 260 °C can be noticed in the DTA curve of the cristobalite sample, which is due to the β/α-cristobalite phase transition.

The thermal expansion of the cristobalite is shown in Fig. 4. The first inflection point around 250 °C is observed, and the thermal expansion increases rapidly until it reaches the second inflection point (290 °C). A comparison with the DTA (Fig. 3) suggests the thermal expansion is caused by phase transition of β/α cristobalite.

Because the expansion coefficient is also the function of temperature, the curve of thermal expansion in Fig. 4 includes the natural expansion and phase transition. The comparison of absorption peak in DTA shows that the phase transition of β/α

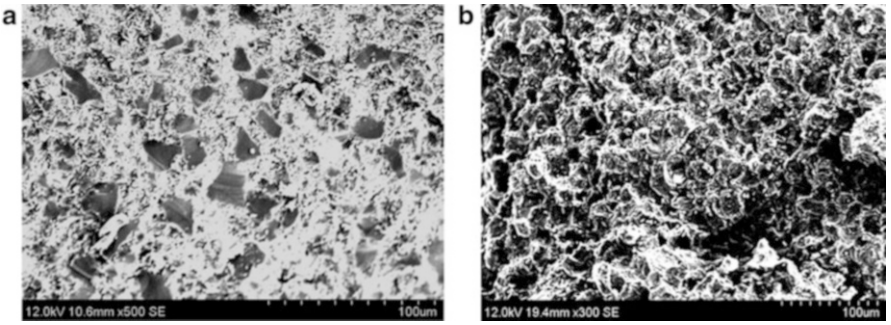

Fig. 2 SEM photograph of fused silica ceramic and cristobalite. (**a**) Fused silica ceramic, (**b**) cristobalite

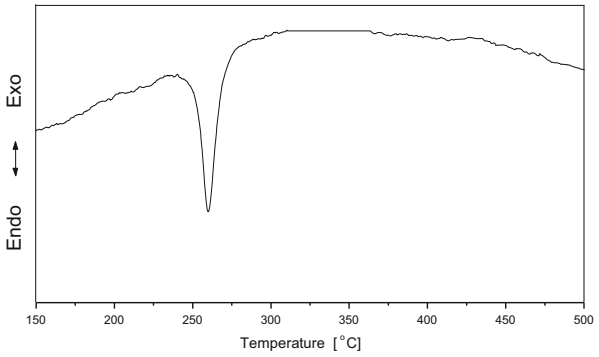

Fig. 3 DTA of the cristobalite

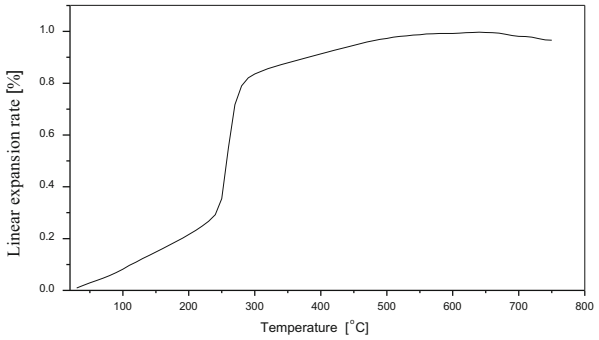

Fig. 4 Thermal expansion of the cristobalite

cristobalite was completed at 290 °C, while the growth of thermal expansion after 290 °C (Fig. 4) reaches 0.99 %.

In order to eliminate the natural expansion of solid, the expansion between 250 and 290 °C has been figured out as the expansion of the phase transition of β/α cristobalite according to DTA. In general the thermal linear expansion rate is 0.5 %. The porous structure of the block cristobalite leading to the actual measurement results is smaller than value of the theoretical calculation, whereas the volume change caused by phase transition will fill the pore spaces.

4 Conclusions

Cristobalite can be manufactured by calcining fused silica ceramic, and it is a kind of porous structural solid block, because the phase transition of silica glass and cristobalite has low volume change. Thermal linear expansion rate of the phase transition of the cristobalite is 0.5 % at the temperature range of 250–290 °C, which is smaller than the theoretical calculation because of its porous structure.

Acknowledgment This work described in this paper is supported by the Key Laboratory of Solid Waste Treatment and Resource Recycle (Southwest University of Science and Technology), Ministry of Education of China, and Project of Guangzhou Education (10B002).

References

1. Stevens SJ, Hand RJ, Sharp JH (1997) Polymorphism of silica. J Mater Sci 32:2929–2935
2. Grimshaw RW, Hargreaves J, Roberts AL (1977) Conversion kinetics of quartz to cristobalite. Trans Br Ceram Soc 76:71–74
3. Wakasa K, Ikeda A, Yoshida Y (1993) Silica investment prepared for dental purposes: effect of cristobalite content on mechanical properties. J Mater Sci Lett 12:1908–1910
4. Pattnaik S, Karunakar DB, Jha PK (2012) Developments in investment casting process—a review. J Mater Process Technol 212:2332–2348
5. Orii K, Ohshima I, Watanale N (1989) Process for producing unsintered cristobalite silica. United States Patent 4853198
6. Shovaf S, Champagnon B, Panczer G (1997) The quartz-cristobalite transformation in heated chert rock composed of micro and crypto-quartz by micro-Raman and FT-IR spectroscopy methods. J Therm Anal 50:203–213
7. Hatch DM, Ghose S (1991) The phase transition in cristobalite, SiO_2. Phys Chem Miner 17:554–562

Removal of Cu (II) from Aqueous Solutions Using Colloidal Pyrite Calcined Under Inert Atmosphere

Yan Yang, Tianhu Chen, Ping Li, Haibo Liu, Yadan Shi, and Xinmin Zhan

Abstract A natural colloidal pyrite calcined in N_2 atmosphere was utilized to remove Cu (II) from aqueous solutions in the present work. Under the effect of calcination temperature, initial solution pH, reaction time, initial Cu (II) concentration, sorption temperature, foreign ions, and the dissolved oxygen (DO) on Cu(II) removal were investigated. The results showed that colloidal pyrite calcined at 500–550 °C (CCPy) has a most promising potential for Cu(II) removal. The increase of pH, initial Cu(II) concentration, and reaction time benefited the improvement of Cu(II) removal efficiency. The isothermal adsorption data of CCPy were well described by Langmuir isotherms and the thermodynamic parameters ($\Delta G < 0$, $\Delta H > 0$), indicating the endothermic nature of Cu(II) sorption on CCPy. The presence of most common ions in acid mine drainage and DO just had little influence on the Cu(II) uptake. The observation implied that CCPy is a low-cost, abundant material for Cu removal from Cu waters.

Keywords Calcined • Colloidal pyrite • Copper removal • Sorption

1 Introduction

Iron sulfide minerals are the most widely occurring sulfide minerals in geological environment and major mining waste products as well. The oxidation and subsequent dissolution of iron sulfide minerals result in acid mine drainage (AMD) with the high acidity of the natural water bodies and the release of dissolved iron, sulfate, and diversity of dissolved metals, such as Fe, Al, Mn, and trace concentrations of lead, copper, cadmium, and arsenic [1, 2]. These compounds can have serious toxicological effects on aquatic ecosystems, such as mortality, growth disorders,

Y. Yang • T. Chen (✉) • P. Li • H. Liu • Y. Shi
Laboratory for Nanomineralogy and Environmental Material, School of Resources & Environmental Engineering, Hefei University of Technology, Hefei, Anhui, China
e-mail: chentianhu@hfut.edu.cn

X. Zhan
Department of Civil Engineering, National University of Ireland, Galway, Ireland

F. Dong (ed.), *Proceedings of the 11th International Congress for Applied Mineralogy (ICAM)*, Springer Geochemistry/Mineralogy,
DOI 10.1007/978-3-319-13948-7_44

lower reproduction rates, deformities, and injuries [3]. Lakes and steams are adversely affected by abandoned mineral and coal mines, corresponding mine wastes, and related AMD. Stringent environmental regulations have called for alternatives to deal with tailing problems of mineral processing. Novel methods for further beneficial uses of tailing wastes are, therefore, becoming increasingly more important. One of the options in sustainable management of mining wastes would be waste trading, that is, treating mining wastes with other wastes [4]. Based on this concept, it is possible to take advantage of the "chemical reactivity and strong affinity for heavy metals" characteristics of iron sulfide minerals to treat wastewater. The use of iron sulfide minerals has been studied as scavengers for the wastewater treatment. For example, redox-sensitive radionuclides (such as U, Se) [5, 6], arsenic [7], and heavy metals, such as Cr^{6+} [8], Zn^{2+} [9], Pb^{2+} [9], Hg^{2+} [10], Cd^{2+} [11, 12], and Cu^{2+} [13] can be reduced and be immobilized by iron sulfide minerals.

Copper is a common hazardous pollutant and considered as one of the most widespread heavy metal contaminants in the environment [14]. Its toxic effects include vomiting, abdominal pain, nausea, diarrhea, liver and kidney damage, chronic disorders, cramps in the calves, and gastrointestinal catarrh [15]. This metal is known for accumulating at high levels in the aquatic food chain, threatening natural ecosystems and human life. To minimize the adverse effects, State Bureau of Technical Supervision in China enforced stringent levels for the maximum allowable limits of heavy metals discharge into the rivers, lakes, and landscapes. The integrated wastewater discharge standard tolerance for Cu (II) concentration in water is 0.5 ppm [16]. Thus, the knowledge of its fate and transport in aquatic environments is of critical importance.

Previous research was concentrated on Cu(II) uptake from wastewater by the natural iron sulfide minerals. However, the reactivity of natural iron sulfide minerals to heavy metals is low. Therefore, the most important problem is how to enhance the reactivity of natural iron sulfide minerals to heavy metals. Chen et al. [17] found an approach to prepare nano-pyrrhotite materials by annealing natural colloidal pyrite in N_2 atmosphere. Therefore, a series of batch experiments were carried out to investigate the feasibility of Cu(II) removal from aqueous solutions using colloidal pyrite calcined in N_2 atmosphere. In the present study, the experimental conditions for adsorption, including calcined temperature, initial solution pH, initial Cu(II) concentration, sorption time, sorption temperature, and foreign ions were investigated with respect to the Cu(II) removal efficiency. Besides, Langmuir and Freundlich models were applied to represent the sorption phenomenon, and some thermodynamic parameters were also determined. In addition, Cu(II) removal efficiency was compared under oxic and anoxic conditions.

2 Materials and Methods

2.1 Experimental Materials

The sample used in this research was hand-picked colloidal pyrite from Xinqiao iron sulfide deposit in Tongling, Anhui Province, China. The particles were washed with 1 % HCl to wipe off the adhesion minerals and oxide film on its surface and washed to neutral with distilled water. XRD analysis showed that the colloidal pyrite samples were primarily composed of pyrite and secondarily of siderite. Samples were crushed and sieved into the desired particle size of less than 0.074 and 0.15–0.28 mm. The sieved samples with a diameter less than 0.074 mm were utilized in the batch sorption experiments, while the calcinate with diameter of 0.15–0.28 mm was used to study the effect of dissolved oxygen.

The stock solution of Cu(II) (1 g/L) was prepared by dissolving $CuCl_2 \cdot 2H_2O$ in distilled water. The working solution was prepared by diluting the stock solution with distilled water. The solution pH was adjusted to 5.0 by using 0.1 M HCl and NaOH solution. All the chemicals used in the study were of analytical reagent grade.

2.2 Experimental Methods and Analysis

2.2.1 Colloidal Pyrite Calcination

The thermally treated experiments were carried out in an electrically heated horizontal tube furnace. The internal diameter of reactor is 2 cm. 1–3 g colloidal pyrite particles were inserted into the reactor with quartz cotton as supporting layer and kept for 1 h in N_2 atmosphere with a flow of 80 mL/min before heating to purge oxygen in this system. After purging, the samples were heated to desired temperature with a rate of 25 °C/min and kept for 1 h. The reactor was took out and cooled in nitrogen to room temperature after heating and then put the samples into sample bag and sealed.

2.2.2 Batch Sorption Experiments

The sorption of Cu(II) on calcined colloidal pyrite was studied by the batch method. Weighed 0.5 g of calcined colloidal pyrite less than 0.074 mm was put into conical flask and mixed with 250 mL of 10 mg/L Cu(II) solution. These conical flasks were sealed and put into a water bath shaker (Jiangsu JINTAN SHY-2) with shaking rate of 150 r/min at 25 °C and kept for 24 h. The suspensions were analyzed for Cu (II) concentration after centrifugation. From the obtained results, optimum

calcination temperature, pH, contact time, sorption temperature, and concentration were selected for further investigation.

The effect of ions and its concentrations including common cations and anions in AMD on removal of Cu(II) was investigated. The cations (cations in chlorine form) were including K^+, Na^+, NH^{4+}, Mg^{2+}, Ca^{2+}, and Fe^{2+}; the anions (anions in sodium form) contained Cl^-, NO^{3-}, SO_4^{2-}, and CO_3^{2-}. The elevated concentrations of 0.1, 0.5, 1, 5, 10, and 50 mM of various ions were selected to study the effect of exotic ions on the sorption of Cu(II) on CCPy.

The effect of dissolved oxygen was studied by comparing Cu(II) removal efficiency under oxic and anoxic solutions, respectively. The effect of dissolved oxygen was investigated in flasks where 250 mL of 50 mg/L Cu (II) as well as 1.0 g of 0.15–0.28 mm CCPy were mixed. Anoxic experiment was carried out in glove box of no oxygen. The supernatant was extracted 2 mL using a syringe at a desired time. All batch experiments were performed in triplicate and only the mean values were reported. The maximum deviation observed was less than ± 1 %.

The final removal efficiency was calculated according to the Eq. (1):

$$\mathrm{RE}(\%) = \frac{C_0 - C_t}{C_0} \times 100 \tag{1}$$

Where C_0 is the initial concentration of Cu(II), and C_t is the concentration of Cu (II) after reaction 1 h.

The suspensions were analyzed for Cu(II) concentration by an atomic absorption spectrophotometer (RUILI WFX-130A, Beijing, China) using the flame atomization technique. A pH meter (pHS-3C, China) was used to determine the pH of solutions.

3 Results and Discussion

3.1 Effect of Calcining Temperature on Cu(II) Removal

As is seen in Fig. 1, the Cu(II) removal experienced a dramatic increase from 5 to 99.84 % and then decreased to 28 % with the increase of calcining temperature from 100 to 900 °C. The maximum of Cu(II) removal (99.84 %) was obtained when the calcining temperature was up to 500 or 550 °C, where pyrite was transformed into monoclinic pyrrhotite in N_2 atmosphere according to the results of XRD [17]. The transformation of pyrite to monoclinic pyrrhotite gave rise to the shift of the disulfide crystal structure to simple sulfide, which weakened the strength of Fe–S bond and increased the vacancy of Fe lattice, resulting in the increase of chemical reactivity [18, 19]. Therefore, monoclinic pyrrhotite has better effect on Cu (II) uptake than colloidal pyrite [20]. The occurrence of Cu(II) removal decreasing from 600 °C was contributed to the transformation of monoclinic pyrrhotite to

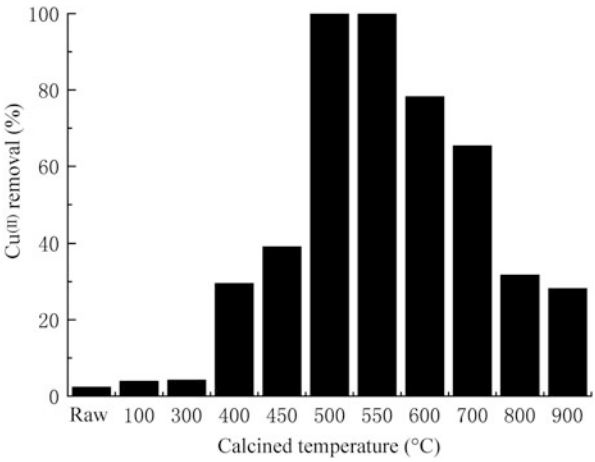

Fig. 1 Effect of calcining temperature on the Cu (II) removal

hexagonal pyrrhotite and troilite. This transformation caused a negative impact on the chemical reactivity and reduced the Cu(II) removal, which agrees well with the previous reports [21]. The result demonstrates the best calcining temperature is 500–550 °C, where monoclinic pyrrhotite is the dominative product. Consequently, optimum calcination temperature of 500 °C was selected for calcining colloidal pyrite for the following experiments.

3.2 Effect of pH

Figure 2 shows the pH (2.0–6.0) dependence of Cu(II) sorption on CCPy by taking precipitation pH value and the acidity of AMD of Cu(II) into account [22, 23]. The pH of the solution played an important role in the sorption of Cu(II) on CCPy as was displayed in Fig. 2. The Cu(II) removal increased from 34 to 99 % as the pH varied from 2 to 5; however, no obvious variation was observed when the pH is over 5. Fornasiero et al. reported that above pH of 2, pyrite had a negative surface charge, the density of which increased as pH increased [24]. Therefore, it is easy for the positive charged Cu(II) to be adsorbed on the negative charged surfaces of CCPy, which is similar to pyrite. Thus, the sorption capacity for Cu(II) increased as the pH increased. The final pH of the solutions is also shown in Fig. 2. The values are below the precipitation pH values of the metal ions. Therefore, it can be stated that the mechanism governing the removal process could not be the metal precipitation.

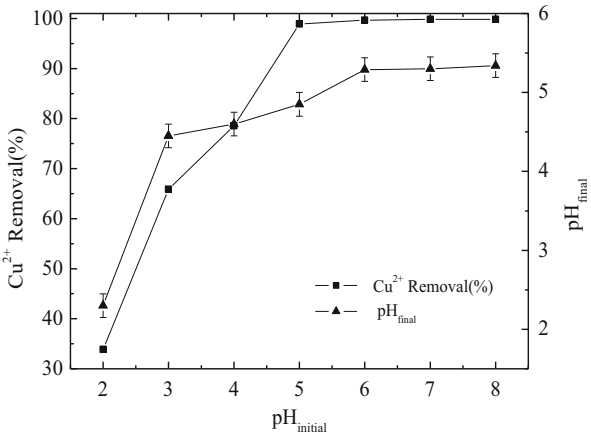

Fig. 2 Effect of pH on Cu (II) removal by CCPy

3.3 Effect of Contact Time

Cu(II) concentrations were measured at regular intervals and the results are shown in Fig. 3. The results showed that the removal efficiency increased with an increase of contact time. The sorption was rapid during the first 2 h and equilibrium was reached after 24 h. Hence, in the present work, 24 h was chosen as the equilibrium time. Generally, the removal rate of sorbent is rapid initially, but it gradually decreases with time until it reaches equilibrium. The removal rate of Cu(II) was higher in the beginning due to the larger surface area of the sorbent being favorable to the sorption of the Cu(II). Sulfur on the CCPy surface serves as an active center for Cu(II) that was adsorbed from the solution by bounding these centers. As the surface sulfur sites become exhausted, the rate of uptake is controlled by the rate of transport from the exterior to the interior sites of the sorbent particles. It is also relevant that, since active sulfur sites in a system have a fixed number and each active sites can sorb only one ion in a monolayer, the metal uptake by the sorbent surface will be rapid initially, slowing down as the competition for the decreasing availability of active sites intensified by the metal ions remaining in the solution [25].

3.4 Effect of Concentrations and Temperature

The batch sorption experiments were performed at different temperatures of 288, 298, and 308 K for the initial Cu(II) concentrations in the range of 5–100 mg/L at optimum pH of 5.5. The sorption capacity increased from 10 to 20 mg/g with the rise of reaction temperature from 288 to 308 K (Fig. 4). This is mainly due to the increase in surface activity suggesting that the sorption process is endothermic and higher temperature favors Cu(II) removal by CCPy. At the

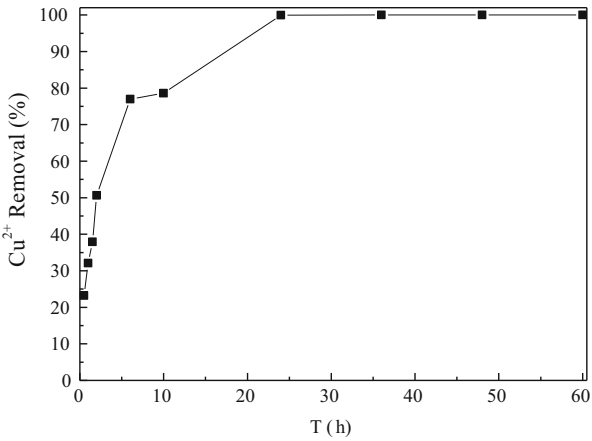

Fig. 3 Effect of contact time on Cu(II) removal by CCPy

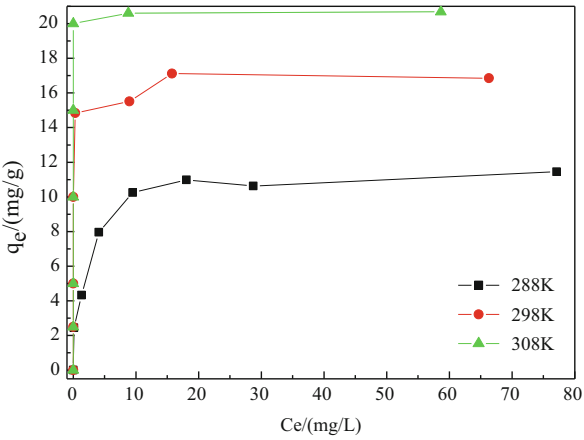

Fig. 4 Effect of initial Cu (II) concentrations and reaction temperatures on Cu (II) removal by CCPy

beginning of initial concentration (5 mg/L for 288 K, 20 mg/L for 298 K and 40 mg/L for 308 K), the removal percentage was very high (nearly 100 %) and the sorption capacity increased linearly. This could be explained by that the sorption was not saturated at low initial concentration. At a higher initial concentration, the ratio of initial number of Cu(II) to the available sorption surface area was higher than that of low initial concentration resulting in the increase of sorption capacity saturation.

3.4.1 Adsorption Isotherms

The most commonly used isotherm equations are Langmuir and Freundlich models which are used to find out the relation between the equilibrium concentrations of Cu (II) in liquid phase and in the solid phase [25, 26]. In this case, the experimental data obtained under various concentrations, and temperatures were plotted in linearized

Table 1 The parameters for Langmuir and Freundlich isotherms at different temperatures

	Langmuir equation			Freundlich equation		
Temperature/K	K_l (L/mg)	q_m	R^2	K_F	$1/n$	R^2
288	0.79	11.57	0.9988	1.30	0.2600	0.921
298	10.21	16.87	0.9990	0.31	0.0200	0.820
308	69.06	20.38	1.0000	0.32	0.0018	1.000

forms of Langmuir and Freundlich adsorption isotherms (Eqs. (2) and (3), respectively) (Table 1):

$$\frac{c_e}{q_e} = \frac{1}{K_l q_m} + \frac{c_e}{q_m} \tag{2}$$

$$\lg q_e = \left(\frac{1}{n}\right)\lg c_e + \lg K_F \tag{3}$$

Where q_e is the amount of metal adsorbed per specific amount of adsorbent (mg/g), C_e is the equilibrium concentration of the solution (mg/L), q_m is the maximum amount of metal ions required to form a monolayer (mg/g), and K_l is the Langmuir constants, K_F and $1/n$ are the Freundlich constants related to adsorption capacity and adsorption intensity, respectively. The Freundlich equilibrium constants were calculated from the intercept and the slope, respectively, of the linear plot of $\lg q_e$ versus $\lg c_e$ based on experimental data.

The experimental data of Cu(II) adsorption were regressively analyzed with the Langmuir and Freundlich isotherm models. The relative values calculated from the two models were listed in Table 2. It can be concluded from the constants that Langmuir model simulates the experimental data better than Freundlich. The fact that the Langmuir isotherm fitted the experimental data very well indicated that almost complete monolayer coverage of the adsorbent particles and chemisorption were considered as the main adsorption. The results of this study with CCPy on the sorption of Cu(II) were similar to the behavior of Cu(II) onto titanate nanofibers prepared by alkali treatment [27]. Moreover, CCPy has a limited sorption capacity, thus the adsorption could be better described by the Langmuir model rather than Freundlich model as an exponentially increasing adsorption is assumed in the Freundlich model.

3.4.2 Adsorption Thermodynamics

Thermodynamic parameters such as free energy (ΔG), enthalpy (ΔH) and entropy (ΔS) change of sorption can be evaluated from the following equations:

$$\Delta G = -RT\ln b \tag{4}$$

Table 2 Values of thermodynamic parameters for the reaction of Cu(II) on the CCPy

Temperature/K	$-\Delta G$/(KJ/mol)	ΔS/(KJ/mol)	ΔH/(KJ/mol)
288	5.30	0.66	145
298	12.75	0.66	145
308	18.60	0.66	145

$$\Delta G = \Delta H - T\Delta S \tag{5}$$

$$\ln b = \Delta S/R - \Delta H/RT \tag{6}$$

where $b = K_{\mathrm{Lqm}}$, is the equilibrium constant (L/mg), ΔG, ΔH, and ΔS are changes in Gibbs free energy (kJ/mol), enthalpy (kJ/mol), and entropy (J/mol/K), respectively. R is the gas constant (8.314 J/mol/K), and T is the temperature (K).

The values of ΔH and ΔS are determined from the slope and the intercept of the plots of $\log K_c$ versus $1/T$. The ΔG values were calculated using Eq. (3). Sorption of Cu(II) on CCPy increased when the temperature increased from 208 to 308 K, which is shown in Fig. 4. The process was thus endothermic in nature. The plots were used to compute the values of thermodynamic parameters (Table 2). The Gibbs free energy ΔG is small and negative but increases with increasing temperature, indicating that the sorption process led to a decrease in Gibbs energy. The negative ΔG value indicates that the process is feasible and spontaneous in the nature of sorption; positive ΔH value suggests the endothermic nature of sorption and the ΔS can be used to describe the randomness at the Cu–solution interface during the sorption. The thermodynamic parameters thus indicate that this sorption process can be used for the removal of Cu(II) ions by CCPy.

3.5 *Effect of Foreign Ion*

The results shown in Fig. 5 demonstrate that compared with the control experiment (100 % of Cu(II) removal), there was almost no interference for the Cu(II) sorption in the presence of foreign ions, except Fe^{2+} and NO^{3-}. The property of CCPy surface was changed by the additive Fe^{2+} which is up to 0.05 M, the oxidation of Fe^{2+} to Fe^{3+}, the mineral surface was covered by a layer of $Fe(OH)_3$ film to prevent further oxidation of mineral surface, thereby inhibiting the Cu(II) removal process. It also can be easily observed from the figure that the NO^{3-} can inhibit Cu (II) sorption on CCPy significantly and mainly due to the strong oxidizability of NO^{3-} in the weak acid solution. Thus, the higher the NO^{3-} concentration was, the worse the Cu(II) removal. The concentration of the common ions (Fe^{2+},SO_4^{2-}, etc.) in most AMD is lower than 0.01 M in reality; thus it showed that CCPy has great application prospect in dealing with AMD.

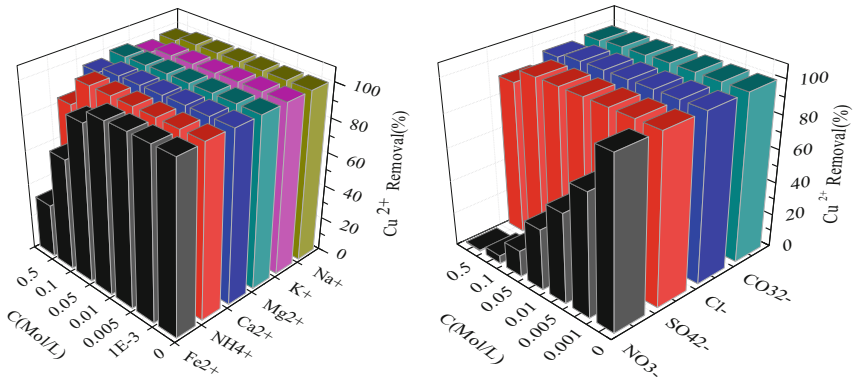

Fig. 5 Effect of ion strength on Cu(II) removal by CCPy

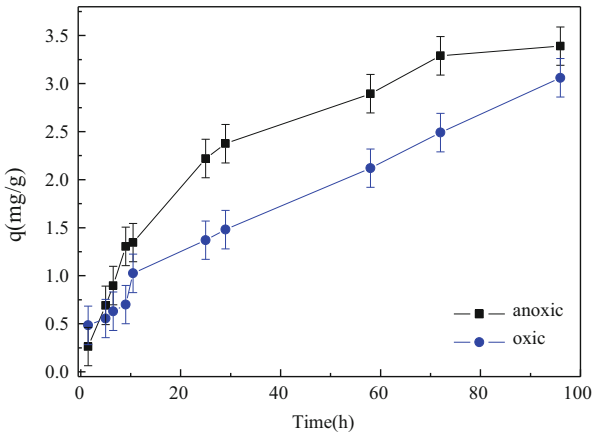

Fig. 6 Effect of DO on Cu(II) removal by CCPy

3.6 Effect of DO

3.6.1 Cu(II) Concentration

Figure 6 shows the effect of DO on Cu(II) uptake by CCPy. CCPy has great purification efficiency on Cu(II) wastewater treatment with removal capacity of about 3.0 mg/g under both oxic and anoxic conditions, indicating that the presence of DO has little effect on Cu(II) removal efficiency. However, the higher Cu (II) removal rate in the presence of oxygen could be due to the formation of ferric hydroxide, which has an adsorption capacity for Cu^{2+} [28].

4 Conclusions

Colloidal pyrite calcined in N_2 at 500 °C has the highest removal efficiency for Cu (II) in aqueous solutions. Cu(II) uptake was highly dependent on pH, and weak acidity promotes reaction. There is no significant effect with the addition of common ions in mine drainage into reaction system, indicating that CCPy has great application prospect in the processing of copper-containing wastewater and AMD.

References

1. Wei X, Viadero RC, Bhojappa JS (2008) Phosphorus removal by acid mine drainage sludge from secondary effluents of municipal wastewater treatment plants. Water Res 42:3275–3284
2. Cheng SA, Dempsey BA, Logan BE (2007) Electricity generation from synthetic acid-mine drainage (AMD) water using fuel cell technologies. Environ Sci Technol 41:8149–8153
3. Buzzia DC, Viegasb LS, Rodriguesc MAS, Bernardesb AM, Tenórioa JAS (2013) Water recovery from acid mine drainage by electrodialysis. Miner Eng 40:82–89
4. Lin YT, Huang CP (2008) Reduction of chromium (VI) by pyrite in dilute aqueous solutions. Sep Purif Technol 63:191–199
5. Descostes M, Schlegel ML, Eglizaud N, Descamps F, Miserque F, Simoni E (2010) Uptake of uranium and trace elements in pyrite (FeS_2) suspensions. Geochim Cosmochim Acta 74:1551–1562
6. Han DS, Batchelor B, Abdel-Wahab A (2012) Sorption of selenium (IV) and selenium (VI) onto synthetic pyrite (FeS_2): spectroscopic and microscopic analyses. J Colloid Interface Sci 368:496–504
7. Jeong HY, Han YS, Park SW, Hayes KF (2010) Aerobic oxidation of mackinawite (FeS) and its environmental implication for arsenic mobilization. Geochim Cosmochim Acta 74:3182–3198
8. Lu AH, Zhong SJ, Chen J, Shi JX, Tang JL, Lu XY (2006) Removal of Cr (VI) and Cr (III) from aqueous solutions and industrial wastewaters by natural clino-pyrrhotite. Environ Sci Technol 40:3064–3069
9. Ozverdi A, Erdem M (2006) Cu2+, Cd2+ and Pb2+ adsorption from aqueous solutions by pyrite and synthetic iron sulphide. J Hazard Mater 137:626–632
10. Jeong HY, Sun K, Hayes KF (2010) Microscopic and spectroscopic characterization of Hg (II) immobilization by Mackinawite (FeS). Environ Sci Technol 44:7476–7483
11. Erdem M, Ozverdi A (2006) Kinetics and thermodynamics of Cd (II) adsorption onto pyrite and synthetic iron sulphide. Sep Purif Technol 51:240–246
12. Coles CA, Rao R, Yong RN (2000) Lead and cadmium interactions with Mackinawite: retention mechanisms and the role of pH. Environ Sci Technol 34:996–1000
13. Chandra AP, Puskar L, Simpson DJ, Gerson AR (2012) Copper and xanthate adsorption onto pyrite surfaces: implications for mineral separation through flotation. Int J Miner Process 114–117:16–26
14. Awual MR, Yaita T, El-Safty SA, Shiwaku H, Suzuki S, Okamoto Y (2013) Copper (II) ions capturing from water using ligand modified a new type mesoporous adsorbent. Chem Eng J 221:322–330
15. Larous S, Meniai AH, Lehocine MB (2005) Experimental study of the removal of copper from aqueous solutions by adsorption using sawdust. Desalination 185:483–490
16. Integrated wastewater discharge Standard (1996) GB 8978-1996, China.

17. Chen TH, Yang Y, Chen D, Li P, Shi YD, Zhu X (2012) The structural evolution of heat-treated colloidal pyrite under inert atmosphere and its application for the purification of Cu (II) ion from wastewater. Environ Eng Manag 12(7):1411–1416.
18. Arnold RG (1967) Range in composition and structure of 82 natural terrestrial pyrrhotites. Can Mineral 9:31–50
19. Janzen MP, Nicholson RV, Scharer JM (2000) Pyrrhotite reaction kinetics: reaction rates for oxidation by oxygen, ferric iron, and for nonoxidative dissolution. Geochim Cosmochim Acta 64:1511–1522
20. Nicholson RV, Scharer JM (1994) Laboratory studies of pyrrhotite oxidation kinetics. Environ Geochem Sulfide Oxid 550:14–30
21. Thomas JE, Skinner WM, Smart RSC (2003) A comparison of the dissolution behavior of troilite with other iron (II) sulfides; implications of structure. Geochim Cosmochim Acta 67:831–843
22. Jackson E (1986) Hydrometallurgical extraction and reclamation. Wiley, New York
23. Ma W, Tobin JM (2004) Determination and modelling of effects of pH on peat biosorption of chromium, copper and cadmium. Biochem Eng J 18:33–40
24. Fornasiero D, Eijt V, Ralston J (1992) An electrokinetic study of pyrite oxidation. J Colloid Interface Sci 62:63–73
25. Langmuir I (1916) The constitution and fundamental properties of solids and liquids. J Am Chem Soc 38:2221–2295
26. Freundlich HMF (1906) Uber die adsorption in lasungen. J Phys Chem 57:385–470
27. Li N, Zhang LD, Chen YZ, Tian Y, Wang HM (2011) Adsorption behavior of Cu(II) onto titanate nanofibers prepared by alkali treatment. J Hazard Mater 189:265–272
28. Martinez CE, Mcbride MB (1998) Solubility of Cd^{2+}, Cu^{2+}, Pb^{2+}, and Zn^{2+} in aged coprecipitates with amorphous iron hydroxides. Environ Sci Technol 32:743–748

N Reagents in the Reverse Flotation of Carbonate-Containing Iron Ores

Wanzhong Yin, Jizhen Wang, and Longhua Xu

Abstract The influence of pulp pH, dispersants, and auxiliary collectors on reverse flotation of carbonate-containing iron ores was explored. Interactions between iron ores and quartz were theoretically analyzed by flotation solution chemistry and DLVO theory. The results indicated that the iron concentrate grade improved sharply when pH increased from 11.0 to 12.0 but changed unobviously when pH was larger than 12.0, which was related to solution chemistry of siderite and interactions among particles. Sodium tripolyphosphate was an effective dispersant and sodium dodecyl sulfate was an effective auxiliary collector of KS-III. Both recovery and grade were enhanced by the action of sodium dodecyl sulfate or sodium tripolyphosphate when pH was 12.0.

Keywords Auxiliary collector • Carbonate-containing iron ores • Reverse flotation • Sodium dodecyl sulfate • Sodium tripolyphosphate

1 Introduction

China's iron ore imports reached 686 million tons in 2011, but more than 60 % of the iron ore relied on foreign supply. At present, due to impure iron-ore deposits, there are problems that the exploitation and utilization of domestic iron ore resource are low grade, low recovery, high smelting cost, and serious metal loss of iron concentrate.

Iron ore in Anshan District contains more than 3 % of siderite, which is very difficult to deal with [1]. Stepped-flotation process was investigated by Yin et al. to separate iron ore from silicate minerals [2]. Mineral dissolution is one of the main causes of interactions among minerals, such as mineral surfaces conversion [3–7], activation caused by dissolved ions [8], and so on. Various forces among particles

W. Yin (✉)
School of Resource and Civil Engineering, Northeastern University, Shenyang, Liaoning, P.R. China
e-mail: jizhenwang@126.com

J. Wang • L. Xu
Key Laboratory of Solid Waste Treatment and Resource Recycle Ministry of Education, Southwest University of Science and Technology, Mianyang, Sichuan, P.R. China

F. Dong (ed.), *Proceedings of the 11th International Congress for Applied Mineralogy (ICAM)*, Springer Geochemistry/Mineralogy,
DOI 10.1007/978-3-319-13948-7_45

are other causes of interactions among minerals [9–12], such as carrier flotation, selective flocculation, and agglomeration flotation. Mineral particles, reagents, and pulp environment complexly interact with each other. The effective way to solve the problem of carbonate-containing iron ores is to study the chemical and physical mechanisms for the microlevel control over interactions among particles and expand the floatability differences by collectors and modifiers.

Herein, we aim at weakening the negative effects of siderite on flotation by using simple direct-reverse flotation, focusing on mineral flotation chemistry and dispersion, and providing the theories foundation for direct-reverse flotation of refractory carbonate-containing iron ores.

2 Materials and Methods

2.1 Materials

The carbonate-containing iron ore was from Anshan Mining Industry Corp and was concentrated by magnetic separation. The distribution of particle sizes was listed in Table 1. Since the particles were very fine, we concluded that dispersants were very important for direct-reverse flotation of carbonate-containing iron ores.

The chemical component for the test material was listed in Table 2. The contents of TFe and SiO_2 were 42.88 % and 33.60 %, respectively. Based on X-ray powder diffraction (XRD) (Fig. 1) measurement and Table 3 results, the main compositions of the iron ore were magnetite (17.04 %), hematite (70.24 %), and siderite (9.19 %).

2.2 Reagents

Sodium hydroxide (analytical grade) was used as pH modifier. Calcium oxide (analytical grade) was used as an activator of quartz. Starch (industrial grade) was used as an inhibitor of iron ore. Sodium silicate (industrial grade), sodium hexametaphosphate (analytical grade), tripolyphosphate, and sodium

Table 1 Particle size distribution of test material

Particle size (μm)	+48	48–37	37–23	−18
Distribution (%)	6.74	0.72	24.57	36.40

Table 2 Analytical results of chemical component for test material (mass fraction, %)

TFe	FeO	CaO	MgO	Al_2O_3	SiO_2	S	P
42.88	6.29	0.31	0.45	0.81	33.60	0.029	0.075

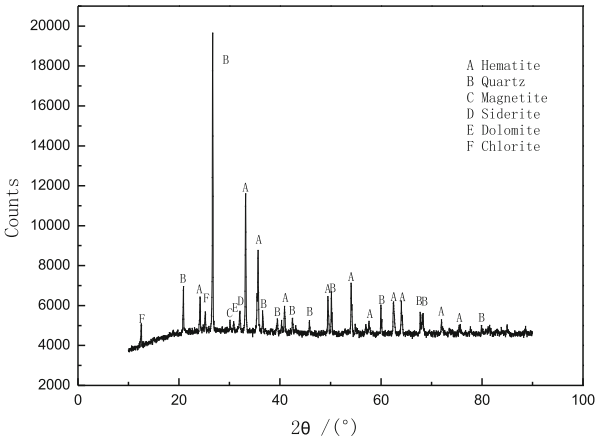

Fig. 1 XRD pattern of test material

Table 3 Minerals composition of test material (mass fraction, %)

Magnetite	Hematite	Ferrosilite	Siderite	Iron sulfide
17.04	70.24	2.12	9.19	1.41

polyphosphate were used as dispersants. Sodium dodecylsulfate and sodium dodecyl benzene sulfonate were analytical grade and were used as auxiliary collectors of KS-III.

2.3 Flotation Experiment

The direct-reverse flotation tests were performed in a 500 mL XFG-III single flotation cell. The flotation was prepared by putting 167 g solid sample and 500 mL water (45 °C) into the cell and then adding sodium hydroxide, various dispersants, starch (2,200 g/t), CaO (600 g/t), and KS-III (1,000 g/t) in turn. Flotation time was 4.5 min. Foam products and tank products were dried and weighed respectively and then got the grade and recovery of iron. The pulp temperature was maintained at around 40 °C. The flow sheet of flotation was shown in Fig. 2.

2.4 Measurement of Zeta Potential

Pure minerals were ground to the desired size (less than 5 μm), and then 0.01 mol/L suspension was prepared by adding distilled water. After pH value was adjusted, zeta potentials were measured by a Brookhaven Zeta Plus Zeta-potential analyzer.

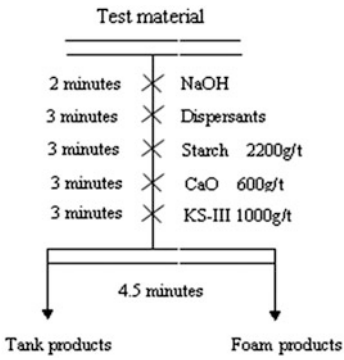

Fig. 2 The flow sheet of test

All measurements were conducted in a 0.1 mol/L KNO_3 background electrolyte solution.

3 Results and Discussion

3.1 Effects of Sodium Hydroxide on Direct-Reverse Flotation of Carbonate-Containing Iron Ores

Figure 3 showed the effects of hydroxide on the iron grade and recovery of concentrate. It indicated that the iron concentrate grade improved sharply when pH increased from 11.0 (the concentration of sodium hydroxide was 1,000 g/t) to 12.0 (the concentration of sodium hydroxide was 2,000 g/t) but changed unobviously when pH was larger than 11.8 (the dosage of sodium hydroxide is 1,600 g/t). By comprehensive analysis of the iron grade and recovery of concentrate, the optimum concentration of sodium hydroxide was 2,000 g/t when pH value was 12.0.

Figure 4 indicated that the highest recovery of quartz was obtained with the action of calcium ions when pH value was 11.3, but the iron grade increased when pH was larger than 11.3 (Fig. 3). We suspected that there were other factors that affected the recovery of iron grade.

3.2 Effects of Inorganic Dispersant on Direct-Reverse Flotation of Carbonate-Containing Iron Ores

In Fig. 5, we found that when the concentration of sodium silicate was less than 400 g/t, the iron grade of concentrate rose with increase in the amount of sodium silicate. However, when the concentration of sodium silicate was more than 400 g/t,

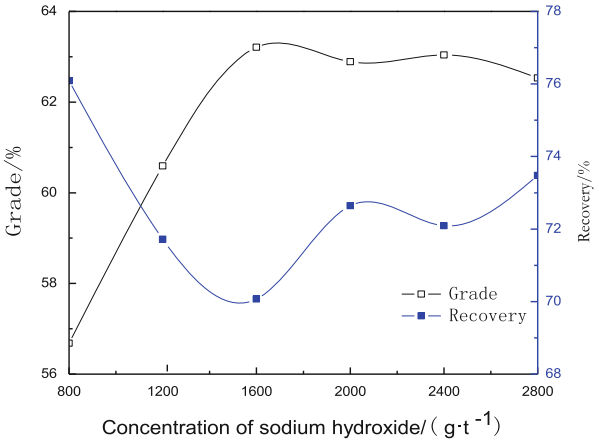

Fig. 3 Effects of sodium hydroxide on reverse flotation of carbonate-containing iron ores

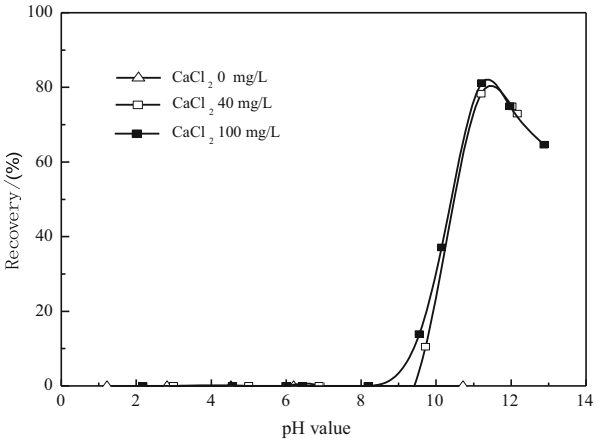

Fig. 4 Effects of $CaCl_2$ on the flotation of quartz

the iron grade of concentrate declined with increase in the amount of sodium silicate. Iron recovery of concentrate showed the opposite trend of grade.

Figure 6 presented that sodium hexametaphosphate can effectively promote the iron concentrate grade, but it also can significantly reduce the iron recovery of concentrate.

Figure 7 showed that when the concentration was less than 50 g/t, both the iron grade and recovery of concentrate increased with increase in the concentration of sodium tripolyphosphate. When the concentration of sodium tripolyphosphate was more than 50 g/t, the iron recovery of concentrate reduced considerably.

As shown in Fig. 8, the iron recovery of concentrate reduced significantly with increase in the concentration of sodium polyphosphate. When the concentration of sodium polyphosphate was less than 200 g/t, the iron concentrate grade increased with the action of sodium tripolyphosphate.

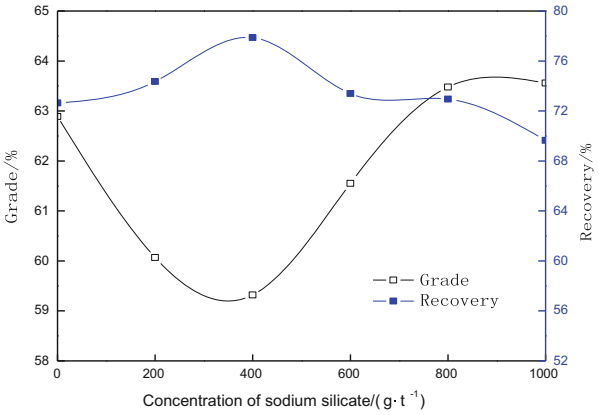

Fig. 5 Effects of sodium silicate on reverse flotation of carbonate-containing iron ores

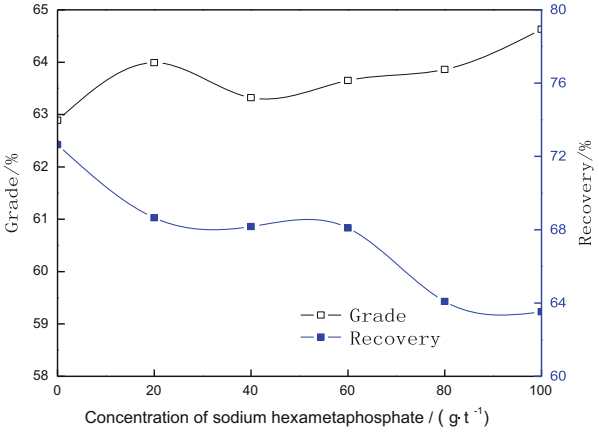

Fig. 6 Effects of hexametaphosphate on reverse flotation of carbonate-containing iron ores

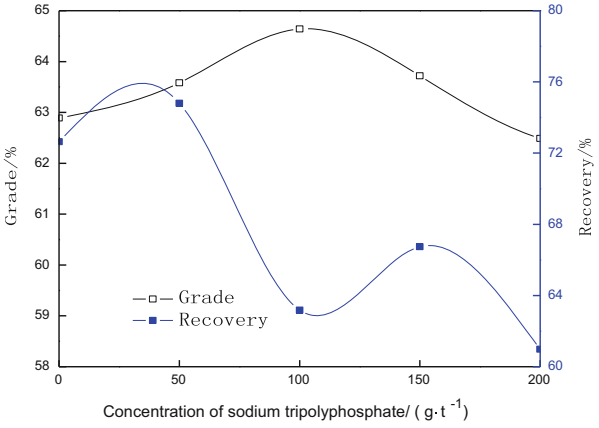

Fig. 7 Effects of sodium tripolyphosphate on reverse flotation of carbonate-containing iron ores

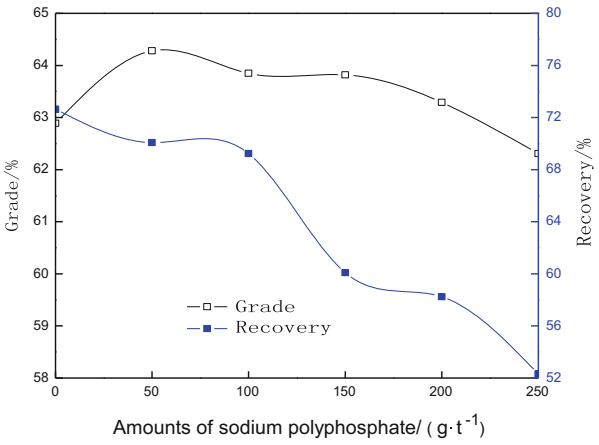

Fig. 8 Effects of sodium polyphosphate on reverse flotation of carbonate-containing iron ores

To sum up, the most effective dispersant was sodium hexametaphosphate, but its concentration should be less than 50 g/t.

3.3 Effects of Auxiliary Collectors on Reverse Flotation of Carbonate-Containing Iron Ores

As shown in Figs. 9 and 10, sodium dodecyl sulfate used as an auxiliary collector of KS-III could be better than sodium dodecyl benzene sulfonate because of hindrance. Both iron grade and recovery can be improved by adding sodium dodecyl sulfate. Therefore, sodium dodecyl sulfate can be used together with KS-III in reverse flotation of carbonate-containing iron ores.

3.4 Mechanism Research

3.4.1 Effects of Minerals Solution on Direct-Reverse Flotation of Carbonate-Containing Iron Ores

Influence of saline minerals on flotation was great, and the main factors included pulp pH, mineral activation, and performances of collectors [8].

Flotation solution chemistry renders that ΔG of ferrous ions reacting with oleic acid ion is minimal when pH remains between 6.0 and 10.0 [8]. ΔG value rises significantly when pH value is larger than 10. Experiments also found that silicate minerals cannot be activated by ferrous ion. Therefore, silicate minerals cannot be activated by saline minerals when $\mathrm{pH} > 11.0$.

Distribution of ferrous ion and polyhydroxy compound is as follows:

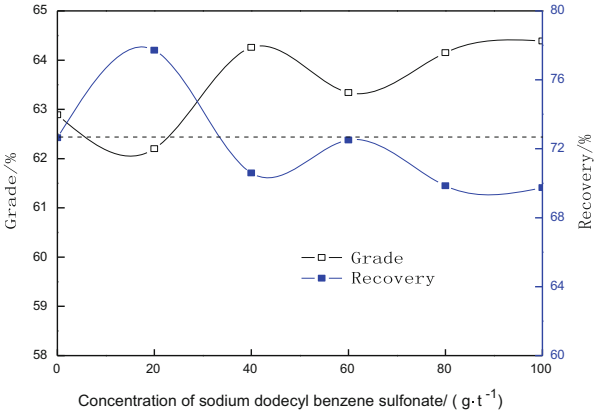

Fig. 9 Effects of sodium dodecyl benzene sulfonate on reverse flotation of carbonate-containing iron ores

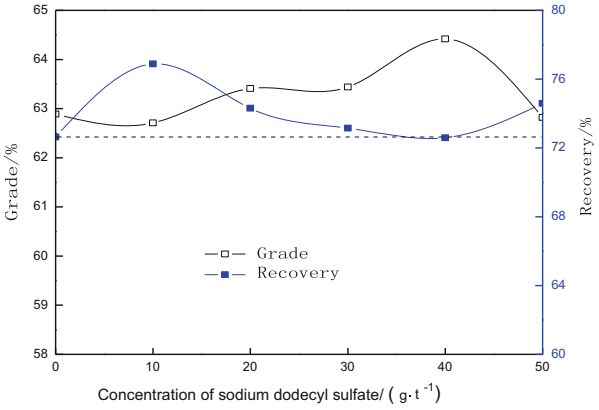

Fig. 10 Effects of sodium dodecyl sulfate on reverse flotation of carbonate-containing iron ores

$$\Phi_{Fe^{2+}} = \frac{100}{1 + \sum_{i=1}^{4} \beta_i [OH^-]^i} (\%) \quad (1)$$

$$\Phi_{Fe(OH)_j^{2-j}} = 100 \frac{\beta_j [OH^-]^j}{1 + \sum_{i=1}^{4} \beta_i [OH^-]^i} (\%) \quad (2)$$

The relationship of pH value and polyhydroxy compound was shown in Fig. 11.

The theoretical PZC of Fe $(OH)_2$ is 11.2, PZC of hematite is 7.8, and PZC of quartz is 2.0–3.0. Figure 11 showed that when pH value was larger than 7.8 but less than 11.2, hematite and quartz adsorbed polyhydroxy compound of ferrous ions because of electrostatic effect, and the difference of mineral floatability became small. When pH was larger than 11.2, the electrical charges of quartz, hematite, and $Fe(OH)_2$ remained the same, and the nonselective adsorption ability of $Fe(OH)_2$ significantly weakened, and the difference of mineral floatability increased.

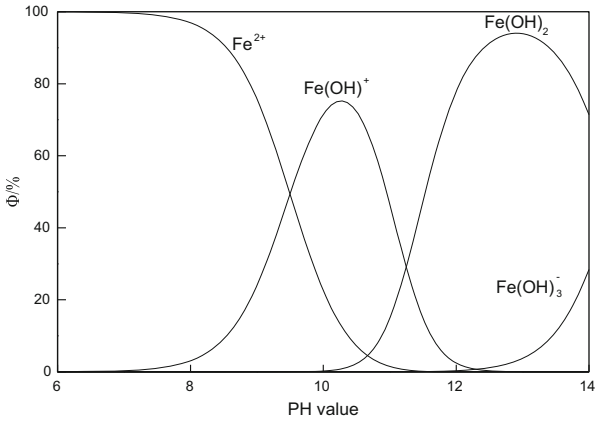

Fig. 11 The relationship of distribution of iron ion and polyhydroxy compound and pH

Therefore, flotation results would significantly improve when pH value was larger than 11.2, which was in accordance with the result in Fig. 3.

3.4.2 Calculation of Interactions Between Particles

The DLVO theory model is as follows. Take the energies of electrostatic interaction and Van der Waals interactions into consideration:

$$V_T = V_W + V_E \tag{3}$$

where V_T is the total interaction energy; V_W is Van der Waals interaction energy; and V_E is electrostatic interaction energy; and

$$V_W = -\frac{A_{132}}{6H}\frac{R_1 R_2}{R_1 + R_2} \tag{4}$$

where $A_{132} = \left(\sqrt{A_{11}} - \sqrt{A_{33}}\right)\left(\sqrt{A_{22}} - \sqrt{A_{33}}\right)$

$$V_E = \frac{\pi \varepsilon_a R_1 R_2}{R_1 + R_2}\left(\varphi_{01}^2 + \varphi_{02}^2\right)\left[\frac{2\varphi_{01}\varphi_{02}}{\varphi_{01}^2 + \varphi_{02}^2}p + q\right] \tag{5}$$

where,

$$p = \ln\left(\frac{1 + \exp(-\kappa H)}{1 - \exp(-\kappa H)}\right)$$

$$q = \ln(1 - \exp(-2\kappa H))$$

Plugging the parameters into Eq. (3), and

$$V_T = V_E + V_W = a[b\ln(1 + e^{-0.104H})/\ln(1 - e^{-0.104H}) + \ln(1 - e^{-0.208H})] - c/H \quad (6)$$

where a, b, and c are constants. The radius of siderite particle R_1 is 5 μm, the radius of hematite and quartz particles R_2 is 38 μm; κ is the thickness of the electric double-layer, $\kappa = 0.104\ \text{nm}^{-1}$; ε_0, ε_r represent the vacuum dielectric constant and the relative dielectric constant of the continuous phase, with given value of $6.95 \times 10^{-10}\ \text{C}^2/(\text{J·m})$, and H represents the distance between particles; φ_1 and φ_2 are the surface potential (mV), and a dynamic potential can be used; A represents the effective Hamaker constant [13], and for quartz $A_1 = 5.0 \times 10^{-20}$ J, for hematite $A_2 = 23.2 \times 10^{-20}$ J, and for water $A_3 = 4 \times 10^{-20}$ J. In highly alkalized solution, the surface of sideriteis similar to $Fe(OH)_2$ dissolution and Fe(II) can be oxidized to Fe(III) [14], which facilitated the dissolution. The A_4 of siderite is approximately equal to that of $Fe(OH)_3$ and the value is 18.0×10^{-20} J.

Zeta potentials (ζ) were measured, and the values of relative parameters in Eq. (6) were listed in Table 4.

Plugging the data in Table 4 into Eq. (6), we could draw the interaction energy, as shown in Figs. 12 and 13.

As shown in Figs. 12 and 13, the total interaction energy between siderite and quartz was higher than that between siderite and hematite. Therefore, the aggregation of siderite and hematite occurred more easily than siderite and quartz. Energy barrier was very low and aggregation occurred easily when the pH value was low, and it was difficult to separate iron ores from quartz. It can also be seen in Figs. 12 and 13 that pH value was important for dispersion of particles, especially when pH value reached 11.0, the energy barrier was high enough to prevent the aggregation of particles. This paper has obtained an iron concentrate grading of 63 % at a recovery of 71 % after one rough dressing when pulp pH value was 11.0. For the same ores, an iron concentrate grading of 62.89 % at recovery of 72.64 % was obtained after one rough dressing without any dispersants when the pH value was 12.0 (as shown in Fig. 1).

Table 4 The values of parameters in Eq. (6)

pH value	8.000	9.000	10.000	11.000
ζ quartz (mv)	−50.000	−58.000	−70.00	−75.000
ζ siderite (mv)	−18.000	−26.000	−32.00	−37.000
ζ hematite (mv)	−24.000	−29.000	−39.00	−46.000
$a_{s\text{-}q}$	2.970	3.860	5.713	6.7430
$b_{s\text{-}q}$	0.637	0.747	0.756	0.793
$c_{s\text{-}q}$	0.390	0.390	0.390	0.390
$a_{s\text{-}q}$	0.868	1.463	2.454	3.365
$b_{s\text{-}q}$	0.960	0.994	0.981	0.977
$c_{s\text{-}q}$	4.650	4.650	4.650	4.650

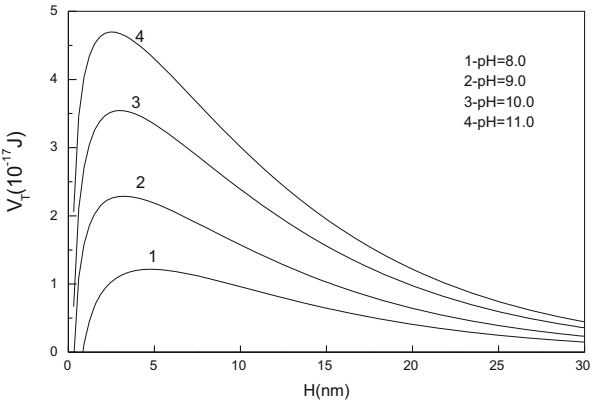

Fig. 12 Interaction energy between siderite and quartz

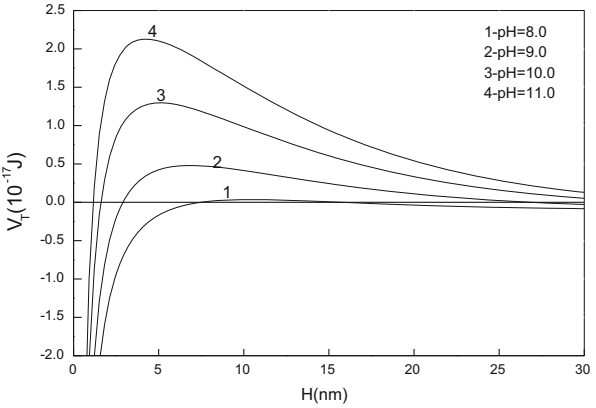

Fig. 13 Interaction energy between siderite and hematite

4 Conclusions

1. Direct-reverse flotation of carbonate-containing iron ores was feasible. Pulp pH was one of the most important factors. Iron concentrate grade improved sharply when pH increased from 11.0 to 12.0 but changed unobviously when pH was larger than 12.0. Iron concentrate grade of 62.89 % at a recovery of 72.64 % can be obtained after one rough dressing without any dispersants when pulp pH was 12.0.
2. Influence of inorganic dispersant on direct-reverse flotation of carbonate-containing iron ores was complicated. Flotation cannot be improved with the action of sodium silicate. Sodium hexametaphosphate and sodium polyphosphate can improve the grade but reduce the recovery. Both recovery and grade rose with the action of sodium tripolyphosphate, but the concentration

should be less than 50 g/t. Sodium dodecylsulfate was effectively auxiliary collector of KS-III, and both recovery and grade rose with the action of sodium dodecylsulfate.

3. Mechanism research showed that when pH value reached 11.0, the energy barrier was high enough to prevent the aggregation of particles. When pH was larger than 11.0, nonselective adsorption ability of $Fe(OH)_2$ would significantly weakened and the difference of mineral floatability enhanced.

References

1. Zhang ZY, Lu ZF, Yin WZ et al (2008) Influence of the siderite in Donganshan iron ore on reverse flotation. Metal Mine 10:52–55
2. Zhang M, Liu MB, Yin WZ et al (2007) Investigation on stepped-flotation process for Donganshan carbonate-containing refractory iron ore. Metal Mine 9:62–64
3. Hu YH, Wang DZ (1992) Dissolution/surface property of salt-type minerals and design of schemes of flotation separation. J Cent South Univ 23(3):273–279
4. Qin QW, Hu YH (1999) Dissolution of sparingly soluble minerals and its effect on floatability of minerals. Min Metall Eng 19(2):30–33
5. Shen HT, Gong ZG (1996) Effect and the way to eliminating the influence of calcite on the flotation of scheelite and mechanism research. Hunan Nonferrous Metals 12(2):36–39
6. Hu YH, Xu J, Luo CQ, Yuan C (1995) Solution chemistry studies on dodecyl-amine flotation of smithsonte/calcalcite. J Cent South Univ 26(5):589–594
7. Luo N, Zhang GF, Feng QM et al (2012) Study on the flotation behavior and mechanism of rhodochrosite and calcite. Nonferrous Metals 4:41–45
8. Wang DZ, Hu YH (1987) Solution chemistry of flotation. Hunan Science and Technology Press, Changsha, pp 271–274
9. Zhang GF, Wang L, Feng QM et al (2010) Influence factors for interparticle interaction between titanaugite and ilmenite. Chin J Nonferrous Metals 20(2):339–345
10. Zhang GF, Wang L, Feng QM et al (2009) Effect of titanaugite on flotation behavior of ilmenite. Chin J Nonferrous Metals 19(6):1124–1129
11. Qin WQ, Qiu GZ, Long HZ (1996) Study on hydrophobic flocculation flotation of fine rhodochrosite and quartz. Metal Mine 9:19–22
12. Ren X, Zhang HE (1993) Interaction of dissolved components on separation flotation of fine-grained rhodochrosite and apatite. J Beijing Gen Res Inst Min Metall 2(4):24–31
13. Qiu GZ, Hu YH, Wang DZ (1993) Interactions between particles and flotation of fine particles. Central South University of Technology Press, Changsha, pp 129–131
14. Yang B (2010) Separation process of siderite and hematite and mechanism research. Central South University, Changsha

The Study on Genotoxicity of $PM_{2.5}$ Mineral Dusts to A_{549} Cells

Yali Zeng, Tingting Huo, Faqin Dong, Limin Wang, and Jianjun Deng

Abstract Object: Detecting the influence of six main ingredients of $PM_{2.5}$ mineral dusts on the A_{549} cell morphology, proliferation inhibition rate, micronuclei, and DNA damage to explore the genotoxicity of $PM_{2.5}$ mineral dusts.

Methods: (1) After exposure to six kinds of dusts of 200 μg mL^{-1} concentration for 24 h, the morphology of A_{549} cells was observed with Wright-Giemsa staining. (2) After exposure to different concentrations of mineral dusts for 24 h, the proliferation inhibition rate of A_{549} cells was detected by MTT assay. (3) Cells were exposed to $PM_{2.5}$ mineral dusts at a concentration of 200 μg mL^{-1} for 24 h. After Wright-Giemsa staining, the rates of micronucleus cells were counted under oil immersion lens. (4) Observe Comet phenomenon by single-cell gel electrophoresis (SCGE). The degree of DNA damage was observed by OTM.

Results: (1) Compared to the control group, membrane destruction, nuclear pyknosis, and mineral surface adhesion were mainly seen in the Sericite group and Albite group. In the Quartz group and Montmorillonite group, Cell gap grew bigger, which was loosely arranged and shrank gradually than control group, showing the absorption of a large number of minerals on the cell surface. (2) The proliferation inhibition rate of the six kinds of dusts to A_{549} cells was (in descending order): KWC-M > Nano-SiO_2 > KWC-S > KWC-Q > KWC-A > KWC-C. The dust concentration was positively related to the inhibition of cell proliferation rate. (3) As the dusts' concentration increased, the incidence of micronuclei gradually increased. The rate was positively correlated to exposure concentration. (4) The six mineral dusts can damage DNA of the A_{549} cells by dose–response relationship. The higher concentration of the mineral dusts was, the more obvious the DNA damage became.

Project supported by the State Key Program of National Natural Science of China (NO. 41130746), and the State On national natural fund project (NO. 41472046).

Y. Zeng (✉) • L. Wang • J. Deng
The Medical Laboratory, 404 Hospital, Mianyang, Sichuan 621000, P.R. China
e-mail: 631734429@qq.com

T. Huo • F. Dong
School of Environmental Resource and Engineering, SWUST, 59 Qinglong Road, Mianyang, Sichuan 621010, P.R. China

F. Dong (ed.), *Proceedings of the 11th International Congress for Applied Mineralogy (ICAM)*, Springer Geochemistry/Mineralogy,
DOI 10.1007/978-3-319-13948-7_46

Conclusion: The six main ingredients of the $PM_{2.5}$ mineral dusts can change A_{549} cell morphology in different degrees, improve proliferation inhibition rate of the cells, increase the number of micronuclei cells, and damage DNA. Then we come to the conclusion that $PM_{2.5}$ mineral dusts can change the genotoxicity of the cells possibly.

Keywords Genotoxicity • Mineral dusts • $PM_{2.5}$

1 Introduction

As air pollution has become one of the primary risk factors that affect public health, increasing importance has been attached to it. $PM_{2.5}$ respirable dust has small particle size but large surface area. It can come into the trachea and bronchi with the person's breathing, then into the alveoli and the blood, which could affect human health seriously [1]. $PM_{2.5}$ has become a hot spot and frontier in the field of international air pollution. The major research has been focused on the organic components that adhere to the particles and hypothesis of the pathogenic heavy metal ions; however, as a main component of the dust, the mineral particles themselves are also the important pathogenic factors. It is also unknown about the biological genetic toxicity of $PM_{2.5}$ grade mineral particles at home and abroad. In this chapter, we selected six major components of $PM_{2.5}$ level mineral dust as the research object, using morphological method, MTT, micronucleus test, and comet assay to study cell genotoxicity of the dust particles and reveal potential biological genetic hazards of $PM_{2.5}$ grade mineral dusts.

2 Materials and Methods

2.1 Materials

2.1.1 Cell Source

A_{549} cells are from human small cell carcinoma, which are bought from biomedical laboratories of Western China Medical Center of Sichuan University.

2.1.2 $PM_{2.5}$ Level of Mineral Dusts

Nano silica dust (Nano-SiO_2), Albite dust (KWC-A), Nano calcite dust (KWC-C), Nano quartz dust (KWC-Q), Nano Sericite dust (KWC-S), and Nano-montmorillonite (KWC-M) are all provided by Southwest University of Science and Technology.

2.1.3 Reagents

Improved RPMI 1640 culture medium and fetal bovine serum (Hyclone, America); MTT, penicillin streptomycin, and 0.25 % trypsin (Biyuntian, Jiangsu); Automatic enzyme immunoassay instrument (Thermo Multiskan, America); CO_2 incubator (Thermo electron corporation, America); Inverted microscope (Chongqing optical instrument factory); ultra-low-temperature–high-speed centrifuge (Thermo electron corporation, America); Horizontal planet ball mill (Lianyungangchunlong, Jiangsu); Malvin laser particle size analyzer (Malvin instrument company, UK); and Fluorescence microscopy (Olympus, Japan).

2.2 Methods

2.2.1 Experimental Dust and Its Suspension Preparation

First, use the Horizontal ball mill for 10 h to break the mineral, clean, use the Malvern laser particle size analyzer to measure granularity; then get suction filtered, dry it. Grind the drying sample again through 200 mesh package for use. Before the test, we dry the mineral in an oven at 110 °C and radiate it under the UV light for 24 h. Use the serum-free medium to compound mineral dust, do swirl mixing for 30 min, then make suspension, there's no particle reunion after measurement, and the average particle diameter is less than 2.5 μm.

2.2.2 Wright-Giemsa Staining to Observe Cell Morphology

Take the logarithmic growth phase cells, adjust the concentration of 1×10^5/mL, and seed the cells to a culture dish which contains coverslips. Culture for 24 h, after the cells adhered, add drought-disinfected dust to the culture dish respectively, make a final concentration of 200 μg mL^{-1}, and make negative control group. Remove the coverslips after another 48 h, gently wash by PBS buffer, dry, fix, do Wright-Giemsa staining for 10 min, wash by PBS, allow for natural drying, and use oil microscope to observe.

2.2.3 Thiazolyl Blue (MTT) Assay to Detect Cell Viability

Take the logarithmic growth phase cells, adjust the concentration of 1×10^5/mL, and seed in 96-well plates, at 37 °C with 5 % CO_2 for 24 h. Discard the culture medium after the cells adhered, add the serum-free mineral dust suspension, make a final concentration of 50–400 μg mL^{-1}, continue incubation for 24 h, add 20 μL MTT solution to each well of the culture plate, culture for 2 h, then suck out the culture medium from each well, add 200 μL dimethyl sulfoxide, mix with shaking,

measure wavelength of 490 nm, measure the absorbance of each well of the culture plate by Automatic enzyme immunoassay instrument, use the relative survival rate of the cells as experimental results, and calculate according to the following formula.

$$\text{Cell viability } \% = \text{the exposed mineral dust group(OD)} - \text{the mineral dust group(OD)}/\text{the control group(OD)} \times 100\ \% \quad (1)$$

2.2.4 Micronucleus Test

Take the logarithmic growth phase cells, adjust the concentration of 1×105/mL, seed in the culture dish for filming at 37 °C, with 5 % CO_2 for 24 h. Discard the culture medium after the cells adhered, add six different serum-free mineral dust suspensions, make a final concentration of 200 μg mL^{-1}, add cell culture medium to the negative control group, add 200 μg mL^{-1} Cyclophosphamide (CP) to the positive control group, go on culturing for 24 h, wash by PBS, dry naturally, use the fixatives (methanol and formaldehyde in a volume ratio of 3:1) to fix as long as 30 min, use Wright-Giemsa staining to observe A_{549} cell morphology by the oil microscope, select 3,000 cells of each slide, count the number of cells containing micronucleus, and express results by ‰ (Fig. 1).

$$\text{FMN} = \text{the number of cells containing the micronucleus}/\text{the total number of cells observed} \times 1,000\ \% \quad (2)$$

2.2.5 Single-Cell Gel Electrophoresis Experiments

Expose the cells to the suspension of mineral dusts (100 μg mL^{-1}) for 48 h, digest the cells with 0.25 % trypsin, move it to the centrifuge tube, use the centrifugation

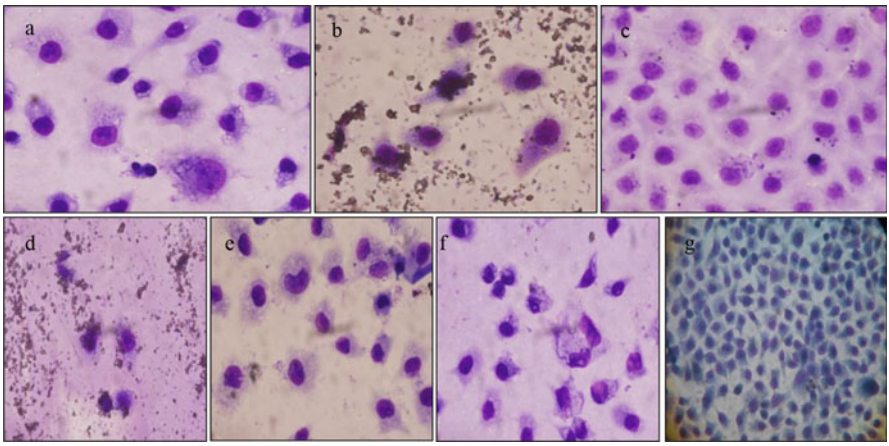

Fig. 1 A_{549} cell treated dusts for 24 h dying Wright-Giemsa staining (10 × 100). (**a**) Nano-SiO_2, (**b**) KWC-Q, (**c**) KWC-C, (**d**) KWC-M, (**e**) KWC-S, (**f**) KWC-A, (**g**) Negative control cells

of 1.0×10^3 r min^{-1} per 10 min, discard the supernatant, resuspend in PBS to 4×10^5/mL, and then get the cell suspension. Take 25 μL of cell suspension, adding 75 μL to preheated 37 °C 0.75 % low melting point agarose, shop the glue after mixing, coverslip immediately, cure for 5 min at 4 °C, remove coverslip, then immerse the slides in lysis buffer, and then do 4 °C cracking for 1.5 h in the dark. Put the slides into the electrophoresis tank, helicase 30 min in electrophoresis buffer, cryogenic dark electrophoresis for 20 min, electrically neutralize to an electrically neutral, dry the slides, use fluorescent staining solution to dye 20 min, observe with fluorescence microscope at excitation wavelength 549 nm, randomly select 100 cells comet image from every piece of slide, use CASP comet analysis software to analyze the comet images, tail length, tail moment (OTM), the rate of tail DNA (*T%*) as the main analysis indicators, and analyze the results by SPSS software.

$$\begin{aligned} \text{OTM} = {} & \text{cells in the tail of comet DNA}\% \\ & \times \text{the center of the head to the tail center distance} \end{aligned} \tag{3}$$

OTM value can more comprehensively reflect the degree of DNA damage than simply using the length of the head length and tail length indicators.

2.2.6 Statistical Analysis

Use $\bar{x} \pm s$ to represent experimental data, EXCEL and SPSS 19.0 software for calculations and statistical analysis, and use single-factor ANOVA analysis for significant test.

3 Results

3.1 Wright-Giemsa Staining for Observation of Morphological

Through 200 μg mL^{-1} mineral suspension for 24 h to treat A_{549} cells. There're more cells in the negative control group, spindle-shaped, or polygon, membrane integrity, ucleoplasm clearly, be round or oval-shaped. There're little cells in quartz and montmorillonite group, the cytoplasm is loose or chromatin is pyknosis with different degrees of mineral particles adsorption on cell surface. In the sericite and albite group, the cell membrane is not completed and karyopyknosis, and there's an increase in the number of dead cells. Different dust groups could cause damage to the morphological properties to varying degrees; montmorillonite and quartz groups cause the largest destruction to the cell morphology, whereas albite and sericite group causes minimum.

3.2 MTT Detects Cell Proliferation Inhibition Rate

Different concentrations of dust act on A_{549} cells for 24 h; the growth-inhibitory effects on A_{549} cells between each mineral dust are different, calcite can promote cell proliferation, the remaining dust cells have different levels of inhibition effect on the cells. Montmorillonite has the strongest inhibition of cell proliferation rate; at 50 μg mL^{-1}, cell mortality reached 46.8 %; at 200 μg mL^{-1}, cell survival rate was only 18.7 %. Through the dust group act on A_{549} cells, the inhibition rate is in descending order: KWC-M > Nano-SiO_2 > KWC-S > KWC-Q > KWC-A > KWC-C, inhibition of cell proliferation increased with dust concentration as seen in Table 1.

3.3 Micronucleus Test for Detection of Chromosomal Changes

Six concentrations of dust act on A_{549} cells for 48 h; in addition to montmorillonite exposed group, the micronucleus rate of remaining dust group is statistically significant ($P < 0.05$) compared with the negative control group. Micronucleus incidence is in descending order: Nano-SiO_2 > KWC-S > KWC-C > KWC-D > KWC-Q > KWC-M. It's worth noting that cells rapidly die after the addition of montmorillonite mineral dust; when exposed to a concentration of 50 μg mL^{-1}, the micronucleus rate is only 5.6 ± 1.5‰; six kinds of dust have different levels of damage on the A_{549} nucleus, exposed to different concentrations of mineral dust suspension; the micronucleus rates are shown in Table 2.

3.4 Single-Cell Gel Electrophoresis Test for Detection of DNA Damage

Six concentrations of dust act on A_{549} cells for 48 h; use fluorescence microscope to observe that with the increase of exposure to dust concentration after lectrophoresis. The result show that the cell tailing rate gradually increase, comet head becomes smaller, the brightness is increased, the tail becomes round, and the fluorescence intensity. Within the scope of the low concentration of mineral dust can cause cellular DNA damage, according to the statistical results (see Table 3). When the mineral dust concentration increases to 200 μg mL^{-1}, the comet assay can be observed that most nucleus fragmented into irregular shapes; there's a significantly increased trend of the tail length of comet cells, Olive tail moment, and tail DNA content. It shows that the mineral dust to the DNA damage of A_{549} cells presents a dose–response relationship. Compared with the negative control group, all six groups have DNA damage; the largest damage rate is in nano-silica

Table 1 The survival rate (%) of A_{549} cells treated by different concentrations of mineral for 24 h

Concentration (μg mL^{-1})	KWC-M	Nano-SiO_2	KWC-S	KWC-Q	KWC-A	KWC-C
50	46.82 ± 6.51	73.70 ± 2.75	95.64 ± 5.22	105.32 ± 15.82	108.00 ± 10.35	100.00 ± 8.05
100	36.25 ± 4.86	60.00 ± 9.52	87.45 ± 4.68	90.64 ± 18.86	100.00 ± 8.74	110.00 ± 8.75
200	18.74 ± 1.68	23.96 ± 8.85	70.55 ± 3.48	87.41 ± 8.65	95.00 ± 6.28	114.5 ± 9.05
400	5.83 ± 1.42	5.00 ± 1.05	62.54 ± 2.98	72.18 ± 9.24	85.00 ± 5.55	116.08 ± 9.37

Table 2 The micronuclei rate (%) of six different concentrations of mineral dust act on A_{549} cells for 24 h

Sample ID	Micronucleus rate (×‰) (μg mL^{-1})			
	50	100	200	400
(−)	5.67 ± 1.58	5.67 ± 1.53	5.67 ± 1.52	5.65 ± 1.53
CP	21.67 ± 1.58	21.66 ± 1.52	21.67 ± 1.54	21.66 ± 1.52
KWC-A	10.67 ± 2.82**	11.33 ± 1.15**	12.00 ± 1.73**	14.00 ± 1.00**
KWC-C	12.33 ± 2.82**	12.33 ± 0.57**	12.50 ± 2.00**	13.50 ± 2.00**
KWC-M	5.67 ± 1.58*	6.33 ± 3.05*	5.00 ± 1.00*	5.00 ± 1.73*
KWC-Q	9.33 ± 2.30**	10.67 ± 2.08**	11.83 ± 1.15**	13.33 ± 1.53**
Nano-SiO_2	14.67 ± 2.51**	16.33 ± 2.08**	17.33 ± 2.08**	18.66 ± 1.53**
KWC-S	13.33 ± 2.08**	14.00 ± 2.00**	16.67 ± 1.53**	17.00 ± 5.29**

Note: Compared with the negative control group, *$p \leq 0.05$; $n = 3$, **$p \leq 0.05$; compared with the positive control (CP)

Table 3 Comet assay data of different concentrations of dust act on A_{549} cells for 24 h

Mineral sample ID	Dose (μg mL^{-1})	TL	*T* %	OTM
Control	/	21.9 ± 9.72	5.08 ± 3.41	2.59 ± 1.71
KWC-C	50	28.3 ± 15.51	5.08 ± 3.41	2.59 ± 1.71
	100	30.52 ± 14.57	11.54 ± 5.86	5.18 ± 2.54
	200	33.70 ± 13.67	14.16 ± 4.88	6.09 ± 2.16
	400	63.30 ± 39.11	15.03 ± 6.61	7.20 ± 3.24
KWC-A	50	20.90 ± 13.03	26.57 ± 14.63	14.01 ± 5.45
	100	26.16 ± 14.01	7.69 ± 3.03	3.23 ± 1.16
	200	37.70 ± 18.78	10.59 ± 4.26	5.61 ± 1.22
	400	50.10 ± 22.08	15.56 ± 7.18	7.43 ± 4.41
KWC-M	50	34.30 ± 29.31	16.82 ± 5.06	8.04 ± 4.41
	100	39.50 ± 14.29	10.22 ± 5.54	5.18 ± 4.29
	200	45.10 ± 19.15	18.37 ± 6.59	6.27 ± 0.85
	400	62.40 ± 12.87	22.8 ± 6.80	8.19 ± 4.35
KWC-Q	50	27.60 ± 22.84	25.38 ± 5.84	14.28 ± 7.30
	100	29.37 ± 15.64	9.24 ± 4.82	4.64 ± 3.66
	200	31.70 ± 11.64	13.93 ± 5.24	5.92 ± 2.84
	400	52.30 ± 21.66	14.86 ± 5.04	7.76 ± 2.87
Nano-SiO_2	50	30.00 ± 10.95	29.71 ± 10.63	13.39 ± 5.97
	100	28.37 ± 8.25	10.05 ± 5.38	5.51 ± 3.03
	200	29.40 ± 9.83	14.95 ± 5.42	7.60 ± 2.67
	400	57.10 ± 14.98	20.36 ± 7.97	9.04 ± 2.80
KWC-S	50	33.3 ± 15.36	29.85 ± 11.31	15.46 ± 6.33
	100	32.25 ± 11.10	10.09 ± 4.35	4.88 ± 2.25
	200	30.20 ± 10.58	15.24 ± 6.87	6.58 ± 1.99
	400	62.00 ± 32.37	17.18 ± 4.23	8.44 ± 1.95

and sericite dust group, the smallest is in albite and quartz dust group. The dust group of DNA damage in descending order: Nano-SiO_2 > KWC-S > KWC-M > KWC-C > KWC-Q > KWC-A.

4 Discussion

Epidemiological research has found that when the quality of atmospheric environment descends, especially air particulate matter concentration increases, the Hospital Respiratory number will rise sharply. $PM_{2.5}$, as an important component of atmospheric particulate matter, is closely related with respiratory and cardiovascular diseases, can cause the germ cell genotoxicity, inducing cancer [2–5]. Many scholars at home and abroad have done a lot of research on the chemical composition, source, and sink of mineral grains in Asia. They think that the main components of the particles of dust in the atmosphere are aluminosilicate particles which account for 61.59 % and calcite and quartz particles almost about 13.59 % [6]. To confirm whether $PM_{2.5}$ mineral dust particles have genotoxicity, in this test, we selected six major components of the $PM_{2.5}$ level within a certain concentration range minerals and human lung adenocarcinoma A_{549} cells as an object of study and used Wright-Giemsa staining cell morphology and MTT experiment to observe inhibition rate of cell proliferation, micronucleus test to observe the formation of chromosomes, and SCGE experiment to observe whether cell DNA synthesis is influenced. Experimental results show that all six kinds of the $PM_{2.5}$ dust change inhibition of cell proliferation, destroy the cell morphology, and interfere with the formation of chromosomes to varying degrees, damage DNA integrity, have Dose–effect relationship, speculate that a certain concentration of $PM_{2.5}$ mineral dust affects stability of the cells genetic material, and have a genetic toxicity to the human body, which coincides with Dal et al [7].

Genotoxicity of $PM_{2.5}$ has toxic effects on the fine particles on chromosomes, DNA, gene, and other different levels of genetic material, including changes in chromosome structure, DNA damage [8], and gene mutation [9], generally considered to be one of the aspects of the development of malignant tumors. In this study, we use different methods to detect the genotoxicity of the respirable mineral dusts and compare the toxicity of different dust. Finally, we can draw the conclusion that: (1) six kinds of dust have different levels of damage on the genetic material of the cells, which prompts us that we should have a new understanding of the biological genetic toxicity of the previously considered safe mineral dust; in addition to the organic component and the metal particles, mineral dust is also an important factor of atmospheric pollution protection object. British Geological Society and the British Mineralogical Society had organized a special environmental geology symposium, which specialized investigation from the mineralogical point of view of atmospheric particulate matter, considering that the mineral compositions of the particles which could not be ignored in the study of atmospheric particulate matter. (2) By comparing cytogenetic virulence among six kinds of mineral dust, the

genotoxicity of calcite and albite is shown to be relatively small; however, Nano-SiO_2 and montmorillonite show a strong genetic toxicity even in low concentrations. How to reduce the atmospheric $PM_{2.5}$ grade Nano-SiO_2 and montmorillonite dust content is the focus of the prevention and control of air pollution, thus to reduce the hazards of mineral dust on human, which is consistent with Berman DW, etc., [10] who thought kidney cancer related to the mineral dust of occupational exposure. (3) From mechanism of the dust genetic damage, the genetic material damage of the cells is multifactorial participate results, but different dusts show different interference of genetic material stability; montmorillonite is mainly through DNA damaging, Nano-SiO_2 is through interfering chromosome formation, and damage cellular DNA in two ways together, quartz dust by changing cell morphology and interfering chromosome formation and sericite dust through damaging cellular DNA and interfering the formation of the chromosome. Calcite and albite formate micronuclei and DNA are damaged by disrupting the cell morphology, but the specific reasons that different mineral dusts damage the stability of the genetic material are not clear yet. This may be associated with different physical and chemical properties of the dust [11, 12].

Summing up the above results can be seen that $PM_{2.5}$ atmospheric mineral dust is not safe to human body, current domestic and international researches often use the extracts (such as organic compounds or heavy metals) or emphasis on the biological toxic effects of particulate matter complex, but studies about mineral dust particles on human cells and genetic toxicity are almost empty at home and abroad, and the mechanism of toxicity is still not very clear, for the evaluation harm of the $PM_{2.5}$ level of absorbing particles to the human body. Minerals as the main component of the absorbent particles are important factors which could not be ignored. Scientific objectivity detect hazards could provide the basis for environment detection indicators.

5 Conclusions

The six main ingredients of the $PM_{2.5}$ mineral dusts can change A_{549} cell morphology from varying degrees; they can improve proliferation inhibition rate of the cells, increase the number of micronuclei cells, and damage DNA. Then we come to the conclusion that $PM_{2.5}$ mineral dusts can change the genotoxicity of the cells.

References

1. Gillissen A, Gessner C, Hammerschmidt S et al (2006) Health significance of inhaled particles. Dtsch Med Wochenschr 12:639–644

2. Kolling A, Ernst H, Ritting S, Hausen U (2011) Relationship of pulmonary toxicity and carcinogenicity of fine and ultrafine granular dusts in a rat bioassay. Inhal Toxicol 23 (9):544–554
3. Ballester F, Rodriguez P, Iniguez C et al (2006) Air pollution and cardiovascular admissions association in Spain. J Epidemiol Community Health 4:328–336
4. Valko M, Rhodes CJ, Moncol J et al (2006) Free radicals, metals and antioxidants inoxidative stress-induced cancer. Chem Biol Interact 160(1):1–40
5. Pope CA III, Burnett RT, Thun MJ et al (2002) Lung cancer, cardiopulmonary mortality, and long-term exposure to fine particulate air pollution. JAMA 9:1132–1141
6. Chen YJ, Shi ZB, He KB et al (2007) Physico-chemical characteristics of individual mineral particles collected during dust storm periods in Beijing. Res Environ Sci 1:52–57
7. Dal M, Malak AT (2012) Effects of SiO_2 in Turkish natural stones on cancer development. Asian Pac J Cancer Prev 10:4883–4888
8. Gao N, Keane MJ, Ong T et al (2000) Effects of simulated pulmonary surfactant on the cytotoxicity and DNA-damaging activity of respirable quartz and kaolin. J Toxicol Environ Health A 60(3):153–167
9. Yauk CL (2004) Advances in the application of germline tandem repeat instability for in situ monitoring. Mutat Res 2:169–182
10. Berman DW, Brorby GP, Sheehan PJ et al (2012) More on the dynamics of dust generation: the effects of mixing and sanding chrysotile, calcium carbonate, and other components on the characteristics of joint-compound dusts. Ann Occup Hyg 7:852–867
11. Zeng YL, Gan SY, Dong FQ et al (2012) Study on correlation between the erosion Characteristic in organic acid with the V79 cell toxicity of chrysotile asbestos and its four major substitute fibers. Mod Prev Med 12:2938–2940
12. Boriana KA, Yigal E, Amir S et al (2009) Mineralogical and chemical characterization of suspended atmospheric particles over the east Mediterranean based on synoptic-scale circulation patterns. Atmos Environ 25:3963–3970

The Effect of Gum Arabic on the Dispersion of Cement Pastes

Cuiting Zhao, Qinglin Zhao, Yulin Zhang, and Mingkai Zhou

Abstract Gum arabic, an inexpensive dispersant widely used in the food industry, has great potential for application in building materials. In order to find out the dispersion effect of gum arabic and the factors influencing the holding capacity of gum arabic in cement during hydration, rheological properties of cement paste with added gum arabic were assessed in this paper. The results show that 0.10–0.60 wt% of gum arabic positively affects dispersion, whereas lower dosages have negligible effect. High speed mixing is required to maintain the dispersion stability of gum arabic in cement paste. The optimum dosage of gum arabic to achieve best disperse-holding capacity of cement paste was 0.3 wt%, and the minimum water–cement ratio needed to obtain a dispersion effect was 0.28.

Keywords Dispersion • Fluidity • Gum arabic • Rheological property • Steric hindrance

1 Introduction

Gum arabic is a polymer forming complex molecules, composed of arabinogalactan spine with multiple branching chains. Molecules are normally furled up to near-spherical shape (Fig. 1). Gum arabic has a dispersing effect on particles by steric hindrance, which is attributed to its hyper-branched structure and spherical shape of gum arabic. An aqueous solution of gum arabic exhibits Newtonian flow over a wide range of shear rates. The viscosity of aqueous solution containing gum arabic is lower than with polysaccharides of similar molecular weight [1, 2]. Gum arabic is

C. Zhao • Y. Zhang
School of Materials Science and Engineering, Wuhan University of Technology, Wuhan, P.R. China

Q. Zhao (✉) • M. Zhou
State Key Laboratory of Silicate Materials for Architectures, Wuhan University of Technology, Wuhan, P.R. China

School of Materials Science and Engineering, Wuhan University of Technology, Wuhan, P.R. China
e-mail: zhaoqinglin@whut.edu.cn

F. Dong (ed.), *Proceedings of the 11th International Congress for Applied Mineralogy (ICAM)*, Springer Geochemistry/Mineralogy,
DOI 10.1007/978-3-319-13948-7_47

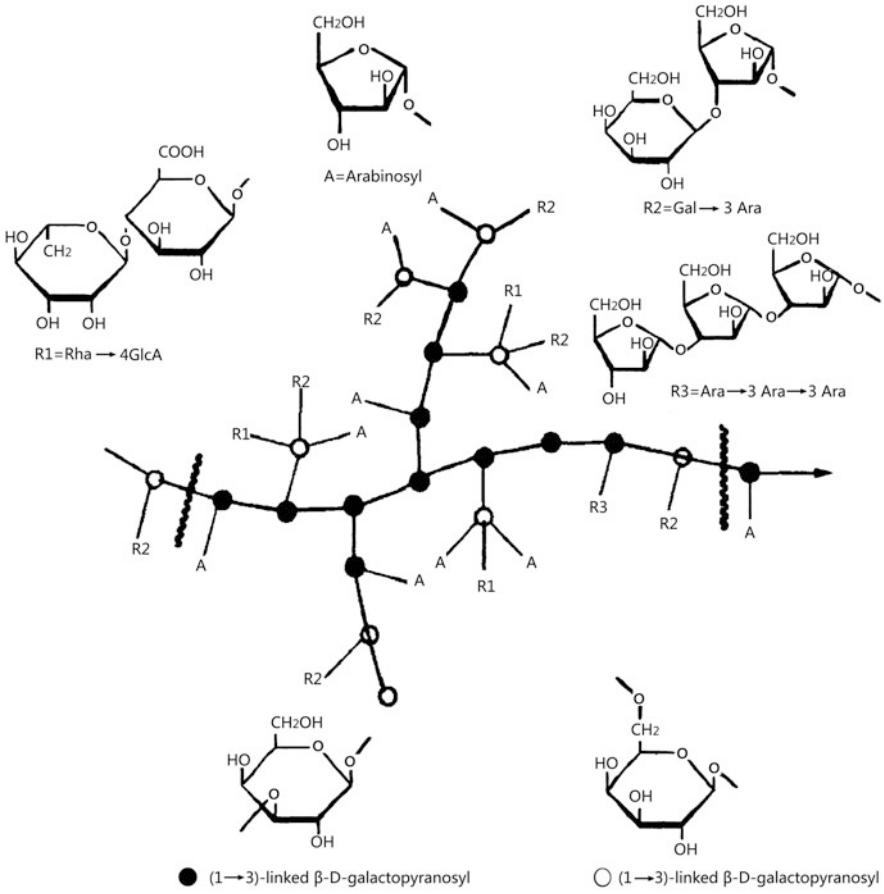

Fig. 1 The molecular structure of gum arabic

a pH-neutral organic dispersant. The long polymer chains of gum arabic adsorb to a particle surface by electrostatic bonding, hydrogen bonding, and/or Van der Waals force, forming a polymer armor of certain thickness covering the particles. By contrast, the hydrophilic groups of gum arabic are attracted to polar fluids like water. When polymer-armored particles approach one another, the increase in local mass concentration or compressive deformation increases mutual repulsion and thereby spacing. In effect, the potential energy of Van der Waals force among (nonpolymer-armored) particles is weakened and they cannot collide nor agglomerate [3].

Seeing away from its wide application in the food industry, gum arabic is currently used as dispersant mainly in the materials field of nanometer materials (e.g., dispersion of carbon nanotubes [4]), industrial ceramics (dispersion of ceramic slurry [5]), and ultrafine powder suspension (preparation of Al_2O_3 and CuO suspensions [6, 7]). However, studies on the application of gum arabic for cement-based materials are very few. This study reports results from initial

investigations into the dispersive and holding capacity of gum arabic on Portland cement during hydration, by determination of rheological and flow properties.

2 Materials and Methods

2.1 Materials

2.1.1 Cement

The cement used in this study was 42.5 ordinary Portland cement (OPC) from the normal production of a cement plant in Hubei province. The chemical composition in main oxides and physical properties of cement are shown in Tables 1 and 2, respectively.

2.1.2 Gum Arabic

Gum arabic used in this study was food-grade dispersing agent. It was available as a light yellow powder. The IR spectrum of gum arabic is shown in Fig. 2 with absorption bands bond at 3,410 cm^{-1} characteristic of OH. Two strong bands at 1,624 and 1,419 cm^{-1} are attributable to (a–) symmetric stretching vibration of carboxylic acid –COO and bands at 1,251 and 1,040 cm^{-1} due to the stretching of the C=O bond.

2.1.3 Mix Designs

All cement pastes made with gum arabic were prepared with 200 g OPC and fixed water/cement ratio of 0.4. Seven dosages of gum arabic were tested, notably 0.02, 0.06, 0.10, 0.20, 0.30, 0.60, and 1.00 in weight percent (wt%) relative to cement, in addition to a blank, without added gum arabic.

2.2 Test Methods

2.2.1 Determination of Rheological Behavior

The mixing process of cement paste was tested according to Chinese standard GB/T 1346-2001 “Test methods for water requirement of normal consistency, setting time, and soundness of the Portland cements.” The rheological properties of the cement pastes were determined by type R/S-SST paddle viscometer from American Brookfield Company and rheological parameters including yield stress and plastic

Table 1 Chemical composition in main element oxides of the 42.5 Ordinary Portland Cement (OPC), in weight percent

Main oxides	CaO	SiO_2	Al_2O_3	Fe_2O_3	MgO	P_2O_5	SO_3	K_2O	Na_2O	LOI	Total
Content (wt%)	60.5	21.6	5.84	3.06	1.61	0.10	3.30	1.00	–	1.75	98.8

Ignition loss determined at 950 °C

Table 2 Main physical properties of 42.5 OPC from Hubei

Specific surface area ($m^2\ kg^{-1}$)	Normal consistency (%)	Setting time (min)		Flexural strength (MPa)		Compr. strength (MPa)	
		Initial	Final	3 days	28 days	3 days	28 days
366	27.6	184	310	6.0	9.2	20.0	45.2

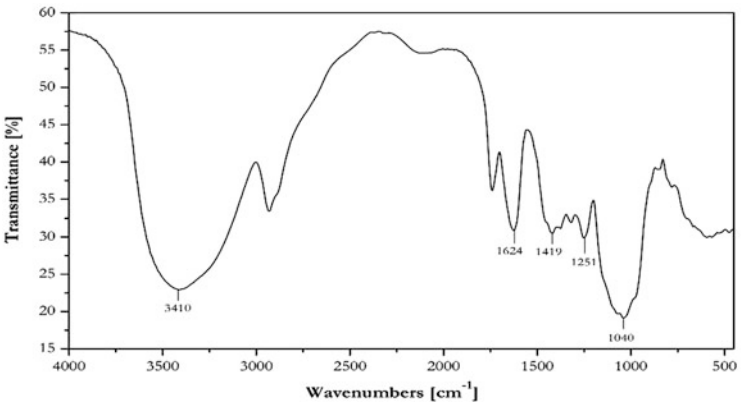

Fig. 2 IR absorption spectrum of gum arabic

viscosity were obtained using the Herschel–Bulkley model. Tests were performed at different shear rates, designed to increase gradually from 0 to 200 s^{-1} over 180 s.

Additional tests were run at fixed shear rates of 5 and 50 s^{-1} over 180 s, respectively, to assess the development of apparent viscosity of cement paste with time.

2.2.2 Determination of Flow Properties over Time

The fluidity through time of the cement paste was tested according to Chinese standard GB/T 8077-2000 "Methods for testing uniformity of concrete admixture." The grout mix investigated in this study was prepared with 300 g OPC at a water/cement ratio of 0.4 by mass. Gum arabic and grout were premixed before water was added. Flow properties were measured at 0, 30, and 60 min after preparation of the pastes.

3 Results

3.1 *Influence of Gum Arabic on Rheological Properties of Cement Pastes*

Figure 3 shows the influence of gum arabic on rheological properties of cement paste. An increasing dosage of gum arabic reduces apparent viscosity, yield stress, and plastic viscosity. With dosages of gum arabic below 0.1 %, the cement paste clearly exhibits shear thinning behavior. Apparent viscosity and yield stress of cement paste containing 0.1 % added gum arabic changed a little, while the plastic viscosity shows a tendency to gradually reduce. With dosages of gum arabic exceeding 0.1 %, apparent viscosity and yield stress reduce dramatically, and shear thinning behavior is completely absent. Instead, apparent viscosity initially decreases and then stabilizes with increasing shear rate. Addition of more than 0.6 % gum arabic results in a slight increase in plastic viscosity of the paste.

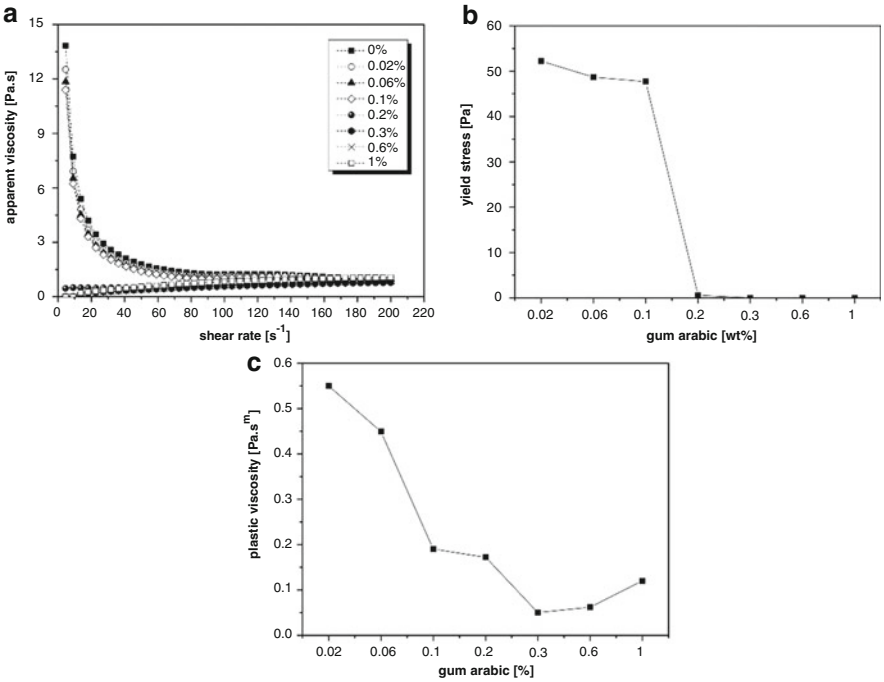

Fig. 3 Effect of gum arabic dosage on various rheological properties of cement paste. (**a**) Apparent viscosity vs. shear rate; (**b**) yield stress vs. dosage, and (**c**) plastic viscosity vs. dosage

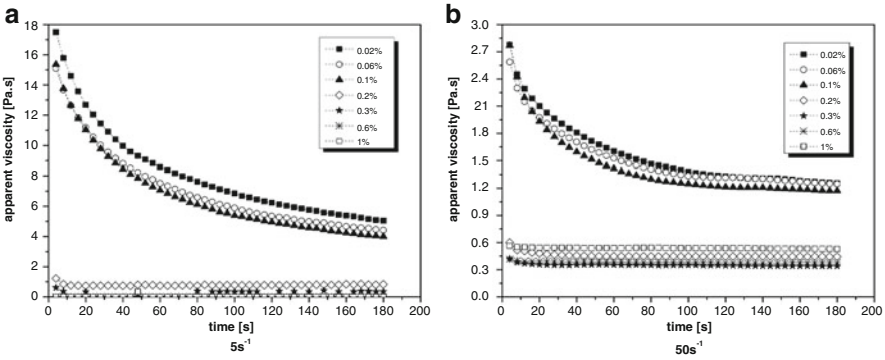

Fig. 4 Relation between the development of apparent viscosity of cement paste (w/c: 0.40) over time at two fixed shear rates, for different dosages of gum arabic

3.2 Relation of Apparent Paste Viscosity with Time in Different Dosages of Gum Arabic at Fixed Shear Rates

The variations of apparent viscosity of cement paste with time for different dosages of gum arabic at a fixed water–cement ratio of 0.4 are shown in Fig. 4. For dosage of gum arabic under 0.1 %, the results from Fig. 4a indicate that the apparent viscosity of cement paste at low shear rate of 5 s^{-1} showed a downward trend as time went on. Cement paste with 0.2 % gum arabic exhibited weak shear thinning behavior. However, when the dosage of gum arabic was greater than 0.2 %, the apparent viscosity of cement paste remained unstable. The results from Fig. 4b indicated that adding no more than 0.1 % gum arabic resulted in a reduction in initial apparent viscosity at high shear rate of 50 s^{-1} and the apparent viscosity gradually stabilizes over time. For dosages of gum arabic over 0.2 %, apparent viscosity of cement paste does not change significantly but tends to stabilize with time. Comparison between Fig. 4a and Fig. 4b indicates that cement paste with gum arabic performs more stable at high speed mixing.

3.3 Influence of Gum Arabic on Fluidity of Cement Paste

To investigate the dispersion effect of gum arabic, fluidity was assessed for cement pastes with fixed water–cement ratio 0.4 with the seven + blank dosages of gum arabic as mentioned above, at time intervals 0, 30, and 60 min. In addition, cement pastes prepared with a fixed dosage of gum arabic 0.30 % but with six different water/cement ratios ranging from 0.40 to 0.27 were tested.

Figure 5 shows that different dosages of gum arabic at constant water/cement ratio greatly affect the fluidity of cement paste. Until 0.10 %, fluidity remains fairly

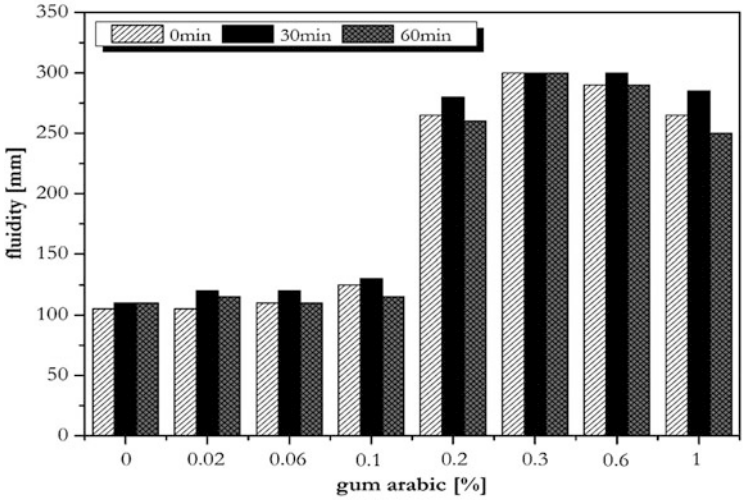

Fig. 5 Effect of gum arabic dosage on cement paste (w/c 0.40) fluidity at 0, 30 and 60 min

Table 3 The influence of different water/cement ratio on fluidity of cement paste with 0.30 % gum arabic

W/C	0.40	0.35	0.32	0.29	0.28	0.27
Fluidity (mm)	300	265	235	200	150	Stopped flowing

constant at just over 100 mm, whereas fluidity jumps up to 250 mm at dosage of 0.20 % and even 300 mm at 0.30 %. Further increase of dosage to 0.60 or 1.00 % of gum arabic again results in slight decline in paste fluidity. Note the variation of fluidity with time where maximum fluidity is attained after 30 min, the effect being most pronounced for the two highest dosages.

The effect of different water–cement ratios on fluidity of cement paste at a constant gum arabic dosage of 0.30 % is shown in Table 3. A decreasing water/cement ratio leads to the reduction of fluidity of cement paste. Fluidity drops increasingly for lower water/cement ratios than 0.40, but pastes essentially remain workable. However, at a very low water/cement ratio of 0.27, the cement paste stops flowing and no longer be poured.

4 Discussion

4.1 Dispersion Effect of Gum Arabic on Cement Particles

The analytical results reported above consistently demonstrate that the addition of gum arabic to OPC decreases apparent viscosity as well as shear rate, which

coincides with an increase in fluidity. Gum arabic has a dispersing effect on the cement particles, the extent of which is related to dosage.

Additions of 0.02 and 0.06 % up to 0.10 % gum arabic have negligible measurable steric stabilization effect on cement particles compared to the blank sample, which may be attributed to an insufficient quantity of gum arabic adsorbed to the cement particles to completely cover their surface. Cement particles show none to only very moderate dispersion after addition of up to 0.10 % gum arabic. For dosages of gum arabic 0.20 and 0.30 %, the dispersion effect of gum arabic becomes more and more significant as the cement particles get gradually surrounded by gum arabic. This armor then keeps the cement particles from coming close to each other, and repulsion among cement particles gradually increases with dosage. In effect, the apparent viscosity and yield stress of the cement paste decreases greatly whereas fluidity increases.

Increase in the dosage of gum arabic further to 0.60 and 1.00 % leads to the decrease of dispersion effect on the cement particles. These high dosages result in a slight increase again of plastic viscosity of cement paste, coinciding with a slight decrease of initial fluidity [5, 6]. This effect may be attributable to "supersaturated adsorption," i.e., there is excess gum arabic relative to the available surface area of cement particles. The long carbon chains with multiple side branches not entirely adsorbed to cement particles get entangled with excess gum arabic in solution, causing cement particles to agglomerate and flocculate.

4.2 Dispersion Stability of Cement Paste with Added Gum Arabic

The results of viscosity measurements indicate that cement paste with 0.20 % or more admixed gum arabic performs more stable at high mixing speeds, presumably by virtue of the increased degree of dispersion. The variation of apparent viscosity of hydrating cement paste depends on the relationship between shear rate and flocculation of cement paste, which latter evolves over time during hydration.

Experimental conditions are kept consistent for all dosages of gum arabic, hence the hydration rates of cement paste are essentially the same, and therefore also the flocculation rates of the pastes in the evolving microstructure. Therefore, observed variations of apparent viscosity of cement paste over time depend on shear rate and do reflect different dosages of gum arabic [8].

Gum arabic adsorbed to the cement particles' surface partially inhibits development of microstructure with interlocking growing paste hydrates, as a consequence of the hyper-branched structure of gum arabic causing steric hindrance. Meanwhile, the network formed by long molecular chains of gum arabic also increases resistance against segregation through agglomeration [9]. These agglomerates are then dissociated by the shear force applied, higher rates leading to finer agglomerate

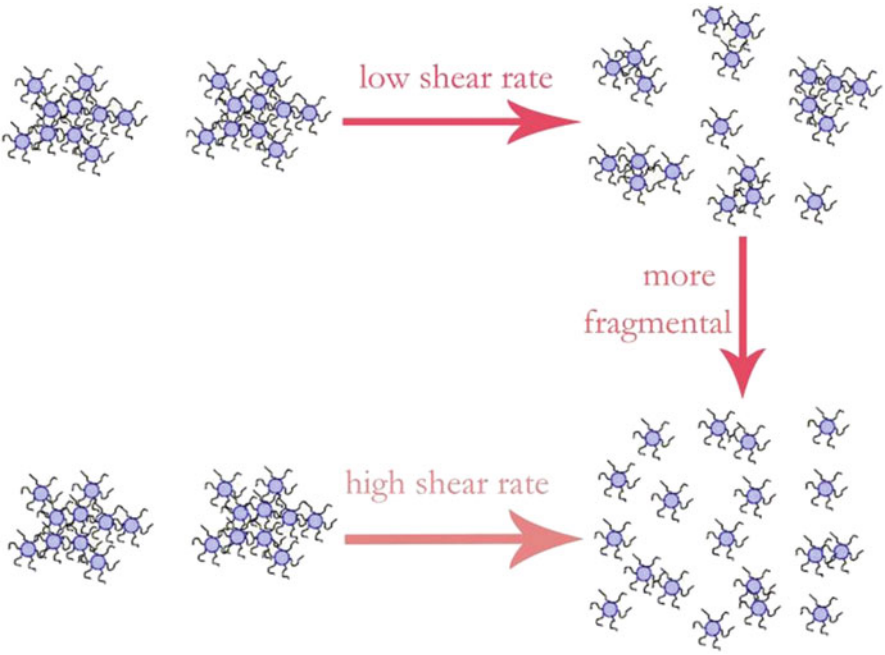

Fig. 6 Assumed effect of shear rate on Portland paste-gum arabic agglomerates

sizes as illustrated in Fig. 6. Therefore, high speed mixing provides the best dispersion stability of cement paste with added gum arabic at suitable dosages.

4.3 Disperse-Holding Capacity of Gum Arabic in Cement Paste

The disperse-holding capacity of gum arabic in cement paste was assessed by measuring the variation of paste fluidity with time, with a fixed water/cement ratio of 0.40 for seven different dosages of gum arabic, plus a blank sample. The results described above show that the fluidity of the paste varies over the duration of the experiment, with a maximum near 30 min (i.e., the second measurement) and slightly lower initial (at 0 min) and final values (at 60 min). The initially lower fluidity may be attributable to cement particles initially (0 min) being covered by water (at least partially), which is then gradually replaced by gum arabic molecules, thus increasing fluidity until a maximum (30 min). Without the paste being agitated, fluidity then drops again as gum-armored cement particles agglomerate towards the end of the experiment (60 min). Thus, the disperse-holding capacity of gum arabic over time seems indeed governed by dosage. For a water/cement ratio of 0.40, the

optimum dosage of gum arabic is at or near 0.30 % but might be different for other water/cement ratios (not investigated here).

The optimum dosage of gum arabic in above experiment (0.30 %) was taken as the starting point to determine the minimum water–cement ratio needed to maintain the dispersibility of gum arabic. Reducing w/c stepwise gradually decreased fluidity down to w/c 0.28, until the paste stopped flowing at w/c 0.27. This illustrates the mutual interaction of water and gum arabic for dispersion and paste fluidity.

5 Conclusions

Based upon results presented and discussed in the preceding sections, the following conclusions can be drawn:

1. The main effect of added gum arabic on the hydration of Portland cement paste is enhanced dispersion contributing to a decrease in apparent viscosity as well as an increase in the fluidity.
2. The extent of the dispersion effect of gum arabic is conveniently controlled by dosage. Low dosages of gum arabic up to 0.10 % have negligible effect on cement particle dispersion, high dosages of gum arabic of 0.60 % or over again appear to reduce dispersion. With a water/cement factor of 0.40, dosages of gum arabic 0.20 or 0.30 % are observed to have the greatest effect on paste dispersion.
3. Mixing at high speed (i.e., with a high shear rate) is a convenient and highly effective means to maintain the dispersion stability of gum arabic in cement paste, compared with mixing at lower speeds/shear rates.
4. The disperse-holding capacity of gum arabic in cement paste depends on a combination of gum arabic dosage and the water/cement ratio. For a water/cement ratio of 0.4, admixing 0.30 % gum arabic relative to cement weight shows the best disperse-holding capacity. The minimum water/cement ratio required to maintain the dispersing action of 0.30 % gum arabic was found to be 0.28.

Acknowledgments The research works in the paper were supported by National Natural Science Foundation of China (No. 51202173).

References

1. Yan ZY, Hüttermann C, Keller J, Kuntsevich M (2011) Application of acacia gum replaced by methylcellulose and hydroxypropyl methylcellulose in perfume emulsion. China Food Addit 1:226–231
2. Hu GH (2003) The application of gum arabic in food industry. Sci Technol Cereals Oils Foods (11/2):7–8
3. Zhang QC, Huang SP (2000) Prospect of dispersant's application in aqueous systems. China Powder Sci Technol (6/4):32–35

4. Bandyopadhyaya R, Nativ-Roth E, Regev O, Yerushalmi-Rozen R (2002) Stabilization of individual carbon nanotubes in aqueous solutions. Nano Lett (2/1):25–28
5. Li FZ (2008) Effect of arabic gum on the sedimentation of Al_2O_3 suspension. Foundry Technol Die Cast (29/9): 1275–1278
6. Li FZ (2009) Study on the stability behavior of α-Al_2O_3 suspension interact with two dispersants. New Technol New Process 9:83–87
7. Li ZL, Li JM, Hu HT, Wang BX (2005) Influence of ingredients of copper oxide nanosuspension on stability and viscosity of suspension. J Therm Sci Technol (4/2):157–163
8. Zhao QL, He T, Tao FY, Guo WH, Zhou MK (2010) Influence of welan gum on rheological properties of high-performance grouting materials. In: Proceedings of the seventh national high strength and high performance concrete academic conference, Shenyang, China
9. Yu DB (2008) A research on molecular association in gum arabic solution. China Master's Theses, Full-text Database, Shanghai Jiao Tong University, Shanghai

Reservoir Features of Carboniferous Sand-Mudstone Member and Effects of Diagenesis in Lunnan Region

Xueqin Zhao, Jin Fang, Jianghua Deng, and Tiejun Yin

Abstract Based on the analysis of the rock characteristics, pore types, pore structure characteristics, and physical characteristics of the reservoir of the Carboniferous sand-mudstone section, it is considered that the rock types of the sand-mudstone section are mainly composed of lithic sandstone and partly of feldspar lithic sandstone; the reservoir pore types are primarily intergranular dissolution pore and intergranular pores, secondarily dissolution pores inside the cements and intragranular dissolution pores, and also a small amount of kaolinite and calcite intergranular micropores, while a small amount of grain boundary fractures and micro fractures is developed; the overall physical properties of the reservoir are inferior and the average porosity of are mostly below 10 % while there are differences; porosity and permeability are basically exponential positively correlated, with the correlation coefficient being 0.78; highly efficient reservoirs mainly develop in the residual primary intergranular pores and intergranular dissolution pores. By combining the diagenesis features of the reservoir, it is concluded that the compaction and pressure solution, cementation, and dissolution affect the reservoir development of the sand-mudstone section in the research area, with dissolution playing a constructive role in porosity development of the reservoir.

Keywords Carboniferous sand-mudstone member • Diagenesis • Lunnan region • Reservoir features

The Foundation of State Key Laboratory of Petroleum Resources and Prospecting, China University of Petroleum, Beijing (No. PRP/open-1303).

X. Zhao (✉)
State Key Laboratory of Petroleum Resources and Prospecting, China University of Petroleum, Beijing 102249, China

Institute of Environment and Resources, Southwest University of Science and Technology, 59 Qinglong Road, Mianyang, Sichuan, People's Republic of China
e-mail: zxqch@sina.com

J. Fang • J. Deng • T. Yin
Institute of Environment and Resources, Southwest University of Science and Technology, 59 Qinglong Road, Mianyang, Sichuan, People's Republic of China

F. Dong (ed.), *Proceedings of the 11th International Congress for Applied Mineralogy (ICAM)*, Springer Geochemistry/Mineralogy,
DOI 10.1007/978-3-319-13948-7_48

1 Introduction

Carboniferous system is a very significant reservoir for clastic rock exploration target in Tarim Basin [1–3] and has contributed 50–60 % to oil and gas yield of Tarim Basin over more than a decade. Oil and gas have been frequently discovered in the wells drilled in Carboniferous sand-mudstone member in Lunnan Region and some wells have achieved high yield, proving the existence of high nonstructural oil-gas reservoir. For large horizontal change of sand body, the effective prediction of reservoir has been always restricting the further exploration and development of this stratum. Meanwhile, common reservoir analysis technologies do not satisfy the functional requirements of reservoir prediction for constant development of exploration. The type and strength of diagenesis are one of the key factors affecting the accumulation property of reservoir. Thus, the quantitative analysis on reservoir and the effects of diagenesis can reveal the geological evolution of oil and gas and the spatial formation and evolution of oil-gas reservoir, so as to provide a solid basis for evaluating high-quality reservoirs.

North Tarim Uplift is a primary tectonic element of Tarim Basin and extends nearly from east to west. Lunnan Region is a secondary tectonic element in the middle of North Tarim Uplift to guide and aggregate the long-term movement of oil and gas [4]. Affected by tectogenesis in Caledonian-Early Hercynian period and Late Hercynian-Indosinian period [5], Lunnan Region is featured by insufficient stratigraphic development. Except the absence of Devonian system, Ordovician system, Silurian system, Carboniferous system, and Permian system are also severely corroded in the region. Other strata exist in the whole region. In Lunnan Region, Upper Devonian Series-Carboniferous system is classified into Bachu formation and Kalashayi formation [6]. Sand-mudstone member in Kalashayi formation is an important oil-gas reservoir in Lunnan Region and contains mainly unbalanced thick subdivision of sandstone and mudstone, which is mingled with extremely thin limestone, carbonaceous mudstone, or thin coal bed. The sediment thickness exceeds 500 m. Also, it is divided into middle mudstone member, standard limestone member, upper mudstone member, sand-mudstone member, and ash-contained member. Through an analysis on reservoir features including lithology, types of space, pore structure, as well as physical characteristics of sand-mudstone member in Kalashayi formation, the study considers the characteristics of reservoir diagenesis to systematically analyze its effects on reservoir.

2 Lithologic Characteristics

As revealed in the observation of rock cores, common chips, and cast chips (Picture Plate I), sand-mudstone member mainly contains coarse-moderate, moderate-fine, and fine sandstone and partially consists of breccia-contained anisometric sandstone, breccia, and fine sandstone, etc. Based on the triangular chart of rock types

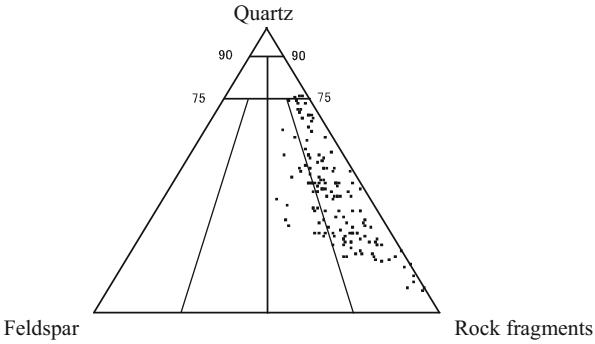

Fig. 1 Triangular chart of rock types of Carboniferous sand-mudstone member in Lunnan Region

(Fig. 1), sand-mudstone member normally contains 20–60 % quartz, which mainly has one color, and 30–60 % rock fragments, or 92 % at some positions, which mainly contain limestone, dolostone, metamorphic rocks, siliceous rocks, tuffaceous rocks, and biotite. The lithology is mainly composed of lithic sandstone and partly feldspar lithic sandstone. Mineral structure and composition are not much mature. Particles are round and separated into moderate-poor condition, and mostly in angular-subangular grain. It also contains 8–25 % interstitial materials, which are mainly argillaceous and calcareous and partially tuffaceous. Cementation is mainly in pores based on particles. Gravel mainly consists of quartz, igneous rocks, limestone, and flint.

3 Pore Types and Pore Structure Characteristics of Reservoir

3.1 Pore Types

Based on the observation of cast chips (Picture Plate I), the reservoir of sand-mudstone member mainly contains intergranular pore and intergranular dissolved pore, and the minor pores are dissolved pores in cement, intragranular dissolved pore, calcite, and kaolinite intercrystalline micropore, with a small amount of grain-edged fracture and micro crack developing.

Sandstone fragments comprise more than 50 % carbonate rocks, which are mainly crumbing argillaceous limestone and dolostone and mostly carbonate cement. Corroded rocks are mainly calcite, feldspar, and rock fragments with rare existence of extra large pores. There is strong effect of metasomatism and recrystallization on pores. Pores are distributed very sparsely and connected poorly, and their average diameter is less than 10 μm as shown in most samples.

At some positions, sand reservoir with breccia-contained moderate-rough sandstone and anisometric sandstone has a high content of quartz with developing pores and shows good separation and connection and low content of interstitial materials.

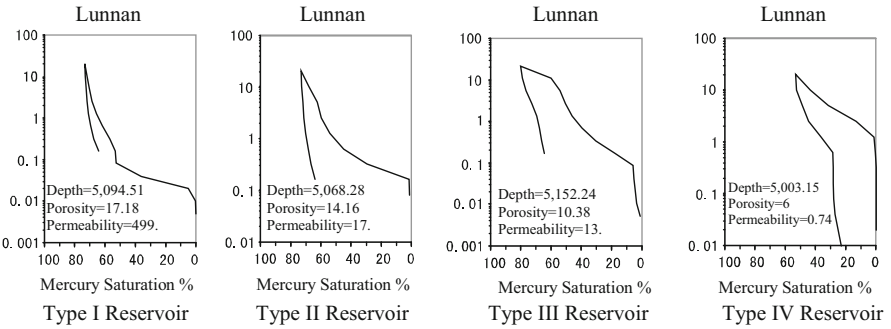

Fig. 2 All kinds of reservoir capillary pressure curve characteristics by mercury intrusion of Carboniferous sand-mudstone member in Lunnan Region

The permeability is between 315.68 and 557.03×10^{-3} μm^2, the porosity is between 13.27 and 20.38 %, the average aperture is higher than 70 μm, and the maximum aperture exceeds 300 μm.

3.2 Pore Structure Characteristics

Accumulation property of rocks depends on the pore and throat size, shape, interconnection, and distribution of reservoir [7]. According to capillary pressure curve by mercury intrusion (Fig. 2) and the pore graphic analysis data of reservoir, the pore structures of sandstone reservoir in sand-mudstone member are categorized into four types in terms of porosity (Table 1).

Type I Reservoir It is characterized by high porosity and permeability, low displacement pressure, long straight section, and coarse skewness of mercury intrusion curve. Its pore and throat are large with good separation, while its pores are mainly residual primary intergranular pore and intergranular dissolved pore.

Type II Reservoir It is featured by moderate porosity and permeability, but poor separation of pores. Its displacement pressure is similar to Type I Reservoir. Pore and throat are moderate with coarse skewness. This type has a poorer pore–throat ratio than Type I, and its pores are mainly intragranular dissolved pore, intergranular pore, and cast pore.

Type III Reservoir This type has high displacement pressure, maximum mercury saturation lower than 60 %, low pore–throat ratio, slightly fine skewness, and poor pore separation. It is characterized by low porosity and permeability and mainly composed of patchy calcite-cemented sandstone and mud-contained sandstone. The major pores are residual primary intergranular pore in carbonate cement and the minor pores are intragranular dissolved pore and dissolved pore in cement.

Table 1 Pore structure characteristic parameters by mercury intrusion of Carboniferous sand-mudstone member in Lunnan Region

Reservoir type	Porosity range	Permeability (10^{-3} μm^2)	Displacement pressure (mpa)	Average aperture (μm)	Sorting coefficient	Minimum unsaturated pore volume (%)	Pore throat ratio	Reservoir evaluation
I	>15	10–500	<0.1	1.5–15	2.6–12	<20	0.12–0.5	High P&PM
II	15–12	1–150	0.08–0.2	0.8–6.8	1.2–6	10–30	0.08–0.24	Medium P&PM
III	12–8	0.4–30	0.08–0.8	0.6–3.6	1–5	30–50	0.027–0.06	Low P&PM
IV	≤8	0.04–3	>0.5	<0.08	0.03–0.5	>50	<0.01	Extra P&PM

Type IV Reservoir Its accumulated percentage of mercury intrusion is less than 50 %. It is characterized by high displacement pressure, fine skewness, extra low porosity, and low permeability. The major pores are sandstone and base micropores in dense carbonate cementation.

4 Physical Characteristics

4.1 Distribution Characteristics of Porosity and Permeability

Physical property analysis data of measured common small rock cores are affected by sampling density, sampling location, and other factors, so the results cannot fully reflect the original and actual characteristics of reservoir under normal circumstances. However, its statistical law can still reflect the accumulation property of reservoir to some extent. This study has a statistics of reservoir physical property of sand-mudstone member in more than ten wells including Lunnan Well 8#, Lunnan Well 9#, and Lunnan Well 14#, etc., as shown in Table 2.

The statistical results reveal the physical property of sandstone reservoir in Carboniferous sand-mudstone member in Lunnan Region is bad on the whole. The average porosity is mostly below 10 % and varies as well (Table 2). In the south of Lunnan buried hill, Lunnan Well 9#, Lunnan Well 22#, Lunnan Well 44#, and Lunnan Well 48# have good physical property with their average permeability between 3.73 and 82.53×10^{-3} μm^2 and average porosity between 9.52 and 11.08 %. The wells in other areas show poor physical property with average permeability between 0.4 and 44.24×10^{-3} μm^2 and average porosity between 5.79 and 8.99 %.

4.2 Relationship Between Porosity and Permeability

Based on data analysis, positive correlation of index exists basically between sandstone reservoir porosity and permeability in the sand-mudstone member in Lunnan Region (Fig. 3). The correlation between porosity and permeability is good at the coefficient of 0.78.

Table 2 Statistical of single-well reservoir physical property of Carboniferous sand-mudstone member in Lunnan Region

Well	Lithology	Porosity (%)				Permeability ($\times 10^{-3}$ μm^2)			
		Average	Max.	Min.	Size	Average	Max.	Min.	Size
LN 8#	Sandstone, siltstone	7.48	19.44	2.31	30	40.135	454.11	0.01	30
LN 9#	Sandstone, siltstone, breccia	10.94	14.47	4.66	27	28.29	139.22	0.17	23
LN 14#	Sandstone, siltstone, breccia	7.98	16.64	1.73	41	44.24	631.35	0.01	35
LN 17#	Sandstone, siltstone, breccia	6.45	10.81	2.37	28	0.4	4.13	0.01	22
LN 18#	Sandstone, breccia	7.9	17.7	2.96	24	5.09	31.65	0.16	22
LN 19#	Sandstone, siltstone, breccia	7.25	15.16	1.92	77	2.89	27	0.01	65
LN 21#	Sandstone, siltstone	7.03	13.43	3.1	9	3.53	17.11	0.1	6
LN 22#	Sandstone, siltstone, breccia	9.52	16.83	2.1	43	15.16	73.785	0.01	40
LN 23#	Sandstone, siltstone, breccia	5.79	16.68	1.42	126	2.33	42.85	0.01	106
LN 32#	Sandstone, siltstone, breccia	8.99	23.85	1.93	184	10	145.87	0.01	169
LN 44#	Sandstone, siltstone	11.08	22.39	4.11	46	82.53	1213.74	0.06	45
LN 48#	Sandstone, siltstone	9.16	15.03	1.35	48	3.73	16.08	0.23	43
LN 54#	Sandstone, siltstone	7.39	16.59	3.46	20	6.91	112.32	0.06	20

5 Effects of Diagenesis on Reservoir

Accumulation property of reservoir is finally determined by different effects of clastic rock diagenesis on reservoir alternation [8, 9]. The analysis shows that compaction and dissolution, corrosion, and cementation are main effects on the reservoir development of sand-mudstone member in the studied region.

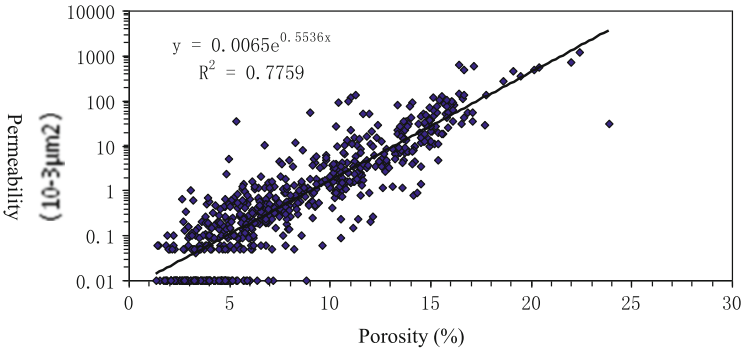

Fig. 3 Relationship diagrams of correlation between porosity and permeability of Carboniferous sand-mudstone member in Lunnan Region

5.1 Compaction and Dissolution

Based on the observation of cast chips (Picture Plate I), the major mechanical compaction effects in the studied region are as follows: compaction and transformation of soft particles (Picture Plate I-5 and I-7), e.g., compaction kink of mica, happened in the early period; fracture of rigid particles leads to irregular cracks and mainly happens to quartz with stable physical properties; particles are mostly embedded (Picture Plate I-2 and I-5) in the wells showing severe compaction; and twin lamellae stress deformation of calcite and dolomite happened at the late stage of diagenesis.

As revealed in chip observation, dissolution gradually develops along with the increased effect of mechanical compaction. Quartz fragments contact each other in the seamed and partially jagged manner (Picture Plate I-2 and I-3). In different layers of every well, linear contact exists among particles. In some chips, calcite cementation prevents further development of compaction, resulting in point contacts and even floating contacts (Picture Plate I-1 and I-4). Above all, the studied region shows severe compaction, which reduces the porous space significantly and affects the accumulation property of sandstone.

5.2 Cementation

The analysis reveals that cementation is the major diagenesis that reduces the reservoir pores of sand-mudstone member in the studied region. There are mainly carbonate and siliceous cements, while the minor ones are clay minerals, pyrites, plaster, self-generated quartz, self-generated feldspar, and sulfate, etc. (Fig. 4 and Picture Plate II).

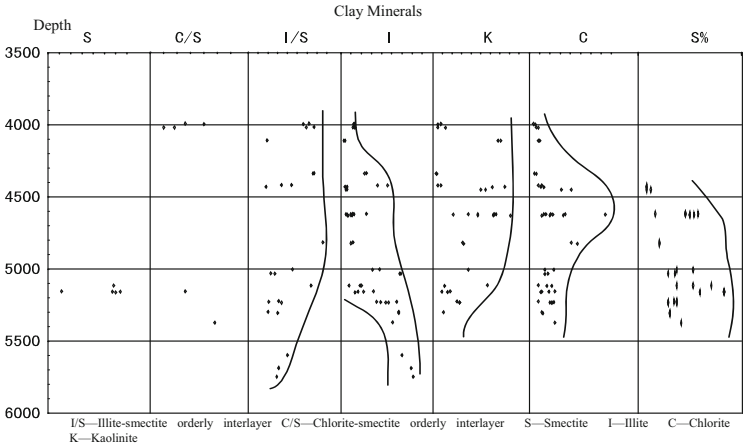

Fig. 4 Variation diagram on the relative content of clay mineral versus the depth of burial of Carboniferous in Lunnan Region

5.2.1 Carbonate Cement

The shape and distribution of carbonate cement are one of the factors controlling the development of reservoir in the studied region. In both macro presentation of rock cores and micro observation of chips, carbonate cement is distributed unevenly in the shape of clump or speck. In the observation of rock cores, gray calcareous clumps and belts are cemented very densely, so they have little accumulation property. Chips also show the development of poikilitic and granular carbonate and the basal or pore-filled cementation or single-crystal filled pores (Picture Plate I-2). While filling pores, carbonate cement enhances the resistance of rock layer to pressure, which prevents the expansion of compaction, preserves early-formed pores, and provides the space for late corrosion by acidic fluids. The study proves that such corrosion pores develop extensively in the studied region and form the important accumulation space and movement channel for oil and gas in the studied region.

5.2.2 Cementation of Clay Minerals

The results of X-diffraction, electron microscopy, and chip observation (Picture Plate II) indicate that clay minerals of sand-mudstone member in the studied region are mainly illite, kaolinite, illite-smectite mixed layer, and chlorite, etc., which are categorized into terrigenous and self-generated. Mostly formed at depositional stage, terrigenous clay minerals often exist in the clay rim that have particles wrapped by membranous minerals and partially filled by minerals. Clay rim has obvious effects on the preservation of pores in the reservoir rocks in the studied region and also inhibits the secondary development of quartz and feldspar

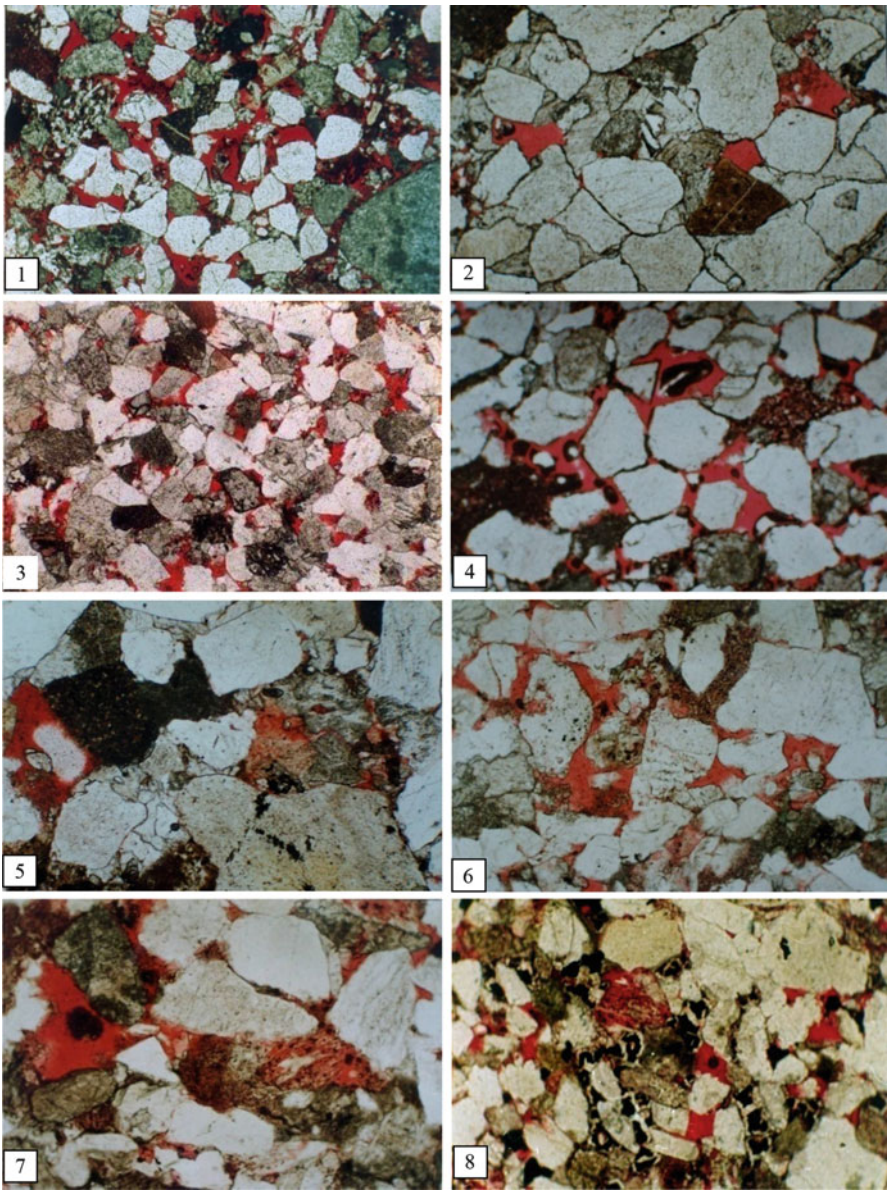

Picture Plate I Reservoir pore cast pictures of Carboniferous sand-mudstone member in Lunnan region. (1) Fine quartz lithic sandstone with partly intergranular pore and intergranular dissolved pore developing and point-linear contact of particles. Lunnan Well 44#, 5,088.1 m. Upper S3 sand group of Carboniferous sand-mudstone member. Cast chips × 20. (2) Fine lithic sandstone cemented by calcite with residual pore and linear contact of particles. Lunnan Well 8#, 5,112.75 m. Upper S3 sand group of Carboniferous sand-mudstone member. Cast chips × 20. (3) Fine lithic sandstone with intergranular pore and intergranular dissolved pore developing. Lunnan Well 48#, 5,085.99 m. Upper S3 sand group of Carboniferous sand-mudstone member. Cast chips × 20. (4) Fine lithic quartz sandstone with partly intergranular pore and intergranular dissolved pore developing. Lunnan Well 8#, 5,120.84 m. Upper S3 sand group of Carboniferous

significantly, facilitating the protection of pores. Chip observation and comparison demonstrate that the section with clay and rim development often has no secondary development. The studied region has a low content of self-generated clay, which is often lined or filled in pores.

Clay minerals convert into each other for the increase of burial depth, pressure, and earth temperature, the release of water between clay mineral layers, and the migration of interlayer cations. As shown in Fig. 4, when burial depth is about 5,200 m, illite-smectite mixed layer and kaolinite decrease, while illite increases in the studied region. At a high depth, kaolinite and smectite disappear and convert into illite and chlorite.

5.3 Corrosion

As revealed in the observation by microscope, scanning electron microscopy and cast chip, sandstone reservoir is exposed to different degrees of corrosion under the effects of carbonic or organic acid, so as to form different types of secondary pores. Corroded materials are mainly unstable particles (e.g., feldspar and deteriorated quartz fragments), carbonate cements (calcite, iron-contained calcite), NaCl, and plaster, etc. Corrosion is the commonest effect on rock fragments in the studied region, and may happen at the edge of particle or along cleavage or form cast pores (Picture Plate I-4 and I-8). Among them, corrosion often happens to quartz fragments selectively. Corrosion is the major contributor to the formation and expansion of accumulation space, but it is very weak in the studied region. Thus, corrosion plays a limited role in improving the reservoir physical property of secondary pores generated.

Picture Plate I (continued) sand-mudstone member. Cast chips × 20. (5) Fine lithic sandstone with intergranular dissolved pore and intragranular pore. Lunnan Well 8#, 5,118.4 m. Upper S3 sand group of Carboniferous sand-mudstone member. Cast chips × 20. (6) Fine quartz lithic sandstone with pores filled by calcite and kaolinite. Lunnan Well 19#, 5,118.10 m. Sub-member S3 sand group of Carboniferous sand-mudstone member in Kalashayi formation. Cast chips × 20. (7) Fine lithic with intragranular pore, intergranular dissolved pore, and some intercrystalline dissolved pore. Lunnan Well 19#, 5,175.80 m. Upper S3 sand group of Carboniferous sand-mudstone member. Cast chips × 20. (8) Fine lithic sandstone with intergranular dissolved pore, intergranular pore, and intragranular pore. Lunnan Well 54#, 5,241.35 m. Lower S3 sand group of Carboniferous sand-mudstone member. Cast chips × 20

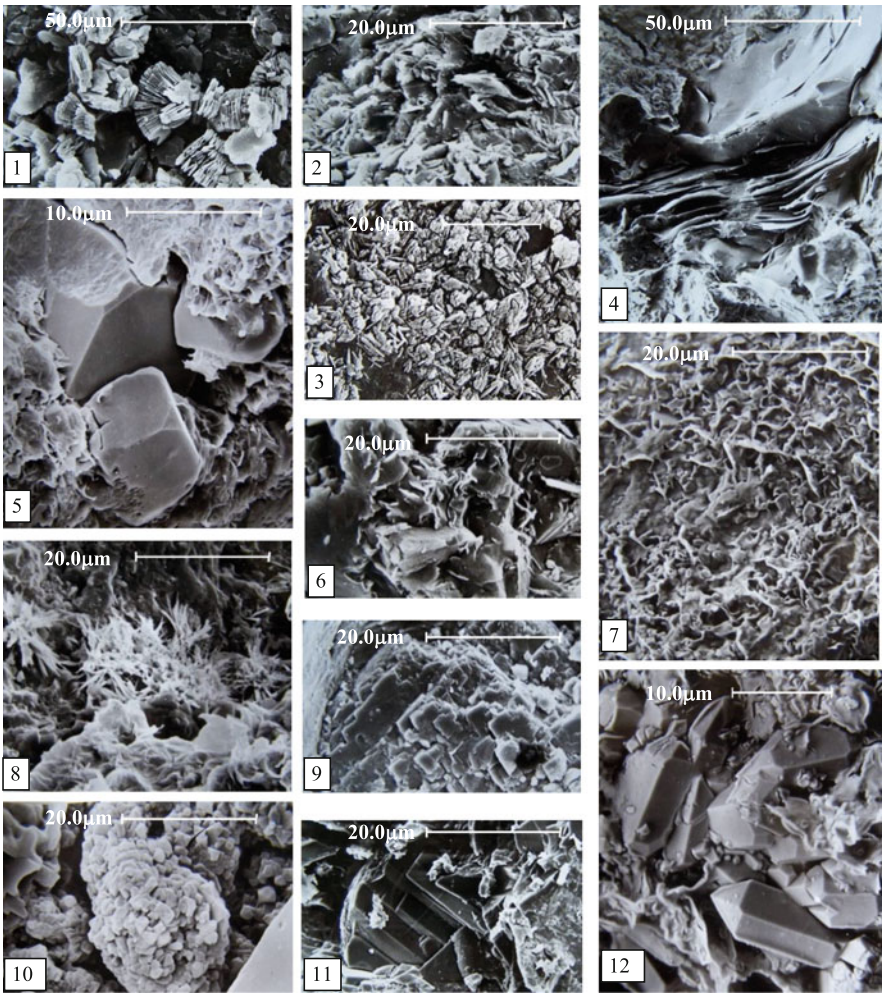

Picture Plate II Reservoir scanning electron microscopy pictures of Carboniferous sand-mudstone member in Lunnan region. (1) Intergranular kaolinite. Lunnan Well 22#, 5,125.35 m, S3, siltstone. (2) Flaky chlorite with irregular surface. Lunnan Well 22#, 5,125.68 m, S3, siltstone. (3) Plaster, Lunnan Well 22#, 5,128.29 m, S3, siltstone. (4) Conversion of mica fragments into illite. Lunnan Well 18#, 5,104.55 m, S3, greenish gray fine sandstone. (5) Clay minerals and dolomite crystal in intergranular honeycomb illite-smectite mixed layer. Lunnan Well 9#, 5,153.58 m, S1, breccia-contained fine sandstone. (6) Illite with curved surface. Lunnan Well 22#, 5,128.89 m, S3, breccia-contained siltstone. (7) Minerals with honeycomb surface in illite-smectite mixed layer. Lunnan Well 18#, 5,128.61 m, S3, gray fine sandstone. (8) Chrysanthemum set formed by fiber plaster. Lunnan Well 9#, 5,153.03 m, S1, muddy siltstone. (9) Corrosion of feldspar fragments. Lunnan Well 22#, 5,126.90 m, S3, siltstone. (10) Pelletized pyrite set. Lunnan Well 9#, 5,153.08 m, S1, grayish white berrica. (11) Carbonate cement. Lunnan Well 22#, 5,128.29 m, S3, siltstone. (12) Self-generated quartz set. Lunnan Well 18#, 5,126.76 m, S3, sandy berrica

6 Conclusion

1. The reservoir lithology of sand-mudstone member is mainly composed of lithic sandstone and partly feldspar lithic sandstone. The reservoir of sand-mudstone member mainly contains intergranular pore and intergranular dissolved pore, and the minor pores are dissolved pores in cement, intragranular dissolved pore, calcite, and kaolinite intercrystalline micropore, with a small amount of grain-edged fracture and micro crack developing. Corroded rocks are mainly calcite, feldspar, and rock fragments with rare existence of extra large pores. It is mostly carbonate cement with strong effect of metasomatism and recrystallization on pores. Pores are distributed sparsely or in clumps with poor connection.
2. The physical property of sandstone reservoir in sand-mudstone member is bad on the whole, and the average porosity is mostly below 10 % with the existence of differences. The porosity, with the correlation coefficient of 0.78, has significant positive correlation with permeability. Effective reservoir mainly develops in residual primary intergranular pores and intergranular dissolved pores.
3. Compaction and dissolution, cementation, and corrosion affect the reservoir development of sand-mudstone member in the studied period, and corrosion plays a constructive role in the development of reservoir pore.

References

1. Sun LX, Zhou Y, Li YP et al (2003) Depositional model and reservoir characteristics of Carboniferous thin sandstone in Hadeson-4 oil field. Xinjiang Pet Geol 24(01):44–46
2. Gu JY (1996) A study of sedimentary environment and reservoir quality of the Carboniferous Donghe sandstone in the Tarim Basin. Acta Geol Sin 9(04):395–406
3. Jia CZ (2004) Structure characteristic and oil-gas of Meso-Cenozoic in Rarim Basin. Petroleum Industry Press, Beijing, p 229
4. Zhang K (2003) Analysis of hydrocarbon prospecting domain in Tabei Uplift of Tarim Basin. Xinjiang Pet Geol 24(3):188–192
5. Xu GQ, Liu SG, Li GR et al (2005) Comparison of tectonic evolutions and petroleum geological conditions in Tazhong and Tabei palaeohighs in Tarim Basin. Oil Gas Geol 26(1):114–119, 129.
6. Xin RC, Jia JH, Yang B (2011) Sequence stratigraphic framework and palaeogeography of the Upper Devonian to Lower Carboniferous in Tarim Basin. J Palaeogeogr 13(06):665–676
7. Huang SJ, Hou ZJ (2001) Spatio-temporal variation of subsurface porosity and permeability and its influential factor. Acta Sedimentol Sin 19(2):224–232
8. Wang R, Shen P, Zhao L (2011) Diagenesis of deep sandstone reservoirs and a quantitative model of porosity evolution: taking the third member of Shahejie Formation in the Wendong Oilfield, Dongpu Sag, as an example. Pet Explor Dev 38(5):552–559
9. Karim A, Pe-Piper G, Piper DJW (2010) Controls on diagenesis of Lower Cretaceous reservoir sandstones in the western Sable Subbasin, offshore Nova Scotia. Sediment Geol 224 (1–4):65–83

The Mineral Geochemistry Identification and Its Influence on the Pore Evolution of the Upper Ordovician Carbonate Cements in Tazhong Oil Field

Xueqin Zhao, Yunfeng Zhang, Zhenyu Wang, Qin Ma, and Tiejun Yin

Abstract According to the crystal morphology and cementation sequence of the calcite cements, with the aid of cathode luminescence and microelement analysis methods, 11 categories of calcite cements are identified in the fracture cave of upper Ordovician Lianglitage Formation in Tazhong Oil Field in the Tarim Basin; three diagenetic environments, that is, submarine diagenetic environment, the meteoric freshwater diagenetic environment, and buried diagenetic environment are determined. The submarine diagenetic environment is Phase I cementation which mainly produces microcrystalline, fibrous, radial fibrous, fasciculate, and radial-axial calcites and subspherical aragonites with a pore filling of 0–30 %. The meteoric fresh water environment is Phase II cementation and its main cements are crescent or pendant calcite, vadose silt, and syntaxial cement with a pore filling of 5–100 %; Phase III cementation occurs in burial diagenetic environment. The crystals of cement are bright and massive and the main categories are calcsparite and poikilotopic calcite with a pore filling of 5–100 %.

Keywords Calcite cement • Carbonate rock • Cementation • Diagenetic environment • Tazhong area

The Foundation of State Key Laboratory of Petroleum Resources and Prospecting, China University of Petroleum, Beijing (No. PRP/open-1303).

X. Zhao (✉) • T. Yin
Institute of Environment and Resources, Southwest University of Science and Technology, 59 Qinglong Road, Mianyang, Sichuan, People's Republic of China
e-mail: zxqch@sina.com

Y. Zhang • Z. Wang • Q. Ma
School of Resources and Environment Engineering, Southwest Petroleum University, Chengdu, Sichuan, People's Republic of China

F. Dong (ed.), *Proceedings of the 11th International Congress for Applied Mineralogy (ICAM)*, Springer Geochemistry/Mineralogy,
DOI 10.1007/978-3-319-13948-7_49

1 Introduction

The upper Ordovician in Tazhong Area of the Tarim Basin is good oil and gas reservoir section consisting of Lianglitage Formation and Sangtamu Formation. The target Lianglitage Formation with both the overlying and underlying formations is in unconformity contact to form a set of limestone deposition with thickness of up to 800 m. During the deposition period, Lianglitage Formation features the platform—slope-basin depositional system (Fig. 1) [1, 2] in the northeast direction. After the deposition of Lianglitage Formation, the basin has experienced karstification of three phases, that is, in the late Ordovician Period—Early Silurian Period, the Late Silurian Period—Early Devonian Period, and the Middle-Late Devonian Period [3], which resulted in the multiple diagenesis categories and diagenetic phases in the Lianglitage Formation and the complex relationship in-between.

Carbonate cement is the important record that manifests the diagenetic history of the carbonate rock and the understanding of its original crystalline habit and the diagenetic time series reflected by the cement stratigraphy mean a lot for the successful recovery of the diagenetic history [4]. Isotope, trace elements, scanning electron microscopy, cathode luminescence, clay mineral transformation, and other techniques have been widely used in the research on discriminating different diagenetic environments and diagenesis phases of carbonate rocks [5, 6] and have achieved good results [7, 8]. The author analyzes the diagenetic environment of the carbonate rocks and discusses the influence of cementation at different diagenetic

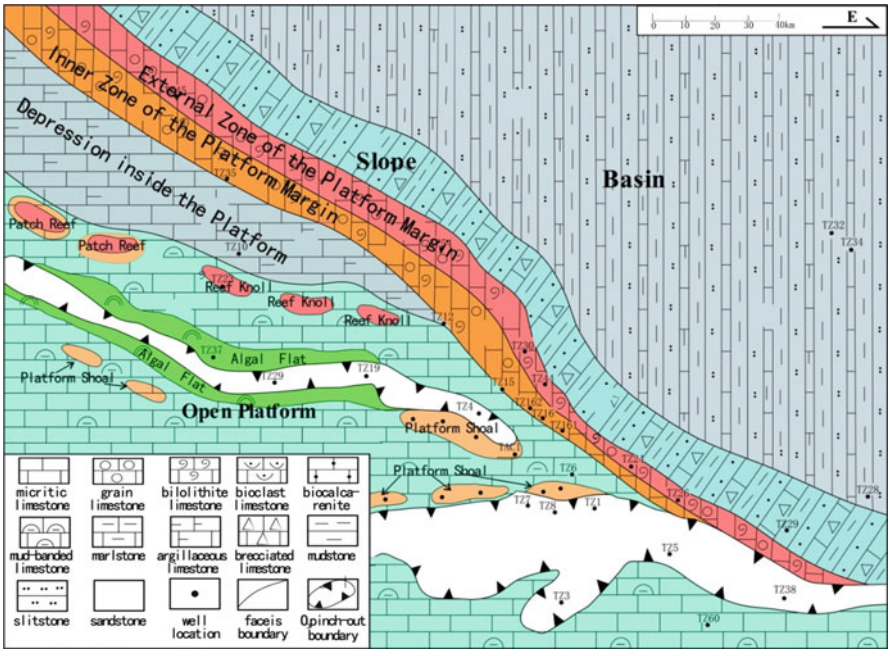

Fig. 1 The plane distribution character of the sedimentary facies of Lianglitage formation of Tazhong area in Late Ordovician Epoch

phases on the pore evolution through observation and description of the characteristics and cause of formation of various cements inside hundreds of pieces of rock slices and polished surface in combination with trace elements and carbon and oxygen stable isotope testing methods.

2 Cement Categories and the Mineral Geochemistry Characteristics

Through observation of the characteristics and cause of formation of various cements inside hundreds of pieces of rock slices and polished surface, the author identified 11 kinds of cement categories of the upper Ordovician Lianglitage Formation in Tazhong Area: microcrystalline calcite, fibrous and fibrous-columnar calcite, radial fibrous calcite, fasciculate and radial-axial calcites, spherical grain fiber skirts, vaterite calcite cement, crescent or pendant calcites, vadose silt, girdle calcite, and calcsparite and poikilotopic calcites; all cements have different distribution characteristics and sequence of formation.

2.1 Mineral Geochemistry Characteristics

To identify the various diagenetic environments and diagenetic phases of the carbonate rocks of the upper Ordovician Lianglitage Formation, the author selects several types of typical cement calcites to carry out isotope, trace elements, scanning electron microscopy, cathode luminescence, and other types of research.

The EPMA (electron probe microanalysis) of the fibrous calcites in the holes of the bond stone and cryptophyta clot limestone shows (Table 1) that its content of MgO, Na_2O, and K_2O is rather high and its content of SrO varies a lot, its content of Ba, Mn, and Fe being generally low; part of the samples contain a bit higher amounts of Fe, which may be attributable to the recrystallization in the late period. The carbon and oxygen isotope analysis of the matrix of the microcrystalline calcite shows that the oxygen and carbon isotope values are −5.24‰ and 0.900‰ (PDB), respectively, which are approximate to the isotope analysis results of the square tube coral and stromatopora shell representing the marine environment in the upper Ordovician carbonate rocks in the same area ($\delta 180 = -5.25$ to −5.36‰ PDB, $\delta^{13}C = 0.77$–0.97‰ PDB).

The electron probe trace element analysis of the radial fibrous calcites in the holes of the reef limestone (Table 2) shows that its content of MgO is high, while its content of SrO is generally low, the content of Na and K changing in an overall consistent manner; the content of MnO is rather low, but in some samples the content of MnO can reach up to 520 $wB/10^{-6}$ and in most of the samples, the content of FeO reaches 420–550 $wB/10^{-6}$; the content of Fe and Mn may be related to the impurities, because all the radial fibrous calcites suffered the effects of the late recrystallization of varying degrees.

The electron probe trace element analysis of the different parts of the radial-axial calcites in the holes of the bond rocks and the frame reef shows that content of trace

Table 1 EPMA of the fibrous calcites in the holes of the bond stone and cryptophyta clot limestone

Number of well	Depth (m)	Lithology	Luminescent characteristic	Trace elements (wB/10^{-6})							Notes
				MgO	SrO	Na_2O	K_2O	BaO	MnO	FeO	
TZ161	4,360	Cryptophyta clot limestone	Nonluminous	6,300	0	570	0	0	0	0	Turbid
TZ161	4,360	Cryptophyta clot limestone	Nonluminous	5,390	330	1,850	240	3,130	130	0	Turbid
TZ30	5,027.8	Bond stone	Dim	6,510	0	1,240	20	0	70	550	Turbid
Tz30	5,065.7	Cryptophyta clot limestone	Dim	6,560	0	4,050	230	0	390	0	Recrystallization being fine grain, turbid
TZ44	5,017.1	Bond stone	Dim–nonluminous	3,820	1,300	100	100	0	0	0	Recrystallization being fine grain, turbid

Table 2 The electron probe analysis of the radial fibrous calcites in the holes of the bond rocks

Well number	Depth (m)	Lithology	EPMA (wB/10^{-6})						
			MgO	SrO	Na_2O	K_2O	BaO	MnO	FeO
TZ30	5,027.8	Bond rock	6,510	0	1,240	260	0	70	550
TZ42	4,378.0	Bond rock	5,110	0	360	60	0	520	420
TZ42	5,375.0	Bond reef limestone	3,090	0	0	0	0	0	450
TZ44	4,843.56	Algae bond calcarenite	1,780	540	800	90	0	0	0

elements and cathode luminescence in different parts of the crystal feature obvious differences. In the middle and lower parts of the crystal, there is higher content of Mg, Sr, and Na, but no content of Fe and Mn, and the manifestation of the cathode luminescence is nonluminous and dim; at the top and on the outer edge of the crystal, the content of MgO, SrO, and Na_2O relatively decreases, while the content of MnO and FeO rises, and the closer to the outer edge, the lower the content of Mg, Sr, and Na and the higher the content of Fe; the manifestation of the cathode luminescence is light in dark orange to orange color (Fig. 2a). This characteristic reflects the changes of medium environment in the growth process of the radial-axial calcites.

The girdle calcite is characterized by the significant growth girdle under the cathode luminescence (Table 2) and generally are mainly fine grained to medium coarse grained; beyond the nonluminous core, there is the development of 2–3 girdles consisting of the bright orange and dark orange light or non-luminescence alternatively. The nonluminous girdle contains a large amount of iron and magnesium, while the luminous girdle contains a large amount of manganese, strontium, and potassium, which reflects the environment variable medium conditions and the environment is mainly formed in the environment under the influence of the underground water in the meteoric water underflow zone–shallow burial zone.

Coarse-grained calcsparites are mostly in medium coarse-giant granular allotriomorphic, hypidiomorphic, or mosaic shapes filling in the center of the holes. Within the incompletely filled holes, the well-developed crystalline forms can also be seen (Table 3). The electron microprobe analysis of their elements shows that their composition changes greatly and the isotope analysis also shows their $\delta^{13}C$ and $\delta^{18}O$ values change greatly as well. Generally speaking, their content of iron and manganese is higher and their cathode luminescence characterized by dim light, dark orange color, and non-luminescence; the significant negative $\delta^{18}O$ value, the high content of two-phase fluid inclusion, and the rather high homogenization temperature reflect that they are formed in the burial environment.

3 Diagenetic Environment Analysis

The category, shape, and filling sequence of the cements can be clearly observed in a variety of pores and cracks through the core, slice, and so on. But the same type of cement may be formed in different diagenetic environments, so the judgment of the

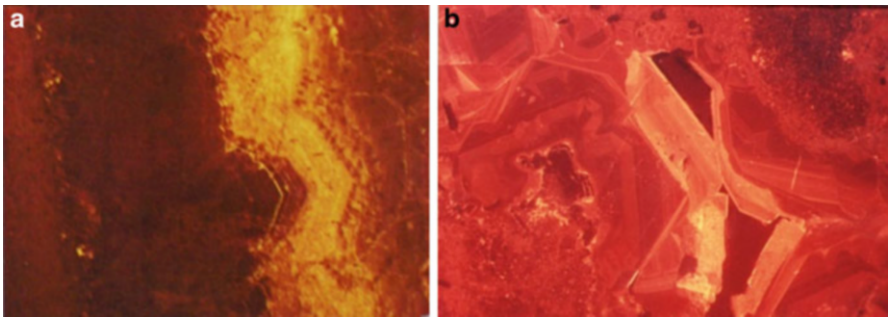

Fig. 2 Picture of cathode luminescence of the cements in the karst cave of Tazhong oil field. (**a**) The cathode luminescence image in the middle chart. The radial fibrous and radial-axial calcites on the edge of the pores are nonluminous. On the outer rim of the radial-axial calcites, there are several luminous girdles in *bright orange*, *dim*, and *dark orange* colors. #42 Well of Tazhong, 5,487.60 m, cathode luminescence, ×10; (**b**) Sparry algal gritty limestone. The intergranular dissolution pores are half-filled with medium-coarse crystalline girdle calcites. Under the cathode ray, there are luminous girdles in *dim* and *dark orange* colors. #44 Well of Tazhong, 4,883.72 m, (−) ×40

diagenetic environment should be based on the integrative analysis of the relationship between shapes of all kinds of cements, geochemistry features, biological effects, deposition, and dissolution [9]. In accordance with the categories of the calcite cements and the isotope, trace elements, and other geochemistry features of the research area (Fig. 3), the author identifies three kinds of diagenetic environments of Lianglitage Formation, that is, submarine diagenetic environment, meteoric freshwater environment, and burial diagenetic environment and all of the three environments feature particular cement categories and cementation sequence.

The products of the submarine diagenetic environment of Lianglitage Formation are mainly microcrystalline calcites, fibrous calcites, radial fibrous calcites, fasciculate calcites, radial-axial calcites, and micrite calcites, that is, six types in total. In the meteoric underflow zone, the typical cement formed is equiaxial and fine grained, and isopachous leaf-shaped, blade-shaped, fang-shaped, diamond-shaped, hexahedral fine-grained calcites, which disperse evenly in the underflow stratum, can either grow along the outer edge of the fibrous rim cements of the filled primary pores and stay in unconformity contact with the fibrous rim cements or fill in the secondary pores formed by the early-phase meteoric freshwater dissolution as Phase I cements. In such kind of diagenetic environment, another common cement is the calcite growing coaxially on the spiny crumb grains, which is clean and bright crystal, almost surrounding the entire spiny crumb grains. The trace elements of the meteoric freshwater cements generally show low Mg, Sr, and Na values, which reflects the dilution of the meteoric fresh water. The common features of the calcite cements from the burial diagenetic environment are coarse and bright crystals, generally larger than 0.1 mm, which fill in the central part of the pores or holes in forms of monocrystal or poikilotope and stay in cementation contact of unconformity with Phase I and Phase II calcites or in direct contact with the cave wall and

Table 3 Electron probe and cathode luminescence analyses of the radial-axial calcite cements in the holes of the bond rocks and frame stones

Well number	Depth (m)	Position	Cathode luminescence	T race element analysis (wB/10^{-6})						
				MgO	SrO	Na_2O	K_2O	BaO	MnO	FeO
TZ42	4,378.0	Middle part of the crystal	Dim	2,900	1,510	2,620	0	2,540	0	0
TZ42	4,378.0	Outer edge of the crystal	Dark orange	3,000	0	540	0	0	0	570
TZ42	4,378.0	Outer edge of the crystal	Orange	3,170	840	1,070	70	0	840	0
TZ42	5,375.0	Middle and upper parts of the crystal	Nonluminous	3,640	0	90	0	0	0	1,010
TZ49	6,398.7	Bottom of the crystal	Nonluminous	3,890	250	400	0	590	0	240
TZ49	6,398.7	Top of the crystal	Dark orange	910	1,900	0	0	1,380	0	480

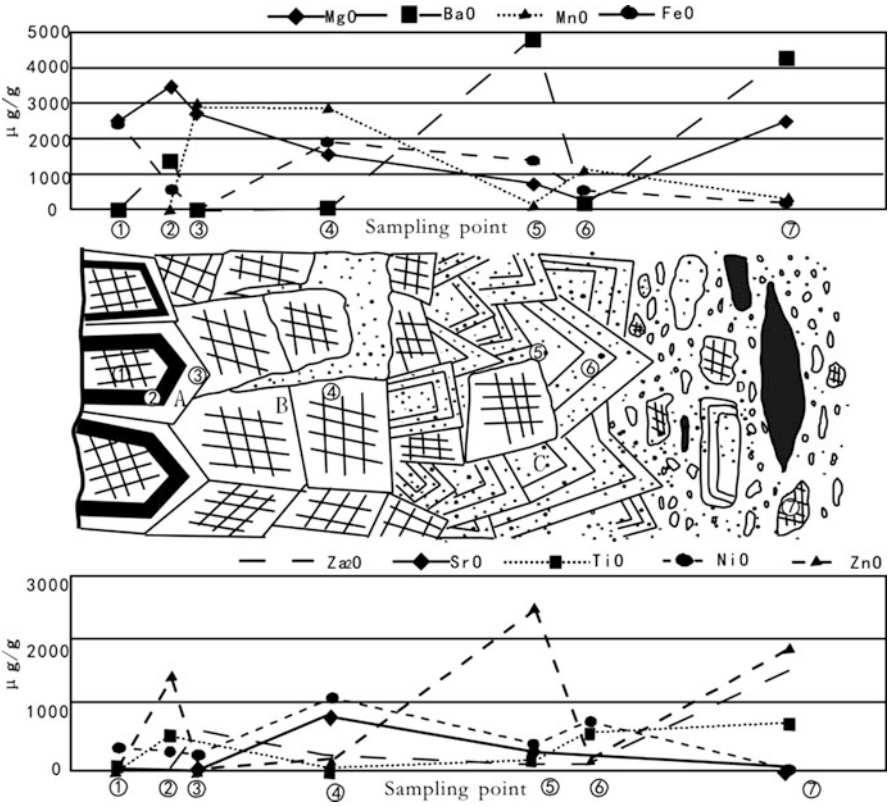

Fig. 3 Filling sequence, cathode luminescence, girdle, and electron probe trace element analysis of the cements in the karst cave at 4,654 m of Tazhong #12 Well. (**a**) Coarse-grained girdle calcite; (**b**) coarse-grained mosaic calcite; (**c**) coarse-grained granular fluorite; (**d**) symbiosis of porphyritic fine-grained calcite and fluorite

grains. This phase of calcites is more common in the pores and holes of the high-energy beach granular limestone and organic reef limestone, and although their content is not high, they often lead to reduced reservoir performance of the primary porosity and secondary porosity.

4 Influence of Cementation on the Evolution of the Pores

4.1 Submarine-Meteoric Freshwater Diagenetic Phase at the Early Diagenesis

At the early diagenesis stage, the original intergranular pores are well developed with the original porosity being 25–40 %. In the submarine cementation phase,

fibrous calcites grow around the edges of the grains, forming the crustified rim cements and resulting in narrowing of the original intergranular pores with their porosity being 5–15 % and their types mainly being residual intergranular pores.

When the sea level declines relatively, the grain shoal will rise above the sea surface and enter the meteoric diagenetic environment. Then near the meteoric vadose zone and the underflow belt, due to the selective dissolution of the meteoric freshwater, intergranular dissolution pores, intragranular dissolution pores, and molded pores and other dissolution seams are formed so that the porosity is increased by 10–15 %. In the middle and lower parts of the meteoric underflow belt, the Phase II leaf-shaped, blade-shaped, fang-shaped, equiaxial, and fine granular, and coaxial calcite cements fill in the pores to reduce the porosity to 10–25 %. Afterward, most of the shoals in the middle and lower parts of Lianglitage Formation usher into the shallow burial stage, when the shallow burial compaction, pressure solution, and cementation occur, resulting in the reduction of the porosity by 10–15 %.

4.2 Porosity Shrinkage Phase at the Shallow Burial Stage

In the subsequent gradual burial process, due to pressure solution and compaction and cementation, the porosity shrinks and the burial cements are mainly fine-grained intergranular calcites with flat and straight crystal surface in equiaxial grain shapes becoming larger while extending toward the pore center. The mass fraction of the burial cements is generally 8–15 %, and after the late Caledonian burial cementation, the porosity reduces to 5–12 % with pore types mainly being residual intergranular solution pores, intergranular dissolution pores, and molded pores. In the stratum with strong cementation section, most of the pores can disappear (Fig. 4).

5 Conclusions

1. Eleven categories of carbonate rock cements of Lianglitage Formation are identified; three diagenetic environments and all cements have distinctive distribution characteristics and sequence of formation.
2. The electron probe analysis shows that the fibrous calcites in the holes of the bond stone and cryptophyta clot limestone have rather high content of MgO, Na_2O, and K_2O and their content of SrO changes a lot, their content of Ba, Mn, and Fe being generally low; the radial fibrous calcite in the holes of the reef limestone has rather high content of MgO, while its content of SrO is generally low, the content of Na and K changing in an overall consistent manner; the radial-axial calcites in the holes of the bond rocks and the frame reef have trace elements and cathode luminescence in different parts of the crystal featuring

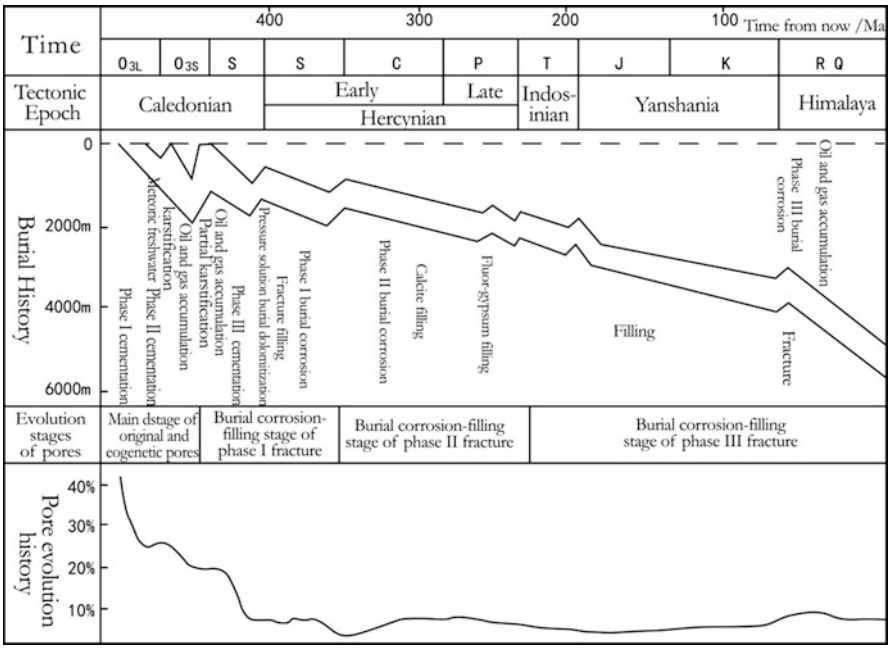

Fig. 4 Ordovician diagenesis and pore evolution history of Tazhong oil field

obvious differences; the composition of the coarse-grained sparry calcites changes greatly.

3. Three diagenetic environments are determined, that is, submarine diagenetic environment, the meteoric freshwater diagenetic environment, and buried diagenetic environment; the submarine diagenetic environment is Phase I cementation, which mainly produces microcrystalline, fibrous, radial fibrous, fasciculate, and radial-axial calcites and subspherical aragonites with a pore filling of 0–30 %; the meteoric freshwater environment is Phase II cementation and its main cements are crescent or pendant calcite, vadose silt, and syntaxial cement with a pore filling of 5–100 %; Phase III cementation occurs in burial diagenetic environment. The crystals of cement are bright and massive and the main categories are calcsparite and poikilotopic calcite with a pore filling of 5–100 %.

References

1. Jia CZ, Wei GQ, Yao HJ et al (1995) Tectonic evolution and regional structural geology of the Tarim Basin (petroleum exploration in the Tarim Basin). Petroleum Industry Press, Beijing, p 203
2. Chen JS, Wang ZY, Dai ZY et al (1999) Study of the middle and upper ordovician rimmed carbonate platform system in the Tazhong Area, Tarim Basin. J Palaeogeogr 1(2):8–17

3. Huang SJ, Wang CM, Huang PP et al (2008) Scientific research frontiers and considerable questions of carbonate diagenesis. J Cheng du Univ Technol 35(1):1–10
4. Aissaoui DM, Cpniglo M, James NP, Purser BH (2002) Diagenesis of a Miocene Reef Platform: Jebel Abu-Shaar, Guif of Suez, Egypt. In: Schroeder JH, Purser BH (eds) Reef diagenesis. Springer, Germany, pp 112–131
5. Macaulay CI, Haszeldine RS, Fallick AE (1993) Distribution, chemistry, isotopic composition and origin and diagenetic carbonates; Magnus Sandstone, North Sea. J Sediment Petrol 63 (1):33–43
6. Moyleg PS, Burns SJ (1993) Oxygen and carbon isotopic composition of marine carbonate concretions: an overview. J Sediment Petrol 63(1):73–83
7. Song ZM (1993) Cathodoluminescence geology basis. China University of Geosciences Press, Wuhan
8. Qiang ZT (1998) Carbonate reservoir geology. University of Petroleum Press, Beijing
9. Kendall AC, Tucker ME (1973) Radiaxial fibrous calcite: a replacement after acicular carbonate. Sedimentology 20(3):365–389

Chemical and Mineralogical Characterizations of High Ti-Bearing Blast Furnace Slag in Panzhihua, China

Guobiao Zhou, Tongjiang Peng, Hongjuan Sun, and Haiyang Xian

Abstract Chemical and mineralogical characterizations of high Ti-bearing blast furnace slag in Panzhihua region, Sichuan province, China, were investigated, and the technical approach "recycling Fe by magnetic separation-extracting Al and Mg by sulfation roasting and water leaching-extracting Ti by acidolysis" was proposed for recycling the valuable elements from the special mineral resources. The results show that the most valuable metal is Ti (20.46 % TiO_2, mass fraction). Other metals, such as Al, Mg, and Fe, can also be seen as valuable components to be recovered. Minerals such as perovskite, diopside, and spinel are disseminated in the slag. The Ti element in the slag is distributed widely in many types of mineral phases and Ti component enriches mainly in perovskite phase. It is highly euhedral and mostly disseminates in the diopside, it usually presents an equiaxed or irregular granular shape, and particles are commonly tiny.

Keywords High Ti-bearing blast furnace slag • Mineral characterization • Valuable components • Comprehensive utilization

1 Introduction

Titanium ore deposits are widely distributed in the southwest part of China, and 95 % of which occurs in vanadium–titanium magnetite ore [1]. Panzhihua-Xichang area, which is the main metallogenic belt of vanadium titanium magnetite, is also

Fund: Supported by Postgraduate Innovation Fund Project by Southwest University of Science and Technology (13ycjj20).

G. Zhou • H. Xian
Key Laboratory of Solid Waste Treatment and Resource Recycle, Southwest University of Science and Technology, Ministry of Education, 59 Qinglong Road, Mianyang, Sichuan, People's Republic of China

T. Peng (✉) • H. Sun
Institute of Mineral Materials & Application, Southwest University of Science and Technology, 59 Qinglong Road, Mianyang, Sichuan, People's Republic of China
e-mail: tjpeng@swust.edu.cn

F. Dong (ed.), *Proceedings of the 11th International Congress for Applied Mineralogy (ICAM)*, Springer Geochemistry/Mineralogy,
DOI 10.1007/978-3-319-13948-7_50

one of the important production areas of similar ore deposits in the world. At present, the ore which contains 10.4 % TiO_2 and 0.3 % V_2O_5 is smelted in blast furnaces. Most of the Ti component in the ore is separated from iron and formed the high Ti blast furnace slag which contains excess of 20 % TiO_2. It is a kind of specific secondary mineral wealth of China. China has accumulated over 60 million tons of Ti blast furnace slag, and it is still increasing at an annual rate of more than 3.6 million tons [2]. Thus, comprehensive utilization of the resources is beneficial, because it helps save natural resources and reduces the tonnage of slag that is stocked every year.

For utilizing the specific secondary mineral resources, several mineral and metallurgy methods such as selective enrichment and separation after metallurgic modified [3–6], preparation of $TiCl_4$ by high-temperature carbonization and low-temperature chlorination [7, 8], recovery titanium by H_2SO_4 leaching [9, 10], and separation of iron droplets from titanium-bearing slag [11] have been studied in the past years. However, the recovery efficiency for Ti components of those processes was poor, and so the slag has not been efficiently utilized. In addition, there were fewer studies which have been undertaken to research the chemical and mineralogical characterizations of high Ti-bearing blast furnace slag that occur in early stage. With the improvement and development of smelting process, there may be some differences in chemical and mineralogical characterizations between the recent slag and slag which occur in early stage. It is essential to identify the chemical and mineralogical characterizations of the recent slag and more efficient use of the specific secondary mineral resources.

Thus, the aim of this study was to undertake systematic and detailed chemical and mineralogical characterizations of high Ti blast furnace slag coupling with several analytical techniques in order to make use of the specific secondary mineral resources. These characterizations were exposed and their results were discussed in this chapter.

2 Materials and Methods

In this work, a kind of high Ti blast furnace slag from Panzhihua, Sichuan Province, China, was investigated by chemical and mineralogical means. The high Ti blast furnace slag was obtained from the slag fields of Panzhihua Iron and Steel Corporation. All of the samples were collected by the method of pick-out sampling to ensure the representativeness of the samples. They were slowly air cooled and have vesicular texture, massive structure, and gray-black color.

2.1 Chemical Characterization

For chemical characterization, some samples in fine powder (−0.074 mm) were obtained after crushing and ball milling by a jaw crusher and a high-energy ball

mill. The multi-element analysis of the bulk samples was determined by X-ray fluorescence (Axios; PANalyticalB.V.). The accelerating voltage and the tube current were 60 kV and 100 mA, respectively.

2.2 Mineralogical Characterization

The main mineral phases contained in the slag were identified using X-ray diffraction (XRD) and complementary analyses were made using metallographic microscope and scanning electron microscopy (SEM) coupled with energy-dispersive spectrometer (EDS).

2.2.1 XRD Analysis

In order to determine the mineralogical compositions of the powder samples, the XRD (X'Pert PRO; PANalyticalB.V.) technique with Cu Kα radiation was used in the present experiments. The accelerating voltage and the tube current were 40 kV and 40 mA, respectively. The X-ray patterns were acquired in the 2θ scanning range from 3 to 80° at a scanning rate of 8° min^{-1}.

2.2.2 Metallographic Microscope Analysis

For optical microscopic observation, the air-cooled slag was mounted in epoxy resin, incised and polished, and then the polished sections were observed in the optical microscope (BX51-P; Olympus) to obtain the grain size, mineral components, and embedded features of minerals in the high Ti blast furnace slag. The optical microscope was associated with polarized light, reflected light, and a photomicrography system. Magnification objectives range from 10 to 50×.

2.2.3 SEM/EDS Analysis

Following the optical microscopic examination, in order to analyze the microstructural aspects, micro-constitution, and microstructure of the slag, the polished sections were determined with a scanning electron microscope (SEM) coupled with EDS. The scanning electron microscope (Libra 200FE; Carl Zeiss SMT Pte Ltd) was equipped with a field emission and coupled with an EDS (IETEM100; Oxford). Analysis conditions were as follows: an acceleration tension of 20 kV and 10 mm for the working distance. For semiquantitative chemical analyses, the counting time was fixed at 40 s/point range.

Table 1 The main chemical composition of Ti-bearing blast furnace slag (mass fraction, %)

TiO_2	Al_2O_3	CaO	SiO_2	MgO	Fe_2O_3	BaO	MnO
20.46	13.54	27.91	25.98	7.68	1.92	0.08	0.68
K_2O	SO_3	Na_2O	Cr_2O_3	SrO	ZrO_2	P_2O_5	Rb_2O
0.60	0.58	0.42	0.04	0.04	0.03	0.02	0.02

3 Results and Discussion

3.1 Chemical Component

In order to research the main chemical component of high Ti blast furnace slag, through the coarse crushing, fine crushing, and dry grinding, five powdered samples below 0.074 mm for chemical analysis were prepared. Table 1 showed the average content of multi-element analysis of the samples by X-ray fluorescence spectroscopy. As shown in this table, the slag was mainly composed of TiO_2, CaO, Al_2O_3, SiO_2, MgO, and Fe_2O_3 and contained small amounts of MnO, BaO, and K_2O.

TiO_2 content in samples fluctuated remarkably in the tiny range, which may be as high as 20 % and even 23 % in some samples. The grade of Ti in the slag was far over the least industrial grade as the associated useful composition. According to some studies [12, 13], the slag was not suitable to produce building materials like other developed countries because the higher content of TiO_2 may affect the performance of building materials. More importantly, traditional extensive mode of utilization was the basic reason for the wastage of the valuable resources in this approach. Nevertheless, owing to the lower content of TiO_2, the slag was not suitable to produce artificial rutile as an ingredient. Compared with natural rocks, the slag has high titanium and low silicon in chemical composition, which can be considered as a kind of silicon-unsaturated rock.

3.2 Mineralogical Characterizations

3.2.1 Main Mineral Phases

Three mineral phases were confirmed by XRD analyses (Fig. 1). Results of XRD test showed that perovskite (characteristic diffraction peaks: 2.703, 1.913, 2.720, 2.690, 1.910 Å) as the major mineral phase in the slag. Secondary minerals were diopside (characteristic diffraction peaks: 2.994, 2.551, 1.425, 2.131 Å) and spinel (characteristic diffraction peaks: 2.436, 2.021, 1.429, 1.555 Å), in which the content of perovskite was 40 %, diopside 51 %, and spinel content 9 %. Perovskite has the strongest diffraction peak in the three kinds of minerals, followed by diopside and spinel. The diffraction peaks were very sharp, showing that the degree of crystallization of minerals was good.

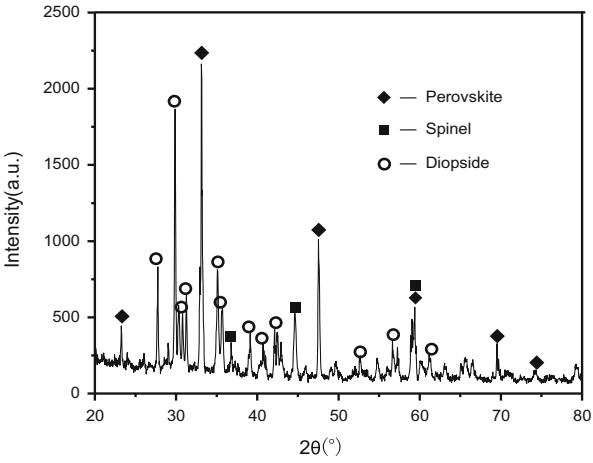

Fig. 1 X-ray diffraction of Ti-bearing blast furnace slag

3.2.2 Optical Specification

After sintering and smelting blast furnace, all unreduced oxides, such as calcium oxide, titanium oxide, magnesium oxide, and aluminum oxide in vanadium titanium magnetite erupted from blast furnace after cooling in the air, formed the high Ti blast furnace slag. The process was very similar with the magma spurting out from the crust. Hand specimen of high Ti blast furnace slag was dark gray block structure, partial for porous structure.

Following XRD examination, the high Ti blast furnace slag samples were made into polished sections and polished thin sections for observation under the optical microscope. The microscopic photos under reflected light (Fig. 2a) and polarized light (Fig. 2b) were obtained. From Fig. 2 it can be seen that high Ti blast furnace slag mainly showed idiomorphic or hypidiomorphic granular structure and disseminated texture. Ore microscopic fabric research results showed that the main minerals in the high Ti blast furnace slag included perovskite, diopside, magnesium aluminium spinel, and metallic iron.

3.2.3 Perovskite

The distributions of perovskite granules were uniform in the high Ti blast furnace slag. Perovskite appeared white in reflected light, dark gray, or brown in polarized light, most of which showed idiomorphic equiaxed or irregular granular shape; individual crystals grew into rules of cube. Some crystals showed cross-shaped section and dendritic skeletal conjoined. Crystal grain size was fine, about 5–20 μm. Perovskite was evenly dispersed in diopside and glass substrate, and the content was about 35–40 %.

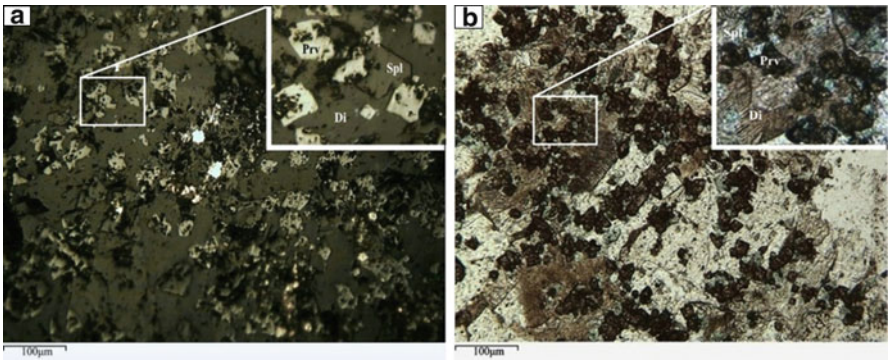

Fig. 2 Optical microscopic characteristic of Ti-bearing blast furnace slag. (**a**) Micrograph of reflected light; (**b**) micrograph of polarized light, *Prv* perovskite, *Di* diopside, *Spl* spinel

3.2.4 Diopside

Diopside appeared taupe and brown yellow in polarized light. Most of the diopside crystals were in irregular, columnar, or plate forms, usually for granular, dense clumps or radial pattern aggregation. Diopside was the most important gangue mineral in the high Ti blast furnace slag, and the content was about 45–55 %. The crystal grain size was about 50–300 μm, usually with unequigranular metallic iron filled in the diopside.

3.2.5 Spinel

Spinel showed light blue or greenblack in polarized light. Mainly, the equiaxial euhedral-hypidiomorphic octahedral crystal appeared, whose forms often were rhombus, square, triangle, and rules under the polarized light, sometimes irregular granular distributed in diopside and glass substrate, distribution around the perovskite, content about 5–10 % in the slag, and small particle size distribution, generally in 15–25 μm.

3.2.6 Metallic Iron

Metallic iron appeared bright yellow under the reflected light. Most of which were pelletized, sometimes massive, banded, embayed, and elliptically distributed in diopside. The particle size distribution was very uneven, from small to a few microns to some hundreds of micrometers. The content in the high Ti blast furnace slag was about 2–5 %.

The above optical identification on Ti-bearing blast furnace slag showed that Ti component enriches mainly in perovskite, and various minerals in the microscopic morphology characteristics were similar to the natural production of perovskite and

diopside ore under the objective characteristics, so that we regarded Ti-bearing blast furnace slag as a kind of artificial rock. The XRD analysis results of Ti-bearing blast furnace slag powder specimens were consistent with above optical identification.

3.3 Micro Area Composition

The scanning electron microscope (SEM) coupled with EDS was used to analyze the microstructural aspects, micro-constitution, and microstructure of the high Ti-bearing blast furnace slag. The electron backscattering micrograph of the polished sections and energy spectrum of all kinds of individual minerals were shown in Fig. 3. As can be seen in Fig. 3, the microstructure aspect characteristics of high Ti-bearing blast furnace slag were similar to the identification results under the optical microscope. The results of energy spectrum analysis showed that the main minerals in the slag were perovskite, diopside, magnesium aluminum spinel, and metallic iron, which were consistent with the XRD and ore microscopy results. In addition, there was a small amount of mist titanium carbonitride solid solution

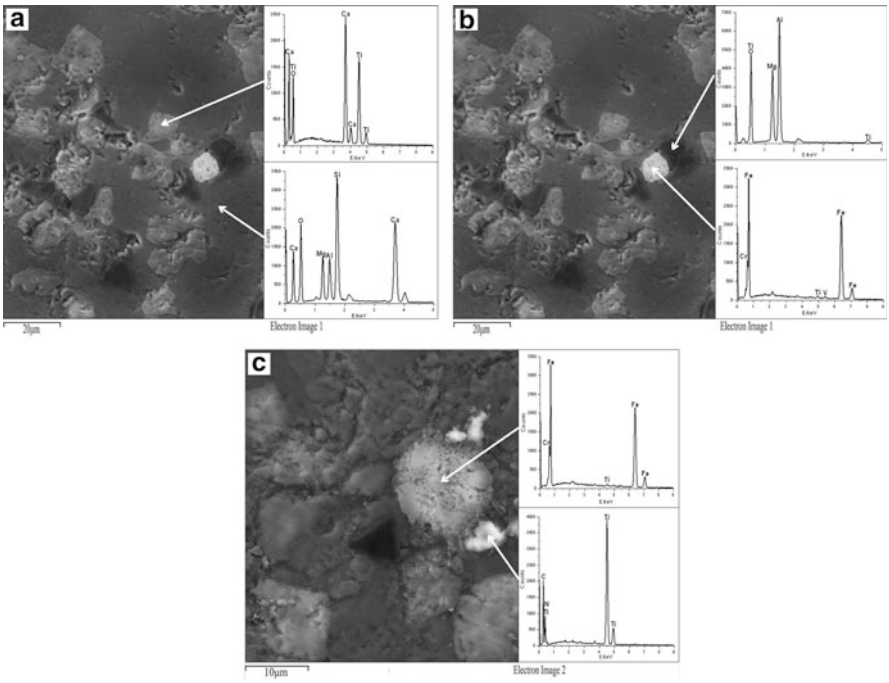

Fig. 3 The electron backscattering micrograph and energy spectrum analysis of Ti-bearing blast furnace slag in SEM-EDS. (**a**) Perovskite and diopside, (**b**) spinel and metallic iron, (**c**) metallic iron and Ti(C,N))

output around the metallic iron. EDS was used to determine the micro area chemical composition of each mineral phase in high Ti blast furnace slag, as indicated in Table 2 and described below.

Perovskite phase contains calcium (27–31 %), titanium (31–37 %), and oxygen (31–43 %). The ratio of calcium, titanium, and oxygen atomic number was close to 1:1:3, and theory empirical formula of perovskite for $CaO{\cdot}TiO_2$. It also contains small amounts aluminium. Diopside phase contains calcium (20–25 %), silicon (12–21 %), and oxygen (37–39 %). It also contains small amounts magnesium, aluminum, and titanium, and titanium content was fluctuated in a wide range, the individual test point mass fraction of titanium was high as 11 %. Spinel contains magnesium (15–18 %), aluminum (29–39 %), and oxygen (44–54 %). The ratio of magnesium, aluminum, and oxygen atomic number was close to 1:2:4, and theory empirical formula of spinel for $MgO{\bullet}Al_2O_3$. In addition, the spinel also contains a certain amount of titanium, and the content was about 2–4 %. Titanium was closely associated with spinel and exists mainly in the form of isomorphism in spinel. Metallic iron contains iron (95–99 %) and oxygen content of only about 2 %, which indicated that the oxidation degree of metal iron was low in the high Ti-bearing blast furnace slag. It also contains small amounts aluminum and vanadium. It was worth noting that there was always a kind of smog-like material around the metallic iron in the electron backscattering micrograph of high Ti-bearing blast furnace slag. Energy spectrum test results showed that the material was titanium carbonitride solid solution, which contains titanium (62–87 %), carbon (12–19 %), and nitrogen (11–25 %). The content of titanium was extremely high in titanium carbonitride solid solution, but the content was very low in slag, the particle size was small, and there was only a small output around the metallic iron.

The studies indicated that high Ti-bearing blast furnace slag in Panzhihua was an important secondary resource, which contains titanium, aluminum, magnesium, iron, and other valuable components. Perovskite was the main Ti-rich mineral in the slag, and granularity is fine, only 5–20 μm, and very scattered distribution of slag, with almost every mineral containing titanium. Titanium was as isomorphism hosting in diopside and spinel which were the secondary hosting slag for titanium. Therefore, with the method of mineral separation of perovskite in order to realize the recycling of titanium in problems of perovskite disintegration difficulties, low comprehensive recovery, and difficult to achieve comprehensive utilization of the special secondary resources.

Iron content was lower in the high Ti-bearing blast furnace slag, but most of which filled in diopside and other mineral grains in the form of metallic iron, lower degree of oxidation, highly magnetic, and easy to disintegrate from the slag. Therefore, metal iron in slag could be recycled effectively by adopting the low-intensity magnetic separation. Aluminum and magnesium in the slag could also be seen as valuable component to be recovered. To extract aluminum and magnesium from high Ti-bearing blast furnace slag by sulfation roasting followed by water leaching was proposed. The content of aluminum and magnesium was enriched in the leaching solution and the content of titanium was enriched in the

Table 2 Chemical composition of the mineral phases contained in the high Ti blast furnace slag obtained by EDS

Mineral phases	Perovskite	Diopside	Spinel	Metallic iron	Ti(C,N)
Elements weight %	Min–max	Min–max	Min–max	Min–max	Min–max
Ca	27.20–31.14	19.78–24.62	0–0.32	–	0–0.70
Ti	31.14–37.27	1.28–10.91	1.65–4.30	0–0.32	61.95–86.80
Si	–	12.36–21.19	–	0–0.24	–
Al	0–0.91	7.44–8.04	29.29–39.07	0–1.88	–
Mg	–	4.70–6.79	14.76–18.35	–	–
O	30.97–42.89	37.09–39.23	43.92–54.38	0.89–2.76	0–12.97
Fe	–	–	–	94.46–99.46	0–2.17
V	–	–	–	0–1.02	0–10.84
Cr	–	–	–	0–0.49	–
Na	–	0.62–1.88	–	–	–
C	–	–	–	–	12.03–19.37
N	–	–	–	–	10.70–25.39

solid phase and formed rich titanium slag. And on this basis we proposed to extract Ti by acidolysis from the rich titanium slag.

There were many studies on extracting Ti by direct acidolysis [9, 14, 15]. However, there were two main reasons that the extraction of titanium from high Ti-bearing blast furnace slag was difficult using direct acidolysis. One reason is that the slag contains plenty of consumption of acid composition like Ca, Al, Mg, and Fe. The other reason was that the component of decomposing titanium liquor was complex, and the impurity content was high. Thereby, the technical approach "recycling Fe by magnetic separation-extracting Al and Mg by sulfation roasting and water leaching-extracting Ti by acidolysis" was proposed for valuable components recycling based this study on research of chemical and mineralogical characterizations of high Ti-bearing blast furnace slag.

4 Conclusions

A careful and detailed chemical and mineralogical characterization of high Ti-bearing blast furnace slag from Panzhihua, Sichuan Province, China, was carried out. The obtained results are summarized as follows.

1. The most valuable metal was Ti in the high Ti-bearing blast furnace slag. Other components, such as Al, Mg, and Fe, can also be seen as valuable element to be recovered. The main minerals in the slag were perovskite, diopside, magnesium

aluminum spinel, and metallic iron. In addition, there was a small amount of titanium carbonitride solid solution output around the metallic iron.
2. Ti component enriches mainly in perovskite in the high Ti-bearing blast furnace slag. The granularity of perovskite is small and Ti component distributes in various minerals. Therefore, hydrometallurgy is more appropriate to recovery valuable components from the high Ti-bearing blast furnace slag than traditional separation processes.
3. Based on research of chemical and mineralogical characterizations of high Ti-bearing blast furnace slag, the technical approach "recycling Fe by magnetic separation-extracting Al and Mg by sulfation roasting and water leaching-extracting Ti by acidolysis" was proposed for valuable components recycling.

References

1. Du HG (1996) Theory of smelting V and Ti-magnetite by blast furnace. Science Press, Beijing
2. Li XH, Pu JT (2011) The latest developments of integrated utilization on Panzhihua high titanium-bearing BF slag. Iron Steel Vanadium Titan 2:10–13
3. Li YH, Lou TP, Sui ZT (2000) Selective enrichment of Ti component in Ti-bearing blast furnace slag and precipitation behavior of perovskite phase. Chin J Nonferrous Metals 5:719–722
4. Sui ZT, Guo ZZ, Zhang L (2006) Green separation technique of Ti component from Ti-bearing blast furnace slag. J Mater Metall 2:93–97
5. Wang MY, Lou TP, Sui ZT (2007) Precipitation behaviour of perovskite phase in oxidized Titanium-bearing slag. Chin J Process Eng 1:110–112
6. Wang MY, Zhang LN, Zhang L (2006) Selective enrichment of TiO_2 and precipitation behaviour of perovskite phase in titania bearing slag. Trans Nonferrous Metals Soc China 16:421–425
7. Peng Y (2005) Thermodynamic analysis on the selective chlorination of carbonized Pangang BF slag at low temperature. Titan Ind Prog 6:45
8. Ke CM, Han BQ, Wei YW (2010) Extracting titanium by plasma smelting reduction from high titanium-bearing BF slag. Papers of the 2010, conference on integrated utilization on Panzhihua high titanium-bearing BF slag, Panzhihua, China, pp 43–48
9. Huang ZQ, Wang MH, Du XH (2003) Recovery of titanium from the rich titanium slag by H_2SO_4 method. J Mater Sci Technol 2:191–192
10. Wang MH, Du XH, Sui ZT (2000) Recovery of titanium from rich titanium blast furnace slag. Multipurpose Util Miner Resour 4:5–7
11. Wang MY, Lou TP, Zhang L (2008) Separation of iron droplets from titania bearing slag. J Iron Steel Res Int 1:45–48
12. Wang XQ (1994) The smelting of vanadium-titanium bearing magnetite by blast furnace. Metallurgical Industry Press, Beijing, pp 67–70
13. Dong HG, Guo YF, Jiang T (2010) Directional enrichment-separation of titanium component from Ti-bearing blast furnace slag. J Wuhan Univ Sci Technol 6:574–578
14. Xiong Y, Li C, Liang B (2008) Leaching behavior of air cooled Ti-bearing blast-furnace slag in hydrochloric acid. Chin J Nonferrous Metals 3:557–563
15. Zhang P, Liu DJ, Mao XH (2012) Leaching of water quenched titanium-bearing blast furnace slag in hydrochloric acid. Iron Steel Vanadium Titan 5:6–9

Secondary Minerals of Weathered Orpiment–Realgar-Bearing Tailings in Shimen Carbonate-Type Realgar Mine, Changde, Central China

Xiangyu Zhu, Rucheng Wang, Xiancai Lu, Huan Liu, Juan Li, Bingjie Ouyang, and Jianjun Lu

Abstract Formation and dissolution of secondary arsenic minerals often play significant roles in controlling arsenic mobility in contaminated environments, especially in sulfide mines. Weathering of the orpiment and realgar-bearing tailings from the Shimen realgar deposit, the largest realgar deposit in Asia, was studied. An integrated mineralogical analysis by using X-ray powder diffraction, Raman spectrum, scanning electron microscope, and transmission electron microscope reveals four kinds of As-bearing secondary minerals, including arsenic oxides, arsenates, As-gypsum, and As-Fe minerals. The precipitation of arsenates is due to interaction of As-bearing runoff waters and the underlying carbonate rocks, or the transformation of gypsum into arsenates or As-bearing gypsum through $SO_4^{2-}/HAsO_4^{2-}$ substitution. Ca-arsenates are mainly weilite and pharmacolite with Ca/As atomic ratio of 1. Scanning transmission X-ray microscope and X-ray absorption fine structure reveal that the valence of arsenic is mainly +3 and +5.

Keywords Weathering • Arsenic • Tailings • Secondary arsenic minerals • Shimen realgar deposits

1 Introduction

Arsenic is known to be essential for life in small amounts, but becomes toxic for plants, animals, and humans when ingested in large amounts [1–3]. Inorganic Arsenic has mutagenic, teratogenic, and carcinogenic effects [4], and the human epidemiologic evidence of inorganic As-induced skin, lung, and bladder cancers is ample [5]. Arsenic is currently regarded as one of the most toxic inorganic elements, causing environmental and health impacts in several areas of the world

X. Zhu • R. Wang (✉) • X. Lu • H. Liu • J. Li • B. Ouyang • J. Lu
State Key Laboratory for Mineral Deposit Research, School of Earth Sciences and Engineering, Nanjing University, Nanjing 210093, China
e-mail: Rcwang@nju.edu.cn

F. Dong (ed.), *Proceedings of the 11th International Congress for Applied Mineralogy (ICAM)*, Springer Geochemistry/Mineralogy,
DOI 10.1007/978-3-319-13948-7_51

[6]. In natural environments, arsenic can exist in −I, −III, 0, III, and V states. Trivalent forms (e.g., arsines, arsenite, and arsenolite) are generally more toxic than pentavalent forms (e.g., arsenate, arsenicals) or metallic arsenic [7]. More specifically, As (III) is about 60 times more toxic than As (V) [8]. Despite of same valence, toxicity can be influenced by the occurrence of arsenic; for example, inorganic arsenic compounds are about 100 times more toxic than organic ones [9]. In general, the toxicity of different arsenic species varies in the order: arsine (AsH_3) > arsenite (ASO_3^{3-}) > arsenate (ASO_4^{3-}) > monomethylarsonate > dimethylarsinate [7, 10, 11].

There are more than 200 arsenic minerals, including elemental arsenic, arsenides, sulfides, sulfosalts, oxides, arsenates, and arsenites. Weathering of these arsenic minerals, especially arsenic sulfides, generally releases arsenic into groundwater and soils and causes serious contamination. Meanwhile, various secondary arsenic minerals, such as scorodite, arsenic oxides, amorphous Fe–As minerals, kaatialait, and pharmacosiderite, precipitated [12, 13]. In such processes, active arsenic species can be adsorbed or coprecipitated into secondary minerals while directly precipitated. Then the arsenic is immobilized and the toxicity is reduced. Thus, in weathering process of arsenopyrite at sulfidic mining sites, at least three kinds of secondary arsenic phases have been identified, including mineral phases, absorption ions, and solid solution precipitations. In local highly As-enriched environments, secondary arsenic mineral, e.g., scorodite ($FeAsO_4{\cdot}2H_2O$), can be precipitated [13–15]. The formation of these secondary phases on the mineral surface could slow down the oxidation of As-bearing sulfides [12]. The stability of these secondary minerals in a changing environment controls the arsenic concentration in waters [13]. For example, scorodite may transform into Fe oxyhydroxide as pH increases and result in As(V) species releasing into the environment [16–18]. While in most cases, arsenic oxyanions can be absorbed in Fe oxyhydroxide via outer-sphere complex or inner-sphere ways [19–21]. But, as the bicarbonate–carbonate concentrations increase, arsenic can also be released again from Fe oxyhydroxide [22, 23]. Furthermore, reduction of the oxides will also cause desorption and secondary mobilization of the adsorbed arsenic species [15], and the released arsenic may be absorbed on or coprecipitated into the reduced Fe (II) phases [24]. Another phase of arsenic in weathered mine wastes is $HAsO_4^{2-}$, commonly substituted structural SO_4^{2-} of jarosite ($KFe_3(SO_4)_2(OH)_6$), and schwertmannite ($Fe_8O_8(OH)_6SO_4$) [14, 25].

So far, the weathering of arsenopyrite has been widely studied [26], whereas the natural weathering of realgar and orpiment is rarely studied despite their wide usage, poison, and large amount in environment. Based on laboratory experiments, Lengke and Tempel [27–29] calculated the reaction rates and activation energies of the oxidation of natural realgar and orpiment at near neutral to alkaline pH values, and found that oxidation of realgar was more rapid than orpiment with the same dissolved oxygen concentration and pH. Increasing pH and high dissolved oxygen concentrations can accelerate the oxidation of both sulfides and the presence of calcite can increase the oxidation rates of orpiment and the release of arsenic [30]. The oxidation of sulfur in realgar is preferentially than arsenic as the oxidation

rate become constant while orpiment does not show this tendency. During oxidation of realgar and orpiment in neutral and alkaline medium, mainly As (III), As (V), sulfate, and intermediate sulfur can be identified [28, 29]. While in acidic medium the oxidation of both realgar and orpiment involve two steps: initial oxidation producing H_3ASO_3, and HSO_4^- followed by the oxidation of H_3ASO_3 into H_3AsO_4 [31]. Besides, both orpiment and realgar are intermediate products in the electrochemical oxidation of arsenopyrite in acid medium [32]. But, the transformation of arsenic phases in the oxidation of realgar and orpiment has not fully recognized.

This study focuses on the behavior of arsenic in the weathered tailings of Shimen arsenic mine, the largest carbonate-type realgar ore in Asia. The secondary arsenic species in weathered tailings together with arsenic concentration in runoff water were analyzed and the natural oxidation of orpiment and realgar were discussed. Then, the transformation, mobility, and toxicity of arsenic in such special tailings characterized by high contents of carbonates were accessed.

2 Essential Background of the Shimen Realgar Mine

The Shimen realgar mine is located in Shimen County, northwest of Hunan province, central China (Fig. 1). It is a tectonic and karst-controlled epithermal deposit [33]. The main orebody is mainly hosted in dolostone of upper Cambrian and limestone of lower Ordovician. The mine has a noticeable three-layer structure with siliceous rocks, lenticular breccia, and massive orpiment–realgar orebody from top to bottom [34] (Fig. 1c). The orebody is restricted to karst breccia pipe and ore structure changes successively from core to edge as massive ore, brecciated ore, and disseminated ore [33].

The Shimen realgar deposit has been mined for more than 1,500 years. Altogether, about one million tons of ores has been produced. But now the mineral reserve is on the verge of exhaustion. At present, the mining is prohibited for environmental concerns [35]. In the mining history, massive mining wastes had been produced [36]. Improper discharge of the wastes led to severe pollution. Average arsenic concentrations in local farmland soils were as high as 99.51 ppm, which were about five times as the background value of the Hunan province and ten times as the local unpolluted soil [37]. Arsenic concentrations in rivers could be as high as 14.5 ppm, which were far beyond the United States Environmental Protection Agency (EPA) standard (10 ppm) [36]. The arsenic concentration in the rice planted near the mine could reach 0.84 ppm [37], which was even higher than the average level of Bangladesh irrigating paddies with elevated arsenic groundwater 0.29–0.51 ppm [38], and far higher than the normal arsenic concentration of world rice 0.08–0.20 ppm [39]. Arsenic concentration in the hair of local residents ranging from 0.972 to 2.459 ppm clearly was higher than the average hair arsenic content from a chronic arsenic poisoning region in Japan 0.64 ppm [36].

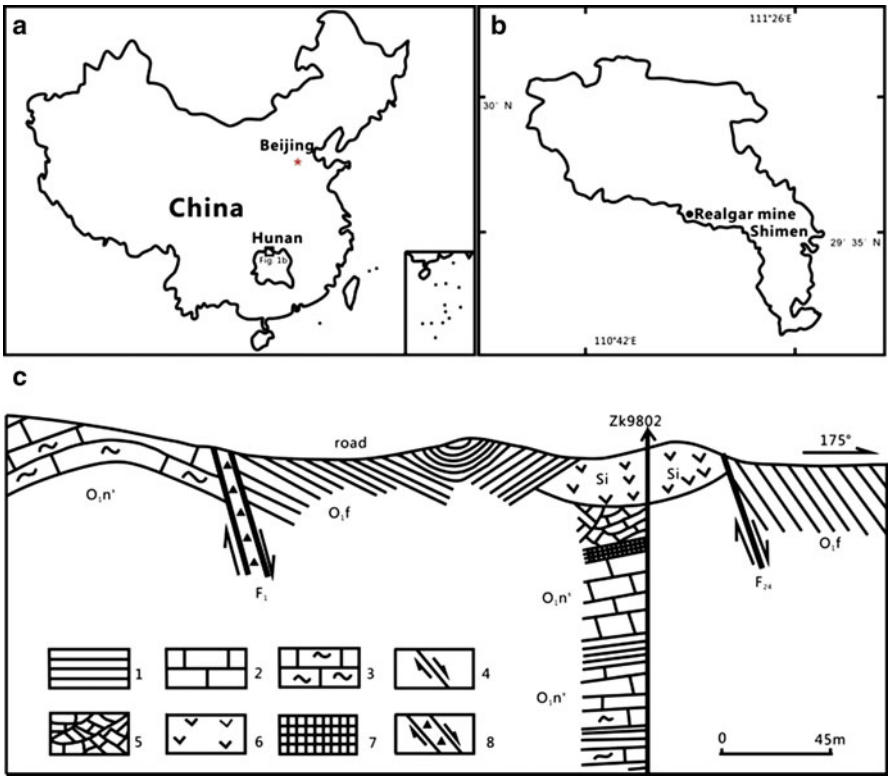

Fig. 1 Schematic maps of the Shimen mine. (**a**, **b**) The location of the Shimen realgar deposit; (**c**) profile map of drill hole 9802 [35], showing the three-layer structure of the mine. *O1f fengxiang formation* Ordovician, *O1ns upper nanjinguan formation* Ordovician, *O1nx lower nanjinguan formation* Ordovician, *1* shale, *2* limestone, *3* marlite, *4* fault, *5* brecciaous limestone, *6* siliceous rocks, *7* ore bed, *8* fault breccia

3 Samples and Measurements

3.1 Samples

The tailings and abandoned orpiment and realgar ores were collected from an ore dressing plant in JiePai (Fig. 2a). Brook water and mine drainage in mining area were also collected (Fig. 2b, c). According to color, the tailings can be cataloged into a gray white group and gray group (Fig. 2d, e). The gray white tailings are very loose and normally covered by a thin frost-like layer. While the gray tailings present as a much hard crust which resulted from a relatively long weathering period (Fig. 2f). In general, the gray white tailings only can be found on the shortly discharged tailings, which suggest a relatively short weathering duration.

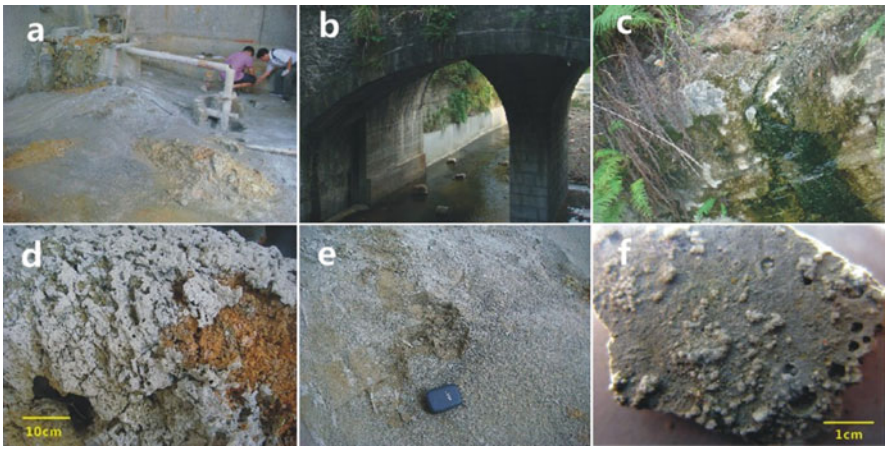

Fig. 2 (**a**) The ore dressing plant, where the tailings were collected; (**b**) the brook near Shimen realgar deposit; (**c**) mine drainage from Shimen realgar deposit which is directly discharged into the brook; (**d**) the gray white tailing. (**e**) The gray tailing. (**f**) Hard crust of the gray tailing

3.2 Measurements

pH of the water samples was measured using a DEL TA320 pH meter, and a Dds 307 conductivity meter was used to analyze the conductivities of the waters.

Whole-rock, major-element compositions of the tailings were measured by using an ARL9800XP + X-ray fluorescence (XRF) spectrometer. The samples were finely grounded and pressed into slice. For arsenic, finely ground fresh orpiment was used to derive calibration curves. Arsenic concentrations in the water samples were detected using an AF-610 atomic fluorescence spectrometer (AFS). All of the measurements were performed in Materials Analytical Center, Nanjing University.

X-ray powder diffraction (XRD) and Raman microprobe spectroscopy were employed to determine the mineral composition in tailings. For XRD analysis, samples were hand-grounded into powders (<2 μm) using an agate mortar and pestle, and then analyzed on a Rigaku D/max-rABede-D1 diffractometer with Cu Kα radiation (scanned at a step of 0.02°, 0.3 s per step, from 3° to 70°2θ, 40 kV, and 20 mA). For the Raman microprobe spectroscopy analysis, raw samples or scraped power were placed on a glass slide on the stage of the Leica microscope of the Renishaw 2000 Raman microscope system, which was equipped with a monochromator, a filter system, and a CCD detector (1,024 pixels). The Raman spectra were excited by a Spectra-Physics model Ar laser producing highly polarized light at 514 nm and collected at a nominal resolution of 2 cm^{-1}.

For observation of morphology of the tailings on scanning electron microscope (SEM), both polished sections and raw samples were coated with Au/C. A JEOL JSM-6490 SEM attached with an Oxford INCA energy-dispersive spectroscopy (EDS) device was operated at an accelerating voltage of 20 kV. A JEOL JEM-2100 transmission electron microscopy (TEM) was used to observe the tailing powders,

which was first dropped on amorphous carbon-coated copper grids and then air dried before observation. Meanwhile, the tailings were embedded in epoxyresin and then prepared as polished thin sections for electron microprobe analyses (EMPA) on a JEOL JXA 8800 electron microprobe (EMP), in order to disclose the spatial relationship between secondary minerals and the primary minerals. The operating conditions were as follows: accelerated voltage 15 kV, beam current 15 nA, and beam diameter 1 μm. Appropriate standards were collected before analyses, and standard ZAF corrections were applied.

In order to reveal the arsenic valences and the coordination station in the tailings, K-edge X-ray absorption fine structure (XAFS) spectra of arsenic were collected on beamline 14 W1 at the Shanghai Synchrotron Radiation Facility (SSRF). Energy ranges from 4 to 22.5 keV with an energy resolution of 1.5×10^{-4} at 10 keV. Minimum size of focusing spot is 0.3×0.3 mm^2, with a flux of over 1×10^{13} phs/s at 10 keV. Both the tailings and reference compounds were ground to fine powders which were stuck to tailor-made S-free adhesive tapes through folding which the thickness of the samples can be changed to get the spectra of high quality. Spectra were collected over the energy range −200 to +800 eV of the arsenic K-edge. The monochromator step size was reduced to 0.2 eV per step in the X-ray adsorption near edge spectra (XANES) region, from −20 to 30 eV. XAFS data were collected at ambient temperature and pressure in transmission modes. Ifeffit software package was used to analyze the spectra data.

Scanning transmission X-ray microscope (STXM) analyses were used on beamline 08U at SSRF, which was equipped with a 10.0-cm period elliptical-polarization undulator (EPU). Photons were focused onto the sample by a zone plate. An order-selecting aperture was placed between the zone plate and sample to filter the zero-order light. The sample was scanned relative to the focused X-ray beam, and the transmitted intensity was recorded using a scintillator with photomultiplier tube or a photodiode. The available energy range on Beamline 08U is 192–2,182 eV. The maximum spatial resolution can reach 30 nm and the energy resolution $E/\Delta E$ is between 2,460 and 17,900. Finely grounded tailings were fixed on the copper grid with coordinates on it. Then the copper grids with samples were mounted on an indicated holder capable of accommodating four copper grids. A 5 μm × 5 μm area was scanned at energy 1,333, 1,336, and 1,338.3 eV (pre-edge, As^{3+} L-edge, As^{5+} L-edge according to standard samples, As_2S_3 for As^{3+}, $Na_2HAsO_4{\cdot}7H_2O$ for As^{5+}) with the step size of 50 nm. Processing the pre-edge and edge images can reveal the spatial distribution of As^{3+} and As^{5+} in tailings particles.

4 Results

4.1 Chemical Composition of the Tailings and Water

The tailings are mainly constituted by Ca, Mg, As, and S besides H and O, in which Ca and Mg are mainly from dolomite and calcite ,while As and S are from realgar

and orpiment. Arsenic is more highly enriched in white gray tailings (33.965 wt%) than the gray ones (5.510 wt%). The low content of iron is the distinguished characteristics of the tailings (Table 1).

The pH of river waters is neutral to alkalescence, while pH of the mine drainage is alkalescence to faintly acid. The conductivity of mine drainage is obviously higher than the river water, which is consistent with the general knowledge. While the arsenic concentrations in the brook waters (0.67–4.00 mg L^{-1}) and mine drainage (33.60–40.10 mg L^{-1}) are all far beyond the long-standing legally acceptable limit imposed by the EPA for the arsenic concentration in drinking water (10 μg L^{-1}), which indicates serious arsenic contamination in this area (Table 2).

4.2 XRD Analysis

The XRD patterns of primary ores and the weathered tailings are shown in Fig. 3. The primary minerals in the tailings are mainly realgar, orpiment, dolomite, calcite, and quartz, while the secondary minerals include gypsum and arsenates (such as pharmacolite, picropharmacolite). According to the peak height, the contents of realgar and orpiment in gray white tailings are much higher than those in gray ones, which is consistent to the higher arsenic content in gray white tailings. Arsenates mainly occurred in the gray tailings, especially in the outmost layer of the crust of gray tailings (Fig. 4).

4.3 Raman Analysis

Raman spectra reveal the existence of gypsum, orpiment, dolomite, sulfur, pharmacolite, arsenolite, and hornesite in the tailings (Fig. 5). Arsenates are characterized by the peak between 800 and 900 cm^{-1}. Particularly, pharmacolite is characterized by an intense Raman band at 865 cm^{-1} assigned to the $v1$ (ASO_3) symmetric stretching mode. The band at 707 and 706 cm^{-1} is attributed to the v As-OH stretching vibrations [40]. There is a major difference between Ca-arsenates and Mg-arsenate in the peak range 800 and 900 cm^{-1}, for peaks of pharmacolite are sharper and smoother than hornesite.

4.4 SEM and TEM Observation

SEM observation shows that arsenates usually exhibit as small needle-shaped crystals arranged as radial aggregations (Fig. 6a, b). Single crystal of Mg-arsenate (about 20 μm long and 1 μm wide) appears slenderer and smaller than that of Ca-arsenate (200 μm long and 5 μm wide). Arsenic oxides were found in both types

Table 1 Chemical compositions of the two kinds of tailings (wt%)

	Ca	Mg	As	S	Si	Fe_2O_3	Al	K	Mn	Sr
White gray tailing	10.744	–	33.965	34.525	0.781	1.383	0.236	0.108	0.015	0.009
Gray tailing	24.490	7.237	5.510	4.391	1.561	0.139	0.091	0.018	0.016	0.008

Table 2 Arsenic concentration, pH, and conductivity of brook water and mine drainage

Sample	Number	As (ppm)	pH	Conductivity (μs/cm)
River water	3	0.67–4.00	7.09–7.13	286–349
Mine drainage	5	33.60–40.10	6.15–7.13	1,053–1,606

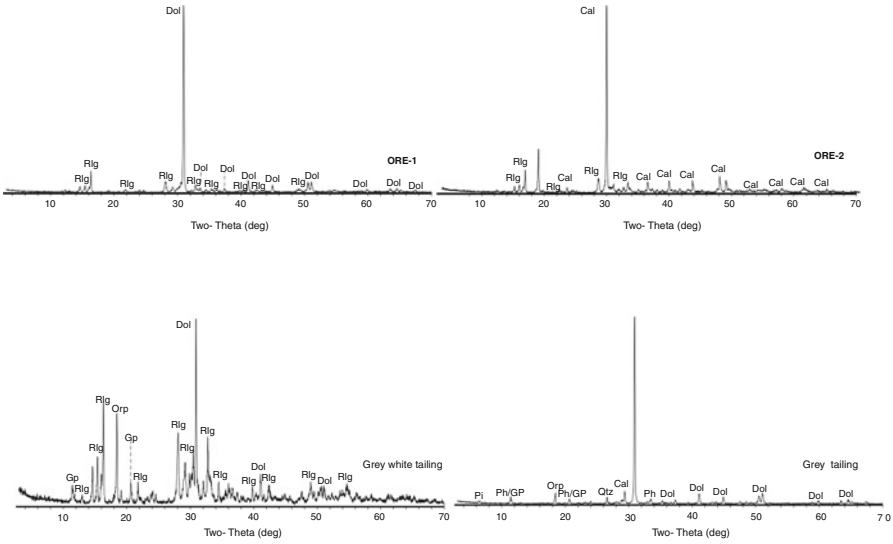

Fig. 3 XRD patterns of tailings and primary ores. *Dol* dolomite, *Orp* orpiment, *Rlg* realgar, *Cal* calcite, *Qtz* Quartz, *Ph* pharmacolite, *Gp* gypsum, *Pi* picropharmacolite

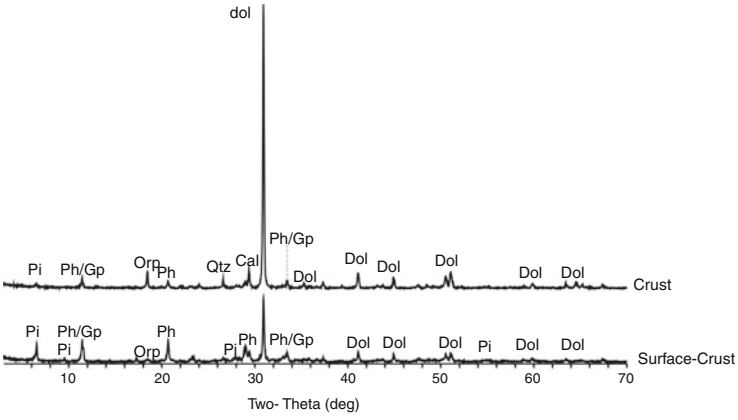

Fig. 4 Sample SM-T-7's XRD patterns of the crust of gray tailings. *Dol* dolomite, *Ph* pharmacolite, *Orp* orpiment, *Gp* gypsum, *Pi* picropharmacolite, *Cal* calcite, *Qtz* quartz

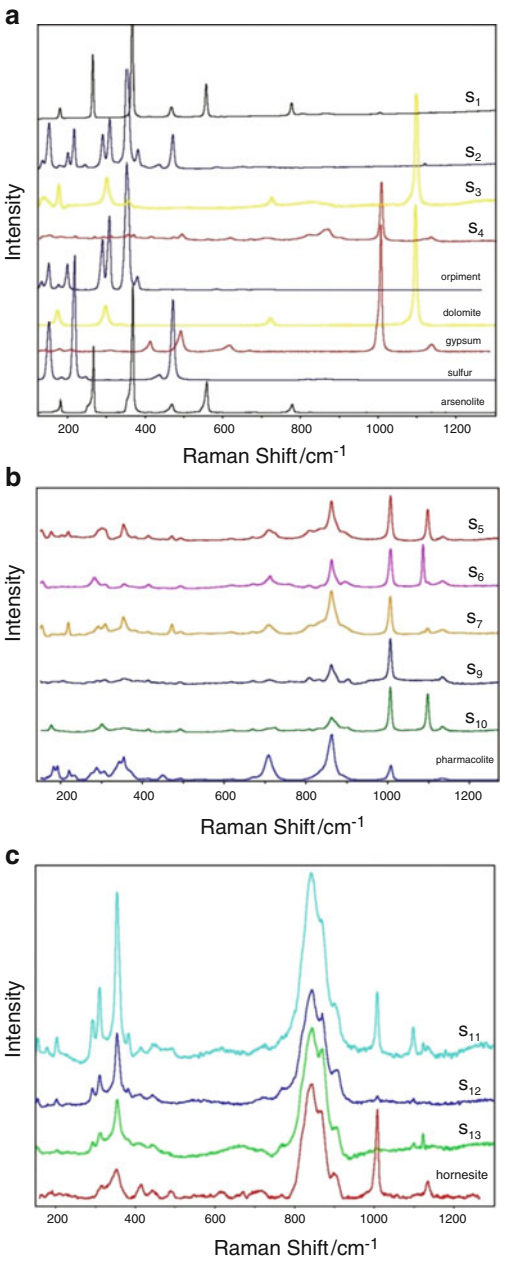

Fig. 5 Raman spectra of tailings and the mineral reference data from RUFF

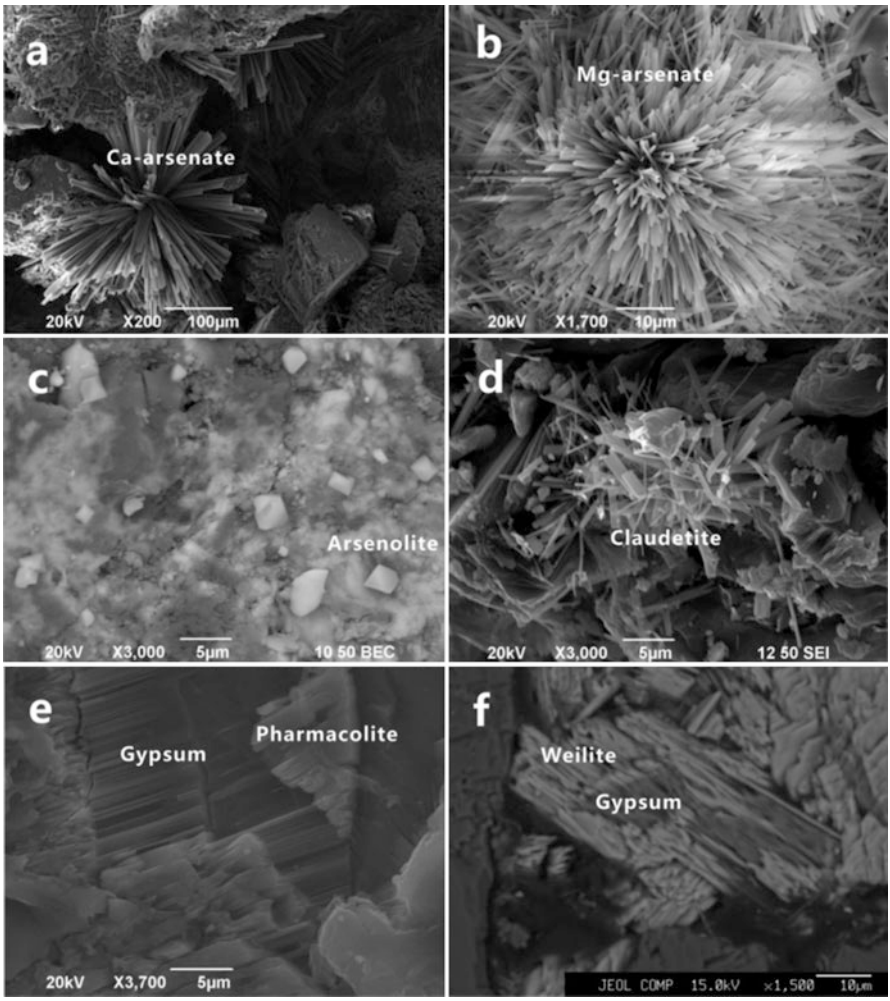

Fig. 6 (**a**, **b**) Acicular to fibrous crystals of Ca-arsenates and Mg-arsenates in spherical radiating groups. (**c**) Octahedrons of arsenolite on gypsum. (**d**) Prismatic crystals of claudetite on matrix. (**e**) Overgrowth of pharmacolite on gypsum. (**f**) Intergrowth of weilite and gypsum

of tailings but more common in the gray white tailings. In the gray tailings, tiny octahedrons of arsenic oxides of about 5 μm covered the gypsum surface (Fig. 6c). Although it is very hard to identify arsenolite, claudetite, or arsenic pentoxide only by EDX, the arsenic oxide is deduced as arsenolite according to crystal morphology and stability in the air. Apart from arsenolite, suspected crystals of claudetite, about 10 μm long and 2 μm wide, were also observed (Fig. 6d). Intergrowth of Ca-arsenate and gypsum is very common (Fig. 6f), as well as overgrowth and epitaxial growth of Ca-arsenate with the gypsum have also been detected (Fig. 6e).

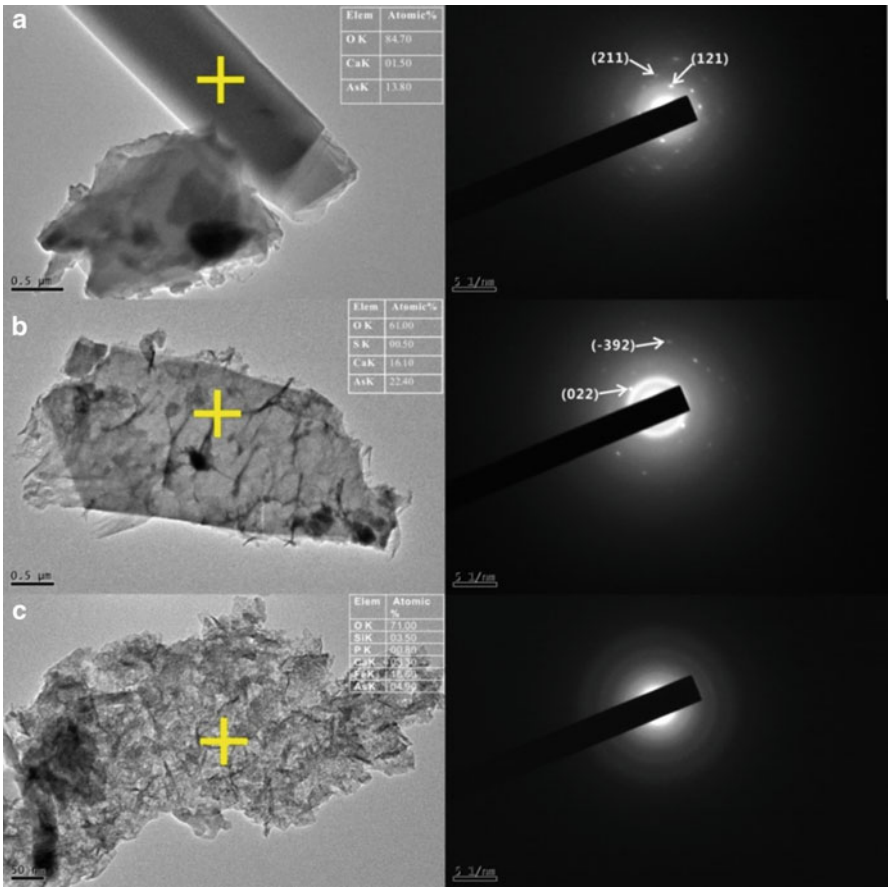

Fig. 7 TEM images with EDS data, and selected area diffraction pattern of claudetite (**a**), pharmacolite (**b**), and As-bearing iron (hydr)oxide (**c**). The *yellow crosses* represent the position where EDS and SAED were conducted

Analysis of the selected area electron diffraction (SAED) and EDS analysis as TEM observation confirmed the existence of claudetite and pharmacolite (Fig. 7a, b). The inferior quality of the SAED pattern is probably due to the over thickness of the sample or mixing with other minerals. SAED of claudetite and pharmacolite are consistent with the data of PDF#83-1548 and PDF#70-2432, respectively. Claudetite crystal is clintheriform and about 0.5 μm wide, which is similar to SEM observation. Because of the scarcity of iron and the high pH in the studied area, As-Fe-bearing species are difficult to be found. But we found amorphous As-Fe bearing (hydr)oxide by using TEM equipped with EDS (Fig. 7c).

4.5 EMPA Measurement

EMPA measurement was performed to determine the chemical composition of the arsenates and to study the spatial relationships between the primary minerals and the secondary ones. The structural formulas of pharmacolite, weilite, and picropharmacolite were calculated by using the EMPA data (Tables 3, 4, and 5). However, in most of the cases, arsenates are not pure and commonly mixed with other minerals, leading to varying chemical composition (Fig. 8). In most cases, there is always little S in arsenate or little As in gypsum (Figs. 9 and 10), which may be caused by the $SO_4^{2-}/HAsO_4^{2-}$ substitution in gypsum or arsenates. Under the backscattered electron (BSE) mode, and it is common to see a dolomite or/and orpiment/realgar core are surrounded from the inside out by gypsum and weilite and then the other Ca-arsenates and Ca-Mg-arsenates (Fig. 11).

4.6 XANES Spectra

XANES spectra of orpiment (As_2S_3) and sodium arsenate heptahydrate ($Na_2HAsO_4{\cdot}7H_2O$) serve as reference spectra. Comparison of XANES spectraof the gray tailing with those of references indicates that the sample contains primarily As (V) and As (III) (Fig. 12).

4.7 STXM Analysis

Arsenic L-edge XANE spectra of model compounds, $Na_2HAsO_4{\cdot}7H_2O$ and As_2S_3, were obtained from total electron yield (TEY), according to which we choose 1,333, 1,336, and 1,338.3 as pre-edge energy, As(III) on-edge energy, and As (V) on-edge energy, respectively, to get the absorption images. The dual-energy method was used to obtain the qualitative distribution of As (V) and As (III) [41]. The element distribution in the particle isolated from gray tailing shows that As (V) is the main composition, while As (III) is secondary one (Fig. 13).

5 Discussion

5.1 Formation of Secondary Minerals

The secondary minerals in the both types of tailings are mainly gypsum, arsenic trioxides, arsenates, As-gypsum, *S*-arsenates, sulfur, and amorphous As-Fe minerals. Arsenic trioxides are more common in the gray white tailings, while most of

Table 3 The formula calculation of pharmacolite

	FeO (wt%)	As_2O_5	SO_3	Sb_2O_5	MgO	CaO	SiO_2	Total	H_2O^a
#1	0.00	46.52	0.28	0.21	3.22	27.72	0.01	77.96	22.04
#2	0.00	49.60	0.27	0.17	1.72	28.07	0.00	79.82	20.18
#3	0.07	50.06	0.30	0.25	2.66	27.81	0.00	81.15	18.85
Average	0.02	48.72	0.28	0.21	2.53	27.87	0.00	79.64	20.36
stdev	0.04	1.93	0.01	0.04	0.76	0.18	0.01	1.60	1.60
Structural formulas calculated based on six O atoms and the average data									
Cation MW	55.85	74.92	32.07	121.76	24.31	40.08	28.09		1.01
Oxide MW	71.85	229.84	80.07	323.52	40.31	56.08	60.09		18.02
Mol #	0.00	0.21	0.00	0.00	0.06	0.50	0.00		1.13
O-Atom prop.	0.00	1.06	0.01	0.00	0.06	0.50	0.00		1.13
Anion prop.	0.00	2.30	0.02	0.01	0.14	1.08	0.00		2.45
#Cation/formula	0.00	0.92	0.01	0.00	0.14	1.08	0.00		4.91

Ideal formula: $Ca(AsO_3OH)\cdot 2H_2O$

Empirical formula: $(Ca1.08Mg0.14)\sum = 1.22((As_{0.92}S_{0.01}Si_{0.07})\sum = 1O_3OH0.91)\cdot 2H_2O$

[a]Estimated by difference. MW: O = 16 g/mol. Mg probably comes from the tiny dolomite grain covering up the pharmacolite

Table 4 The formula calculation of weilite

	FeO (wt %)	As_2O_5	SO_3	Sb_2O_5	CaO	SiO_2	Al_2O_3	Total
#1	0.04	65.27	0.87	0.00	32.04	0.00	0.10	98.32
#2	0.00	63.46	0.83	0.00	31.74	0.11	0.12	96.26
#3	0.00	68.03	0.50	0.13	31.03	2.13	0.00	101.81
#4	0.00	64.77	0.63	0.09	30.87	0.56	0.20	97.11
Average	0.01	65.38	0.70	0.05	31.42	0.70	0.10	98.37
stdev	0.02	1.92	0.17	0.06	0.56	0.98	0.08	2.44
Structural formulas calculated based on 3.5 O atoms and the average data								
Cation MW	55.85	74.92	32.07	121.76	40.08	28.09	26.98	
Oxide MW	71.85	229.84	80.07	323.52	56.08	60.09	101.96	
Oxide mol #	0.00	0.28	0.01	0.00	0.56	0.01	0.00	
O-Atom prop.	0.00	1.42	0.03	0.00	0.56	0.02	0.00	
Anion prop.	0.00	2.44	0.05	0.00	0.96	0.04	0.01	
# Cation/ formula	0.00	0.98	0.02	0.00	0.96	0.02	0.00	

Ideal formula: $Ca(ASO_3OH)$
Empirical formula: $(Ca_{0.96}Mg_{0.04})\sum = 1(As_{0.98}S_{0.02}Si_{0.02})\sum = {}_{1.02}O_3OH$
MW: H = 1.01 g/mol, O = 16 g/mol

the arsenates occur in the gray tailings. Thus, according to assemblage of secondary minerals in different tailings, the formation of secondary minerals can be divided into two stages, i.e., As (III) stage and As (V) stage.

5.1.1 As (III) Stage

In this stage, orpiment and realgar are oxidized in the air and transformed into sulfur and arsenic trioxides (Reactions 1 and 2):

$$As_2S_3(s) + 1.5O_2(g) \rightarrow As_2O_3(s) + 3S(s) \quad (1)$$

$$2AsS(s) + 1.5O_2(g) \rightarrow As_2O_3(s) + 2S(s) \quad (2)$$

Sulfur can be further oxidized into SO_4^{2-} and simultaneously release H^+ into the surrounding water. The H^+ will be consumed by the reactions with underlying carbonates and form gypsum (Reactions 3, 4, and 5).

$$S(s) + 1.5O_2(g) + H_2O(l) \rightarrow SO_4^{2-}(aq) + 2H^+ \quad (3)$$

$$CaCO_3(s) + H_2O + 2H^+ + SO_4^{2-} \rightarrow CaSO_4 \bullet 2H_2O + CO_2 \quad (4)$$

$$CaMg(CO_3)_2 + 6H_2O + 4H^+ + 2SO_4^{2-} \rightarrow CaSO_4 \bullet 2H_2O + MgSO_4 \bullet 6H_2O + 2CO_2 \quad (5)$$

Arsenic trioxides are amphoteric oxides, and their aqueous solutions are weakly

Table 5 The formula calculation of picropharmacolite

	FeO (wt%)	As_2O_5	SO_3	Sb_2O_5	MgO	CaO	SiO_2	Al_2O_3	Total	H_2O^a
#1	0.06	50.11	0.21	0.05	4.13	23.43	0.18	0.23	78.39	21.61
Structural formulas calculated based on 27 O atoms										
Cation MW	55.85	74.92	32.07	121.76	24.31	40.08	28.09	26.98		1.01
Oxide MW	71.85	229.84	80.07	323.52	40.31	56.08	60.09	101.96		18.02
Oxide mol #	0.00	0.22	0.00	0.00	0.10	0.42	0.00	0.00		1.20
O-Atom prop.	0.00	1.09	0.01	0.00	0.10	0.42	0.01	0.01		1.20
Anion prop.	0.01	10.40	0.08	0.01	0.98	3.98	0.06	0.06		11.44
# Cation/formula	0.01	4.16	0.03	0.00	0.98	3.98	0.03	0.04		22.87

Ideal formula: $Ca_4Mg(AsO_3OH)_2(AsO_4)_2{\cdot}11H_2O$

Empirical formula: $(Ca_{3.98}Mg_{0.98}Al_{0.04}Fe_{0.01})\sum = 5.01((As_{1.08}S_{0.01}5Si_{0.015})\sum = 1.11O_3OH_{0.435})_2(AsO_4)_2{\cdot}11H_2O$

[a]Estimated by difference. MW: O = 16 g/mol

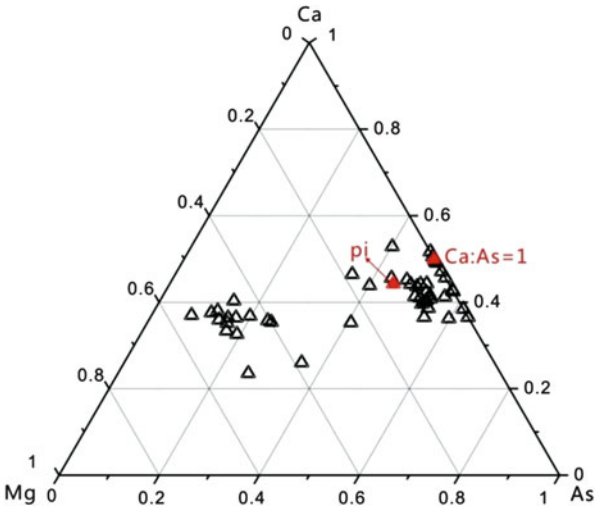

Fig. 8 EMPA composition of secondary minerals in gray white crusts in the Ca–As–Mg ternary diagram. *Pi* picropharmacolite

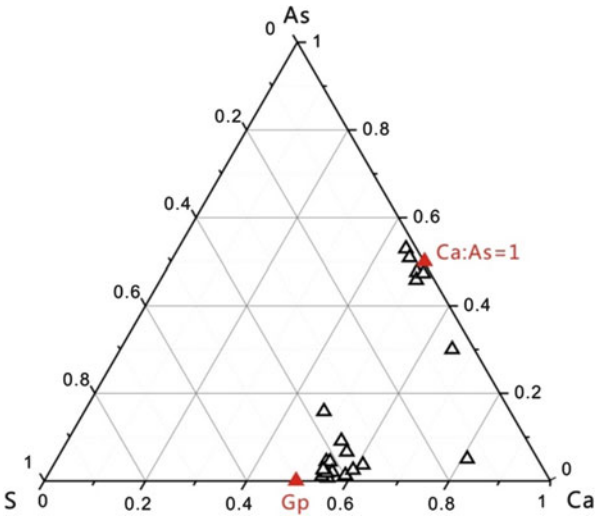

Fig. 9 Electron microprobe analyses (EMPA) of mineral precipitates in white crusts in the Ca–As–S ternary diagram. *Gp* gypsum

acidic. Thus, they can dissolve readily in alkaline solutions to give arsenites [42]. This can explain why arsenolite dissolves on the surface of gypsum (Fig. 6c) and arsenic trioxides are so rare in the long-term weathered gray tailings.

5.1.2 As (V) Stage

In this stage, As(III)-bearing runoff waters are oxidized (Reaction 6) and then reacted with underlying carbonates resulting in the precipitation of weilite

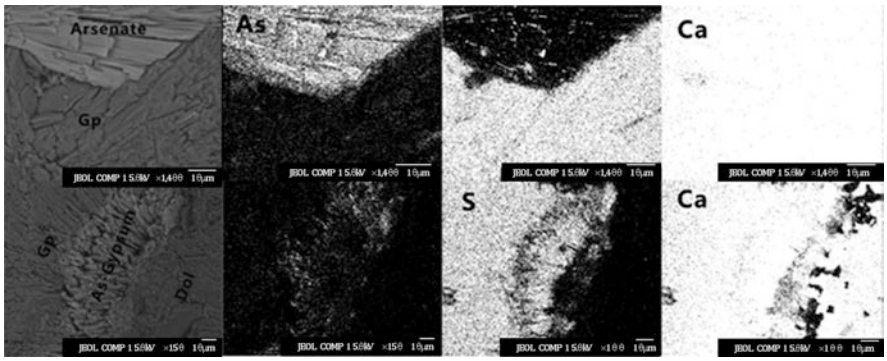

Fig. 10 EMP backscattered electron and the corresponding As, S, Ca distribution images of S-bearing arsenate and As-bearing gypsum. *Gp* gypsum

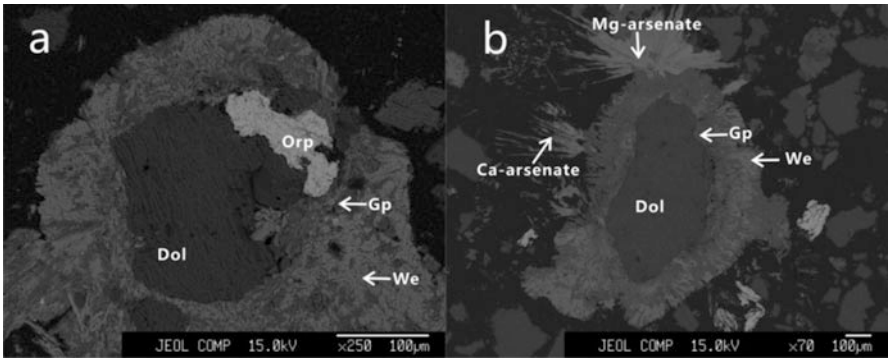

Fig. 11 (**a**) EMP backscattered electron images of dolomite and orpiment core surrounded by gypsum and weilite. (**b**) EMP backscattered electron images of dolomite core surrounded by gypsum and arsenate. *Orp* orpiment, *We* weilite, *Gp* gypsum, *Dol* dolomite

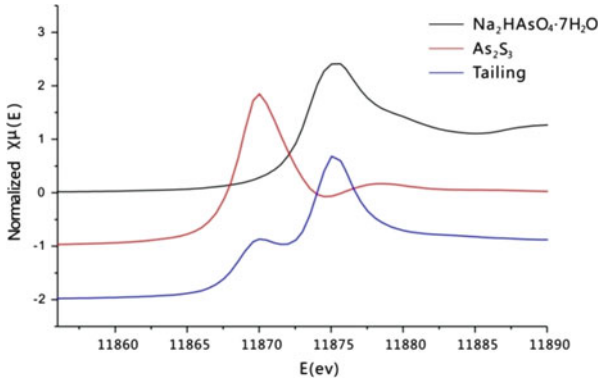

Fig. 12 Normalized As K-edge XANE spectra of gray tailing contrasting to those of reference samples

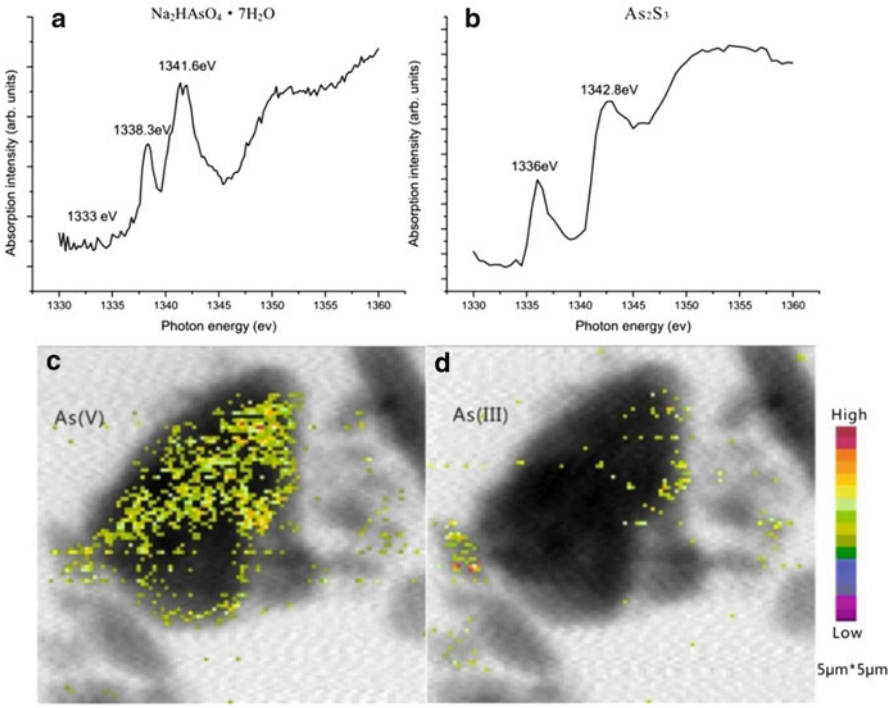

Fig. 13 (**a**, **b**) Normalized As L2-edge XANE spectrum of model compounds, $Na_2HAsO_4 \cdot 7H_2O$ and As_2S_3 obtained from total electron yield (TEY). (**c**, **d**) False-color micro-X-ray fluorescence maps showing the qualitative distribution of As (III), As(V) in a particle isolated from the gray tailing

(Reaction 9), pharmacolite (Reaction 10), hornesite (Reaction 11), and picropharmacolite (Reaction 12).

$$2HAsO_2(aq) + O_2(g) + \text{bacteria} + 2H_2O \rightarrow 2HAsO_4^{2-}(aq) + 4H^+(aq) \quad (6)$$

$$CaCO_3 + 2H^+ \rightarrow Ca^{2+} + H_2O + CO_2 \quad (7)$$

$$CaMg(CO_3)_2 + 4H^+ \rightarrow Ca^{2+} + Mg^{2+} + 2H_2O + 2CO_2 \quad (8)$$

$$Ca^{2+} + HAsO_4^{2-} \rightarrow CaHAsO_4 \quad (9)$$

$$Ca^{2+} + HAsO_4^{2-} + 2H_2O \rightarrow CaHAsO_4 \bullet 2H_2O \quad (10)$$

$$3Mg^{2+} + 2AsO_4^{3-} + 8H_2O \rightarrow Mg_3(AsO_4)_2 \bullet 8H_2O \quad (11)$$

$$4Ca^{2+} + Mg^{2+} + 2HAsO_4^{2-} + 2AsO_4^{3-} + 11H_2O \rightarrow Ca4Mg(ASO_3OH)_2(AsO_4)_2 \bullet 11H_2O \quad (12)$$

In this transformation from As (III) to As (V), atmospheric oxygen and oxidizing bacteria may play important roles, and carbonates maintain the pH as neutral to

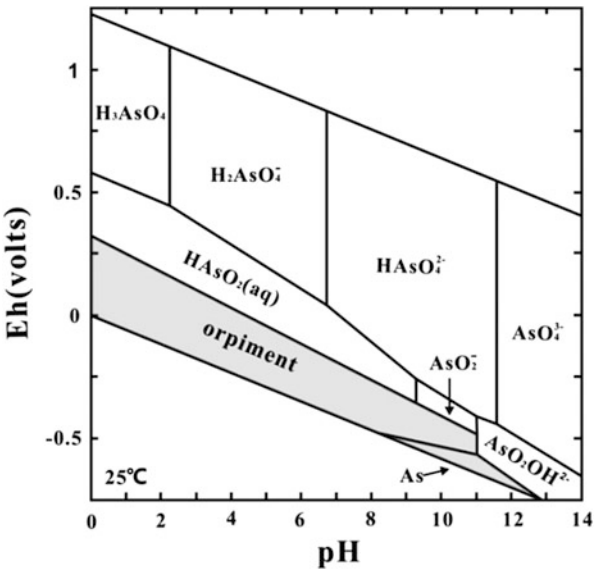

Fig. 14 Eh-pH stability diagram of As [47]

alkalinity (Reactions 7 and 8). The species of As (V) is generally pH dependent [43]. In the pH range of between 2.19 and 6.94, the main aqueous arsenate species is H_2AsO^{4-}. As pH above 6.94, H_2AsO^{4-} will be replaced by $HAsO_4^{2-}$ and AsO_4^{3-} (Fig. 14). According to the types of secondary arsenates in the studied tailings, $HAsO_4^{2-}$ and AsO_4^{3-} are obviously the main occurrence of As(V), which could be attributed to the pH regulation of carbonate.

EMP backscattered electron observation shows that a dolomite or/and orpiment/realgar core are surrounded by gypsum and weilite and then the other Ca-arsenates and Ca-Mg-arsenates from inside out (Fig. 11). We propose that the arsenates precipitated following certain sequence. At first, the pH is low, and only gypsum can form. The following reactions raise pH and weilite forms. When the pH remains steady at neutral, the other arsenates form. Anhydrous arsenate weilite was the first Ca-arsenate precipitated between pH 3 and 5, followed by haidingerite for pH up to 6, and finally followed by pharmacolite at pH above 6 [44].

5.2 Evaluation of Arsenic Activity

The amount of Arsenic accommodated in Shimen Realgar Tailings is huge, which imposes serious environmental threat on mining area. In other Fe-rich areas, arsenic mainly forms Fe-arsenates or occurs in Fe (III) oxyhydroxides and sulfates via adsorption and coprecipitation. However, in this study of Fe-lacking and Ca-rich site, arsenic is mainly fixed in Ca-arsenates, and therefore, the arsenic activity is determined by the solubility and chemical stability of Ca-arsenates. The solubility

of weilite ranges from 2,170 to 3,610 mg/L and that of pharmacolite varies from 3,120 to 4,360 mg/L [45]. As arsenic concentrations in mine drainage are as high as 33.6–40.1 mg/L, which are far below the equilibrium concentration. Meanwhile, the Ca-arsenates in tailings exhibit nearly perfect crystal morphology without any dissolution features. It is considered that the solubility of Ca-arsenates decreases greatly, down to <0.1 mg/L, with excess free lime [13].

The release of large amounts of dissolved CO_2 accompanying with carbonates' decomposition by acidic solutions may influence the stability of arsenates. For example, at a pH > 8.3, $Ca_3(AsO_4)_2$ decomposes to calcite and soluble arsenate oxyanions (Reactions 13 and 14) [13, 46]:

$$Ca_3(AsO_4)_2(s) + 3HCO^{3-}(aq) + OH^-(aq) \rightarrow 3CaCO_3(s) + 2HAsO_4^{2-}(aq) + H_2O(l) \quad (13)$$

$$Ca_3(AsO_4)_3(s) + 3CO_3^{2-}(aq) \rightarrow 3CaCO_3(s) + 3AsO_4^{2-}(aq) \quad (14)$$

The former studied the stability of 1:1, 5:4, 4:2, and 3:2 Ca-arsenates as a function of dissolved CO_2 and found that dissolved CO_2 hardly affects the stability field of 1:1 Ca-arsenates, whereas it can strongly decrease the stability field of 4:2 and 3:2 Ca-arsenates. Above discussion may explain the phenomenon that Ca-arsenates we found in tailings are all 1:1 type weilite and pharmacolite.

6 Conclusions

Based on identified mineralogical composition of two types of tailings, the naturally weathering of orpiment and realgar in the presence of carbonate can be separated into two stages: As(III) stage and As(V) stage. In the first stage, arsenic are primarily oxidized into As(III) minerals (claudetite, arsenolite). While in the second stage, As(III) is converted to As(V). The oxidation of sulfides accompanied with the dissolution of carbonates causes the precipitation of gypsum and arsenates. Gypsum and arsenates precipitated following certain sequence. Gypsum precipitated first and then weilite, which was followed by the formation of pharmacolite and minor contents of picropharmacolite and hornesite. pH of the environmental fluids and CO_2 released from carbonates' dissolution controls the secondary minerals. The oxidation of the tailings can fix arsenic into arsenic oxide and arsenates. Although some secondary minerals are not good As-immobilizers due to high solubility, high Ca and Mg concentrations due to dolomite dissolution in surrounding environment can decrease the solubility of arsenate by Ca-arsenates precipitation.

References

1. Huang CP, Fu PLK (1984) Treatment of arsenic (V)-containing water by the activated carbon process. J Water Pollut Control Fed 56:233–242
2. Hutton M (1987) Human health concerns of lead, mercury, cadmium and arsenic. In: Hutchinson TC, Meema KM (eds) Lead, mercury, cadmium and arsenic in the environment. Wiley, New York
3. Tseng WP (1989) Blackfoot disease in Taiwan: a 30-year follow-up study. Angiology 40 (6):547–558
4. Eisler R (1989) Tin hazards to fish, wildlife, and invertebrates: a synoptic review (No. FWS-85/1.15). Patuxent Wildlife Research Center, Laurel
5. Ng JC (2005) Environmental contamination of arsenic and its toxicological impact on humans. Environ Chem 2(3):146–160
6. Mandal BK, Suzuki KT (2002) Arsenic round the world: a review. Talanta 58(1):201–235
7. Penrose WR, Woolson EA (1974) Arsenic in the marine and aquatic environments: analysis, occurrence, and significance. Crit Rev Environ Sci Technol 4(1–4):465–482
8. Ferguson JF, Gavis J (1972) A review of the arsenic cycle in natural waters. Water Res 6 (11):1259–1274
9. Jain CK, Ali I (2000) Arsenic: occurrence, toxicity and speciation techniques. Water Res 34 (17):4304–4312
10. Sturgeon RE, Siu KM, Willie SN, Berman SS (1989) Quantification of arsenic species in a river water reference material for trace metals by graphite furnace atomic absorption spectrometric techniques. Analyst 114(11):1393–1396
11. Vaughan DJ (2006) Arsenic. Elements 2(2):71–75
12. Lengke MF, Sanpawanitchakit C, Tempel RN (2009) The oxidation and dissolution of arsenic-bearing sulfides. Can Mineral 47(3):593–613
13. Drahota P, Filippi M (2009) Secondary arsenic minerals in the environment: a review. Environ Int 35(8):1243–1255
14. Foster AL, Brown GE Jr, Tingle TN, Parks GA (1998) Quantitative arsenic speciation in mine tailings using X-ray absorption spectroscopy. Am Mineral 83(5):553–568
15. Lu XC, Wang H (2012) Microbial oxidation of sulfide tailings and the environmental consequences. Elements 8(2):119–124
16. Dove PM, Rimstidt JD (1985) The solubility and stability of scorodite, $FeAsO4•2H_2O$. Am Mineral 70(7–8):838–844
17. Richardson S, Vaughan DJ (1989) Arsenopyrite: a spectroscopic investigation of altered surfaces. Mineral Mag 53(370):223–229
18. Nesbitt HW, Muir IJ, Prarr AR (1995) Oxidation of arsenopyrite by air and air-saturated, distilled water, and implications for mechanism of oxidation. Geochim Cosmochim Acta 59 (9):1773–1786
19. Rancourt DG, Fortin D, Pichler T, Thibault PJ, Lamarche G, Morris RV, Mercier PH (2001) Mineralogy of a natural As-rich hydrous ferric oxide coprecipitate formed by mixing of hydrothermal fluid and seawater: implications regarding surface complexation and color banding in ferrihydrite deposits. Am Mineral 86(7–8):834–851
20. Majzlan J, Lalinská B, Chovan M, Milovská S, Göttlicher J (2007) The formation, structure, and ageing of As-rich hydrous ferric oxide at the abandoned Sb deposit Pezinok (Slovakia). Geochim Cosmochim Acta 71(17):4206–4220
21. Catalano JG, Park C, Fenter P, Zhang Z (2008) Simultaneous inner-and outer-sphere arsenate adsorption on corundum and hematite. Geochim Cosmochim Acta 72(8):1986–2004
22. Anawar HM, Akai J, Sakugawa H (2004) Mobilization of arsenic from subsurface sediments by effect of bicarbonate ions in groundwater. Chemosphere 54(6):753–762
23. Stachowicz M, Hiemstra T, van Riemsdijk WH (2007) Arsenic-bicarbonate interaction on goethite particles. Environ Sci Technol 41(16):5620–5625

24. Herbel M, Fendorf S (2006) Biogeochemical processes controlling the speciation and transport of arsenic within iron coated sands. Chem Geol 228(1):16–32
25. Savage KS, Tingle TN, O'Day PA, Waychunas GA, Bird DK (2000) Arsenic speciation in pyrite and secondary weathering phases, Mother Lode gold district, Tuolumne County, California. Appl Geochem 15(8):1219–1244
26. Corkhill CL, Vaughan DJ (2009) Arsenopyrite oxidation–a review. Appl Geochem 24 (12):2342–2361
27. Lengke MF, Tempel RN (2001) Kinetic rates of amorphousAs2S3 oxidation at 25 to 40°C and initial pH of 7.3 to 9.4. Geochim Cosmochim Acta 65:2241–2255
28. Lengke MF, Tempel RN (2002) Reaction rates of natural orpiment oxidation at 25–40°C and pH 6.8–8.2 and comparison with amorphous As2S3 oxidation. Geochim Cosmochim Acta 66:3281–3291
29. Lengke MF, Tempel RN (2003) Natural realgar and amorphous AsS oxidation kinetics. Geochim Cosmochim Acta 67:859–871
30. Lengke MF, Tempel RN (2005) Geochemical modeling of arsenic sulfide oxidation kinetics in a mining environment. Geochim Cosmochim Acta 69:341–356
31. Lázaro I, González I, Cruz R, Monroy MG (1997) Electrochemical study of orpiment (As_2S_3) and realgar (As_2S_2) in acidic medium. J Electrochem Soc 144(12):4128–4132
32. Lázaro I, Cruz R, González I, Monroy M (1997) Electrochemical oxidation of arsenopyrite in acidic media. Int J Miner Process 50(1):63–75
33. Huang Q, Xiong XX (1996) Study on no. 1 tunnel orebody's structure of Shimen arsenic deposit. Guangxi Geol 9(3):7–15
34. Xiong XX (1999) Geological characteristics and major types of realgar and orpiment deposit of china. Guangxi Geol 12(4):23–26
35. Yang RS, Xu YJ, Xiong XX (1999) Probing into the further looking for minerals in Shimen realgar mine. Hunan Geol 18(2–3):91–92
36. Wang ZG, He HY, Yan YL, Wu CY, Yang Y, Gao XY (1999) Arsenic exposure of residents in areas near Shimen arsenic mine. J Hyg Res 28(1):12–14
37. Li LF, Zheng XB, Bai LY, Li SH (2010) Soil arsenic content and its health risk assessment for agricultural products in the region surrounding Shimen arsenic sulphide mine. Chin J Appl Ecol 21(11):2946–2951
38. Williams PN, Islam MR, Adomako EE, Raab A, Hossain SA, Zhu YG, Meharg AA (2006) Increase in rice grain arsenic for regions of Bangladesh irrigating paddies with elevated arsenic in groundwaters. Environ Sci Technol 40(16):4903–4908
39. Zavala YJ, Duxbury JM (2008) Arsenic in rice: I. Estimating normal levels of total arsenic in rice grain. Environ Sci Technol 42(10):3856–3860
40. Frost RL, Bahfenne S, Čejka J, Sejkora J, Plášil J, Palmer SJ (2010) Raman spectroscopic study of the hydrogen-arsenate mineral pharmacolite Ca (ASO_3OH)•$2H_2O$-implications for aquifer and sediment remediation. J Raman Spectrosc 41(10):1348–1352
41. Zhang XZ, Xu ZJ, Tai RZ, Zhen XJ, Wang Y, Guo Z et al (2010) Ratio-contrast imaging of dual-energy absorption for element mapping with a scanning transmission X-ray microscope. J Synchrotron Radiat 17:804–809
42. Pokrovski G, Gout R, Schott J, Zotov A, Harrichoury JC (1996) Thermodynamic properties and stoichiometry of As (III) hydroxide complexes at hydrothermal conditions. Geochim Cosmochim Acta 60(5):737–749
43. Cherry JA, Shaikh AU, Tallman DE, Nicholson RV (1979) Arsenic species as an indicator of redox conditions in groundwater. J Hydrol 43(1):373–392
44. Juillot F, Ildefonse P, Morin G, Calas G, Kersabiec AD, Benedetti M (1999) Remobilization of arsenic from buried wastes at an industrial site: mineralogical and geochemical control. Appl Geochem 14(8):1031–1048
45. Swash PM, Monhemius AJ (1996) The characteristic of calcium arsenate compounds relevant to the disposal of arsenic from industrial processes. In: Proceedings of mineral metals and the environment II, 3–6 Sept, Prague. IMM, London, pp 353–361

46. Nordstrom DK, Archer DG (2003) Arsenic thermodynamic data and environmental geochemistry. In: Welch AH, Stollenwerk KG (eds) Arsenic in ground water. Springer, Berlin, pp 1–25
47. Reeder RJ, Schoonen MA, Lanzirotti A (2006) Metal speciation and its role in bioaccessibility and bioavailability. Rev Mineral Geochem 64(1):59–113

Appendix

The post-conference publication of the 11th ICAM consists of two parts, including these electronic Proceedings in charge of Springer and the special issue published in Mineralogy and Petrology. Of 60 accepted contributions, 15 better-qualified papers were recommended to Mineralogy and Petrology, and nine papers have been finally accepted after going through standard journal review processes.

The nine papers are as follows:

Characterization of mineralogy and surface zeta potential of atmospheric dust fall in northwest China
Author: Dong Faqin

Magnetite–hematite transformation: Correlation between natural and synthetic features
Author: Paola Ferreira Barbosa

Effect of particle size on kaolinite flotation with quaternary ammonium salts collectors
Author: Xu Longhua

Psammoma bodies in two types of human ovarian tumours: A mineralogical study
Author: Wang Changqiu

Non-isothermal kinetic analysis of thermal decomposition of the Ca-bentonite from Santai, China
Author: Wang ling

Flotation characteristics of two different types of ilmenite with sodium oleate
Author: Wang Weiqing

Genesis of the Ordovician fluorite in the Tazhong area and its geological significance
Author: Wang Zhenyu

F. Dong (ed.), *Proceedings of the 11th International Congress for Applied Mineralogy (ICAM)*, Springer Geochemistry/Mineralogy,
DOI 10.1007/978-3-319-13948-7

The structure of montmorillonites modified with zwitterionic surfactants and their sorption ability
Author: Zhu Jianxi

Study on the dissolution of natural dusts and artificial dusts in glutamic acid
Author: Zhang Ling

Index

A
Alaabed, Sulaiman, 291
Angora, Marco Antonio, 71
Antoniassi, Juliana L., 39, 173
Azarnova, Liudmila, 223

B
Baibatsha, Adilkhan, 1
Broekmans, Maarten A.T.M., 325

C
Cao, Chao, 253
Cao, Xi, 29
Carmo, Sheila S., 233
Chen, Jie, 187
Chen, Shu, 107
Chen, Tianhu, 425, 447
Chen, Wu, 305
Chen, Xiaoling, 405
Chen, Yinghua, 213
Chuan, Xiuyun, 29, 263, 373
Çiftçi, Emin, 91, 99

D
Dai, Qunwei, 59, 305
Deng, Dayi, 405
Deng, Jianghua, 495
Deng, Jianjun, 59, 159, 471
Deng, Yuequan, 305
Dong, Faqin, 59, 81, 159, 283, 305, 471
Du, Jianguo, 197
Dyussembayeva, Kulyash, 1

F
Fang, Jin, 495
Fei, Huang, 51
Feng, Taiwei, 115
Fu, Kaibin, 107

G
Gao, Shang, 115, 213
Gao, Wenpeng, 137
Gao, Wenyuan, 115, 213
Gasaleeva, Galina, 241
Goryainov, Sergey, 313
Gu, Xiaobin, 125
Guan, Yufeng, 405
Gütller, Rainer A.S., 233

H
Han, Tao, 343
He, Hua, 81
He, Ping, 81
Hong, Hanlie, 137
Hong, Qiuyang, 151, 205
Huang, Dubin, 373
Huang, Fei, 115, 213
Huo, Tingting, 159, 471

F. Dong (ed.), *Proceedings of the 11th International Congress for Applied Mineralogy (ICAM)*, Springer Geochemistry/Mineralogy,
DOI 10.1007/978-3-319-13948-7

I
İsmail Erdağ, 99

J
Ji, Junfeng, 425
Jia, Shaohui, 335
Jiang, Fenfen, 405

K
Kahn, H., 233
Kahn, Henrique, 39, 71, 173
Kassenova, Aimkhan, 1
Ke, Lihua, 187
Kotova, Olga, 241
Kovalev, Konstantin, 313
Kullerud, Kåre, 19

L
Larionov, Piter M., 9
Lé Tassinari, M. Manuela M., 71, 173
Lermi, Abdurrahman, 91
Li, Bo, 151, 205
Li, Guanglu, 51, 115, 213
Li, Juan, 531
Li, Lin, 373
Li, Ping, 447
Li, Ying, 197
Li, Zengsheng, 343
Li, Zhaohui, 137
Liang, Dongyun, 205
Ling, Kunyue, 343
Liu, Chao, 275
Liu, Haibo, 447
Liu, Huan, 531
Liu, Jia, 115, 213
Liu, Qiang, 115
Lu, Huayu, 425
Lu, Jianjun, 531
Lu, Junda, 59
Lu, Shaoyou, 405
Lu, Xiancai, 531
Lu, Xirui, 283
Luo, Deqiang, 107

M
Ma, Qin, 509
Meng, Lin, 213
Moroz, Tatyana, 313

N
Nadur, Angela V., 233
Nery, Guilherme, 39
Niu, Jingjing, 125

O
Onufrienok, Victor V., 325
Ouyang, Bingjie, 531

P
Palchik, Nadezhda, 313
Peng, Han, 51
Peng, Tongjiang, 253, 521
Ponomarchuk, Victor, 313
Pryadunenko, Anna, 19

Q
Qin, Lang, 263
Qin, Shan, 125
Qiu, Gao, 425

R
Ramanaidou, E.R., 387
Rui, Liu, 51

S
Shi, Guiming, 397
Shi, Yadan, 447
Song, Bei, 275
Song, Dan, 115
Su, Sijin, 283
Sun, Hongjuan, 253, 521
Sun, Shiyong, 159
Sun, Xiaohui, 343

T
Tang, Jingyou, 283
Tang, Jun, 305
Titov, Anatoly T., 9

U
Uliana, Daniel, 39, 71, 173
Ulsen, Carina, 39, 173

V
Vakhrushev, Aleksandr, 241

W
Wan, Jun, 335
Wan, Zhongyan, 351
Wang, Chaowen, 137
Wang, Chong, 351
Wang, Fudong, 343
Wang, Jianwei, 351
Wang, Jizhen, 459
Wang, Limin, 471
Wang, Maoli, 351
Wang, Mingcui, 159
Wang, Rucheng, 531
Wang, Tongtong, 275
Wang, Weifeng, 213
Wang, Xiaoli, 283
Wang, Xiaoyong, 425
Wang, Yong, 365
Wang, Yuesong, 373
Wang, Zhe, 351
Wang, Zhen, 107
Wang, Zhenyu, 509
Wang, Zhonggang, 343
Wells, M.A., 387
Wu, Caibin, 397
Wu, Honghai, 405

X
Xian, Haiyang, 521
Xiao, Junhui, 107
Xie, Chao, 197
Xie, Qiaoqin, 425
Xu, Huifang, 425
Xu, Longhua, 81, 459
Xu, Xiaochun, 425

Y
Yalçınalp, Bülent, 91
Yan, Ya'nan, 365
Yan, Ying, 441
Yang, Qingyu, 51
Yang, Wei, 81
Yang, Yan, 447
Yi, Facheng, 351
Yin, Ke, 137
Yin, Tiejun, 495, 509
Yin, Wanzhong, 459
Yu, Haoran, 213
Yu, Siwang, 159
Yunhong, Cheng, 51

Z
Zaikovskii, Vladimir I., 9
Zeng, Yali, 471
Zhan, Xinmin, 447
Zhang, Lili, 151, 205
Zhang, Qingbi, 159
Zhang, Yulin, 483
Zhang, Yunfeng, 509
Zhao, Cuiting, 483
Zhao, Jian, 275
Zhao, Qinglin, 483
Zhao, Ran, 115
Zhao, Xueqin, 495, 509
Zhao, Yulian, 59
Zheng, Shuilin, 275
Zhou, Guobiao, 521
Zhou, Mingkai, 483
Zhou, Shiping, 305
Zhou, Yongheng, 441
Zhou, Zhihua, 197
Zhu, Xiangyu, 531
Zhu, Xiaoqing, 343